MAX-PLANCK-INSTITUT FÜR EXTRATERRESTRISCHE PHYSIK

The Origin of the Cosmic Gamma-Ray Background in the COMPTEL Energy Range

Georg Weidenspointner

Vollständiger Abdruck der von der Fakultät für Physik
der Technischen Universität München zur Erlangung des akademischen Grades
eines Doktors der Naturwissenschaften (Dr. rer. nat.)
genehmigten Dissertation.

Vorsitzender	:	Univ. Prof. Dr. M. Lindner
Prüfer der Dissertation:		1. apl. Prof. Dr. V. Schönfelder
		2. Univ. Prof. Dr. H.-J. Körner

Die Dissertation wurde am 20.01.1999 bei der Technischen Universität München
eingereicht und durch die Fakultät für Physik am 25.02.1999 angenommen.

. . . I'm standing next to a mountain,
and I chop it down with the edge of my hand . . .

Voodoo Child (Slight Return), Jimi Hendrix

Summary

The goal of this thesis is to study spectrum and isotropy of the cosmic diffuse γ-ray background in the energy range 0.8–30 MeV with the Compton telescope COMPTEL. The γ-ray background at MeV energies is of interest for a number of reasons. Possible origins of the low-energy γ-ray background are the superposed emission of a variety of source populations, such as different types of galaxies, in particular active galaxies, or of Type Ia supernovae. In addition, truly diffuse processes such as the annihilation of matter and anti-matter in the early universe, or the decay or annihilation of certain types of exotic elementary particles, are expected to give rise to spectral features at MeV energies. The measurement of spectrum and isotropy of the low-energy γ-ray background is one of the many small steps towards understanding the emission and evolution of these sources in particular, and — since these sources are connected to other domains of the overall background radiation — towards understanding the origin and evolution of the universe as a whole.

In this work the spectrum of the cosmic diffuse γ-ray background has been determined in the 0.8–30 MeV range with the Compton telescope COMPTEL. In addition, the isotropy of the cosmic diffuse γ-ray background has been investigated for the first time on large angular scales. The measured spectrum can be adequately described by a power law. Fitting a power-law spectrum of the form

$$I(E) = A \cdot (E/E_0)^{\alpha}$$

to the final spectrum of the cosmic diffuse γ-ray background, with the reference energy E_0 being fixed at 5 MeV, yields the following results for the normalization A and the power-law index α:

$$A = (1.12 \pm 0.22) \times 10^{-4} \quad \mathrm{ph/(cm^2\ sec\ ster\ MeV)}$$

and

$$\alpha = -2.20 \pm 0.24$$

with the reduced chi-squared of the fit being $\chi^2_\nu = 0.27$ with 7 degrees of freedom. This result is in agreement with earlier COMPTEL analyses (see e.g. Kappadath 1998), which employed a less advanced analysis method and were based on data from a smaller fraction of the sky. Furthermore, the resulting spectrum is consistent with extrapolations of recent results derived at lower (Kinzer *et al.* 1997) and higher (Sreekumar *et al.* 1998) energies. No evidence for the existence of the so-called MeV-bump, an excess emission at MeV energies above the extrapolations from lower and higher energies, is found. The MeV-bump was consistently measured by different groups in the 1970's and

early 1980's and interpreted as evidence for the annihilation of matter and anti-matter in the early universe. The COMPTEL results render such a process insignificant for the cosmic diffuse γ-ray background. The shape of the overall high-energy background spectrum appears to be greatly simplified, but nevertheless is not easily explained by current models for the emission of individual source populations. The emission of Seyfert galaxies, which produce the bulk of the X-ray background radiation, cuts off exponentially above about 100 keV. Similarly, the emission of blazars, which may be significant contributors to the γ-ray background above about 100 MeV, exhibit a spectral break at energies ranging from about 1 MeV to about 100 MeV. Hence their emission at MeV energies is too low to consitute a significant fraction of the γ-ray background in this energy range. γ-ray line emission from Type Ia SNe may offer a solution to this problem, since their spectrum peaks at MeV energies. In addition, there are indications for the existence of special classes of AGN, such as MeV-blazars or radio-loud Seyfert galaxies, which may provide substantial contributions to the diffuse γ-ray background at MeV energies.

Within the limits of the statistical uncertainty no significant deviations of the intensity of the cosmic diffuse γ-ray background from isotropy could be found. Assuming that the background intensity is, indeed, isotropic, upper limits on the relative deviations from isotropy consistent with the data at the 95% confidence level were derived. In the 0.8–4.3 MeV band an upper limit of about 34% was obtained from comparing two regions subtending a solid angle of about 3 ster each. At higher energies, the deviations could still be investigated with scales as small as about 1.5 ster. The upper limits on the deviations from isotropy in the 4.3–30 MeV, 4.3–9 MeV, and 9–30 MeV bands are about 26%, 45%, and 24%, respectively.

In the following the content of the individual chapters of this thesis is briefly summarized. In Chapter 1 the basic motivation for studying the background radiation across the electromagnetic spectrum is introduced with the well-known example of Olbers' paradox. The background radiation provides unique information on origin and evolution of the universe as a whole, and on the formation and evolution of various constituents, such as galaxies, in particular.

An overview of current results on the background radiation, from radio wavelengths to the γ-ray regime, is given in Chapter 2. In addition, a large variety of possible origins of the γ-ray background is discussed in detail. Finally, the history of the measurements of the γ-ray background radiation is reviewed briefly.

A description of the COMPTEL instrument can be found in Chapter 3, together with a discussion of instrumental aspects relevant for the analysis. For example, the validity of the Monte Carlo modelling of the instrument response is demonstrated. The analysis requires knowledge of the instrument response to the isotropic background radiation, as well as to a number of radioactive isotopes in the telescope material which produce a considerable amount of instrumental background. These responses can only be determined by Monte Carlo simulation.

The properties of the COMPTEL instrumental background, which by far dominates the celestial signal, are discussed in Chapter 4. The instrumental background is composed of various components, such as γ-radiation from radioactive isotopes. To date, eight different isotopes have been identified. Detailed understanding of the instrumental background, in particular, its specific dataspace distribution and variation in time and as a function of geophysical parameters, is indispensible for its elimination from the data so that the sought-after signal from the cosmic diffuse γ-ray background can be uncovered.

The analysis method employed to study the cosmic diffuse γ-ray background is described in Chapter 5. In addition to taking advantage of differences in the dataspace distributions of celestial signal and instrumental background, the separation of these two components rests mainly on the fact that the instrumental background — in contrast to the cosmic diffuse γ-ray background — is variable.

Finally, the results on spectrum and isotropy of the cosmic diffuse γ-ray background obtained in this thesis are summarized in Chapter 6, which also provides a discussion of their astrophysical implications.

Zusammenfassung:

Der Ursprung der diffusen, kosmischen Gamma-Hintergrundstrahlung im COMPTEL-Energiebereich

Das Thema dieser Dissertation ist die Untersuchung des Ursprungs der diffusen, kosmischen γ-Hintergrundstrahlung mit dem Compton-Teleskop COMPTEL. Dieses Teleskop, sensitiv für γ-Strahlung im Energiebereich von etwa 1–30 MeV, ist eines der vier Instrumente auf dem Compton Gamma-Strahlen-Observatorium (Compton Gamma-Ray Observatory, CGRO), einem Satelliten, der im April 1991 mit dem Space Shuttle Atlantis der NASA in seine Umlaufbahn gebracht worden ist. Das Studium des diffusen, kosmischen γ-Hintergrunds ist, aufgrund seiner großen Bedeutung für die Kosmologie und der Entstehung und Evolution von Galaxien, eines der wissenschaftlichen Hauptziele der COMPTEL-Mission. Wegen der hohen Transparenz des Universums für γ-Strahlung ist es möglich, im Licht der γ-Photonen hochenergetische Prozesse bis in sehr große Entfernungen, und somit bis weit in die kosmische Vergangenheit, direkt zu beobachten. Der experimentell schwer zugängliche und deshalb bisher wenig untersuchte Energiebereich von COMPTEL ist dabei von besonderem Interesse, da er im Übergang zwischen den deutlich besser untersuchten Energiebereichen der harten Röntgenstrahlung ($E \sim$ 10–500 keV) und der hochenergetischen γ-Strahlung ($E \gtrsim 100$ MeV) liegt.

Im Laufe der Zeit ist eine Vielzahl von Modellen zur Entstehung des diffusen, kosmischen γ-Hintergrunds vorgeschlagen worden, welche in zwei Kategorien unterteilt werden können. Der diffuse, kosmische γ-Hintergrund könnte in echt-diffusen Prozessen erzeugt worden sein, oder er entsteht durch die Überlagerung der Emission einer Vielzahl einzelner, unaufgelöster Punktquellen. Ein Beispiel für einen möglichen, echt-diffusen Ursprung der γ-Hintergrunds ist die kosmische Annihilationsstrahlung aus den frühen Phasen eines Baryon-symmetrischen Universums. Zu den möglichen Populationen diskreter Quellen der γ-Hintergrundstrahlung zählen unter anderem verschiedene Klassen aktiver Galaxien und Supernovae vom Typ Ia. Eine Untersuchung der Beiträge der verschiedenen Quellen erfordert zum einen die Messung des Spektrums des diffusen, kosmischen γ-Hintergrunds, das sich über mehr als sechs Größenordnungen in der Energie erstreckt. Da die von den verschiedenen Quellen emittierte Strahlung unterschiedliche spektrale Verteilungen aufweist, ergibt sich daraus eine Möglichkeit die Beiträge der verschiedenen Objekt-Klassen zu bestimmen. Zum anderen ist auch eine Untersuchung der Isotropie der γ-Hintergrundstrahlung von Interesse. Sind ihre

Quellen extragalaktischen Ursprungs, so sollte die Intensität des γ-Hintergrunds isotrop verteilt sein. Es ist jedoch möglich, daß die γ-Hintergrundstrahlung teilweise, oder sogar überwiegend, aus einem ausgedehnten Halo unserer eigenen Galaxis stammt. Je nach Art des Halos sollten dann charakteristische Anisotropien auf großen Winkelskalen in der γ-Hintergrundstrahlung beobachtbar sein. Die meisten der verausgesagten Anisotropien entziehen sich jedoch noch dem Leistungsvermögen derzeit verfügbarer Experimente. In der Zukunft sollte es auch möglich sein, Fluktuationen der Intensität des γ-Hintergrunds auf kleinen Winkelskalen zu untersuchen. Dies würde dann eine zusätzliche Möglichkeit zur Trennung der Beiträge verschiedener Quell-Klassen eröffnen, da diese sich auch in ihrer Verteilung am Himmel unterscheiden.

Im Rahmen dieser Arbeit wurde mit dem Compton-Teleskop COMPTEL sowohl das Spektrum der diffusen, kosmischen γ-Hintergrundstrahlung im Energiebereich von 0.8–30 MeV bestimmt, als auch erstmalig deren Isotropie auf großen Winkelskalen untersucht. Das gemessene Spektrum kann mit einer Potenzfunktion der Form

$$I(E) = A \cdot (E/E_0)^{\alpha}$$

beschreiben werden. Eine Anpassung dieser Funktion an das Spektrum ergab einen Wert von

$$A = (1.12 \pm 0.22) \times 10^{-4} \quad \mathrm{ph/(cm^2\ sec\ ster\ MeV)}$$

für die Normierung des differentiellen Photonen-Spektrums, und einen Wert von

$$\alpha = -2.20 \pm 0.24$$

für die Potenz, wobei die Stützenergie E_0 bei 5 MeV, dem logarithmischen Mittel des Meßbereichs, festgehalten wurde. Dieses Ergebnis ist konsistent mit früheren Ergebnissen von COMPTEL (z.B. Kappadath 1998), die mit einer einfacheren Methode und für einen kleineren Teil des Himmels bestimmt worden sind. Darüber hinaus ist das in dieser Arbeit gewonnene Spektrum konsistent mit den Extrapolationen der Ergebnisse bei niedrigeren (Kinzer *et al.* 1997) und höheren (Sreekumar *et al.* 1998) Energien. Das COMPTEL Spektrum zeigt keine Hinweise auf die Existenz des sogenannten MeV-Exzesses im Spektrum des γ-Hintergrunds, der von zahlreichen Experimenten in den 70er und frühen 80er Jahren gemessen worden, und als Evidenz für die Annihilation von Materie und Anti-Materie im frühen Universum interpretiert worden ist. Somit scheint dieser Prozeß für den γ-Hintergrund unbedeutend zu sein. Der jetzt deutlich vereinfachte Verlauf des Spektrums ist allerdings mit den derzeitigen Modellen für die Emissionen der einzelnen Quell-Klassen nicht ohne weiteres erklärbar. So bricht die Emission der Seyfert-Galaxien, einer Klasse aktiver Galaxien, die den Großteil des extragalaktischen Röntgen-Hintergrunds beitragen, nach bisherigem Wissen bei wenigen 100 keV ab. Die Situation ist ähnlich bei den Blasaren, einer Klasse aktiver Galaxien, die unter Umständen den γ-Hintergrund oberhalb von etwa 100 MeV erklären. Das Spektrum eines Blasars weist, individuell verschieden, einen Knick bei Energien von etwa 1 MeV bis 100 MeV auf, wodurch deren MeV-Emission im allgemeinen zu gering

ist, um den γ-Hintergrund bei diesen Energien erklären zu können. Einen möglichen Ausweg bildet die γ-Linien-Emission von Supernovae vom Typ Ia, deren Maximum im MeV-Bereich liegt. Auch haben sich schon Hinweise auf die Existenz spezieller Klassen aktiver Kerne ergeben, zum Beispiel MeV-Blasare oder radio-laute Seyfert-Galaxien, die wesentlich zum γ-Hintergrund im MeV-Bereich beitragen könnten.

Im Rahmen der statistischen Meßunsicherheit konnten keine signifikanten Abweichungen der Intensität von der Isotropie gefunden werden. Unter der Annahme, daß die γ-Hintergrundstrahlung in der Tat isotrop ist, wurden dann obere Grenzen für die noch mit den Daten verträgliche, relative Abweichung der Intensität von der Isotropie für eine Konfidenz von 95% bestimmt. Im 0.8–4.3 MeV Bereich ergibt sich für die relative Abweichung eine obere Grenze von etwa 34% aus einem Vergleich zweier Gebiete mit einem Raumwinkel von jeweils etwa 3 ster. Bei höheren Energien konnten die Abweichungen bis zu Skalen von etwa 1.5 ster untersucht werden. In den Energiebereichen 4.3–30 MeV, 4.3–9 MeV und 9–30 MeV wurden obere Grenzen von 26%, 45% und 24% bestimmt.

Im folgenden wird der Inhalt der einzelnen Kaptiel der vorliegenden Arbeit jeweils kurz zusammengefaßt. Im ersten Kapitel wird anhand des Beispiels von Olbers' Paradoxon die Grundidee aller Untersuchungen der extragalaktischen Hintergrundstrahlung erläutert. Das Spektrum des extragalaktischen Hintergrunds ist eine wesentliche Randbedingungen für alle Modelle der großräumigen Struktur und der Evolution des Universums. Die in den Modellen existierenden und sich entwickelnden Quell-Klassen müssen das Spektrum des extragalaktischen Hintergrunds reproduzieren, wenn das Modell als ein gültiger Entwurf des Universums gelten soll.

Im zweiten Kapitel werden zunächst aktuelle Ergebnisse über den extragalaktischen Hintergrund über das gesamte, der Bobachtung zugängliche, elektromagnetische Spektrum zusammenstellt, von den Radiowellen bis zur γ-Strahlung. Im Anschluß wird dann eine Vielzahl verschiedener Modelle zur Entstehung des diffusen, kosmischen γ-Hintergrunds diskutiert. Schließlich wird noch ein kurzer Überblick über die Historie der Messungen des γ-Hintergrunds gegeben.

Eine detailierte Beschreibung des Compton-Teleskops COMPTEL ist in Kapitel 3 zu finden. Dabei wird nicht nur der Aufbau des Experiments beschrieben, sondern es werden auch Korrekturen der Rohdaten, die sich für die wissenschaftliche Analyse als vorteilhaft erwiesen haben, erläutert. Ein Schwerpunkt dieses Kapitels ist die erfolgreiche Beschreibung der Eigenschaften des Teleskops in Monte Carlo Simulationen. Dies ist von großer Bedeutung für die Untersuchung des diffusen, kosmischen γ-Hintergrunds, da die Antwortfunktion des Instruments für eine isotrope Quell-Verteilung nur in der Simulation, aber nicht im Experiment bestimmt werden kann. Außerdem konnte der instrumentelle γ-Linien-Hintergrund nur durch Monte Carlo Simulation beschrieben werden.

Das folgende Kapitel ist ganz dem instrumentellen Hintergrund gewidmet. Das Verständnis des instrumentellen Hintergrunds ist von zentraler Bedeutung für die Un-

tersuchung der diffusen, kosmischen γ-Hintergrundstrahlung, da der instrumentelle Hintergrund das Signal des γ-Hintergrunds deutlich dominiert. Die Trennung des Signals der γ-Hintergrundstrahlung vom wesentlich stärkeren instrumentellen Hintergrund beruht zum einen auf Unterschieden in den Verteilungen der beiden Komponenten im Datenraum des Instruments, zum anderen auf der Tatsache, daß der instrumentelle Hintergrund auf verschiedenen Zeitskalen variiert, während das Signal des γ-Hintergrunds konstant ist. Eines der größten Probleme in den Untersuchungen des instrumentellen Hintergrunds war die Identifizierung und Monte-Carlo Modellierung der instrumentellen Hintergrund-Linien. Diese stammen aus dem Zerfall radioaktiver Isotope, die meist durch Wechselwirkungen der kosmischen Strahlung mit dem Material des Teleskops erzeugt werden. Bis jetzt konnten acht verschiedene Isotope identifiziert werden.

In Kapitel 5 wird die Analyse-Methode, aufbauend auf den Ergebnissen für den instrumentellen Hintergrund, entwickelt und beschrieben. Die Schwerpunkte sind dabei die Bestimmung der Aktivität der identifizierten Hintergrund-Isotope und die Untersuchung der Systematik der Veto-Raten-Extrapolation. Die Bestimmung der Isotopenaktivitäten erfolgt durch Anpassung simulierter Modellspektren für die Energie-Verteilung der einzelnen Isotope an geeignet gewählte Energiespektren. Die Extrapolation der Ereignisrate mit der Zählrate der Veto-Dome dient der Eliminierung des in vielen Wechselwirkungen der kosmischen Strahlung im Instrument erzeugten, sehr kurzlebigen instrumentellen Hintergrunds.

Im letzten Kapitel werden schließlich die Ergebnisse dieser Arbeit bezüglich Spektrum und Isotropie der diffusen, kosmischen γ-Hintergrundstrahlung zusammengestellt und diskutiert.

Contents

Chapter 1

Introduction or: Why is the Sky Dark at Night?

Why is the sky dark at night? Soon after the Copernican revolution in the sixteenth century it became clear that this seemingly naive question poses an intriguing and tantalizing riddle in a universe consisting of unbounded space populated endlessly with luminous stars. In such a universe a line of sight in any direction, extended into the depth of space, eventually intercepts the surface of a star. Visible stars should therefore cover the entire sky without any separating gaps, and every part of the sky should shine as brightly as any point on the sun's disk. The hemisphere of the night sky is about 90000 times larger in solid angle than the sun's disk, and therefore the starlight falling on Earth should be about 90000 times more intense than sunlight. Hence the riddle of cosmic darkness: Why is the sky dark at night? (Harrison 1990)[1]. The riddle played an important role in the development of astronomy, and in particular of cosmology, as it drew the attention of many brilliant minds to questions concerning the physical nature and large-scale structure of the universe as a whole — and linked these cosmic properties to the intensity of the background radiation, which is accessible to observation. The study of background radiation therefore is truly the oldest problem in cosmology (Longair 1994b), and remained a prime objective in astronomy and astrophysics until the present, as described in the next chapter.

Nowadays, the riddle of cosmic darkness is usually referred to as Olbers' paradox. Olbers, however, was only one in a long row of thinkers that ventured to cope with the dark night-sky riddle. Kepler was the first to clearly state the riddle in 1610, but it was not until Loys de Chéseaux (1744) and Olbers (1823) that the problem was treated in

[1]The introduction of this thesis provides all but a glimpse of the cornucopious material on the dark night-sky riddle compiled by Harrison (1987) in his highly recommendable account of the history of the riddle of cosmic darkness in his book *Darkness at Night: A Riddle of the Universe*, Harvard University Press, covering the scientific ideas as well as anecdotal detail concerning the scientists involved. A summary of the scientific aspects of Olbers' paradox can also be found in an elucidating overview article by Harrison (1990).

a lucid and quantitative manner. Loys de Chéseaux estimated that the stars within a radius of about 10^{15} times the average star-separating distance, as inferred from the distance to the closest star, cover the entire sky. In addition, Olbers, by virtue of the line-of-sight argument, realized that the riddle remains little affected when the stars are not distributed uniformly, but form clusters or galaxies. The vastness of the estimated background distance[2] lead both Loys de Chéseaux and Olbers to the conclusion that most starlight, on its way through space, is absorbed by a tenuous interstellar medium such that we only observe the foreground stars, while the distant stars are hidden from our view.

Both Loys de Chéseaux and Olbers, as almost everyone else from the sixteenth to the twentieth century, assumed that the sky is actually covered by stars. In their interpretation of the riddle of cosmic darkness most of the stars remain unseen, raising the question: What has happened to the missing starlight? Their suggestion that the interstellar medium absorbed most of the radiation emitted by stars contained a fundamental flaw, however, which was first identified by Herschel (1848): if the integrated starlight from the full celestial sphere were, indeed, about 180000 times more intense than the sunlight at the Earth's surface, then the absorbing medium would soon heat up until emission equalled absorption.

An alternative interpretation of the riddle of cosmic darkness assumes that the dark gaps between the visible stars are actually empty of stars — even in an infinite universe containing an infinity of stars — raising the question: What has happened to the missing stars? A solution based on this second interpretation is to arrange stars hierarchically, at larger and larger scales, as proposed by Herschel and a number of other astronomers and scientists. Their solution of the dark night-sky riddle by cosmic hierarchy, however, only succeeds for an infinite number of hierarchical levels on progressively larger scales. A finite number of levels fails to solve the riddle, because the homogeneous distribution at some high level inevitably creates a bright starlit sky in an infinite universe.

The discovery of the finiteness of the speed of light by Römer in 1676 provided a natural solution to the riddle of cosmic darkness. Owing to the finite speed of light, c, starlight travels only a finite distance in an unbounded universe of age t. The region visible to the observer therefore has a radius (in a static universe) of $c \cdot t$. Beyond the visible universe lie objects whose light has yet to reach the observer, hence a possible solution of the dark night-sky riddle is that stars fail to cover the sky because the light from numerous background stars is still in transit. This solution applies to static as well as non-static universes as long as the background distance exceeds the size of the visible universe. If the luminous lifetime of stars, t_*, is much less than the age of the universe, then the size of the visible universe decreases accordingly to $c \cdot t_*$. This

[2]For a sky covered with stars the background distance denotes the average distance a line of sight can extend into space before intercepting the surface of a star. Hence the background distance is the mean free path of starlight between emission and absorption.

finite-age solution for the riddle of cosmic darkness was first explicitly put forward in a cosmological essay by Poe (1848). The first quantitative treatment of the finite-age solution was provided by Thomson (1901), the later Lord Kelvin, who estimated that the luminous lifetime of the sun cannot exceed 10^8 years. In addition, Thomson realized that a sky as bright as the surface of the sun implies thermodynamic equilibrium, in which the stars emit as much radiation as they receive, and showed that the fraction of the sky covered by stars equals the ratio of the apparent brightness of the starlit sky to the brightness of the sun's disk.

After the discovery of the expansion of the universe in the 1920's and 1930's by Hubble and others static universes were ruled out, and the two leading cosmological concepts were the steady-state universe and the big-bang cosmology. The first possesses an infinite past and future and stars are perpetually luminous, with continuous creation of matter ensuring that newborn suns replace dying stars. In the latter, the universe is of finite age and was created, matter and energy, even space and time itself, in a ubiquitous explosion.

In an expanding steady-state universe of infinite age a solution of the riddle of cosmic darkness based on the finite lifetime of individual stars is not viable, because the average number of luminous stars at any point in time remains unchanged. The night sky may still remain dark, even though it is covered with stars, owing to the expansion of the universe, which redshifts most of their light-rays into invisibility (Bondi and Gold 1948). This solution seemed so plausible that is was generally believed to solve the riddle of cosmic darkness in all expanding universes, whether steady-state or evolving like the big-bang universe.

While indeed correct for an expanding steady-state universe, the redshift solution of the dark night-sky riddle is insufficient for an evolving universe. In general, in an evolving universe, either static or expanding, the sky at night is dark when stars shine for a period considerably less than the background distance divided by the speed of light (Harrison 1964). The distribution of stars in the current universe corresponds to a background distance of the order of 10^{23} light-years. The luminous lifetime of a sun-like star, however, is on the order of 10^{10} years, hence a starlight intensity of only 10^{-13} of that anticipated by Olbers' paradox is to be expected — consistent with observations — and darkness at night, as already inferred by Thomson (1901), results from the finite age of the luminous sources (see e.g. Harrison 1974, Wesson *et al.* 1987, Wesson 1991, and references therein). The night sky remains dark because stars fail to cover it. Other effects in an evolving and expanding universe, such as the redshifting of radiation, are of second order and merely decrease a radiation intensity already sufficiently low to be consistent with the observed dark night sky.

As astronomy evolved in the twentieth century, more and more regions of the electromagnetic spectrum became accessible to observation. Less than 100 years ago our view of the universe was still limited to the tiny optical window, covering only a factor of ~ 2 in frequency, while today we have knowledge on the background radiation over more than 20 decades in frequency. The night sky is dark almost all across the elec-

tromagnetic spectrum, for the same reason that it is dark in the optical — the finite age of the luminous sources. The night sky, however, is not dark at all wavelengths. Between the stars we look out into the depth of space and far back in time, before the birth of the first stars, to the horizon of the visible universe. In all directions, we see the once incandescent light of the big bang, redshifted by expansion into an infrared glow.

In the next chapter an overview is given of current results on the background radiation, from radio wavelengths to the γ-ray regime. Intensity and shape of the background radiation across the electromagnetic spectrum provide unique information on cosmic properties such as the formation of structure and the evolution of galaxies and of individual source populations over cosmic time. None of these topics can be addressed thoroughly by studying only a small portion of the electromagnetic spectrum, because the many different sources of the background radiation emit over a wide range in energy. In addition, there are interactions of matter and background radiation, such as absorption and re-emission by dust, and even interactions of photons from different portions of the background radiation, such as γ-γ pair production of high-energy γ-ray photons with photons at lower energies, particularly at optical and infrared wavelengths.

The topic of this thesis is to study spectrum and isotropy of the background radiation in the energy range 0.8–30 MeV with the Compton telescope COMPTEL. As described in Sec. 2.2, the low-energy γ-ray background radiation is of interest for a number of reasons. Possible origins of the low-energy γ-ray background are the superposed emission of a variety of source populations, such as different types of galaxies, in particular active galaxies, of Type Ia supernovae, or of evaporating black holes. In addition, truly diffuse processes such as the annihilation of matter and anti-matter in the early universe, or the decay or annihilation of certain types of exotic elementary particles, are expected to give rise to spectral features at MeV-energies. The measurement of spectrum and isotropy of the low-energy γ-ray background is one of the many small steps towards understanding the emission and evolution of these sources in particular, and — since these sources are connected to other domains of the overall background radiation — towards understanding the origin and evolution of the universe as a whole.

Chapter 2

The Extragalactic Gamma-Ray Background

2.1 The Extragalactic Background Radiation — A Multiwavelength Overview

The extragalactic background radiation (hereafter EBR), defined here to signify all diffuse radiation arising external to our galaxy, provides a unique window on a variety of fundamental topics in cosmology, astrophysics, and particle physics. These topics include the origin of the universe, the formation of structure and the evolution of galaxies, the formation of stars and the production of metals and gas and dust, and the properties of (exotic) elementary particles. Opening this window is, however, an exceedingly difficult task in almost all observable wavebands, as it requires the absolute measurement of the intensity of a presumably isotropic radiation field — one of the most challenging measurements in astronomy. A determination of the EBR intensity involves the complete elimination of all instrumental background in addition to accounting for the emission from point sources and extended foreground emission, in particular, diffuse galactic emission.

There are two distinct possibilities for the origin of the EBR: it may result from the superposition of unresolved point sources or originate from truly diffuse mechanisms. The EBR may also originate from a combination of diffuse sources and point sources, with different origins dominating in different portions of the electromagnetic spectrum. An answer to the question of the origin of the EBR can be found only in an iterative process of observation and modelling of the radiative properties of various extended and discrete sources in the sky. Progress in this endeavour depends crucially on the capabilities of the telescopes and detectors available in each waveband. If the EBR is due to discrete sources, instruments with high angular resolution are needed to resolve and study the large number of expected faint sources. If the EBR has a truly diffuse origin it is crucial to determine its energy spectrum as accurately as possible in order

to reveal its physical production process. Even if the EBR arises solely from discrete sources, a precise measurement of the energy spectrum of the total diffuse emission is needed to determine the absolute EBR intensity in the presence of appreciable galactic diffuse foreground emission by spectral fitting. A further important diagnostic for the origin of the EBR is the spatial fluctuation of its intensity on large and small angular scales. The detection of large-scale isotropy of the EBR is a crucial test for its cosmological origin and can be exploited to separate the EBR from galactic diffuse emission. The angular-fluctuation spectrum of the EBR intensity on fine angular scales can be compared to the expected angular fluctuations due to different sources of radiation, which allows one to assess the EBR contributions from different source populations.

In the following, a brief overview[1] is given of the observations of the extragalactic background radiation from radio wavelengths to the γ-ray regime and their relevance for the above mentioned issues in cosmology, astrophysics and particle physics. The terminology used throughout this section is defined in Appendix A, which also summarizes some of the basic equations frequently used in extragalactic astronomy. In addition, useful conversion factors for multiwavelength studies are given there.

2.1.1 The Extragalactic Radio Background

In studies of the extragalactic radio background (hereafter ERB) the radio waveband usually is restricted to frequencies $\lesssim 300$ MHz (corresponding to wavelengths $\gtrsim 1$ m) because the cosmic microwave background (see next section) starts to dominate at higher frequencies.

A major difficulty for measurements of the intensity of the ERB is the synchrotron radiation from our galaxy, which dominates the radio sky even at high galactic latitudes. What is observed in the sky is

$$I_\nu(l,b) = I_{gal,\nu}(l,b) + I_{ERB,\nu} \tag{2.1}$$

with $I_{gal,\nu}(l,b)$ representing the anisotropic galactic component in galactic coordinates (l,b), and $I_{ERB,\nu}$ representing the isotropic extragalactic component. The two components can be separated by mapping the sky at different frequencies, assuming that the anisotropic component has the same radio spectrum in all directions and exploiting the fact that the ERB spectrum is significantly steeper than the galactic continuum spectrum (Longair 1995). Above about 10 MHz the ERB intensity can be approximated by

$$I_{ERB,\nu} \simeq 6 \cdot 10^3 \left(\frac{\nu}{1\,\mathrm{GHz}}\right)^{-0.8} \quad \mathrm{Jy\ ster^{-1}} \tag{2.2}$$

[1]For further reading the following proceedings are recommended: *The Galactic and Extragalactic Background Radiation*, eds. S. Bowyer and Ch. Leinert, Cambridge University Press, 1990; *The Deep Universe*, eds. B. Binggeli and R. Buser, Springer, 1994; *Extragalactic Background Radiation*, eds. D. Calzetti, M. Livio and P. Madau, Cambridge University Press, 1995.

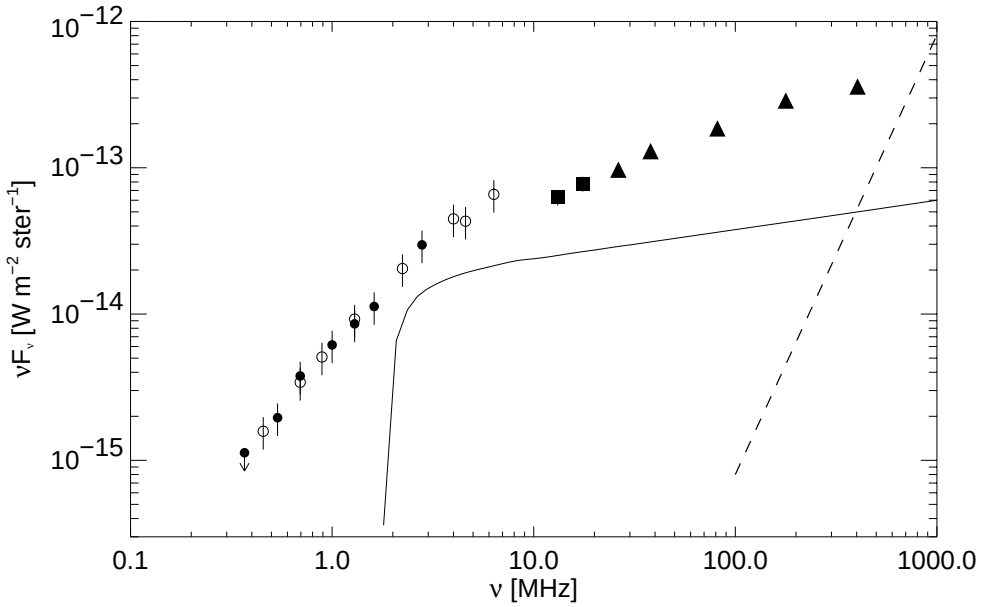

Figure 2.1: *The spectrum of the total radio emission from a region close to the galactic north pole, where the galactic component is at its minimum. The data are from Alexander* et al. *(1969) (open and filled circles), Bridle (1967) (filled squares) and Purton (1966) (filled triangles). The solid line indicates an estimate of the ERB spectrum according to Simon (1977) and Peacock (1995). The dashed line represents the 2.7 K blackbody radiation of the cosmic microwave background.*

with an uncertainty of about 20% in amplitude and 0.1 in spectral index (Peacock 1995). At lower frequencies the extragalactic spectrum cuts off below ~ 4 MHz. The spectrum of the total radio emission from a region close to the galactic north pole, where the galactic component is at its minimum, is depicted in Fig. 2.1, together with an estimate of the ERB spectrum and the spectrum of the cosmic microwave background. Most of the ERB is accounted for by the superposition of extragalactic radio sources, the ERB low-frequency cut-off is due to synchrotron self-absorption in the discrete sources (Simon 1977).

Later surveys revealed that various populations of extragalactic radio sources contribute to the ERB: at high luminosities mostly FR II radio galaxies and quasars[2], at intermediate luminosities predominantly FR I radio galaxies, and at low luminosities radio-quiet quasars, starburst galaxies and normal galaxies (Peacock 1995). These data allow us now to study the evolution of different populations of galaxies with cosmic epoch, in particular their radio-emission properties. Also, these observations provide useful constraints on galaxy formation, since one of the unique capabilities of radio astronomy is the detection of neutral hydrogen via the 21 cm line back to high redshifts (Peacock 1995). In addition, detailed analysis of the spatial distribution of the

[2]The various types of active galactic nuclei, such as radio galaxies and quasars, are explained in Sec. 2.2.1.2

extragalactic sources offers the prospect of mapping the large-scale structure in the universe (Wall 1990). Finally, it has to be emphasized that the study of the evolution of different populations of galaxies at radio wavelengths is not only interesting in its own right, but is of considerable importance for all other wavelengths, since quite often a linear correlation between the radio flux and the flux at other wavelengths (e.g. at γ-ray energies, see Sec. 2.1.7) is supported or at least not excluded by the available data.

2.1.2 The Cosmic Microwave Background

Among all accessible wavebands pride of place is due to the cosmic microwave background (CMB). It is the sole radiative remnant of the initial conditions governing the early universe[3], and it is one of the best-studied extragalactic radiation fields. The CMB was discovered in 1965 at centimeter wavelengths (Penzias and Wilson 1965). It was quickly established that this background radiation is remarkably uniform over the sky and that its spectrum closely follows the form of a blackbody spectrum at a radiation temperature of about 3 K. The maximum intensity of such a spectrum occurs at about 1 mm, at which atmospheric emission makes a precise absolute intensity measurement impossible from the surface of the Earth.

This limitation was overcome with the launch of the Cosmic Background Explorer (COBE) in 1989, a satellite dedicated to studies of the CMB and the cosmic infrared background (see next section). The spectrum of the CMB was determined with unprecedented accuracy and precision by the COBE Far Infrared Absolute Spectrophotometer (FIRAS), which was designed to compare the CMB spectrum to a blackbody spectrum. The CMB spectrum is an almost perfect blackbody spectrum with an absolute temperature of (2.728 ± 0.004) K (95% confidence limit), with rms deviations being less than 0.05% of the peak intensity in the wavelength range 0.5–5 mm (Mather *et al.* 1994, Fixsen *et al.* 1996). As can be seen in Figs. 2.1, 2.2 and 2.5, the CMB completely overwhelms all other emission components in the sky at cm and mm wavelengths, in particular in the Rayleigh-Jeans region of the spectrum, which greatly facilitates an absolute intensity measurement. The near-blackbody shape of the CMB is expected in the hot big bang model of cosmology, in which the universe evolves from a very hot and dense initial state in thermal equilibrium. As the universe expands, the blackbody spectrum could be distorted by energy release after a redshift of $z \sim 3 \times 10^6$ (see the review by Sunyaev and Zel'dovich 1980). After the decoupling of neutrinos and the annihilation of positrons and electrons until $z \sim 3 \times 10^4$, the CMB was the

[3]In principle, a second radiative remnant exists — the cosmic neutrino background (CNB). The CNB is expected to have a blackbody spectrum at a radiation temperature of ~ 2 K. The temperture of the CNB is less than that of the CMB because the neutrinos dropped out of thermal equilibrium, or "decoupled", before the annihilation of electrons and positrons, which resulted in a reheating of the photons (Weinberg 1977). A detection of the CNB, which unfortunately by far exceeds the capabilities of current technology, would be a dramatic confirmation of the hot big bang hypothesis.

dominant energy field, thus large amounts of energy are required to produce deviations from the pure blackbody spectrum. The FIRAS measurements allow us to strictly limit energy release after the first year of expansion. There are two likely distortions of the primeval spectrum produced during the plasma period before recombination. Energy release or conversion in the redshift range $10^5 < z < 3 \times 10^6$ produces a Bose-Einstein distortion, where the Planck law is modified by a chemical potential μ[4]. At later times, $z < 10^5$, a Comptonization spectrum is produced, a mixture of blackbody spectra at a range of temperatures, which can be described by the Kompaneets equation with the dimensionless parameter y (Sunyaev and Zel'dovich 1980)[5]. Possible sources of such energy augmentations include decay of primeval turbulence, elementary particles, cosmic strings or black holes. The growth of black holes, quasars, galaxies, clusters and superclusters might also convert energy from other forms (Mather 1995). After recombination at $z \sim 1100$ stars, galaxies and quasars form, leading to new classes of possible spectral distortions. Reionization of the universe at $5 < z < 1000$, in particular by Population III stars, will lead to Compton distortions of the CMB spectrum due to semirelativistic electrons in the hot intergalactic medium (IGM). The most recent limits on the chemical potential μ and the Comptonization parameter y are given by Fixsen *et al.* (1996), with $|\mu| < 9 \times 10^{-5}$ and $|y| < 16 \times 10^{-6}$ at the 95% confidence limit. As will be elaborated in Sec. 2.1.6, it was suggested that the extragalactic X-ray background is produced in a hot IGM. This possible origin of the X-ray background is, however, clearly ruled out by the tight limits on the CMB distortion from a blackbody spectrum. The FIRAS data can also be used to limit the amount of hydrogen burned in Population III stars and evolving IR galaxies following decoupling (Wright *et al.* 1994a, Mather 1995).

Of equal cosmological interest is the extent of the remarkable isotropy of the CMB, which was studied with the COBE Differential Microwave Radiometer (DMR) on 7° angular scales (and also with FIRAS). The largest anisotropy in the CMB is the (3.358± 0.023) mK dipole assumed to result from the Doppler effect due to our galactic velocity of about (369.0 ± 2.5) km/sec in the direction $(l, b) = (264.31° \pm 0.17°, 48.05° \pm 0.09°)$ with respect to the CMB rest frame (Fixsen *et al.* 1994, Lineweaver *et al.* 1996). In

[4]The energy density of the photons is then given by

$$u_\nu \, d\nu = \frac{8\pi h\nu^3}{c^3} \left[\exp\left(\frac{h\nu}{kT} + \mu\right) - 1\right]^{-1} d\nu$$

with the chemical potential μ being a measure of the deficit in the number of photons relative to that required for a Planck distribution at the same temperature.

[5]The parameter y gives the optical depth for Compton scattering:

$$y = \int \frac{kT_e(z)}{m_e c^2} \frac{\sigma_T \, N_e(z)}{(1+z)} \, dr$$

with $T_e(z)$ and $N_e(z)$ being the electron temperature and density at redshift z, respectively, σ_T being the Thomson cross-section, and dr being an element of proper comoving coordinate distance.

this analysis it was necessary to take into account the galaxy, which has a comparable amplitude as the dipole ($\Delta T/T \sim 10^{-3}$). After removing the contributions of both the dipole and the galaxy, random large-scale fluctuations at a level of $\Delta T/T \sim 10^{-5}$ could be detected (Smoot *et al.* 1992, Bennett *et al.* 1994, Fixsen *et al.* 1997). These fluctuations are consistent with expectations from scale-invariant primordial density perturbations[6] and with inflationary scenarios (Wright *et al.* 1994b, Mather 1995). The large-scale fluctuations on 7° angular scales observed by DMR and FIRAS probe structures that are currently much larger than 100 Mpc (Smoot *et al.* 1992). Additional measurements of the CMB anisotropies at smaller angular scales corresponding to the current galaxy cluster and even galaxy scales, allow us to better probe the primeval density perturbations in the early universe, which are the seeds for subsequent structure formation, and to determine cosmological parameters such as Ω, Λ, Ω_b and H_0 (Mather 1995, Lubin 1995).

2.1.3 The Cosmic Infrared Background

The cosmic infrared background (CIB) covers the wavelengths longwards of about 1 μm up to about 400 μm, where it is overwhelmed by the steep rise of the Wien region of the CMB (see previous section). The CIB is of great cosmological interest as it is expected to arise from the cumulative emissions from pregalactic, protogalactic, and galactic systems. Its observation would provide new insight into the cosmic "dark ages" following the decoupling of matter from the CMB (see e.g. Bond *et al.* 1986, Hauser 1995, Lonsdale 1995). Also, the combination of direct measurements of the extragalactic background in the infrared[7], optical (see Sec. 2.1.4) and ultraviolet (see Sec. 2.1.5) can provide important constraints on the integrated cosmological history of star formation, metal, gas and dust production, and the conversion of starlight into IR emission by dust (see e.g. Dwek *et al.* 1998). The energy density contained in the CIB may be higher than in any other spectral range of the extragalactic radiation field, yet detections of the CIB are exceedingly difficult because of abundant foreground emissions and the need to use cooled optics to reduce instrumental background, even

[6] Fluctuations in the initial gravitational potential reveal themselves in primordial density perturbations $\Delta = \delta\rho/\rho$. The power spectrum of these perturbation is given by

$$\langle \Delta^2 \rangle = \frac{V}{(2\pi)^{3/2}} \int |\Delta_k|^2 \, d^3k$$

Making the ansatz that the power spectrum has no preferred scale (scale invariance) implies

$$|\Delta_k|^2 \propto k^n$$

(see e.g. Longair 1994b, p. 486 ff.).

[7] The infrared spectral region customarily is crudely divided into three subranges: near, mid and far infrared. In the following, these terms will denote the wavelength ranges 1–5 μm, 5–50 μm and 50–400 μm, respectively. Wavelengths beyond 400 μm will be referred to as submillimeter range.

in space environments.

The strong emission from the terrestrial atmosphere[8] can be eliminated by observing from space, but even then the pronounced foreground emissions from interplanetary dust, interstellar dust and faint stars have to be accounted for. The interplanetary dust causes two kinds of diffuse emissions: scattered sunlight and thermal emission. The scattered sunlight, the so-called zodiacal light, peaks below 1 μm in the optical and falls into the IR, the thermal emission peaks above 10 μm. The integrated light of faint stars forms a diffuse, extended emission peaking above 1 μm, but is less bright than the zodiacal light. Finally, interstellar dust heated by the interstellar radiation field emits thermally beyond 100 μm, although this emission is less intense than the thermal emission from interplanetary dust (see Fig. 2.2). It follows that observations at the minima between the various foreground components and the CMB at ~ 3 μm and ~ 300 μm, the so-called "cosmological windows", are best suited for detecting the CIB (Matsumoto 1990, Hauser 1995, Lonsdale 1995).

The best results on the CIB have been obtained by two instruments on the COBE satellite. The Diffuse Infrared Background Experiment (DIRBE) was designed to conduct a sensitive search for the CIB in the wavelength range from 1.25–240 μm (Hauser 1995). The Far-Infrared Absolute Spectrometer (FIRAS), whose primary objective was a precise measurement of the CMB, was also a powerful instrument for the CIB at the longest wavelengths. The final result of the DIRBE/COBE search for the CIB was reported by Hauser *et al.* (1998). After modeling and subtraction of the bright foregrounds from interplanetary dust (scattering and emission), stars, and interstellar dust the CIB was detected at 140 μm and 240 μm, as depicted in Fig. 2.2. At shorter wavelengths from 1.25 μm to 100 μm assessment of the uncertainties in the residual after foreground subtraction showed that the CIB has not yet been detected, hence 2σ upper limits at the 95% confidence level are given at these wavelengths (see Fig. 2.2). As was to be expected in the case of incomplete foreground subtraction, the upper limits are lowest in the cosmological windows, and highest in the wavelength ranges of the zodiacal light and of the thermal emisson from interplanetary dust. At wavelengths longer than ~ 100 μm the foreground from dust emission falls rapidly, hence the CIB could be detected. The CMB, which overwhelms the CIB at wavelengths greater than ~ 400 μm, can be accounted for since its spectrum and dipole are well known. The spectrum of the CIB from 125–2000 μm was determined from FIRAS observations by Fixsen *et al.* (1998), which confirms an earlier, tentative detection of the CIB in the 400–1000 μm range with FIRAS by Puget *et al.* (1996), as depicted in Fig. 2.2.

Alternative to observations at infrared wavelengths, the observed MeV to TeV spectra of extragalactic γ-ray sources may be used as probes of the density of the CIB along the line of sight to the source (Stecker *et al.* 1992). TeV photons can be absorbed by γ-γ pair production, primarily by intervening infrared photons. Applying this approach

[8]In addition, the Earth's atmosphere is opaque to extraterrestrial infrared radiation from 20–320 μm due to absorption by H_2O.

to the observed spectrum of the BL Lacertae object Mrk 421, Dwek and Slavin (1994) were able to report a tentative detection of the CIB in the 15–40 μm wavelength regime. A similar analysis was also reported by De Jager *et al.* (1994). It has to be noted that the derived CIB intensities depend on the assumed spetrum of the CIB as well as on the intrinsic spectrum of the observed γ-ray source. Krennrich *et al.* (1997), however, have recently reported the detection of TeV γ-rays from Mrk 421. They concluded that there is presently no evidence in the data for attenuation by pair production, although given the uncertainty in the intrinsic spectrum of the γ-ray source, the possibility of some attenuation can not be totally ruled out. As was already emphasized by Dwek and Slavin (1994), lack of evidence for attenuation turns their determination of the CIB intensity into an upper limit, which is well below the present direct limits from observations (see Fig. 2.2).

Another approach to searching for evidence of the CIB is to study the fluctuations in maps of the IR sky intensity. If the spatial correlation function of the sources is known, the diffuse background produced by them can be estimated from the measured correlation function of sky brightness. Kashlinsky *et al.* (1996) determined the rms fluctuations in the 2.2–100 μm DIRBE/COBE maps and argued that their analysis implies that the CIB due to matter clustered like galaxies is less than about 10–15 nW/(m^{2}ster) over this wavelength range, which is comparable to the result of Dwek and Slavin (1994). Again it has to be noted that the result of such a fluctuation analysis is dependent on assumptions about the clustered sources of radiation.

Lower limits on the CIB can be obtained by integrating the brightness of observed galaxies. The near-IR results of Cowie *et al.* (1994), and the far-IR results of Hacking and Soifer (1991), amended at 60 μm by Gregorich *et al.* (1995), are included in Fig. 2.2. The intensities from integrated source counts are still well below the diffuse sky-brightness residuals. This gap, however, should decrease as future space missions will allow us to probe the galaxy number counts more deeply.

The CIB is of great cosmological interest as it allows us to study the early history of the universe, in particular the formation of structure and the formation and evolution of galactic systems. The infrared spectral region is well suited for searching for the integrated light of galaxies and protogalaxies for several reasons. The near-infrared range, as compared to the optical region, is advantageous for extragalactic searches because of weaker foreground emission. With increasing distance the optical and ultraviolet emission of galaxies, in particular of primeval galaxies, which are expected to go through a dramatic initial star formation event, is redshifted into the near-infrared region (Matsumoto 1990, Lonsdale 1995). The results from galaxy counts in the near-infrared will be reported in Sec. 2.1.4 covering the optical waveband.

Similarly, the second cosmological window in the far-infrared region is a rich hunting ground for the redshifted dust emission of galaxies. Young galaxies and protogalaxies may have been much more luminous at far-infrared wavelengths, compared to the optical and ultraviolet, than galaxies at the present epoch. Metallicity can increase rapidly during the early evolution of galactic systems. With the return of enriched gas

from evolved stars to the interstellar medium the dust content grows with time as the metallicity increases. Thus the dust optical depth, and consequently the far-infrared luminosity, can rise dramatically at the expense of the absorbed and re-radiated optical-ultraviolet luminosity (see e.g. Lonsdale 1995, and references therein). Hence, the far infrared background is of complementary nature to the near-infrared background, and fluctuations in the near and far infrared are predicted to be anticorrelated (Matsumoto 1990, Bond *et al.* 1991).

Finally, intervening galaxies at low to moderate redshifts may obscure galaxies and protogalaxies at high redshifts from observations in the optical and near-infrared wavebands. At far-infrared wavelengths, however, not only will absorption be insignificant, but the dust which is responsible for extinguishing the ultraviolet and optical light of high-redshift galaxies will re-emit this light at far-infrared and submillimeter wavelengths (Lonsdale 1995).

The cosmic epoch of galaxy formation and the sequence of events which took place when galaxies formed are still far from being understood. The two most popular pictures for the process of galaxy formation are the "pancake" model (see e.g. Zel'dovich 1984) and the quite different hierachical clustering model (see e.g. Press and Schechter 1974), which correspond closely to the expectations in the hot and cold dark matter[9] scenarios for galaxy formation. Briefly, in the pancake and hot dark matter models small-scale structure is dampened at early epochs and thus the largest-scale structures (superclusters and clusters) form first and the smaller-scale structures such as galaxies form by the process of fragmentation. In the hierarchical clustering and cold dark matter models the smallest structures are formed first, larger-scale structures are formed later by mergers or coalescence, thus smaller galaxies are formed before larger galaxies which later become gravitationally bound in clusters and superclusters.

One possibility for testing these models is through determination of the luminosity function, in particular in the far-infrared region. A large fraction of the total energy output of normal galaxies, and even more so for some starburst galaxies and AGN, is in this spectral range, as was shown from IRAS (Infrared Astronomy Satellite) observations (Lonsdale 1995). Comparison of the predicted far-infrared background intensity to COBE limits already constrains some of the models, and it is now clear that models that simply translate a local luminosity function in luminosity and/or density are not sufficient. Models of galaxy evolution have to take into account the evolution of physical galaxy properties such as metallicity and dust temperature.

Another option is to use far-infrared and submillimeter observations of redshifted thermal dust emission as a tool for studying the star-formation rate (SFR) in galaxies. The stars responsible for the intense optical and ultraviolet luminosity during star formation have short lifetimes, and thus the total thermal radiation by obscuring

[9] The essential difference between hot and cold dark matter is their streaming velocity, which may arise from differences in their masses. Typically, the terms hot and cold dark matter are used to describe particles with rest masses of $\lesssim 30$ eV and $\gtrsim 1$ GeV, respectively.

dust may act as a tracer of the star-formation history. Over the redshift interval in which substantial amounts of star-formation activity are expected to have taken place, thermal dust emission is redshifted into the far-infrared and submillimeter wavebands (Blain and Longair 1993b,a). According to the latest DIRBE/COBE results the energy level of the far-IR background in the 140–240 μm range is about 10.3 nW/(m^{2}ster) (Hauser *et al.* 1998), which is higher than the integrated optical light from galaxies in the Hubble Deep Field in the 3600–8100 Å range of 4.2 nW/(m^{2}ster) (Pozzetti *et al.* 1998) by a factor of ~ 2.5. These numbers indicate that a substantial fraction of the stellar luminosity from galaxies might have been reradiated by dust in the far-IR at the expense of the obscured UV-optical luminosity and that star formation might be heavily enshrouded by dust at high redshifts (Hauser *et al.* 1998). Based on the far-IR and optical background intensities from COBE and HST Dwek *et al.* (1998) estimated that the SFR at $z \approx 1.5$ must be larger than that inferred from UV-optical observations by at least a factor of 2, as the latter systematically underestimated the SFR due to dust absorption at these wavelengths. The exact magnitude of the absorption by dust at UV and optical wavelengths is, however, still quite controversial, as the currently available data on the extragalactic background from far-IR through UV does not allow to unambiguously resolve the history of star formation in the universe. For example, the UV to near-IR and far-IR estimates of the extragalactic background imply that $\sim$10–30% of the total baryonic mass density inferred from big-bang nucleosynthesis was processed in stars into heavier elements (Dwek *et al.* 1998).

In addition to the galactic and protogalactic sources of the CIB discussed so far, there may be contributions from pregalactic sources, albeit these are more speculative (see Bond *et al.* 1986, and references therein). In some cosmological scenarios the density fluctuations in the early universe extend to scales as small as $\sim 10^6$ M$_\odot$. Thus the first objects to form could be pregalactic clouds of this mass which could fragment into pregalactic stars. It is also conceivable that black holes were formed, which may be the precursors of the central engines of quasars. It has also been suggested that the decay of weakly interacting relic particles from the big bang may generate an electromagnetic background, whose amplitude and wavelength regime depend upon particle properties such as mass and lifetime (see also Secs. 2.1.5 and 2.1.7).

2.1.4 The Extragalactic Background Light

The optical spectral region extends from about 300 nm to about 1000 nm, whereas the wavelengths visible to the human eye cover the range $\sim$400–800 nm. The great cosmological importance of an isotropic background component in the optical range was recognized more than 300 years ago, as outlined in Chapter 1. The absence of a bright background light, expected as the cumulative effect of the emission of stars in an infinite universe, is generally known as Olbers' paradox and poses one of the oldest problems in astronomy. Despite the long history in the optical region, the extragalactic background radiation was first detected in the X-ray and millimeter wavebands (see

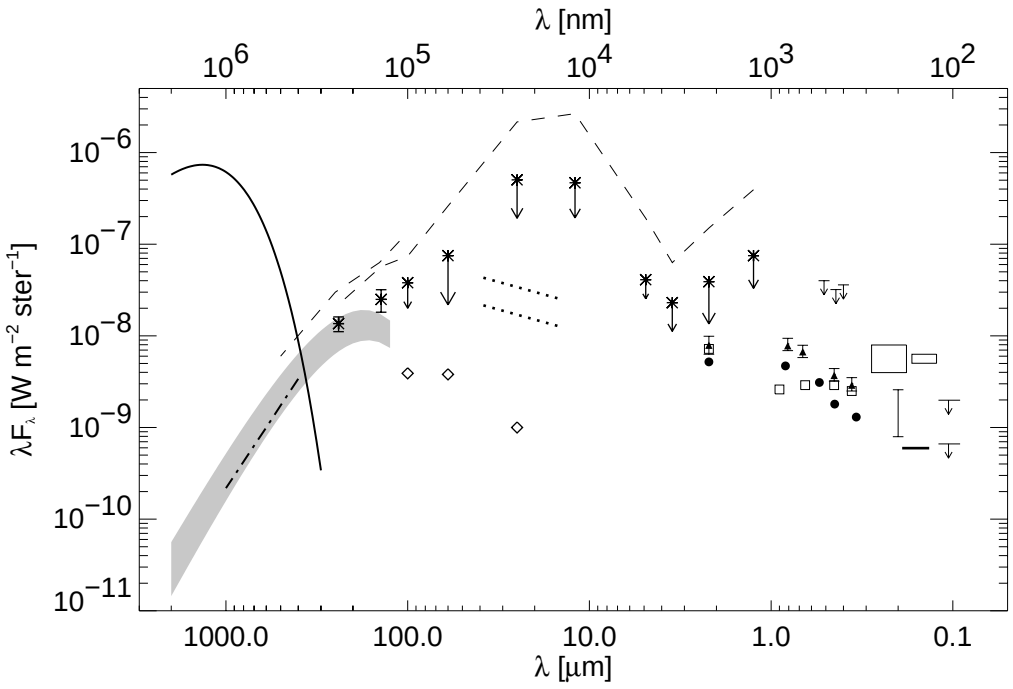

Figure 2.2: *A summary of present measurements and observational limits on the extragalactic background from submillimeter and far-infrared wavelengths to the far ultraviolet region. The 2.728 K blackbody spectrum of the CMB (Fixsen* et al. *1996) is shown as a thick solid line. The grey shaded area and the dash dotted line represent measurements of the CIB at 125–2000 μm and 400–1000 μm by Fixsen* et al. *(1998) and Puget* et al. *(1996), respectively. The thin dashed lines indicate the dark-sky brightnesses (the minimum observed sky brightnesses) between 1.25 μm and 500 μm, which are strict upper limits to the CIB (Hauser 1996). The dark sky brightness illustrates the emission due to zodiacal light peaking below 1 μm, and the thermal emissions from interplanetary and interstellar dust around 10 μm and beyond 100 μm, respectively. The asterisks at 140 μm and 240 μm are detections of the CIB, the asterisks with downward arrows are upper limits on the CIB at the 95% confidence limit, with the arrows extending to the measured residuals after subtraction of foreground emission (Hauser* et al. *1998). The diamonds are lower limits to the CIB in the far infrared from the integrated emission of galaxies (Hacking and Soifer 1991, Gregorich* et al. *1995). An upper limit to the intensity of the CIB at 10–40 μm from γ-γ pair production derived by Dwek and Slavin (1994) is shown for $H_0 = 100$ km/sec Mpc (upper dotted line) and $H_0 = 50$ km/sec Mpc (lower dotted line). The lower limits on the extragalactic background in the near-infrared and optical regions from galaxy counts are shown with different symbols. The results by Cowie* et al. *(1994), Tyson (1995), and Pozzetti* et al. *(1998) are represented by filled circles, open squares and filled triangles, respectively. The downward pointing arrows at 400 nm, 440 nm and 511.5 nm depict the photometric upper limits on the EBL by Mattila (1990), Toller (1983) and Dube* et al. *(1979) as revised by Leinert* et al. *(1998), respectively. The two boxes at 1800–2800 Å and 1230–1680 Å show the estimates of the EUB of (300 ± 100) units (units are defined in Sec. 2.1.5) and (285 ± 32) units by Tennyson* et al. *(1988) and Anderson* et al. *(1979), respectively. Also shown are the results from extrapolated galaxy counts of 40–130 units at 2000 Å by Armand* et al. *(1994) and of a fluctuation analysis of ~ 30 units at 1350–1900 Å by Martin and Bowyer (1989). The downward pointing arrows at 912–1200 Å represent the Voyager upper limits on the EUB from Holberg (1986) (upper arrow) and Henry and Murthy (1995) (lower arrow) using different calibrations.*

Secs. 2.1.6 and 2.1.2). The extragalactic background radiation in the optical spectral range, usually referred to as extragalactic background light (EBL), is extremely difficult to observe because it is swamped by much stronger foreground emissions such as airglow[10], zodiacal light, bright stars and diffuse galactic light, which consists of the integrated light of faint stars and starlight scattered in intergalactic dust and gas clouds. On average, the EBL amounts to only about 2×10^{-3} of the sum of these diffuse optical backgrounds (Tyson 1995). Often the EBL intensity is quoted in units of $S_{10}(\lambda)$, which is the equivalent bolometric surface brightness of a 10^{th} magnitude star of specified spectral type measured at wavelength λ, if its light is uniformly spread over a square degree of sky[11]. Although this unit is not particularly helpful for multi-wavelength comparisons, it illustrates the faintness of the EBL, which has an intensity of about one S_{10}. A variety of approaches have been pursued to measure the EBL (see e.g. the reviews by Toller 1990, Tyson 1990, and Mattila 1990), a few of which are sketched in the following: direct photometry, the dark-cloud method, galaxy counts, and fluctuation analysis.

Direct photometry starts with the total brightness of the night sky, from which all foreground emission has to be eliminated. In general, a disadvantage of direct photometry is that it requires a very accurate determination of the absolute intensities of foreground components such as zodiacal light and airglow, which are much brighter than the EBL. Furthermore, the method does not differentiate between the EBL and the diffuse galactic light and hence only allows one to derive an upper limit to the EBL. Very thorough ground-based photometry of the night sky has been carried out by Dube *et al.* (1979), who dealt differently with each of the accessible foreground components. For example, stars in the field-of-view were blocked by star masks, the zodiacal light was separated on the basis of its solar-like spectrum, and the airglow was measured assuming a secant-law dependence on zenith angle for its intensity. Elimination of the foregrounds yielded an upper limit on the EBL of 3.4 S_{10} (see Fig. 2.2). An unprecedented opportunity for photometry in absence of atmospheric and interplanetary foregrounds was offered by the Pioneer 10 spacecraft as it passed the asteroid belt. Because of the crude spatial resolution of the Pioneer photometer experiment the dominating starlight had to be subtracted based on available star-count data, which was rather uncertain. In addition, the Pioneer photometry had limited accuracy, hence only an upper limit to the EBL of 3.9 S_{10} was obtained (Toller 1983, see Fig. 2.2).

The principal problem of subtracting large absolute intensities in direct photometry is avoided in the dark-cloud method. A differential measurement of the night-sky brightness in the direction of a high galactic latitude dark cloud and its surrounding area, which is (almost) free of obscuring dust, provides a signal that is due to two

[10]Airglow is a dim afterglow of atoms and molecules in the upper atmosphere, which have been excited, usually via dissociation or ionization, by the incident solar radiation.

[11]In physical units, $1\ S_{10}(V)_{G2\,V} = 1.16 \times 10^{-9}$ erg cm^{-2} sec^{-1} ster^{-1} Å^{-1} at blue wavelengths, and 1.09×10^{-9} erg cm^{-2} sec^{-1} ster^{-1} Å^{-1} at red wavelengths (Toller 1990).

components only: the EBL and the diffusely scattered starlight from the dark cloud (Mattila 1990). The main problem here is that the intensity of the scattered starlight in the dark nebula is expected to be equal to or larger than the EBL. The two components can be separated, however, by utilizing a Balmer discontinuity in the intensity of the scattered starlight at about 400 nm. Such features do not occur in the EBL, which arises from the accumulated emission over a large range in redshift, such that any spectral features are washed out. With this approach Mattila (1990) obtained a preliminary estimate of the EBL intensity of $(6.5 \pm 2.5) \times 10^{-9}$ erg cm^{-2} sec^{-1} ster^{-1} Å^{-1} at 400 nm (see Fig. 2.2).

The contribution of galaxies to the EBL can be estimated from deep galaxy counts, which are based on the detection of discrete objects in very deep CCD (Charge-Coupled Device) images of dark sky regions. The method is not sensitive to any uniform or extended component in the EBL, hence its results must be considered lower limits to the EBL. The data imply, however, that the objects dominating the EBL appear smaller than 5 arcsec, making direct CCD imaging a very sensitive technique (Tyson 1995). Lower limits for several wavebands between 340 nm and 2.2 μm have been provided by Cowie *et al.* (1994) from a K-band limited sample with $K \leq 22$ mag, by Tyson (1995) from a sample to an isophotal limiting B_j magnitude of 29 arcsec^{-2}, and by Morgan and Driver (1995) from counts with a limiting magnitude of B = 26 mag [12]. The latter authors not only gave the result of the summed number counts to the limiting magnitude, but also extrapolated the observed number counts down to a limiting magnitude of 38 using a dwarf-dominated luminosity function. The EBL values from the extrapolation are higher than from the summation by factor of 2 to 5 and give an impression of the possible importance of the contribution by very faint galaxies, $m \geq 30$, to the EBL. The best view to date of the optical sky at faint flux levels is provided by the Hubble Deep Field (HDF)[13], which reaches down to 5σ limiting AB magnitudes of roughly 27.7, 28.6, 29.0 and 28.4 in the F300W, F450W, F606W and F814W bandpasses (Williams *et al.* 1996). Using ground-based and HDF data on differential number counts down to the detection threshold, Pozzetti *et al.* (1998) computed the EBL intensity in 3600 Å $\leq \lambda \leq$ 22000 Å (see Fig. 2.2). An extrapolation of the observed differential number counts $N(m)$ to brighter and/or fainter magnitudes was estimated to typically increase the integrated light by less than 20%.

Because galaxies cluster in space, the EBL due to galaxies is not smoothly dis-

[12]The magnitude of a galaxy can be determined in many different ways. The most common magnitudes are metric magnitudes, isophotal magnitudes, and total magnitudes. Metric magnitudes are determined from the light contained within a certain aperture. Isophotal magnitudes are estimates of the light contained within a certain isophotal contour, i.e. a contour of constant brightness [mag/arcsec^2]. Total magnitudes are estimated from metric or isophotal magnitudes by some sort of galaxy-type dependent extrapolation and represent the total light emitted by a galaxy (see e.g. de Vaucouleurs *et al.* 1976b, Mihalas and Binney 1981, de Vaucouleurs *et al.* 1976a, and references therein).

[13]The HDF is centered at 12h 36min 49.4s +62° 12′ 58" (epoch J2000) in the constellation Ursa Major and is the so-far deepest observation obtained with the Hubble Space Telescope.

tributed on the night sky, but exhibits a characteristic anisotropy on the order of $\sim 20 - 30\%$ at scale lengths of a few arc minutes. These fluctuations may be the most efficient means of detecting the galaxy component in the EBL (Tyson 1995). In a statistical analysis of the fluctuations in the EBL at 650 nm Shectman (1974) found a close resemblance to expectations from the clustering of nearby galaxies, providing evidence that galaxies are substantial contributors to the EBL.

The principal interest in the EBL stems from the prospect of using it as a probe of galaxy formation and evolution, because the bulk of the EBL is expected to originate in young stellar populations in galaxies at moderate to high redshift (see e.g. Mattila 1990, Tyson 1995, and references therein). Besides galaxies, the intergalactic gas may also contribute to the EBL (see e.g. Hogan and Rees 1979, Sherman and Silk 1979), but this component is not expected to be significant (see Sec. 2.1.5). It has often been suggested that the integrated background light due to galaxies could be used as a test to discriminate different cosmological models (see e.g. McVittie and Wyatt 1959, Withrow and Yallop 1965, Patridge and Peebles 1967). The intensity of the EBL, however, is influenced much more strongly by galaxy evolution (stellar lifetimes and population evolution) than by the specific expanding or non-expanding cosmological model (see e.g. Harrison 1964, Wesson *et al.* 1987, Wesson 1991), particularly at wavelengths where much of the redshifted ultraviolet emission from early star formation appears.

One way to probe galaxy evolution is to study galaxy number counts $N(m)$ as function of magnitude m in different passbands. These analyses revealed an increase in the $N(m)$ slope with decreasing wavelength, indicating a blue trend at faint magnitudes (Tyson 1995). The average $\log N(m)$ slopes in the B and U passbands are even super-critical, i.e. the slopes would result in a divergent EBL intensity in these bands if there were no decrease in slope below the critical value of 0.4 at the faintest magnitudes $\gtrsim 26$, as observed[14]. The observed blue trend is highlighted by the existence of a population of faint blue galaxies, which have a number density of ~ 300000 deg^{-2}. Their typical apparent magnitude is between 25 and 28 and their redshift range presumably extends between 0.7 and 3. Observations suggest that these galaxies are seen at an epoch of formation of much of their stellar content (Tyson 1995). It will be interesting to see if the sky is similarly crowded with faint galaxies in the K-band as it is in the U and B bands, once surveys in the first passband extend to magnitudes as faint as in the latter two. The counts at the faint end of the K-band data seem to be less than expected, which could indicate negligible galaxy formation for $z > 5$, or the presence of an adequate amount of dust from an even earlier star-formation epoch to hide a later luminous phase (Tyson 1995). Galaxy number-magnitude data alone can not constrain galaxy evolution models sufficiently, and thus it will be crucial to improve number-redshift data, which is more sensitive to cosmology. Then it should be possible to decide whether the EBL indeed is due to normal galaxies.

[14]The calculation of the EBL intensity from number magnitude counts is explained in Appendix A.4.3.

2.1.5 The Extragalactic Ultraviolet Background

The ultraviolet spectral region covers the wavelengths from about 3000 Å down to about 10 Å ($\sim$ 120 eV). Due to absorption by O_3 and O_2 the Earth's atmosphere is opaque at all wavelengths shorter than 2850 Å, and so the ultraviolet universe has to be studied from space. The zodiacal light decreases rapidly into the ultraviolet range, making it far better suited for studies of galactic and extragalactic diffuse backgrounds than the optical region (see previous section). At wavelengths shorter than the Lyman limit of neutral hydrogen[15] at 912 Å, however, the interstellar gas becomes opaque. Hence direct measurements of the extragalactic ultraviolet background (EUB) are not possible at shorter wavelengths. The diffuse ultraviolet background at wavelengths shorter than Lyman α is of galactic and local origin. Since the photoelectric absorption cross-section decreases with increasing energy, $\sigma(E) \sim E^{-3}$, the optical depth of the ISM becomes less than unity again in the soft X-ray band (see next section).

The major challenge for measurements of the EUB at the accessible wavelengths longward of 912 Å, often referred to as the far-ultraviolet region, is to disentangle the extragalactic radiation from galactic foreground emissions. Possible sources of a diffuse galactic background include fluorescence of interstellar molecular hydrogen, atomic emission lines from hot gas in the ISM and/or galactic halo, two-photon emission from the ionized component of the ISM, and the light of hot stars scattering from the interstellar dust grains (see e.g. Henry and Murthy 1995, and references therein). Detailed observations of the galactic ultraviolet emission could provide valuable information on the composition, properties and distribution of interstellar gas and dust. There is a strong correlation between the intensity of the diffuse ultraviolet background radiation and the column depth of neutral hydrogen, $\int N_H dl$, in the same direction (Paresce *et al.* 1980), presumably due to scattering of ultraviolet radiation of O and B stars by interstellar dust[16]. Thus two different approaches have been pursued to measure the intensity of the EUB, photometry and spectroscopy. With photometry one extrapolates to zero neutral-hydrogen column-depth and spectroscopy is used to observe in regions of minimal neutral-hydrogen column-depth.

These measurements indicate that the spectrum of the EUB is most remarkable, featuring quite an abrupt rise at about 1216 Å: shortward of Lyman α so far only upper limits of $\lesssim 100$ units[17] have been obtained, longward of Lyman α a strong intensity

[15]The hydrogen Lyman series comprise all atomic transitions to or from the $n = 1$ level. The Lyman limit refers to the minimum energy required for photoionization from the $n = 1$ level, which is 13.6 eV, corresponding to a wavelength of 912 Å. Similarly, Lyman α denotes the transition between the $n = 1$ and $n = 2$ levels, corresponding to a wavelength of 1216 Å.

[16]The observed correlation follows from the fact that the column densities of dust and neutral hydrogen are strongly correlated.

[17]In ultraviolet astronomy, photon intensities are customarily quoted in "units" or "photon units", which are defined to be the photon intensity per unit wavelength interval in cgs units: photons/cm^2 sec ster Å (see Appendix A.6).

of about 300 units is positively detected (see Fig. 2.2 and Henry and Murthy 1995). There is some scatter in the absolute EUB intensity longward of Lyman α, but this scatter demonstrably reflects a spatial variation in the overall intensity of the ultraviolet background on the sky, presumably due to the patchiness of the ISM, rather than uncertainties in the observations or spectral variations. At a given location the EUB intensity remains unchanged longward of 1216 Å. Given this spectral shape it seems unlikely that significant contamination from galactic diffuse emission is present, however, owing to the lack of an all-sky survey in the far ultraviolet a general uncertainty remains (see e.g. Henry and Murthy 1995, and references therein).

In addition to photometric and spectroscopic results on the EUB, two estimates of the background intensity due to galaxies are available. Martin and Bowyer (1989) presented evidence that part of the isotropic far-ultraviolet background exhibits fluctuations which are consistent with those expected from galaxies, with an intensity of ~ 30 units. A different approach was taken by Armand *et al.* (1994), who used data on galaxy counts at 2000 Å to estimate the diffuse far-ultraviolet intensity due to the integrated light of galaxies. The observed galaxy counts with a limiting magnitude of 18.5 amount to 30 units, the small extrapolation to fainter magnitudes leads to an expected intensity of 40–130 units, comparable to EUB estimates from direct background measurements (see Fig. 2.2). Hence it seems that some extragalactic component is present in the observed far-ultraviolet background.

At present, there are three candidate extragalactic sources of ultraviolet radiation that could conceivably produce a diffuse background at the observed intensity level: radiative decay of exotic particles of cosmological origin, diffuse thermal emission from the intergalactic medium, and the integrated ultraviolet light of galaxies and quasars. The first, more speculative source is of great potential cosmological interest because such exotic particles are prime candidates for non-baryonic dark matter. For example, it was suggested by De Rújula and Glashow (1980) that the dark matter might be massive neutrinos that decay with the emission of an ultraviolet photon. The spectrum of such a decay displays a characteristic jump at the decay-line wavelength and drops steeply, $I_\lambda \sim \lambda^{-5/2}$, towards longer wavelengths (see e.g. Kimble *et al.* 1981). Such a decline is not supported by the observations, making a contribution from the decay radiation of an exotic particle to the EUB unlikely (Henry and Murthy 1995, Jakobsen 1995).

If the ledge around 1216 Å were, indeed, abrupt, the EUB spectrum could be due to redshifted hydrogen recombination radiation from the IGM, which could constitute a significant fraction of the baryonic matter in the universe. Standard big-bang nucleosynthesis predicts that a baryonic IGM must consist primarily of a mixture of about 90% hydrogen and 10% helium atoms. The emission of such a medium can readily be calculated as a function of temperature in collisional and thermal equilibrium. By far the most stringent limits on the IGM come from its absorption properties as observed

in the spectra of high-redshift quasars. The Gunn-Peterson test[18] and the Lyman α forest[19] severely constrain the density of intergalactic neutral hydrogen at high redshift and the structure and evolution of the IGM. In addition, the intensity of the background ultraviolet radiation ionizing the IGM at high redshift can be estimated from the so-called "proximity effect"[20]. Combining all these constraints, Jakobsen (1995) demonstrated that the IGM contributes only marginally to the EUB.

As indicated by the results from the extrapolation of ultraviolet galaxy counts and ultraviolet background-fluctuation measurements, galaxies and quasars must at some level contribute to the EUB. Unfortunately, the observed integrated far-ultraviolet spectra of the different classes of galaxies are not particularly well modelled or understood at present, as the emergent ultraviolet fluxes depend sensitively not only on the details of the assumed star-formation history, but also on the amount, detailed geometry, and other properties of any absorbing dust present in the galaxies. The global galaxy luminosity function at ultraviolet wavelengths is dominated by the emission from massive O and B stars in star-forming regions. Thus spiral and irregular galaxies most likely account for close to 90% of the local galaxy luminosity density and therefore dominate the integrated galaxy background. Compared to visible and longer wavelengths, however, the integrated ultraviolet light of galaxies originates from relatively modest redshifts. As late-type galaxies are generally surrounded by neutral-hydrogen halos which permit little or no radiation to escape below the Lyman α limit, such that this radiation is redshifted out of the observed far-ultraviolet wavelengths at moderate redshifts. Taking into account the fact that main-sequence OB stars have short lifetimes (a few 10^6 years), the integrated far-ultraviolet light of galaxies is primarily a measure of the level of on-going star formation in the local universe, as opposed to the extragalactic background at longer wavelengths which provides a measure of the total accumulated star formation (see Jakobsen 1995, and references therein). Predictions by current evolution models generally span the observed EUB intensity, although with a rather wide range of spectral shapes, implying that the edge in the EUB spectrum at 1216 Å rather is a steep decline (Jakobsen 1995). Quasars seem to contribute only marginally to the EUB, as models for quasar evolution, albeit uncertain, predict only a small contribution to the EUB intensity (Paresce and Jakobsen 1980, Jakobsen 1995,

[18]The Gunn-Peterson test (Gunn and Peterson 1965) constrains the density of intergalactic neutral hydrogen at high redshift from the observed lack of an intense redshift-smeared Lyman α absorption trough seen just shortward of emitted Lyman α in the spectra of high redshift quasars. The test implies that the IGM must be highly ionized and have a temperature $T \gtrsim 10^5$ K. Thus, the IGM was re-heated and re-ionized after recombination, either by dissipative processes, such as shock heating, or by ionizing radiation.

[19]The Lyman α forest is due to Lyman α absorption in intervening hydrogen clouds at different redshifts along the line of sight.

[20]The proximity effect (Murdoch *et al.* 1986) is a deficit of Lyman α absorption systems close to the emission line redshift of the quasar relative to the expected average number density. This effect is attributed to the additional ionization by the Lyman continuum radiation of the quasar on top of the intergalactic Lyman continuum background radiation.

and references therein).

No definite conclusion on the spectrum and the origin of the EUB is possible at the current state of ultraviolet astronomy. The EUB may be produced by galaxies, mostly spirals, and to a lesser extent by quasars.

2.1.6 The Extragalactic X-Ray Background

The existence of a diffuse X-ray background (XRB) was discovered by Giacconi *et al.* (1962) — three years before the detection of the CMB (see Sec. 2.1.2). About a decade later, it had been realized that the origin of the XRB had to be mainly extragalactic, based on the high degree of isotropy revealed by the first X-ray all-sky surveys with the UHURU and ARIEL V satellites (see Zamorani 1995). In fact, the X-ray band, covering the energies from about 120 eV to about 511 keV, is one of the few ranges of the electromagnetic spectrum where the extragalactic emission dominates a large fraction of the sky (Hasinger *et al.* 1998), and thus is ideally suited for studying the extragalactic background. Two alternative hypotheses were discussed for the origin of the XRB: a truly diffuse origin in a hot IGM and the superposition of unresolved, discrete sources. Both possibilities seemed to be supported by the data, which are depicted in Fig. 2.3. On the one hand, Marshall *et al.* (1980) showed that the shape of the XRB in the 3–50 keV range as measured with HEAO-1 (High Energy Astrophysics Observatory) is well fitted by an isothermal bremsstrahlung model corresponding to an optically thin, hot plasma with $kT \approx 40$ keV. In addition, none of the individual classes of known X-ray emitters, in particular AGN, seemed to be characterized by an energy spectral distribution similar to that of the XRB (the so-called "spectral paradox", see e.g. Mushotzky 1984, Boldt 1987). On the other hand, the first deep surveys with the imaging instruments on the EINSTEIN satellite could resolve $\sim 20\%$ of the soft XRB in the 1–3 keV range into discrete sources, a large fraction of which were identified with AGN (see Zamorani 1995, and references therein). Thus the debate continued until the hot IGM hypothesis for the origin of the XRB was convincingly eliminated by the FIRAS/COBE results on the spectrum of the CMB (see Sec. 2.1.2). The tight limits on the Comptonization parameter y derived from the minute deviations of the CMB from a pure blackbody spectrum imply that a hot IGM can at most produce 10^{-4} of the observed XRB (Wright *et al.* 1994a), reducing the question of the origin of the XRB to identifying the responsible point sources.

Substantial contributions to understanding the origin of the soft XRB came from very deep observations of the Lockman Hole[21] with ROSAT (Röntgen Satellit) in the

[21]The so-called Lockman Hole, a small region of $\lesssim 1\,\mathrm{deg}^2$ centered at $(l,b)^{II} \approx (149.5°, 53.2°)$, is the direction of the absolute minimum in the galactic neutral hydrogen column density (Lockman *et al.* 1986). The Lockman Hole was chosen for these soft X-ray observations to minimize the absorption by neutral hydrogen, thus improving the chance of detecting faint sources and, more importantly, removing as far as possible any potential biases caused by variations in the absorbing column density.

0.5–2 keV range. Based on the $\log N - \log S$ function derived from these observations 70–80% of the 0.5–2 keV XRB is resolved into discrete sources (Hasinger *et al.* 1998). Fluctuation analyses have shown that the remaining XRB intensity can be accounted for by source fluctuations at the faintest fluxes (Hasinger *et al.* 1993, Branduardi-Raymont *et al.* 1994). The uncertainty in the resolved fraction at soft X-rays is not dominated by the source counts, but by the systematic error in the determination of the absolute background intensity (see Fig. 2.3). Models of the diffuse X-ray emission in the 0.1–10 keV range have to take into account at least three components: a soft thermal component with $kT \approx 0.07$ keV (the Local Hot Bubble, presumably the remnant of a recent, local supernova) dominating in 0.1–0.3 keV, a hard thermal component with $kT \approx 0.14$ keV (probably associated with the galactic halo), and the XRB, which can be represented by a single power law or a broken power law with break energy $\lesssim 1$ keV. A further complication for spectral fits of the X-ray emission arises from absorption of the latter two components by neutral hydrogen, in addition to response cross-calibration problems and uncertainties in the subtraction of instrumental background (see e.g. Miyaji *et al.* 1998). Identification of the optical counterparts of the X-ray sources in the Lockman Hole survey revealed that they are mostly QSOs and Seyfert galaxies with broad emission lines (Schmidt *et al.* 1998). A large fraction of the faint X-ray sources are optically resolved low-luminosity active galactic nuclei (mostly Seyfert galaxies), some of which show clear evidence of gas and dust obscuration in the soft X-ray and optical bands (Hasinger 1998).

Based on pure luminosity-evolution models, however, these broad line AGN are predicted to contribute only 30–50% of the soft XRB, and much less to the hard XRB (Hasinger *et al.* 1998). It has been reported that a new population of X-ray active, but optically relatively normal narrow-emission-line galaxies (NELG) start to dominate the X-ray counts at the faintest X-ray fluxes, and could ultimately contribute the majority of the soft XRB. These claims are, however, based on survey data that are severely limited by source confusion at the faintest X-ray fluxes, and are challenged by the results of the deepest ROSAT Lockman Hole survey (see Hasinger *et al.* 1998, Hasinger 1998, Schmidt *et al.* 1998, and references therein). In the framework of current unification schemes of active galactic nuclei (see e.g. Antonucci 1993, Urry and Padovani 1995) some models postulate a large population of faint, intrinsically absorbed AGN, such that most of the soft XRB, and possibly all of the hard XRB, is due to AGN (see e.g. Madau *et al.* 1993, Comastri *et al.* 1995, Zdziarski 1996)[22]. It has to be noted, however, that above about 100 keV all of these models fall short of the hard XRB intensity as determined by Gruber (1992) and Kinzer *et al.* (1997), possibly implying that new or additional source populations such as radio-loud Seyfert galaxies or so-called misaligned blazars (see Sec. 2.2.1.2) or Type Ia supernovae (see Sec. 2.2.1.4) are needed to account for the hard XRB at these energies. It has also been

[22]As discussed in more detail in Sec. 6.5, in these synthesis models the decrease of the XRB below about 30 keV results from intrinsic photoelectric absorption in the AGN, while the roll-over at higher energies arises from the red-shifted intrinsic exponential cut-offs at about 100 keV.

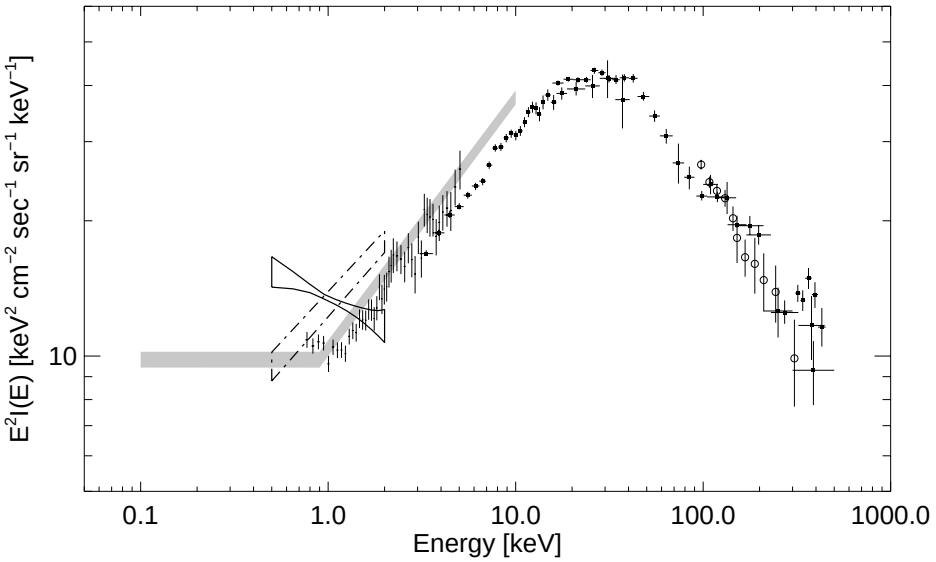

Figure 2.3: *The spectrum of the XRB as it is known today. At soft X-ray energies the solid and dash-dotted regions indicate the ROSAT results by Hasinger (1992) and Georgantopoulos* et al. *(1996), respectively. The grey shaded region is the result of a broken power law fit to the combined ROSAT and ASCA data by Miyaji* et al. *(1998). The data points at keV energies were derived by Geandreau* et al. *(1995) using ASCA. At higher energies, the HEAO-1 data from Gruber (1992) and Kinzer* et al. *(1997) are shown with filled squares and open circles, respectively.*

proposed that reflection-dominated AGN (Zdziarski *et al.* 1993) and starburst galaxies (Griffiths and Padovani 1990) are important contributors to the XRB, in particular above 2 keV.

A crucial test for the competing models is a direct measurement of a sample of sources at harder X-rays, where the bulk of the energy density of the XRB resides (see Fig. 2.3). A first step in this direction is the medium-survey program conducted in the 2–10 keV band with ASCA (Advanced Satellite for Cosmology and Astrophysics), which carries the first imaging instruments for these energies. This survey already resolved $\sim$ 27% of the XRB in the 2–10 keV band into discrete sources (Cagnoni *et al.* 1998). The $\log N - \log S$ distribution derived from this survey is in very good agreement with the predictions from models based on AGN unification schemes. It is therefore possible that the sources of the hard XRB, e.g. the heavily absorbed AGN in the models of Madau *et al.* (1993) and Comastri *et al.* (1995), are undersampled in the soft X-ray surveys because absorption makes them too faint to be detected at these energies. The question of whether or not the XRB is mainly due to various classes of AGN may be be finally resolved by the next X-ray missions covering the 1–10 keV range with improved sensitivity and resolution.

Finally, it is worth mentioning that a dipole anisotropy of the XRB, consistent

within instrumental uncertainties with the dipole of the CMB (see Sec. 2.1.2), has been determined with HEAO-1 data. Using the A-2 High-Energy Detector (HED), Shafer (1983) measured a dipole component with amplitude of $(0.5 \pm 0.2)\%$ and apex at $(l,b)^{II} = (282° \pm 75°, 30° \pm 60°)$ at 95% confidence in the 2.5–60 keV range. With kinematic interpretation a velocity of (475 ± 165) km/sec is obtained. A similar dipole anisotropy with amplitude $(2.2 \pm 0.7)\%$, corresponding to a peculiar velocity of (1450 ± 440) km/sec, and apex at $(l,b) = (304°, 26°)$ was derived by Gruber (1992) using the A-4 Medium-Energy Detector (MED) data from 95–165 keV. The latter result may be influenced by a concentration of hard X-ray sources in the general vicinity of the apex. Recently, Kinzer *et al.* (1997) reported that the XRB appears to be isotropic within 4% in the 80–400 keV range.

2.1.7 The Extragalactic Gamma-Ray Background

The γ-ray regime covers the highest photon energies above about 511 keV. Historically, the measurement of the extragalactic γ-ray background (EGB) has always been beset with great experimental difficulties. Due to the opaqueness of the Earth's atmosphere to γ-radiation observations at these energies can only be performed from balloons at the top of the atmosphere or from space. The high cosmic-ray intensity in these environments produces an intense background of secondary γ-rays in the detectors, in addition to the bright γ-ray albedo from the Earth's atmosphere, against which the much weaker signal of the EGB has to be discerned (see Sec. 4.1).

The history of measurements of the EGB is reviewed in Sec. 2.3. Briefly, the hard XRB in the 100–400 keV range (e.g. Mazets *et al.* 1975) and the EGB from 35 MeV to about 150 MeV (Thompson and Fichtel 1982) were found to follow power laws with spectral indices -2.8 and -2.35, respectively. In the MeV range, an excess of emission above the extrapolations from lower and higher energies was determined quite consistently with a number of different experiments operated in different environments (see e.g. Trombka *et al.* 1977, Schönfelder *et al.* 1980), as illustrated in Fig. 2.9. Doubt remained concerning the existence of the MeV bump, because the energy range from $\sim$ 500 keV to $\gtrsim$ 10 MeV is experimentally the most challenging and plagued with exceptionally high instrumental backgrounds due to locally produced nuclear γ-rays (see e.g. Daniel and Lavakare 1975).

Recent studies of the EGB with the instruments COMPTEL (Kappadath 1998, Bloemen *et al.* 1999, Weidenspointner *et al.* 1999, and this thesis) and EGRET (Sreekumar *et al.* 1998) onboard the Compton Gamma-Ray Observatory (CGRO), and also an analysis of data from the Gamma-Ray Spectrometer (GRS) onboard the Solar Maximum Mission (SMM) (Watanabe *et al.* 1997), have greatly simplified the overall shape of the EGB spectrum and extended the observed energies to 100 GeV, as depicted in Fig. 2.4. No evidence for the existence of the MeV bump was found, instead the recent results suggest that we see the transition from a softer, low-energy component to a

harder, high-energy component, both power-law shaped, with the transition occuring at a few MeV (see Weidenspointner *et al.* 1999, and Sec. 6.3.3 of this thesis).

The large-scale anisotropy of the EGB above 100 MeV was examined with EGRET. A comparison of 36 independent regions of the sky showed that the integrated sky intensity above 100 MeV is consistent with a uniform distribution in regions outside the inner galaxy (Sreekumar *et al.* 1998). The average integrated intensity above 100 MeV in the 36 independent sky regions is $(1.47 \pm 0.33) \times 10^{-5}$ph/(cm^{2}sec ster), the corresponding result from the combined data is $(1.45 \pm 0.05) \times 10^{-5}$ph/(cm^{2}sec ster). Of the 36 measurements, 69% fall within 1σ, and 97% fall within 2σ of the mean. It has to be noted that there is evidence that these observations contain galactic diffuse emission that has not yet been accounted for. Excluding the inner regions of the galaxy which are not more than 60° from the galactic center results in a sample of 28 independent observations, whose intensity distribution again is consistent with isotropy. A first attempt to examine the fine-scale anisotropy of the EGB above 100 MeV was made in a fluctuation analysis on EGRET data (Willis 1996). Unfortunately, it turned out that the quality of the data was not sufficient to rule out a significant, truly diffuse component in the EGB. The contribution of unresolved point sources was found to be 6–100% of the observed EGB intensity. It has to be emphasized, however, that the fluctuation analysis is sensitive to all intensity variations, independent of the nature of the background sources. Therefore it cannot be used to determine the contribution of a specific class of sources, such as blazars.

As part of this thesis, the isotropy of the CDG was studied on scales of a few steradian with COMPTEL (see Sec. 6.4). No significant anisotropies in the diffuse emission at $|b| > 30°$ could be found in the 0.8–30 MeV energy range. This result is consistent with the assumption of an extragalactic origin of the CDG, which implies isotropy on large angular scales. Upper limits on the relative deviations from isotropy at the 95% confidence level were derived, which constrain the relative deviations to less than about 25–45%.

The EBG is of particular interest to cosmology because of the transparency of the universe to γ-rays back to very high redshifts (see e.g. Stecker 1971). A large number of possible origins for the EGB have been proposed, all of which fall into one of the following two distinct categories: the superposition of unresolved, discrete sources or a truly diffuse origin. Individual models and physical concepts are described in detail in Sec. 2.2. None of the proposed models can, however, explain by itself the entire spectrum of the EGB, which spans at least 6 orders of magnitude in energy. Most likely, the EGB is the sum of a number of different components, each dominating a specific energy range, which may be disentangled once the spectrum of the EGB is known with sufficient accuracy and precision. In the future, additional leverage for the separation of the supposedly different contributions to the EGB may come from observations of the large-scale and fine-scale anisotropy of the intensity of the EGB. First steps towards studying these anisotropies have already been made with EGRET and COMPTEL. Better instruments with improved sensitivity and resolution are needed to address the

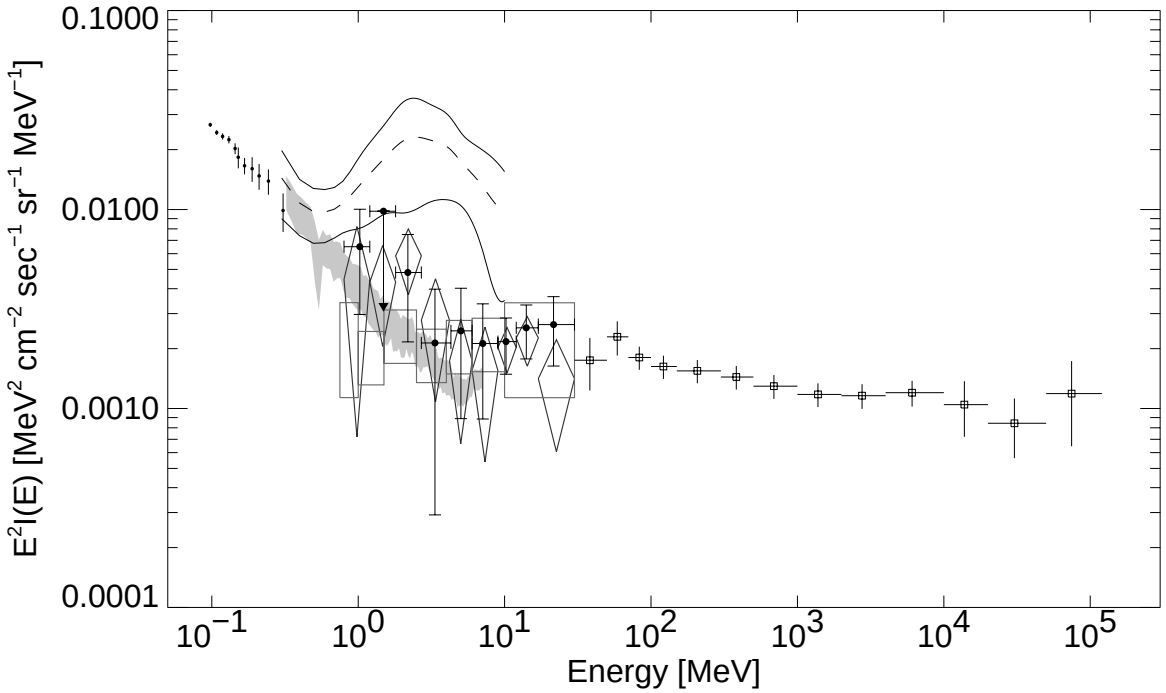

Figure 2.4: *A comparison of current results on the spectrum of the EGB. The hard X-ray data are from Kinzer* et al. *(1997) obtained with HEAO-1, the grey shaded band depicts the preliminary GRS/SMM result of Watanabe* et al. *(1997). The historic 'MeV bump' is illustrated by the Apollo result of Trombka* et al. *(1977) (compare the illustration of the historic measurements of the EGB in Fig. 2.9). The recent COMPTEL results by Bloemen* et al. *(1999), Kappadath (1998), and Weidenspointner* et al. *(1999)/this work are depicted by boxes, diamonds and data points (filled circles), respectively. The results of the analyses by Kappadath (1998) and Weidenspointner* et al. *(1999)/this work are plotted with their total 1σ errors, taking onto account the statistical as well as the various systematic uncertainties (the arrow depicts a 2σ upper limit and reaches down to the intensity value). The high energy data above 30 MeV have been derived by Sreekumar* et al. *(1998) with EGRET (open squares). To date, no extragalactic diffuse γ-radiation has been detected above 100 GeV.*

large-scale and fine-scale anisotropy of the EGB in more detail.

The current results suggest that the EGB up to 100 GeV is more likely to have originated from the superposed emission of various classes of unresolved discrete, extragalactic sources than from a truly diffuse origin (see Sec. 2.2). Above about 30 MeV a significant fraction of the EGB seems to be due to the blazar class of AGN, other contributors may be starburst galaxies and normal galaxies. At MeV energies and below, candidate source populations are radio-loud Seyfert galaxies, misdirected blazars and MeV-blazars, as well as cosmological Type Ia supernovae[23] and perhaps starburst

[23]A determination of the EGB contribution from Type Ia SNe would provide a probe for the history

galaxies. The contributions from these different source populations are, however, still quite uncertain, and it is possible that another, yet unidentified, source population may be required to account for the observed intensity at these energies.

Above 100 GeV no extragalactic diffuse γ-radiation has been detected so far, but atmospheric Čerenkov telescopes have already measured significant emission from BL Lac objects in the ~ 300 GeV to ~ 30 TeV range (Weekes *et al.* 1997). These telescopes detect the Čerenkov light from the electromagnetic cascade initiated by the primary photon in the Earth's atmosphere, which serves as a convertor. At energies above ~ 30 TeV, there are enough residual particles in the electromagnetic cascades that they can be detected at high mountain altitudes using arrays of particle detectors. To date, no verifiable detections have been reported by these particle air shower arrays (Weekes *et al.* 1997). The extension of the spectra of extragalactic sources well beyond 1 TeV opens a new, exciting aspect of γ-ray astronomy. The absorption features in the γ-ray spectra of distant extragalactic sources due to γ-γ pair production of primary γ-rays of very high energy with the diffuse extragalactic background radiation at lower energies, in particular the CMB and the CIB, as well as the radiation from secondary pair cascades contain unique cosmological information about the intergalactic photon and magnetic fields, and their evolution in time (see e.g. Stecker *et al.* 1992, Weekes *et al.* 1997, Coppi and Aharonian 1997, and references therein). For example, Dwek and Slavin (1994), De Jager *et al.* (1994), and others have claimed tentative determinations of the CIB based on the apparent evidence for attenuation of TeV γ-rays from the BL Lac Mrk 421. Recently, however, Krennrich *et al.* (1997) have reported the detection of γ-rays from that source exceeding 5 TeV, concluding that there is at present no evidence for attenuation by pair production on optical or near-IR photons, turning the tentative determinations of the CIB into upper limits, as already emphasized by Dwek and Slavin (1994) (see Sec. 2.1.3).

2.1.8 Summary and Multiwavelength Overview

The previous sections provided a glimpse on the very wide range of observations, experimental techniques and astrophysics that have to be considered when studying the physics of the extragalactic background radiation (EBR). The EBR provides a unique window on a variety of fundamental topics in cosmology, astrophysics and particle physics, ranging from the origin of the universe, the formation of structure and the evolution of galaxies, the formation of stars and the production of metals, gas and dust, to the properties of (exotic) elementary particles. The multitude of objects and processes that manifest themselves in the EBR can only be disentangled by observing the EBR at all accessible wavelengths. The full multiwavelength spectrum of the EBR from radio wavelengths to γ-rays as it is known today is depicted in Fig. 2.5. From

---

of star formation independent of measurements in the optical/UV and far-IR (see Secs. 2.2.1.4 and 2.1.3).

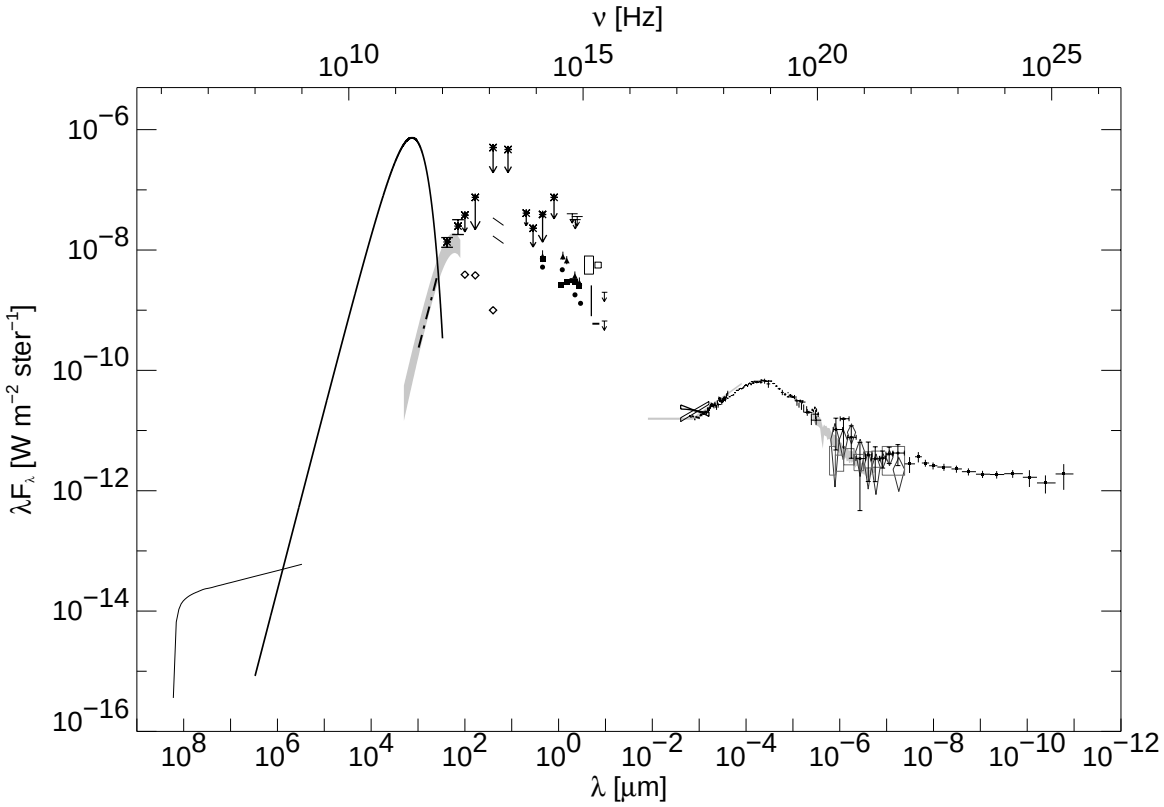

Figure 2.5: *The full multiwavelength spectrum of the extragalactic background radiation from radio wavelengths to the γ-ray regime as it is known today. The spectrum summarizes the data on individual wavebands depicted in Figs. 2.1–2.4.*

the point of view of astrophysics, the wavebands divide naturally into those in which the physics involves "thermal" processes, and those which are probably dominated by high-energy astrophysical processes, often referred to as "non-thermal" processes[24] (Longair 1994b).

The millimeter, infrared, optical and ultraviolet wavebands (see Secs. 2.1.2–2.1.5) are probably dominated by thermal processes. Among all wavebands, the cosmic microwave background (CMB) is unique in a number of ways. The CMB is the only truly "cosmic" EBR component containing information on the very distant past of the cosmos, as the CMB is the cooled thermal spectrum of the hot early stages of the universe as a whole. In addition, the CMB seems to be the only EBR component of truly diffuse origin. The spectrum of the CMB is the most perfect example of a blackbody spectrum that has been found in nature to date. The almost perfect blackbody

[24]The distinction between thermal and non-thermal processes is not defined by energy, but by the distributions that the involved particles and photons follow. In thermal processes particles follow a Maxwell distribution, photons have a blackbody spectrum. In non-thermal processes both particles and photons follow other distributions, which often can be approximated by power laws.

shape of the CMB spectrum places severe constraints on the thermal history of the universe, even before recombination, thereby e.g. ruling out a significant contribution of a hot intergalactic medium to the XRB (see Secs. 2.1.2 and 2.1.6). The anisotropy of the CMB offers a unique opportunity to probe the initial density fluctuations that were the seeds for subsequent structure formation, as well as to determine cosmological parameters such as Ω, Λ and H_0.

The EBR at infrared, optical and ultraviolet wavelengths is most likely dominated by thermal emission from galaxies and thus ultimately by thermal emission of stars and dust. The EBR in these wavebands allows us to probe the formation and evolution of galaxies as well as the formation of stars and the production of gas and dust. As was pointed out in the previous sections, it is of utmost importance for this endeavour to observe the EBR at all wavelengths from far-IR to near-UV as the intensities in each of the individual wavebands are intimately connected. For example, studies of the star-formation rate have to take into account that a significant fraction of the primary star emission at optical and ultraviolet wavelengths is absorbed and reradiated in the far-infrared. In this context it has to be noted that star-formation activity may also reveal itself in conspicuous edges or steps in the EGB at MeV energies due to γ-ray line emission from Type Ia SNe (see Sec. 2.2.1.4). The current EBR detections and limits already impose severe constraints on models for the formation and evolution of galaxies, requiring the models to include the chemical evolution of the galaxies and the production of dust. The IR to UV EBR is much less suited to discriminate different cosmological models than the CMB, because the intensity in the former is influenced by galaxy evolution much more than by the specific cosmological model.

The wavelengths involving high-energy astrophysical processes are the radio, X-ray and γ-ray regions of the electromagnetic spectrum (see Secs. 2.1.1, 2.1.6 and 2.1.7). In these wavebands, the EBR seems to be dominated by the non-thermal emission of various classes of AGN. In contrast to the emission from normal galaxies, which is powered by nuclear fusion, the ultimate energy source of AGN is gravity, specifically the accretion of matter onto a massive black hole (see Sec. 2.2.1.2). In all models of galaxy evolution mergers and tidal interactions have a major impact not only on normal galaxies, but also on the formation of active galactic nuclei. Unravelling the contributions of the various AGN classes to the non-thermal wavebands of the EBR will therefore provide valuable constraints on the evolution of normal galaxies dominating the thermal EBR wavebands, and vice versa.

To conclude this summary, typical energy and photon-number densities in each waveband in which the EBR has been positively detected are listed in Table 2.1 (based on Table 1.3 in Longair 1994b, p. 347). It has to be emphasized that these numbers are usually very rough estimates and, for any precise calculation, integrations should be carried out over the relevant regions of the spectrum[25], as was done to redetermine

[25]For an isotropic radiation field the photon-number density n is connected to the photon intensity I through $n = \frac{4\pi}{c} I$, with c denoting the speed of light (see Appendix A.5).

Waveband	Energy Density of Radiation [eV m^{-3}]	Number Density of Photons [m^{-3}]
Radio	$\sim 5 \times 10^{-2}$	$\sim 10^{6}$
Microwave	3×10^{5}	5×10^{8}
Infrared	?	?
Optical	$\sim 2 \times 10^{3}$	$\sim 10^{3}$
Ultraviolet	?	?
X-Ray	75	3×10^{-3}
γ-Ray	8.2	1.3×10^{-6}

Table 2.1: *The energy densities and photon densities of the EBR in different regions of the electromagnetic spectrum at the current epoch. Numbers are only given for those wavebands in which the EBR has been positively detected. Note that the quoted densities are usually rough estimates and, for any precise calculation, integrations should be carried out over the relevant regions of the spectrum. The table is adapted from Table 1.3 on p. 347 in Longair (1994b) except for the numbers for the γ-ray waveband, which were recalculated based on the current results on the EGB (see Sec. 2.1.7).*

the densities in the γ-ray waveband from the current results on the EBR (see previous section). These rough figures are often useful for making simple estimates of the importance of physical processes in a cosmological setting.

As can be seen in Fig. 2.5 and Table 2.1, the majority of the EBR photons are due to the CMB, which also contains the bulk of the EBR energy density. The integrated EBR energy density in the infrared, optical and ultraviolet wavebands most likely is less than that in the CMB, although the CIB intensity still has not been positively detected except at the longest wavelengths. The EBR photon-number density in the radio waveband is rather large, however, the corresponding energy density is minute. Finally, in the X-ray and in particular the γ-ray wavebands the photon densities are exceedingly low, and the energy densities are very small compared to those in the thermal sections of the EBR.

2.2 Possible Origins of the Extragalactic Gamma-Ray Background

A large number of possible origins for the EGB have been proposed over the years (see e.g. Fichtel and Trombka 1981, Ramana Murthy and Wolfendale 1993, Gehrels and Cheung 1996, Sreekumar *et al.* 1997). Exhaustively covering this vast literature would by far exceed the scope of this thesis, thus the overview presented in this section is restricted to those models that either have stood the test of time, or are of historical

importance, or great potential physical interest. All of these models fall into one of the two distinct categories for the origin of the EGB, both of which are discussed separately below: the superposition of unresolved, discrete sources or a truly diffuse origin.

None of the proposed models can by itself explain the entire spectrum of the EGB, which spans at least six decades in energy. Most likely, the EGB therefore is the sum of a number of different components, each dominating a specific energy range, which may be disentangled once the spectrum of the EGB is known with sufficient accuracy and precision. In the future, additional leverage for the separation of the supposedly different components contributing to the EGB may come from observations of the large-scale and fine-scale anisotropy of the intensity of the EGB. First steps towards studying the large-scale and fine-scale anisotropy have already been made (see Sec. 2.1.7), however, better instruments with improved sensitivity and resolution are needed to address the large-scale and fine-scale anisotropy of the EGB in more detail.

Historically, diffuse mechanisms were favoured over the superposition of discrete point sources until the launch of the Compton Gamma-Ray Observatory (CGRO) in 1991, simply because the detection of only four extragalactic sources had been reported at γ-ray energies until then[26], all active galactic nuclei (AGN): Cen A (Hall *et al.* 1976), NGC 4151 (Di Cocco *et al.* 1977), 3C 273 (Swanenburg *et al.* 1978) and MCG 8-11-11 (Perotti *et al.* 1981). Of these four AGN 3C 273 was the only one detected above 10 MeV. The dire state of extragalactic γ-ray astronomy was improved dramatically by CGRO, which has thus far detected more than 80 active galaxies (see e.g. Johnson *et al.* 1997, Hartman *et al.* 1997), reversing the current thinking on the origin of the EGB: it now seems more likely that the EGB originates from the superposition of various classes of discrete, extragalactic sources than from truly diffuse mechanisms.

2.2.1 Models based on the Superposition of Unresolved Point Sources

2.2.1.1 Normal Galaxies

Normal galaxies are an obvious candidate class of discrete sources that may contribute to the EGB as they are abundant in the universe and known to emit at all observable γ-ray energies. The diffuse emission from our galaxy stands out clearly against the isotropic glow of the EGB as an intense band of emission along the galactic plane dominating the γ-ray sky (see e.g. Strong *et al.* 1996, Hunter *et al.* 1997a). In addition, emission from the Magellanic Clouds[27], which are our closest neighbouring galaxies

[26]In fact, a fifth extragalactic γ-ray source had been observed, SN 1987A in the Large Magellanic Cloud (Matz *et al.* 1988), confirming that supernovae may indeed contribute to the EGB around 1 MeV (see Sec. 2.1.7). Supernovae, however, cannot explain γ-ray emisson that extends over many orders of magnitude in photon energy.

[27]More precisely, only the Large Magellanic Cloud has been observed above 100 MeV (Sreekumar *et al.* 1992). The non-detection of the Small Magellanic Cloud, which in contrast to the Large Mag-

at a distance of about 50 kpc, has been detected at γ-ray energies above 100 MeV (Sreekumar *et al.* 1992, 1993).

The diffuse galactic (continuum) emission arises from three different physical mechanisms: decay of π^0 mesons produced in nuclear interactions between cosmic-ray particles and nuclei of the interstellar medium, bremsstrahlung produced in Coulomb scatterings of cosmic-ray electrons on the nuclei and electrons of the interstellar medium, and γ-rays produced in inverse Compton scatterings of high-energy cosmic-ray electrons on soft photons of the interstellar radiation field (see e.g. Bloemen 1989, Strong 1996, Hunter *et al.* 1997b, Strong *et al.* 1999, and references therein, see also Sec. 2.2.2.3). Below about 8 MeV, γ-ray line emission from nuclear deexcitation may add a little to the total galactic luminosity at γ-ray energies (e.g. Bloemen and Bykov 1997, and references therein). The contribution of point sources to the total galactic γ-ray luminosity is uncertain but expected not to exceed 10–20% (Strong 1996). In particular, pulsars have been shown to add very little to the diffuse emission at low γ-ray energies, but may account for up to 25% of the observed intensity above 1 GeV (Pohl *et al.* 1997). To good approximation, the galactic γ-ray emission is therefore due to diffuse production processes which are proportional to the cosmic-ray energy density and to either the density of the interstellar medium or the density of the interstellar radiation field, depending on which of the production processes is dominant.

A reliable estimate of the contribution of normal galaxies to the EGB is currently hampered by our ignorance concerning their γ-ray luminosity function. A determination of the γ-ray luminosity function of normal galaxies, describing the evolution of the space density and emission of these sources with cosmic epoch, is beyond the capabilities of current instruments, which lack the required sensitivity and spatial resolution. It is therefore necessary to resort to simplifying asumptions and models to predict the diffuse γ-ray intensity from normal galaxies. Three different approaches have been pursued so far.

The first approach is to estimate the mean γ-ray luminosity and density of normal galaxies based on some indicator which is observationally accessible. For lack of other data, the ratio between the γ-ray luminosity and the chosen indicator is determined from our own galaxy, assuming that the Milky Way is a "typical" normal galaxy. If in addition evolutionary effects and absorption processes are neglected, then the diffuse γ-ray background from normal galaxies is proportional to the mean of the product of luminosity and density (see e.g. Strong *et al.* 1976). Using the optical luminosity and the mean neutral hydrogen density as an indicator for the γ-ray luminosity of normal galaxies, Strong *et al.* (1976) estimated a contribution of about 5% and 2% to the EGB above 100 MeV, respectively. Similarly, Erlykin and Wolfendale (1995) obtained a contribution of about 3% above 100 MeV based on a direct estimate of the density of normal galaxies and the luminosity of our galaxy. These results are consistent and in

---

ellanic Cloud is believed to be in a non-equilibrium state, strongly suggests that the bulk of the cosmic-ray energy density is galactic, and not metagalactic, in origin (Sreekumar *et al.* 1993).

agreement with other first-order estimates by Kraushaar *et al.* (1972) and Fichtel *et al.* (1978), who concluded that the emission from normal galaxies can at best account for 10% of the observed EGB intensity at energies above 100 MeV.

An alternative approach is to assume that the γ-ray luminosity of a normal galaxy is proportional to the luminosity in another waveband, specifically the radio luminosity. A rough proportionality between the γ-ray and the radio luminosity of a normal galaxy may be expected since the emission in both wavebands is produced by cosmic rays (see e.g. Setti and Woltjer 1994). Again, the assumed proportionality is determined from data on our galaxy. Assuming in addition that this proportionality is the same at all cosmic epochs, the diffuse γ-ray background from normal galaxies, including evolutionary effects as inferred from radio observations, is proportional to the contribution of normal galaxies to the extragalactic radio background (ERB) (see e.g. Strong *et al.* 1976). Following this line various consistent results for the contribution of normal galaxies to the EGB above 100 MeV have been obtained: 4% (Strong *et al.* 1976), 10% (Setti and Woltjer 1994) and 5.7% (Erlykin and Wolfendale 1995).

Finally, a more self-consistent approach is to derive the γ-ray luminosity of normal galaxies as a function of cosmic epoch from evolutionary models of the galaxy, in particular its cosmic-ray density and gas density, which were developed to explain the observed elemental abundances and the chemical composition of the solar system and its neighbourhood (see e.g. Lichti *et al.* 1978). In a first attempt Lichti *et al.* (1978) considered three different models for the galactic supernova rate (assuming that supernovae are the source of the cosmic radiation) and gas density, and three different emission models, in which the γ-ray luminosity was taken to be proportional to the optical luminosity. For most of the nine combinations of galaxy evolution and γ-ray emission the predicted contribution to the EGB above 100 MeV is $\lesssim 20\%$, however, in a few cases normal galaxies may contribute significantly above 100 MeV, although the predicted spectrum is somewhat harder than the spectrum of the EGB. In the 10–100 MeV range none of the models can account for the EGB. Similarly, Bignami *et al.* (1979) reached the conclusion that normal galaxies only contribute significantly to the EGB from 1–150 MeV in the presence of evolution. By comparison with the observed EGB intensity above 200 MeV they found that evolution can enhance the γ-ray background due to normal galaxies by no more than a factor of 10. Another attempt to estimate the γ-ray background from normal galaxies based on their chemical evolution was made by Prantzos and Aubert (1995). From the fact that B and Be were much more abundant in the early galaxy than at present, while their ratio remained constant at a value consistent with what is expected from cosmic-ray production they concluded that galactic cosmic rays were more efficiently confined in the early (halo) phase of the galaxy than at present. As a result, the galactic cosmic-ray intensity was very high and consequently the production of γ-rays from π^0 decay enhanced. This scenario might apply to all normal galaxies, in particular spiral galaxies. In their calculation Prantzos and Aubert (1995) did not self-consistently derive the γ-ray spectrum of normal galaxies, but rather adopted a model for the current galaxy, with

pure luminosity evolution. They found that a "bright" early phase in the evolution of normal galaxies can entirely explain the EGB at 30–150 MeV. In the absence of evolution, the EGB contribution is expected to be negligible.

In summary, it cannot be ruled out that normal galaxies can account for an appreciable fraction of the EGB intensity. The importance of their contribution, howver, depends upon still uncertain evolutionary effects.

2.2.1.2 Active Galaxies

Up to 10% of all galaxies in the observable universe harbour an active nucleus (Robson 1996), a very small region at the center of the host galaxy in which a very high luminosity is produced, probably by physical processes other than the nuclear fusion that powers stars. This luminosity can exceed by far the luminosity of the remainder of the host galaxy. In contrast to the spectral energy distribution (SED) of normal galaxies, which peaks around the optical waveband as it is dominated by the thermal emission from stars, the SED of these active galaxies or active galactic nuclei (AGN) is usually dominated by non-thermal emission and often has maxima in the radio-/far-infrared waveband, in the infrared waveband, and at ultraviolet and γ-ray energies. In addition, the luminosity of these "active" galactic nuclei is highly variable at all energies, in contrast to the steady emission from "normal" galaxies. There are indications that AGN are formed at early epochs of the universe through mergers of normal galaxies, and that the AGN activity decreases with cosmic time, so that some of the normal galaxies at the current epoch may actually be dormant active galaxies (see e.g. Robson 1996, and references therein).

Empirically, AGN have been classified according to a large number of different detection criteria and morphological, spectral, polarization, and variability characteristics, giving rise to a confused variety of different names and classifications. One way to impose order on this chaos is to organize the principal classes of AGN according to their radio loudness, their optical and ultraviolet spectra and, within each of the groupings, their luminosity, as is done in Table 2.2 (Urry and Padovani 1995). Roughly 15–20% of all AGN are classified as radio-loud, meaning that the ratio of their 5 GHz radio flux to their optical B-band flux F_5/F_B is greater than ~ 10 (Kellermann *et al.* 1989). The characteristic of radio loudness may somehow be related to the type of host galaxy (most radio-loud AGN are ellipticals, most radio-quiet AGN are spirals) or to the spin of the central black hole (see below), which might enable the formation of relativistic jets (see e.g. Urry and Padovani 1995, and references therein). Based on the characteristics of their optical and ultraviolet radiation, AGN can be divided into three broad types. Type 1 AGN have bright continua and broad (and sometimes also narrow) emission lines, Type 2 AGN have weak continua and only narrow emission lines, Type 0 AGN, which are rare, have very unusual spectra. In the following, the basic properties of these AGN tpyes are given, more detailed information can be found e.g. in Urry and Padovani (1995).

Radio Loudness	Optical Emission Line properties		
	Type 2 (Narrow Line)	Type 1 (Broad Line)	Type 0 (Unusual)
radio-quiet (80–85%)	Sy 2	Sy 1 QSO	
radio-loud (15–20%)	NLRG { FR I FR II	BLRG SSRQ FSRQ	Blazars { BL Lac (FSRQ)

↓ ? BH spin ? ? gal. type ? ↓

⟶ ? decreasing angle between jet and line of sight ? ⟶

Table 2.2: *Classification of the principal types of AGN according to their radio loudness and their optical emission line properties. Within each grouping, the AGN are additionally distinguished by their luminosity, which increases from top to bottom. Physically, the optical emission line properties may reflect the angle between the jet and the line of sight to the observer. The radio loudness may be determined by the spin of the putative black hole at the center of the active nucleus or result from properties of the host galaxy. This table is a simplified version of the Table 1 in Urry and Padovani (1995).*

The radio-quiet group of Type 1 AGN includes Seyfert 1 galaxies (Sy 1), which have relatively low luminosity, and the higher-luminosity radio-quiet quasars (QSO[28]). As Sy 1 galaxies can only be observed if they are rather close, the host galaxy can often be resolved, in contrast to the more distant quasars, which rarely show an obvious galaxy surrounding the bright central source. The radio-loud Type 1 AGN are called Broad-Line Radio Galaxies (BLRG) at low luminosities and radio-loud quasars at high luminosities. Depending on the power law index α_r of the radio spectrum at a few GHz (radio flux density $S_\nu \propto \nu^{-\alpha_r}$ [Jy]), the latter are divided into Steep-Spectrum Radio Quasars (SSRQ) for $\alpha_r > 0.5$ and Flat-Spectrum Radio Quasars (FSRQ) for $\alpha_r \leq 0.5$. Except for the differences in luminosity, Sy 1s and QSOs are very similar, as are BLRGs and SSRQs/FSRQs.

Radio-quiet Type 2 AGN include, among others, the Seyfert 2 galaxies (Sy 2). The radio-loud Type 2 AGN are often called Narrow-Line Radio Galaxies (NLRG) and encompass two distinct morphological types: Faranoff-Riley I radio galaxies (FR I), which have rather symmetric radio jets whose emission is brightest close to the active

[28]Historically, the first active galaxies were observed at radio wavelengths and referred to as quasars (quasi stellar radio sources). Later, objects with the same optical properties, but without radio emission, were discovered and called QSG (quasi stellar galaxies). Both types were subsequently summarized as QSO (quasi stellar objects). Today, the terms quasar and QSO are usually used interchangeably and are synonymous to AGN, QSO being preferred in optical astronomy, quasar being more customary in radio and high-energy astronomy.

nucleus, and Faranoff-Riley II radio galaxies (FR II), which have more collimated radio jets leading to well-defined, bright radio lobes.

Most of the rare Type 0 AGN are radio-loud. These include the BL Lacertae (BL Lac) objects, which have no or only very weak emission lines. Their emission is characterized by rapid variability (on time scales from less than a day to months) and strong polarization. In many cases, superluminal motion[29] of compact radio cores moving outward from the active nucleus has been observed. Some of the radio-loud Type 1 AGN, in particular FSRQs, exhibit many of the BL Lac characteristics, even though they have strong emission lines. Probably the two most "active" types of AGN are BL Lacs and FSRQs. They are collectively referred to as blazars (BL Lac quasars).

The AGN classification scheme summarized in Table 2.2 is not always based on very distinct criteria. For example, the dividing lines between radio-loud and radio-quiet AGN, or steep-spectrum and flat-spectrum radio quasars, are not defined precisely. The same is true for the (sub-)classifications based on luminosity, exemplified in the Sy 1/QSO division, suggesting that the numerous, empirically different classes of AGN can be attributed to a much smaller number of different astrophysical objects.

There is a large body of evidence indicating that the emission from AGN is intrinsically anisotropic due to obscuration and beaming, and that much of the variety in AGN types is the result of varying orientation relative to the line of sight (see e.g. Antonucci 1993, Urry and Padovani 1995, Robson 1996). In fact, it was possible to devise a single astrophysical scenario, the so-called standard model illustrated in Fig. 2.6, capable of broadly accounting for the observed multitude of different types of AGN. It is commonly believed that the ultimate source of the AGN luminosity is the gravitational potential energy of a central, supermassive black hole (BH) with a mass of 10^6–10^8 $M_\odot$. Before matter falls into the potential well of the BH it forms an accretion disk and loses angular momentum through viscous or turbulent processes, resulting in bright emission at ultraviolet and X-ray energies. Broad optical and ultraviolet emission lines are produced in clouds rapidly orbiting in the vicinity of the BH, the so-called broad-line clouds (dark blobs in Fig. 2.6). The accretion disk and the broad-line region are obscured along some lines of sight by a thick dust and gas torus or warped disk. Some continuum and broad line emission can be scattered into these lines of sight by a hot electron corona (black dots in Fig. 2.6) pervading the broad-line region. Slower moving gas clouds (grey blobs in Fig. 2.6) beyond the torus or warped disk are the source of narrow emission lines. In many AGN, in particular those that are radio-loud, bipolar outflows of energetic particles emanate perpendicular to the plane of the obscuring dust and gas from the region near the BH (illustrated in Fig. 2.6 as FR I type radio jets). The origin of these jets is poorly understood. One of the biggest mysteries associated with AGN is why these jets are sometimes strong radio emitters

[29] "Superluminal motion" refers to proper motion with an apparent speed exceeding the speed of light. This relativistic phenomenon occurs for emitting regions moving at very high (but still subluminal) velocities at small angles to the line of sight (Rees 1966).

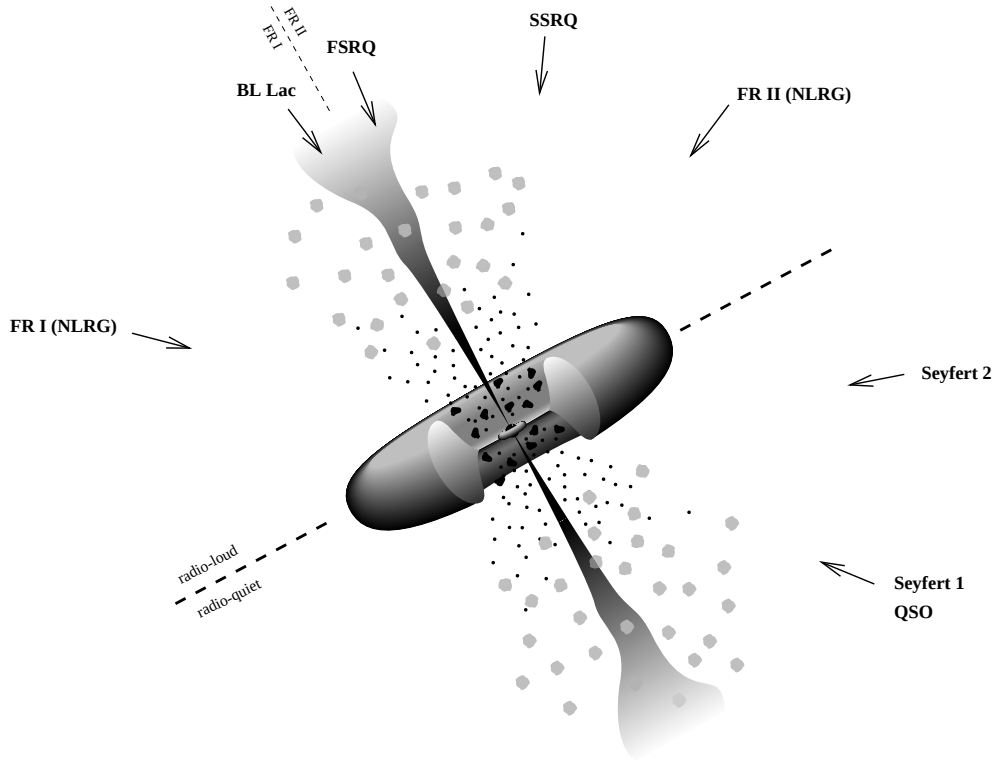

Figure 2.6: *An illustration of the so-called standard AGN model capable of broadly accounting for the observed multitude of different types of AGN (not to scale). The ultimate source of the AGN luminosity is the gravitational potential energy of a central, supermassive BH, which is surrounded by an accretion disk. Broad emission lines are produced in clouds rapidly orbiting in the vicinity of the BH (depicted as dark blobs). The accretion disk and the broad-line region are obscured from transverse lines of sight by a thick torus or warped disk of gas and dust. Some continuum and broad-line emission can be scattered into these lines of sight by a hot electron corona (symbolized by black dots) pervading the broad-line region. Slower moving gas clouds (depicted as grey blobs) beyond the torus or warped disk are the source of narrow emission lines. Perpendicular to the plane of the obscuring dust and gas bipolar outflows of energetic particles emanate from the region near the BH (shown as FR I type radio jets). The schematic drawing is taken from Urry and Padovani (1995).*
In addition, the approximate lines of sight for the principal AGN types of Table 2.2 according to the unification schemes proposed by Antonucci (1993) and Urry and Padovani (1995) are indicated. The upper half of the scheme gives the radio-loud AGN, the lower half the radio-quiet AGN. In the case of radio-loud AGN there is evidence that SSRQs and FSRQs are a subsample of FR IIs (right side of upper half), and that FR Is are the parent population of BL Lacs (left side of upper half).

(most likely the host galaxy then is an elliptical), and why they are sometimes only weak radio sources (most likely the host galaxy then is a spiral). Initially, the plasma in the jets streams out at relativistic velocities, producing γ-radiation that is beamed in the forward direction. Also indicated in Fig. 2.6 are the approximate lines of sight

for the principal AGN types of Table 2.2 according to the unification schemes proposed in Antonucci (1993) and Urry and Padovani (1995). In the case of radio-loud AGN there is evidence that SSRQs and FSRQs are a subsample of FR IIs, and that the FR Is comprise the parent population of BL Lacs.

Recent observations of the high-energy emission of AGN revealed the existence of two classes of γ-ray emitting AGN: radio-quiet Seyferts and quasars (QSOs), and the jet-dominated blazars, as illustrated in Fig. 2.7 (Dermer and Gehrels 1995, Johnson *et al.* 1997). Within the sensitivity limits of current instruments the spectra of radio-quiet AGN exhibit an exponential cutoff around 100 keV. No photons have been observed at or beyond the 511 keV annihilation line (see the spectra of the Seyferts IC 4329A and NGC 4151, and the "average Seyfert" spectrum in Fig. 2.7). This hard X-ray/soft γ-ray emission is probably produced very close to the central engine, as it is seen to vary on very short timescales. The astrophysical environment in the vicinity of an accreting, supermassive BH is of exceeding complexity, with a multitude of radiative processes simulaneously at work, whose relative importance may be different for each individual active nucleus. The inner, hot accretion disk and infalling gas above are expected to emit at ultraviolet and X-ray energies, with photon densities at the BH that may be high enough for γ-γ pair production to be important (e.g. Done and Fabian 1989). There is strong evidence from X-ray observations of Fe K_α emission features, absorption edges and spectral hardenings above $\gtrsim 10$ keV, however, that a large fraction of the emission emanating from the central region has been "reprocessed" in a very hot electron plasma by thermal Comptonization, or reflected by cold (neutral) or warm (partly ionized), optically thick material (see e.g. Robson 1996, Johnson *et al.* 1997, and references therein).

In marked contrast, the γ-ray emission of blazars extends to GeV and even TeV energies, the FSRQs being intrinsically much brighter than the BL Lacs (see the spectra of the FSRQ 3C 279 and the BL Lac object Mrk 421 in Fig. 2.7). Assuming isotropic emission, the high-energy emission often dominates the total luminosity of these sources[30] (see e.g. Dermer and Gehrels 1995, Hartman *et al.* 1997). All blazar type AGN detected so far in high-energy γ-rays have compact radio-cores and flat radio spectra (radio flux density power law index $\alpha \leq 0.5$, where $S_\nu \propto \nu^{-\alpha}$), show strong, rapid time variability in both optical and radio wavebands, as well as strong optical polarization (in particular BL Lac objects) (Mattox *et al.* 1997). In addition, in many cases superluminal motion of radio-jet components resolved with VLBI (Very Long Baseline Interferometry) has been observed. Above 100 MeV the blazar spec-

[30] As is explained in Appendix A.2, assuming isotropic emission the luminosity per natural logarithmic energy interval is given by $E\,L_E = 4\pi d_L^2 \cdot E^2\,I(E)$, with d_L denoting the luminosity distance. For beamed components the subtended solid angle is less than 4π ster, in addition the observed photon energy E may be much higher than the intrinsic photon energy. Thus the assumption of isotropy for a beamed component may overestimate greatly its contribution to the bolometric luminosity of the source by several orders of magnitude, despite the fact that the beamed component does indeed dominate the observed SED.

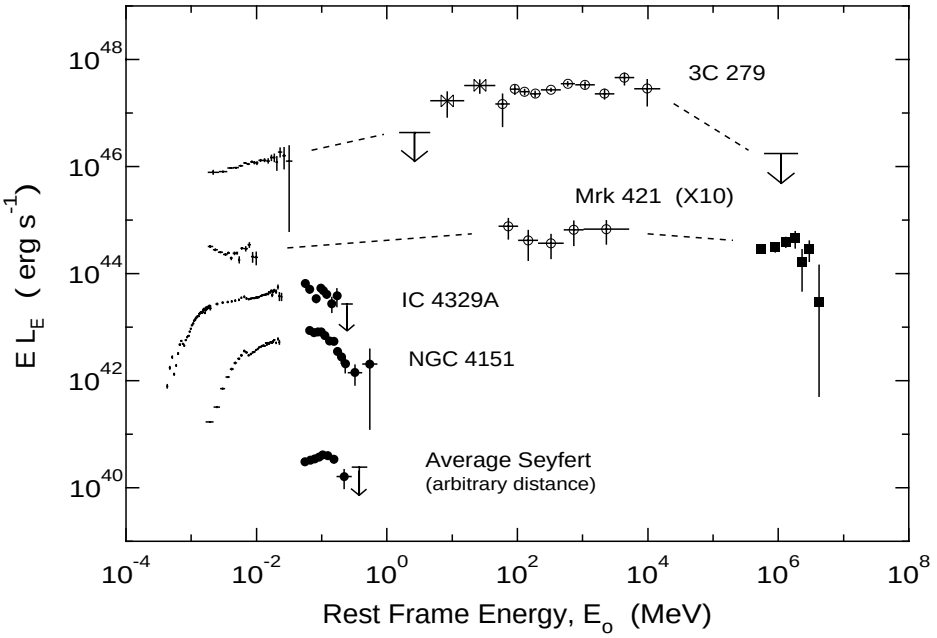

Figure 2.7: *The luminosity per natural logaithmic energy interval, $E\,L_E = 4\pi d_L^2 \cdot E^2\,I(E)$ (see Appendix A.2), for the Seyferts IC 4329A and NGC 4151, the FSRQ 3C 279 and the BL Lac object Mrk 421, as a function of the rest frame energy $E_0 = (1+z)\,E$. Also shown is the "average Seyfert" spectrum. Note that the Mrk 421 spectrum is multiplied by 10. The figure is from Dermer and Gehrels (1995).*

tra are well described by a power law, the power law index of the "average blazar" photon-number spectrum $I(E) \propto E^{-\alpha}$ being $\alpha = -2.16 \pm 0.31$ (Hartman *et al.* 1997). At lower energies the spectra harden, implying a spectral break. There are indications that BL Lacs are less variable than quasars and that BL Lac objects have slightly harder spectra than FSRQs. So far, only BL Lac objects have been detected at TeV energies (see Fig. 2.7), which could also be due to intrinsic absorption of high-energy γ-rays by an ambient soft photon field only present for FSRQs, or due to γ-γ interactions of TeV photons with the intergalactic infrared radiation field attenuating the flux from the high-z FRSQs much more severely than from the low-z BL Lacs. In addition, there seems to be a tendency for spectral hardening at higher flux levels for all blazars. At lower energies a spectral break is observed for blazars at energies between about 1 MeV and 100 MeV (e.g. McNaron-Brown *et al.* 1995, Collmar 1996). For a sub-class of the blazar population, the so-called MeV-blazars, however, a time-variable spectral bump is found at MeV energies instead of a break (Bloemen *et al.* 1995, Blom *et al.* 1995a,b). The high-energy blazar emission is most likely produced in plasma blobs[31] moving along a jet pointing close to the line of sight, such that the radiation is strongly

[31]It is still an open question whether the plasma blobs consist of non-thermal electrons with a thermal proton component or of non-thermal electrons and positrons. For simplicity, only electrons are considered in the following.

enhanced and beamed in the jet direction due to relativistic effects. The γ-rays are due to Compton up-scattering of ambient soft photons by non-thermal electrons and positrons, which also produce the blazar radio-through-optical continuum emission by synchrotron radiation. The ambient soft photons could be synchrotron photons produced in the jet, as proposed by the so-called synchrotron self-Compton (SSC) model, or external photons from the accretion disk or surrounding clouds of gas and dust, as proposed by the so-called external inverse-Compton (EIC) models (see e.g. Hartman *et al.* 1997, Dermer *et al.* 1997). Most likely, at some level all processes contribute, and might be discerned by the different beaming factors produced by synchrotron radiation and Compton scattering of soft, external photons. To date it is not clear whether leptons or hadrons are the primary accelerated particles. The detection of neutrinos from blazars would unambiguously answer this question, as neutrino emission is only expected in the hadronic models from the decay of secondary charged pions.

In addition to the two "standard" classes of γ-ray emitting AGN briefly described above, namely radio-quiet Seyferts/quasars (QSOs) and radio-loud blazars, there is growing evidence for the existence of an intermediate class of γ-ray emitting AGN, which are referred to as radio galaxies with Seyfert nuclei, radio-loud Seyfert galaxies or misdirected/misaligned blazars. The best-studied of these objects is the well-known FR I radio galaxy Centaurus A (Cen A), which is the by far closest AGN at a distance of less than 4 Mpc. In the optical and ultraviolet Cen A resembles a Sy 2 galaxy, but its emission does not cutoff above $\sim$ 100 keV, as is typical for radio-quiet Seyferts. Indeed, it extends beyond 100 MeV — the first such case among non-blazar AGN (Johnson *et al.* 1997, Steinle *et al.* 1998). The spectral shape changes with the intensity state of the source, but can always be described by a doubly-broken power law in the 50 keV to 1 GeV range. The detection of emission at high energies beyond 100 MeV implies that non-thermal processes must be present in Cen A. It is likely that Cen A is a member of the blazar class that is observed from outside the opening angle of the beamed radiation (see Johnson *et al.* 1997, Steinle *et al.* 1998, and references therein). There are also a few examples of radio-loud Sy 1 galaxies whose emission is clearly different from blazars and somewhat different from ordinary, radio-quiet Sy galaxies. Unlike the spectra of the latter, the spectra of the radio-loud Seyferts do not exponentially cutoff at $\sim$ 100 keV, but break at $\gtrsim$ 100 keV to another power law. Nevertheless, no emission at MeV energies has been detected so far within the sensitivity limits of current instruments. It is remarkable that the spectrum of Cen A is similar to that of the radio-loud Sy galaxies which could entail the presence of non-thermal processes in the latter sources (Johnson *et al.* 1997).

The various types of AGN may be the dominant source of the EGB, as was first proposed more than 20 years ago (e.g. Strong *et al.* 1976, Bignami *et al.* 1979, Kazanas and Protheroe 1983). At that time, however, very little was known about the γ-ray properties of AGN and therefore these early studies were as much intended to derive constraints and upper limits on the γ-ray spectra and evolution of these sources as to estimate their contribution to the EGB. After the launch of CGRO a large number of

γ-ray emitting AGN have been detected (see e.g. Johnson *et al.* 1997, Hartman *et al.* 1997), providing a more solid basis for calculations of the diffuse γ-ray background due to the different types of AGN, inasmuch as it is now possible to estimate the evolution function as well as the intensity distribution of these objects.

The approaches utilized to determine the diffuse γ-ray background produced by the multitude of AGN classes are the same as those utilized for normal galaxies (see Sec. 2.2.1.1). It is either assumed that the γ-ray evolution of AGN is similar to that at other wavelengths, or the γ-ray evolution is determined from the data itself. Provided that the assumption of a common evolution is correct, the former approach clearly allows one to obtain an estimate with less uncertainty. The merit of the latter approach is that no assumptions of this kind are being made. Due to the smallness of the AGN sample, however, the uncertainties are inevitably larger.

The intrinsic spectra of radio-quiet AGN, in particular Seyferts and QSOs, exhibit an exponential cutoff around 100 keV (see Fig. 2.7) and therefore these objects are not expected to be important contributors to the EGB. The radio-quiet AGN do, however, provide a substantial contribution to, or may even account for, the XRB from ~ 0.1 keV to ~ 100 keV. At soft X-rays about 70–80% of the XRB already is resolved into discrete sources in the 0.5–2 keV band, mostly different types of AGN (Hasinger *et al.* 1998). Extrapolation of the observed $\log N - \log S$ distribution can account for the entire soft XRB (Hasinger *et al.* 1993). The relative contributions of the different AGN types are still under investigation (e.g. Hasinger 1996, Chen *et al.* 1997). Up to ~ 100 keV the hard XRB, characterized by the pronounced peak in the SED at ~ 30 keV, can be accounted for by combined emissions from different types of Seyfert galaxies, the dominant contribution being due to strongly absorbed Sy 2 galaxies, in accordance with the unification paradigm (e.g. Madau *et al.* 1993, Zdziarski and Zycki 1993, Comastri *et al.* 1995, Zdziarski *et al.* 1995, Zdziarski 1996). Due to differences in the model spectra for the different AGN there is still some ambiguity as far as relative contributions are concerned. The margin for any additional component, however, is quite small in all calculations, which are mostly based on soft X-ray luminosity functions.

As was already mentioned in Sec. 2.1.6, the Seyfert galaxy based models for the hard XRB fall short of the observations above ~ 100 keV. One of the few known sources emitting above ~ 100 keV are radio-loud Sy galaxies and so-called misdirected blazars, as previously stated. Members of this intermediate class of γ-ray emitting AGN are promising candidates for the XRB/EGB in the energy range from about 100 keV to a few MeV (see e.g. Steinle *et al.* (1998), Dermer (1998), private communication). Very few of these intermediate AGN have been observed thus far, which may be due to the limited sensitivity of current instruments. Thus their contribution to the XRB/EGB cannot be reliably determined at the moment. The situation is similar to that of the so-called MeV-blazars. Few of these sources have been observed so far, only a small fraction of all detected blazars being MeV-blazars. Therefore the latter are expected to contribute only marginally to the diffuse emission due to blazars above about 30 MeV. At MeV energies, however, emission from MeV-blazars could exceeed the emission

from standard blazars and constitute a significant fraction of the total EGB intensity (Comastri *et al.* 1995).

The close agreement of the average spectrum of radio-loud blazars above 100 MeV and the spectrum of the EGB immediately establishes γ-ray blazars as the prime candidate source population for the diffuse γ-ray background. Both spectra are well described by a power law, the spectral index of the EGB in the 30 MeV to 100 GeV range being 2.10 ± 0.03 (Sreekumar *et al.* 1998), the spectral index of the "average blazar" spectrum being 2.16 ± 0.31 (Hartman *et al.* 1997). It is worth noting that a cosmological integration of a power law in energy yields the same functional form and slope (see Appendix A.3).

Most calculations of the blazar contribution to the EGB are based on the proposition that there is a correlation between the radio and the γ-ray emission of these objects (e.g. Stecker *et al.* 1993, Padovani *et al.* 1993, Setti and Woltjer 1994, Salamon and Stecker 1994, Erlykin and Wolfendale 1995, Stecker and Salamon 1996b, Comastri *et al.* 1996). The diffuse γ-ray background is then determined by either integrating a scaled radio luminosity function or by scaling the blazar contribution to the extragalactic radio background. The general conclusion from these calculations is that most of the EGB can be explained as originating from unresolved blazars, albeit the uncertainties are still quite large, even more so for the relative contributions from BL Lacs and FSRQs. It has to be pointed out, however, that the degree and nature of the correlation between the radio and the γ-ray emission is still under debate (Padovani *et al.* 1993, Mücke *et al.* 1996, Mattox *et al.* 1997). There is substantial scatter in the data, and a correlation could be a selection effect as the samples are flux-limited. In addition, the number of blazars actually detected at γ-ray energies is much smaller than what is expected from a tight correlation with the radio emission, with most γ-ray detections being for high radio luminosities. This might be explained by the fact that the beamed γ-rays have a smaller opening angle than the radio photons (as predicted by EIC models). It is also possible that blazars are detected in γ-rays only during brief flaring episodes, with their quiescent emission (if it exists at all) being below the current sensitivity limits. Another possibility is that the γ-ray emission of blazars is steady, but with a broad luminosity distribution, such that only the high-luminosity wing is observed. It was concluded by Stecker and Salamon (1996b) and Kazanas and Pearlman (1997) that blazars have been preferentially detected in "flaring" states. Including a spectral hardening during flare emission as compared to the softer quiescent emission results in a curvature of the calculated spectrum of the diffuse γ-ray background (Stecker and Salamon 1996b, Salamon and Stecker 1998), which is already constrained by the latest EGRET measurements (Sreekumar *et al.* 1997).

The variability of the blazar γ-ray emission is also a major source of uncertainty for the γ-ray luminosity function deduced from the γ-ray data itself by Chiang *et al.* (1995) and Chiang and Mukherjee (1998). Using the V/V_{max} and V_e/V_a approaches

[32] they could show that there is indeed evolution of the γ-ray emitting blazars, which is consistent with pure luminosity evolution and similar to that seen at other wavelengths. While the conclusion of the original work was that radio-loud AGN contribute a significant fraction of the EGB above 100 MeV, the improved calculation of the low-luminosity end of the luminosity function in the latter analysis reduces the emission of unresolved blazars to $\sim 25\%$ of the observed EGB intensity. Clearly, a much improved evaluation of the γ-ray luminosity function is needed.

A unique approach to estimating the contribution of unresolved radio-loud AGN to the EGB was taken by Mücke and Pohl (1999). They calculated the non-thermal emission of blazars in the framework of leptonic models, with the inverse-Compton scattering of external soft photons from the accretion disk (EIC process) dominating the synchrotron self-Compton (SSC) process, and then proceeded to estimate the diffuse γ-ray background due to these sources in the context of the AGN unification paradigm. The model was constrained by observations of resolved BL Lacs and FSQRs: their $\log N - \log S$ distribution, their relative number, and their redshift distribution. It was found that the model is consistent with the observed FSRQ number density, but underpredicts the number of BL Lacs, which might indicate that the SSC process is more important than the EIC process in the latter objects. This model can only account for 20–40% of the EGB. If the model is relaxed, however, such that it also reproduces the BL Lac number density, then unresolved BL Lacs and FSRQs can produce the observed EGB, with BL Lacs contributing 70–90% of the intensity.

To summarize, emission from radio-quiet AGN can account for the entire XRB up to about 100 keV. In the 100 keV to a few MeV range radio-loud Seyfert galaxies and misaligned blazars, and also MeV-blazars, could conceivably contribute significantly to the XRB/EGB. Finally, there are strong indications that radio-loud AGN may provide a substantial fraction of, or even account for, the EGB above a few MeV. Estimates of their contribution, however, are still uncertain.

2.2.1.3 Infrared-Luminous Galaxies

The infrared emission of infrared-luminous galaxies exceeds that of normal galaxies by 1–2 orders of magnitude. The origin of this strong IR emission is not yet fully understood, but may involve starburst activity, galactic winds, or a buried AGN (see e.g. Dermer 1996, and references therein). Infrared-luminous galaxies may also be stronger emitters at γ-ray energies than normal galaxies for two reasons. In scenarios of galaxy

[32]The V/V_{max} test provides a check of the assumption that the sources of a complete sample are homogeneously distributed. V is the volume in which a source has been found (which is determined by the source distance), V_{max} is the maximum volume in which the source could have been found (which is determined by the distance at which the source would have the limiting brightness of the sample). For an isotropic distribution the sample average of $V/V_{max} = 0.5$, in the presence of evolution $V/V_{max} > 0.5$. The V_e/V_a test is a generalization of the V/V_{max} test to determine the degree of evolution (see e.g. Weedman 1986, Chiang *et al.* 1995, and references therein).

unification through evolution, mergers and interactions of galaxies are supposed to lead to infrared-luminous sources which harbor active nuclei that are fueled and uncovered as the dust settles (see e.g. Dermer 1996, and references therein). In addition, the star-formation rate is high in many infrared-luminous galaxies, in particular starburst galaxies, resulting in a high density of cosmic rays. The cosmic-ray electrons produce γ-ray photons in interactions with the interstellar medium through emission of bremsstrahlung and in interactions with low-energy photons of the CMB and the intrinsic galaxy radiation via the inverse-Compton process (see e.g. Soltan and Juchniewicz 1999, and references therein).

A recent estimate of the EGB contribution of galaxies luminous at far-infrared wavelengths was given by Soltan and Juchniewicz (1999). Based on the observational correlation of the luminosities at far-IR and radio wavelengths, the latter of which is due to synchrotron emission, a correlation between the number of cosmic-ray electrons and the far-IR luminosity was derived, which finally was transformed into a correlation between the luminosities at far-IR and γ-ray energies. Using a far-IR luminosity function Soltan and Juchniewicz (1999) estimated that these galaxies may account for 20–25% of the observed EGB intensity above about 1 MeV. In addition, the predicted γ-ray spectrum of IR-luminous galaxies does not break down at lower energies, hence these galaxies may also contribute in the 100 keV to a few MeV region. It has to be noted that the bremsstrahlung emission is not yet included in these numbers, thus the EGB contribution of IR-luminous galaxies may even be larger.

Direct testing of the viability of this picture by observation at γ-ray energies will be difficult. Although the number density of far-IR-luminous galaxies is relatively high, individual members of this population are fainter than AGN by orders of magnitude.

2.2.1.4 Supernovae

The explosion of a star in a supernova (SN) is a truly cosmic event, releasing in total an energy of about $\sim 10^{51}$ erg. Over the first few days the optical luminosity of a SN rises dramatically, when it can be as bright as a small galaxy, before it dims again exponentially. The total energy emitted by a SN in photons over the first months is $\sim 10^{48} - 10^{49}$ erg.

Observationally, SNe are divided into two different types, based on spectral characteristics and the form of their light curves (Minkowski 1941). Type I SNe are spectroscopically characterized by the absence of hydrogen lines, their light curves being very similar and regular. In contrast, the spectra of Type II SNe, despite being inhomogeneous, exhibit strong hydrogen lines. Type I SNe are further subdivided spectroscopically. Early Type Ia spectra can be distinguished by a pronounced absorption feature at about 615 nm presumably due to a blue-shifted SiII line, whereas the presence or absence of He lines at the maximum of the light curve is characteristic of SNe Type Ib and Ic, respectively (Branch *et al.* 1991). Type II SNe are subdivided mainly based on their (blue) light curves, with SNe II-P being characterized by a "plateau" in the light

curve after its maximum and SNe II-L by a "linear" decrease (on a logarithmic scale) in luminosity after the maximum (Wheeler and Swartz 1994).

Physically, all these different types of SNe may be attributed to only two different explosion mechanisms: thermonuclear carbon burning (Type Ia) and core collapse (Types Ib,c and Type II).

Type Ia SNe are believed to belong to binary systems in the star population II, which consists of relatively old stars with low masses (a few $M_\odot$)[33]. These stars hardly evolve beyond He buring and end their lifes as white dwarfs (WD), stabilized by the degeneracy pressure of electrons, most of them consisting predominantly of carbon and oxygen[34]. If the two members of such a binary system have sufficiently different masses, the heavier star ($M \approx 2 - 8\,M_\odot$) will have evolved to a carbon-oxygen WD while its low mass companion ($M \approx 1 - 2\,M_\odot$) is still on the main sequence burning hydrogen. As the low-mass star evolves further it expands and the carbon-oxygen WD may accrete matter from its companion. In case the total mass exceeds a critical value[35] the pressure from the degenerate electrons can no longer stabilize the WD and the temperature and density in the core rise until the onset of a thermonuclear runaway reaction which releases so much energy that the WD is completely disrupted[36]. During the brief moments of the explosion the temperatures and densities in the inner regions of the WD are high enough to reach nuclear statistical equilibrium, so that the elements with the maximum binding energy (Fe group) are preferentially produced (see e.g. Niemeyer *et al.* 1996, Woosley 1997). The lack of hydrogen lines in the spectrum of Type Ia SNe is explained by the fact that the WD consisted predominantly of carbon and oxygen (the accreted hydrogen is immediately burned). Even if there were some hydrogen or helium left at the time of the explosion, it would be burned to heavier elements as the shock front passes through the thin outer layers of the WD.

SNe of Types Ib, Ic and II (often referred to as core-collapse SNe) are considered to be linked to young, massive population I stars with main-sequence masses $M \gtrsim 8\,M_\odot$. Stars in this mass range go through all steps of nuclear fusion during their hydrostatic evolution. Once the core of such a massive star is dominated by Fe group elements

[33]The mass of our sun, often referred to as solar mass, is $M_\odot = 2 \times 10^{33}$ g.

[34]The heavier members of population II may end as WDs with neon-oxygen cores. These are not believed to explode but rather collapse to a neutron star, the gravitational energy being carried away by neutrinos (Woosley 1997).

[35]In general, the fate of such a binary system depends critically on its many characteristic parameters, such as the masses of the WD and the companion star, their composition, the accretion rate etc., and is therefore very hard to predict. It is clear, however, that such a binary system is much more likely to produce one or more nova explosions, in which accreted matter on the WD goes through thermonuclear burning, than to end in a supernova that completely disrupts the WD (see e.g. Longair 1994a).

[36]In degenerate matter pressure is independent of temperature, therefore the degenerate WD cannot cool by expansion once nuclear reactions commence in its core. Thus the temperature can rise very quickly until the WD is no longer degenerate and finally expands violently, i.e. explodes.

nuclear energy can no longer be released by fusion to balance gravity and the core collapses. As the temperature rises the Fe group nuclides are dissociated (endotherm) by γ-rays into α particles, protons and neutrons, which are subsequently all converted into neutrons as the collapse proceeds. The gravitational energy of the emerging proto neutron star is converted into neutrinos from electron capture by protons and from radioactive decays. The core collapse continues until the neutron gas degenerates at nuclear matter densities, at which it can not be compressed any further and bounces, generating an outgoing shock that can hold up the infalling outer shell for a few seconds, but is not sufficient to blow away the shell. However, in particular during the core bounce huge numbers of neutrinos are produced which cannot escape freely from the core because of the very high density of the infalling matter. The neutrinos deposit a small fraction of their energy ($< 1\%$), which is the gravitational energy of the (proto-)neutron star of about 10^{53} erg, heating the infalling material so rapidly that the old, standing shock is "revived" or a new shock wave is formed, now powerful enough to eject the envelope of the star ("delayed explosion") (see Thielemann *et al.* 1996). In a core-collapse SN the star is not disrupted completely, as was the case for SNe Type Ia, but depending on the mass of the core a neutron star ($M_{\rm core} \lesssim 2-3\,{\rm M}_\odot$) or a black hole ($M_{\rm core} \gtrsim 2-3\,{\rm M}_\odot$) is left. The absence of hydrogen lines in Type Ib SNe, and of hydrogen and helium lines in Type Ic SNe, can be explained if the progenitor star lost its hydrogen or hydrogen and helium envelopes before the explosion, respectively, either by a strong stellar wind or to a companion in a binary system (Wheeler and Swartz 1994).

Supernovae are a copious source of radioactivity, in particular of γ-ray line emission from iron production, as was first advanced by Clayton *et al.* (1969). Soon afterwards Clayton and Silk (1969) showed that SNe could provide a significant fraction of the EGB around 1 MeV and that the observation of characteristic steps or edges in the composite spectrum due to individual γ-ray lines could provide valuable information on the history of nucleosynthesis in the universe — provided that the γ-ray lines can emerge from the source without degradation. These basic considerations were refined by Clayton and Ward (1975) and put on solid grounds by observations of γ-ray lines from SN 1987A (see e.g. Leising and Share 1990, and references therein). Recently, improved calculations of the cosmic γ-ray background from SNe Type Ia (The *et al.* 1993) and from Type Ia and Type II SNe (Watanabe *et al.* 1997) have been provided.

The predominant contribution to the EGB comes from Type Ia SNe. The product of SN rate and γ-ray yield is comparable for Type Ia SNe and for core-collapse SNe. The massive envelopes of core-collapse SNe, however, inhibit the γ-ray escape, making them much less luminous in γ-rays than Type Ia SNe (The *et al.* 1993, Watanabe *et al.* 1997). The composite spectrum of Tpye Ia SNe is due to the line emission from the decay chain $^{56}{\rm Ni} \rightarrow {}^{56}{\rm Co} \rightarrow {}^{56}{\rm Fe}$ (0.85 MeV, 1.24 MeV, 1.77 MeV, 2.03 MeV, 2.60 MeV and 3.25 MeV), the spectrum of SNe Type Ib/c and II results from the decay of isotopes with much longer half-lives (1.8 MeV from ^{26}Al, 1.16 MeV from ^{44}Ti and 1.17 MeV and 1.33 MeV from ^{60}Co). The time averaged photon-number spectrum from

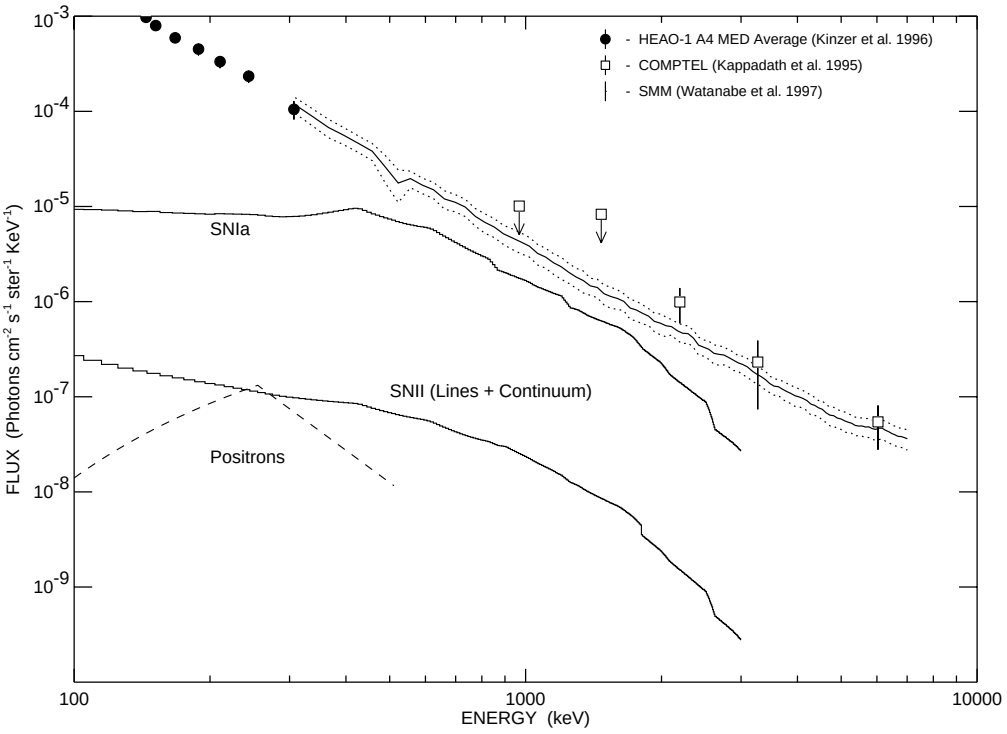

Figure 2.8: *The diffuse γ-ray intensity from SNe Type Ia and Type II as predicted by Watanabe* et al. *(1997), compared to recent determinations of the CDG intensity. The figure is taken from Watanabe* et al. *(1997).*

a Type Ia SN peaks between 20 keV and 80 keV and breaks down at energies of about 3.25 MeV. On top of this continuum some structure is expected due to the integrated line emission from different redshifts: with decreasing energy for each ^{56}Co γ-ray line a sudden increase or step is expected near the rest energy, which should be followed by a drop at lower energies (The *et al.* 1993). The shape of the steps at the rest energies of the lines and of the corresponding drops at lower energies indicate the distribution of the current ($z \approx 0$) Fe nucleosynthesis and the distribution of its onset in space and time, respectively.

Once the time averaged spectra for Type Ia SNe and Type II SNe (representing all core-collapse SNe, including Type Ib/c) are calculated there are several routes which may be followed to derive the SN contribution to the EGB. The *et al.* (1993) assumed that SN Ia nucleosynthesis started at $z = 2.5$ and adopted simple models for the rate of nucleosynthesis with cosmic epoch, which were normalized to the current Fe mass fraction in the sun, supposing that 2/3 of the Fe in the universe is produced by Type Ia SNe. The calculation of Watanabe *et al.* (1997) is slightly different in that the history of nucleosynthesis is decribed with current observations for the star formation rate, normalized to the current SN rate. In addition, Watanabe *et al.* (1997) assume that SNe Type II occur three times as frequently as SNe Type Ia at all epochs. The

predictions of both approaches are in agreement, and consistent with measurements of the EGB intensity, which may be dominated around 1 MeV by the integrated emission from Type Ia SNe, as shown in Fig. 2.8.

These calculations have to be considered preliminary for a number of reasons. According to Timmes *et al.* (1995) there is some uncertainty in the fraction of Fe in the sun produced by Type Ia SNe, with a plausible range of 1/3 to 2/3. In addition, the rates of Type Ia SNe and core collapse SNe are expected to vary differently with cosmic epoch. In particular, a time delay between the onset of core-collapse SNe from massive stars and Type Ia SNe from low-mass stars is expected because the former have much shorter lifetimes than the latter (see e.g. Timmes *et al.* 1995, Prantzos and Aubert 1995). Finally, in both calculations the nucleosynthesis or SN rates are normalized to values derived in our galaxy, which does not take into account that these values depend sensitively on the Hubble type of the galaxy. The total SN rate is lowest for early-type galaxies and increases along the Hubble sequence, with the dependence of different types of SNe on the Hubble type being quite different (e.g. van den Berg and Tammann 1991, Tammann *et al.* 1994).

Despite these uncertainties SNe are promising contributors to the EGB at about 1 MeV, but a definite assessment of the intensity due to SNe may have to wait until the detection of the predicted steps and drops in the EGB spectrum.

2.2.1.5 Deuterium Formation

In analogy to Clayton and Silk (1969), who considered the γ-ray lines from iron production in SNe, it was suggested by Leventhal (1973) that the emission of 2.2 MeV photons from the production of deuterium by neutron capture on hydrogen may contribute to the EGB around 1 MeV. The emission of the 2.2 MeV deuterium line is believed to be the most important neutron capture emission in any astrophysical environment in which energetic neutrons are produced and where these liberated neutrons can interact with matter before they decay.

Neutron capture occurs in solar flares (Chupp *et al.* 1973) and may also occur in the outer envelope of a SN explosion (Hoyle and Fowler 1973) or in accreting compact objects (see McConnell *et al.* 1997, and references therein). Thus far, no 2.2 MeV line emission from SNe has been observed, and, except for one candidate, only upper limits for deuterium line emission from accreting compact objects have been obtained (McConnell *et al.* 1997).

It therefore seems unlikely that the formation of deuterium makes a significant contribution to the EGB.

2.2.1.6 Primordial Black Holes

At the present cosmic epoch the only known process for the formation of black holes (BHs) is self-gravitational collapse, which requires that the mass of the modern BH must exceed a few solar masses ($\gtrsim 2-3\,\mathrm{M}_\odot$). In the early universe, however, so-called primordial black holes (PBHs) of almost arbitrarily small masses may have formed. A variety of mechanisms for the formation of PBHs has been proposed, e.g. the collapse of overdense regions in the presence of significant density fluctuations, cosmic phase transitions or the collapse of oscillating loops of cosmic string (see MacGibbon and Carr 1991, Halzen *et al.* 1991, and references therein). As was first suggested by Hawking (1974), BHs thermally emit particles created by the strong gravitational fields with a temperature of about $1.2\times 10^{26} M^{-1}$ K, where M is the BH mass in grams. For stellar-mass BHs ($M \approx \mathrm{M}_\odot$) this Hawking radiation is negligible, as the temperature would be less than 10^{-7} K, but for much smaller PBHs the effects of this quantum-mechanical decay through particle emission are significant (Page and Hawking 1976). PBHs with the critial mass $M_* \approx 10^{15}$ g evaporate at the current epoch, PHBs with mass less than M_* have evaporated at earlier epochs.

The particle emission from PBHs and the possibilities of their detection have repeatedly been investigated (e.g. Page and Hawking 1976, MacGibbon and Carr 1991), since both the existence or the non-existence of PBHs provide important information or constraints on the conditions in the early, radiation dominated universe. In particular, if PBHs do not exist, then the early universe was probably nearly homogeneous and isotropic with a hard equation of state (Page and Hawking 1976).

An individual PBH emits particles with approximately a black-body spectrum once the PBH temperature exceeds the particle's rest mass. About 9% of the energy is radiated in photons, whose number spectrum peaks at about 120 MeV (Page and Hawking 1976). To be seen above the EGB, an individual PBH must be within the solar system, which is extremely unlikely since an upper limit of 10^4 PBHs per pc^3 (see below) corresponds to $\sim 10^{-7}$ PBHs within the solar system (Page and Hawking 1976). The integrated emission of a uniform distribution of PBHs with $M \lesssim M_*$ over the universe's lifetime, however, results in an isotropic γ-ray background with a photon-number spectrum $\sim E^{-3}$ for $E \gtrsim 100$ MeV due to the evaporation at the present epoch and an E^{-1} part below $E \approx 100$ MeV due to emission in the present and previous epochs (MacGibbon and Carr 1991). Thus a break at an energy of about 100 MeV is expected in the EGB spectrum if PBHs make a significant contribution. Comparison with the observed EGB allows us to put an upper limit on the average number density of PBHs with initial masses less than M_*. Page and Hawking (1976) derived a value of about $10^4\,\mathrm{pc}^{-3}$, MacGibbon and Carr (1991) obtained a PBH mass density of $\Omega_{\mathrm{pbh}} \lesssim (7.6 \pm 2.6) \times 10^{-9} \cdot h^{-1.95\pm0.15}$ for a closed universe with vanishing cosmological constant, which for $h = 0.6$ corresponds to a PBH number density of about $4\times 10^3\,\mathrm{pc}^{-3}$ at the current epoch[37]. Assuming a specific initial mass spectrum, PBH

[37]Here the dimension-less parameter h denotes Hubble's constant H in units of [100 km/sec Mpc].

evaporation may also possibly explain the putative MeV bump in the EGB (MacGibbon and Carr 1991). To conclude, a substantial contribution of evaporating PBHs to the EGB seems unlikely, since the spectral shape of the EGB is quite different from what is predicted from PBHs.

It is worth mentioning that a second possibility for the observation of PBHs arises in the final stage of the evaporation process. As the PBH loses mass its temperature rises and particles of increasing rest mass are emitted. If the number of particle species increases exponentially with mass as in the statistical bootstrap approach of Hagedorn (1968) about 10^{34} erg would be emitted by the PBH in γ-rays peaked at about 250 MeV in its last 10^{-7}sec (Page and Hawking 1976). If the number of quarks, leptons and gauge bosons is finite, as suggested by the current standard model of particle physics, then the final evaporation of a PBH proceeds much more slowly over $\sim$ 1 sec (MacGibbon and Carr 1991). Searches for PBH "explosions" have been conducted and upper limits on the number density of PBHs with mass $\approx M_*$ have been deduced (e.g. Porter and Weekes 1977, Cline and Hong 1992, Fichtel *et al.* 1992, and references therein). Currently, these limits are on the order of $\sim 10^{10}$ pc^{-3} and therefore much less stringent than the upper limits derived from comparisons to the EGB spectrum.

2.2.1.7 Massive Black Holes Collapsed at High Redshift

Another possible origin of the EGB involving BHs was proposed by Gnedin and Ostriker (1992). They constructed a cosmologocal model in which shortly after decoupling much of the matter collapsed into massive black holes (MBHs) of about 10^6 M$_\odot$, which today consitute the dynamically observed dark matter galactic halos. After their formation, the MBHs would accrete gas from their vicinity, and it is expected that spectra similar to those of quasars or galactic BHs such as Cyg X-1 are emitted. Most of the energy is emitted at high redshift of about 100 and results in a truly diffuse background of high-energy photons with a spectrum that parallels the observed XRB and EGB rather well at the level of about 5–10%.

2.2.2 Truly Diffuse Sources

2.2.2.1 Matter-Antimatter Annihilation

Unmistakable evidence for the presence of antimatter comes from the observation of matter-antimatter annihilation. The primary products of matter-antimatter annihilation are pions, which subsequently decay into myons which further decay into electrons, positrons and neutrinos (from $\pi^\pm$ decay) and into γ-rays (from π^0 decay). Roughly one third of the energy released in a typical annihilation is deposited in γ-rays, the easiest-to-detect secondaries, making them the most useful probe for antimatter (Steigman 1976). The typical restframe γ-ray spectrum produced by π^0 decay from proton-antiproton annihilation has a nearly flat maximum at $m_{\pi^0}c^2/2 \sim 70$ MeV and a

minimum and maximum cutoff at $\sim$ 5 MeV and $\sim$ 1 GeV , respectively (Stecker 1971). However, γ-rays with energies $\gtrsim$ 100 MeV do not provide a unique signature of annihilation, since other processes such as π^0 production in cosmic-ray collisions, or the inverse-Compton scattering of low-energy photons and cosmic-ray electrons, or bremsstrahlung emitted by cosmic-ray electrons will also produce γ-rays in this energy range (see Steigman 1976, and references therein)[38].

Two different approaches have been pursued to apply existing γ-ray data to the question of cosmic matter-antimatter symmetry. The first approach is to construct a symmetric cosmology and explore whether its parameters can be adjusted such that it is consistent with observations. In addition to γ-ray observations, constraints imposed from the element abundance produced in primordial nucleosynthesis and from distortions of the spectrum and the isotropy of the cosmic microwave background are of particular importance. Early symmetric cosmologies were proposed by Harrison (1967, 1968) and Omnès (1969, 1970), in which at the earliest stages of the universe matter and antimatter were separated into distinct regions which subsequently formed the foundations of a structured universe. Based on these and later (see below) symmetric cosmologies Stecker and collaborators repeatedly calculated the cosmological γ-ray spectrum from annihilations occuring on the boundaries of colliding domains of matter and antimatter up to redshifts of $\lesssim$ 100 (see e.g. Stecker *et al.* 1971, Stecker and Puget 1972, Stecker 1989). They obtained an annihilation spectrum with a flat peak near 1 MeV due to photon absorption and scattering at the highest redshifts. At higher energies the annihilation spectrum could be approximated by an $E^{-2.86}$ power law breaking down above 50 MeV. This spectrum was in good agreement with observations of the EGB spectrum at that time, in particular with the observed excess intensity around 1 MeV, which was claimed to be strong evidence for the validity of the matter-antimatter hypothesis[39]. These early symmetric cosmologies, however, were ruled out (see e.g. Steigman 1976, and references therein)[40]. Later, Stecker (1985) proposed that

[38]In principle, 511 keV line emission from electron-positron annihilation could also be used as a probe for the existence of antimatter. This line, however, does not provide unambiguous evidence since positrons are also produced in cosmic ray interactions with matter. In addition, matter-antimatter annihilations give rise to roughly the same numbers of photons at 511 keV (e^+-e^- annihilation) as at $\sim$ 100 MeV (p-$\bar{p}$ annihilation), while there are about 3 orders of magnitude more photons in the EGB at 511 keV than at $\sim$ 100 MeV . Thus upper limits obtained from 511 keV γ-rays are less significant than those derived from $\sim$ 100 MeV photons, unless a high-resolution detector for the keV region is available (Steigman 1976).

[39]At that time other possible origins for the excess emission in the MeV range, such as supernovae (see Sec. 2.2.1.4) were already proposed, but all of them could only account for the lower part of the excess.

[40]Briefly, it can be demonstrated that the most naive symmetric big bang cosmology, in which photons, baryons and anti-baryons are distributed homogeneously, fails to reproduce the observed ratio η of the photon-number density N_γ and the baryon number density N, $\eta = N/N_\gamma \approx 10^{-9}$ by 8–10 orders of magnitude. To avoid the catastrophic annihilation of matter and antimatter various mechanisms have been proposed for their separation, such as statistical fluctuations or phase transitions at high temperatures, all of which have been demonstrated to be inconsistent with current astrophysical and

very large matter and antimatter domains, which constitute galaxy clusters or superclusters at the current epoch, may have evolved in a cosmology based on a grand unified field theory with spontaneous CP (charge parity) violation. Thus the possibility that matter-antimatter annihilation might produce the EGB above $\sim$ 1 MeV was restated.

The large-scale fluctuation patterns or anisotropies resulting from annihilation in symmetric universes and from active galactic nuclei were investigated by Cline and Gao (1990) and Gao *et al.* (1990b,a). They found that the fluctuations produced by annihialtion on the boundaries of matter and antimatter domains, which resemble diffuse "ridges" in the 100 MeV range, are intrinsically different from EGB fluctuations produced by AGN, thus providing a probe for cosmological antimatter.

Recent observations of the spectrum of the EGB show no evidence for an excess intensity around 1 MeV (see Sec. 2.1.7). In addition, at energies above 30 MeV the spectrum of the EGB is flatter than predicted from matter-antimatter annihilations and the intensity of the EGB is consistent with isotropy. Thus it appears from the first approach that matter-antimatter annihilations do not contribute significantly to the EGB.

The second approach is to derive upper limits to the possible antimatter fraction from upper limits set to the annihilation rate by γ-ray observations. Following this line of thought Steigman (1976) showed conclusively that antimatter must remain separated from ordinary matter on scales at least as large as clusters of galaxies ($\sim$ 10 Mpc)[41], if present at all (see also Allen 1981). A separation of matter and antimatter on the supercluster scale was ruled out by Dudarewicz and Wolfendale (1990) based on the assumption that the models for the halo gas of galaxy clusters derived from X-ray observations can also be applied to the halo gas of superclusters, as the resulting EGB intensity in this model exceeds the observed intensity. Moreover, they could not find a geometry separating matter and antimatter on even larger scales that was consistent with γ-ray observations. In a more general approach Cohen *et al.* (1998) analysed the dynamics of a patchwork universe consisting of distinct regions of matter and antimatter (as e.g. suggested by Stecker 1985) together with the resulting contribution to the EGB and distortion of the microwave background. The domains were characterized by their current size, which had to exceed $\sim$ 20 Mpc. To be conservative, only annihilations from the time of decoupling to the onset of structure formation ($1000 \lesssim z \lesssim 20$) were considered. They found that for empirically allowed Roberston-Walker universes the expected contribution to the EGB exceeds by far observational limits for all domain sizes $\lesssim 10^3$ Mpc, comparable by order of magnitude to the size of the visible universe, and arguably for even larger domains, thus excluding a matter-antimatter symmetric

---

particle physics data. This is the reason why $\Delta N = N - \bar{N} = \eta N_\gamma$ is chosen as an initial value in the standard non-symmetric big-bang cosmologies.

[41]Typical dimensions of clusters of galaxies and super-clusters of galaxies are $\sim$ 10 Mpc and $\sim$ 100 Mpc, respectively (Unsöld and Baschek 1988).

universe[42].

To conclude, there is currently no evidence from either of the two approaches requiring the presence of antimatter in the universe[43]. Therefore a contribution from matter-antimatter annihilation to the EGB seems unlikely.

2.2.2.2 Exotic Elementary Particles

It has been suggested that the EGB may originate from the decay or the annihilation of some sort of exotic, relic elementary particle from the early universe not yet discovered. This speculative notion is motivated by astrophysical as well as particle physics considerations (see e.g. Silk and Srednicki 1984, Ellis *et al.* 1988, Rudaz and Stecker 1988, Kamionkowski 1995). Astrophysical observations strongly suggest the existence of dark matter, in particular in galactic halos. This dark matter may be composed of non-baryonic, massive, weakly interacting particles, which are natural consequences of many, in particular supersymmetric, extensions to the standard model of particle physics. There are three possible signatures of heavy dark matter particles which might be exploited for their detection (see Ellis *et al.* 1988, Kamionkowski 1995, and references therein). These particles may elastically or inelastically scatter off nuclei in the laboratory, they may annihilate in the sun and produce high energy neutrinos, or they may annihilate in the galactic halo or decay and produce antiprotons, positrons and γ-rays. Thus observations of the EGB can be used to constrain the parameter space of new particle theories (e.g. Daly 1988, Rudaz and Stecker 1988, Kamionkowski 1995) or, which would be more exciting, may lead to the discovery of new physics.

Depending on the choice of particle theory, a large number of different exotic particles may exist, which may produce characteristic features in the EGB. None of the predicted spectral features, such as a cutoff at the rest energy of an annihilating particle (Rudaz and Stecker 1988), a series of γ-ray lines in the GeV range (Srednicki *et al.* 1986), or a broad distribution or a single line (Kamionkowski 1995), has been observed so far, and in many cases their observation is beyond the capabilities of current instruments. This is also true for the predicted angular features, namely anisotropies due to the annihilation or decay in a galactic halo or enhanced emission above the general EGB intensity from other galaxies or clusters of galaxies (e.g. Kamionkowski 1995).

2.2.2.3 Extended Galactic Halo

A major concern for measurements of diffuse extragalactic emission at any wavelength is the subtraction of the diffuse galactic emission. In particular, in case an extended

[42]The calculated distortions of the spectrum of the cosmic microwave background were well below the observed limit and therefore provided no constraint at all.

[43]Neither of the two approaches, however, can exclude the existence of small and distant pockets of antimatter (Dolgov and Silk 1993).

galactic halo[44] exists the diffuse galactic emission may extend to the highest galactic latitudes and may thus preclude the possibility of directly determining the EGB intensity in the absence of any galactic "foreground" emission. Even worse, the isotropy of the emission from a very extended halo could mimic truly extragalactic diffuse emission so well that the components could no longer be distinguished.

In general, two diffuse components can only be separated on the basis of models for their energy spectra and/or the spatial distribution of their intensities on the sky. The galactic diffuse emission is produced by the interaction of cosmic rays with the interstellar medium and the interstellar radiation field via electron bremsstrahlung, nucleon-nucleon processes (π^0 decay) and inverse-Compton scattering of low-energy photons and cosmic-ray electrons (see e.g. Bloemen 1989, Strong 1996, Hunter *et al.* 1997b, Strong *et al.* 1999, and references therein). The galactic diffuse emission depends on the type and distribution of the cosmic-ray sources, on the propagation of cosmic rays, on the structure, distribution and composition of the interstellar medium, and on the interstellar radiation field. Not all of these quantities are well known, making the modelling of the galactic diffuse emission a very complex and involved task. There are, however, observational data of many kinds related to the cosmic-ray origin and propagation that provide independent constraints on any model of the galactic diffuse emission: measurements of the cosmic-ray composition and of the intensity and energy spectra of individual components of the cosmic radiation and observations of γ-rays and synchrotron emission at radio wavelengths (see e.g. Strong and Youssefi 1995, Strong *et al.* 1999, and references therein). Using astrophysical input data on the interstellar medium and the interstellar radiation field, investigators constructed models of the diffuse galactic emission that agree well with the γ-ray observations at most energies and most regions on the sky (see e.g. Hunter *et al.* 1997b,a, Strong *et al.* 1999). Employing these models allows investigators in principle to subtract the diffuse galactic emission from the total observed intensity to derive the intensity of the EGB (e.g. Sreekumar *et al.* 1998).

The question arises whether the diffuse galactic emission is known well enough to determine the intensity of the EGB. Of even more importance is the question: could the diffuse galactic emission account for all the observed diffuse emission? It has repeatedly been pointed out that there may exist a large-scale, yet non-isotropic component of γ-ray emission that is not accounted for in models of the diffuse galactic emission which may be galactic (e.g. Strong 1983, Chen *et al.* 1996, Sreekumar *et al.* 1998, Dixon *et al.* 1998, and references therein) as well as local (e.g. Strong 1984) in origin. Despite the fact that there is statistical evidence for such an additional component its magnitude is very difficult to assess, and it remains to be seen if improved calculations of the diffuse galactic emission, taking into account recent results on neutral and ionized gas components with a scale height of about 4.4 kpc (e.g. Kalberla *et al.* 1998, Pietz *et al.*

[44]Here "galactic halo" is used very generally, denoting a region around the disc of the galaxy in which the matter density is higher than in intergalactic space. The existence of some sort of galactic halo can be inferred e.g. from the dynamics of the galaxy (rotation curve).

1998), can account for this as yet unexplained emission. There are also indications for an extended baryonic dark galactic halo consisting of very low mass stars and H_2 clouds at distances $\gtrsim (10 - 20)$ kpc (e.g. De Paolis *et al.* 1995). Thus far, no evidence for emission from such H_2 clouds has been found. It has also been argued that a cosmic-ray galactic halo extending to some 100 kpc may exist, which could produce an almost isotropic intensity that may account for about 40% of the current best values for the EGB intensity (Erlykin *et al.* 1997b,a). Such a giant halo may indeed exist, but at present this scenario is still lacking support from detailed calculations[45] and is therefore considered unlikely. Finally, there have been suggestions that cosmic rays leak into intergalactic space. In that case cosmic-ray interactions in the intergalactic medium of galaxy clusters, as identified by X-ray observations, could contribute to the EGB (e.g. Dar and Shaviv 1995). Again, this notion seems unlikely considering that it seems to predict the wrong spectral shape and that the intergalactic cosmic-ray density seems to be considerably lower than the cosmic-ray density inside a galaxy (see Stecker and Salamon 1996a, and references therein). Another possibility is that cosmic-ray electrons and protons up-scatter photons of the 2.7 K microwave background radiation (e.g. Strong *et al.* 1973). These contributions, however, were shown to be insignificant (Chi and Wolfendale 1989, Wdowczyk and Wolfendale 1990).

It is clear that the subtraction of the diffuse galactic emission, which is still far from being understood in detail, is a major concern for measurements of extragalactic diffuse emission. At the same time, it seems unlikely that any kind of giant halo component exists, although this possibility should always be kept in mind. Current models for the diffuse galactic emission appear to provide a reliable basis for the determination of the intensity of the EGB.

2.3 History of Measurements of the Extragalactic Gamma-Ray Background

The potential of γ-ray astronomy for exploring the most energetic and violent astrophysical environments was recognized by theoreticians around the end of the first half of this century (see e.g. Morrison 1958). Many different γ-ray producing processes were examined, and estimates of the expected fluxes and intensities were derived, increasing the incentive of experimentors to put these predictions to the test. Interesting accounts of the early days of γ-ray astronomy, which returned upper limits only on the intensity of the putative cosmic γ-rays, can be found in, e.g., Chupp (1976), Longair (1992) and Ramana Murthy and Wolfendale (1993).

The history of measurements of the extragalactic gamma-ray background (EGB) is intimately tied to the history of γ-ray astronomy as a whole. As was the case in

[45]For example, the models of Strong and Youssefi (1995), Strong *et al.* (1999) and Hunter *et al.* (1997a) do not predict such a giant halo.

microwave and X-ray astronomy, the first signal detected by γ-ray astronomy was the EGB, which has remained a prime objective of research ever since. Soon after its discovery, the γ-ray sky could be resolved at high energies above about 50 MeV into an apparently isotropic extragalactic component and a diffuse galactic component. At lower energies this separation could not be made for a long time as the available detectors lacked the required sensitivity and angular resolution. Thus it became customary at low and medium γ-ray energies below about 50 MeV to refer to the EBR as cosmic diffuse gamma-ray background (CDG).

2.3.1 Measurements until $\sim$1965

It was not until 1962 that the first convincing evidence for the existence of primary cosmic γ-rays was obtained. Kraushaar and Clark (1962) reported the detection of 22 γ-ray photons with energies above 50 MeV from space, using an instrument consisting of a crystal scintillator and subsequent Čerenkov detectors onboard the satellite Explorer 11. In the same year, Arnold *et al.* (1962) announced the first indication of diffuse cosmic radiation around 1 MeV using an omnidirectional CsI detector mounted on a telescoping boom onboard the moon probe Ranger 3.

The latter experiment was flown again on the moon probe Ranger 5, and based on the combined data Metzger *et al.* (1964) claimed the detection of a substantial interstellar flux of γ-rays between 0.09 MeV and 4.3 MeV at a level consistent with extrapolations of the early results for the diffuse X-ray intensity detected in rocket flights (Giacconi *et al.* 1962, Gursky *et al.* 1963). As we know today, however, these early measurements of the CDG were heavily contaminated by instrumental background.

The final analysis of the Explorer 11 data for energies above 100 MeV was given by Kraushaar *et al.* (1965). In addition to studying the Earth's γ-ray albedo as a function of zenith angle and geomagnetic latitude, they reported 31 events from the sky, distributed isotropically. This small dataset represents one of the first important successes of γ-ray astronomy, as it allowed Kraushaar *et al.* (1965) to effectively refute the steady-state cosmology based on a severe upper limit on the proton-antiproton creation rate.

2.3.2 Measurements until $\sim$1981

In 1967-1968 an upgraded version of the γ-ray counter telescope on Explorer 11 was flown on the third Orbiting Solar Observatory (OSO-3). The telescope, sensitive to γ-rays above about 50 MeV, consisted of a multilayer scintillation conversion detector on top of a directional Cerenkov counter above a NaI(Tl) sandwich energy detector. Based on the detection of 621 cosmic γ-ray events Kraushaar *et al.* (1972) provided the first evidence for the existence of a galactic component concentrated in a band around the galactic equator with a broad maximum toward the galactic center. In addition,

the presence of an isotropic component was confirmed. This component seemed to be of extragalactic origin with a softer spectrum. Various (mostly balloon borne) experiments conducted between 1968 and 1972, however, did not always give consistent results, and thus there remained some doubt concerning the galactic component (see e.g. Chupp 1976).

The situation improved dramatically with the launch of the second Small Astronomy Satellite (SAS-2) in 1972, carrying a wire spark-chamber γ-ray telescope sensitive to γ-rays above about 35 MeV with much improved sensitivity and angular response compared to that of the telescope onboard OSO-3. The data obtained with SAS-2 allowed Fichtel *et al.* (1975) to end all existing uncertainties: the galactic γ-radiation was clearly detected and seemed to be generally correlated with galactic structural features, in particular with arm systems. Moreover, at high galactic latitudes an apparently uniform background radiation was found, whose photon spectrum could be descibed by a power law with a spectral index of 2.4 ± 0.2 based on data with $|b^{\rm II}| > 30°$. A more detailed examination of the diffuse γ-radiation, making use of the full SAS-2 data base, was presented by Fichtel *et al.* (1978). The galactic component was found to be linearly correlated to the atomic hydrogen column density and the radio continuum emission. The photon spectrum of the apparently isotropic component between 35 MeV and $\sim$ 150 MeV was described by a power law with index $-2.7^{+0.3}_{-0.4}$. The final derivation of the spectrum of the EGB above 35 MeV from SAS-2 data has been carried out by Thompson and Fichtel (1982) using galaxy counts as a tracer of galactic matter, yielding a power-law index of $-2.35^{+0.3}_{-0.4}$.

In 1975 the COS B satellite was launched, carrying a spark-chamber γ-ray telescope similar to that on SAS-2. COS B performed excellently for six and a half years and greatly improved our knowledge on emission from the galactic plane above about 100 MeV. However, unlike the near circular orbit of SAS-2 that remained mostly below the radiation belts, COS B was placed on a highly eccentric orbit extending far above the radiation belts, resulting in an incident cosmic-ray intensity that was an order of magnitude higher. Together with an unfavourable design of the telescope[46] the consequence was a rather large background of secondary γ-rays produced in the detector which precluded a measurement of the EGB (Ramana Murthy and Wolfendale 1993, Kanbach 1998b, private communication).

In the meantime progress in the MeV range was slow due to the presence of additional instrumental background from induced radioactivity and due to the difficulty in building detectors with even moderate spatial resolution. A variety of experiments similar to those flown on the Ranger spacecraft have been performed on various satellites. For example, Vette *et al.* (1970) used an omnidirectional NaI scintillation counter with a

[46]Compared to the SAS-2 experiment, the design of COS B was such that a larger amount of passive material, such as a thermal shield, was present in the instrument aperture above the veto dome. High-energy cosmic-ray electrons and protons can produce energetic secondary γ-ray photons in this passive material by emission of bremsstrahlung or pion production, which may not be rejected if the charged particles involved do not reach the veto dome.

plastic scintillation anticoincidence shield aboard the Environmental Research Satellite (ERS) 18 to measure the cosmic diffuse γ-ray background. Mazets *et al.* (1975) also used an omnidirectional NaI(Tl) crystal, without anticoincidence protection against charged particles, mounted on a long boom outside the satellite Kosmos 461. Of particular interest are the results of Trombka *et al.* (1977) obtained with an omnidirectional NaI(Tl) spectrometer crystal with plastic anticoincidence shield on an extensible boom flown on the lunar missions Apollo 15, 16, and 17.

In parallel to these satellite-borne experiments, considerable effort was devoted to determining the spectrum of the CDG from balloons. Among the first to attempt such a measurement were Vedrenne *et al.* (1971) and Daniel *et al.* (1972), using omnidirectional organic stilbene and NaI(Tl) scintillators with 4π anticoincidence shielding, respectively. More sophisticated balloon-borne experiments with a restricted field-of-view were the Compton telescopes employed by Schönfelder and Lichti (1974), White *et al.* (1977), Schönfelder *et al.* (1977), Schönfelder *et al.* (1980) and Lockwood *et al.* (1981). A collimated detector system consisting of a central NaI(Tl) crystal surrounded by a cylindrical NaI(Tl) counter and an active CsI(Tl) aperture shutter was used by Fukada *et al.* (1975).

While instrumental background is of little concern for high-energy γ-ray telescopes such as SAS-2[47], its elimination is the major challenge for experiments at MeV energies. Most of the above mentioned measurements of the CDG exploited, among other background characteristics, the fact that the background (instrumental background and/or atmospheric γ-radiation), in contrast to the sought-after signal, is variable. For example, in the analysis of Mazets *et al.* (1975) the atmospheric γ-ray background was removed based on its dependence on rigidity. The modulation of the albedo γ-ray continuum was modelled by the readily observable modulation of the atmospheric 511 keV line, which was approximated by an exponential in rigidity. Both atmospheric components were then eliminated by an extrapolation to infinite rigidity[48]. A major instrumental-background component for the analysis of Trombka *et al.* (1977) resulted from γ-ray photons due to cosmic-ray and secondary interactions in the Apollo spacecraft and due to natural radioactivity of spacecraft materials. These backgrounds were extracted from the data based on their dependence on the extension of the boom carrying the detector. Finally, the intense atmospheric γ-ray background at balloon altitudes was separated using a growth-curve technique: at the top of the atmosphere the flux of vertically downward-moving photons is expected to increase linearly with

[47]This is mostly due to the principle of measurement employed by these instruments. Since the direction of the incident γ-ray photons is determined rather accurately, all photons that do not originate from the telescope aperture, and may thus be due to instrumental background, can effectively be excluded from the data. As pointed out above, the only source of instrumental background therefore is production of secondary γ-ray photons in passive material above the veto system and within the aperture.

[48]An analogous technique is used in the COMPTEL CDG analysis to remove the prompt, cosmic-ray induced instrumental background, as described in chapter 5.

atmospheric depth, which is the amount of rest atmosphere above the balloon in units of [g/cm^2], while the cosmic γ-ray photons are exponentially attenuated with increasing atmospheric depth (see e.g. Schönfelder and Lichti 1974, Schönfelder *et al.* 1980, and references therein). This atmospheric growth-curve technique is particularly suited for the Compton telescopes of e.g. White *et al.* (1977), Schönfelder *et al.* (1980), and Lockwood *et al.* (1981), since these instruments are capable of selecting downward-moving photons, in contrast to omnidirectional detectors as those employed by e.g. Vedrenne *et al.* (1971) or Daniel *et al.* (1972). Being aware of this drawback, Fukada *et al.* (1975) therefore relied on artificially modulating the count rate of their omnidirectional detector with an aperture shutter to eliminate the instrumental and atmospheric backgrounds from outside the entrance aperture.

An illustration of the status of measurements of the CDG/EGB above about 100 keV in 1982 is depicted in Fig. 2.9. It has to be emphasized that this compilation of experimental results is not exhaustive, but only intended to give a rough qualitative and quantitative impression of the results on the CDG/EGB available at that time. Of particular interest is the so-called MeV bump, an excess of emission at MeV energies above the extrapolations of the spectra at lower and higher energies. A popular physical interpretation of the MeV bump was to attribute it to redshifted γ-radiation from the decay of neutral pions at an early epoch of the universe (see Sec. 2.2.2.1). The existence of the MeV bump was, however, regarded with scepticism for two reasons (see e.g. Daniel and Lavakare 1975): the energy region 0.5–30 MeV is experimentally most difficult because the cross-section for the interaction of photons with matter reaches its absolute minimum, and in addition the instrumental background due to locally produced nuclear γ-rays is most important from energies of ~ 0.5 MeV to a few MeV. On the other hand, the fact that the MeV bump was measured rather consistently with a variety of different experiments operated in different environments producing different backgrounds (see e.g. Gruber 1992) provided considerable support for the existence of this excess emission. In the end, a shadow of doubt remained on the existence of the MeV bump, and it was felt that new measurements with improved instrumentation were needed to clarify the situation.

At lower, hard X-ray, energies the HEAO-1 mission launched in 1977 was of prime importance, as it carried two experiments, A2 and A4, whose primary goal was the measurement of the CDG from keV to MeV energies. The results obtained with these detectors have important implications on the interpretation of the results at higher, γ-ray, energies, as discussed in Secs. 2.1.6 and 2.1.7 and in the following.

2.3.3 Measurements since $\sim$1980

A large number of γ-ray observations have been performed with balloon-borne and satellite-borne experiments since ~ 1980. Only two of these missions delivered data that allowed us to determine the CDG/EGB, however, these measurements constitute a milestone in the study of the extragalactic γ-radiation. The Solar Maximum Mission

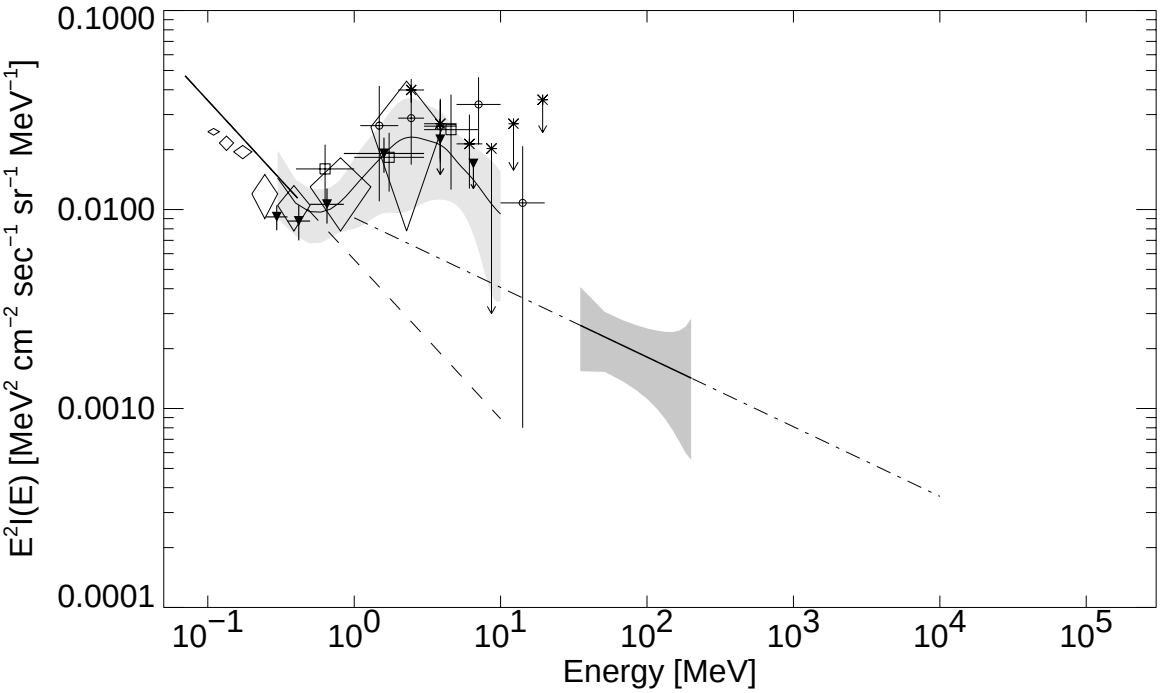

Figure 2.9: *An illustration of the status of CDG/EGB measurements above about 100 keV in 1982. The following results are plotted: Fukada* et al. *(1975): diamonds, Daniel* et al. *(1972) and Daniel and Lavakare (1975): filled triangles, Mazets* et al. *(1975): solid line up to 400 keV (the results at higher energies are not plotted as they are fully consistent with the MeV bump), White* et al. *(1977): asteriks, Trombka* et al. *(1977): light grey-shaded band, Schönfelder* et al. *(1980): circles, Lockwood* et al. *(1981): squares, Thompson and Fichtel (1982): grey-shaded bow tie. The dashed line illustrates the extrapolation of the hard X-ray spectrum to higher energies, the dash-dotted line is an extrapolation of the SAS-2 result to lower and higher energies. The MeV bump, an excess of emission at MeV energies above the extrapolations of the spectra at lower and higher energies, is clearly present. The depicted compilation of experimental results is not exhaustive, but only intended to give the qualitative and quantitative picture at that time. For comparison, the current results on the CDG/EGB spectrum are depicted in Fig. 2.4.*

(SMM) was launched in 1980 and carried a wide-field NaI γ-ray spectrometer (GRS). The GRS operated stably for more than 9 years and was pointed at the sun for most of this time, thereby scanning the ecliptic. Due to its large field-of-view the GRS monitored a considerable fraction of the sky. The Compton Gamma-Ray Observatory (CGRO) was launched in 1991 and is described in more detail in Sec. 3.1. Two of its instruments, namely the Compton telescope COMPTEL and the spark chamber telescope EGRET, sensitive to γ-rays from about 1 MeV to 30 MeV and 30 MeV to 100 GeV, respectively, performed the first all-sky surveys at these energies during the first 18 months of the mission, and since then a large number of pointed observations

across the full sky.

As with earlier measurements of the CDG, the SMM/GRS and COMPTEL analyses relied heavily on the variable nature of the instrumental background for its elimination. In the case of SMM/GRS even the signal itself exhibited a characteristic variation. The SMM/GRS had a large field-of-view of 140° FWHM, hence the largest contributor to the measured count rate, after internal and atmospheric background, was the CDG. To extract the spectrum of the CDG, the observed count rate in each energy channel was fitted with a model consisting of the varying count rates due to CDG and albedo γ-radiation[49], due to decay of radioactivity within the instrument and the spacecraft, and due to prompt and delayed cosmic-ray induced backgrounds (Watanabe *et al.* 1996, Watanabe 1996). The COMPTEL analysis method is described in detail in chapter 5. It is worth noting that the EGRET instrumental background was demonstrated by Sreekumar *et al.* (1998) to be more than an order of magnitude less than the EGB intensity derived from SAS-2 data by Thompson and Fichtel (1982).

Current results on the CDG/EGB from these experiments are discussed in Secs. 2.1.6 and 2.1.7, and in particular in Sec. 6.5. As can be seen in Fig. 2.4, the shape of the CDG/EGB spectrum appears to be much simplified as compared to the situation around 1982 (see Fig. 2.9). The COMPTEL and SMM/GRS measurements provide no evidence for the existence of the putative MeV bump, which therefore must have been due to instrumental background not accounted for in previous analyses. Instead, the overall spectrum seems to consist of a softer low-energy component and a harder high-energy component, with the transition occurring at a few MeV. The high-energy component is now determined over a much larger energy range with greatly improved accuracy and precision.

[49]The variation of these two components results from the variation of the position of the Earth relative to the instrument pointing direction, with the CDG term being the 4π integral of the GRS response minus about 4 ster blocked by the Earth.

Chapter 3

The Compton Telescope COMPTEL

3.1 Introduction

γ-ray astronomy entered a new era on April 5, 1991, when the space shuttle Atlantis (mission STS-37) successfully launched the Compton Gamma-Ray Observatory (CGRO), illustrated in Fig. 3.1. The observatory, with a mass of 16 tons the heaviest scientific satellite to date, was released into a near circular orbit of inclination 28° at an altitude of 450 km. CGRO carries four γ-ray instruments, designed to monitor and image the sky in different, overlapping energy bands ranging from $\sim$ 20 keV to $\sim$ 30 GeV, with an unprecedented combination of high sensitivity, energy resolution and spatial resolution. Each of these instruments is briefly introduced below[1].

The Burst And Transient Source Experiment (BATSE) consits of eight uncollimated detector modules located at the eight corners of the CGRO platform (only one of the eight BATSE detectors is indicated in Fig. 3.1). Each individual module is composed of two NaI(Tl) scintillation sub-detectors: a Large Area Detector (LAD) and a Spectroscopy Detector (SD), sensitive to energies from 20 keV to 1.9 MeV and from 10 keV to 100 MeV, respectively (Fishman *et al.* 1989). BATSE is optimized to continuously monitor the full sky to study γ-ray bursts and X-ray transients. Based on the relative count rates in each of the detector modules, BATSE can localize γ-ray bursts on the celestial sphere with an accuracy of a few degrees. In addition, using the Earth-occultation technique, BATSE also monitors a large number of transient and non-transient hard X-ray sources such as X-ray binaries.

The Oriented Scintillation Spectrometer Experiment (OSSE) uses four actively shielded NaI(Tl)-CsI(Na) phoswich detectors to provide γ-ray line and continuum de-

[1]More information on the Compton Gamma-Ray Observatory is, e.g., available at NASA's Compton science support center under `http://cossc.gsfc.nasa.gov/cossc/cossc.html`.

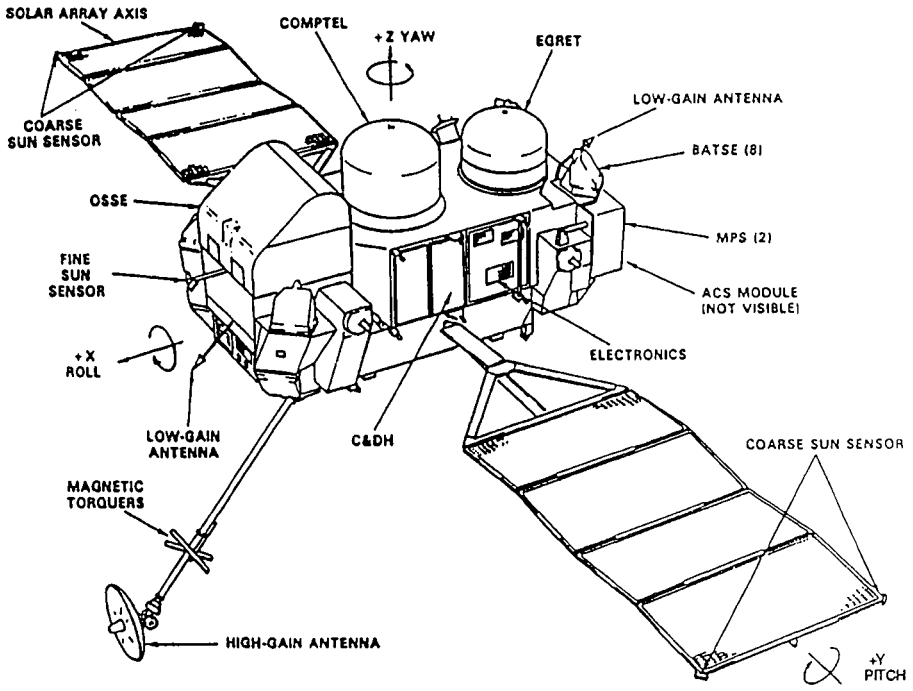

Figure 3.1: *An illustration of the Compton Gamma-Ray Observatory (CGRO), according to Gehrels* et al. *(1994).*

tection capability in the 50 keV to 10 MeV range (Johnson *et al.* 1993). The detectors have a rectangular $3.8° \times 11.4°$ (FWHM) field-of-view defined by tungsten collimators, and can be oriented independent of each other, and relatively independent of the spacecraft orientation, around the CGRO y-axis (see Fig. 3.1), permitting offset pointings for background measurements. The major scientific objectives of OSSE include observations of galactic and extragalactic sources such as X-ray binaries or AGN, studies of the galactic diffuse emission, or γ-ray line and neutron emission from solar flares.

The Energetic Gamma-Ray Experiment Telescope (EGRET) is sensitive in the energy range from ~ 20 MeV to ~ 30 GeV (Thompson *et al.* 1993). EGRET is a spark chamber γ-ray telescope, detecting high-energy photons through electron-positron pair production. The arrival direction of the incident γ-ray is inferred from the tracks of the electron-positron pair in the spark chamber, its energy is determined in a NaI(Tl) calorimeter below. The instrument's field-of-view has a Gaussian shape with a FWHM of $\sim 40°$. EGRET is dedicated to mapping the entire sky and to investigating all categories of astrophysical sources of high-energy γ-radiation, among which are pulsars and AGN, as well as the diffuse γ-ray emission of our galaxy and the extragalactic γ-ray background.

Finally, the COMPton TELescope COMPTEL, the first instrument of its kind operated on a satellite, explores the $\sim 1 - 30$ MeV energy range (Schönfelder *et al.* 1993). The 1σ angular resolution of COMPTEL is $\sim 1° - 2°$ within its wide field-

of-view of about 1 steradian, which can be approximated by a triangular distribution with $\sim 50°$ FWHM. The energy resolution of the instrument ranges from about 10% to 5% FWHM at the lowest and highest energies, respectively. The pointing direction of COMPTEL is identical to that of EGRET. Among the major scientific objectives of COMPTEL is the realization of the first all-sky survey in the little studied $\sim 1-30$ MeV energy range, the observation of galactic sources such as pulsars and X-ray binaries, of extragalactic sources such as AGN, of γ-ray line sources such as the diffuse galactic 1.8 MeV line emission, of diffuse γ-ray emission from interstellar space, of γ-ray bursts and solar flares, and the study of the cosmic diffuse γ-ray background. COMPTEL was designed and built by an international collaboration of four institutes: the Max-Planck-Insitut für extraterrestrische Physik (MPE) in Garching, Germany, the Space Science Institute at the University of New Hampshire (UNH) in Durham, USA, the Laboratory for Space Research (SRON) in Leiden (now in Utrecht), the Netherlands, and the Space Science Departement (SSD) of the European Space Agency in Noordwijk, the Netherlands.

The remainder of this chapter is intended to explain the principle of measurement of a Compton telescope, to describe the COMPTEL instrument, and to present specific instrumental aspects which are of particular importance for the analysis of the cosmic diffuse γ-ray background.

3.2 Principle of Measurement

The principle of measurement of a Compton telescope was first described by Schönfelder *et al.* (1973). It follows naturally from the attempt to make use of the dominating interaction process between matter and photons at MeV energies — Compton scattering[2]. In this process an incident γ-ray photon of energy E_γ inelastically scatters on a free electron at rest, resulting in an energy transfer ΔE_γ from the photon to the electron, and a deflection of the photon from its original direction by an angle φ. From the laws of conservation of energy and momentum it can be shown that the following relation between the scatter angle φ and the energy of the photon before and after the scattering, E_γ and $E'_\gamma = E_\gamma - \Delta E_\gamma$, holds true:

$$\cos\varphi = 1 - \frac{m_0c^2}{E'_\gamma} + \frac{m_0c^2}{E_\gamma} \tag{3.1}$$

with $m_0c^2 = 511$ keV being the rest mass of the electron. The energy-dependent cross-section for the Compton scattering, describing the distribution of the scatter angle φ,

[2]At lower and higher energies photoelectric absorption and pair production are the dominant interaction processes, respectively. Because the three interaction processes have a different dependence on the atomic number Z, with $\sigma_{\rm photo} \propto Z^5$, $\sigma_{\rm Compton} \propto Z$, and to a good approximation $\sigma_{\rm pair} \propto Z^2$ (see e.g. Longair 1992), the energy range in which Compton scattering is the most likely interaction process also depends on Z. For example, in carbon ($Z = 6$) and lead ($Z = 82$) Compton scattering dominates in $\sim 0.03 - 30$ MeV and in $\sim 0.6 - 5$ MeV, respectively.

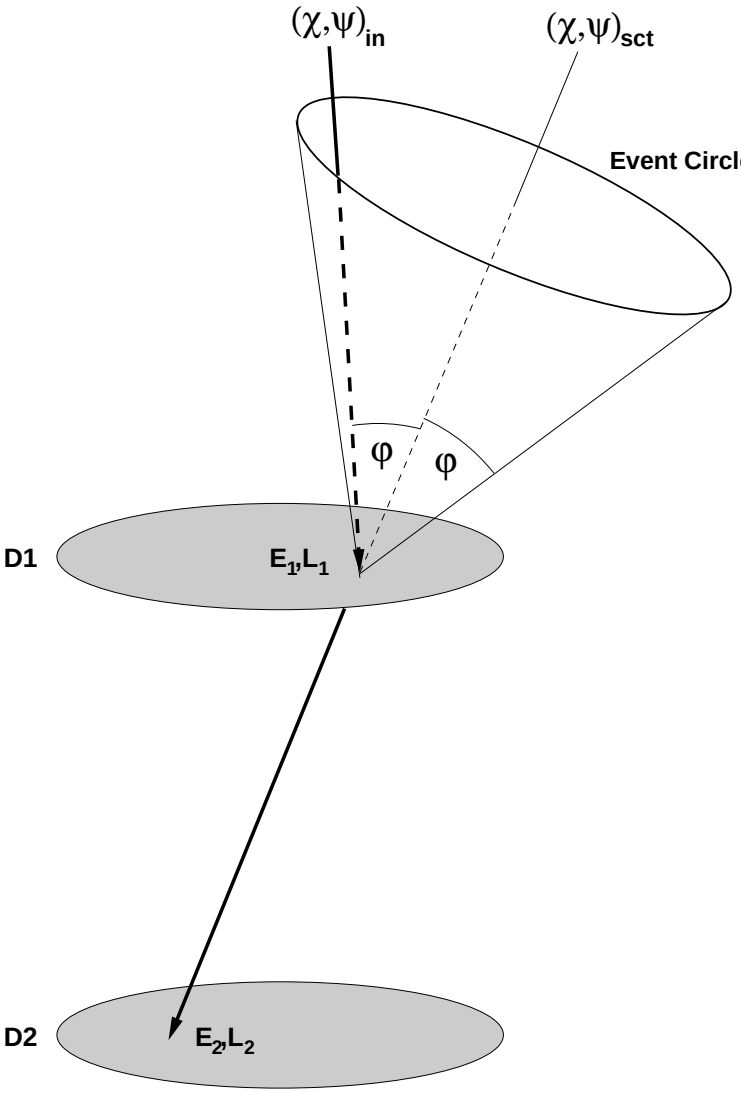

Figure 3.2: *Illustration of the realization of the principle of measurement of Compton telescopes in the COMPTEL instrument for an ideal event. A celestial photon with energy E_γ coming from the direction $(\chi,\psi)_{\rm in}$ is Compton scattered once in the upper detector (D1), thereby being deflected by an angle φ into direction $(\chi,\psi)_{\rm sct}$. Finally, the scattered photon is completely absorbed in the lower detector (D2). For each event the energy deposits E_1 and E_2 in the D1 and D2 detectors are measured, as well as the interaction locations L_1 and L_2. From these measured quantities the energy of the incident photon can be determined, and its direction of incidence can be restricted to lie on a cone around the scatter direction $(\chi,\psi)_{\rm sct}$ with half opening angle φ. The projection of this cone on the celestial sphere defines the so-called event circle.*

is given in the so-called Klein-Nishina formula (see e.g. Longair 1992, p. 96 ff.). The maximum deflection of the photon occurs for back-scattering, $\varphi = 180°$, and results in a maximum energy loss of the photon:

$$\Delta E_\gamma^{\rm max} = \frac{E_\gamma}{1 + m_0c^2/2E_\gamma} \stackrel{E_\gamma \gg m_0c^2}{\longrightarrow} E_\gamma - \frac{1}{2}m_0c^2 \qquad (3.2)$$

which defines the well-known Compton-edge in the continuous energy-loss spectrum of photons in matter. It follows that the determination of energy and direction of the incident photon require the measurement of energy and direction of both the scattered photon and of the recoil electron.

So far the best realization of this principle of measurement has been achieved in the Compton telescope COMPTEL, which utilizes two detector layers for tracking the Compton scattering of the incident photon, as illustrated in Fig. 3.2. Let us

assume for the moment that both detectors are "ideal", i.e. free of any losses of energy deposited in the detectors and with infinitely good energy and positional resolutions. In this ideal COMPTEL a celestial photon with unknown energy E_γ coming from the unknown direction $(\chi,\psi)_{\rm in}$ is Compton scattered once in the upper detector (D1). In this scattering process the incident photon transfers an energy of ΔE_γ to the recoil electron, and is deflected by an angle φ into direction $(\chi,\psi)_{\rm sct}$. Finally, the scattered photon is completely absorbed in the lower detector (D2). The quantities that are measured for such an event[3] are the energy deposits in the two detectors, E_1 and E_2, and the two interaction locations, $L_1 = (x_1, y_1)$ and $L_2 = (x_2, y_2)$. From these measured quantities the energy of the incident photon can be determined:

$$E_{\rm tot} \stackrel{\rm def}{=} E_1 + E_2 \tag{3.3}$$

which for an ideal event is equal to E_γ. The scatter angle $\bar{\varphi}$ can be calculated according to Eq. 3.1 from the measured energy deposits:

$$\cos\bar{\varphi} \stackrel{\rm def}{=} 1 - \frac{m_o c^2}{E_2} + \frac{m_0 c^2}{E_1 + E_2} \tag{3.4}$$

which for an ideal event is equal to φ. Furthermore, the direction of the scattered photon $(\chi,\psi)_{\rm sct}$ can be inferred from the interaction locations L_1 and L_2. A unique reconstruction of the direction of the incident photon $(\chi,\psi)_{\rm in}$ would in addition require the measurement of the direction of the recoil electron in D1 which, however, is beyond the capabilities of COMPTEL[4]. Therefore the possible incident directions of the photon can only be restricted to lie on a cone around the scatter direction $(\chi,\psi)_{\rm sct}$ with half opening angle $\bar{\varphi}$. The projection of this cone on the celestial sphere defines the so-called event circle, which is the locus of all possible origins of the incident photon (see Fig. 3.2). The COMPTEL response to an inividual source in the sky consists of many such event circles, each having a different origin and radius, corresponding to different scatter directions and scatter angles. In the ideal case, the source position simply is the common intersection point of all these event circles.

The real COMPTEL instrument obviously has a response that is not ideal, as described in Sec. 3.5. There is some uncertainty in the measured energy deposits E_1

[3]The occurrence of coincident interactions in both detectors within the coincidence time window of 40 nsec in the absence of a veto signal is referred to as event, as is described in more detail in the next section.

[4]In the COMPTEL D1 detector, the range of the recoil electron is, depending on the energy of the incident photon and the scatter angle, only $\sim 10^{-2}$ cm to a few cm at the most. In addition, low-energy electrons are frequently scattered, rendering a determination of their direction after the initial Compton scatter very difficult. For these reasons no attempt is made with COMPTEL to determine the scatter direction of the recoil electron. This is a goal for the next-generation Compton telescopes such as MEGA, a detector for Medium Energy Gamma-ray Astronomy currently developed at MPE, which utilizes silicon-strip detectors as D1 detector (more information on MEGA is e.g. available under `http://www.gamma.mpe-garching.mpg.de/mega.html`).

and E_2, and in the measured interaction locations L_1 and L_2, resulting in uncertainties in the calculated values of the scatter angle $\bar{\varphi}$ and in the inferred scatter direction $(\chi, \psi)_{\rm sct}$. As a result, the celestial values of the total energy of the incident photon $E_{\rm tot}$ and the scatter angle $\bar{\varphi}$ have complicated distributions around their true values E_γ and φ, respectively. In general, $E_{\rm tot} \lesssim E_\gamma$ and $\bar{\varphi} \gtrsim \varphi$ (see Secs. 3.5.2 and 3.5.4). Due to the combined effects of the uncertainty in the direction of the cone axis, $(\chi, \psi)_{\rm sct}$, and in the half opening angle of the cone, $\bar{\varphi}$, the ideal event circle becomes a blurred event annulus on the celestial sphere.

This is not a major concern for the studies of the cosmic diffuse gamma-ray background presented in this thesis for which COMPTEL is utilized as a pointed collimator, thereby making only limited use of the instrument's imaging capabilities. For dedicated imaging analysis, however, the blurring of the event circle has to be carefully modelled in the instrument response (see e.g. van Dijk 1996, Oberlack 1997).

3.3 Instrument Description

After having introduced the principle of measurement of the Compton telescope COMPTEL, a brief description of the instrument is given in the following. COMPTEL consists of two detector layers D1 and D2, separated[5] by 1.58 m, both of which are surrounded by a pair of charged-particle or anti-coincidence domes (see Fig. 3.3). The in-flight performance of the instrument is continuously monitored with a calibration system. Each of these instrument components is further described below. A comprehensive description of the instrument's design, characteristics and performance has been presented by Schönfelder *et al.* (1993).

The D1 detector consists of 7 cylindrical detector modules filled with the organic scintillator NE 213A, which is composed of hydrogen and carbon. The low average atomic number Z of this material maximizes the energy range over which Compton scattering is the dominant interaction process. In addition, together with the modules' thickness of 8.5 cm, the chance for the occurrence of a single Compton scattering in the D1 detector is optimized. The modules, with a radius of 13.8 cm, are mounted on an aluminium support structure, from which circular holes were removed below each of the modules to minimize the amount of passive material along the γ-ray paths from the D1 to the D2 detector. Each of the 7 D1 modules is viewed from the side by 8 photomultiplier tubes (PMTs) through regularly spaced quartz windows in the aluminium housing. The individual signals from the PMTs allow us to determine the energy deposit and the location of the interaction in the module[6] from the summed signal and the relative signals, respectively, according to the Anger camera principle

[5] The distance of 1.58 m refers to the separation of the centers of the two detector layers.

[6] Only the x and y coordinates of the interaction location can be determined, but not its depth in the module, as is described in more detail in Sec. 3.5.3. This limitation also applies to the D2 modules.

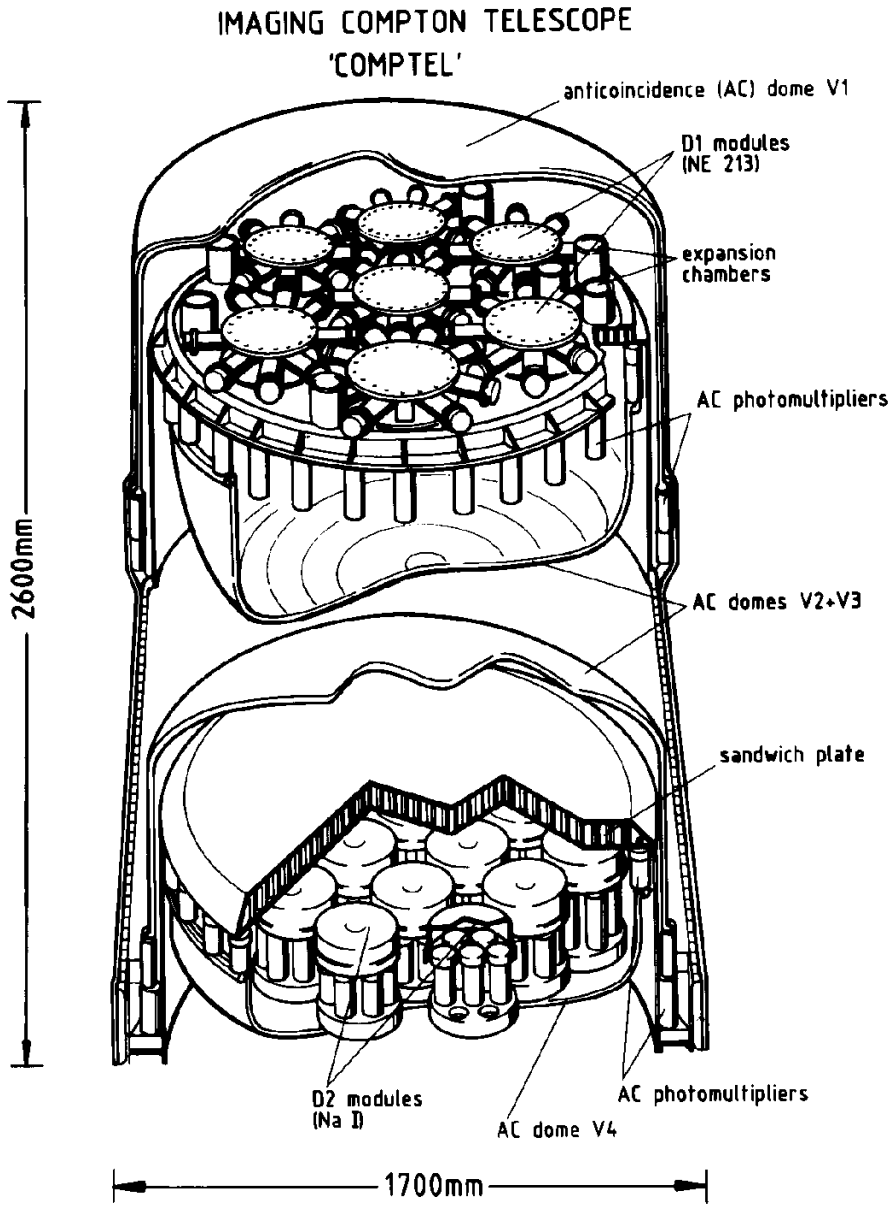

Figure 3.3: *A schematic view of the Compton telescope COMPTEL according to Schönfelder* et al. *(1993).*

(Anger 1958). Each D1 module is equipped with a scintillator expansion chamber used to maintain a constant pressure in the modules. The active geometrical area of the D1 detector is 4188 cm^2.

The D2 detector consists of 14 cylindrical detector modules made of NaI(Tl) crystals of radius 14.085 cm and depth 7.5 cm in an aluminium housing, mounted beneath a low-density aluminium honeycomb sandwhich plate. The high average atomic number

Z of the crystals optimizes the photon absorption properties of the D2 detector. Each module is viewed from the bottom by 7 PMTs through openings sealed with quartz windows. Again, the signals of the individual PMTs are used to determine the energy deposit and the interaction location according to the Anger camera principle. The total geometrical area of the 14 cylindrical crystals is 8744 cm^2.

Each of the two detectors D1 and D2 is completely surrounded by a pair of overlapping, Cassini-shaped charged-particle or anti-coincidence domes to reject charged-particle triggers of the telescope (see Fig. 3.3). In order to allow an overlap these two domes have different sizes: a large dome fits over each detector from above, with a smaller shield below. Each of these so-called veto domes is manufactured of 1.5 cm thick plastic scintillator (NE 110) and viewed by 24 PMTs mounted to the cylindrical extension at the open end. The efficiency of each veto dome to reject charged particles was tested on ground using atmospheric muons and was estimated to exceed 99.99%. The frequency of veto triggers is an important parameter for the CDG analysis (see Chapter 5). It is monitored utilizing a deadtime meter, the principle of which is explained in Sec. 3.10.

The in-flight performance of the instrument is continuously monitored with a calibration system consisting of two ^{60}Co-doped scintillators, the so-called CAL-units, that are placed midway between the D1 and D2 detectors out of the γ-ray light path. The radioactive isotope ^{60}Co has a half-life of 5.3 years and β^--decays by emitting two photons of energies 1.17 MeV and 1.33 MeV. Upon the decay of a ^{60}Co nucleus the β^--particle produces a light-pulse in the scintillator which is detected with very high efficiency by two 1/2 inch PMTs (Snelling *et al.* 1986). This allows us to flag the interaction of one or both ^{60}Co photons in the D1 and/or the D2 detector as so-called CAL-events, which are the basis of the in-flight calibration of the instrument. In addition, each detector module (and each veto dome) is equipped with a light-emitting diode (LED) for calibration and testing purposes.

The COMPTEL instrument accepts and registers all coincident interactions in an individual D1 and D2 detector module within the coincidence time window of $\sim$ 40 nsec in the absence of a veto signal from all charged-particle shields as so-called events, irrespective of whether the interactions are caused by a single photon or by multiple photons and/or particles (see Sec. 3.4.1). Besides the energy deposits and the interaction locations in the two detectors, three additional parameters are measured to characterize each event: the absolute time[7], the so-called time-of-flight (ToF) value and the so-called pulse-shape discriminator (PSD) value. The latter two of these event parameters are of prime importance for background identification and suppression (see Chapter 4) and are briefly described below.

The ToF is a measure for the time difference between the interactions in the D1 and D2 detectors. It is the single most important event parameter for the character-

[7]The absolute point in time of the occurrence of an event is determined with an accuracy of 125 μsec.

ization and elimination of instrumental background (see Sec. 4.3), and consequently considerable effort has been spent on determining its value as accurately as possible (see Sec. 3.7). The ToF is measured in units of [channels], with one channel corresponding to ~ 0.26 nsec. This level of timing accuracy is made possible by the quick rise and decay times of the D2 and in particular the D1 scintillator materials. Photons travelling vertically from the D1 to the D2 detector (so-called downward- or forward-scattered photons) have ToF values of ~ 120 channels, photons travelling the opposite way (so-called upward- or backward-scattered photons) have ToF values of ~ 80 channels. A ToF value of zero (simultaneous interactions in the two detectors) corresponds to channel 100.

The PSD is a measure for a combination of the rise and decay time of the scintillation light-pulse in the D1 detector (Macri 1997a, private communication). It is used to distinguish photons scattering off electrons (short rise and decay times) from neutrons scattering off protons (long rise and decay times). The event parameter PSD is measured in units of [channels], with photon events clustering around channel 80, while neutron events usually appear at channels above 100 — independent of the D1 energy deposit (see Sec. 3.8).

3.4 Data Description

In this section a consise overview is given on the collection of the raw telescope data onboard the satellite, on the processing of the raw data on ground, and on those of the final high-level datasets that are used in scientific analysis in general and in this thesis in particular.

3.4.1 Data Collection

The collection of the telescope event data starts in the Front End Electronics (FEEs), which are electronic devices that exist for each of the D1 and D2 detector modules as well as for each of the veto domes. The FEEs process the relevant output from these instrument components, which in any case includes a fast-logic pulse for timing analysis. The D1 and D2 detector module FEEs also process the signals of the individual PMTs. In addition, the D1 FEEs generate a raw PSD value. The output of the various FEEs is then fed into the Remote Electronics Assembly onboard CGRO, which consists of the Analogue Electronics (AE) and the Digital Electronis (DE) and further processes the raw signals.

In the AE the time delay between the coincident interactions in the D1 and D2 detectors is checked against the coincidence time window of ~ 40 nsec by the FCC (Fast-Coincidence Circuitry). The zero point of this coincidence window is commandable from ground and during nearly the complete mission the settings were such that

the ToF range for events was $\sim 40 - 200$ channels. If in addition there was no coincident trigger of any of the four veto domes[8] the coincident D1 and D2 interactions are accepted as an event. It has to be emphasized that a very substantial background suppresion is achieved at this stage: by selecting only those events for which there is no signal from any of the four veto domes[9] the event rate is reduced by $\sim 99\%$. Each event is subsequently time stamped with an accuracy of 125 μsec, and the detector modules that have been triggered are determined. Furthermore, the FCC forms a raw ToF value from the fast-logic pulses of the triggered modules, and in addition pre-classifies the events as either calibration events (in case of a coincidence between an interaction in a D1 and/or a D2 module and a signal from a calibration unit or a module LED) or as gamma event (in case of a coincidence between interactions in a D1 and a D2 module in absence of a signal from a calibration unit or a module LED).

The DE then classifies the calibration events and gamma events according to a set of criteria which are commandable from ground. All gamma events are first checked against the criteria for the so-called `Gamma-1` class, which in `NORMAL` telescope mode[10] include a minimum energy deposit in both detectors of more than 20 channels, corresponding to $\gtrsim 50$ keV for D1 and $\gtrsim 550$ keV for D2, and a raw ToF value between 95 channels and 150 channels to select downward-moving events and reject those moving upward. In addition, it is required that only one module in each the D1 and D2 detectors was triggered. Events that do not meet the `Gamma-1` criteria are checked against the relaxed `Gamma-2` criteria, which accept all raw ToF values (0–255 channels) and require D1 and D2 detector energy deposits of at least 5 channels, again in the absence of any so-called multi-hits in the D1 and D2 detectors. Events that also fail these criteria, including events for which multi-hits in the D1 and/or the D2 detector occurred, are classified as `Gamma-3`.

The calibration events are sorted into 5 classes: `CAL-1` and `CAL-2` events are coincident triggers of a calibration source and a D1 or D2 detector module, `CAL-3` events are coincident interactions of a calibration source and in both a D1 and D2 detector module. The latter are most valuable for the in-flight calibration (see below). `CAL-4` and `CAL-5` events are LED stimulated triggers of a D1 or D2 module, respectively.

The CGRO telemetry cannot transmit more than 48 COMPTEL events per packet, a packet being a time interval of 2.048 sec. Because of this limitation the selection criteria for `Gamma-1` events, which are scientifically most useful, have been chosen such that they contain nearly all of the celestial photons while their rate does not exceed $\sim$ 20 events/sec on average, thereby keeping signal loss due to telemetry saturation

---

[8] The typical length of the fast-logic veto signal is $\sim$ 200 nsec (see Sec. 3.10).

[9] Because there may be delayed signals from the veto domes, one still has to require the absence of any anti-coincidence signals when selecting events in scientific analysis (see Sec. 4.2.3).

[10] In addition to the standard or `NORMAL` telescope mode for γ-ray observations of the sky, there are also special modes in which the instrument is optimized e.g. for data collection during a γ-ray burst, solar flare observations (γ-rays and neutrons), or measurements of the Earth's albedo neutron flux.

negligible for most parts of the orbit. The `Gamma-2` event rate typically is a factor of 4 higher than the `Gamma-1` event rate, mainly due to the unrestricted ToF range. Since `Gamma-1` events and calibration events have higher priority in the telemetry than `Gamma-2` events, the instrument's deadtime for `Gamma-2` events is significantly higher than for `Gamma-1` events, mostly due to telemetry losses (see Sec. 3.9).

Finally, the AE/DE electronics samples and integrates various house-keeping parameters such as detector and veto dome trigger rates, temperatures of detector and electronics components, or voltages applied to various groups of PMTs. Usually, these parameters are sampled or integrated over the time interval of a packet once per superpacket, a superpacket being 8 packets, hence lasting 16.384 sec ($= 8 \times 2.048$ sec).

3.4.2 Data Processing

The raw data telemetered from the spacecraft are written on tapes, one for each day, at Goddard Space Flight Center (GSFC) in Greenbelt, MD, USA. These tapes are then sent to MPE for further processing into higher-level data that can be used for scientific analysis[11]. For both the processing of raw telescope data and the subsequent scientific analysis of the higher-level data the COMptel Processing and Analysis Software System (COMPASS) has been developed by the COMPTEL collaboration, which is also responsible for the maintenance and continuous improvement of this software package. Reports on the COMPASS system have been presented by den Herder *et al.* (1992) and de Vries (1994), an introductory guide has been written by Stacy (1995)[12].

As a first step in the processing of the raw data the tapes are read by the COMPASS task `ENGCTR`, which writes the different types of data such as telescope events, orbital and house-keeping parameters, to different data files. Except for the calculation of the telescope livetime for each superpacket (see Sec. 3.9) no corrections or calibrations are applied to the raw data.

The conversion from raw event data to calibrated event data is performed in two major steps. The PMT gains needed for the calibration of the detector energy deposits are determined in the In-Flight Calibration (`IFC`) subsystem using the CAL-events. The actual energy calibration is then applied in `EVPRNN`, which converts the analogue sum of the PMT outputs measured in units of [channels] to energy deposits in units of [keV]. In addition, `EVPRNN` determines the event interaction locations based on a neural network (see Sec. 3.5.3) and corrects the raw ToF and PSD values (see Secs. 3.7 and 3.8).

---

[11] Since about mid 1998 the raw data are electronically transferred from GSFC to MPE via ftp.

[12] This guide, and other information on the COMPASS system, is e.g. available under `http://www.gamma.mpe-garching.mpg.de/comptel/compass.html`.

3.4.3 Datasets

In the following, the main types of high-level datasets used in the analysis of the cosmic diffuse gamma-ray background, EVP, OAD, HKD, SHD, and TIM, are briefly described.

- EVP data contain EVent Parameters. For each individual event class an individual EVP dataset is generated. The EVP event parameters include: the D1 and D2 energy deposits (in keV) and interaction locations, the corrected PSD and ToF values, the scatter angle, and the direction of the scattered photon.

- OAD data summarize Orbit and Aspect Data, which are sampled for every superpacket. Orbital parameters are e.g. the location of the CGRO spacecraft above the Earth including the orbit altitude. The aspect (orientation) of the telescope is defined by the pointing directions of its z-axis (the instrument's pointing or observing direction) and x-axis on the celestial sphere (see Fig. 3.1). The instrument's pointing direction is also given relative to the center of the Earth.

- HKD data are House-Keeping Data, such as detector and veto dome trigger rates, temperatures of detector and electronics components, or voltages applied to various groups of PMTs. As already mentioned, usually these parameters are sampled or integrated over the time interval of a packet once per superpacket.

- SHD (Superpacket HeaDer (and livetime)) data give the livetime of the instrument per superpacket (see Sec. 3.9). The livetime of the instrument is defined as the time over which it was able to process and transmit a potential event, hence the livetime is complementary to the instrument's deadtime. SHD data are generated for Gamma-1 and Gamma-2 events only.

- TIM data provide TIMe information, i.e. the operating mode of the telescope as a function of time, allowing us to conveniently select data from those periods of time during which the instrument collected data in the appropriate mode. For standard γ-ray observations the instrument is operated in the so-called NORMAL mode.

3.5 Instrument Response

The response is the most important characteristic of an instrument for scientific analysis, as it describes the distribution of the measured event parameters as a function of energy and direction of the incident photons. The COMPTEL response has been determined with three different approaches (Diehl *et al.* 1992, Schönfelder *et al.* 1993):

1. empirically by calibrating the instrument with γ-ray line sources located at different positions.

2. analytically by convolving analytical representations of the reponses of the individual detectors D1 and D2.

3. in Monte Carlo simulations using the COMPASS `SIM` sub-system (Kippen 1991, Stacy *et al.* 1996) based on the GEANT simulation code developed and maintained by CERN.

Each of these approaches has its unique advantages and disadvantages. In principle, the empirical calibration of the instrument is the most straight-forward and reliable approach, however, its applicability is limited by the finite number of source energies and positions that can actually be measured. In addition, the sources could not be positioned at distances larger than ~ 8 m during calibration for technical reasons, limiting the applicability of the calibration for celestial sources located at practically infinite distance. The former problems also apply to the calibration of the individual D1 and D2 detector systems, however, their individual responses can be modelled analytically or be reproduced by simulation much more easily. The most severe concern regarding the convolution of the analytical responses of the individual detectors to model the telescope response is that this approach cannot sufficiently describe the full telescope, because effects such as photon scattering in the instrument structure can at best be approximated. The potentially most powerful approach is the determination of the instrument response in Monte Carlo simulations by propagating the incident photons and secondary particles through a detailed mass model of the telescope[13], taking into account instrumental characteristics such as energy resolutions as determined in the calibration measurements. Once the capability of the simulation package to reproduce the calibration results has been verified, this approach can be used to determine the response to any source distribution with any energy spectrum. The main disadvantage of the simulation approach is that it requires considerable computer resources.

In the following, some of the basic characteristics of the COMPTEL response are addressed briefly, in particular of the spectral response relevant to the CDG analysis[14]. Emphasis is put on the understanding of the physical origin and nature of the COMPTEL telescope events, and on the validity of the simulation approach. The latter is of fundamental importance for the CDG analysis, because the instrument's response to an isotropic source (see Sec. 3.6) and to internal radioactivity (see Sec. 4.4.2) can *only* be determined by Monte Carlo simulation.

---

[13]The most recent descriptions of the various COMPTEL mass models can be found in Kippen (1996) and Weidenspointner *et al.* (1996b).

[14]Thorough discussions of the spatial (imaging) aspects of the instrument response can be found, e.g., in van Dijk (1996) and Oberlack (1997).

3.5.1 D1 and D2 Detector Energy Resolution

The D1 detector was designed to maximize the probability of a single Compton-interaction (see Sec. 3.3), hence incident photons are not absorbed in the D1 detector and the energy-loss spectrum does not show a photopeak. Therefore the energy resolution of the D1 detector was determined with a Compton-backscatter method, utilizing a coincidence setup with two detectors, in which the photons scatter by an angle close to 180° (Diehl and Graser 1981, Schönfelder *et al.* 1993). For technical reasons the D1 detector could only be calibrated with radioactive sources in the energy range 339 keV to 4.438 MeV. The response for single Compton-scatter events can be well represented by a Gaussian function. The average energy resolution of the D1 detector as a function of energy deposit is to a good approximation described by a power law

$$\sigma_1 = 1.10 \cdot E_1^{0.57} \tag{3.5}$$

with σ_1 and E_1 in [keV].

The response of the D2 detector is much more complicated due to various energy-loss mechanisms that allow a fraction of the deposited energy to escape from the D2 module (a detailed description of the D2 energy response can be found in van Dijk 1996). The D2 energy response was empirically determined by placing calibration sources at large zenith angles as seen from COMPTEL, such that parts of the D2 detector could be directly reached by the photons without having to pass through the D1 detector. The energies of the calibration sources (radioactive isotopes and accelerator targets) ranged from 511 keV to 20.5 MeV (Schönfelder *et al.* 1993). A first model for the energy response of the D2 detector consisted of the following components: a photopeak, a Compton component, and two escape-peaks (see Fig. 3.4). The photopeak consists of photons that are fully absorbed. This component includes photons that undergo multiple Compton-scattering and pair production, as long as the scattered photon and all secondary particles eventually deposit all of their energy in the same module. The Compton component is due to photons that Compton scatter once and subsequently escape from the module. Its shape is described by the differential cross-section for Compton scattering, the so-called Klein-Nishina formula. The two escape-peaks are only present for photon energies above the electron-positron pair-production threshold of 1.022 MeV. If both the electron and the positron are fully absorbed, the photon contributes to the photopeak component. It is quite likely, however, that one or both of the 511 keV photons created in the annihilation of the positron leave the module, resulting in the two peaks that are located 511 keV and 1.022 MeV below the photopeak energy. This model was not sufficient to adequately describe the D2 energy response, in particular at the lowest energies. From Monte Carlo simulations of the response it became clear that an additional component, the so-called Compton background, needed to be included. The Compton background, which to a good approximation is a constant distribution up to the photopeak energy, is due to Compton scatterings of the photons in the telescope structure before entering the D2 detector (van Dijk

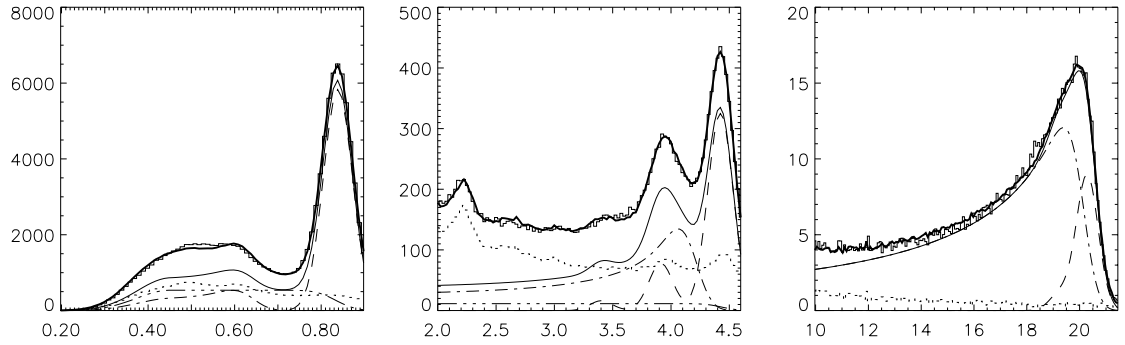

Figure 3.4: *The empirical D2 detector response (counts/bin versus energy [MeV]) for the calibration energies 0.835 MeV, 4.438 MeV and 20.525 MeV from left to right, respectively (figure taken from van Dijk 1996). The histograms are the data from calibration measurements consisting of a source and a background component. The latter was determined in measurements with the source blocked, and is given by the dotted line. The components of the response model are the photopeak and the two escape-peaks (dashed line), the Compton component (dash-dotted line) and the Compton background (dash-tripple-dotted line). The simultaneous fit of the D2 response model and the background is given by the thick solid line, the response model alone is given by the thin solid line.*

1996). Now the D2 energy response could be adequately described at all energies (see Fig. 3.4). Based on fits of this improved model response to the measured energy-loss spectra the D2 energy resolution as a function of the energy deposit was obtained:

$$\sigma_2 = 0.01 \cdot \sqrt{9.86\, E_2 \ + 4.143\, E_2^2} \tag{3.6}$$

with σ_2 and E_2 in [MeV]. It has to be noted that at energies above $\sim$ 10 MeV no distinct photopeak is present in the D2 spectra any more, because the modules are too small to fully absorb the energy of the incident photon and its secondaries (e.g., bremsstrahlung emitted by recoil or secondary electrons can escape from the modules, resulting in a continuous distribution of energy losses). The D2 spectrum then has a shape similar to a Compton distribution, which results from the superposition of photopeak, escape-peaks and Compton component (modified by an energy-dependent empirical factor above $\sim$ 12 MeV), and the entire distribution peaks slightly below the input energy. Because the energy-loss mechanisms responsible for this Compton-like distribution could only be modelled semi-empirically, it is the width of the peak of this distribution that was used in the calibration above 10 MeV, not the width of the photopeak as at lower energies.

3.5.2 Combined Instrument Energy Resolution

The response of the combined telescope was empirically determined at energies ranging from 511 keV to 20.5 MeV, and could successfully be reproduced by semi-empirical models combining the responses of the individual detectors, and in particular by Monte

Carlo simulation. Because the energy resolution of the D1 detector is poorer than that of the D2 detector (see Eqs. 3.5 and 3.6) the energy resolution of the combined instrument depends on the scatter angle $\bar{\varphi}$ (see Eqs. 3.3 and 3.4). In addition, the average scatter angle of a source increases with increasing source zenith angle[15], implying a dependence of the energy resolution of the combined instrument on the zenith angle of the source. The measured $E_{\rm tot}$ spectra resemble the D2 spectra (see Fig. 3.4). Most photons Compton scatter only once in D1, with their D1 energy deposit being totally absorbed, in contrast to the D2 detector, for which losses of the deposited energy are not unlikely, in particular at high photon energies. It follows from Eq. 3.3, that in general $E_{\rm tot} \lesssim E_\gamma$. For an on-axis source the full-energy peak resolution as a function of the input energy can be described by (Schönfelder *et al.* 1993, Much 1994)

$$\sigma_{\rm tot} = 0.01 \cdot \sqrt{14.61\, E_{\rm tot} \ + 2.53\, E_{\rm tot}^2} \tag{3.7}$$

with $\sigma_{\rm tot}$ and $E_{\rm tot}$ in [MeV].

3.5.3 Event Localisation Resolution

The event localization resolution of the D1 and D2 detector modules has been determined by mapping each module in (x, y) with a collimated beam of γ-rays from radioactive sources: approximately 900 positions were mapped with ^{60}Co photons (1.173 MeV and 1.332 MeV) for each D1 module, 686 positions were mapped with ^{22}Na photons (511 keV and 1.275 MeV) for each D2 module. Based on the set of relative PMT signals associated with each location, the so-called location map, a neural-net learning algorithm was used to derive a set of characteristic weights for each of the modules (Connors *et al.* 1992). Application of the neural net allows us to effectively interpolate the calibration grid to infer the interaction location from the set of relative PMT signals according to the Anger camera principle (Anger 1958).

The absolute spatial (x, y)-resolution of the D1 and D2 modules was measured by comparing the event locations for collimated photons, derived with the module maps, with the known collimator position. In both the D1 as well as the D2 modules the spatial (x, y)-resolution was found to depend on the interaction location, as depicted in Fig. 3.5. In the D1 modules the 1σ event location varies from 0.6 cm (in front of the PMTs) to 6.1 cm (between the PMTs). The average 1σ resolution, the average over all collimator positions, is 2.3 cm. The spatial (x, y)-resolution of the D2 modules is better on average (1.5 cm average 1σ resolution) and shows less variation (0.5–2.5 cm). At a given D1 or D2 location, however, the (x, y)-resolution is not symmetric. For example, for the location of events that interacted between the PMTs there is a tendency of being reconstructed in front of one of the adjacent PMTs, resulting in an apparent clustering of the event interaction locations in front of the PMTs and a depletion of interaction

[15]The zenith angle of a source, ζ, is defined as the angle between the pointing direction of the telescope and the direction to the source location.

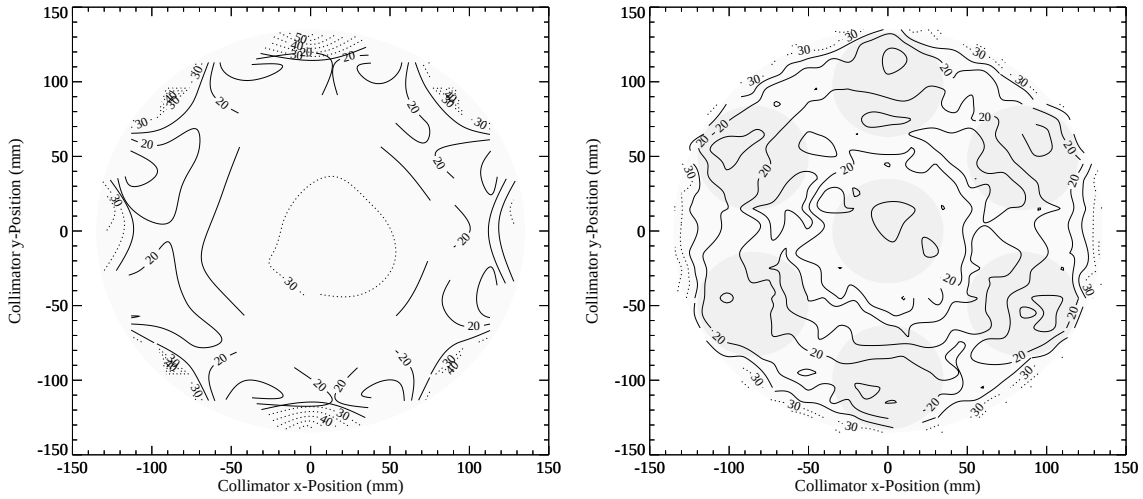

Figure 3.5: *Contour plots of the 1σ spatial (x,y)-resolution for a single D1 (left) and a single D2 (right) module (the figure is taken from Oberlack 1997). The contour levels are given in units of [mm]. The 8 PMTs viewing the D1 module from the side are located were the spatial resolution is best (compare Fig. 3.6). The location of the 7 D2 PMTs is indicated by the grey-shading.*

locations between the PMTs (see Fig. 3.6). Also, interaction locations close to the edge of a module have the tendency to be reconstructed further inside the module, resulting in an apparent depletion of event interaction locations around the modules' edge.

The energy dependence of the event localization process was assessed for one D2 module by comparing the location map obtained at 1.27 MeV to location maps determined at 6.1 MeV and 20.5 MeV (Böhm 1984). These three maps were found to compare well, and therefore the 1.27 MeV map is used for determining the event interaction locations at all energies. Studying the event interaction locations in the D1 and D2 modules, however, it was found that the systematic artifacts produced by the neural-net reconstruction do significantly change with energy, as can be seen in Fig. 3.6. In both the D1 and the D2 modules these artifacts become more pronounced with increasing energy, indicating that the used location maps, which were derived at low energies, become less applicable with increasing energy. The presence of these systematic effects is expected to affect the instrument's imaging capabilities as a function of energy. First results of a study of these effects can be found in Appendix C.

Finally, the z-response of the D1 and D2 detector modules, giving the height of the interaction location, cannot be unambiguously inferred with the neural-net algorithm or any other algorithm for a number of reasons (see Connors *et al.* 1992, and references therein). First of all, no calibration measurements have been made that allow us to study the PMT signals as a function of the z-position of the interaction location in the modules. Since the D1 PMTs are positioned symmetrically on the walls of each D1 module, there is clearly limited depth information, and it is expected that the D1 PMT z-response is symmetric about the central plane of the modules. In principle,

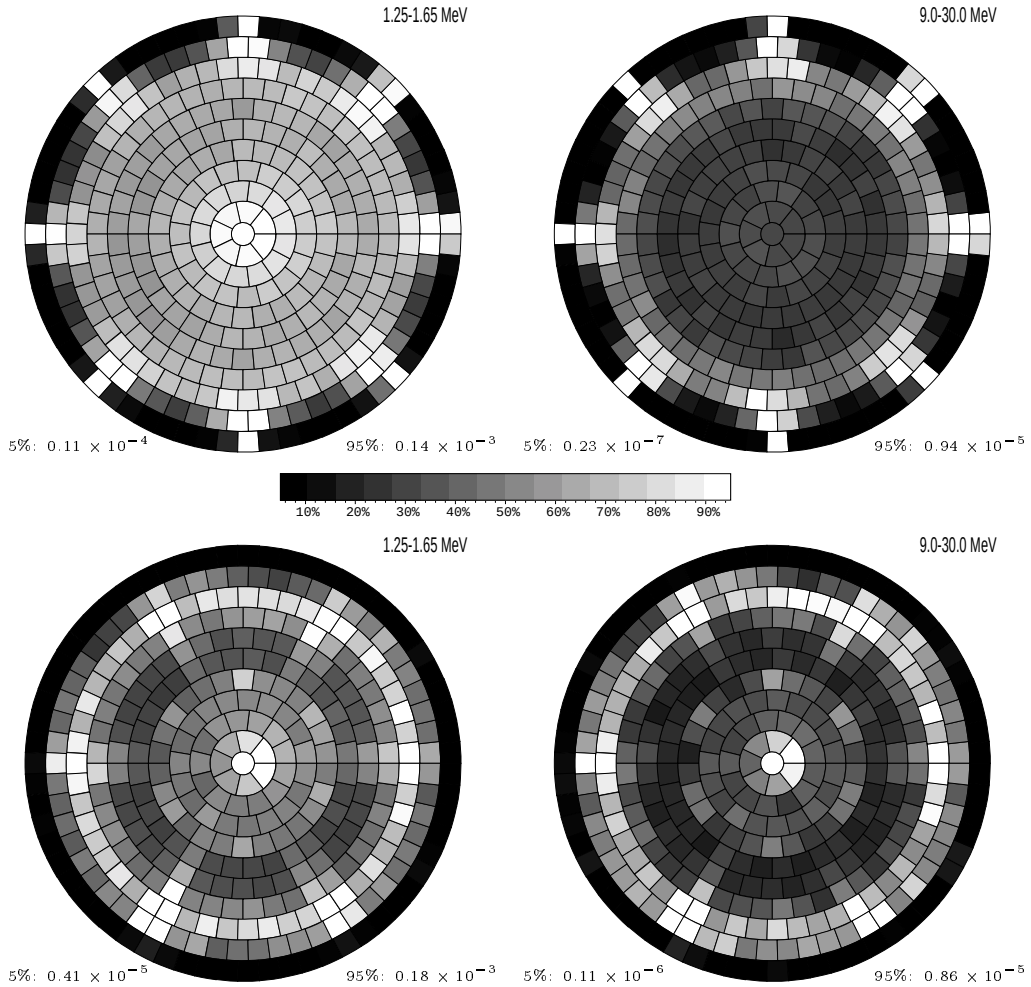

Figure 3.6: *The energy dependence of the neural-net reconstruction of the event interaction location in the D1 (upper row) and the D2 (lower row) detector. The event rates in individual localization bins are depicted for the energy ranges 1.25–1.65 MeV (covering the calibration energies used for the derivation of the location maps) and 9–30 MeV in the left and right column, respectively. The linear grey scale covers 5–95% of the full dynamic range of the event rates, which are in units of [1/(sec · 1.9cm^2)] and [1/(sec · 2.0cm^2)] for D1 and D2, respectively. To minimize statistical fluctuations, the event rates of the individual D1 and D2 modules have been overlayed, taking into account their 8-fold and 7-fold symmetry. In D1, the location of the 8 PMTs is clearly indicated by the bright spots around the module edge. At low energies, the D1 event localizations are still quite homogeneous, whereas there is a pronounced trend for the reconstructed event locations to cluster in front of the PMTs at high energies. Similarly, in D2 the locations of the 7 PMTs are again indicated by bright spots, which also become more pronounced at higher energies, but both of these trends in D2 are present to a lesser extent than in D1. In comparing with Fig. 3.5 it has to be noted that there the D1 and D2 modules are rotated by 22.5° and 30° relative to the orientation in this figure, respectively.*

the situation is more favourable for the D2 modules, as they are viewed by the PMTs from the bottom. It has been demonstrated with light propagation models, however, that even in the D2 modules there is some remaining ambiguity in the PMT signals that precludes a unique reconstruction of the z-coordinate of the interaction location. For these reasons only the (x, y)-information on the event interaction locations can be used in COMPTEL analyses, and for simplicity the z-coordinates of the D1 and D2 interaction locations are set equal to the mid-planes of the respective detectors.

3.5.4 Angular Resolution Measure

The spatial (imaging) response of COMPTEL is most suitably described in terms of an energy-dependent distribution in a three-dimensional dataspace $(\chi_{\rm sct}, \psi_{\rm sct}, \bar{\varphi})$, with $(\chi_{\rm sct}, \psi_{\rm sct})$ being the direction of the scattered photon in spherical coordinates (see Sec. 3.2) and $\bar{\varphi}$ being the scatter angle determined from the D1 and D2 energy deposits according to Eq. 3.4 (Schönfelder *et al.* 1993). In this three-dimensional dataspace the distribution of ideal events from a point source at position $(\chi_{\rm in}, \psi_{\rm in})$ in the sky is a cone with half opening angle 45° located at $(\chi, \psi) = (\chi_{\rm in}, \psi_{\rm in})$. In real life some fraction of the energy deposited in D1 and D2 may escape from the modules, in addition to other imperfections, resulting in a broadening or smearing of the cone structure.

The width of the spatial response, i.e. the effective angular resolution, can be well illustrated by the distribution of the difference between the scatter angle $\bar{\varphi}$ and the true geometrical scattering angle $\varphi_{\rm geo}$, defined as the angle between the scatter direction $(\chi_{\rm sct}, \psi_{\rm sct})$ of the photon as inferred from the interaction locations L_1 and L_2 and the direction to the source. This is the so-called angular resolution measure ARM:

$$\mathrm{ARM} = \bar{\varphi} - \varphi_{\rm geo} \tag{3.8}$$

Examples of ARM distributions determined with three different methods for each of three different calibration energies are given in Fig. 3.7. For ideal, totally absorbed events $\bar{\varphi} = \varphi_{\rm geo}$ and therefore ARM = 0°, hence the ARM distributions peak at about zero. The most frequent energy losses occur in the D2 detector, resulting in a $\bar{\varphi}$ that is larger than in the ideal case ($\bar{\varphi} \gtrsim \varphi$, see Eqs. 3.1 and 3.4) and producing a tail towards positive ARM values. Similarly, incomplete energy deposits in the D1 detector result in an underestimate of $\bar{\varphi}$ and produce a tail towards negative ARM values. It is important to note that the three different methods for determining the ARM distribution, namely direct measurement, modelling with analytical functions and Monte Carlo simulation, yield consistent results. In particular, the close agreement of calibration data and simulation again indicates that the instrumental characterists of COMPTEL can indeed be reproduced in Monte Carlo simulations.

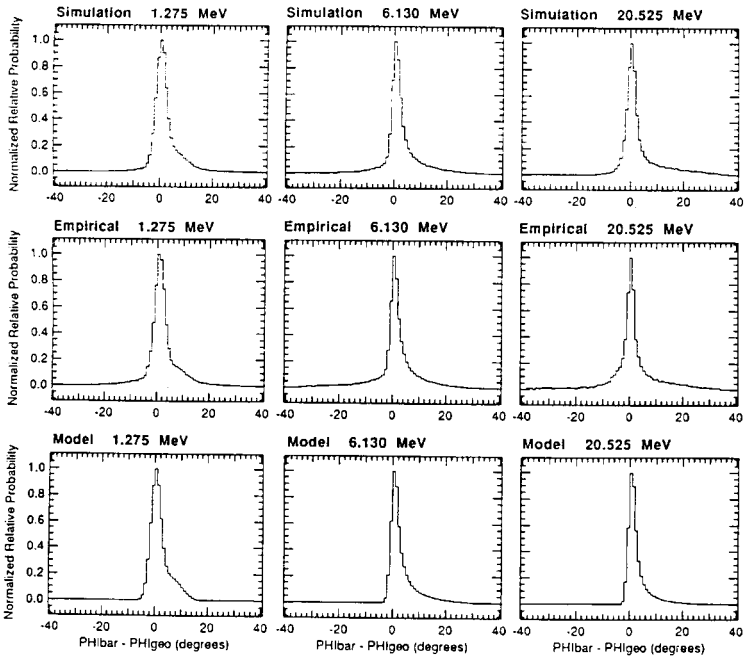

Figure 3.7: *ARM spectra at three different γ-ray energies (1.275 MeV, 6.130 MeV and 20.525 MeV) obtained with three different methods each: Monte Carlo simulation (top row), direct measurement (middle row) and analytical modelling (bottom row). The figure is from Schönfelder* et al. *(1993).*

3.5.5 Effective Area

A telescope is not only characterized by its spectral and spatial resolution, but also by its efficiency in detecting incident photons. The latter aspect is characterized by the effective area $A_{\rm eff}$ [cm^2], which is defined by

$$A_{\rm eff}(\vartheta,\varphi,E) = A_{\rm geo}(\vartheta,\varphi)\cdot\varepsilon(\vartheta,\varphi,E) \tag{3.9}$$

with $A_{\rm geo}(\vartheta,\varphi)$ being the geometrical area of the detector projected in the direction of incidence (ϑ,φ), and $\varepsilon(\vartheta,\varphi,E)$ being the detector efficiency for photons incident from (ϑ,φ) with energy E. The effective area can be considered the geometrical detector area that is effectively "seen" by the incident photons, i.e. the geometrical area of an ideal detector with detection efficiency 100%.

A comparison between the COMPTEL effective area as determined from calibration measurements and from Monte Carlo simulations as a function of energy is given in Fig. 3.8. The results from the two methods are in good agreement, given the uncertainties in the calibration measurements due to background and uncertainties in the source intensities, which again validates the simulation approach. The decrease of $A_{\rm eff}$ at low energies is due to the D1 and D2 energy thresholds, the decrease of $A_{\rm eff}$ at high energies mainly results from the decrease of the Compton-scatter cross-section at these energies.

The CDG analysis requires the COMPTEL effective area for an isotropic photon intensity, which cannot be derived from existing calibration measurements, but only by Monte Carlo simulation. A detailed description of the derivation of the effective area for an isotropic intensity is given in Sec. 3.6.

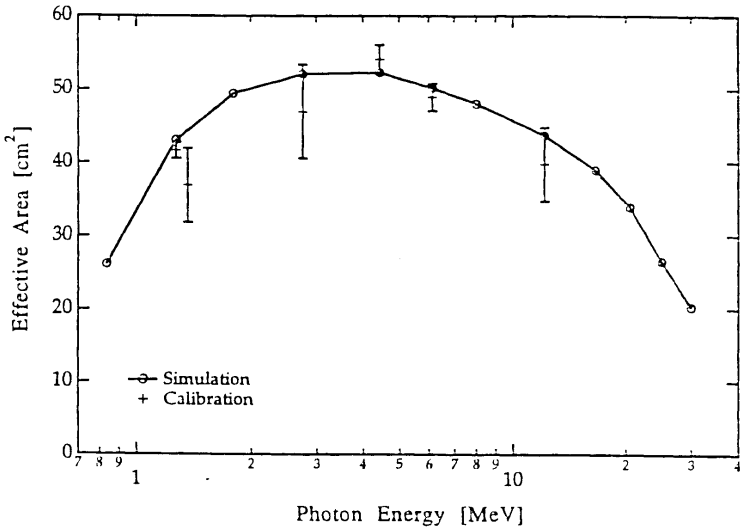

Figure 3.8: *A comparison of the COMPTEL effective area determined from calibration measurements and from Monte Carlo simulations for vertical incidence (from Stacy* et al. *1996).*

3.5.6 Physical Nature of Telescope Events

To conclude this concise account of the COMPTEL response some comments are given below on the origin and nature of the telescope events. A qualitative and quantitative understanding of the different interaction types resulting in the triggering of an event has been obtained by a detailed tracking of the events performed in the COMPASS task `SIMTRK` (see e.g. Kappadath 1994, Stacy *et al.* 1996, Kappadath 1998). These studies showed that the most efficient interaction channels or processes for producing a valid telescope event are:

- The incident photon Compton scatters in the D1 detector and subsequently interacts in the D2 detector. For an ideal event a single Compton-scatter in D1 with no loss of deposited energy and a complete absorption of the scattered photon in the D2 detector are required.

- The incident photon Compton scatters in the D1 detector and a bremsstrahlung photon emitted by the recoil electron triggers the D2 detector.

- The incident photon undergoes pair production in the D1 detector and a bremsstrahlung photon from either the electron or the positron interacts in the D2 detector.

- Again, the incident photon pair-produces in the D1 detector, but one of the two photons from the positron annihilation triggers the D2 detector.

The relative importance of the various interaction types to produce valid telescope events is exemplified in Figs. 3.9 and 3.10 for mono-energetic sources at normal incidence. A detailed decomposition of valid telescope events according to the mechanism that, in the D1 detector, produced the photon triggering the D2 detector is given in

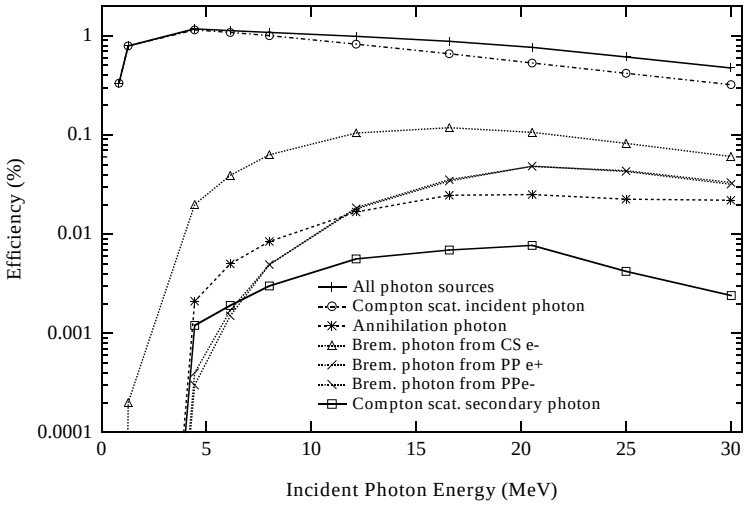

Figure 3.9: *A detailed decomposition of valid telescope events according to the mechanism that, in the D1 detector, produced the photon triggering the D2 detector: Compton scattering of the incident photon, annihilation of positrons produced in pair productions, bremsstrahlung photons from the recoil electron or either the electron or positron from pair production, or Compton scattering of a secondary photon (from Stacy* et al. *1996).*

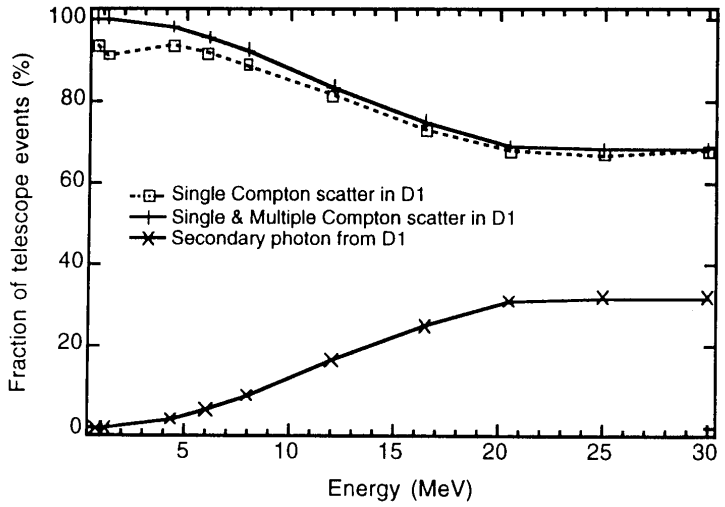

Figure 3.10: *The fraction of valid telescope events involving the Compton-scattered incident photon or a secondary photon (from Kappadath 1998).*

Fig. 3.9. As can be seen, the most efficient photon interaction in the D1 detector for the triggering of valid telescope events is Compton scattering. If the photon interacting in the D2 detector is not the Compton-scattered incident photon, then the secondary photon most likely is a bremsstrahlung photon produced either by the recoil electron or by one of the two leptons from a pair-production interaction of the primary photon. The fractions of telescope events involving single or multiple Compton-scatters of the incident photon in the D1 detector, or the production of a secondary photon, is given in Fig. 3.10. At all energies, most telescope events are due to photons that Compton-scatter once in the D1 detector before triggering the D2 detector. Only a minority of telescope events are due to photons that underwent multiple Compton-scattering in the D1 detector. The fraction of telescope events that are triggered by secondary photons travelling from the D1 to the D2 detector is much smaller than that

of Compton-scattered events, but increases with energy.

3.6 Calculation of Effective Area for Isotropic Intensity

The effective area is the characteristic quantity of a telescope that allows us to convert the measured event rate r [photons/sec] into the incident source flux F [photons/cm^{2}sec] or intensity I [photons/cm^{2}sec ster] from a point-like source or an extended source distribution, respectively[16]. Let the telescope be exposed to an intensity distribution $I(\vartheta, \varphi, E)$ of photons with energy E and direction of incidence (ϑ, φ). Then the resulting event rate measured by the telescope at energy E can be determined from

$$r(E) = \int A_{\rm eff}(\vartheta, \varphi, E)\, I(\vartheta, \varphi, E)\, d\Omega \tag{3.10}$$

with the effective area $A_{\rm eff}(\vartheta, \varphi, E)$ for photons with energy E and incident direction (ϑ, φ) being defined according to Sec. 3.5.5. In the special case of an incident isotropic intensity $I(\vartheta, \varphi, E) = I_0(E)$, which is assumed to apply for the CDG, the relation between the measured event rate $r(E)$ and the isotropic intensity $I_0(E)$ reduces to:

$$r(E) = I_0(E) \cdot \int A_{\rm eff}(\vartheta, \varphi, E)\, d\Omega \tag{3.11}$$

The calculation of the effective area of COMPTEL as a function of the direction of incidence (ϑ, φ) is complicated by the fact that the instrument does not have a well-defined aperture. As described in Sec. 3.3, the D1 detector consists of 7 cylindrical scintillator modules, therefore incident photons can enter these modules not only from the top, but also from the sides. In addition, some D1 modules can be "shaded" by others for directions of incidence with large zenith angles. Also, incident photons can scatter or produce secondary photons in the passive material surrounding the D1 modules. These and other effects[17] have to be taken into account carefully if the

[16] In this section the intensity I is defined as the number of photons incident from direction (ϑ, φ) on a unit area $d\sigma$ per unit solid angle $d\Omega$. The flux F is defined as the number of photons that pass through a unit area $d\sigma$. Letting ϑ be the angle between the normal to $d\sigma$ and the direction of incidence, it follows that:

$$F = \int I(\vartheta, \varphi) \cos\vartheta\, d\Omega.$$

[17] For example, in orbit not all detector modules have performed perfectly all the time due to PMT failures, which is accounted for in the scientific analysis by rejecting events that interacted in parts or all of the sensitive area of these malfunctioning modules. This can easily be reproduced by the simulations. Detector modules that have been switched off, however, represent passive material that is not correctly taken into account in the simulations at the moment. E.g., multiple hits involving an interaction in a switched off module are identified in the simulation, but not onboard the telescope. For incident γ-radiation these effects are minor (which may not be the case for background produced by incident particles, in particular neutron-induced background in the D1 scintillators).

isotropic intensity of the CDG is to be measured correctly.

In the following the algorithm used in SIMGAM[18] to calculate the COMPTEL effective area $A_{\rm eff}(E)$ for an isotropic intensity at energy E is summarized briefly (see the illustration in Fig. 3.11):

1. A random direction (ϑ, φ) is drawn from a hemispherical distribution around the center of the D1 detector[19].

2. A square $A_{\rm vtx}$ perpendicular to that direction is defined on which the vertex position (the starting position) of the random photon will be chosen. $A_{\rm vtx}$ is located outside the structure of the telescope, in particular the veto domes. The size of $A_{\rm vtx}$ is independent of (ϑ, φ) and is chosen such that the projected area of the D1 detector on the plane of $A_{\rm vtx}$ along (ϑ, φ) is always inside $A_{\rm vtx}$[20].

3. A random vertex position is chosen from $A_{\rm vtx}$.

4. A random photon energy E is drawn, usually from a power law distribution.

5. The photon is started from the chosen vertex position with the chosen energy in direction (ϑ, φ) and propagated through the COMPTEL mass model.

The architecture of the COMPASS subsystem SIM is such that the task SIMGAM does not return any information on either the starting location and direction or the starting energy of the individual photons propagated. Nevertheless, the effective area for an isotropic intensity can be determined from the available SIMGAM output, consisting of the total number of simulated photons and of the simulated event parameters of all photons that triggered the telescope, as explained below.

The following considerations are purely geometrical, therefore the energy dependence of the effective area is dropped for the moment. As defined above, the effective area $A_{\rm eff}(\vartheta, \varphi)$ for an incident intensity from direction (ϑ, φ) is determined by the projection of the geometrical area of the detector on the direction of incidence, $A_{\rm geo}(\vartheta, \varphi)$,

[18] SIMGAM is the standard Monte Carlo simulation task used to simulate the COMPTEL response to incident photons and internal radioactivity (see Sec. 4.4.2). It is based on the GEANT Monte Carlo package released and maintaned by CERN and part of the SIM subsystem of COMPASS, the COMptel Processing and Analysis Software System. Further information on the COMPTEL SIM package can be found on http://wwwgro.unh.edu/comptel/compass/sim/SIM.html.

[19] The data selections applied in the CDG analysis (see Sec. 4.2) restrict the COMPTEL field-of-view to about 1 steradian, centered on the telescope's pointing direction. To correctly simulate this situation, the photons have to be started from a solid angle larger than the field-of-view. Starting the photons from the hemisphere above the telescope takes into account the possible range of measurement uncertainties (events originating from outside the nominal field-of-view may be accepted) and provides flexibility to apply the results of the simulations to different event selections.

[20] The D1 detector can be inscribed in a cylinder of depth 25 cm and radius 78 cm. Thus an $A_{\rm vtx}$ of dimensions $2 \cdot 78$ cm and $(2 \cdot 78 + 25)$ cm, yielding a total area of 28236 cm^2, meets the requirements.

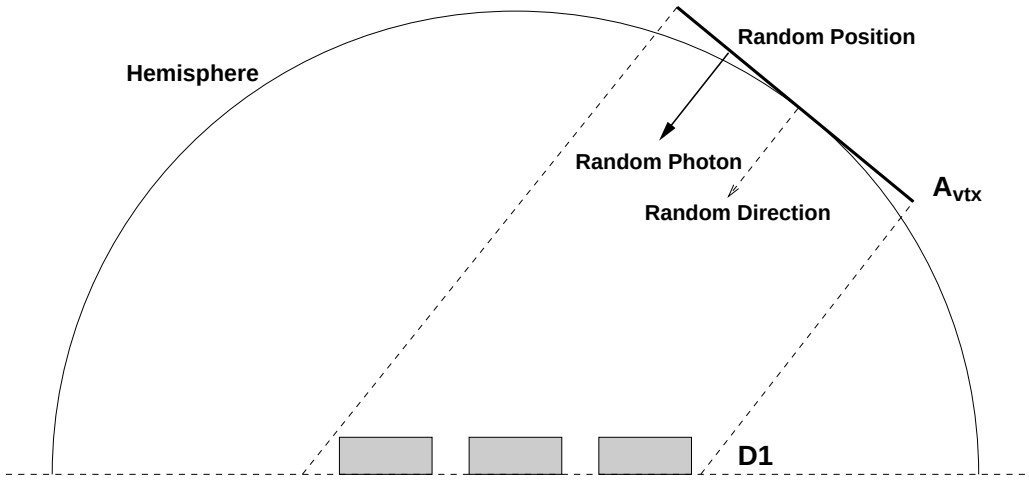

Figure 3.11: *Illustration of the algorithm used in* `SIMGAM` *to determine the total effective area* $A_{\rm eff}(E)$ *for the CDG analysis.*

and the detector efficiency $\varepsilon(\vartheta,\varphi)$. In principle, the detector efficiency can be derived from

$$\varepsilon(\vartheta,\varphi) = \frac{n_{\rm acc}(\vartheta,\varphi)}{n_{\rm in}(\vartheta,\varphi)} \tag{3.12}$$

where $n_{\rm acc}(\vartheta,\varphi)$ is the number of accepted photons incident from (ϑ,φ) under a specific set of event selections, and $n_{\rm in}(\vartheta,\varphi)$ is the number of simulated photons incident on the D1 detector modules from (ϑ,φ). As stated above, however, these numbers are not available directly from the simulation since the direction of incidence of each individual simulated photon as well as the number of photons incident from a given direction are not held in memory in the `SIM` subsystem.

In the simulation a total number of $N_{\rm vtx}$ photons is drawn from a hemispherical, isotropic distribution:

$$N_{\rm vtx} = \int\limits_{2\pi} \nu_{\rm vtx}\, d\Omega = 2\pi \cdot \nu_{\rm vtx} \tag{3.13}$$

where the photon density is $\nu_{\rm vtx}(\vartheta,\varphi) = \text{const}$. From these $N_{\rm vtx}$ photons $N_{\rm acc}$ are accepted:

$$N_{\rm acc} = \int\limits_{2\pi} \nu_{\rm vtx}\, \varepsilon_{\rm vtx}(\vartheta,\varphi)\, d\Omega = \frac{N_{\rm vtx}}{2\pi} \cdot \int\limits_{2\pi} \varepsilon_{\rm vtx}(\vartheta,\varphi)\, d\Omega \tag{3.14}$$

with $\varepsilon_{\rm vtx}(\vartheta,\varphi)$ being defined according to

$$\varepsilon_{\rm vtx}(\vartheta,\varphi) = \frac{n_{\rm acc}(\vartheta,\varphi)}{n_{\rm vtx}(\vartheta,\varphi)} \tag{3.15}$$

where $n_{\rm vtx}(\vartheta,\varphi)$ is the number of photons started in direction (ϑ,φ) from $A_{\rm vtx}$. Again, neither $n_{\rm in}(\vartheta,\varphi)$ nor $n_{\rm vtx}(\vartheta,\varphi)$ can be inferred directly from the simulation, but since

the photons are started homogeneously from $A_{\rm vtx}$ the following relation between these quantities holds true:

$$\frac{n_{\rm in}(\vartheta,\varphi)}{n_{\rm vtx}(\vartheta,\varphi)} = \frac{A_{\rm geo}(\vartheta,\varphi)}{A_{\rm vtx}}. \tag{3.16}$$

From Eqs. 3.9, 3.12, 3.15 and 3.16 it follows that

$$\varepsilon_{\rm vtx}(\vartheta,\varphi) = \frac{A_{\rm eff}(\vartheta,\varphi)}{A_{\rm vtx}} \tag{3.17}$$

and therefore from Eqs. 3.14 and 3.17

$$\int\limits_{2\pi} A_{\rm eff}(\vartheta,\varphi)\, d\Omega = \frac{N_{\rm acc}}{N_{\rm vtx}} \cdot A_{\rm vtx} \cdot 2\pi \tag{3.18}$$

Comparison of this result with Eq. 3.11 shows that Eq. 3.18 gives a solution for the effective area of COMPTEL for an incident isotropic intensity that can be inferred directly from the simulation. This result is independent of the solid angle from which the photons are started (here 2π) and is also independent of the size of $A_{\rm vtx}$ — as long as the solid angle is larger than the field-of-view of the telescope for a given set of event selections and as long as the area of $A_{\rm vtx}$ is larger than the projected area of the D1 detector. Under these conditions the number of accepted photons will always be the same, and the same is true for the value of $A_{\rm vtx} \cdot 2\pi / N_{\rm vtx}$ (where 2π represents the solid angle from which the photons are started).

The result for the effective area for an isotropic intensity given in Eq. 3.18 is in units of [cm^2 ster]. In Appendix B, describing the calculation of the total incident flux and intensity in the CDG analysis, the effective area $A_{\rm eff}$ is formally defined as

$$A_{\rm eff} \equiv \frac{N_{\rm acc}}{N_{\rm vtx}} \cdot A_{\rm vtx} \tag{3.19}$$

with $A_{\rm eff}$ now being in units of [cm^2].

After having solved the geometrical aspects of the calculation of the effective area, its energy dependence can be addressed. At present, the energy spectrum of the CDG intensity is not obtained from an explicit spectral deconvolution, but rather from the measurement of the average CDG intensity in each of a set of predefined energy intervals ΔE[21]. The effective area for a given energy interval is calculated according to (compare Eq. 3.19):

$$A_{\rm eff}(\Delta E) = \frac{n_{\rm acc}(\Delta E)}{n_{\rm vtx}(\Delta E)} \cdot A_{\rm vtx} \tag{3.20}$$

[21]The CDG analysis is peformed in relatively wide energy intervals. In addition, the CDG spectrum is expected to be a continuum spectrum without any line features. Therefore the determination of the incident CDG intensity using an effective area provides a good approximation to an explicit deconvolution of the spectrum — provided the assumed spectral shape in the simulation is reasonably close to the true CDG spectrum.

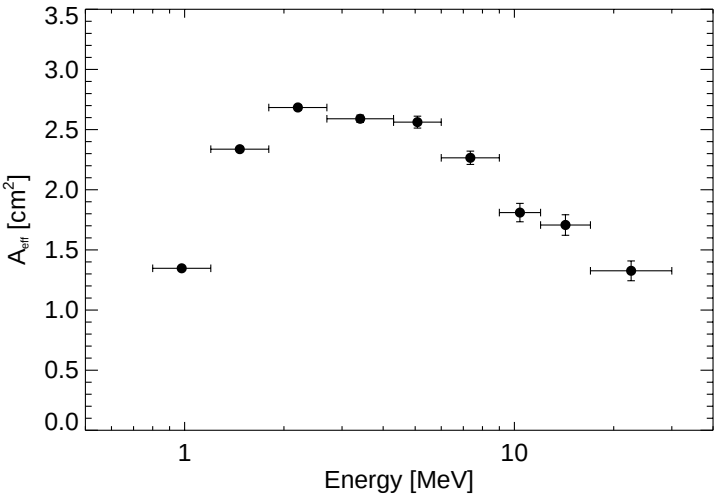

Figure 3.12: *The CDG effective area, calculated for an $E^{-2.5}$ power law and standard CDG selections. All D1 and D2 detector modules were used in the simulations.*

with $n_{\rm acc}(\Delta E)$ being the number of selected events with total energy E in ΔE and $n_{\rm vtx}(\Delta E)$ being the total number of events started with total energy E in ΔE[22]. The effective area for standard CDG selections (see Sec. 4.2.3) and with all D1 and D2 detector modules on is given in Fig. 3.12 (compare to the effective area for a point source in Fig. 3.8).

3.7 Time-of-Flight Corrections

The ToF, a measure for the time difference between the interactions in the D1 and D2 detectors, is of fundamental importance for instrumental-background suppression and identification (see Sec. 4.3), and consequently considerable effort has been spent on determining its value as accurately as possible. The goal of the ToF corrections is

[22]The starting energy of a photon in the simulations is usually drawn from a power law distribution

$$\nu_{\rm vtx}(E) = \nu_0 E^{-\alpha}$$

The simulated energy range usually extends from $E_{\rm low} = 0.6$ MeV to $E_{\rm up} = 90$ MeV. The normalization constant ν_0 of the energy distribution can be determined from

$$N_{\rm vtx} = \nu_0 \cdot \int_{E_{\rm low}}^{E_{\rm up}} E^{-\alpha}\, dE = \frac{\nu_0}{1-\alpha}\,(E_{\rm up}^{1-\alpha} - E_{\rm low}^{1-\alpha)})$$

for $\alpha \neq 1$, with $N_{\rm vtx}$ being the total number of photons started in the simulations. Now $n_{\rm vtx}(\Delta E)$ can be computed easily:

$$n_{\rm vtx}(\Delta E) = \nu_0 \cdot \int_{\Delta E} E^{-\alpha}\, dE$$

to align the ToF forward-peak distributions of all minitelescopes[23] approximately at channel 120 as independently as possible of any kind of influence, such as energy deposit or temperature, so that the event parameter ToF characterizes the instrument as a whole for all events. One of the benefits for scientific analysis is that these corrections will narrow the ToF forward-peak, allowing us to improve the signal-to-noise ratio in our data by rejecting unwanted background events more effectively. The basic approach to deriving the corrections is to study the ToF forward-peak position as a function of various parameters. This is done for events from the Earth's atmosphere, which is bright in γ-rays and hence produces a very pronounced forward peak.

3.7.1 History

The first, and longest, stretch of corrections applied to the raw ToF on the way to the best possible ToF for scientific analysis has been derived and explained in detail by van Dijk (1996). A concise summary of this first set of corrections is given in the following, before recent attempts to further improve the ToF values are described.

The raw ToF formed by the FCC of the instrument (see Sec. 3.4.1), denoted ToF_0 hereafter, can not be used for scientific analysis for a number of reasons. For example, differences in the geometrical separation between minitelescopes and in the lengths of the cables used in module-specific electronics result in ToF_0 shifts of up to 20 channels. Also, a dependence of ToF on the D1 and D2 PMT analogue sums was observed, in addition to other, more subtle effects described below.

A milestone in the history of the ToF corrections was the implementation of the COMPASS task `IFCTCF`, which accounted for the following dependences of ToF_0 (van Dijk 1996):

- *The minitelescope dependence*: Differences in the average path lengths between minitelescopes and in the module-specific cable lengths and electronics result in different positions of the ToF_0 forward-peak for each minitelscope. This minitelescope dependence is corrected by aligning the 98 individual ToF_0 peaks at channel 120, corresponding to a path length of 1.58 m.

- *The D1 and D2 analogue-sum dependences*: The analogue sum (measured in units of [channels]) is derived from the original PMT outputs (in units of [V]) and is a measure for the total amount of energy deposited in a module. A detailed study of the position of the ToF_0 forward-peak as a function of the D1 and D2 analogue sums showed that there are channel ranges in which the peak position depends considerably on the pulse height of the signal. Simple analytical functions could

[23]The combination of an individual D1 detector module with an individual D2 detector module is referred to as minitelescope. The 7 D1 modules and 14 D2 modules can be combined to 98 different minitelescopes.

be determined that describe the observed D1 and D2 analogue-sum dependences sufficiently accurate to allow us to align the ToF_0 forward-peaks for all energy deposits.

- *The detector-temperature dependence*: The measurement of the ToF involves the scintillation material in the modules and the electronic circuitry in both the FEEs and the FCC. The possible dependence of the ToF on the temperature of these instrument components was studied using calibration data. It was found that for in-orbit conditions the only relevant effect is a linear dependence of ToF on the average detector temperature. This walk can be neutralized by correcting ToF_0 for the detector temperatures at the time of the event with respect to a reference temperature of 20°C.

- *The D2 hardware-threshold dependence*: The hardware "energy" thresholds for interactions in the D1 and D2 detectors are represented by numbers between 0 and 7, corresponding to decreasing amounts of energy deposits required to trigger events. It was found that the ToF depends on the hardware threshold for low D2 analogue sums. This effect can be accounted for by using analogue-sum corrections for ToF_0 that depend on the setting of the hardware thresholds.

- *The sub-minitelescope dependence*: Due to the large surface areas of the D1 and D2 modules there is a non-negligible spread in the path lengths between different locations within one minitelescope. The corresponding broadening of the ToF resolution can be reduced by correcting ToF_0 for the deviation of the path length inferred from the interaction locations L_1 and L_2 with respect to the distance between the module centers.

- *The sub-D1-module dependence*: A large energy deposit very close to one of the D1 PMTs produces a trigger more quickly then a medium energy deposit at other locations in the module[24]. In addition, each D1 PMT has its own response time that may differ up to several nanoseconds from that of the other PMTs in the same module. This results in a dependence of ToF on the D1 interaction location, which can be undone by using a module map for each D1 module, containing the difference of the ToF_0 peak with respect to channel 120.

All ToF values obtained with `IFCTCF` are referred to as $\mathrm{ToF}_{\mathrm{III}}$ in the following[25]. Comparison of the resolution of $\mathrm{ToF}_{\mathrm{III}}$ data to older $\mathrm{ToF}_{\mathrm{I}}$ and $\mathrm{ToF}_{\mathrm{II}}$ data clearly showed a

[24]Such an effect should also occur in D2 modules for interaction locations above PMTs, however, there the vertical positions of the locations, which are unknown (see Sec. 3.5.3), probably play a major role. Simple corrections based on the (x_2, y_2)-location were expected to be smaller than for D1, but due to statistical limitations it was not possible to obtain a coherent picture of a possible dependence of the ToF value on the interaction location in D2 (van Dijk (1996) and van Dijk (1997), private communication).

[25]$\mathrm{ToF}_{\mathrm{I}}$ and $\mathrm{ToF}_{\mathrm{II}}$ represent previous stages of ToF corrections, inferior to those applied in `IFCTCF`. For test purposes `IFCTCF` can also be used to produce $\mathrm{ToF}_{\mathrm{IV}}$ and $\mathrm{ToF}_{\mathrm{V}}$ values, for which the differences

significant narrowing of the forward-peak by 0.3–1.4 channels with increasing energy going from $\mathrm{ToF_I}$ to $\mathrm{ToF_{III}}$. It was expected that this narrowing of the ToF forward-peak should increase the signal to noise ratio, in particular at high energies were it should be possible to select events from a smaller $\mathrm{ToF_{III}}$ range than the $\mathrm{ToF_I}$ and $\mathrm{ToF_{II}}$ ranges. Indeed, the detection significances of the Crab pulsar improved by 0.3–0.7σ in a first test, with the largest improvement at the highest energies (van Dijk 1996).

High ToF resolution is of prime importance also for the CDG analysis described in this thesis (see Chapter 5). For this reason the ToF distribution around the forward-peak was repeatedly studied, for example as a function of energy (Weidenspointner and Varendorff 1996a,b). These investigations confirmed the narrowing of the ToF forward-peak using $\mathrm{ToF_{III}}$ data as opposed to $\mathrm{ToF_{II}}$ data. More importantly, the benefit of the improved $\mathrm{ToF_{III}}$ resolution for the CDG analysis could be clearly demonstrated: the statistical quality of fits of the ToF distribution improved going from $\mathrm{ToF_{II}}$ to $\mathrm{ToF_{III}}$, in particular at high energies, thereby reducing systematic uncertainties in the results for the ToF peak. This was one of the incentives to try to improve upon `IFCTCF`, as described below.

3.7.2 Further Improvements

The next level in ToF resolution was achieved by correcting the dependence on the D2 interaction location to the first order (Weidenspointner *et al.* 1997a). These corrections were obtained from a study of the sub-D1-module and sub-D2-module dependences of the $\mathrm{ToF_{III}}$ forward-peak position, in which the D1 and D2 modules were divided in 9 and 7 so-called localization bins of equal area, respectively[26]. In the D1 modules 8 localization bins are each positioned before one of the 8 PMTs, one localization bin covers the module center. In the D2 modules the 7 localization bins are each centered above one of the 7 PMTs. For each of these D1 and D2 localization bins the $\mathrm{ToF_{III}}$ spectrum was investigated in 7 energy intervals: 0.8–1.25 MeV, 1.25–1.65 MeV, 1.65–2.0 MeV, 2.0–2.45 MeV, 2.45–4.3 MeV, 4.3–9.0 MeV and 9.0–30.0 MeV, according to the general structure of the instrumental background in E_{tot}.

The deviation of the $\mathrm{ToF_{III}}$ forward-peak position in the individual D1 modules from the average D1 detector $\mathrm{ToF_{III}}$ forward-peak position for all 7 energy ranges is depicted in the top left panel of Fig. 3.13. Except for D1 module 5, which will play a major role in the PSD corrections described in the next section, the $\mathrm{ToF_{III}}$ forward-peak is at the same position for all modules to a high accuracy, independent of energy. Even the deviation of D1-05 from the other D1 modules is very small (less than 0.1 channels). The situation is slightly worse in D2, as can be seen in the top right

in path lengths between minitelescopes are used to align the ToF backward-peaks or to simultaneously align both the forward- and the backward-peaks, respectively (see e.g. Fig. 4.10).

[26] In contrast to the studies by van Dijk (1996), in which each module was divided into about 1000 (x, y)-bins, this study is not limited by statistics because the spatial resolution is much cruder.

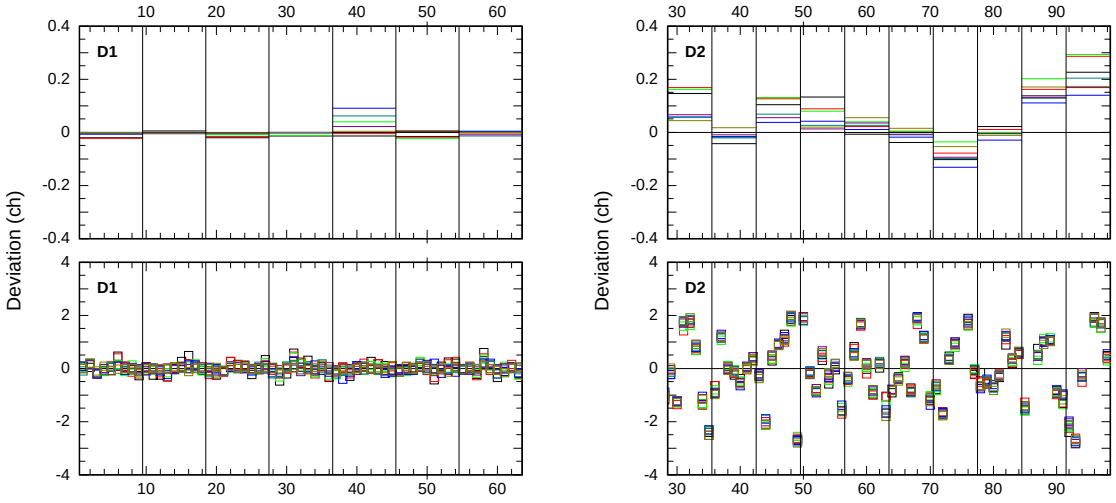

Figure 3.13: Top left: *The deviation of the ToF_{III} forward-peak position in the individual D1 modules from the average D1 detector ToF_{III} forward-peak position.* ***Top right:*** *The same as top left for D2.* ***Bottom left:*** *The deviation of the ToF_{III} forward-peak position in the individual D1 localization bins from the average D1 module ToF_{III} forward-peak position.* ***Bottom right:*** *The same as bottom left for D2.*

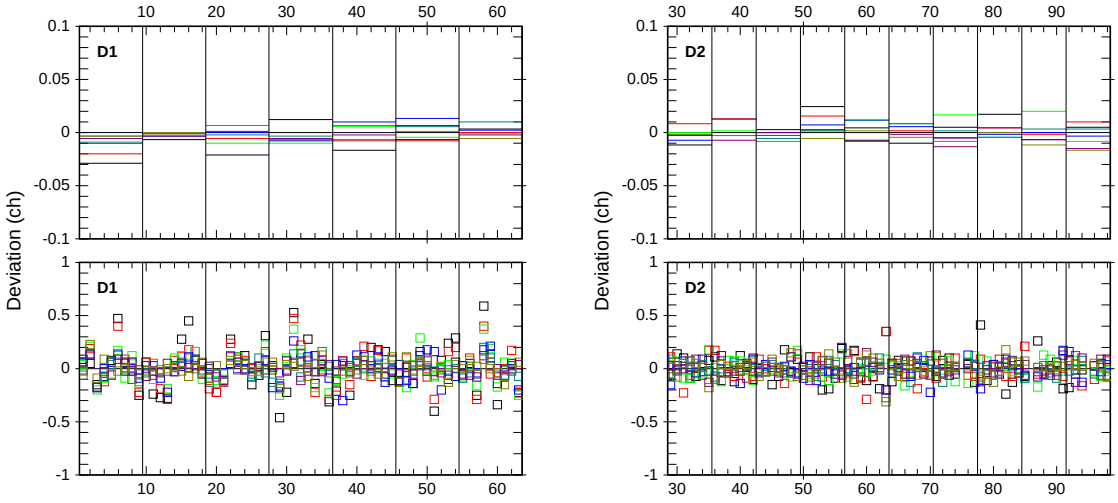

Figure 3.14: Top left: *The deviation of the ToF_{VI} forward-peak position in the individual D1 modules from the average D1 detector ToF_{VI} forward-peak position.* ***Top right:*** *The same as top left for D2.* ***Bottom left:*** *The deviation of the ToF_{VI} forward-peak position in the individual D1 localization bins from the average D1 module ToF_{VI} forward-peak position.* ***Bottom right:*** *The same as bottom left for D2.*

Note: *The y-axis ranges are different from that in Fig. 3.13.*

panel of Fig. 3.13. The ToF_{III} forward-peak position deviates at most 0.4 channels between individual D2 modules. The deviation of the ToF_{III} forward-peak position in the individual D1 localization bins from the average D1 module ToF_{III} forward-peak position for all 7 energy ranges is depicted in the bottom left panel of Fig. 3.13. The largest deviations of 0.5 channels occur at the lowest energies, where the systematic uncertainties of the ToF fits are greatest. In general, the ToF_{III} forward-peak position is very homogeneous independent of energy — showing the excellent quality of ToF_{III} data for D1. In D2 the situation is considerably worse, as can be seen in the bottom right panel of Fig. 3.13. The ToF_{III} forward-peak position can deviate by more than 4 channels within individual D2 modules, independent of energy!

These results were obtained by combining data from 1991 through 1997 and thus represent the average deviations over this period of time. To assess a possible time dependence of these deviations the analysis was repeated for data from 1991 to mid-1993 and for data from late-1995 to late-1997. In general, the results for data from early and late in the mission agree quite well, the differences being less than 0.2 channels. For some localization bins, however, the difference can be as large as 0.7 channels, much larger than the statistical uncertainties of the ToF fits, which in general are less than 0.1 channel, but smaller than the magnitude of the D2 deviations, which may indicate the presence of a weak time dependence for some localizaton bins (see below). For simplicity, it was assumed for the sub-D2-module corrections that there is no time dependence.

The scatter of the ToF_{III} forward-peak position in the D2 localization bins was corrected as follows:

- First, the average of the ToF_{III} forward-peak positions in all D2 modules except D2-11, 13 and 14 (having failed PMTs) was determined in each energy range (the module D2-01, and the modules D2-11, D2-13 and D2-14 with all PMTs working, were corrected separately because they were not included in the original data base, the module D2-02 was omitted completely because it is not used in scientific analysis due to a failure of the central PMT). This defines the D2 detector reference ToF_{III} forward-peak position as a function of energy.

- The deviation of the ToF_{III} forward-peak position in each D2 localization bin from the reference ToF_{III} forward-peak position was determined in each energy range.

- Then the average of the deviations in each energy range was determined for each localization bin, defining energy-independent D2 module maps of the deviations.

- Finally, these D2 module maps were used to correct the ToF_{III} values according to the D2 interaction location.

These ToF corrections have been implemented in the COMPASS task `EVPTPC` (for

details refer to Weidenspointner *et al.* 1997a). The ToF values obtained with these corrections are denoted by $\mathrm{ToF_{VI}}$ in the following.

The resulting deviation of the $\mathrm{ToF_{VI}}$ forward-peak position in the individual D1 and D2 modules from the average D1 and D2 detector $\mathrm{ToF_{VI}}$ forward-peak positions for all 7 energy ranges is depicted in the top left and right panels of Fig. 3.14, respectively. Now all D1 and D2 modules are very consistent (which is also true for D2-01 which is not included in the plots). The deviation of the $\mathrm{ToF_{VI}}$ forward-peak position in the individual D1 and D2 localization bins from the average D1 and D2 module $\mathrm{ToF_{VI}}$ forward-peak positions for all 7 energy ranges is depicted in the bottom left and right panels of Fig. 3.14, respectively. As was to be expected, the scatter of the $\mathrm{ToF_{VI}}$ forward-peak positions in D2 is now even less than in D1. As a result, the $\mathrm{ToF_{VI}}$ forward-peak width (1σ) decreased by about 0.1 channels at the lowest energies and by about 0.3 channels at the highest energies compared to $\mathrm{ToF_{III}}$ data, which again reduces systematic uncertainties in the CDG analysis. In addition, $\mathrm{ToF_{VI}}$ data offer considerable potential for improving imaging analysis with COMPTEL, as is summarized briefly in App. C. Because of these advantages for COMPTEL analyses it was decided to incorporate `EVPTPC` into `EVPRNN` for a complete reprocessing of all COMPTEL event data to raise the generally available level of ToF resolution in one step from $\mathrm{ToF_{II}}$, which currently is the level of the standard data, to $\mathrm{ToF_{VI}}$ (see also next section).

For the time being, the lastest ToF correction was serendipitously discovered in a study of the instrumental background as a function of time: a seemingly linear drift of the $\mathrm{ToF_{VI}}$ forward-peak position in time. The magnitude of this drift was assessed in the energy ranges 4.3–6 MeV, 6–9 MeV, 9–12 MeV, 12–17 MeV and 17–30 MeV. Lower energies could not be used for this purpose because of the presence of instrumental line background from activated isotopes, which dominates the time variation of the ToF forward-peak. As an example, the $\mathrm{ToF_{VI}}$ forward-peak position in the 4.3–6 MeV and 17–30 MeV ranges are plotted as a function of time in units of [TJDs][27] in Fig. 3.15, together with linear fits. The squares indicate the $\mathrm{ToF_{VI}}$ forward-peak positions derived from the combined data, which are very consistent with the observed trend.

It has to be emphasized that the $\mathrm{ToF_{VI}}$ time variation was studied using sky-viewing data, therefore variations of the instrumental background may possibly pretend the assumed instrumental effect. Above about 4.3 MeV, however, the instrumental background is prompt and does not vary with time. In addition, above 9 MeV the sky-viewing ToF forward-peak position should be very close to the position of the Crab signal (see Sec. ??? and Appendix C). The black dot in the bottom panel of Fig. 3.15 indicates the position of the Crab signal in the 17–30 MeV range, derived from data with an average time of TJD 9682.5. The small shift between the position of the Crab signal and the $\mathrm{ToF_{VI}}$ forward-peak position can be explained by the differences in the models used for the ToF spectrum in the two analyses. The $\mathrm{ToF_{VI}}$ forward-peak position was

[27] For a definiton of TJD (Truncated Julian Day) please refer to Appendix D.

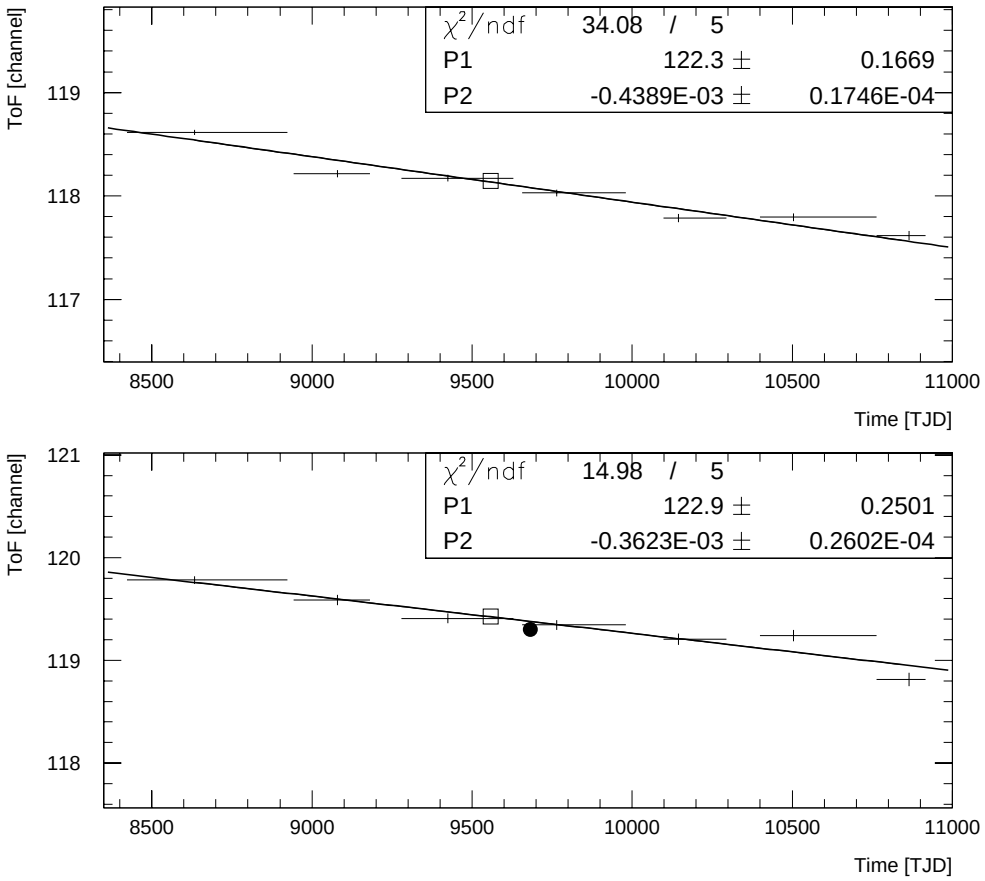

Figure 3.15: *The drift of the ToF_{VI} forward-peak position in time in the 4.3–6 MeV (upper panel) and the 17–30 MeV energy ranges. The squares are the peak positions derived from the combined data, the black dot is the position of the 17–30 MeV Crab signal.*

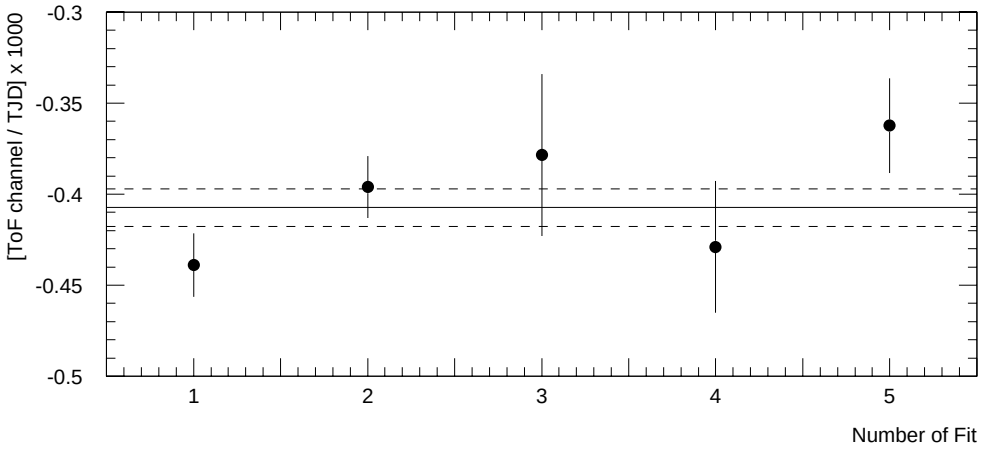

Figure 3.16: *The best-fit slopes of the assumed linear ToF_{VI} drift in time in the five energy intervals studied, and their weighted average and its 1σ error.*

determined by describing the forward-peak by a single Gaussian, while the position of the Crab signal was determined from a fit in which the ToF forward-peak was described by two gaussian components: the dominating, so-called signal component and a small background component at slightly higher ToF values. It was therefore concluded that the observed drift of the ToF forward-peak is indeed an instrumental effect[28].

The best-fit slopes of linear fits to the $\mathrm{ToF_{VI}}$ drift in the five energy intervals are depicted in Fig. 3.16, along with their weighted average and corresponding 1σ error, indicated by the solid and dashed lines. To first order the drift of the $\mathrm{ToF_{VI}}$ value is independent of energy, with a slope of $(-4.074 \pm 0.103) \times 10^{-4}$ channels/TJD. The drift can be compensated by correcting $\mathrm{ToF_{VI}}$ with respect to a reference point in time, chosen to be TJD 9682.5, resulting in the new $\mathrm{ToF_{VII}}$ level:

$$\mathrm{ToF_{VII}} = \mathrm{ToF_{VI}}(t) + 4.074 \times 10^{-4}\ \mathrm{channels/TJD} \cdot (t - 9682.5) \qquad (3.21)$$

where $\mathrm{ToF_{VI}}$ and $\mathrm{ToF_{VII}}$ are in [channels] and t is in [TJD].

The final results on the CDG presented in Chapter 6 are derived with $\mathrm{ToF_{VII}}$ data.

3.8 PSD Corrections

The (only) purpose of the event parameter PSD is to provide an efficient separation of photon and neutron events. The `IFC` algorithm for the PSD correction is set up such that a corrected PSD value of 100 channels separates photons and neutrons best — independent of E_1. It is not the aim of the PSD correction in `IFC` to provide energy-independent PSD values, only the separation between photons and neutrons is intended to be independent of E_1 (de Vries 1997, private communication). In the following, the raw, uncorrected PSD values measured onboard COMPTEL are denoted by $\mathrm{PSD_0}$, and the `IFC`-corrected (standard) PSD values are denoted by $\mathrm{PSD_I}$ (following the ToF nomenclature).

The $\mathrm{PSD_0}$ distribution depends on the D1 analogue sum. In addition, the correlation of uncorrected $\mathrm{PSD_0}$ values and D1 analogue sum is different for different D1 modules. Thus the PSD correction in `IFC` starts with fitting $\mathrm{PSD_0}$ spectra as function of D1 analogue sum for each individual D1 module. With increasing energy the photon and neutron peaks tend to become narrower, at the same time they tend to come closer to each other, which may cause problems at the highest D1 energy deposits. The final PSD corrections, however, were checked to separate photons from neutrons independent of energy. The resulting $\mathrm{PSD_I}$ values have been extremly stable over time ever since the launch of CGRO. Since the $\mathrm{PSD_I}$ distribution can be energy dependent, selections on this event parameter should be made over a relatively wide range (de Vries 1997, private communication).

[28] It is interesting and important to confirm the observed $\mathrm{ToF_{VI}}$ drift in time with Earth-viewing data. Such an analysis is currently in progress.

The investigation of the PSD distributions of individual D1 modules was performed using standard PSD_I data (PSD_I range 0-110 channels) and was triggered by peculiarities in the E_1 and E_{tot} spectra of D1 module 5. It was recognized quickly that D1-05 was different from the other D1 modules *only* when a narrow PSD range was selected. The PSD_I distribution as a function of E_1 for module D1-05 is depicted in the top left panel of Fig. 3.17. Obviously, the PSD_I distribution of this module is strongly dependent on E_1 - both the photon and the neutron distributions are shifted to lower PSD_I values with increasing E_1 energies, resulting in a significant decrease of events from this module when a narrow PSD cut such as 70-90 channels is applied. Even worse, at the highest E_1 energies only neutrons are accepted, but no photons! The peculiar PSD_I distribution of D1-05 is most likely due to the fact that for this module the PSD_0 photon and neutron peaks are very close to each other, making it very hard to obtain proper fits in `IFC` and thus to correct PSD_0 properly (de Vries 1997, private communication). For other D1 modules the E_1 dependence of the PSD_I distribution at the highest E_1 energies is much less pronounced.

The E_1-dependence of the PSD_I distributions does not allow photons to be separated from neutrons independent of energy. The best way to correct this energy dependence would be to improve `IFC` such that the fits of the PSD_0 distributions are based on more than just the data of a single day. This approach, however, would be very time consuming. In addition, it is not clear that the benefits could justify the required amount of work. Therefore a much simpler and quicker approach was adopted. Empirical corrections of the PSD_I distributions were determined such that the separation of photons and neutrons is as independent of energy as possible. The empirical corrections are (with PSD_I and PSD_{II} in [channels], and E_1 in [MeV]):

- **D1-01:** no correction
- **D1-02:** for $E_1 > 10$ MeV:
  $PSD_{II} = PSD_I - 0.5 \cdot E_1 + 5$
- **D1-03:** for $E_1 > 12$ MeV:
  $PSD_{II} = PSD_I - 1.25 \cdot E_1 + 15$
- **D1-04:** for $E_1 > 8.6$ MeV:
  $PSD_{II} = PSD_I + 0.0234 \cdot (E_1 - 14.219)^3 - 0.34077 \cdot (E_1 - 14.219) + 2.2123$
- **D1-05:** for $E_1 > 6$ MeV:
  $PSD_{II} = PSD_I + 0.043541 \cdot (E_1 + 12.676)^2 - 15.12$
- **D1-06:** no correction
- **D1-07:** same as D1-02

These corrections for PSD_I data have been implemented in the COMPASS program `EVPTPC`, along with the ToF corrections described in the previous sections. In analogy

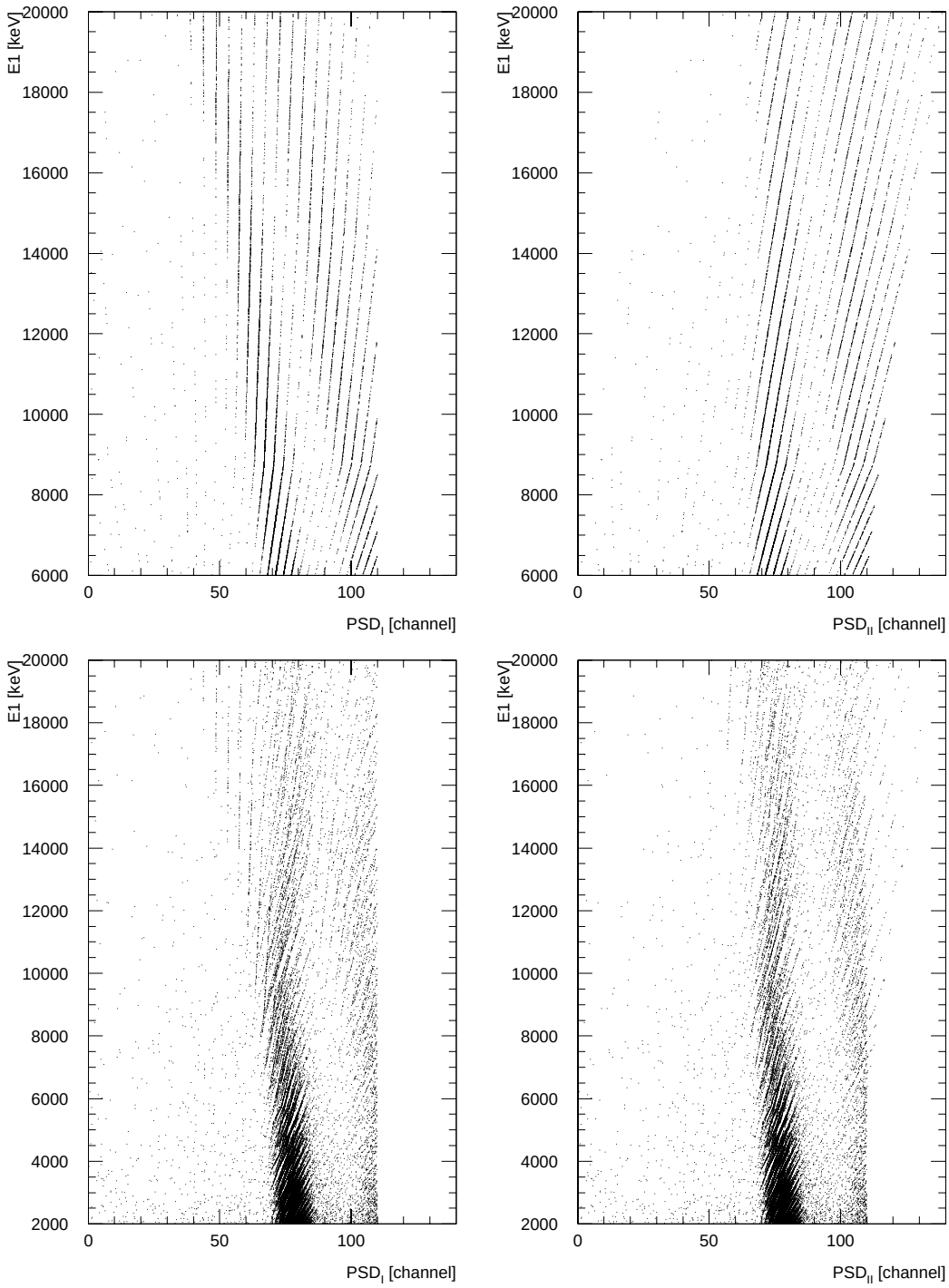

Figure 3.17: Top left: *The PSD_I distribution of D1-05.* ***Top right:*** *The PSD_{II} distribution of D1-05.* ***Bottom left:*** *The PSD_I distribution of all D1 modules.* ***Bottom right:*** *The PSD_{II} distribution of all D1 modules.*
Note: the "stripes" are electronic artifacts, reflecting the discrete values of PSD_0.

to the ToF nomenclature, the corrected PSD_I values are denoted by PSD_{II} in the following. The PSD_{II} distribution as a function of E_1 for module D1-05 is depicted in the top right panel of Fig. 3.17.

To address the question of a possible time dependence of these PSD_I corrections the PSD_I distributions for individual Observation Periods (OPs)[29] from 1991 through 1997 were compared. No significant deviations could be found within the available statistics. Therefore it is assumed that the PSD values are indeed stable and that the PSD_I corrections are independent of time.

As already mentioned above, `EVPTPC` has been incorporated into `EVPRNN` for a complete reprocessing of all COMPTEL event data. The final results on the CDG presented in Chapter 6 are derived with PSD_{II} data.

The combined PSD_I and PSD_{II} distributions of all D1 modules for $E_1 >$ 2 MeV are shown in the bottom left and right panels of Fig. 3.17, respectively. For PSD_I the photon and neutron distributions are somewhat blurred at the highest E_1 energies, rendering a separation difficult. For PSD_{II} the two distributions are more clearly separated, allowing a cleaner separation between photons and neutrons at these high E_1 energies. The combined PSD_I distribution of all D1 modules for E_1 in 70–2000 keV is shown in Fig. 3.18 (note that at these low E_1 energies the PSD_I and PSD_{II} values are identical).

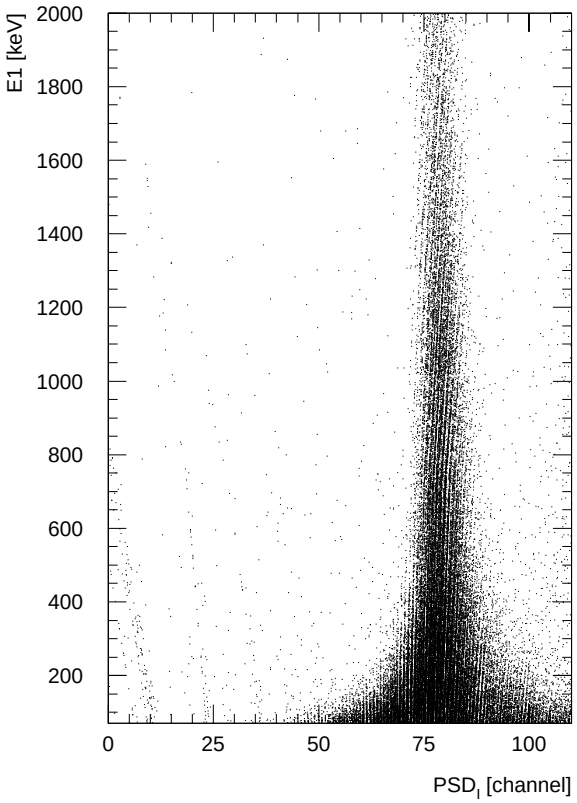

Figure 3.18: *The combined PSD_I distribution of all D1 modules for E_1 in 70–2000 keV. At these low energies the PSD_I and PSD_{II} values are identical.*

As can be seen from Fig. 3.18 and the bottom panels of Fig. 3.17, the standard PSD selection of 0–110 channels is not the best choice. This standard selection does not reject the "artifacts" at low PSD values for E_1 below about 1 MeV. More important, with increasing energy an increasing fraction of all accepted events is due to neutrons. This problem, however, can easily be solved by introducing an E_1-dependent PSD selection. The goal of this energy de-

[29]COMPTEL observations are organized in so-called Observation Periods (OPs), as described in Appendix D.

pendent selection should be to accept as many photons as possible while rejecting as many neutrons as possible. From the PSD_{II} distributions in Fig. 3.18 and the bottom right panel of Fig. 3.17 the following E_1-dependent PSD_{II} ranges seem to be reasonable:

- $E_1 = 70$ keV: 40–110 channels
- $E_1 = 1$ MeV: 55–95 channels
- $E_1 = 10$ MeV: 55–92 channels
- $E_1 = 20$ MeV: 40–90 channels

At intermediate energies these ranges are linearly interpolated. The low value of the lower boundary of the $PSD_{II,\,low}$ range at the highest E_1 energies is due to a peculiarity of module D1-01: the lower PSD boundary of its photon-PSD distribution decreases from about 60 channels to about 40 channels for E_1 energies between 10 MeV and 20 MeV.

3.9 Livetime Calculation

A photon counting experiment such as the Compton telescope COMPTEL may lose potential events due to busy electronics, coincident triggers of the veto domes, full buffers, in particular of the telemetry, or other causes. To account for these inevitable losses of valid events the livetime of the instrument is calculated for each superpacket in units of [sec]. The livetime is defined as the time over which the telescope was able to process and transmit a potential event, hence it is complementary to the instrument's deadtime. It follows from this definition that the maximum livetime is the length of a superpacket = 16.384 sec.

The COMPTEL livetime can be written as

$$L_{kl}^{\gamma i} = f_T^{\gamma i} \times f_{DE} \times f_{AE} \times f_V \times f_{F1} \times f_{F2} \times f_{D1-k} \times f_{D2-l} \times 16.384 \text{ sec} \qquad (3.22)$$

with $L_{kl}^{\gamma i}$ being the livetime for class `Gamma-`i data ($i = 1, 2$) for the minitelescope consisting of the detector modules D1-k ($k = 1, 7$) and D2-l ($l = 1, 14$). The derivation of this expression, and a detailed explanation of each of the factors, was given by van Dijk (1996). Briefly, the functions $f_{\{\}}$ are the livetime factors, with values in [0,1], of the different components involved: $f_T^{\gamma i}$ for the telemetry, f_{DE} and f_{AE} for the digital and analogue electronics, f_V for random coincidences in the FCC with veto signals, f_{F1} and f_{F2} for random coincidences in the FCC with signals from the D1 and D2 detector, respectively, and f_{D1-k} and f_{D2-l} for the D1-k and D2-l FEEs (see Sec. 3.4.1). This improved calculation was implemented in the separate COMPASS program `ENGSHD` to replace the erroneous algorithm originally used in the standard processing of the data (van Dijk 1996). Since the differences in livetime between individual minitelescopes

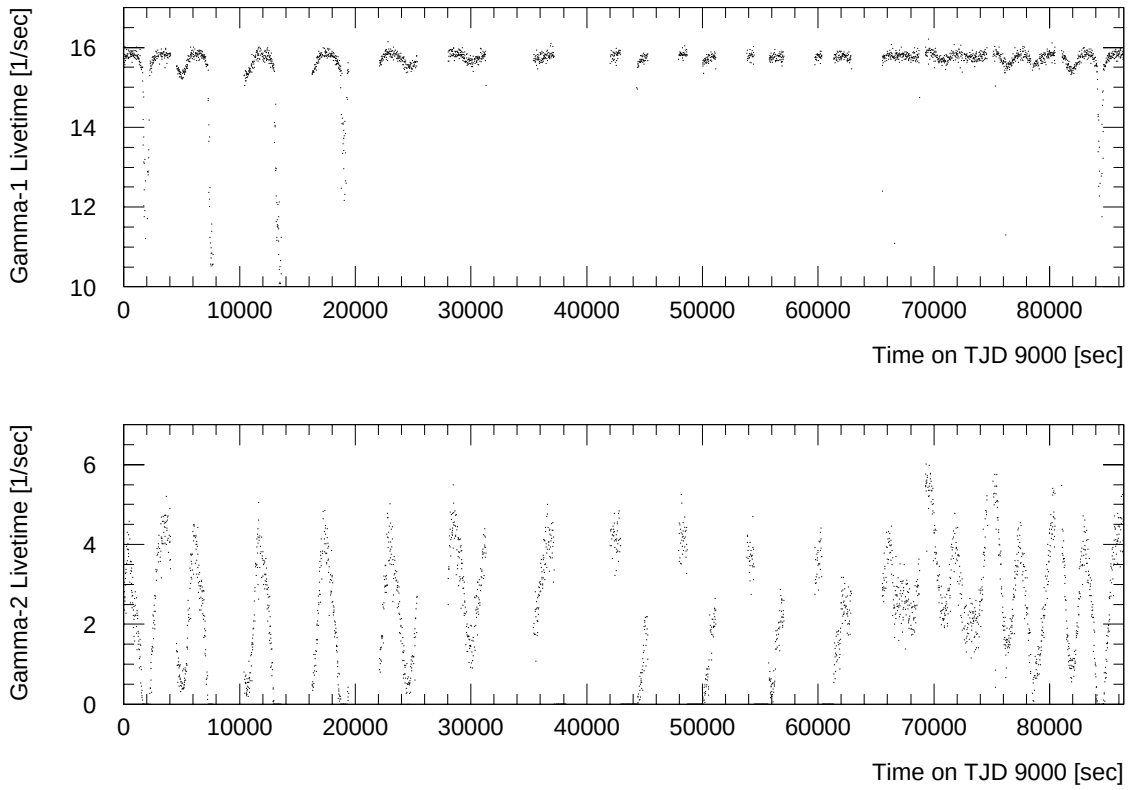

Figure 3.19: *The* `Gamma-1` *(upper panel) and the* `Gamma-2` *(lower panel) livetimes on the arbitrary day TJD 9000. The dips in the* `Gamma-1` *livetime occur when the telecope is pointed close to the Earth's center while the vertical cut-off rigidty is low. Note the different scalings in the two panels.*

caused by differences in f_{D1-k} and f_{D2-l} are negligible[30] (Weidenspointner 1995b) the corrected `SHD` data usually only contain an average livetime value, the so-called composite livetime, but no longer also the 98 minitelescope livetimes, which were routinely included in the erroneous `SHD` data.

As an example, the corrected livetime for `Gamma-1` and `Gamma-2` events is depicted as a function of time on arbitrary day TJD 9000 in Fig. 3.19. The large difference in the composite `Gamma-1` and `Gamma-2` event livetimes is due to the different telemetry buffer sizes in combination with the higher priority of `Gamma-1` events. As can be seen in Fig. 3.19, in general all `Gamma-1` events are telemetered, while a large fraction of the `Gamma-2` events is lost, mostly due to the filling of the telemetry buffer. Both livetimes slightly modulate with vertical cutoff rigidity and geocenter elevation. The `Gamma-1` livetime usually is close to 15.9 sec, therefore it is sufficient for most COMPTEL analyses to apply an a posteriori flux/intensity correction of 3%. In the CDG analysis, however, among other things the event rate is determied as a function of rigidity or veto

[30]This is no longer the case for very high incident γ-ray fluxes as during solar flares or γ-ray bursts (see e.g. Rank 1996).

rate. In this case the livetime has to be properly taken into account, as described in Appendix B, because the average livetime varies with rigidity/veto rate (see Fig. 3.19).

3.10 The Veto Deadtime Meter

As described above in Sec. 3.4.1, the purpose of the COMPTEL veto system is to suppress background events produced by interactions of charged particles in the D1 and D2 detectors. In order to be accepted, the FCC requires an anti-coincidence between the event's fast-logic signals from the D1 and D2 detectors and the fast-logic signals from all four veto domes. The length of the fast-logic signal from a veto dome τ_{vs}, which is typically ~ 200 nsec, depends on the amount of energy deposited in the dome, which in turn depends on the type of the penetrating particle, its energy, and the length of its path through the dome. Inevitably, the veto system contributes to the telescope deadtime, since photon events that incidentially coincide with a fast-logic signal from a veto dome are lost for scientific analysis.

In COMPTEL the deadtime due to the veto system is determined utilizing a deadtime meter. The fast-logic signals from the veto system are gated by deadtime-clock pulses τ_{dc} of duration 50 nsec at a deadtime-clock frequency f_{dc} of 312.5 kHz. The deadtime-meter counts the number of deadtime-clock pulses that occur during the presence of a veto signal. For each veto dome the deadtime-clock counts are accumulated over the length of a packet (2.048 sec) once for each superpacket (16.384 sec) and recorded in the `HKD` datasets in units of [deadtime-clock counts/2.048 sec]. The `HKD` deadtime scalers based on the main FEE signals from the veto domes Vi are denoted `SViM`, $i = 1, 4$. The combined deadtime scaler representing the veto system as a whole is denoted `SCVCOM`. The fractional deadtime of the veto system $t_V = 1 - f_V$ (see Eq. 3.22) is then determined by

$$t_V = \frac{\texttt{SCVCOM}}{2.048 \text{ sec} \cdot f_{dc}} \tag{3.23}$$

Although the pulses of the deadtime clock cover only a fraction of $\tau_{dc} \cdot f_{dc} \approx 0.016$ of the time, the fractional deadtime t_V is an accurate statistical estimate of the actual fractional deadtime because of the *random* nature of the coincidences between the veto signals and the deadtime-clock pulses. This is the deadtime-meter principle.

At first glance one might think that a straight-forward measurement of the rate of triggers of the veto system should allow us to precisely determine the deadtime of the veto system. This is not the case, however, because the length of the veto signal determining the deadtime due to an individual veto trigger depends on the deposited energy. If the deadtime would be simply inferred from the veto trigger rate, then the same amount of deadtime would be assigned to each veto trigger, irrespective of the length of the individual veto signal. If the deadtime is determined according to the deadtime-meter principle this effect is taken into account, because a longer veto signal

(resulting in a longer deadtime) is more likely to be counted than a shorter veto signal. One might also argue that a larger fraction of the time could be covered by utilizing a faster deadtime clock. In principle this is true, but since the rate of deadtime-clock counts (a few 100 per sec) already is about an order of magnitude higher than the event rate ($\sim$ 20 Hz) the veto deadtime already is determined with sufficient accuracy (Macri 1996, Swanenburg 1997, both private communication).

The rate of veto dome triggers r_{V} can be inferred from the number of veto deadtime-clock counts SCVCOM. According to the deadtime-meter principle

$$\frac{\mathtt{SCVCOM}}{2.048 \text{ sec}} = r_{\mathrm{V}} \times f_{dc} \times \tau_{coinc} \tag{3.24}$$

with τ_{coinc} being the length of the coincidence interval for the veto signal and the deadtime-clock pulse. τ_{coinc} is given by

$$\tau_{coinc} = \tau_{dc} + \tau_{vs} \approx 50 \text{ nsec} + 200 \text{ nsec} = 250 \text{ nsec} \tag{3.25}$$

Inserting this value in Eq. 3.24 it follows that r_{V} can be estimated by

$$r_{\mathrm{V}} = 12.8 \times \frac{\mathtt{SCVCOM}}{2.048 \text{ sec}} \tag{3.26}$$

This conversion from deadtime-clock counts to veto trigger rate is valid only when the fractional veto deadtime is much less than 1, since the deadtime-clock counts also reflect the amount of deadtime in the veto domes themselves. Typical in-orbit values of the deadtime scalers for the individual and combined veto domes are on the order of a few to several thousand, implying a fractional deadtime of less than 1%. It is therefore expected that the deadtime-clock counts are proportional to the veto trigger rate for typical in-orbit conditions.

Chapter 4

The Instrumental Background

4.1 Introduction

Historically, γ-ray astronomy at MeV energies has always been haunted by excessively high instrumental backgrounds (see Sec. 2.3). The Earth's atmosphere is opaque to γ-ray photons, and in addition prevents incident high-energy cosmic-ray particles from reaching the surface of the Earth. To conduct astronomical observations at γ-ray energies the detectors therefore have to be placed at the top of the atmosphere by balloons ($\sim$ 40 km) or into space by rockets. It is inevitable, however, that the instruments are then exposed to a continuous bombardement of energetic particles such as high-energy cosmic-rays or secondary particles produced in the Earth's atmosphere. These particles interact with the spacecraft and detector materials through a multitude of processes which result in the emission of instrumental background photons that may ultimately be accepted as valid events (see Sec. 4.1.3). For example, MeV photons are emitted by activated radioactive isotopes or by excited nuclei produced in nuclear interactions upon their decay or de-excitation, respectively. The incident particle fluxes are so high that the background events by far outnumber proper double-scattering events due to celestial photons. Therefore, a detailed qualitative and quantitative understanding of the intense and complex instrumental background is crucial for studies of the CDG. Contrary to the signal of most celestial sources, in particular the CDG, the intensity of the instrumental background varies in time as the telescope encounters a varying background environment, e.g. due to the orbital motion of the spacecraft around the Earth. In fact, variability in time or with geophysical parameters is one of the most useful and powerful discriminators between the instrumental background and the CDG signal.

Below, the varying radiation environment to which COMPTEL is exposed is briefly described, followed by an overview of different types of background events in terms of their interaction process and location. As indicated, only a fraction of the various background event types can easily be identified and rejected based on their event

parameters.

4.1.1 The COMPTEL Environment

Orbiting the Earth at altitudes of $\sim 350 - 500$ km with an inclination[1] of 28.5° CGRO encounters a complex and variable radiation environment (see e.g. Stassinopoulos 1989, Klecker 1996). The main constituents of the particle environment in near-Earth orbit are high-energy cosmic rays, geomagnetically trapped particles, solar energetic particles, particles from the anomalous component of cosmic rays, and secondary particles and γ-ray photons produced in the Earth's atmosphere. In addition, secondary particles and γ-ray photons are also produced in interactions of particles of the external radiation environment with the spacecraft itself. Below, each of these constituents of the radiation environment is briefly described, followed by a concise assessment of the interaction mechanisms through which the different types of particles may contribute to the triggering of valid events due to the instrumental background.

- *High-energy cosmic rays*: Protons are the most abundant component of this particle radiation ($\sim 85\%$), followed by He nuclei ($\sim 12\%$) and electrons ($\sim 2\%$); the remaining $\sim 1\%$ are heavier nuclei (see e.g. Longair 1992, p. 270 ff.). These particles can be extremely energetic (up to $\gtrsim 10^{20}$ eV). Above ~ 10 GeV nucleon^{-1} the energy spectra of the cosmic-ray particles follow a power-law distribution with spectral indices in the range 2.5–2.7 for the nucleons and about 3.3 for the electrons. As an example, the intensity of the cosmic-ray protons at these energies is well described by

$$I(E) \approx 1.5 \times E^{-2.7} \text{ protons cm}^{-2}\text{ster}^{-1}\text{sec}^{-1}\text{GeV}^{-1} \tag{4.1}$$

with E the kinetic energy in [GeV] (from Fig. 9.1 in Longair 1992). In order to reach the near-Earth orbit of COMPTEL, the cosmic-ray particles have to penetrate the Earth's magnetic field, whose effect on the incident particles can be described by a so-called cut-off rigidity $\Re_c$ [GV], which is a function of the location in the geomagnetic field and of the direction of incidence [2]. Particles with a rigidity $\Re < \Re_c$, with $\Re$ defined by

$$\Re = \frac{p\,c}{Z\,e} \tag{4.2}$$

[1] The inclination of a satellite orbit is defined as the angle between the orbital plane and the Earth's equatorial plane.

[2] The motion of charged particles in the geomagnetic field in a dipole approximation was first considered by Størmer (1955). For a given location, the allowed incident directions for a given particle rigidity, or the allowed particle rigidities for a given incident direction, are described by extremely complex relations. For practical reasons it is therefore attempted to quantify to a first approximation the actual effects of the geomagnetic field on the incident cosmic-ray particles by a single parameter, a so-called cut-off rigidity. Popular choices for cut-off rigidities are the cut-off for vertical incidence, the so-called vertical cut-off rigidity, or the western cut-off rigidity, the cut-off for incidence from the magnetic-western direction. The former cut-off rigidity is aimed at proving a representative average over all directions, while the latter cut-off rigidity is the lowest occurring cut-off for positively charged particles (see e.g. Klecker 1996).

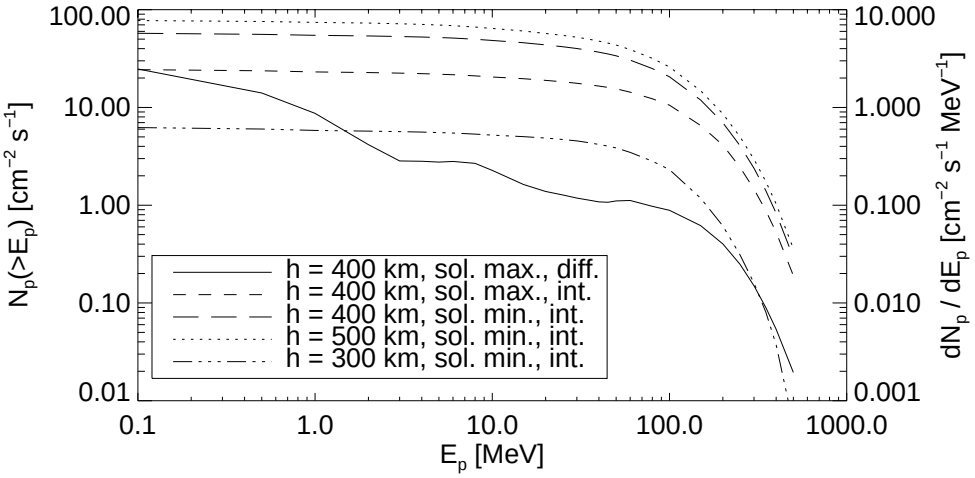

Figure 4.1: *Integral (left scale) and differential (right scale) energy spectra of SAA protons encountered in an 28.5° inclination orbit at various altitudes at solar minimum and solar maximum. The data are available at the U.S. National Space Science Data Center at NASA's Goddard Space Flight Center:* `http://nssdc.nasa.gov/space/model/models/trap.html` *(Stassinopoulos 1989).*

where p is the particle momentum, c is the speed of light, and $Z\,e$ is the particle charge, cannot reach a location with cut-off rigidity $\Re_c$. The Earth's magnetic field therefore acts as a momentum (energy) filter for cosmic rays. Typical cut-off rigidities along the COMPTEL orbit range from $\sim$ 5 GV to $\sim$ 15 GV (see Fig. 4.2 below), and it follows from Eqs. 4.1 and 4.2 that intensity and energy distribution of the cosmic-ray particles incident on COMPTEL exhibit a pronounced variation in time due to the orbital motion of the spacecraft in the geomagnetic field.

• *Geomagnetically trapped particles*: The magnetic field of the Earth can be well approximated by a dipole out to a few Earth radii. Charged particles can be magnetically trapped in such a dipole field and stored in so-called radiation or Van Allen belts centered in the geomagnetic equatorial plane (see e.g. Stassinopoulos 1989, and references therein). By number, the most frequent trapped charged-particle species populating the radiation belts are protons and electrons. The protons are trapped in a single belt, with the maximum proton flux occuring at an altitude of $\lesssim$ 1 Earth radius. The energies of the trapped protons range from less than 1 MeV to several 100 MeV (see Fig. 4.1). The electron belt is divided into two zones. The electron flux in the inner zone peaks at about the same altitude as the proton belt, with the total number of electrons exceeding that of the protons by roughly two orders of magnitude. The energy spectrum of the inner zone electrons is very soft and hardly extends beyond $\sim$ 10 MeV. The fluxes of the lowest-altitude trapped particles are modulated by the solar activity[3] (as exemplified in Fig. 4.1, the proton flux varies by a factor of $\sim$ 2 be-

[3]The increased energy output of the sun during the active phase of its cycle causes the upper layers of the atmosphere to expand, which results an increased depletion of low-altitude protons

tween solar minimum and solar maximum). Most parts of the CGRO orbit are below the radiation belts, however, because the geomagnetic dipole is offset from the Earth's center, the radiation belts reach down into the upper layers of the atmosphere over the coast of Brazil. This apparent extension of the radiation belts to low altitudes is usually referred to as South Atlantic Anomaly (SAA). On average, CGRO passes through the SAA 6–8 times each day. In 1991 (at solar maximum and hence at minimum SAA proton flux) the daily average of the incident flux of SAA protons with $E_p > 100$ MeV was about 38 times higher than the corresponding incident cosmic-ray proton flux (Dyer *et al.* 1994). Obviously, each SAA passage constitutes a dramatic change of the radiation environment. During its mission, the altitude of CGRO ranged from $\sim 350 - 500$ km, which corresponds to a variation of the SAA proton flux of a factor ~ 10 (see Fig. 4.1).

• *Solar energetic particles*: Violent energy releases on the sun, such as flares or coronal mass ejections, result in the emission of energetic particles, mostly protons, but also electrons and neutrons. The energies of these solar energetic particles can extend up to several 100 MeV nucleon^{-1} (see e.g. Klecker 1996, and references therein). The COMPTEL orbit is shielded by the geomagnetic field from most of the charged solar energetic particles. In addition, these solar events, whose frequency follows the solar cycle, rarely last for longer than a day. Therefore the contribution of solar energetic particles to the COMPTEL radiation environment is negligible.

• *The anomalous cosmic-ray component*: The anomalous component of cosmic rays[4] is of great potential interest because its most abundant particle species are heavy nuclei, such as He, N, O or Ne, which are very efficient producers of secondaries in nuclear interactions. Like high-energy cosmic-ray particles, the particles of the anomalous component can be trapped in radiation belts[5], however, their fluxes are below those of the trapped cosmic-ray protons by about 2 orders of magnitude (Selesnik *et al.* 1995 and Klecker 1998, private communication). In addition, the anomalous cosmic-ray belts are located at higher altitudes than the proton belt and therefore are hardly encountered by CGRO.

---

through Coulomb scattering. Hence the trapped-proton flux is anti-correlated to the solar cycle. The opposite is the case for the trapped electrons at low altitudes. The trapped electrons have been accelerated in the magnetosphere before being trapped, and this acceleration mechanism is powered by the solar wind. The increased replenishment of trapped electrons during solar maximum outweights the increased depletion by Coulomb scattering.

[4]This component of the radiation environment represents interstellar neutral particles that have drifted into the heliosphere, where they were ionized by solar UV radiation or charge exchange with the solar wind, convected into the outer heliosphere, and then accelerated at the termination shock to energies of $\sim 10 - 100$ MeV nucleon^{-1} (see e.g. Cummings *et al.* 1993, Klecker 1996, and references therein).

[5]In contrast to high-energy cosmic rays, anomalous cosmic rays are singly-charged. Therefore their rigidity is high (see Eq. 4.2) and they can penetrate deeply into the magnetosphere. In the upper atmosphere they then lose some or all of their electrons; now their rigidity is low and they may be trapped in the geomagnetic field (see e.g. Selesnik *et al.* 1995, and references therein).

• *Secondary particles from the Earth's atmosphere*: When entering the Earth's atmosphere the primary cosmic-ray particles interact violently with the air nuclei, initiating nuclear interaction cascades that ultimately result in the production of a multitude of secondaries of relatively low energy. The most important of these secondaries for COMPTEL are the so-called atmospheric albedo neutrons (see e.g. Newkirk 1963, Armstrong *et al.* 1973) and atmospheric albedo γ-rays (see below). The intensity and spectral distribution of the albedo neutrons were studied from balloons at the top of the atmosphere and from satellite altitudes (see e.g. Lockwood *et al.* 1973, Kanbach *et al.* 1974, Preszler *et al.* 1976, Ait-Ouamer *et al.* 1988, and references therein). The spectral distribution extends from thermal energies to several 100 MeV, and can be approximated with a broken power-law spectrum with a break energy at about 70 MeV (Morris *et al.* 1995). The intensity of the albedo neutrons was found to be sufficient to constitute the dominating source for the population of the energetic protons in the inner radiation belt as predicted by the so-called CRAND (cosmic-ray albedo-neutron decay) theory. The local flux of fast neutrons ($E_n > 12.8$ MeV) in the COMPTEL D1 detector was measured by Morris *et al.* (1995). It was found that the flux varied linearly with `GCEL`, the angle between the geocenter and the instrument pointing, and exponentially with vertical cut-off rigidity. The inferred fluxes were consistent with the expected albedo neutron flux at the COMPTEL altitude, indicating that neutron production in the spacecraft itself seems to be negligible (see below). This was a surprise, since calculations of the induced radioactivity in OSSE onboard CGRO indicated that a significant flux of secondary neutrons is produced in the spacecraft material (Dyer *et al.* 1994). On the other hand, preliminary Monte Carlo calculations of high-energy protons interacting in CGRO supported the measurements (Morris 1996a). To a good approximation the intensity of the albedo neutrons is proportional to the number of incident cosmic-ray primaries, which depends on the local cut-off rigidity and to a lesser extent on the solar cycle. The albedo-neutron intensity encountered by COMPTEL therefore varies with the local cut-off rigidity, and in addition depends on the orbit altitude and the solar cycle.

• *Atmospheric γ-radiation*: As mentioned above, γ-rays are produced in the Earth's atmosphere by the incident cosmic radiation. The principal processes that result in the production of γ-ray photons are the decay of neutral pions and bremsstrahlung from the decay of charged pions (see e.g. Graser and Schönfelder 1977, Thompson and Simpson 1981). Similar to albedo neutrons, albedo γ-rays have been studied from balloon and satellite altitudes (see e.g. Ryan *et al.* 1979, Thompson and Simpson 1981, and references therein). The γ-ray albedo is very intense, for example at energies above about 35 MeV it is 10–100 times more intense than the extragalactic γ-ray background (Thompson and Simpson 1981). Since the γ-ray albedo and the neutron albedo are both produced by cosmic-ray primaries in the atmosphere, the intensity of the former exhibits the same variations and dependences as discussed above for the intensity of the latter.

• *Locally produced radiation*: In general, the particles of the external radiation

environment outlined above do not simply produce instrumental background events by directly triggering the detectors or by producing γ-ray photons in the spacecraft material, but produce a multitude of different secondary particles and γ-ray photons through the same interactions that produce the instrumental background (see below). In fact, the secondaries produced in the spacecraft material and the instrumental background are intricately connected, indeed, in a certain sense the secondaries *are* the instrumental background. As will be examined in Sec. 4.1.3, the location within the spacecraft at which secondary particles are produced greatly influences the probability that a valid event is triggered in COMPTEL, and also is crucial for the rejection of this background event through selections on the measured event parameters. In this context it has to be noted that the spacecraft material not only is a potential source of secondaries, but also acts as a shield that inhibits particles of the external background environment from producing secondaries close to the detectors, in particular the D1 detector. For example, the linear dependence of the fast-neutron flux in the D1 detector on `GCEL` observed by Morris *et al.* (1995) was attributed to mass shielding, e.g. by the CGRO aluminium platform (see Fig. 3.1). This linear dependence on `GCEL` has also been found for other quantities, such as the instrumental 2.2 MeV line from thermal-neutron capture on hydrogen in the D1 detector (Weidenspointner 1994, Weidenspointner *et al.* 1996a, see Sec. 4.4.2.1). The effects of mass shielding were also evident in a neural network simulation of the rate of events used in scientific analysis (Varendorff *et al.* 1996, see below).

To summarize this concise description of the radiation environment to which COMPTEL is exposed, the dominating constituents over long time scales are particles of the cosmic radiation, geomagnetically trapped particles and secondary particles and photons produced in the Earth's atmosphere and the spacecraft material. The intensity of all of these particle populations varies in time due to modulation by the geomagnetic field and the solar cycle and due to orbit altitude dependences. In the following, the interaction mechanisms through which different types of particles may contribute to the triggering of valid events due to instrumental background are briefly assessed.

Protons are an important source of instrumental background. The most intense particle population (except for trapped electrons) irradiating CGRO are the geomagnetically trapped protons encountered during passages through the SAA. These protons are the main source of long-lived instrumental background (see next section), as they cover the medium energies of $\sim 10 - 100$ MeV (see Fig. 4.1) at which the cross-sections for the production of radioactive isotopes are highest. The *delayed*[6] decay of these radioactive isotopes does not trigger the veto system and is a prime source of instrumental background events at a few MeV. Conversely, the majority of the telescope triggers due to photons from *prompt*[7] de-excitations of nuclei excited in nuclear proton interactions are rejected because the incident proton or a charged secondary triggered

[6] For the remainder of this thesis "delayed" refers to time scales longer than the typical length of the fast-logic veto signal of ~ 200 nsec (see Sec. 3.4.1).

[7] For the remainder of this thesis "prompt" refers to timescales shorter than the coincidence window

the veto system. Only prompt photons from proton interactions outside the veto domes may create a valid event. Radioactive isotopes may also be produced by high-energy cosmic-ray protons, which for the CGRO orbit have energies $E_p \gtrsim 4$ GeV (Dyer *et al.* 1994). In addition, cosmic-ray protons are efficient in breaking up the target nucleus into lighter fragments (spallation), or in producing lower-energy secondaries such as pions, protons or neutrons, which may subsequently decay or interact in turn within the telescope material and ultimately produce γ-ray photons. Again, unless all these interactions occur in the satellite structure outside the veto domes, the telescope triggers due to promptly emitted photons are rejected by the veto system.

A major fraction of the instrumental background is due to neutrons. Because of their charge-neutrality, neutrons can travel to any location in the satellite to produce γ-ray photons without triggering the veto system. Depending on their energy, neutrons contribute to the instrumental background through a multitude of channels. Low-energy neutrons ($E_n \lesssim 10$ MeV) may lose their energy in inelastic collisions in which the target nuclei may be left in an excited state. Nuclei may also be excited by capturing neutrons, in particular thermal neutrons (see below). The excited nuclei may then return to their ground states by emission of one or more photons. Nuclear interactions of higher-energy neutrons may also result in the direct emission of γ-ray photons, or in the production of radioactive isotopes that decay with a delay characterized by their half-life. Of particular concern are neutron interactions in the D1 detector (see Sec. 4.1.3). A neutron interaction in the D1 scintillator can be identifyed by its PSD value, which allows to reject prompt γ-ray photons. If a longer-lived radioactive isotope is produced in the D1 scintillator, however, the photons from the delayed decay cannot be rejected. Another source of neutron-induced background events from the D1 scintillator that cannot be rejected by PSD selections is thermal-neutron capture on hydrogen, producing a pronounced instrumental line at 2.2 MeV (see Sec. 4.4.2.1). The time scale for the moderation of an incident higher-energy neutron usually is long enough to evade an association of the initial scatters (which in principle are identifyable through PSD) and the delayed neutron capture that produces the γ-ray photon. Prompt or delayed γ-ray photons due to neutron interactions in the structure of the D1 detector also can not be rejected. Finally, neutrons may also undergo a proper double-scattering from D1 to D2, thereby mimicking a celestial γ-ray photon except for the PSD value, which allows them to be identified.

Heavy nuclei with atomic numbers $Z > 1$ are not expected to significantly contribute to the instrumental background, although they are much more efficient in producing secondary particles than protons or neutrons (see e.g. Dyer *et al.* 1994), the reason being the very small number of heavy nuclei encountered by COMPTEL. As pointed out above, anomalous cosmic rays can be neglected for the CGRO orbit. Also, because heavy cosmic-ray particles have low rigidities due to their high charge, and therefore must have correspondingly higher momenta/energy to penetrate the geomag-

---

of 40 nsec for the triggering of a valid event (see Sec. 3.4.1). In particular, prompt background components instantaneously follow the incident local cosmic-ray flux.

netic field (see Eq. 4.2), their number is greatly reduced for the CGRO orbit.

Electrons with $E_e \gtrsim 1$ MeV contribute to the instrumental background through bremsstrahlung emission[8]. Relativistic electrons deposit most of their energy in a few photons with an average energy of about $\frac{1}{3}E_e$ (see e.g. Longair 1992, p. 82 ff.). To avoid rejection by the veto system, valid events due to bremsstrahlung photons must be produced outside the veto domes in the satellite structure. An exception is bremsstrahlung from β-particles emitted in the decay of radioactive isotopes produced within the detector material, in particular the D1 assembly.

Finally, the intense atmospheric γ-radiation is an important source of background events which, however, can be rejected very effectively by careful data selections (see Sec. 4.2.2). Valid events due to γ-ray photons of the instrumental background can be triggered through many different types of interactions (see Sec. 4.1.3) and, in general, are much harder to eliminate.

4.1.2 Instrumental-Background Variations

In this section emphasis is put on the different variations of the COMPTEL radiation environment introduced above, and how these variations manifest themselfes in the data. As will be explained in detail in Chapter 5, the fact that the instrumental background is variable is of fundamental importance for its separation from the constant signal due to the CDG.

The variation of the measured `Gamma-1` event rate, which is available in the `HKD` parameter `GAM1CNT`, is depicted for the arbitrarily selected day TJD 9725 in Fig. 4.2. Also shown are the simultaneous variations of the veto rate[9] observed in veto dome V2 (`SCV2M`), the vertical cut-off rigidity at the location of the spacecraft (`RIGIDITY`), and the angle between the COMPTEL pointing direction and the Earth horizon (`EHORA`)[10].

There is a pronounced positive correlation between the `Gamma-1` event rate and the veto rate, and an anti-correlation between these two parameters and the vertical cut-off rigidity, indicating that a large fraction of the instrumental background events is due to

[8] At lower energies electons become non-relativistic and their dominant energy-loss mechanism is ionization (see e.g. Longair 1992, p. 82 ff.).

[9] For the remainder of this thesis "veto rate" will be used to refer to the number of veto deadtime-clock counts per packet (see Sec. 3.10). To avoid confusion with a genuine event rate, the veto rate will be quoted in units of [DT] = [1/2.048 sec].

[10] To a good approximation the `OAD` parameters `GCEL`, the angle between the COMPTEL pointing direction and the direction to the geocenter, and telescope Earth-horizon angle `EHORA` are related through

$$\texttt{EHORA} \approx \texttt{GCEL} - 70^\circ$$

since the angle between the direction to the geocenter and the Earth horizon is about 70° as seen from an altitude of about 450 km. As will be described in Sec. 4.2.2, the angle `EHORA` is the relevant quantity for the rejection of atmospheric γ-rays in the CDG analysis.

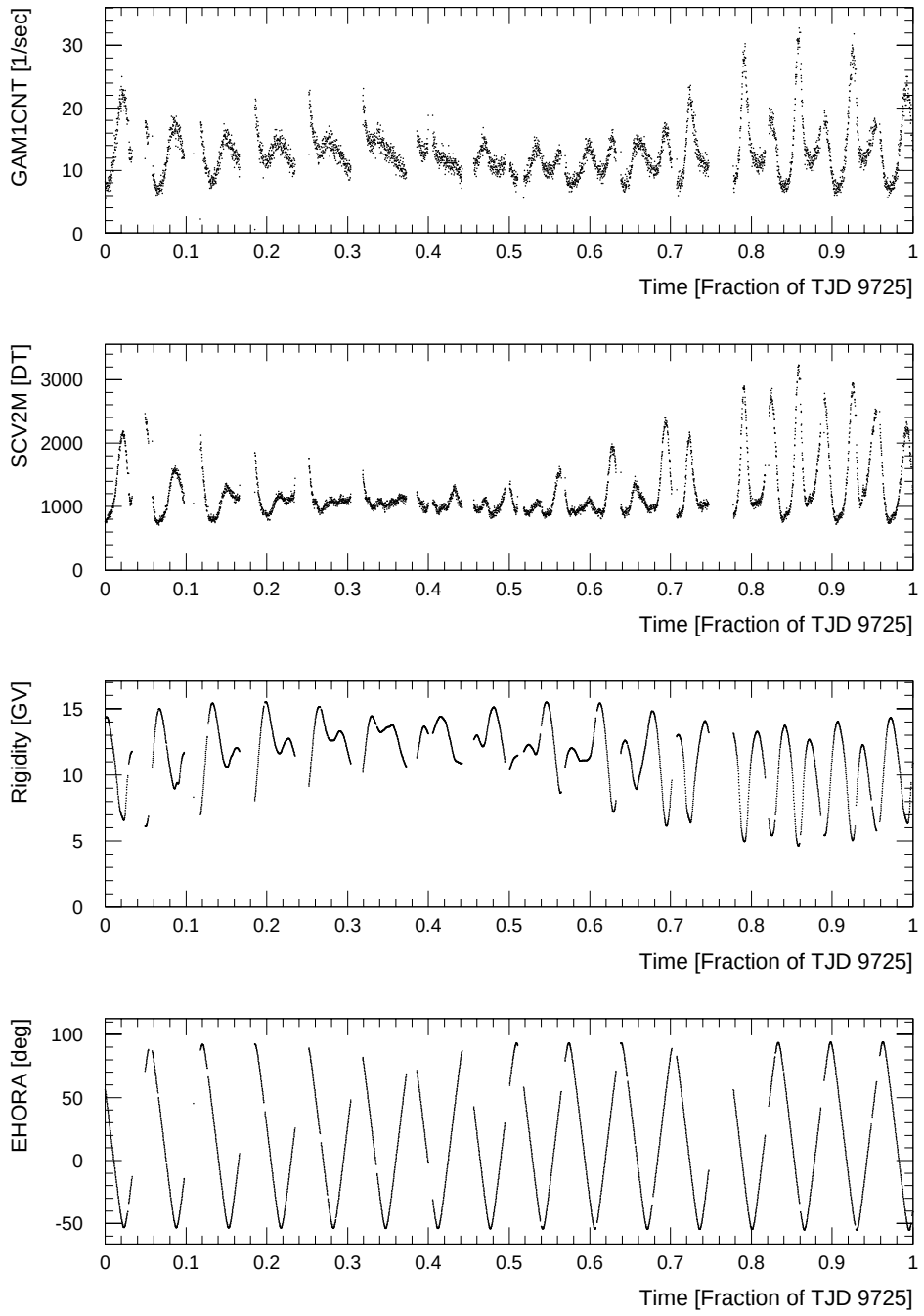

Figure 4.2: *The variation of the* `Gamma-1` *event rate (*`GAM1CNT`*), the V2 veto rate (*`SCV2M`*), the local vertical cut-off rigidity (*`RIGIDITY`*), and the Earth-horizon angle of the telescope pointing direction (*`EHORA`*) on the arbitrary day TJD 9725. The data gaps are either due to SAA passages or lack of TDRSS (Tracking and Data Relay Satellite System) coverage. The rapid decay of short-lived isotopes produced during SAA passages is clearly seen following the SAA exits at, e.g. day fractions 0.05, 0.12, 0.19, 0.25, and 0.32.*

prompt interactions of cosmic-ray protons or atmospheric neutrons. As CGRO orbits the Earth the local cut-off rigidity changes incessantly in time, and so do intensity and spectral distribution of the incident cosmic radiation: the higher the cut-off rigidity, the lower the incident cosmic-ray intensity and the higher the average cosmic-ray energy (see Eqs. 4.2 and 4.1). In addition, the rate of prompt background events to a good approximation is proportional to the incident cosmic-ray intensity. It follows that the prompt background event rate should be positively correlated with veto rate, and anti-correlated with rigidity, as observed. The correlation between the `Gamma-1` event rate and the veto rate and the vertical cut-off rigidity is illustrated, for `EHORA` $\geq 45°$, in the top and bottom panels of Fig. 4.3, respectively. To the first order the event rate increases linearly with veto rate, and decreases exponentially with rigidity. A similar dependence on rigidity has been observed with COMPTEL for the fast-neutron flux in the D1 detector (Morris *et al.* 1995) and for the event rate due to the instrumental 2.2 MeV line (Weidenspointner *et al.* 1996a). Other instruments such as the Gamma-Ray Spectrometer onboard the Solar Maximum Mission (Forrest 1989) or the γ-ray detectors onboard Kosmos 461 (Mazets *et al.* 1975) have found the same dependence of the event rate on rigidity.

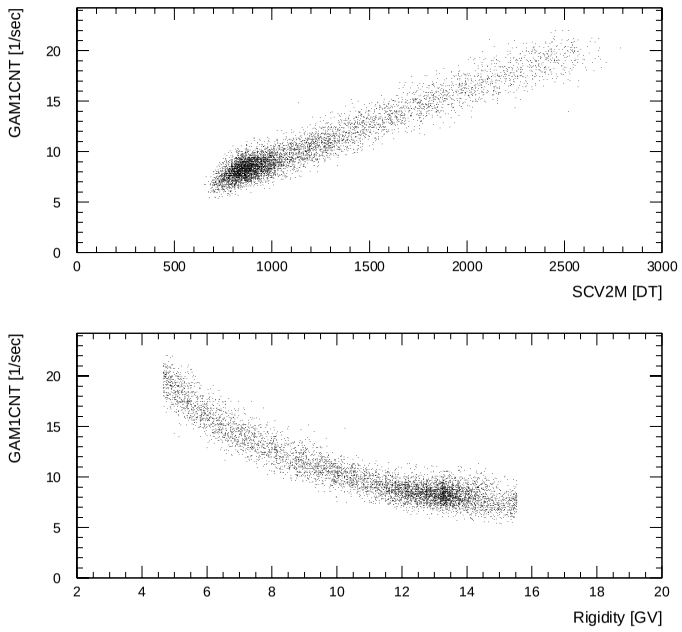

Figure 4.3: *The correlation between the* `Gamma-1` *event rate (*`GAM1CNT`*) and the V2 veto rate (*`SCV2M`*, upper panel) and the vertical cut-off rigidity (*`RIGIDITY`*, lower panel), for the arbitrary observation period 204.*

Superposed on this veto rate or rigidity dependence of the event rate is a dependence on the angle `EHORA` (or `GCEL`) due to the varying solid angle subtended by the intensely bright disk of the Earth in the telescope field-of-view, and due to mass-shielding effects. At an altitude of $\sim$ 450 km CGRO orbits the Earth every $\sim$ 90 min, resulting in about 15 orbits per day, as can be seen in the bottom panel of Fig. 4.2. Because the Earth's atmosphere is much brighter in γ-rays than the sky, the event rate increases with decreasing `EHORA` due to double-scatterings of atmospheric γ-rays and events produced by atmospheric neutrons[11]. Conversely, the event rate decreases with increasing `EHORA`, not only because the Earth moves out of the field-of-view, but also because increasing

[11]See the interplay of the effects of the cosmic radiation (`SCV2M`) and of `EHORA` on `GAM1CNT` at the end of TJD 9725 in Fig. 4.2.

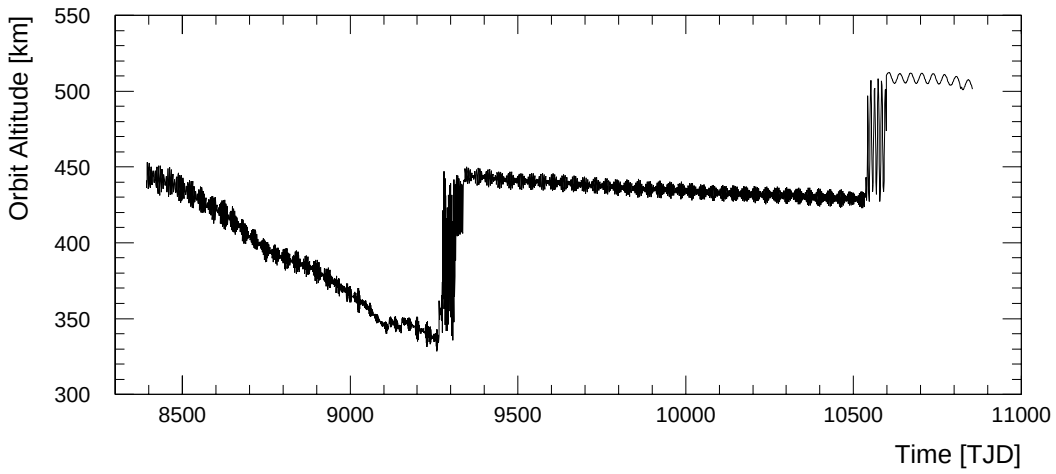

Figure 4.4: *The altitude of the CRGO orbit as a function of time. The two reboosts of the orbit around TJD 9280 (Oct.–Dec. 1993) and TJD 10560 (Apr.–May 1997) are clearly seen. The rapid decay of the orbit at the beginning of the mission results from the increased drag of the expanded atmosphere at solar maximum.*

mass shielding prevents atmospheric neutrons from reaching the D1 detector (see e.g. Morris *et al.* 1995, Weidenspointner *et al.* 1996a).

Passages through the SAA, which for the COMPTEL orbit with an inclination of 28.5° occur 6–8 times each day, are another source of variation of the instrumental-background event rate on time scales less than an orbital period. During these SAA passages the instrument's high-voltages are switched off to prevent damage, therefore very little information is available for these periods of time. Nevertheless, the rapidly decaying high event rate due to short-lived isotopes[12] produced during SAA passages is clearly visible for five SAA exits at the beginning of TJD 9725 (see Fig. 4.2).

As long as the build-up of long-lived[13] activation can be neglected (see below), the two parameters `RIGIDITY` and `GCEL` (or `EHORA`) are sufficient to model the event rate as a function of time to a first approximation. A more refined model of the event rate, including the short-lived effects of SAA passages, was obtained in a neural-network simulation using the following free parameters (Varendorff *et al.* 1997): the position of the Earth in the field-of-view (azimuth and elevation), the position of the satellite above the Earth (geographic longitude and latitude), the ascending node (the time since the last crossing of the equator from negative to positive latitude), the altitude of the spacecraft above the Earth, and the angle between the projection of the satellite

[12]For the remainder of this thesis, "short-lived" background will refer to instrumental-background components with short half-lives compared to an orbital period of ~ 90 min: $T_{1/2} \lesssim 10$ minutes.

[13]For the remainder of this thesis, "long-lived" background will refer to instrumental-background components with half-lives $T_{1/2}$ longer than about 10 minutes. These background components may not completely decay away during the time between two successive SAA passages, and their activity may thus build up over time due to periodical episodes of activation in SAA passages (see Sec. 4.5.

z-axis on the surface of the Earth and the local meridian. The neural network was successfully applied to Phase 2 (Nov. 1992 to Aug. 1993) data, were the activity due to long-lived isotopes, and in particular its variation[14], was at its minimum (see below and Sec. 4.5). It is worth noting that even though variations of long-lived background components are negligible for these data, a dependence of the event rate on altitude had to be taken into account in the neural network model, indicating that the event rate is also subject to changes on time scales much longer than an orbital period.

The two main causes for variations of the event rate on time scales much longer than an orbital period are changes of the altitude of the satellite orbit (see Fig. 4.4) and the solar modulation. The effect of these two parameters on the prompt background components is small since the incident local cosmic-ray flux is hardly affected by them. Conversely, the SAA proton flux encountered by CGRO, and consequently the activation of radioactive isotopes during SAA passages, strongly depends on these two parameters. The altitude and solar-cycle dependence of the SAA proton flux encountered by CGRO is depicted in Fig. 4.1: the SAA proton flux increases by a factor of ~ 10 over the altitude range 300–500 km, and is a factor of $\sim$ 2 higher at solar minimum than at solar maximum. As already mentioned above, the COMPTEL data provide little information on the time periods during SAA passages. Among the few HKD parameters always measured are the trigger rates in the two calibration units (see Sec. 3.3). Fortunately, these are very well suited to monitor the SAA proton flux since the plastic scintillators are sensitive to the protons, but hardly to secondary γ-ray photons. As an example, the values of SCCALBH[15] during SAA passages at

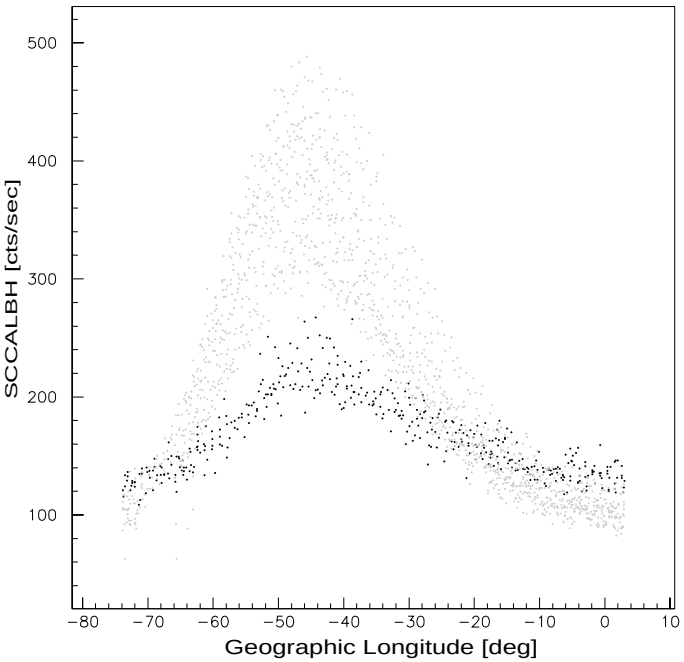

Figure 4.5: *The values of* SCCALBH *during SAA passages at solar minimum (black dots) and solar maximum (grey dots).*

[14]Empirical models of the event rate as a function of time can easily account for long-lived background, as long as it does not vary in time, by introducing a constant baseline event rate.

[15]The trigger rate of both of the two CAL-units, A and B, is measured for a low (parameters SCCALAL and SCCALBL) and a high (parameters SCCALAH and SCCALBH) threshold. The rates of CAL-unit B are more stable than those of CAL-unit A, and the high-threshold rates are more stable than the low-threshold rates. Therefore the parameter SCCALBH was used to monitor the SAA proton flux.

solar minimum and solar maximum are plotted in Fig. 4.5, which exhibit the expected variation by a factor of ~ 2. To a good approximation, the production of radioactive isotopes during SAA passages is proportional to the proton flux. It follows that the production of radioactive isotopes strongly depends on the orbit altitude and on the solar cycle (see Fig. 4.1). For short-lived isotopes this has little consequences, since they decay away between successive SAA passages. For long-lived background components, however, the effect is dramatic. Depending on whether the number of decays of a particular long-lived isotope between successive SAA passages is smaller or greater than the number of isotopes produced, the average event rate due to this isotope can increase or decrease considerably over long time scales. The complex variation of the activity of a long-lived isotopes is determined by its half-life and the time history of the activation episodes during SAA passages. Using the `HKD` parameter `SCCALBH` as a measure for the proton flux during SAA passages, and assuming that a particular isotope is exclusively produced during SAA passages, the isotope activity could be modelled successfully as a function of time, as is described in detail in Sec. 4.5.

4.1.3 Instrumental-Background Event Types

The particle and photon environment to which COMPTEL is exposed produces, through many different channels, coincident interactions in the D1 and D2 detectors that pass all the logic and electronic criteria for a valid gamma event described in Sec. 3.4.1. Below, an overview of different types of background events in terms of their interaction process and location, illustrated in Fig. 4.6, is given. This classification of background events, which evolved over the years (see e.g. van Dijk 1996), is by no means comprehensive, but represents a simplistic, albeit useful, framework for future discussions of the COMPTEL instrumental background. Event types that are easily rejected or identified because of veto triggers or based on event parameter characteristics are indicated.

• **A and B**: *events caused by the double-scattering of a single photon.* Any photon created in CGRO may produce this type of event, which, if the scattering is from D1 to D2, is completely analogous to a proper celestial event (compare Fig. 3.2). Back-scattered photons (D2 $\rightarrow$ D1) are easily rejected by a ToF selection. Many of the photons that originate from below the D1 detector (such as event **B**) have to scatter by a large angle to arrive at D2, hence the energy of the scattered photon may be too low to produce a signal above the energy threshold in the D2 detector. In addition, type **B** events may be eliminated by a selection on the scatter angle $\bar{\varphi}$. A good example for this is the rejection of the 1.46 MeV photons from the natural decay of ^{40}K contained in the glass ceramic of the EGRET spark chamber frame (see Sec. 4.4.2.3).

The instrumental background from single photons is therefore mostly due to photons originating in, around and above the D1 detector (such as event **A**). The best-studied examples for this event type are the natural decay of ^{40}K in the D1 PMTs (see Sec. 4.4.2.3) and thermal-neutron capture on hydrogen in the D1 scintillator (see

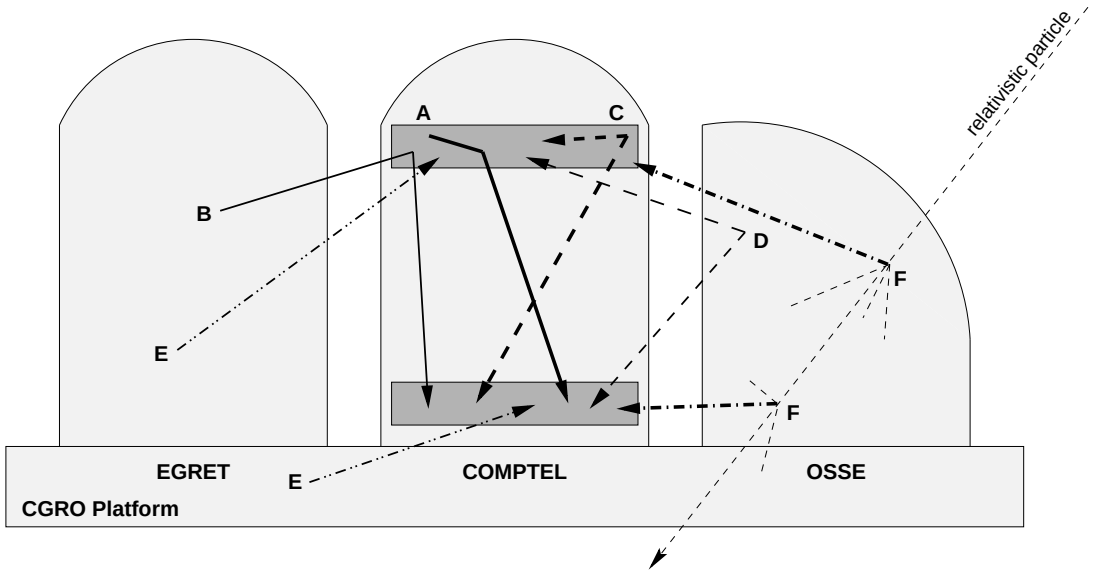

Figure 4.6: *An illustration of the main channels for the triggering of valid events due to instrumental background. For simplicity, BATSE was excluded in this schematic view of CGRO. The various event types are explained in the text.*

Sec. 4.4.2.1), resulting in prominent line features in the $E_{\rm tot}$ spectrum at 1.46 MeV and 2.22 MeV, respectively.

Finally, high-energy neutrons can undergo a double-scattering process analogously to photons, however, these neutron events can be identified by their PSD value (see Sec. 4.1.1).

• **C and D:** *events caused by two or more photons both spatially and temporally correlated (so-called multiple-photon or cascade events).* A number of processes can result in the emission of two or more photons from a small region on a time scale shorter than the coincidence window of 40 nsec. Nucleons that have been excited above the first nuclear level, e.g. by proton or neutron interactions, may promptly emit a cascade of photons. In general, the multitude of nuclear excitation levels will result in a featureless continuun spectrum in $E_{\rm tot}$. If, however, only a few photons are emitted characteristic line-like features appear in the E_1, E_2, and $E_{\rm tot}$ spectra (see e.g. Sec. 4.4.2.2 for a detailed description of the ^{24}Na cascade).

Nuclear interactions may also produce isotopes that are unstable against $\beta^{\pm}$-decay. Upon their decay these $\beta^{\pm}$-isotopes often populate an excited level of the daughter nucleus, which usually decays on time scales of pico-seconds or less (unless an isomeric state has been populated). The range of the β-particle is small (less than a few cm at MeV energies), but bremsstrahlung photons can travel to one of the detectors and interact in coincidence with a trigger of the other detector due to a γ-ray from the de-excitation of the daughter nucleus (see e.g. the β^--decay of ^{28}Al to ^{28}Si described in Sec. 4.4.2.5). In case of a β^+-decay, the positron not only emits bremsstrahlung

photons, but also two 511 keV photons upon its annihilation, one[16] of which again may trigger a valid event together with a γ-ray from the daughter nucleus (see e.g. the β^+-decay of ^{22}Na described in Sec. 4.4.2.4).

High-energy neutrons may induce the emission of one or more γ-ray photons outside of the D1 scintillator (to elude rejection by PSD) and then continue their path downward to interact in the D2 detector.

More complicated nuclear reactions such as the spallation (break-up) of a nucleus or the initiation of a shower of secondaries by an incident cosmic-ray particle may also produce multiples of photons.

In general, photons are emitted near-simultaneously in these processes, i.e. on time scales much shorter than the coincidence window, hence the ToF of this type of events is determined by the location of the emitting nucleus relative to the D1 and D2 detectors. Photons originating above the D1 detector will be found at ToF $\sim$ 120 channels, photons emitted in and around the D1 detector (such as type **C** events) will have a ToF that is slightly below channel 120. Photons emitted by nuclei in the satellite material between the D1 and D2 detectors (such as type **D** events) will interact in the two detectors near-simultaneously and acquire ToF values between the forward- and backward-peak. Photons originating in and around the D2 detector will contribute to the backward-peak at ToF $\sim$ 80 channels. The ToF distribution of these so-called multiple-photon events is therefore determined by the mass distribution of the satellite relative to the D1 and D2 detectors and the effective areas of the detectors as a function of the location in the spacecraft.

• **E:** *events that are both spatially and temporally uncorrelated (the so-called random coincidences).* The COMPTEL detectors are continuously exposed to a large flux of γ-ray photons, which inevitably will result in coincident interactions that qualify as valid events. The photons producing these random coincidences are mostly of local or atmospheric origin. Since the two photons creating the event are not correlated in any way, and in particular not correlated in time, these events are homogeneously distributed in ToF (see Sec. 4.3.1).

• **F:** *events caused by two photons that are temporally correlated, but spatially uncorrelated.* High-energy cosmic-ray particles or atmospheric neutrons may interact at several different locations along their path through CGRO. The individual interactions include those generating type **C** and **D** events (e.g. spallations or showers). The whole interaction chain creating type **F** events is very similar to multiple-photon events, the main difference being that now the ToF depends on both the location of the interactions as well as the (relativistic) velocity of the primary particle. The ToF distribution of this type of event is very broad and covers the whole coincidence window.

[16]The two 511 keV photons are emitted in opposite directions. Since the D2 energy threshold usually is above 511 keV, only the one 511 keV photon interacting in the D1 detector, which has a threshold energy below 100 keV, is available for the creation of a valid event.

Other processes not mentioned, such as the interaction of a neutron in the D2 detector (which has no PSD capability) after producing a photon in the D1 detector material except the scintillators, or direct ionizational losses of β-particles created in the housings of the D1 scintillators may also play an important role. The event signatures of these and other, more complicated processes, however, will be similar to the event types described above.

4.2 Data Selections

Attempting to study the CDG amounts to facing one of the most formidable problems in astronomy — the determination of the absolute intensity of an apparently isotropic radiation field. A detailed qualitative and quantitative understanding of the instrumental background is crucial if the CDG intensity is to be reliably determined. In general, accurate modelling of the complex instrumental background in the three-dimensional COMPTEL dataspace as a function of energy is exceedingly difficult. Such detailed modelling, however, is only required for imaging analysis. The primary goals of the CDG studies performed with COMPTEL are the determination of its energy spectrum and the derivation of upper limits on possible deviations of its intensity from isotropy. These objectives do not require the use of the full imaging capability of the instrument. It is sufficient to use COMPTEL as a pointed collimator, which facilitates considerably the modelling of the instrumental background as the dataspace is reduced to one dimension, the scatter angle $\bar{\varphi}$. The collimation of the COMPTEL field-of-view through event selections is described below.

In addition, the intense atmospheric γ-radiation has to be removed from the data if the CDG is to be studied, as explained in Sec. 4.2.2. Finally, some types of background events can be eliminated from the data, or at least reduced in number, by additional selections on event parameters, as summarized in Sec. 4.2.3.

4.2.1 COMPTEL as a Collimator

The collimation of the COMPTEL field-of-view (FoV) through selections on event parameters is illustrated in Fig. 4.7. Let ζ be the zenith angle of the direction of the scattered photon in the telescope system, $(\chi, \psi)_{\rm sct}$ (compare Fig. 3.2), i.e. ζ is the angle between $(\chi, \psi)_{\rm sct}$ and the poining direction of the telescope. Further, let ξ be the maximum angular distance between the event circle and the pointing direction:

$$\xi = \zeta + \bar{\varphi} \tag{4.3}$$

Then a collimated FoV can be defined by setting an upper limit to the accepted values of the angle ξ. Such a selection defines a circular FoV with half opening angle $\xi_{\rm FoV}$, centered on the pointing direction of the instrument. Only events whose event circle is

fully within this FoV are accepted. For the CDG studies presented in this thesis the FoV was defined by (see also Kappadath 1998)

$$\zeta + \bar{\varphi} \leq 40^\circ = \xi_{\mathrm{FoV}} \tag{4.4}$$

thus covering a solid angle of about 1.47 ster. It is worth noting that this FoV collimation requires selections on event parameters only.

4.2.2 Removal of Atmospheric Gamma-Radiation

During an observation period the pointing direction of COMPTEL remains unchanged while the satellite orbits the Earth, which therefore periodically enters or crosses the FoV (see the variation of `EHORA` in the bottom panel of Fig. 4.2). Defining the COMPTEL FoV for the CDG analysis according to Eq. 4.4, however, allows us to effectively remove the intense atmospheric γ-radiation, as illustrated in Fig. 4.8. By selecting data only from those periods of time when the Earth was outside the FoV, i.e. from times when the Earth-horizon angle of the telescope pointing direction, `EHORA`, is greater than the half opening angle of the FoV, ξ_{FoV}, all photons originating from the Earth's atmosphere are eliminated.

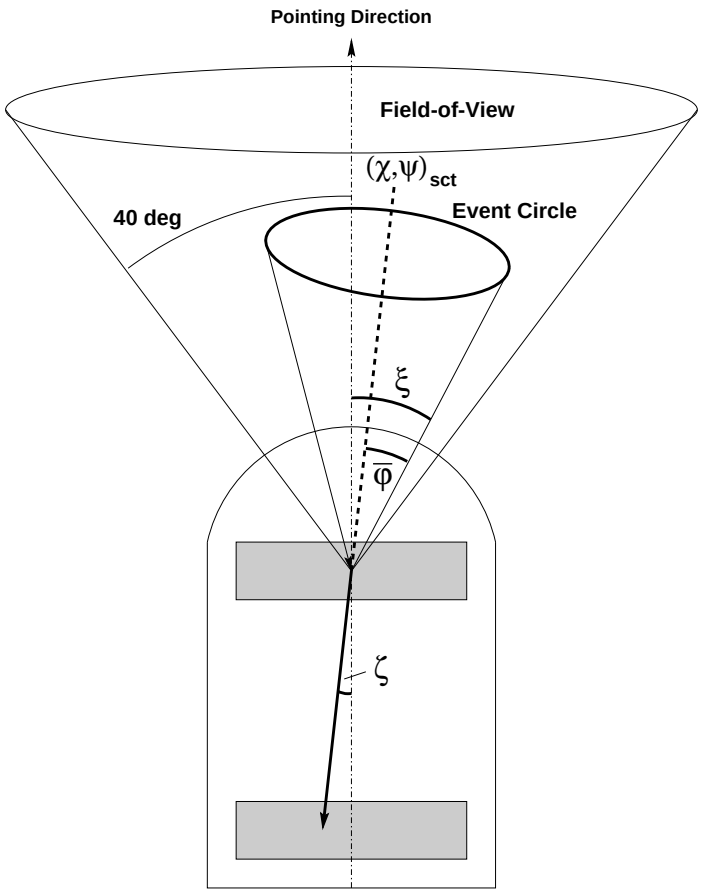

Figure 4.7: *An illustration of the collimation of the COMPTEL field-of-view through selections on event parameters. Only events whose event circle is fully within this field-of-view are accepted.*

The Earth's atmosphere has no well-defined upper boundary, but is gradually thinning out with increasing altitude. In addition, the Earth's atmosphere tends to be brighter close to the horizon than at the nadir, in particular at high energies (Thompson and Simpson 1981). In general, a minimum angular separation of 5° between the edge of

the FoV and the Earth horizon is therefore required in studies of the CDG (see also Kappadath 1998). For $\xi_{\mathrm{FoV}} = 40°$ (see Eq. 4.4) this implies:

$$\texttt{EHORA} \geq 45° \tag{4.5}$$

It follows that if COMPTEL is used as a collimator with a FoV defined according to Eq. 4.4 a selection on a single `OAD` parameter is sufficient to remove the atmospheric γ-radiation[17]. In addition, for these selections the instrument response is independent of the position of the Earth relative to the telescope, unlike in standard imaging analysis (see e.g. van Dijk 1996, Oberlack 1997). About 30% of the observing time are accepted by these selections for CDG studies.

In Secs. 3.2 and 3.5.4 it was discussed that the determination of the scatter angle $\bar{\varphi}$ is subject to various uncertainties, in particular due to losses of deposited energy from the D1 and D2 detectors, which may affect the effectiveness of the removal of atmospheric γ-ray photons. Below about 10 MeV incomplete absorption of deposited energy most likely occurs in the D2 detector, resulting in a measured scatter angle $\bar{\varphi}$ greater than the true scatter angle φ, corresponding to a positive ARM value (see Sec. 3.5.4). Events with positive ARM value, whose event circle is within the FoV, therefore have truly originated from there. A fraction of these events with $\bar{\varphi} > \varphi$ that originated from within the FoV will be rejected falsely, however, this is properly taken into account in the determination of the effective area (see Sec. 3.5.5). Above about 10 MeV the fraction of events with loss of deposited energy in the D1 detector increases to a few percent, which results in an underestimate of $\bar{\varphi}$ and hence a negative ARM value (see Sec. 3.5.4). Accepted events with incomplete absorption of the D1 energy deposit therefore could have originated from outside the FoV. As long as the brightness of the sky around the edge of the FoV

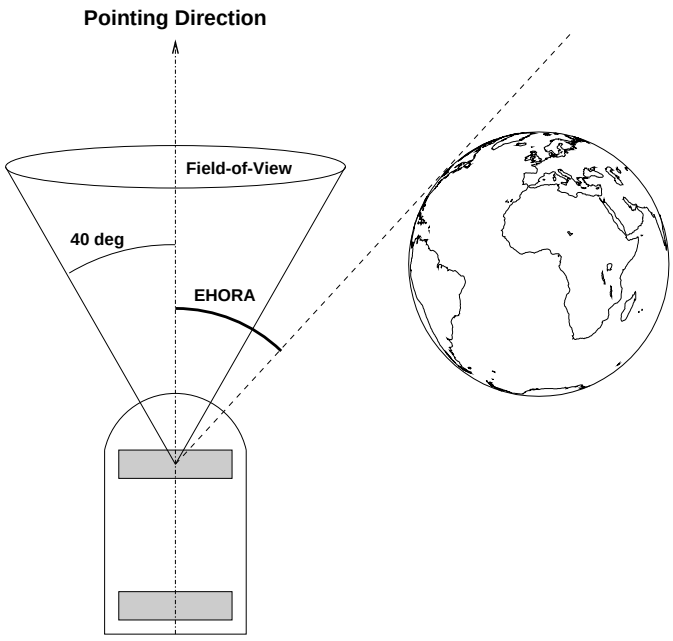

Figure 4.8: *An illustration of the removal of atmospheric γ-ray photons in studies of the CDG through a combination of FoV and orbital selections.*

[17]In principle, an analoguous selection could be achieved using the `OAD` parameter `GCEL` instead of `EHORA`, however, at different orbital altitudes the same value of `GCEL` corresponds to different values of `EHORA`. Since it is the angular separation between the Earth horizon and the edge of the FoV that is relevant, a selection on `EHORA` is more convenient since it is independent of altitude.

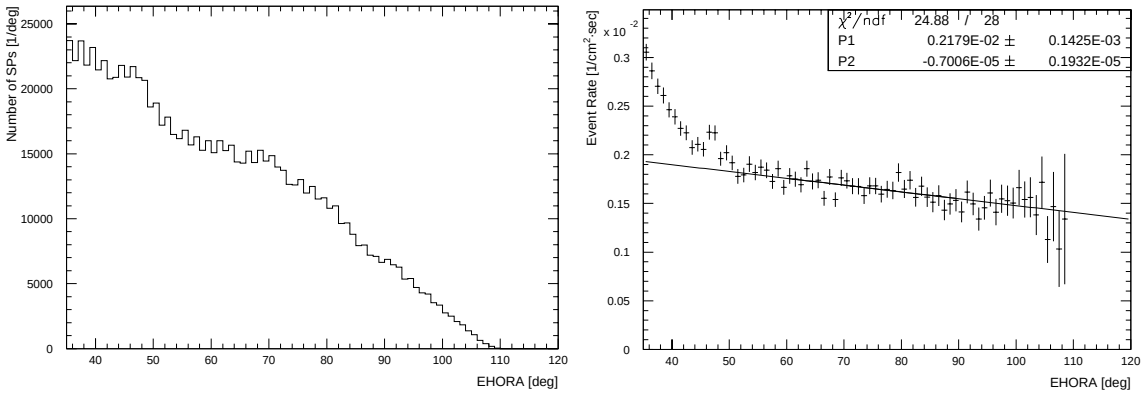

Figure 4.9: *Assessment of the possible contribution of atmospheric γ-ray photons to the CDG intensity. The superpacket distribution and the 17–30 MeV event rate are depicted as a function of* EHORA *in the left and right panel, respectively. Also shown is a linear fit to the event rate in* EHORA *$60° - 90°$, extrapolated over the full* EHORA *range.*

is the same as inside the FoV this is properly accounted for in the effective area and of no concern. A problem my arise if the Earth is closest to the edge of the FoV.

To assess this effect, the event rate for standard CDG selections (see next section), corrected for the effective area (see Sec. 3.5.5), was studied as a function of EHORA in dependence on energy using the full CDG data base used in this thesis (see Appendix D). As expected, the effect was most clearly seen at the highest energies. The superpacket distribution and the 17–30 MeV event rate are both depicted as a function of EHORA in the left and right panel of Fig. 4.9, respectively. For EHORA $\gtrsim 50°$ the event rate varies to a good approximation linearly with EHORA, consistent with the findings of Morris *et al.* (1995) and Weidenspointner *et al.* (1996a), which may be attributable to mass shielding. At lower values of EHORA the event rate increases rapidly, which most likely is due to double-scattering atmospheric γ-ray photons. To assess the event rate due to these double-scattering atmospheric photons, a linear function was fitted to the data in $60° - 90°$, which was then extrapolated to lower angles assuming that the linear variation of the general instrumental background holds for all values of EHORA (see right panel of Fig. 4.9). The excess event rate above the general, linear background in the EHORA ranges $45° - 50°$ and $\geq 45°$ was then compared to the event rate due to the CDG as determined in this thesis (see Sec. 6.3.3). According to this simplistic comparison the excess event rate due to double-scattering atmospheric photons is about the same as the event rate due to the CDG in the $45° - 50°$ range. On average, however, the instrument's pointing is in the $45° - 50°$ EHORA range only about 15% of the observation time defined by Eq. 4.5 (see left panel of Fig. 4.9). For EHORA $\geq 45°$ the excess event rate is less than 10% of the CDG event rate, which is well within the systematic uncertainty of the CDG intensity determination (see Sec. 6.3.3). The CDG intensity was therefore first determined for EHORA $\geq 45°$ (see Eq. 4.5) to reduce statistical uncertainties by using a maximum number of events. To assess a possible systematic effect due to atmospheric photons, the analysis was repeated for EHORA $\geq 50°$. In all cases

the differences were considerably less than the statistical uncertainty.

4.2.3 Standard CDG Data Selections

As already mentioned above, some types of background events may be minimized or rejected by applying appropriate selections on the event parameters, thus optimizing the signal-to-background ratio. Below, the full set of data selections applied in the early stages of the CDG analysis is described[18]. In the following, these CDG selections will be referred to as "standard CDG data selections" (see also Kappadath 1998), since they will be slightly optimized in the final analysis (see Secs. 5.3.6.2 and 5.4). All five basic dataset types listed in Sec. 3.4.3 are affected: `EVP`, `OAD`, `HKD`, `SHD`, and `TIM`.

The event (`EVP`) data used in the CDG analysis consists of `Gamma-1` events (see Sec. 3.4.1) with the best available ToF and PSD values: $\mathrm{ToF}_{\mathrm{VII}}$ (see Sec. 3.7) and $\mathrm{PSD}_{\mathrm{II}}$ (see Sec. 3.8). The following selections are applied to the event data.

$$70 \text{ keV} \leq E_1 \leq 20 \text{ MeV}$$

$$730 \text{ keV} \leq E_2 \leq 30 \text{ MeV}$$

$$\mathrm{PSD}_{\mathrm{low}}(E_1) \leq \mathrm{PSD} \leq \mathrm{PSD}_{\mathrm{up}}(E_1)$$

with $\mathrm{PSD}_{\mathrm{low}}(E_1)$ and $\mathrm{PSD}_{\mathrm{up}}(E_1)$ as defined in Sec. 3.8

$$6^\circ \leq \bar{\varphi} \leq 38^\circ$$

$$\zeta + \bar{\varphi} \leq 40^\circ = \xi_{\mathrm{FoF}}$$

(see Eq. 4.4)

D1 and D2 modules used: see Table D.9

In addition, it is required that there is no coincident signal from any of the four veto domes, indicated by a `VETO FLAG` value of zero (see Sec. 3.4.1).

The purpose of the various selection criteria is as follows. The upper boundaries on the energy deposits E_1 and E_2 reflect the inadequate knowledge of the instrument response above these energies. The lower boundaries have been chosen such that they are above the `Gamma-1` thresholds of all detector modules (see Sec. 3.4.1). These thresholds have in general increased over time, and have different values for different modules. The lower boundaries are sufficiently far above the respective thresholds of all detector modules to render the effects of threshold variations on the instrument response insignificant. The purpose of the PSD selection is to reject a large fraction of the background events due to neutron interactions in the D1 detector (see Secs. 3.8, 4.1.1 and 4.1.3). The lower boundary on the scatter angle is due to the fact that the instrumental

[18]These selections differ in some respects from those usually used for standard analyses by the COMPTEL collaboration (see Appendix C, Footnote 3).

background is exceptionally high at the lowest $\bar{\varphi}$-values. The upper boundary follows from the FoV collimation (see Eq. 4.4), which implies $\bar{\varphi} \lesssim 40°$.

The only selection on an OAD parameter is the cut EHORA $\geq 45°$ (see Eq. 4.5) for removing atmospheric γ-ray photons.

In general, the veto rates in the four veto domes are very well correlated (see Sec. 5.5.1). To eliminate data from superpackets with unusual veto rates in individual veto domes the following selections are applied on HKD data:

$$1.6 \leq \texttt{SCV1M/SCV2M} \leq 2.2$$

$$0.8 \leq \texttt{SCV1M/SCV3M} \leq 1.3$$

The livetime L of the instrument usually is ~ 16 sec (see Sec. 3.9). By requiring $L \geq 10$ sec for superpackets to be accepted for the CDG analysis, times during which the telescope performance may have been reduced or for which the livetime value may be uncertain are rejected. In addition, a SHD quality-flag value of 1 or 2 is required.

Finally, only those periods of time during which COMPTEL was operated in NORMAL mode are selected based on TIM data.

4.3 Instrumental-Background Time-of-Flight Signatures

4.3.1 Overview

The ToF, a measure for the time difference between interactions in the D1 and D2 detectors (see Sec. 3.7), is the most valuable event parameter for instrumental-background suppression and identification. The event distribution in ToF over the full coincidence time window[19] is exemplified in Fig. 4.10 in the four standard COMPTEL energy ranges. The most prominent features in these so-called ToF spectra are the two Gaussian-like features located at ToF channels ~ 80 and ~ 120, the so-called ToF backward- and forward-peaks, respectively. These peaks consist of, among other things, double-scattered single photons. In particular, all of the forward-scattered celestial photons are contained in the ToF forward-peak, together with instrumental-background events (see Sec. 3.3). The forward-peak comprises less than about 10% of all events.

The vast majority of the events are, however, due to the instrumental background, with different types of background events contributing to different portions of the ToF

[19]The coincidence time window has a length of ~ 40 nsec, covering ToF channels $\sim 40 - 200$ (see Sec. 3.4.1).

spectrum. The ToF distribution of background events of type **A** and **B** (see Fig. 4.6), which are events caused by the double-scattering of a single photon, naturally peaks at ToF channels ~ 80 and ~ 120. For multiple-photon events of type **C** and **D** the ToF distribution is determined by the mass distribution of the satellite and the effective areas of the two detectors as a function of the location in the spacecraft. Again, the ToF distribution of these events is expected to contribute mainly to the ToF forward- and backward-peaks. In particular, type **C** events constitute a substantial fraction of the ToF forward-peak, as demonstrated in the following sections.

The ToF forward- and backward-peaks cannot account for the full ToF spectrum, as demonstrated by van Dijk (1996) in two ways. First, the two peaks were subtracted from the full ToF distribution by fitting each with a Gaussian on top of a parabolic background. The remaining ToF distribution, which will be referred to as ToF continuum-background in the following, is depicted by dashed lines in the four panels of Fig. 4.10. The exact shape of the ToF continuum is unknown due to uncertainties in the fit functions used to model the individual ToF peaks, however, the residual is significant. Similarly, a pronounced non-zero ToF component remains between the two ToF peaks when the left wing of the backward-peak is mirrored on the line ToF = 80, as shown by dotted lines in Fig. 4.10. Part of the ToF continuum is due to type **E** events, which are expected to be homogeneously distributed in ToF. The contribution due to these random coincidences was assessed by van Dijk (1996) by comparing the event rate at very low ($\lesssim 30$ channels, measured in a dedicated low-ToF instrument mode) and very high ($\gtrsim 160$ channels) ToF values with the rate of random coincidences expected from the trigger rates in the individual detectors[20]. These investigations showed that random coincidences contribute only a minor fraction of the ToF background, indeed, there is evidence for the presence of additional background components (e.g. type **F** events) at the extremes of the ToF distribution.

Most likely, the majority of the ToF continuum-background arises from type **D** and **F** events. The D1 and D2 energy distributions in the ToF range 104.5–106.5 (to minimize contributions from the forward- and backward-peaks) were studied by van Dijk (1996). The presence of line features in these energy distributions indicates that part of the ToF continuum between the ToF peaks must be due to 2-photon events such as type **D** and **F**. Moreover, the de-convolved E_1 and E_2 distributions are very similar, suggesting that type **D** and **F** events in fact dominate the ToF continuum between the ToF peaks. The relative importance of these two event types, however, cannot be determined from the data and is still uncertain, which is also true for the types of interacting primary particles. Extensive Monte Carlo simulations of the telescope response to interactions of incident cosmic-ray particles and atmospheric secondaries in the satellite material should in principle allow us to answer these questions (see

[20]The trigger rates in the individual detectors were determined at the very beginning of the mission, when the instrument was operated for testing purposes in so-called singles mode, which does not require a coincident interaction in the other detector for an individual interaction in D1 or D2 to be recorded.

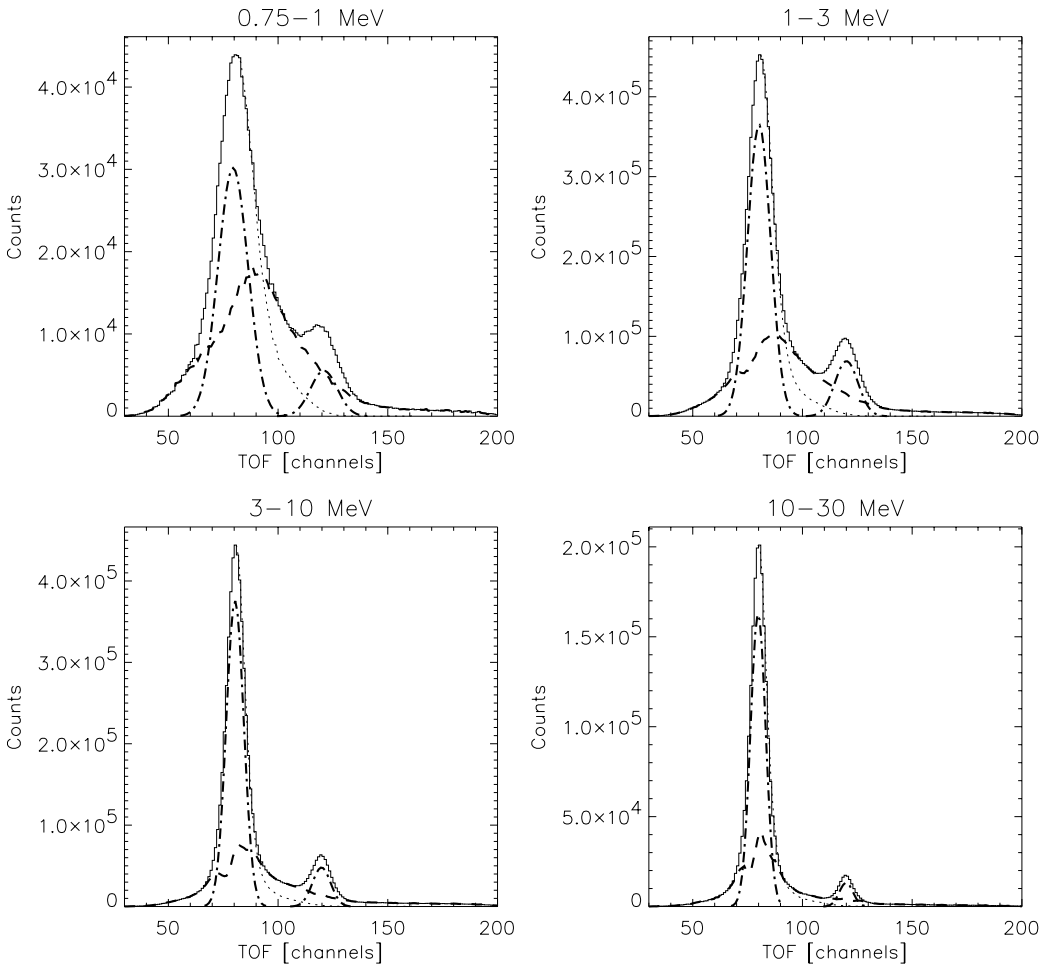

Figure 4.10: *The ToF_V (see Sec. 3.7) distributions over the full coincidence window in four energy ranges, using livetime-corrected* `Gamma-1` *and* `Gamma-2` *data from OPs 204, 205 and 206 (figure from van Dijk 1996). The event distributions are plotted as line histograms. In addition, individual components of the ToF distributions are indicated: Gaussian fits to the backward- and forward-peaks (dash-dotted lines), the remaining distributions after subtraction of the Gaussian fits from the histograms (dashed lines), and the left wings of the backward-peaks mirrored at ToF channel 80.*

e.g. Dyer *et al.* 1994). Additional information on the origin of the ToF continuum-background can be obtained from studying its variation with cut-off rigidity or veto rate (see Sec. 4.3.5).

If not indicated otherwise, the following discussion of the ToF signatures of the instrumental background is based on earlier work by Weidenspointner and Varendorff (1996a,b), Weidenspointner *et al.* (1997b) and Kappadath (1998).

4.3.2 Modelling the ToF Forward-Peak Region

The signal of the CDG, together with various instrumental-background components, is contained in the ToF forward-peak located at ToF $\sim$ 120 ch. The first step in extracting the CDG signal from the total event rate therefore is a fit of the ToF spectrum in the $\sim 105-135$ ch range of the ToF forward-peak, the so-called ToF forward-peak region, which is covered by the `Gamma-1 EVP` data extending over the ToF range $\sim 100-150$ ch (see Sec. 3.4.1). The ToF fit allows us to remove the ToF continuum and to determine the event rate in the ToF forward-peak (see Sec. 5.2).

4.3.2.1 Three Different Models

Three different models are used to describe the `Gamma-1` ToF spectrum in the CDG analysis. In each of these models the ToF forward-peak is approximated by a Gaussian (or two Gaussians in more refined models for specific energy ranges, see Sec. 5.2). The models differ, however, in the analytical function used to approximate the ToF continuum-background: a parabola, an exponential, a Gaussian. This variety of models reflects the fact that the true shape of the ToF continuum-background is unknown.

With $\mathtt{t}$ denoting the ToF value in [channels], the three models, each having six free parameters, are defined as follows.

- *Parabolic Model*:

$$f_p(\mathtt{t}) = p_1 \cdot \exp\left[-\frac{1}{2}\left(\frac{\mathtt{t}-p_2}{p_3}\right)^2\right] + p_4 \cdot (\mathtt{t}-p_5)^2 + p_6 \tag{4.6}$$

- *Exponential Model*:

$$f_e(\mathtt{t}) = p_1 \cdot \exp\left[-\frac{1}{2}\left(\frac{\mathtt{t}-p_2}{p_3}\right)^2\right] + p_4 \cdot \exp\left(\frac{97.5-\mathtt{t}}{p_5}\right) + p_6 \tag{4.7}$$

- *Gaussian Model*:

$$f_g(\mathtt{t}) = p_1 \cdot \exp\left[-\frac{1}{2}\left(\frac{\mathtt{t}-p_2}{p_3}\right)^2\right] + p_4 \cdot \exp\left[-\frac{1}{2}\left(\frac{\mathtt{t}-80}{p_5}\right)^2\right] + p_6 \tag{4.8}$$

The restrictions imposed on the exponential and the Gaussian model by fixing the exponential and Gaussian function describing the ToF continuum relativ to $\mathtt{t} = 97.5$ ch and $\mathtt{t} = 80$ ch, respectively, are very minor since the results of ToF fits with f_e and f_g proved to be very insensitive to these values. To illustrate the quality of these three models, fits of ToF spectra with each of the three ToF models for three different energy ranges are depicted in Fig. 4.11, which also exemplifies the variation of the ToF distribution in energy discussed in Sec. 4.3.3.

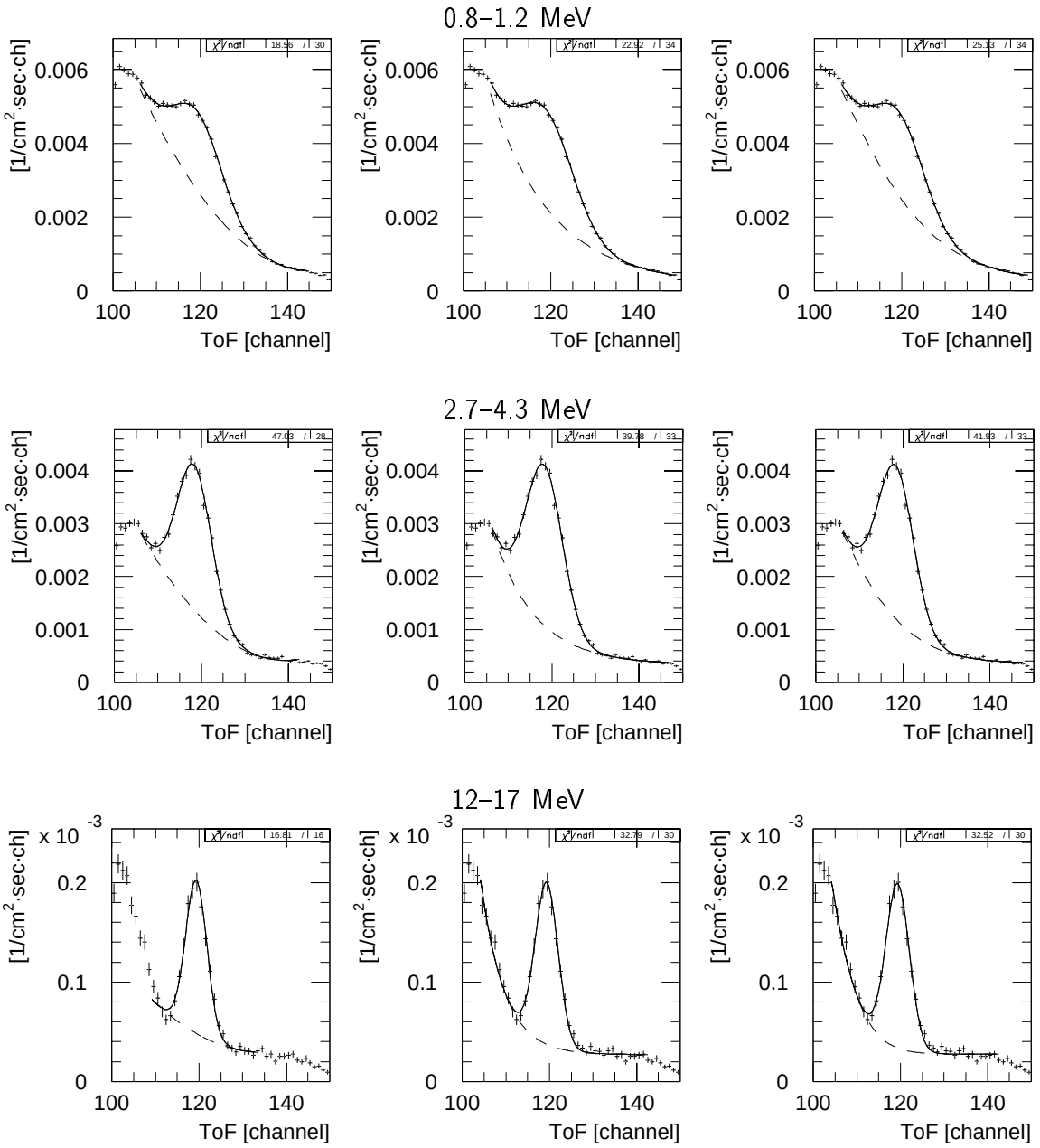

Figure 4.11: *Fits of ToF spectra with each of the three ToF models (parabolic, exponential and Gaussian from left to right) for three energy ranges (0.8–1.2 MeV, 2.7–4.3 MeV, and 12–17 MeV from top to bottom. The solid lines indicate the full fit results, the dashed lines represent the modelled continuum backgrounds only.*

4.3.2.2 Systematic Differences

The different analytical approximations of the ToF background, whose exact shape is unknown, result in different separations of the ToF distribution into ToF forward-peak and ToF background, as illustrated in Fig. 4.11. In particular, the event rate attributed

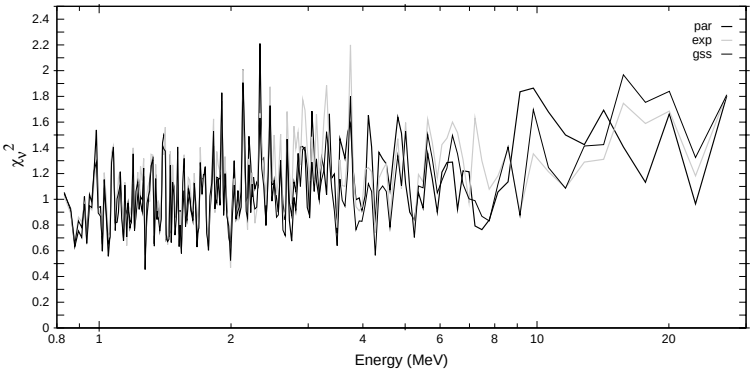

Figure 4.12: *A comparison of the χ^2_ν-values obtained in ToF fits with the three ToF models as a function of energy.*

to the ToF forward-peak is systematically different for different ToF models. This systematic is of great importance for the CDG analysis because it is a major source of uncertainty in the final result (see Sec. 6.3.2), and was therefore studied in detail, together with the different statistical qualities of the three ToF models.

The statistical quality of the three ToF models, i.e. their ability to describe the ToF distribution, was assessed by comparing the χ^2_ν-values obtained for the models in fits of ToF spectra as a function of energy. It is important to note that the level of the ToF data used in these studies has significant influence on the quality of the ToF fits, in particular at energies above about 9 MeV, where fits to $\mathrm{ToF_{III}}$ data are significantly better than fits to $\mathrm{ToF_{II}}$ data. At these high energies acceptable χ^2_ν-values can only be obtained for ToF data of at least level III. Also, the ToF range over which the ToF distribution is fitted affects the χ^2_ν-values obtained in the fits. The ToF range over which acceptable χ^2_ν-values can be obtained for the parabolic model is significantly narrower than the fit range of the other two models, especially at the highest energies (see bottom panels of Fig. 4.11). Below and above 9 MeV the ToF ranges for the fits with the exponential and the Gaussian model are $\sim 106 - 147$ ch and $\sim 105 - 143$ ch, respectively, while the fits with the parabolic model have to be restricted to ranges of $\sim 106 - 140$ ch and $\sim 109 - 134$ ch.

A comparison of the χ^2_ν-values obtained in ToF fits with the three models as a function of energy is depicted in Fig. 4.12. Clearly, the χ^2_ν-values are very similar at all energies, hence none of the three ToF models is statistically superior to any of the other models. At energies above about 9 MeV, however, the parabolic model is nevertheless considered inferior to the other two models because it cannot follow the ToF distribution over such a wide ToF range as the other two models, as can be seen in the lower left panel of Fig. 4.11. Therefore the assessment of the systematic error of the final result on the CDG intensity due to the uncertainty in the ToF fit was based on comparisons of all three ToF models below 9 MeV, and of the exponential and Gaussian models at higher energies (see Sec. 6.3.2). For any energy range and any model the absolue χ^2_ν-value increases with the number of events contained in the fitted ToF distribution, which is expected since the ToF models are only approximations to the unknown shape of the ToF distribution. Nevertheless, all three models provide acceptable approximations to the ToF spectrum. The small trend for the values of χ^2_ν

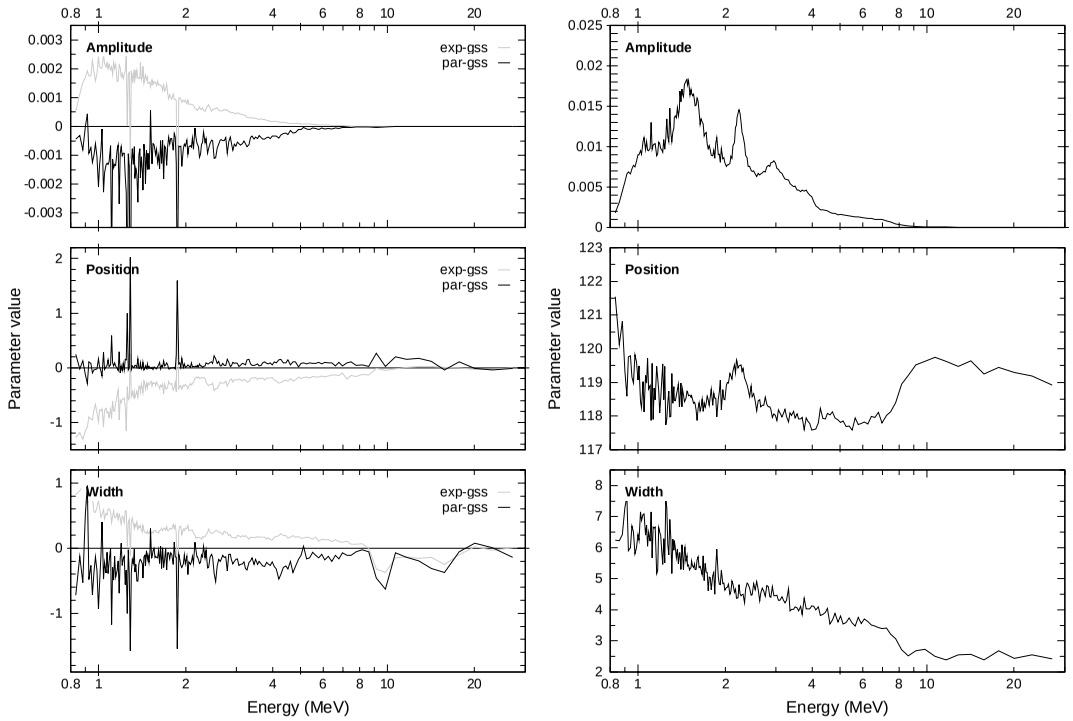

Figure 4.13: **Left panel**: *The differences in the ToF forward-peak parameter values for the three ToF models obtained from ToF fits as a function of energy.* **Right panel**: *The variation of the ToF forward-peak parameter values from ToF fits as a function of energy. Depicted are the averages of the values obtained with the three models.*
Note: The unit of the forward-peak amplitude is [cnts/(sec MeV)], the unit of width and position is [ToF ch].

to increase with energy is most likely due to the fact that the increasing instrumental ToF resolution (see next section) reveals deficiencies of the ToF models more easily with increasing energy.

A comparison of the best-fit values of the forward-peak parameters obtained for the three ToF models from ToF fits as a function of energy in terms of their differences is given in the left panels of Fig. 4.13. Qualitatively, the differences in the ToF forward-peak parameters result from the different curvatures and slopes of the functions used to approximate the ToF continuum: the normalization and the width of the Gaussian approximating the ToF forward-peak increase with increasing curvature of the approximation to the ToF background, while the position of the ToF forward-peak Gaussian decreases with increasing background curvature. In general, below about 9 MeV the exponential and the parabolic model provide the most and least curved approximations to the ToF continuum, while above about 9 MeV these two extremes are provided by the Gaussian and parabolic model (see Fig. 4.11). Consequently, below about 9 MeV the normalization and the width of the ToF forward-peak Gaussian are largest and smallest for the exponential and the parabolic model, with their difference exceeding 1 channel at the lowest energies. The Gaussian model to a good approximation repre-

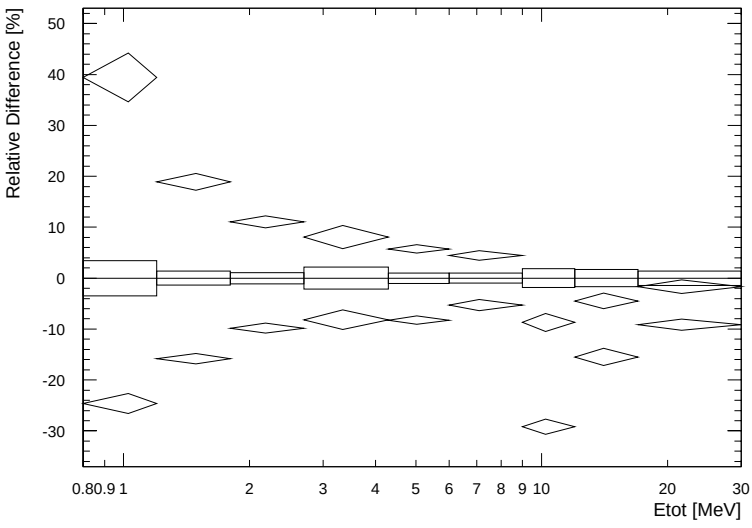

Figure 4.14: *The relative differences in the ToF forward-peak event rate as obtained from the three ToF models for the data used in the final CDG analysis. The differences are normalized to the Gaussian model forward-peak event rate (boxes). The exponential and the parabolic model are depicted with thick and thin diamonds, respectively. (Compare to the top and bottom left panels of Fig. 4.13.)*

sents an "average model" below about 9 MeV. At higher energies the normalization and width of the forward-peak are largest and smallest for the Gaussian and the parabolic model. As far as the position of the ToF forward-peak is concerned, the parabolic and the Gaussian model are very similar, while the exponential model yields a position at lower ToF values for energies below about 9 MeV.

Inevitably, these systematic differences in the ToF forward-peak parameters translate into systematic differences in the forward-peak event rate. The relative differences in the ToF forward-peak event rate as obtained from the three ToF models for the data used in the final CDG analysis (see Sec. 6.2) is depicted in Fig. 4.14. As expected from the differences in the parameter values (see Fig. 4.13), the models yield significantly different forward-peak event rates below 4.3 MeV, with the exponential model and the parabolic model yielding the highest and lowest rates. Between 4.3 MeV and 9 MeV the results are quite consistent. In the transition region of the ToF spectrum around 9 MeV the differences become once again siginificant and then decrease with increasing energy. The general decrease of the systematic differences with increasing energy follows from the decrease of the forward-peak width. It has to be noted that the differences below 4.3 MeV also depend on the activity level of the instrumental lines. The differences decrease with increasing activity, because the forward-peak is the more pronounced the higher the activity. The systematic differences shown in Fig. 4.14 were derived from data with the lowest activity levels used to determine the CDG intensity below 4.3 MeV (see Sec. 6.2), hence the systematic differences are at their maximum. The implications of these ToF fitting systematics for the uncertainty in the CDG intensity values are discussed in Sec. 6.3.2.

4.3.3 Variations of the ToF Distribution in Energy

Valuable insight into the multitude of instrumental-background components present in the ToF forward-peak region can be gained from studying the ToF distribution as a function of energy. As an example, the variation of the average parameters of the ToF forward-peak Gaussian with energy obtained in fits with the three ToF model is shown in the right panels of Fig. 4.13.

The Gaussian amplitude is a measure of the event rate contained in the ToF forward-peak and hence closely resembles the ToF forward-peak energy spectrum, which is discussed below.

The position of the ToF forward-peak deviates considerably from its nominal position at ~ 120 channels over large portions of the energy spectrum. Specifically, the forward-peak positions shifts down to ~ 118.5 chnnels between 1 MeV and 2.2 MeV, and down to ~ 118 chnnelsw between 2.2 MeV and 9 MeV. At the lowest energies and above about 9 MeV the forward-peak position is close to the expected value. The ToF corrections described in Sec. 3.7 were designed for single forward-scattering photons only, hence the shifts indicate the presence of strong instrumental-background components in the ToF forward-peak in at least some parts of the energy spectrum. Of all background event types discussed in Sec. 4.1.3, only types **A** and **C** are expected to contribute mainly to the ToF forward-peak. Type **A** events, caused by double-scattering single photons, do not result in a ToF forward-peak shift, since they peak at ToF channel 120. This is best illustrated by the instrumental 2.22 MeV line from thermal neutron capture on hydrogen in the D1 scintillators (see Sec. 4.4.2.1). At the line energy, this background component is strong enough to move the ToF forward-peak back to its nominal position, despite the presence of other background components which are mostly due to type **C** events. It is suggestive that these multiple-photon events, which peak slightly below ToF 120 ch, seem to be the dominant source of general instrumental forward-peak background in the nuclear γ-ray line regime below about 9 MeV (except around 2.2 MeV, as explained above). At the lowest energies and above about 9 MeV the forward-peak is either free of instrumental background, or the instrumental background is mostly due to type **A** events.

The width of the ToF forward peak decreases steadily with increasing energy up to about 7 MeV, then drops more steeply between $\sim 7-9$ MeV, above which it remains at a roughly constant value. Part of this variation is due to the increasing ToF resolution with energy: as was pointed out in Sec. 3.7, the width of the ToF distribution of the intense atmospheric γ-radiation decreases with increasing energy. Furthermore, the instrumental background causes an additional broadening of the ToF forward-peak, indicated by the drop in the width between $\sim 7-9$ MeV. In particular, an additional broadening of the ToF forward-peak is expected in the $\sim 1-9$ MeV range if type **C** events are the dominant background component, since the forward peak would then be the sum of a component peaking at ToF ~ 120 ch and a component peaking slightly below. This is supported by the slight additional decrease of the forward-peak width

around 2.2 MeV.

The energy spectrum of the ToF forward-peak, derived by integrating the best-fit result for the Gaussian approximation over a ToF range of 107–130 ch, is depicted for the Gaussian model in the top panels of Fig. 4.15 (compare with the energy variation of the peak amplitude shown in the top right panels of Fig. 4.13). Three distinct energy ranges are apparent, namely $\sim 0.8 - 4.3$ MeV, $\sim 4.3 - 9$ MeV, and $\sim 9 - 30$ MeV. Below about 9 MeV the spectrum exhibits characteristics of a nuclear continuum on top of which, below about 4 MeV, there is evidence for a component due to nuclear-line emission. Above about 9 MeV, beyond the nuclear regime, another continuum component appears, which is dominated at lower energies by the nuclear components.

The line-like structures in the ToF forward-peak spectrum below about 4 MeV suggest strong contributions from the decay or cascading de-excitation of a limited number of activated isotopes through type **A** and **C** events[21], such as ^{2}D and ^{40}K (type **A** at 2.2 MeV and 1.4 MeV, respectively, see Secs. 4.4.2.1 and 4.4.2.3) or ^{22}Na and ^{24}Na (type **C**, contributing to the line features at 1.4 MeV and at ~ 2.8 MeV and ~ 3.9 MeV, respectively, see Secs. 4.4.2.4 and 4.4.2.2). Taking into account the shift of the forward-peak position at these energies, type **C** events are expected to dominate the contribution of type **A** events at these energies, with the exception of the 2.2 MeV line. Long-lived isotopes contributing to the line structure could be activated by neutrons as well as protons. Events from isotopes that decay promptly (see Sec. 4.1.1), however, must have been induced by neutrons, otherwise they would not have evaded the veto system.

Underlying this line component is a broad continuum component that dominates the ToF forward-peak spectrum above about 4 MeV until its rapid decline around 9 MeV. This sudden decline at an energy coinciding with the highest energies of the γ-ray line regime, together with the shift of the forward-peak position at these energies, suggests that this component is due to cascading de-excitations of excited nuclei (type **C** events). In general, these de-excitations occur on time scales much shorter than a nanosecond and therefore this component is expected to vary with the incident cosmic-ray intensity (see Sec. 4.3.5). In order to contribute to the ToF forward-peak, the de-excitations must have occurred in the material of the D1 detector (type **C** events), which due to the prompt nature of the cascading photon emission must have been induced by neutrons. Proton-induced prompt cascades are rejected by the veto system.

Beyond the nuclear regime, above about 9 MeV, the nature of the ToF forward-peak background is different. The position of the forward-peak suggests that now type **A** events dominate, presumably electromagnetic in origin (Ryan *et al.* 1997). For

[21] An astrophysical origin of the line structure below about 4 MeV can be excluded. In order to be of astrophysical origin, the line emission had to be persistent and from an extended region of the sky, since in this study many observation periods have been combined covering the regions at high galactic latitudes. Such persistent and extended γ-ray emission, however, has only been observed from the galactic plane.

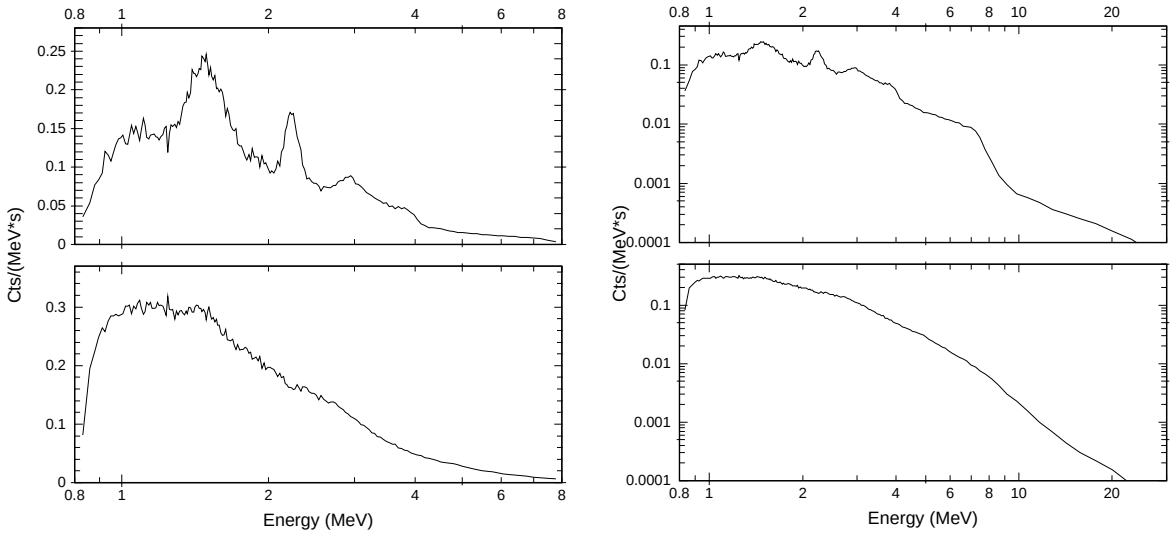

Figure 4.15: *The ToF forward-peak (upper panels) and continuum background (lower panels) energy spectra. The left panels depict the energy spectra below 8 MeV in linear scaling, the right panels give the overall spectra in logarithmic scaling.*

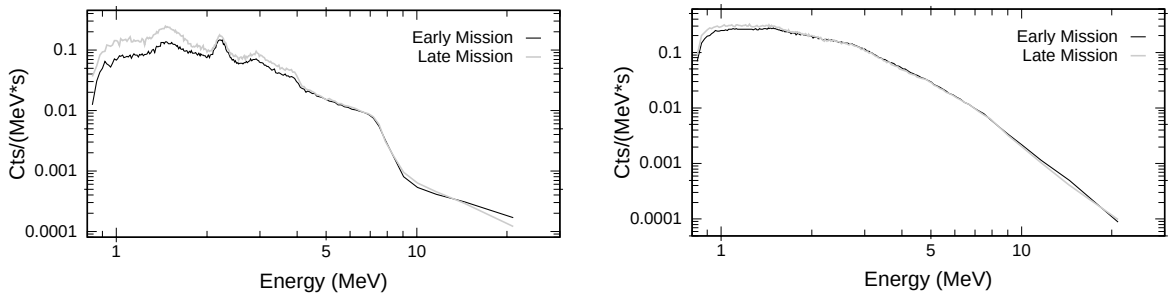

Figure 4.16: *An illustration of the long-term variation of the energy spectra of the ToF forward-peak (left) and the ToF continuum-background (right).*

example, events may arise from prompt processes such as emission of bremsstrahlung by electrons in the material outside the veto domes, or an electromagnetic cascade initiated in the D1 detector by very energetic photons or neutral pions from a nuclear cascade (that occurred outside the anti-coincidence subsystem of D1 detector if proton-induced). This electromagnetic component should also be present below 9 MeV, except that it is dominated at these energies by the much more intense nuclear components.

Finally, the energy spectrum of the ToF continuum-background, again derived from an integration over the ToF range 107–130 ch, is discussed briefly. As an example, the ToF background spectrum obtained with the Gaussian model is depicted in the bottom panels of Fig. 4.15. In marked contrast to the forward-peak spectrum (see top panels), the background spectrum is very smooth. There is at best weak evidence for the presence of line emission, which may also be an artifact of the ToF fitting. Also, there are no sudden declines or transitions around 4 MeV and 9 MeV, which would indicate significant contributions from nuclear components, as is the case for the forward-peak.

It follows that the type **D**, **E**, and **F** events causing the ToF continuum are mostly due to processes such as bremsstrahlung from cosmic-ray electrons, or photons from electromagnetic cascades initiated by high-energy photons or pions, or photons directly produced in nuclear cascades. All these interactions have to take place outside the veto domes to avoid the rejection of the background events.

To conclude, the ToF continuum-background differs from the ToF forward-peak background not only in the geometrical origin of the events, but also in the dominating physical processes causing the events since prompt proton-induced photons are no longer vetoed. The processes dominating the ToF continuum are prompt, hence it is expected to vary strongly with the instantaneous incident cosmic-ray intensity (see Sec. 4.3.5).

4.3.4 Variations of the ToF Distribution with Time

The long-term variation of the ToF forward-peak and ToF continuum-background is illustrated in Fig. 4.16 (see also Fig. 4.19). The energy spectra of both ToF components from early in the mission (1991 – 1994) are compared to the respective spectra from later in the mission (1992 – 1996). On average, the activation of radioactive isotopes during SAA passages is expected to be stronger later in the mission, in particular after the first reboost at the end of 1993 (see Fig. 4.4), because of the increase in the average orbit altitude and the approaching solar minimum (see Fig. 4.1). Consequently, the activity of long-lived isotopes is expected to be higher later in the mission. This picture is supported by the long-term variations depicted in Fig. 4.16. The event rate in the line structures of the ToF forward-peak increased significantly from the beginning of the mission[22], suggesting that these line structures are mostly due to long-lived isotopes, while the prompt nuclear and electromagnetic forward-peak components are unaffected. Similarly, there is no variation in the ToF background, except for a small increase in the event rate below about 2 MeV, indicating that the ToF background is dominated by prompt or short-lived emission.

4.3.5 Variations of the ToF Distribution with Veto Rate

Studying the ToF distribution as a function of veto rate is a powerful diagnostic for identifying prompt instrumental-background components. The veto rate and the incident cosmic-ray intensity are expected to be linearly correlated to a good approximation (see Sec. 3.10), hence prompt components of the instrumental background are expected to be linearly correlated to the veto rate. The variations of the six parameters of the

[22]The activation of long-lived isotopes and the time history of their activity will be addressed in detail in Sec. 4.5.

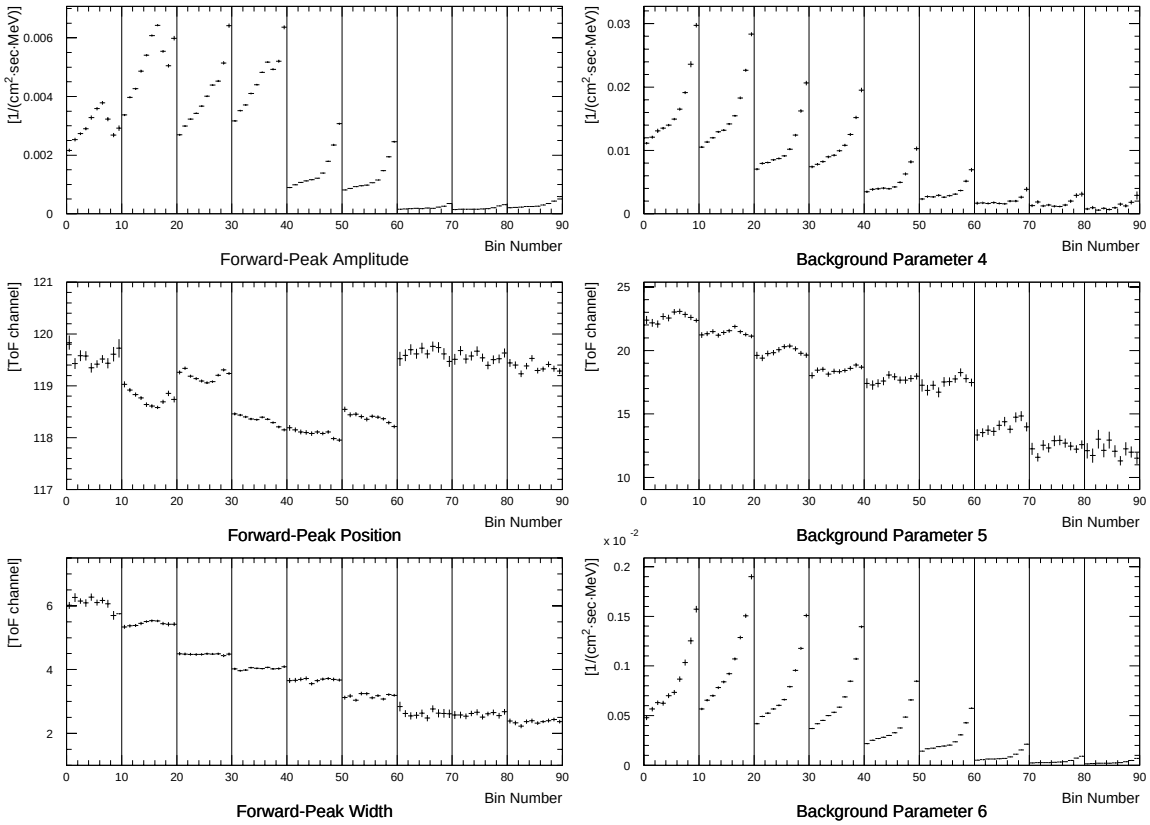

Figure 4.17: *The variation of the six parameters of the Gaussian model with veto rate in each of the nine energy ranges used in the CDG analysis. Each energy range, separated by the vertical lines, was studied in ten veto-rate intervals. The bins are numbered as follows: bins 1–10 correspond to the 10 veto-rate intervals for energy interval 1, bins 11–20 correspond to the 10 veto-rate intervals for energy interval 2, and so on. Note that the veto-rate binning is not equidistant, i.e. the individual widths of the veto-rate intervals are different (compare Fig. 4.18).*

Gaussian model with veto rate in the nine energy ranges used in the CDG analysis[23] are summarized in Fig. 4.17.

In general, the normalization of the ToF forward-peak increases with increasing veto rate, indicating that a large fraction of the instrumental background is due to prompt processes. At the lowest energies, below 4.3 MeV and in particular below 1.8 MeV, however, the background in the forward-peak is strongly influenced by long-lived components that do not linearly follow the veto rate. The veto-rate dependence of these long-lived components and its implications for the CDG analysis will be discussed in detail in Sec. 4.6. The position of the ToF forward-peak has a tendency to decrease with increasing veto rate between $\sim 1.8 - 9$ MeV, confirming that the bulk of the

[23]The energy ranges used in the CDG analysis are (see Sec. 5.1): 0.8–1.2 MeV, 1.2–1.8 MeV, 1.8–2.7 MeV, 2.7–4.3 MeV, 4.3–6 MeV, 6–9 MeV, 9–12 MeV, 12–17 MeV, and 17–30 MeV.

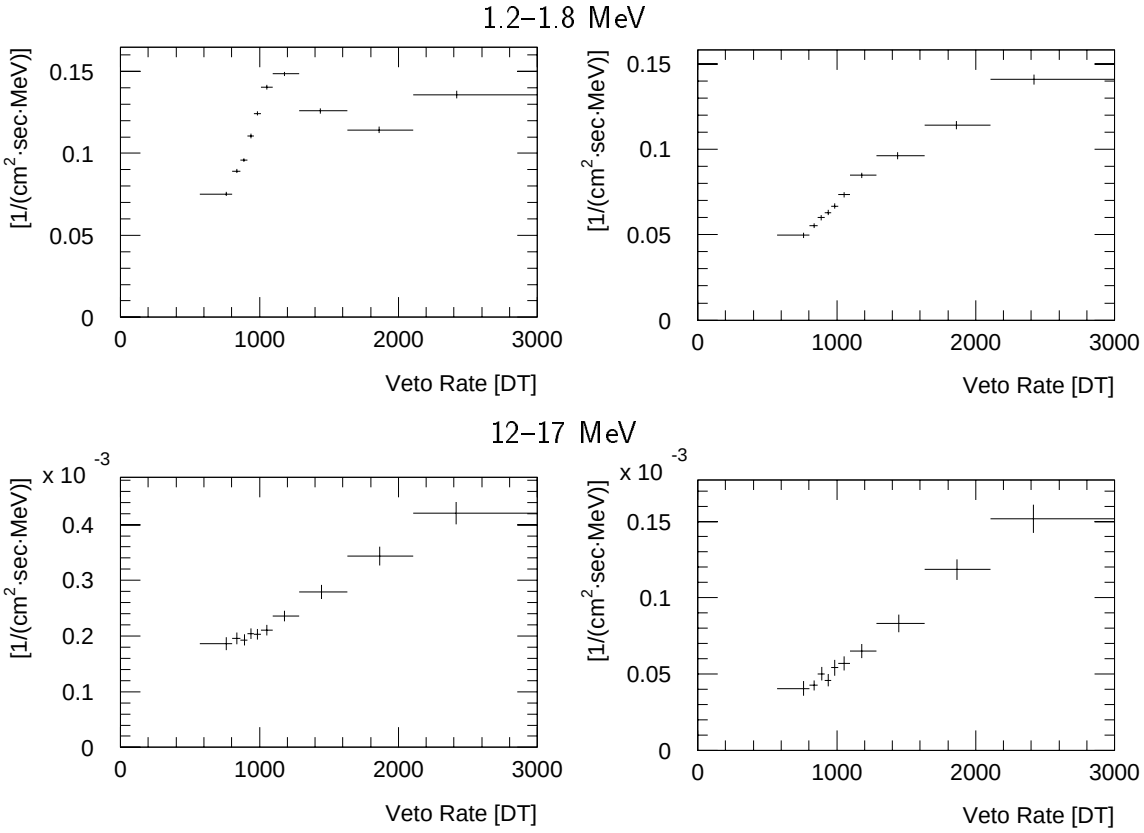

Figure 4.18: *The variation of the ToF forward-peak (left panels) and the ToF continuum-background (right panels) event rate with veto rate at 1.2–1.8 MeV (top) and 12–17 MeV.*

multiple-photon (type **C**) events dominating the forward-peak background at these energies are indeed prompt. Below 1.8 MeV and above 9 MeV there is little variation of the forward-peak position with veto rate, as expected for type **A** background events. The width of the ToF forward-peak does not exhibit any obvious trend in veto rate.

The normalization parameters of the ToF continuum, p_4 and p_6, exhibit a strong variation with veto rate in all energy ranges[24], confirming that the mechanisms producing the bulk of the ToF continuum are indeed prompt. Similar to the width of the forward-peak, the "shape" of the ToF continuum, which is mostly determined by the background parameter p_5, does not exhibit any significant variation with veto rate.

To better illustrate the variation of the ToF distribution with veto rate at different energies, the ToF forward-peak and continuum-background event rates in the energy ranges 1.2–1.8 MeV and 12–17 MeV are depicted in the top and bottom panels of Fig. 4.18, respectively. The 1.2–1.8 MeV ToF forward-peak rate exhibits a pronounced bump-like feature due to long-lived background components, the so-called veto-rate bump, as is explained in detail in Sec. 4.6. At the same energy the ToF

[24]Note that the width of the bins in veto rate is not equidistant in Fig. 4.17, therefore the variation is not linear as in Fig. 4.18.

continuum-background varies more smoothly with veto rate, indicating that prompt background processes dominate. Above 4.3 MeV no significant long-lived background components are present, exemplified by the variation of the 12–17 MeV forward-peak and continuum-background event rates, which are linear to a good approximation.

4.4 Instrumental-Background Energy Signatures

4.4.1 Overview

The majority of the COMPTEL instrumental-background events are due to γ-ray photons whose spectral distribution is either continuous or consists of a large number of individual γ-ray lines blending into a quasi-continuum. There are, however, a few processes that lead to distinguishable spectral features and lines, as can be seen in Fig. 4.19 illustrating the low-energy parts of the spectral distributions in $E_{\rm tot}$, E_2 and E_1. The spectra have been summed as a function of time for standard CDG selections (see Sec. 4.2.3) with an additional ToF 115–130 ch cut, hence the spectra represent the energy distribution in the ToF forward-peak region. The dramatic increase of the event rate with time is, as demonstrated in Secs. 4.3.3 and 4.3.4, due to long-lived background in the ToF forward-peak.

The diagnostic power of the three spectra for the identification of the isotopes responsible for the spectral features is very different. The $E_{\rm tot}$ and E_2 distributions exhibit photopeaks, which are indispensable for the determination of the line energies. The E_1 distribution lacks such prominent features, exhibiting only Compton edges. Therefore the investigation of the instrumental-line background is mostly based on the $E_{\rm tot}$ and E_2 distributions, which are particularly useful for the identification of isotopes that give rise to single-photon (type **A**) or multiple-photon (type **C**) events, respectively. In addition to the spectral characteristics of an individual isotope, the variation of its activity with veto rate (see Sec. 4.6) or time (see Sec. 4.5) proved to be another extremely useful characteristic for separating prompt from long-lived components and for roughly distinguishing different half-lifes.

4.4.2 Isotopes Identified in the Instrumental-Line Background

To date, eight different isotopes have been identified in the instrumental-line background, as described in the following sections. The isotopes, their half-lifes, decay modes, and principal production channels are summarized in Table 4.1. Identification of these isotopes was achieved in an iterative process, starting from the most prominent lines in $E_{\rm tot}$ and E_2. Viable isotope identifications were required to account self-consistently for spectral features in $E_{\rm tot}$ and E_2 as well as for their variation with veto rate and time. The telescope response to individual isotopes was modelled

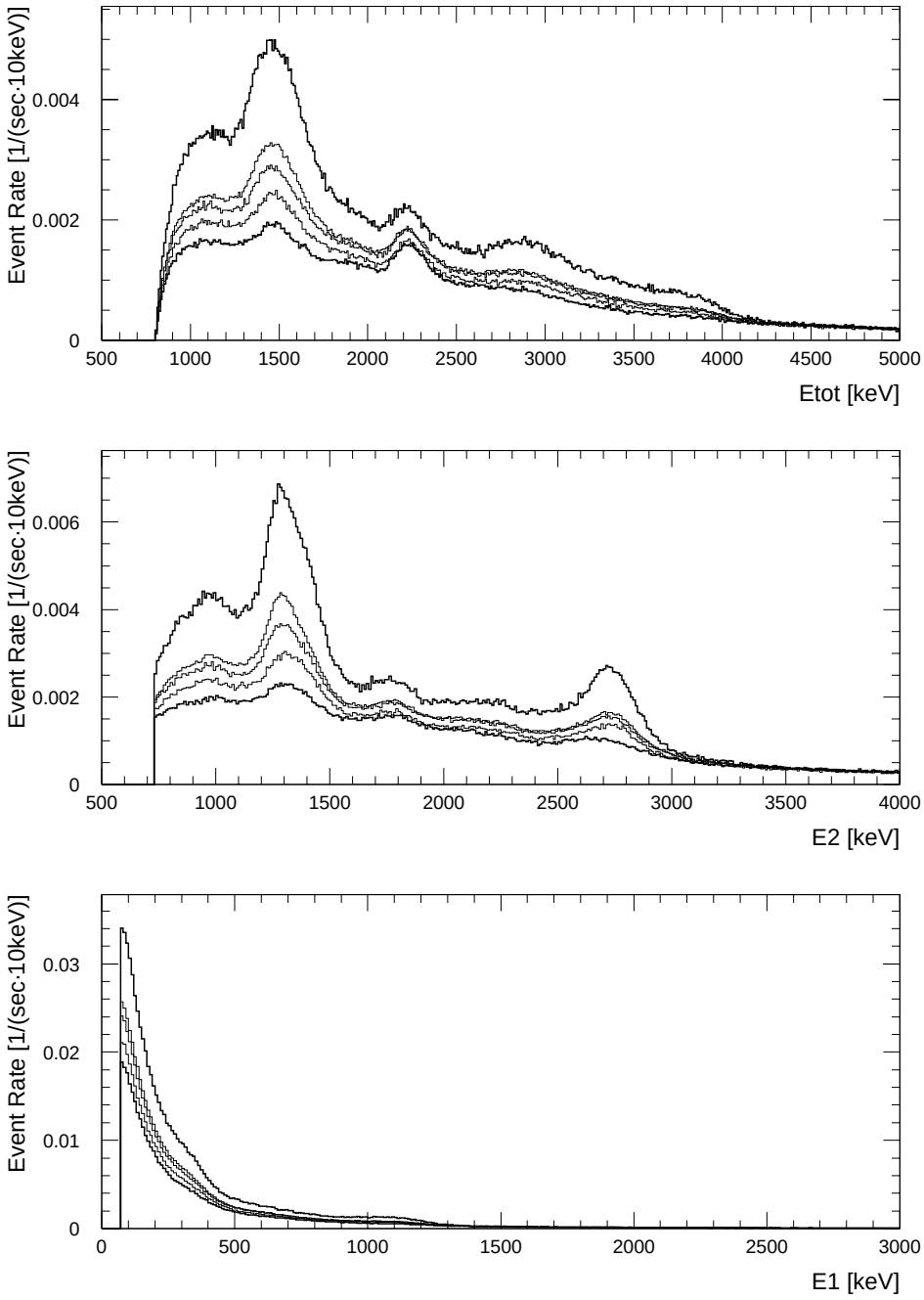

Figure 4.19: *An Illustration of the spectral distributions in $E_{\rm tot}$, E_2, and E_1 as a function of time. The two spectra plotted with thick solid lines represent the times of highest (after the second reboost in May 1997) and lowest (from the beginning of the mission until the first reboost, May 1991 – Nov. 1993) activity due to long-lived background (see Sec. 4.5). The three intermediate spectra cover the time periods Nov. 1993 – Oct. 1994, Oct. 1994 – Oct. 1995, and Oct. 1995 – May 1997, ordered according to increasing event rate.*

Isotope	Half-Life	Decay Modes and Photon Energies [MeV]	Main Production Channels
^{2}D	prompt	2.224	^{1}H(n_{ther},γ)
^{22}Na	2.6 y	β^+ (91%): 0.511, 1.275 EC (9%) : 1.275	^{27}Al(p,3p3n), Si(p,4pxn)
^{24}Na	14.96 h	β^-: 1.37, 2.75	^{27}Al(n,α), ^{27}Al(p,3pn)
^{28}Al	2.2 min	β^-: 1.779	^{27}Al(n_{ther},γ)
^{40}K	1.28×10^{9} y	EC (10.7%): 1.461	natural
^{52}Mn	5.6 d	EC (64%): 0.744, 0.935, 1.434 β^+ (27%): 0.511, 0.744, 0.935, 1.434	Fe(p,x), Cr(p,x), Ni(p,x)
^{57}Ni	35.6 h	β^+ (35%): 0.511, 1.377 EC (30%): 1.377	Ni(p,x), Cu(p,x)
^{208}Tl	1.4×10^{10} y (^{232}Th)	β^- (50%): 0.583, 2.614 β^- (25%): 0.511, 0.583, 2.614	natural

Table 4.1: *A summary of the isotopes identified in the COMPTEL instrumental-line background. For simplicity, only the photon energies of the most frequent decay modes are listed. If β-decays are involved, the β-particles have been included in the response simulations.*

through Monte Carlo simulations. Subtraction of the modelled contributions of identified isotopes then revealed weaker and less pronounced spectral features in $E_{\rm tot}$ and E_2.

The following description of the isotopes identified so far loosely follows the historic development of this subject. The identified isotopes can account for the major instrumental-background lines, as will be discussed in Sec. 5.3. Some minor spectral features still remain unidentified. Their effect on the CDG spectrum, however, can be strongly reduced, as demonstrated in Chaper 5. The final procedure for determining the event rate due to individual isotopes, which is based on the results presented in the following sections, will be explained in detail in Sec. 5.3.

4.4.2.1 The Isotope ^{2}D

The presence of a pronounced line feature at 2.2 MeV in $E_{\rm tot}$ due to thermal-neutron capture on hydrogen was expected and studied in detail by Weidenspointner (1994). The liquid scintillator NE 213A in the D1 detector modules consists of 9.2% hydrogen and 90.8% carbon, making it a very efficient moderator for incident atmospheric and secondary neutrons[25]. Once slowed down to thermal energies of $\sim$ 0.025 eV the

[25]Neutron moderation and capture also occurs in other hydrogen-rich components of the instrument, in particular in the plastic scintillator of the veto domes and in the hydrazine propellant tanks below

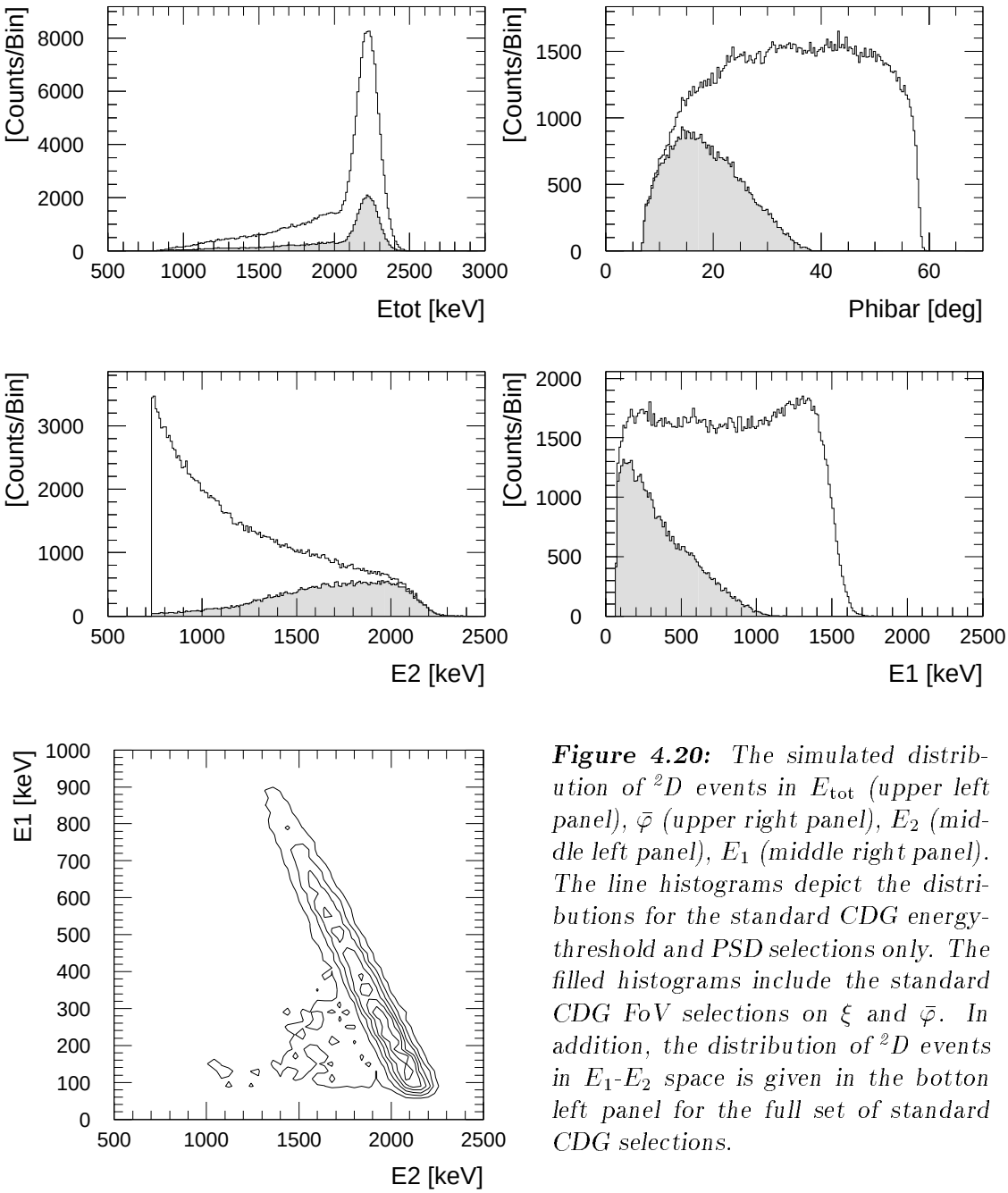

Figure 4.20: *The simulated distribution of ^{2}D events in $E_{\rm tot}$ (upper left panel), $\bar{\varphi}$ (upper right panel), E_2 (middle left panel), E_1 (middle right panel). The line histograms depict the distributions for the standard CDG energy-threshold and PSD selections only. The filled histograms include the standard CDG FoV selections on ξ and $\bar{\varphi}$. In addition, the distribution of ^{2}D events in E_1-E_2 space is given in the botton left panel for the full set of standard CDG selections.*

neutrons are captured by hydrogen[26] ($\sigma_{\rm abs,H} = 0.33$ b), with the resulting deuterium

the satellite platform, but the contributions of these components to the observed 2.2 MeV line is expected to be minor (Weidenspointner 1994). The veto domes are too thin for efficient thermalization of incident neutrons and 2.2 MeV photons from the hydrazine tanks are eliminated by selections on $\bar{\varphi}$ and the D2 energy deposit.

[26]The D1 detectors are kept at a temperature of about 20° C. At low energies the cross-section for neutron absorption is inversely proportional to the neutron velocity, provided that there are no

nucleus releasing its binding energy in form of a single 2.224 MeV photon (Firestone *et al.* 1996).

$$n_{ther.} + {}^1H \longrightarrow {}^2D + \gamma(2.224\ MeV) \tag{4.9}$$

The instrumental 2.22 MeV photons from the D1 scintillators therefore are bona fide type **A** events, which are confined in the ToF forward peak. The average absorption time in the D1 scintillator for an incident neutron is about 3×10^{-4} sec (Weidenspointner 1994), hence the instrumental 2.2 MeV line is a prompt background component. In principal, the initial scatterings of the incident neutrons are identifiable by their PSD values, but because of the $\sim 3\times10^{-4}$ sec delay between the first neutron scatterings and the final emission of the 2.22 MeV photon, which is much longer than the coincidence window of $\sim$ 40 nsec (see Sec. 3.3), these PSD values cannot be used to reject these background events.

The distribution of instrumental 2.22 MeV photons in E_{tot}, $\bar{\varphi}$, E_2, and E_1, as determined in Monte Carlo simulations[27], is depicted in Fig. 4.20. The line histograms give the distributions for the standard CDG energy-threshold and PSD selections only, while the filled histograms include the standard CDG FoV selections on ξ and $\bar{\varphi}$ (see Secs. 4.2.1 and 4.2.3). In addition, the distribution of ^{2}D events in E_1-E_2 space is given in the botton left panel for the full set of standard CDG selections. As is characteristic for type **A** events, the E_{tot}-distribution exhibits a photopeak, while the distributions in E_2 and E_1 are continuous. Also, in E_1-E_2 space the event distribution follows the diagonal $E_1 + E_2 = E_\gamma = 2.22$ MeV. Because the 2.22 MeV photons are emitted isotropically within the D1 scintillators, many of these photons must scatter through large angles. The line activity can therefore effectively be reduced by setting upper limits on $\bar{\varphi}$ or lower limits on the D2 energy deposit.

The orbital variation of the 2.2 MeV line event rate to a good approximation can be modelled by an exponential (or power-law) dependence on vertical cut-off rigidity, confirming the prompt origin of the line, and a linear dependence on `GCEL` (Weidenspointner 1994, Weidenspointner *et al.* 1996a). This variation is very similar to what has been found for the fast-neutron flux ($E_n > 12.8$ MeV) in the D1 detector (Morris *et al.* 1995), implying that the bulk of the neutrons producing ^{2}D are of atmospheric origin, with secondary neutrons produced in the spacecraft being of minor importance (see Sec. 4.1).

As expected due to its prompt nature, the 2.2 MeV line exhibits a linear variation with veto rate, which will be further examined in Sec. 5.5.2.

---

resonances, therefore absorption can be assumed to occur at thermal energies only (Beckurts and Wirts 1964). In comparison, thermal-neutron capture on carbon, which has an absorption cross-section of $\sigma_{abs,C} = 0.5$ mb, can be neglected.

[27] In the simulations, the 2.22 MeV photons were started homogeneously from the volume of the liquid scintillator in the D1 modules, their starting directions being drawn from an isotropic distribution.

4.4.2.2 The Isotope ^{24}Na

Just as the single-photon emission by ^{2}D discussed above exemplifies the characteristics of type **A** events, so does the two-photon cascade emitted upon the decay of ^{24}Na exemplify the characteristics of type **C** events and is therefore discussed in fair detail in the following. The presence of ^{24}Na in the instrumental-line background was recognized very early in the mission, based on the line features at $\sim$ 1.3 MeV and $\sim$ 2.7 MeV in E_2 (see Fig. 4.19). The decay scheme of ^{24}Na is depicted in Fig. 4.21. The isotope β^--decays with a half-life of $\sim$ 15 h into an excited state of ^{24}Mg. In 99.9% of all cases a ^{24}Mg state is populated which further decays by successively emitting two photons with energies of 1.37 MeV and 2.75 MeV on the time scale of a picosecond (in this decay channel the end-point energy of the β^--particle is about 1.39 MeV). Compared to the coincidence window of $\sim$ 40 nsec the two cascade photons are emitted simultaneously and can therefore trigger a valid event.

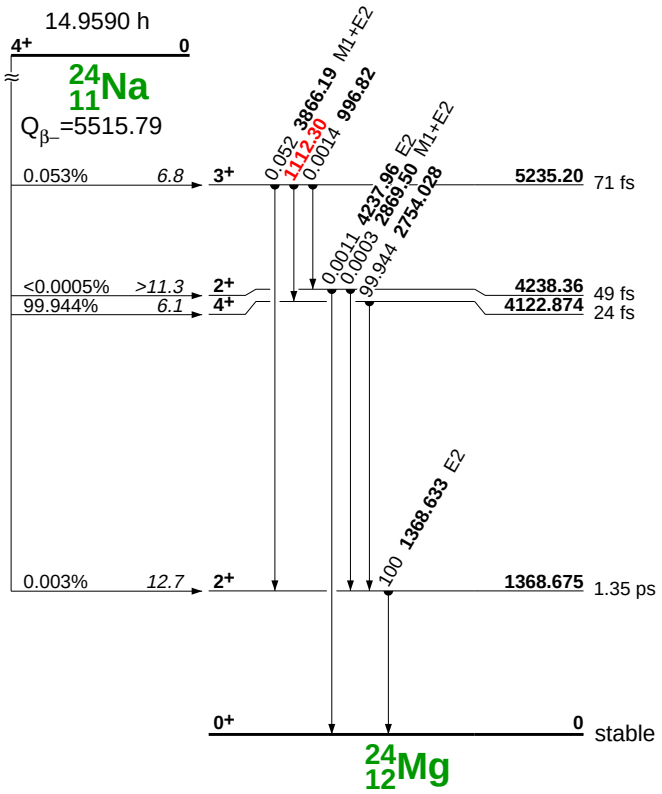

Figure 4.21: *The decay scheme of the isotope ^{24}Na according to Firestone* et al. *(1996).*

The simulated[28] distribution of ^{24}Na events in selected event parameters, taking into account the β^--particle, is depicted in Fig. 4.22. The most important characteristic of ^{24}Na, and any other isotope emitting multiple photons, is the E_2 distribution, which exhibits photopeaks at the line energies. In E_1 only the corresponding Compton edges are present, which are much harder to discern. The $E_{\rm tot}$ spectrum is more complex. It exhibits line features just above the individual photon energies, which result from the absorption of one photon in D2 with the other photon scattering in D1 with an energy deposit near the D1 threshold. In addition, there is a feature at about 3.9 MeV

[28]The simulations cover the ^{24}Na decays in the aluminium in the D1 detector and in the upper half of the instrument structure (^{24}Na decays in the D2 detector and the lower half of the instrument structure only contribute to the ToF backward-peak). The starting directions of the two photons and of the β^--particle emitted in each decay are drawn from an isotropic distributon.

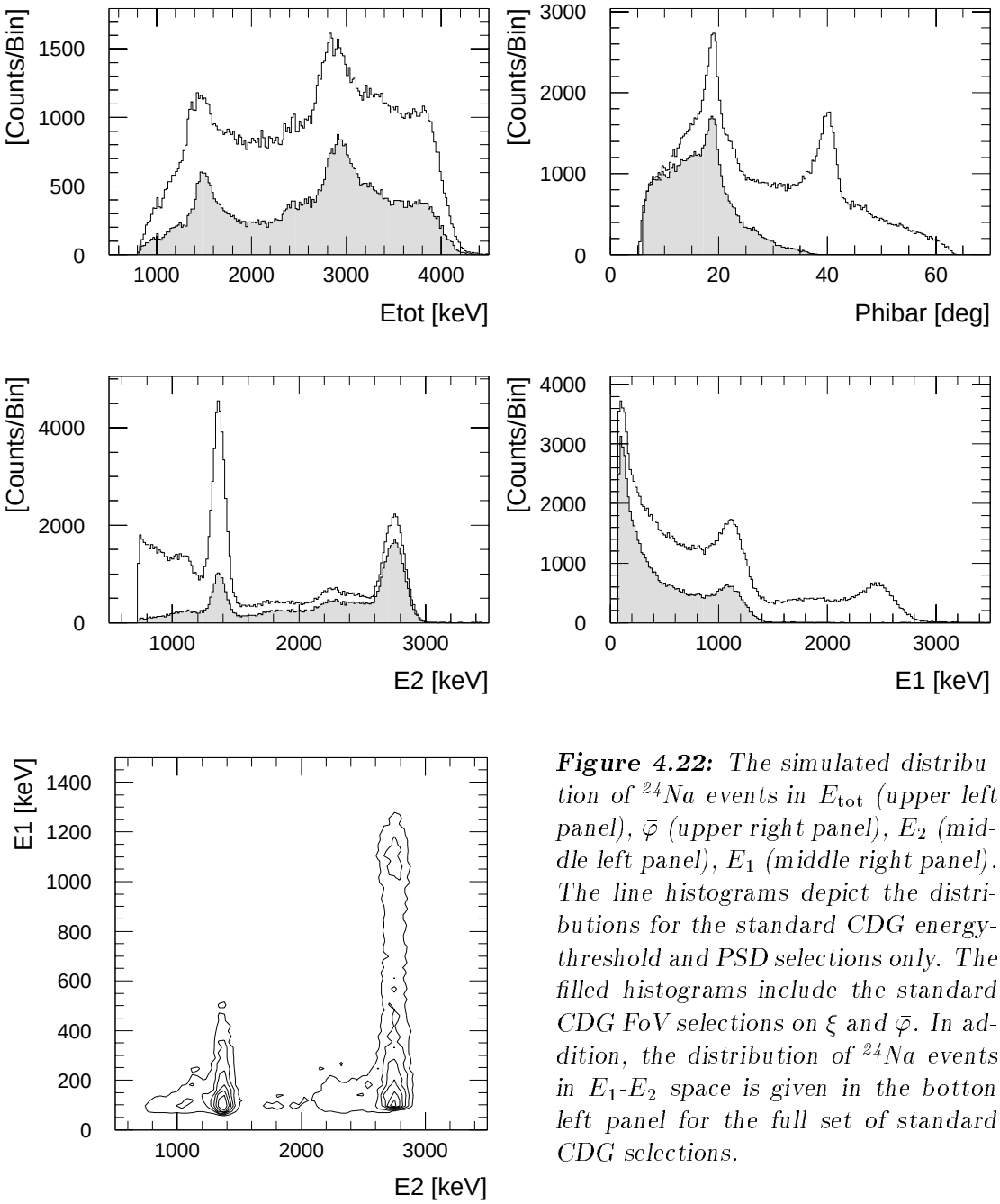

Figure 4.22: *The simulated distribution of ^{24}Na events in $E_{\rm tot}$ (upper left panel), $\bar{\varphi}$ (upper right panel), E_2 (middle left panel), E_1 (middle right panel). The line histograms depict the distributions for the standard CDG energy-threshold and PSD selections only. The filled histograms include the standard CDG FoV selections on ξ and $\bar{\varphi}$. In addition, the distribution of ^{24}Na events in E_1-E_2 space is given in the botton left panel for the full set of standard CDG selections.*

in $E_{\rm tot}$, which is due to the absorption of one photon in D2, while the other photon deposits energy at the Compton edge[29]. The $\bar{\varphi}$-values corresponding to this "sum

[29]This feature is the COMPTEL analogon to a sum peak in standard spectroscopy. The energy of the feature is the sum-peak energy minus $m_0c^2/2$, since the Compton-edge energy is about $m_0c^2/2$ less than the photopeak energy (see Eq. 3.2). The energy of the "sum-peak" feature then is 2.75 MeV + 1.37 MeV $- m_0c^2/2 \approx 3.9$ MeV.

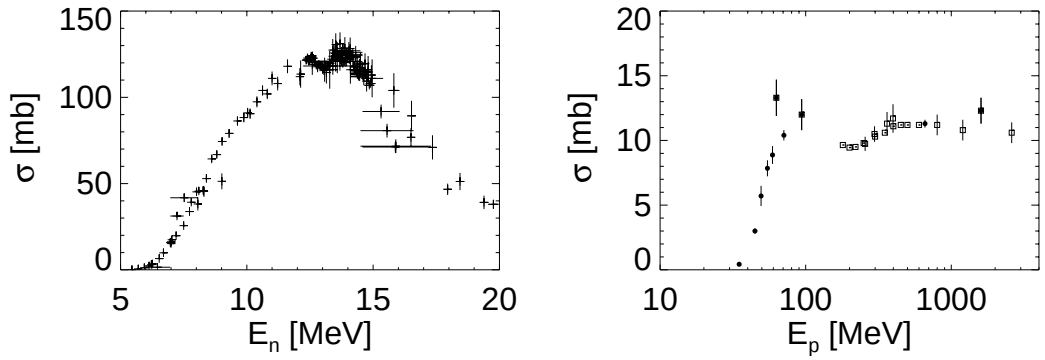

Figure 4.23: *The cross-sections for the production of ^{24}Na by neutrons (left panel) and protons (right panel) in aluminium. The neutron cross-sections are from NNDC (National Nuclear Data Center, USA,* `http://www.nndc.bnl.gov/`*). The proton cross-sections are from NNDC (filled circles) and Bodemann* et al. *(1993), Michel* et al. *(1995) and Schiekel* et al. *(1996) (open squares).*

peak" are $\sim 19°$ and $\sim 41°$ for the 1.37 MeV and the 2.75 MeV photon interacting in D1, respectively. The ^{24}Na event distribution in E_1-E_2 space is also very characteristic. The events cluster along two bands parallel to E_1 located in E_2 at the line energies. In E_1, the two bands extend up to the energy of the Compton edge of the other photon. As can be seen in Fig. 4.22, the CDG FoV selection severely suppresses the channel in which the 2.75 MeV photon interacts in D1, hence the E_1-E_2 correlation is dominated by a line at $E_2 = 2.75$ MeV extending to the Compton edge of the other photon at ~ 1.1 MeV.

The main production channels for ^{24}Na are interactions in the aluminium structure of the telescope and the satellite in general, and interactions in the sodium contained in the D2 detectors (and e.g. in the OSSE detectors). The dominant production channels in aluminium are neutron-capture reactions such as ^{27}Al(n,α)^{24}Na and ^{27}Al(n,α)^{24m}Na and proton reactions such as ^{27}Al(p,3pn)^{24}Na. The production cross-sections for these nuclear reactions[30] are shown in Fig. 4.23. The highest proton and (secondary-)neutron fluxes encountered by COMPTEL occur in the SAA. Assuming that ^{24}Na is exclusively produced during SAA passages, it was, indeed, possible to model the ^{24}Na activity as a function of time, as explained in detail in Sec. 4.5. ^{24}Na can also be produced through neutron capture by ^{23}Na, but this channel does not contribute to the line-background in the ToF forward-peak region.

In contrast to type **A** events such as the instrumental 2.2 MeV photons, which are confined in the ToF forward-peak at ToF $\sim$ 120 ch, the ToF distribution of the type **C** ^{24}Na events should reflect the aluminium and sodium distribution in the spacecraft. The ToF distribution of ^{24}Na events in the ToF forward-peak region as determined by Varendorff and Weidenspointner (1995) is depicted in Fig. 4.24. The ^{24}Na events

[30]The isomeric state ^{24m}Na decays predominantly to the ground state ^{24}Na with a half-life of 20 msec.

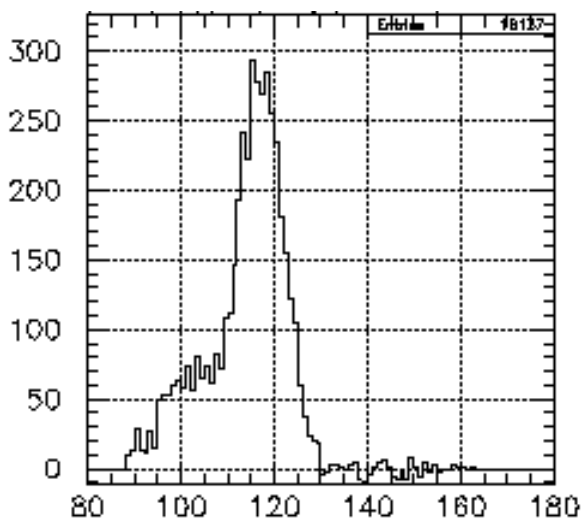

Figure 4.24: *The ToF distribution of ^{24}Na events in the ToF forward-peak region as determined by Varendorff and Weidenspointner (1995).*

peak at $\sim$ 117 ch, indicating[31] that the average distance of the location of the photon emission from the D1 modules is about 20–30 cm, consistent with an origin in the D1 aluminium structure. ^{24}Na is also prominent in the ToF backward-peak due to ^{24}Na production the D2 aluminium structure and the NaI scintillator (van Dijk 1996).

4.4.2.3 The Isotope ^{40}K

The isotope ^{40}K is one of the contributors to the spectral line-feature at about 1.4 MeV in $E_{\rm tot}$ (see Fig. 4.19). A prominent line at this energy was already present before launch in some of the calibration data, and at that time was tentatively identified with natural ^{40}K radioactivity, contained e.g. in the concrete of the buildings. The line was still present after launch, however, and it became clear that there had to be other origins as well. An instrumental origin of the line was strongly suggested by the fact that the line rate was independent of the pointing direction of the telescope. In additon, early in the mission the line rate did not vary with neither vertical cut-off rigidity nor `GCEL` (Weidenspointner 1995a).

Although the spatial origin of the line in the satellite remained unclear for some years, based on the position of the line there was little doubt about the responsible physical process: electron capture by ^{40}K. This decay channel, which has a branching ratio of 10.5%, is illustrated in Fig. 4.25. Electron capture by ^{40}K produces excited ^{40}Ar, which immediately decays to its ground state with a half-life of 1.1 psec through emission of a single 1.46 MeV photon. Other decay channels are β^--decay (89.3%) and β^+-decay (0.001%), leading directly to the ground states of ^{40}Ca and ^{40}Ar, respectively. Also possible is EC decay (0.2%) leading directly to the ground state of ^{40}Ar. No photon emission is involved in the last three decay modes, hence they are not considered

[31] As described in Sec. 3.3, 1 channel in ToF corresponds to a time difference of $\sim$ 0.26 nsec.

further. Because of its half-life of 1.28×10^9 y, any ^{40}K contribution to the instrumental background is practically constant in time.

One suspected source of ^{40}K radioactivity was the frame of the EGRET spark chamber, which was known to contain a considerable amount of potassium (see Sec. 5.5.3.4). In order to undergo a proper double-scattering process, however, these photons must scatter in the D1 detector by an angle larger than 60°. Not only are these photons rejected by the standard CDG selections on $\bar{\varphi}$, the energy of the scattered photons ($\sim$ 0.6 MeV) is lower than the standard CDG D2 energy threshold as well (see Sec. 4.2.3). Finally, a much more viable origin of the 1.4 MeV line was found: the potassium in the glass of the D1 photomultiplier tubes (PMTs) (van Dijk 1994). According to the manufacturer's specifications, the potassium mass fraction in the D1 PMTs (EMI model 9755NA) is 6% in the front glass and 0.14% in the side and back glass. This origin was supported by the fact that a significantly higher fraction of the photons at 1.46 MeV interact in the outer parts of the D1 modules than at other energies, indicating that the photons enter the D1 modules from the sides (van Dijk 1994). Also, the observed $\bar{\varphi}$ distribution at 1.46 MeV peaks at high $\bar{\varphi}$ values, again indicating that the photons enter from the sides.

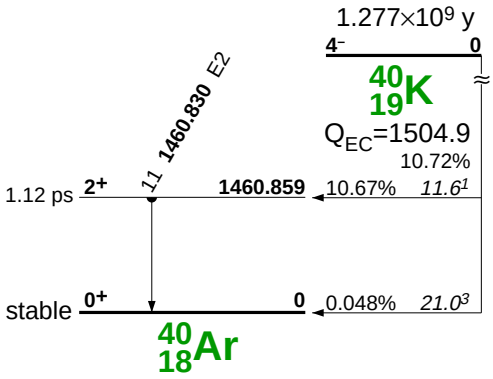

Figure 4.25: *The decay scheme of the isotope ^{40}K according to Firestone* et al. *(1996).*

These characteristics were reproduced in Monte Carlo simulations, which in addition provided the basis for inferring the potassium content in the D1 PMTs from the observed 1.4 MeV line rate (van Dijk 1996, Weidenspointner *et al.* 1996b, Weidenspointner 1996a). The simulated distribution of ^{40}K events, taking into account only the photon-emitting EC decay channel, in selected event parameters for standard CDG selections is depicted in Fig. 4.26. The dataspace distribution of ^{40}K (type **A**) events is fully analogous to the distribution of ^{2}D (type **A**) events (compare Fig. 4.20) and therefore not discussed any further. To model the ^{40}K dataspace distribution as accurately as possible, the representation of the D1 PMTs in the COMPTEL mass model used in these simulations was improved (Weidenspointner *et al.* 1996b). Specifically, the positioning of the PMTs in the D1 modules was corrected, which has considerable influence on the detection efficiency because of the closeness of the PMTs and the scintillator. In addition, the sub-structure of the PMTs, such as the different glass components or the dynodes, was introduced into the mass model for the first time, together with improved material compositions and masses for the individual PMT components. Particular attention was given to the potassium contents of individual PMT components. These were determined by γ-ray spectroscopy of spare PMTs and of parts of a disas-

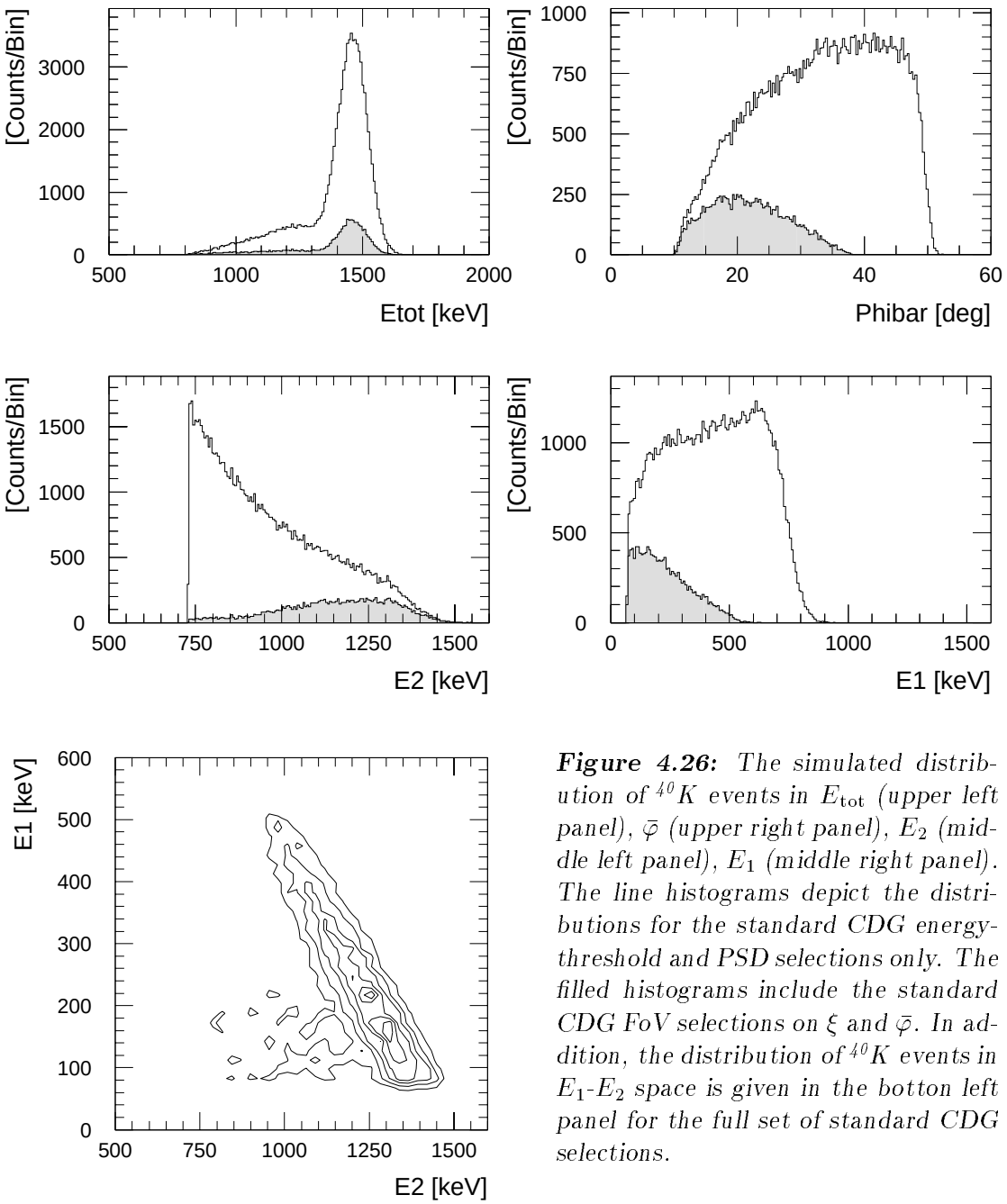

Figure 4.26: *The simulated distribution of ^{40}K events in $E_{\rm tot}$ (upper left panel), $\bar{\varphi}$ (upper right panel), E_2 (middle left panel), E_1 (middle right panel). The line histograms depict the distributions for the standard CDG energy-threshold and PSD selections only. The filled histograms include the standard CDG FoV selections on ξ and $\bar{\varphi}$. In addition, the distribution of ^{40}K events in E_1-E_2 space is given in the botton left panel for the full set of standard CDG selections.*

sembled PMT, using a NaI(Tl) crystal. The background-subtracted spectra from these measurements are summarized in Fig. 4.27. The results for the potassium contents and mass fractions derived from these spectra, which are consistent with the manufacturer's specifications of 6% and 0.14% potassium mass fraction in the front glass and in the side and back glass, respectively, are summarized in Table 4.2. In the simulations, the 1.46 MeV photons were isotropically started from the glass components of the D1 PMTs according to their relative potassium contents (Weidenspointner 1996a).

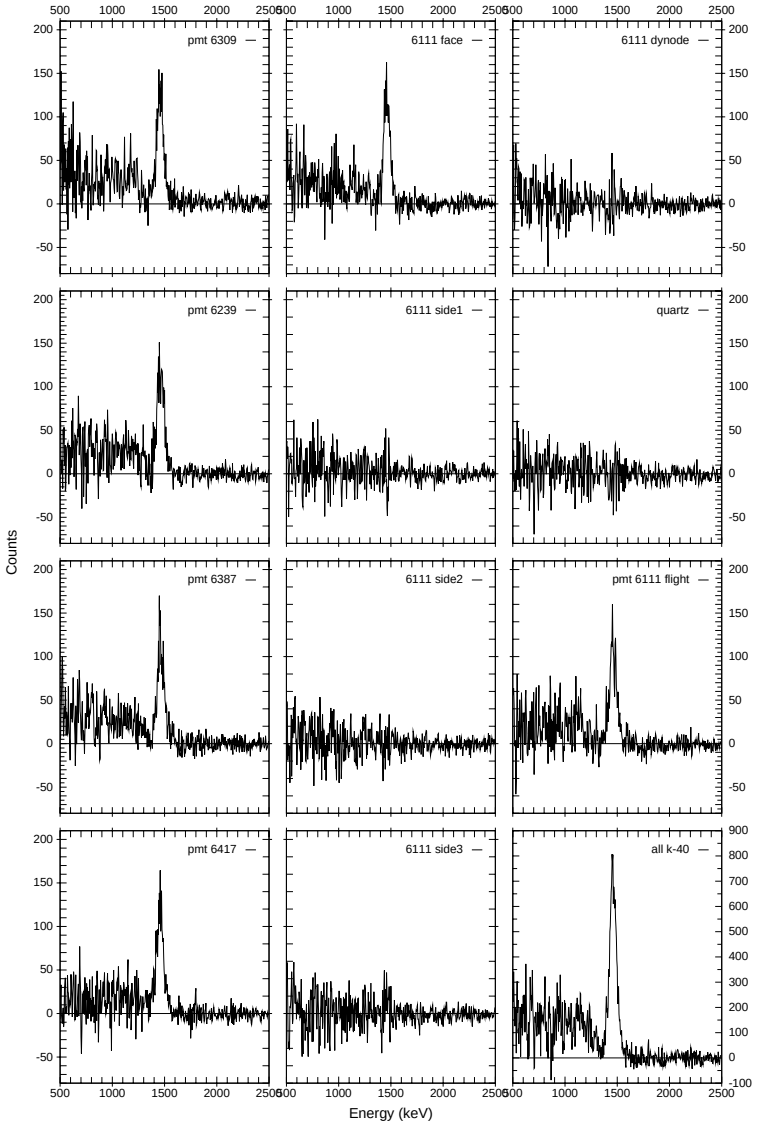

Figure 4.27: *The background-subtracted γ-ray spectra for the determination of the D1 PMT ^{40}K content. The left panel depicts the spectra of four different PMTs (serial numbers 6239, 6309, 6387, and 6417). For the dissassembled PMT 6111 the spectra of the front window (face) and three measurents of the side glass are shown, as well as a spectrum of dynodes, pin pinch and back glass (dynode). "quartz" is a spectrum of the quartz glass, "flight" is a spectrum of PMT 6111 with Al-housing and quartz window. "all k-40" is the sum of the six spectra with a prominent ^{40}K line.*

Comparison of the simulated $\bar{\varphi}$ distribution with the observed distribution of the 1.4 MeV line showed discrepancies at the lowest $\bar{\varphi}$ values, indicating that the line is not entirely due to ^{40}K, but other isotopes contribute as well[32] (van Dijk 1994). To investigate whether the high-$\bar{\varphi}$ component of the 1.4 MeV line is consistent with originating from the D1 PMTs, the event rate in the 1.4 MeV line was determined for $\bar{\varphi}$ in $25° - 50°$ by fitting a simulated line template to the data (Weidenspointner 1996a). Assuming that the event rate is, indeed, due to ^{40}K in the D1 PMTs, the event rate was converted into a D1 PMT potassium content based on the ^{40}K detection efficiency from the Monte Carlo simulation. This analysis was performed for four time intervals with data from 1993 and 1994. No systematic variation with time was

[32]Later in the mission these additional components became much stronger than the ^{40}K contribution to the 1.4 MeV line, as illustrated in Fig. 4.19.

Source	K Content [g]	K Mass Fraction [%]
front window	1.33 ± 0.06	5.3 ± 0.6
side glass average	0.061 ± 0.06	0.15 ± 0.17
back glass	-0.02 ± 0.06	-0.2 ± 0.7
"plain" PMT average	1.39 ± 0.06	
in-flight PMT	1.32 ± 0.06	

Table 4.2: *The potassium content derived from the background subtracted source spectra shown in Fig. 4.27. The errors of the potassium mass fractions include a systematic 10% error due to uncertainties in the detector efficiency. The "plain" and the "in-flight" results refer to measurements of a whole PMT and a whole PMT together with quartz window and aluminium housing, respectively.*

	Sky-Viewing		Earth-Viewing	
	Shift [keV]	K Content [g]	Shift [keV]	K Content [g]
D1 total	16.5 ± 1.3	82.4 ± 1.5	12.7 ± 1.9	97.5 ± 2.9
D1-01	21.9 ± 1.4	12.7 ± 0.5	2.7 ± 2.7	13.6 ± 1.1
D1-02	14.4 ± 3.5	10.9 ± 0.6	24.6 ± 2.1	11.3 ± 1.1
D1-03	12.2 ± 1.9	13.4 ± 0.6	5.4 ± 1.8	15.9 ± 1.1
D1-04	21.5 ± 3.9	11.4 ± 0.6	3.4 ± 5.8	15.6 ± 1.2
D1-05	12.6 ± 2.9	12.7 ± 0.6	17.3 ± 3.1	14.9 ± 1.1
D1-06	18.5 ± 2.9	10.4 ± 0.5	-2.4 ± 1.8	15.4 ± 1.2
D1-07	16.8 ± 3.0	11.6 ± 0.6	22.9 ± 2.7	14.1 ± 1.0
Sum		82.8 ± 1.5		100.8 ± 2.9
Average	16.8 ± 1.1	11.8 ± 0.2	10.6 ± 1.2	14.4 ± 0.4

Table 4.3: *The time-averaged template shifts and potassium contents for sky-viewing and Earth-viewing observations. "Sum" indicates the sum of the potassium contents in the individual D1 modules, "Average" the average template shift and potassium content for the seven D1 modules.*

found, the time-averaged results are summarized in Table 4.3. The results are in good agreement with the expected potassium contents of 12.8 g and 87.4 g for an individual D1 module and the total D1 detector, respectively (consistent results were obtained by van Dijk 1996, in a similar analysis). The presence of a systematic shift of the ^{40}K

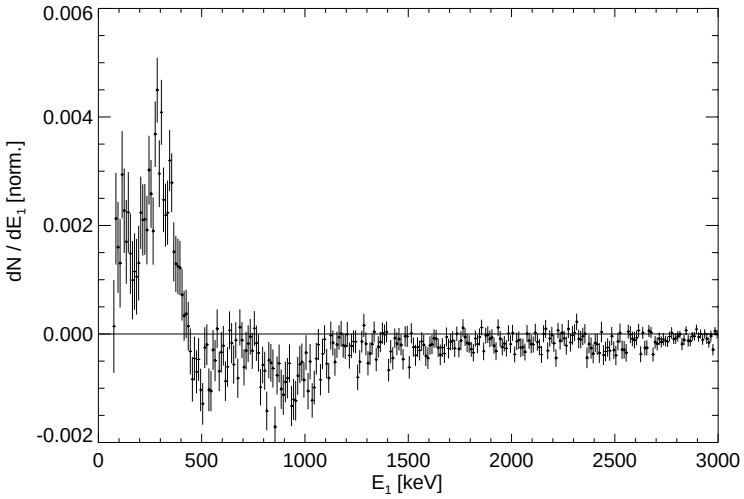

Figure 4.28: *The difference of the E_1 spectra of OPs 511 and 11 for the E_2 range 1.20–1.35 MeV (Oberlack* et al. *1996). The residuum is consistent with the response of the D1 detector to 511 keV photons.*

template relative to the nominal line energy in the fits, and the systematic difference between the results from Earth- and sky-viewing data, however, may indicate that other background components contribute to the 1.4 MeV line even at high $\bar{\varphi}$ values. Nevertheless, these analyses firmly established the natural ^{40}K radioactivity in the D1 PMTs as a component of the instrumental-line background.

4.4.2.4 The Isotope ^{22}Na

Evidence for the presence of ^{22}Na in the instrumental-line background was literally growing with time in a long-term study of the $E_{\rm tot}$ spectrum (Morris 1996b) and in the routine processing of the background datasets for the 1.8 MeV all-sky database (Oberlack 1997). Both studies indicated the build-up of a broad background component at about 1.5 MeV in $E_{\rm tot}$.

Detailed investigations of the $E_{\rm tot}$, E_2 and E_1 distributions of this background feature, as well as of its ToF dependence, finally lead to its identification with the β^+-decay of ^{22}Na produced in the D1 detector material (Oberlack *et al.* 1996, Oberlack 1997). The energy distributions were studied by comparing spectra summed early and late in the mission, which quickly established that the background component must be produced by a two-photon cascade with energies $\sim$ 500 keV and $\sim$ 1.3 MeV. For example, the difference of the E_1 spectra of OPs 511 and 11 for the E_2 range 1.20–1.35 MeV is shown in Fig. 4.28. The pronounced residuum is consistent with the response of the D1 detector to 511 keV photons. In addition, the ToF distribution of the 1.27 MeV line in E_2 was found to peak at ToF $\sim$ 116 ch, consistent with the findings for the ^{24}Na cascade (see Sec. 4.4.2.2), indicating a type **C** event. Finally, the slow build-up of the feature also supports the identification with ^{22}Na, which has a half-life of 2.6 y. Such a build-up has already been observed in the instrumental background of the γ-ray spectrometer onboard SMM (Kurfess *et al.* 1989, Share *et al.* 1989).

The decay scheme of ^{22}Na is illustrated in Fig. 4.29. Two ^{22}Na decay channels, electron capture and β^+-decay with branching ratios of 9.9% and 90.1%, respectively, populate the first excited state of ^{22}Ne, which decays to its ground state through emission of a 1.27 keV photon with a half-life of 3.6 ps. In addition, there is a second β^+-decay mode with a branching ratio of 0.04% that directly leads to the ground state of ^{22}Ne.

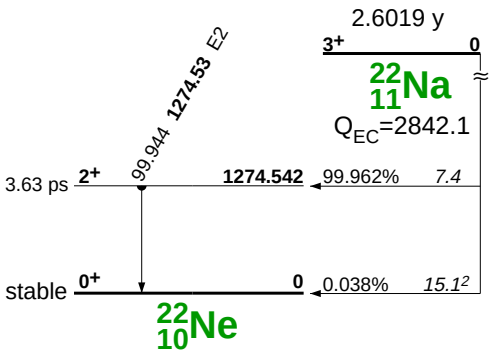

Figure 4.29: *The decay scheme of the isotope ^{22}Na according to Firestone et al. (1996).*

The latter decay mode is neglected in the simulations[33] of the telescope response, which is illustrated for standard CDG selections in Fig. 4.30. In principle, the distributions of the ^{22}Na (type **C**) events are analogous to those of the ^{24}Na (type **C**) events (compare Fig. 4.22). The only difference between the two sets of distributions results from the fact that for ^{22}Na the lower-energy 511 keV photon is below the D2 energy threshold. Therefore only one of the two possible combinations of photon interactions is present in the dataspace in the case of ^{22}Na, namely the lower-energy photon interacting in D1 while the higher-energy photon triggers D2.

The most important process for the production of ^{22}Na in the D1 detector are proton interactions in the aluminium structure, the main channel being ^{27}Al(p,3p3n)^{22}Na. As shown in Fig. 4.31, the cross-section for this interaction peaks at about 50 MeV, and decreases very slowly above about 70 MeV. The average daily flux of SAA protons, covering the energy range from $\lesssim 1$ MeV to several 100 MeV where the cross-section is highest, is much larger than the daily average flux of cosmic-ray protons, which have energies above $\gtrsim 4$ GeV (see Sec. 4.1.1). Therefore it is expected that most of the ^{22}Na production occurs during SAA passages, as is demonstrated in Sec. 4.5. In general, the cross-section for the production of ^{22}Na in proton interactions with silicon is very similar to that for aluminium, except that the silicon cross-section has no resonance around $E_p = 35$ MeV (see Fig. 4.31). Silicon is an abundant element in the glass of the PMTs, and based on yield estimates from preliminary thin-target simulations (Jean 1997) [34] it is expected that about 25% of the ^{22}Na produced in the D1 detector is due

[33]The ^{22}Na decays are simulated analogously to the decays of ^{24}Na (see Sec. 4.4.2.2).

[34]In these hadron simulations, using the GCALOR/GEANT simulation package, a geometrically thin target of depth 0.5 cm was irradiated. In such a thin target the effect of secondary particles, such as neutrons produced in proton interactions, is expected to be small. The following components of the COMPTEL radiation environment were simulated: cosmic-ray protons, SAA protons, atmospheric protons and atmospheric neutrons. Since the results of Morris *et al.* (1995) on the fast-neutron flux in the D1 detector imply that secondary neutrons are a minor component, no attempt was made to estimate the yields due to secondary neutrons outside the SAA. During SAA passages the secondary-

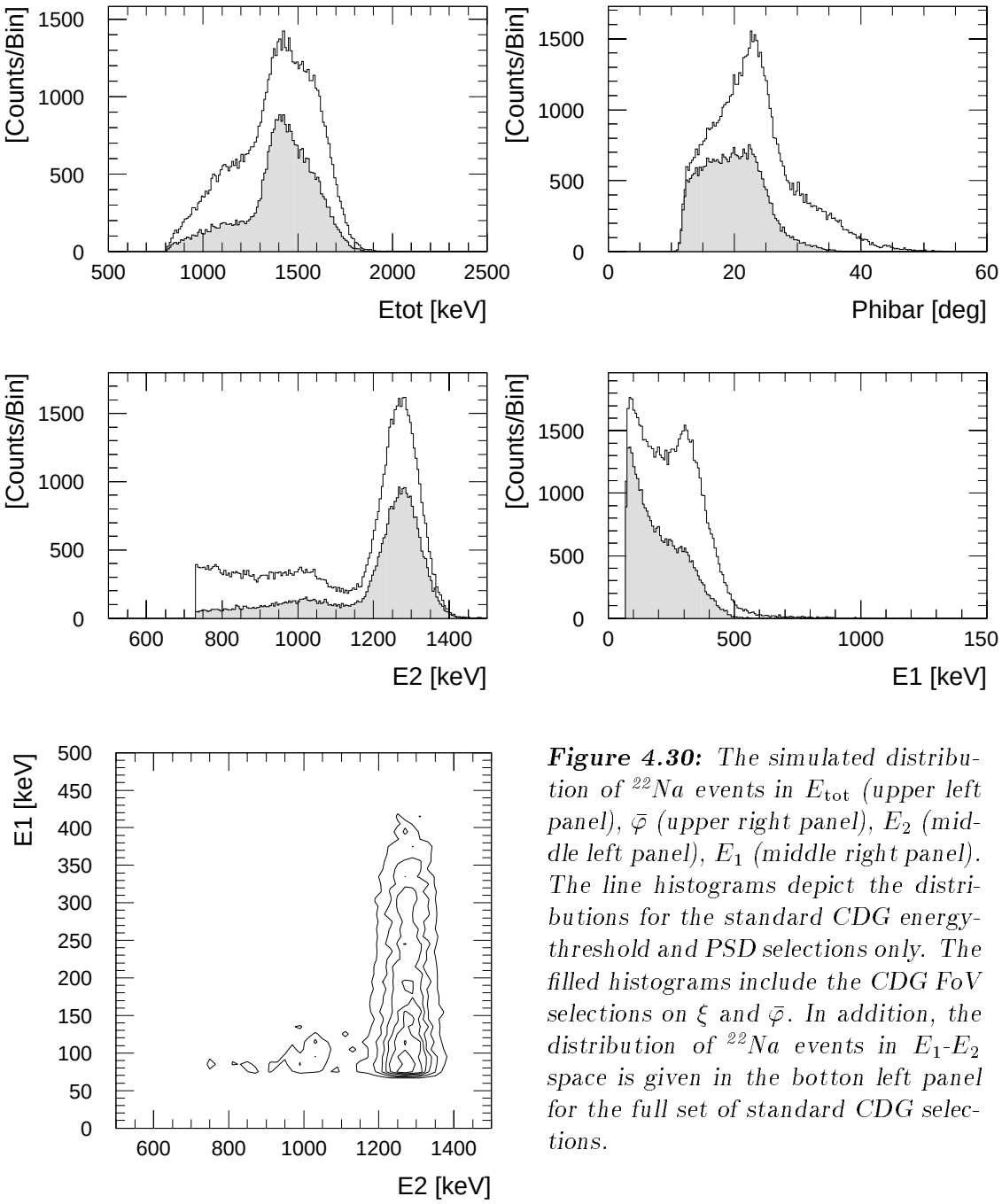

Figure 4.30: *The simulated distribution of ^{22}Na events in $E_{\rm tot}$ (upper left panel), $\bar{\varphi}$ (upper right panel), E_2 (middle left panel), E_1 (middle right panel). The line histograms depict the distributions for the standard CDG energy-threshold and PSD selections only. The filled histograms include the CDG FoV selections on ξ and $\bar{\varphi}$. In addition, the distribution of ^{22}Na events in E_1-E_2 space is given in the botton left panel for the full set of standard CDG selections.*

to Si(p,4pxn) interactions. Thus far, it is assumed in simulations of the ^{22}Na telescope response that all decays take place in the aluminium structure.

neutron flux was estimated to be three times the atmospheric-neutron flux. In addition, thermal-neutron yields were determined for elements/isotopes with large cross-sections for thermal-neutron capture, such as ^{1}H or ^{28}Al.

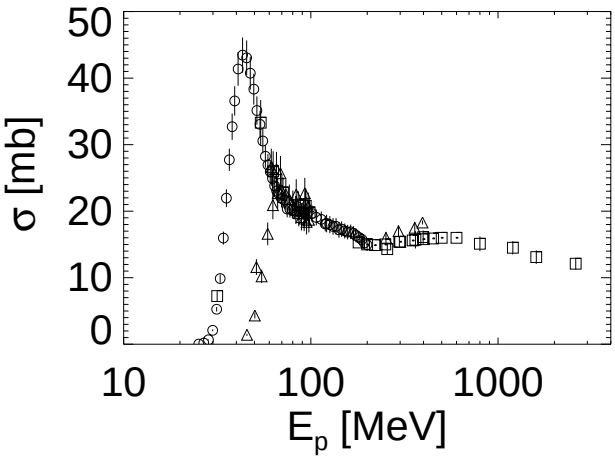

Figure 4.31: *The cross-sections for the production of ^{22}Na by protons in aluminium (circles and squares) and silicon (triangles). The data are from NNDC (circles) and Bodemann* et al. *(1993), Schiekel* et al. *(1996) (squares and triangles) and Michel* et al. *(1995) (squares).*

4.4.2.5 The Isotope ^{28}Al

From the beginning of the mission a weak, albeit significant, line feature at about 1.8 MeV has consistently been present in the E_2 distribution. The position of this feature does not vary with E_1, indicating a multiple-photon (type **C**) origin, which at first remained unclear. The existence of the strong ^{2}D line due to thermal-neutron capture on hydrogen, however, clearly demonstrates the presence of a considerable thermal-neutron flux in the D1 scintillators. In addition, the cross-section for thermal-neutron capture on aluminium, the most abundant element in the D1 detector, has a high value of 0.28 mb (remember, the cross-section for hydrogen is 0.33 mb). It was therefore suggested that the 1.8 MeV feature might possibly be due to thermal-neutron capture on aluminium, in particular, in the D1 scintillator housings, resulting in the production of ^{28}Al (Morris *et al.* 1997)[35]. As illustrated in Fig. 4.32, ^{28}Al β^--decays ($T_{1/2}$ = 2.24 min) to an excited level of ^{28}Si which immediately decays with a half-life of 0.5 psec to its ground state through emission of a single 1.78 MeV photon. The β^--particle has an end-point energy of 2.86 MeV, sufficiently high to produce a second photon through bremsstrahlung emission that may lead to the triggering of a type **C** event[36]. There is, however, also a finite probability that the

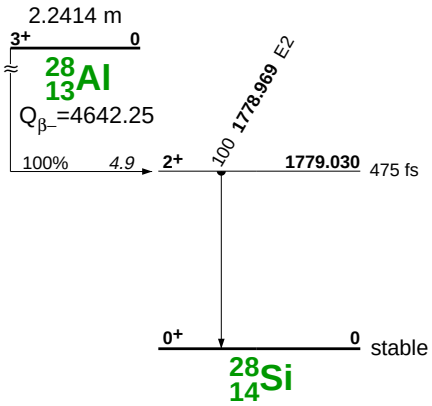

Figure 4.32: *^{28}Al decay scheme according to Firestone* et al. *(1996).*

[35]The isotope ^{28}Al can also be produced in (n,p) interactions on ^{28}Si, but based on the yields from the thin-target simulations (Jean 1997) the contribution from this production channel appears to be negligible.

[36]It is worth mentioning that the ^{28}Al neutron-separation energy of $\sim$ 7.7 MeV is released in γ-ray cascades on psec time scales upon the production of this isotope in a neutron-capture process. These

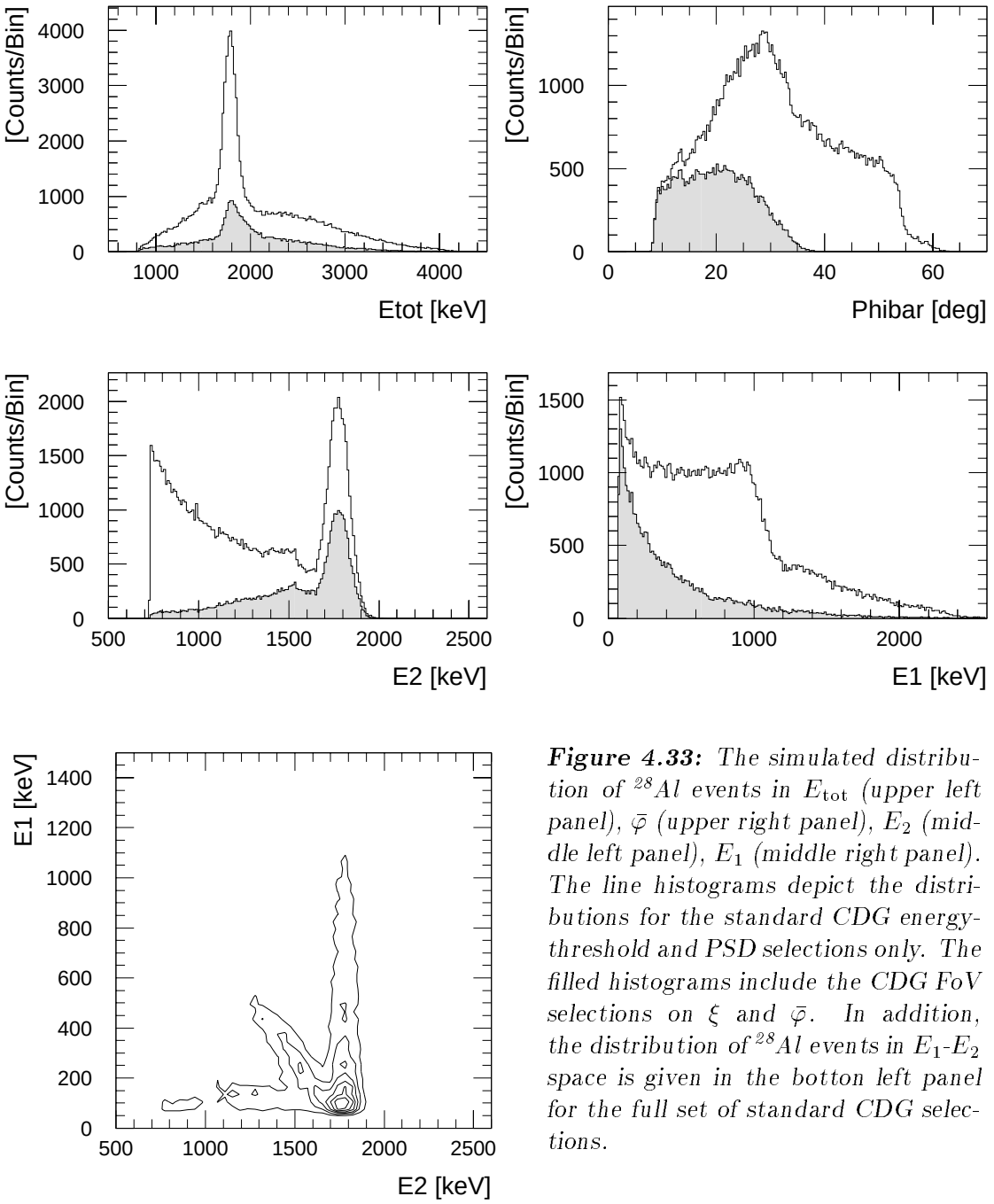

Figure 4.33: *The simulated distribution of ^{28}Al events in $E_{\rm tot}$ (upper left panel), $\bar{\varphi}$ (upper right panel), E_2 (middle left panel), E_1 (middle right panel). The line histograms depict the distributions for the standard CDG energy-threshold and PSD selections only. The filled histograms include the CDG FoV selections on ξ and $\bar{\varphi}$. In addition, the distribution of ^{28}Al events in E_1-E_2 space is given in the botton left panel for the full set of standard CDG selections.*

single 1.78 MeV photon creates a type **A** event.

The simulated telescope response to ^{28}Al decays in the D1 aluminium structure is depicted in Fig. 4.33 for standard CDG selections. The mixed nature of the ^{28}Al

prompt ^{28}Al cascades may contribute significantly to the instrumental nuclear-continuum background and should therefore be studied in some detail to further improve the CDG analysis.

background characteristics is best illustrated in the E_1-E_2 distribution, exhibiting the typical features of type **C** events (the band parallel to E_1 at $E_2 = 1.78$ MeV) and type **A** events (the diagonal band at $E_1 + E_2 = 1.78$ MeV) at the same time. The high-energy tail in the $E_{\rm tot}$ distribution that extends beyond 1.78 MeV is due to bremsstrahlung photons.

In general, events with the 1.78 MeV photon interacting in D1 and one of the lower-energy bremsstrahlung-photons[37] interacting in D2 have $\bar{\varphi}$ values larger than 38° and therefore are rejected. The tentative identification of the 1.78 MeV line in E_2 with ^{28}Al was slowly substantiated as the line-fitting procedure for the CDG analysis (see Sec. 5.3) evolved. Although clearly present over a large fraction of the E_1-E_2 data space, the ^{28}Al structure is usually coincident with contributions from other isotopes and therefore cannot be easily isolated by tailored event selections. Taking into account the simulated ^{28}Al response in the CDG line-fitting procedure, however, allowed us to self-consistently account for the 1.78 MeV line in all E_1-E_2 ranges. Additional support for the identification of ^{28}Al comes from the fact that, as expected, the 1.78 MeV line is short-lived, as demonstrated in Sec. 5.3.4.

4.4.2.6 The Isotope ^{208}Tl

The five isotopes mentioned above are not sufficient to account for all the major instrumental lines as exemplified in Fig. 4.34, showing a fit of an E_2 spectrum obtained at an early stage of the CDG line-fitting procedure (see Sec. 5.3). Obviously, there are two pronounced residuals at $\sim$ 1.4 MeV and $\sim$ 2.6 MeV, the latter of which is discussed in this section.

An important clue to the origin of the line at about 2.6 MeV came from its variation with veto rate, depicted in Fig. 4.35. As can be seen, there is very little variation of the 2.6 MeV line with veto rate, indicating that the bulk of the line signal is long-lived in origin (the small, apparently linear increase is most likely due to another, prompt, background component, as will be explained in Sec. 5.3.5). Even more, the lack of any indication of a veto-rate bump in Fig. 4.35 (compare to top left panel of Fig. 4.18), strongly suggests that the 2.6 MeV line events in Fig. 4.34 are mostly due to an isotope with a half-life much longer than that of ^{22}Na. Taken together, these pieces of evidence make ^{208}Tl, which is part of the natural ^{232}Th decay chain, the most viable candidate.

The decay scheme of ^{208}Tl is depicted in Fig. 4.36. The isotope undergoes β^--decay through several channels, all of which involve the emission of at least two photons, implying that the ^{208}Tl multiple-photon (type **C**) events are quite efficient in triggering the telescope. It follows that a relatively small amount of ^{208}Tl could produce significant instrumental lines. The half-life of ^{208}Tl is only 3.1 min. If the isotope is part of a natural decay chain, however, then its effective half-life is equal to the longest half-life

[37] Most likely the bremsstrahlung photons have energies less than the end-point energy of the β-particle (see Sec. 4.1.1).

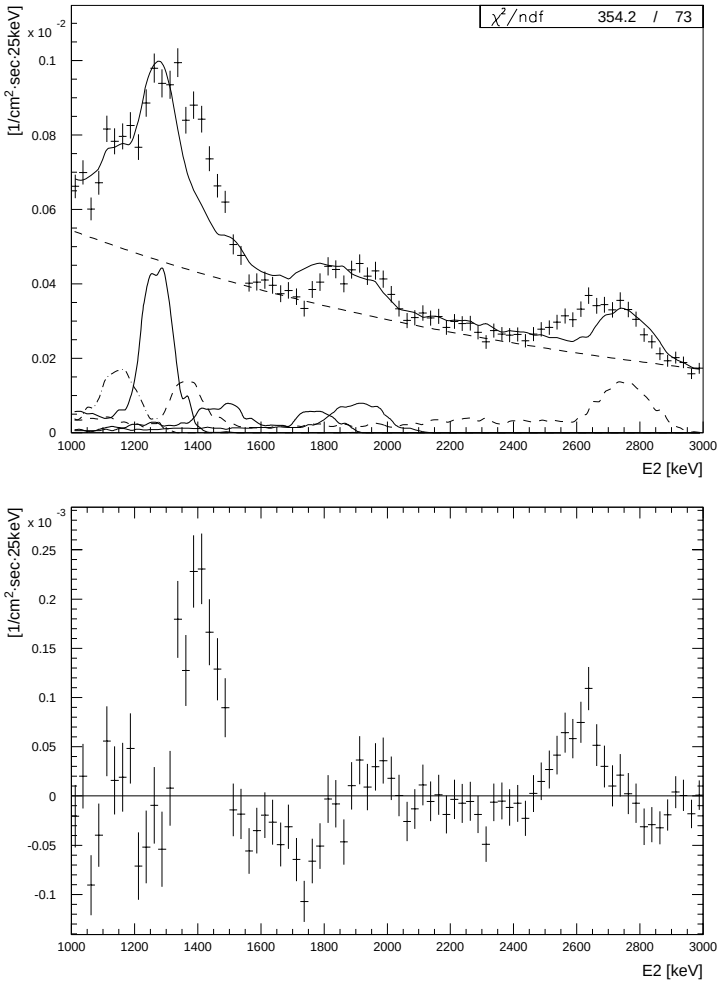

Figure 4.34: *The fit of an E_2 spectrum (top) and its residuals (bottom) at an early stage of the CDG line-fitting procedure. The E_2 spectrum has been summed for E_1 in 250–370 keV, which covers the range of the 511 keV Compton edge, to optimize the signals from β^+-decays such as that of ^{22}Na. The isotopes ^{2}D (thin solid line), ^{22}Na (thick solid line), ^{24}Na (dashed line), ^{28}Al (thick solid line), and ^{40}K (dash-dotted line) have been included in the fit. The ^{22}Na contribution has not been determined in this fit, but was scaled from a previous fit in a different E_1 window that was optimized for the signal of this isotope (see Sec. 5.3.2). Obviously, there are two pronounced residuals at $\sim$ 1.4 MeV and $\sim$ 2.6 MeV (the negative residual at $\sim$ 1.7 MeV is an artifact of the inadequacy of the fit model, as will be explaied in Sec. 5.3 line fitting procedure).*

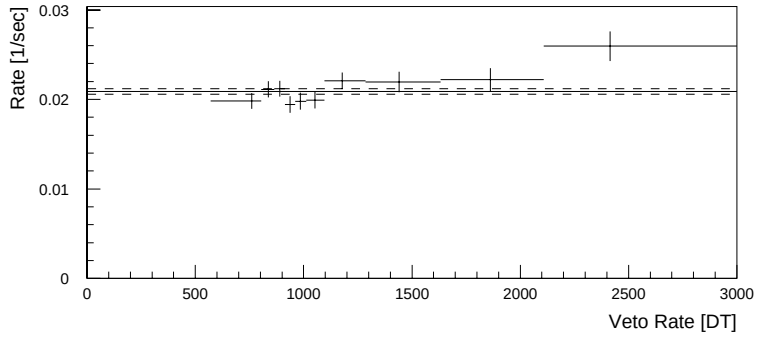

Figure 4.35: *The veto-rate variation of the 2.6 MeV line in E_2 for the E_1 range 250–370 keV. The data cover the time interval from 1991 to 1997. The solid and dashed lines indicate the weighted average and its 1σ error, respectively.*

of any of its mother isotopes, which in this case is the isotope ^{232}Th with a half-life of 1.4×10^{10} y.

As far as the potential location of ^{208}Tl in the telescope is concerned no final conclusions can be drawn yet. As a working hypothesis, it was assumed that ^{208}Tl is distributed as ^{40}K and only present in the front and side glass of the D1 PMTs. The simulated telescope response to ^{208}Tl decays in the D1 PMTs is depicted in Fig. 4.37

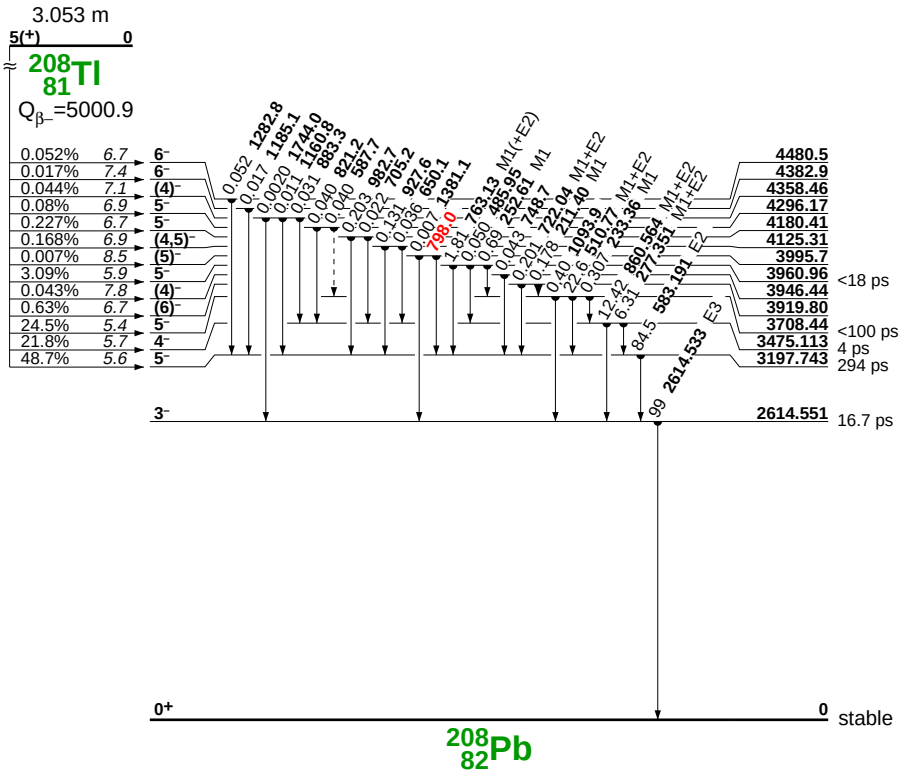

Figure 4.36: The decay scheme of the isotope ^{208}Tl according to Firestone *et al.* (1996).

for standard CDG selections. The multiple-photon (type **C**) characteristic of ^{208}Tl background events is best illustrated in the E_1-E_2 distribution.

Using a Ge-spectrometer, γ-ray spectra of a spare D1 PMT were recorded to test the working hypothesis for ^{208}Tl (Georgii and Plass 1998, private communication). Taking the COMPTEL results for the ^{40}K and ^{208}Tl lines at face value, and assuming that both isotopes are equally distributed in the D1 PMTs, one expects that the ^{208}Tl activity is about 6% of that of ^{40}K, based on the simulated efficiencies, corresponding to a ^{232}Th mass fraction of a few 10^{-6}%. Unfortunately, the measured γ-ray spectra, accumulated over 20 h, do not allow one to draw definite conclusions on ^{208}Tl. The 1.46 MeV ^{40}K line is clearly detected at the 12σ level above the general background (1700 ± 140 counts). The strongest ^{208}Tl lines at 2.61 MeV and 0.58 MeV however, with intensities of 100% and 85.5%, are only detected at the 0.9σ (50 ± 56 counts) and 1.4σ (128 ± 92 counts) level, respectively. Although consistent with expectations, these numbers are insufficient to either verify or falsify the assumptions. Much longer integration times are needed, together with careful gain correction, to obtain γ-ray spectra of sufficient quality. These measurements will be resumed once the experimental set-up has been reassembled after moving it to another laboratory. For the time being ^{208}Tl is included in the CDG analysis.

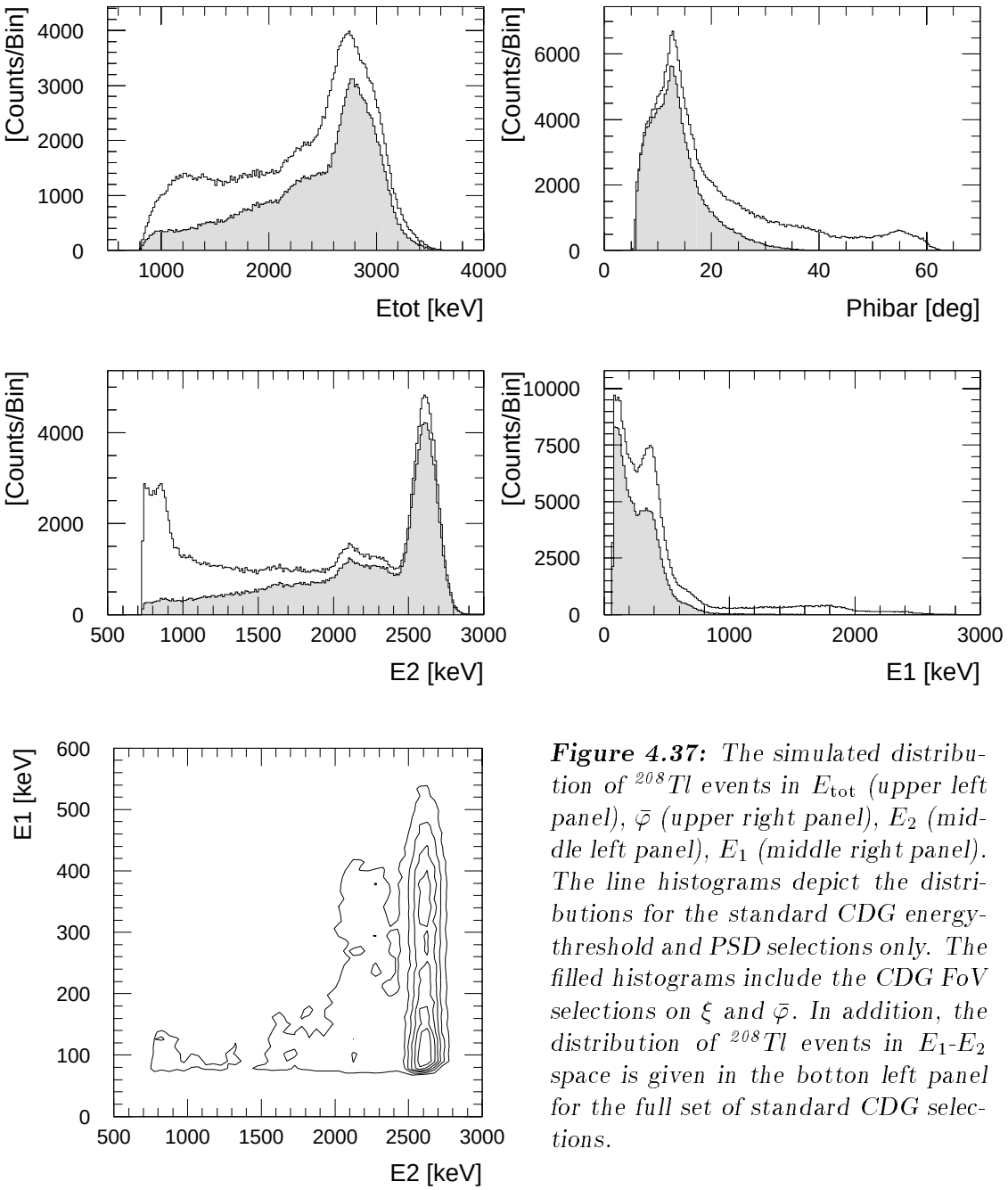

Figure 4.37: *The simulated distribution of ^{208}Tl events in $E_{\rm tot}$ (upper left panel), $\bar{\varphi}$ (upper right panel), E_2 (middle left panel), E_1 (middle right panel). The line histograms depict the distributions for the standard CDG energy-threshold and PSD selections only. The filled histograms include the CDG FoV selections on ξ and $\bar{\varphi}$. In addition, the distribution of ^{208}Tl events in E_1-E_2 space is given in the botton left panel for the full set of standard CDG selections.*

4.4.2.7 The Isotope ^{52}Mn

Similar to the identification of the 2.6 MeV residual in Fig. 4.34, an important clue for the identification of the 1.4 MeV residual came from its veto-rate and time variation, which were both studied by modelling the 1.4 MeV line with a Gaussian. In these fits, the position of the Gaussian was a free parameter, while the width was fixed at the instrumental resolution of the D2 detector of $\sigma_2(1.4\ \text{MeV}) = 46.8$ keV (see Eq. 3.6).

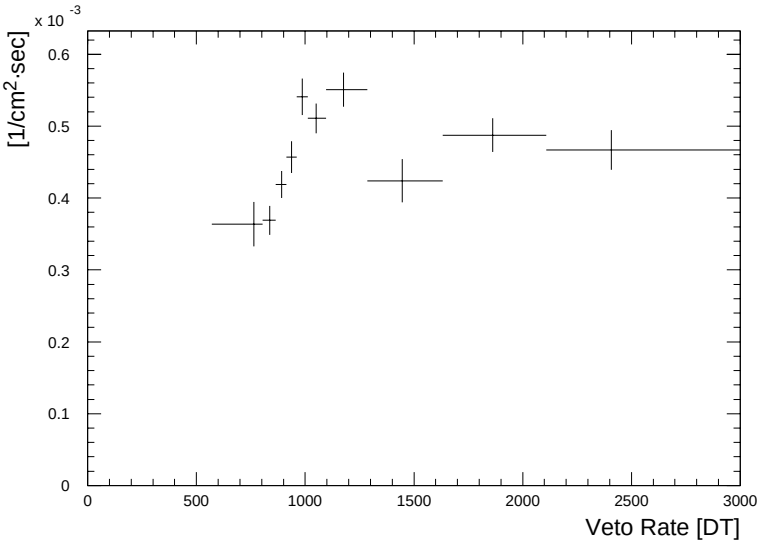

Figure 4.38: *The veto-rate variation of a Gaussian describing the 1.4 MeV line in E_2.*

The veto-rate variation of the 1.4 MeV line is depicted in Fig. 4.38. The pronounced veto-rate bump (see Sec. 4.6) provides unmistakable evidence for the build-up of long-lived activation. The average position of the Gaussian was found to be at about 1.41 MeV. The long-term variation of the line was examined by Oberlack (1997) during the processing of the data base for the ^{26}Al all-sky map. As expected, there was clear evidence for a build-up of the 1.4 MeV line. If due to a single isotope, its half-life could crudely be estimated to be between that of ^{24}Na and that of ^{22}Na. The superior statistics in this long-term study yielded an improved estimate for the line energy: (1409 ± 16) keV. Finally, the E_1 dependence of the 1.4 MeV strongly suggested that the line is due to a β^+-decay.

Assuming that the 1.4 MeV line is due to a single isotope, the evidence suggested that the line is due to the β^+-decay of ^{55}Co Weidenspointner (1997), which has a half-life of 17.5 h and emits a line at 1.41 MeV. Considering the cross-sections for the production of ^{55}Co by proton interactions in iron, nickel and copper, the presence of ^{55}Co necessarily implies the presence of ^{56}Co (Weidenspointner 1997), for which the proton production cross-sections are even higher. Applying the simulated telescope responses (Weidenspointner 1997) to these two isotopes to the data, however, clearly showed that ^{55}Co cannot be responsible for the 1.4 MeV line, since then there should have been a very strong line at 0.93 MeV (see e.g. Fig. 4.19). Similarly, significant contributions of ^{56}Co to the lines at 1.2 MeV and 2.6 MeV are ruled out by the utter lack of any indication for a line at 3.25 MeV in E_2 (see e.g. Fig. 4.19).

The failure of the simplest approach forced us to try to explain the 1.4 MeV line by a blend of contributions of two different isotopes. The most promising candidates for this approach are ^{52}Mn and ^{57}Ni. The isotope ^{52}Mn can be produced in SAA-proton interactions with the iron, chrominium, and nickel abundant in the D1 detector, in particular the electronics components (see production cross-section in Fig. 4.39). The relative yields were estimated by scaling the individual yields from thin-target simula-

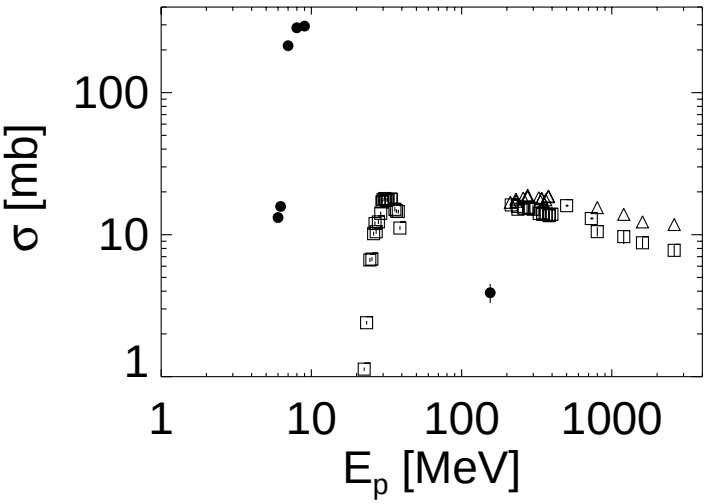

Figure 4.39: *The cross-section for the production of ^{52}Mn in proton interactions with Cr (filled circles), Fe (squares) and Ni (triangles). The data are from NNDC.*

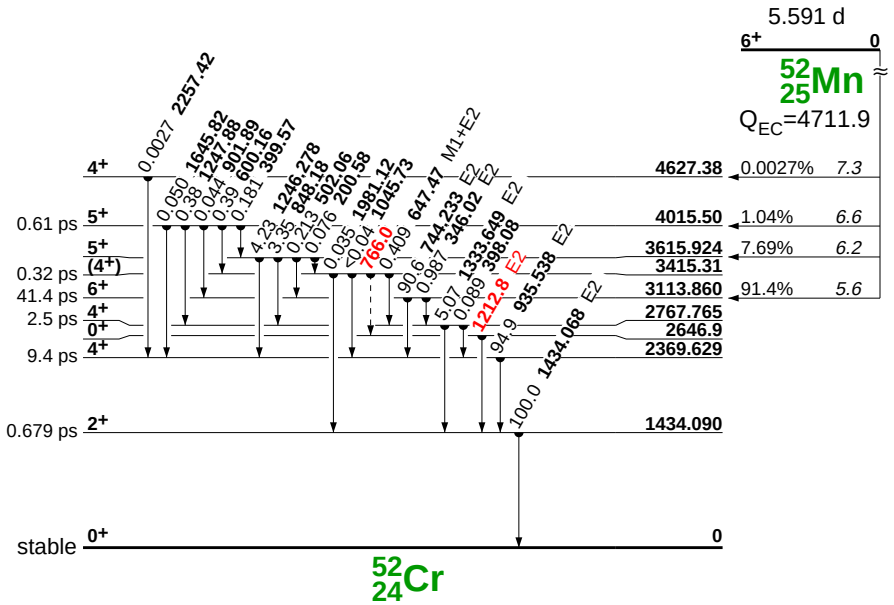

Figure 4.40: *The full decay scheme of the isotope ^{52}Mn according to Firestone* et al. *(1996).*

tions (Jean 1997) with the respective D1 mass fractions. In the response simulations the photons and the β^+-particle were started accordingly from those components of the D1 detector containing iron, chrominium, and/or nickel. Matters are complicated by the fact that ^{52}Mn might be produced in its ground state as well as an isomeric state, with both having different decay schemes. Also, both states have different half-lifes, which finally suggested that ^{52}Mn is more likely produced in the ground state ($T_{1/2} = 5.6$ d) than in the isomeric state ($T_{1/2} = 21.1$ min), as described below.

The decay scheme of the ground state of ^{52}Mn is illustrated in Fig. 4.40. The simulated response, including more than 99% of the decay modes, is depicted in Fig. 4.41

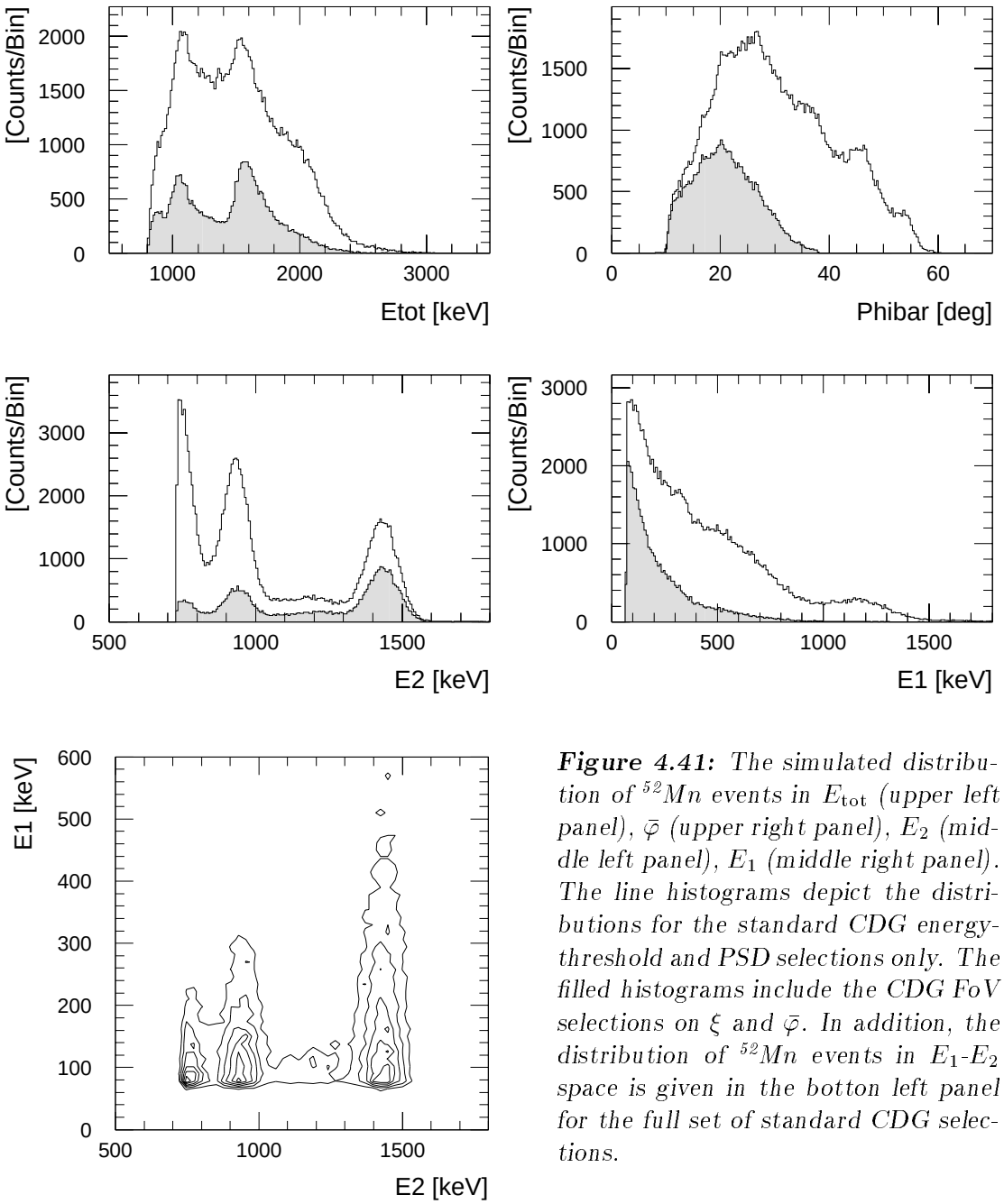

Figure 4.41: *The simulated distribution of ^{52}Mn events in $E_{\rm tot}$ (upper left panel), $\bar{\varphi}$ (upper right panel), E_2 (middle left panel), E_1 (middle right panel). The line histograms depict the distributions for the standard CDG energy-threshold and PSD selections only. The filled histograms include the CDG FoV selections on ξ and $\bar{\varphi}$. In addition, the distribution of ^{52}Mn events in E_1-E_2 space is given in the botton left panel for the full set of standard CDG selections.*

for standard CDG selections. The ground state of ^{52}Mn mostly decays through electron capture ($\sim 71\%$), the remaining decay channels involve β^+-decay. The multiple-photon (type **C**) characteristic of these decays is best illustrated by the bands in the E_1-E_2 distribution at 0.74 MeV, 0.94 MeV, and 1.43 MeV (the 511 keV photon is below the D2 energy threshold).

The identification of part of the 1.4 MeV line with the EC/β^+-decay of the ground

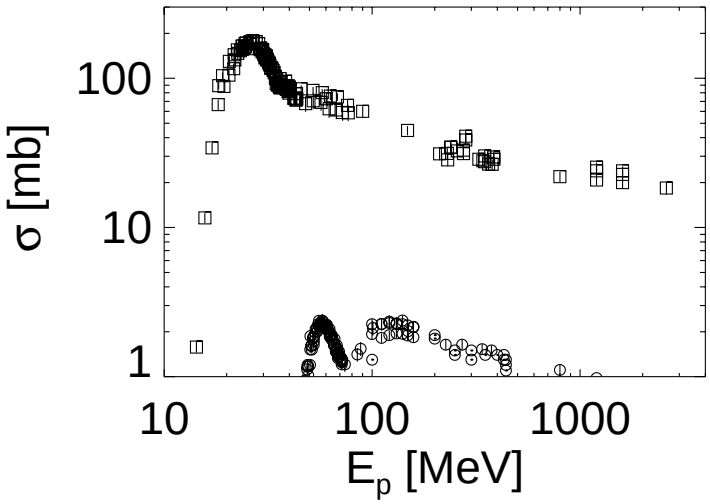

Figure 4.42: *The cross-section for the production of ^{57}Ni in proton interactions with Ni (squares) and Cu (circles). The data are from NNDC.*

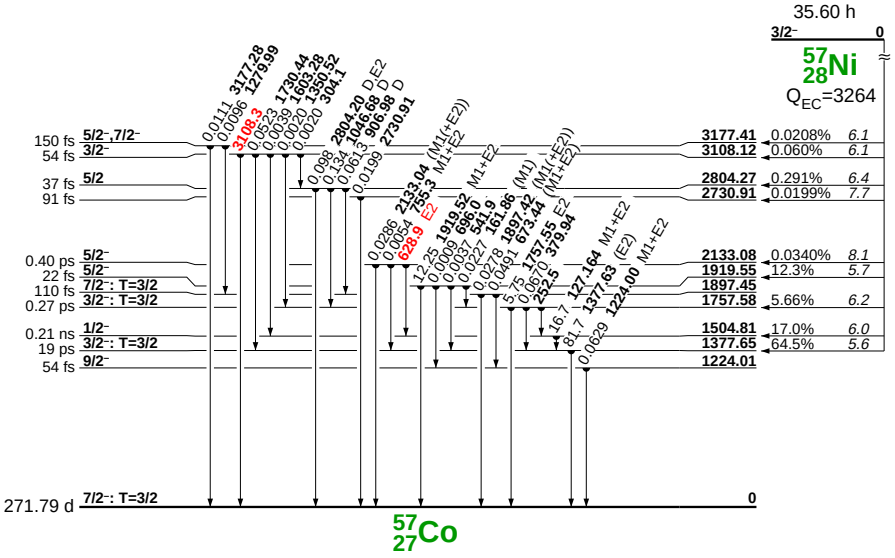

Figure 4.43: *The full decay scheme of the isotope ^{57}Ni according to Firestone* et al. *(1996).*

state of ^{52}Mn is strongly supported by the successful modelling of the observed long-term variation with the activation model, assuming a half-life of 5.6 d (see Sec. 4.5). Finally, it is interesting to note that the signature of this decay has also been recognized in the instrumental background of the SMM γ-ray spectrometer (Share *et al.* 1989).

4.4.2.8 The Isotope ^{57}Ni

As described above, identification of part of the 1.4 MeV line in E_2 with ^{52}Mn implies a significant contribution from the β^+/EC-decay of ^{57}Ni. The isotope is expected to be mostly produced by proton interactions with nickel and copper in the D1 detector

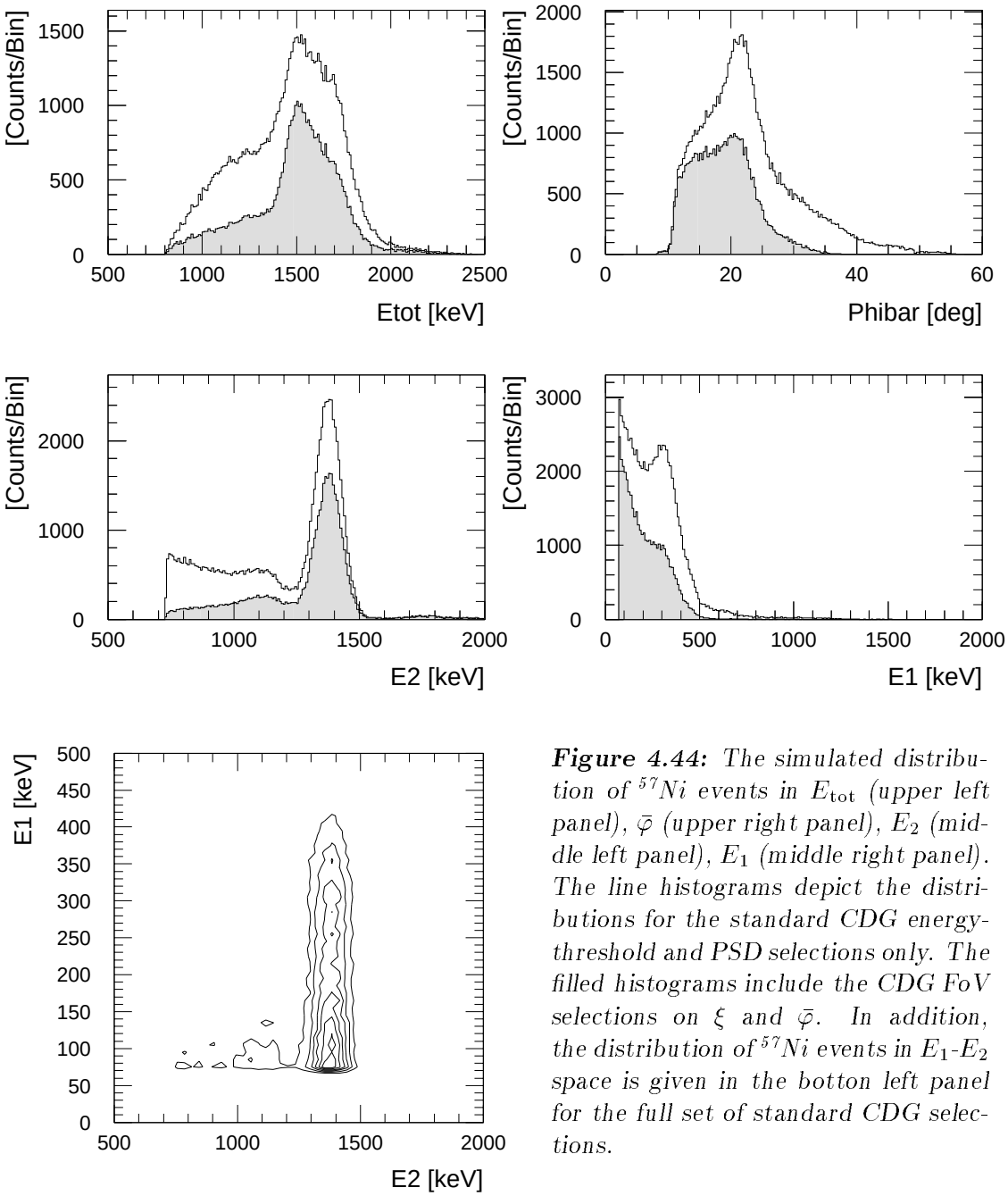

Figure 4.44: *The simulated distribution of ^{57}Ni events in $E_{\rm tot}$ (upper left panel), $\bar{\varphi}$ (upper right panel), E_2 (middle left panel), E_1 (middle right panel). The line histograms depict the distributions for the standard CDG energy-threshold and PSD selections only. The filled histograms include the CDG FoV selections on ξ and $\bar{\varphi}$. In addition, the distribution of ^{57}Ni events in E_1-E_2 space is given in the botton left panel for the full set of standard CDG selections.*

during SAA passages (based on the yield estimates of Jean 1997). The cross-sections for proton interactions on nickel and copper are shown in Fig. 4.42. The decay scheme of ^{57}Ni, which has a half-life of 35.6 h, is illustrated in Fig. 4.43. The simulated[38]

[38]Analogous to the ^{52}Mn simulations (see previous section), the photons and β^+-particles in the ^{57}Ni simulations are started from those D1 detector components containing nickel and/or copper according to the relative yields estimated from the thin-target simulations.

response, including more than 99% of the decay modes, is depicted in Fig. 4.44 for standard CDG selections. The overall branching ratio between decay modes involving electron capture and β^+-decay is about 56.2% and 43.8%, respectively. Both single-photon and multiple-photon decays occur, but the latter (type **C**) events are clearly more efficient in triggering the telescope than the former (type **A**) events, as is best illustrated in the E_1-E_2 response.

Similar to ^{52}Mn, the identification of ^{57}Ni is strongly supported by the successful modelling of the observed long-term variation with the activation model, assuming a half-life of 35.6 h (see Sec. 4.5). Again, it is worth mentioning that evidence for the presence of this isotope in the instrumental background of the γ-ray spectrometer onboard SMM has been reported (Share *et al.* 1989).

4.4.2.9 The Isotope ^{27}Mg

For the sake of completeness it is briefly mentioned that indications for the presence of ^{27}Mg have been obtained during a search for cosmic line-emission from ^{56}Co (Morris *et al.* 1997). The isotope ^{27}Mg is produced by atmospheric or secondary neutrons in ^{27}Al(n,p) reactions with a cross-section of about 100 mb, comparable to the ^{27}Al(n,α)^{24}Na reaction (see left panel of Fig. 4.23). The decay scheme and the simulated response for ^{27}Mg, which is short-lived with a half-life of 9.5 min, are illustrated in Figs. 4.45 and 4.46. A search for the signal of ^{27}Mg by comparing data from the first 30 min after an SAA passage, during which the short-lived isotope should be most pronounced, to the overall data returned inconclusive results. In any case, the ^{27}Mg isotope, if present, is of minor importance for the CDG analysis, since the ^{27}Mg signal is severely reduced by the CDG selections (see Fig. 4.46). The isotope therefore is not explicitely taken into account in the CDG analysis.

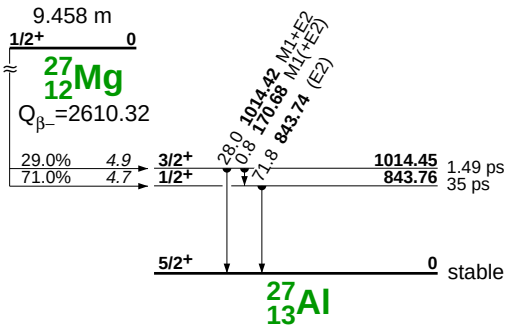

Figure 4.45: *The decay scheme of the isotope ^{27}Mg according to Firestone* et al. *(1996).*

It is interesting to note that if ^{27}Mg indeed is a minor instrumental line, this implies that the bulk of the ^{24}Na activation is due to SAA protons, with production by neutrons being of minor importance, which is also suggested by the yield estimates obtained from thin-target proton and neutron simulations (Jean 1997).

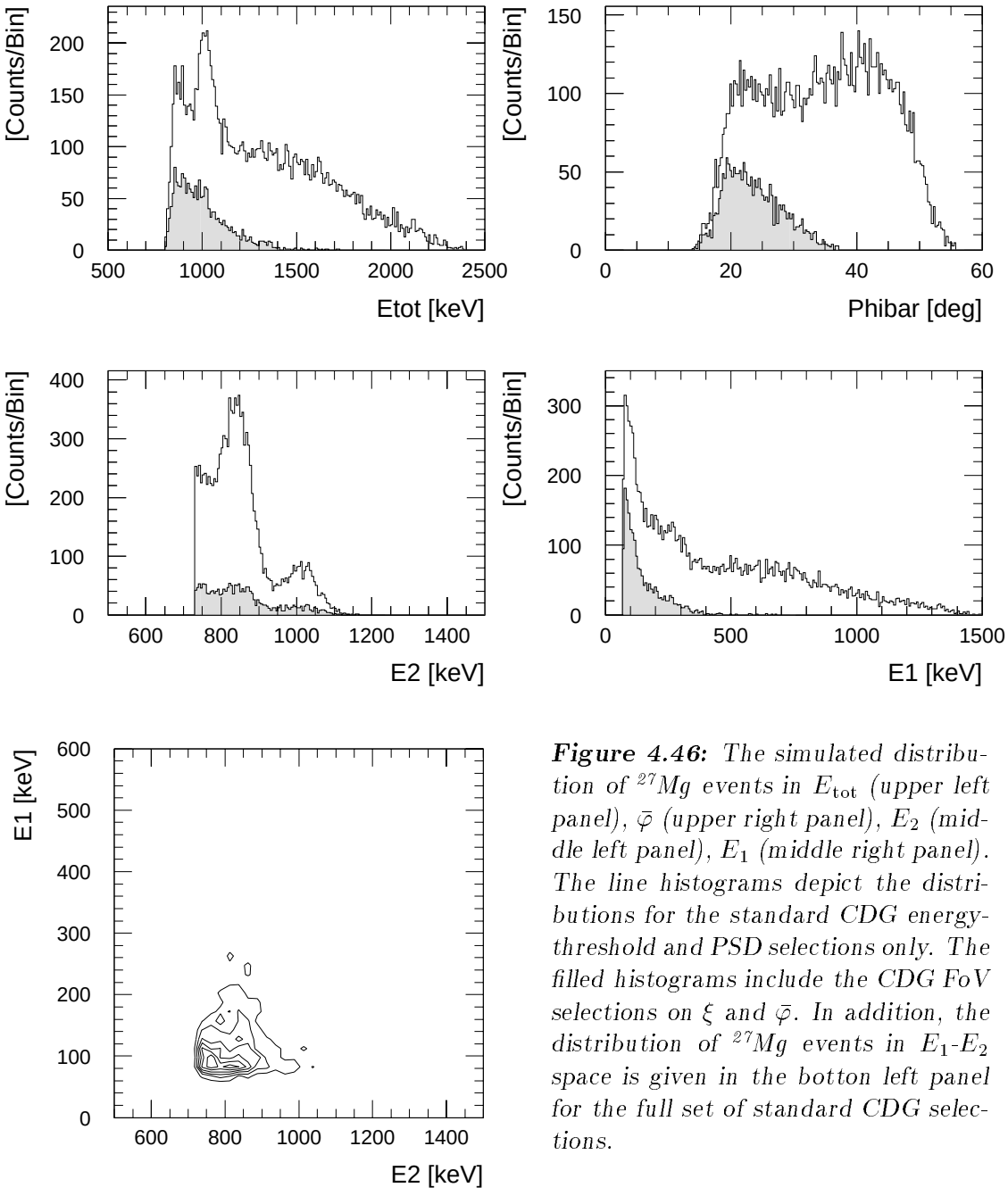

Figure 4.46: *The simulated distribution of ^{27}Mg events in $E_{\rm tot}$ (upper left panel), $\bar{\varphi}$ (upper right panel), E_2 (middle left panel), E_1 (middle right panel). The line histograms depict the distributions for the standard CDG energy-threshold and PSD selections only. The filled histograms include the CDG FoV selections on ξ and $\bar{\varphi}$. In addition, the distribution of ^{27}Mg events in E_1-E_2 space is given in the botton left panel for the full set of standard CDG selections.*

4.5 Variation of Long-Lived Activity in Time — the Activation Model

The activity of long-lived isotopes such as ^{22}Na, ^{24}Na, ^{52}Mn, and ^{57}Ni exhibits a complex variation in time [39]. It is expected that this variation mostly arises from the combined effects of the long-lived isotope's decay and the time history of the activation episodes during SAA passages, with activation outside the SAA by cosmic-ray particles being negligible (see e.g. Kurfess *et al.* 1989).

Assuming a linear correlation between the count rate in the CAL-units[40], in particular the high-level trigger rate of CAL-unit B (SCCALBH), and the production of long-lived isotopes during SAA passages, a model for the activity of long-lived isotopes was developed by Varendorff *et al.* (1997)[41]. Because the CAL-unit count rates are not available for every SAA passage, the data gaps being mostly due to lack of TDRSS (Tracking and Data Relay Satellite System) coverage, the parameter SCCALBH was modelled with a neural net as a function of six free parameters: the orbit altitude, geographic longitude and latitude, time since launch (to include variations due to the solar cycle), and the orientation (azimuth and zenith) of the satellite relative to its velocity vector (to account for asymmetries in the incident proton flux, see e.g. Watts *et al.* 1989). Based on the neural net output for SCCALBH, the number of nuclei of a particular isotope as a function of time, $N(t)$, is given by:

$$\begin{aligned} N(t+\delta t) &= N(t)\cdot e^{-\lambda\cdot\delta t} + N_{new}(t) \\ &\text{and} \\ N_{new}(t) &= \alpha\cdot\delta t\cdot(\mathtt{SCCALBH}(t) - \mathtt{SCCALBH}_0) \end{aligned} \tag{4.10}$$

with the time interval δt usually being a superpacket (= 16.384 sec), $\lambda = \ln 2/T_{1/2}$ being the decay constant of the isotope with half-life $T_{1/2}$, α being the scaling factor between the CAL-unit trigger rate and the isotope activation, and $\mathtt{SCCALBH}_0$ being the approximately constant value of SCCALBH outside the SAA. The isotope activity $A(t)$ then is

$$A(t) = \lambda\cdot N(t) \tag{4.11}$$

The scaling factor α depends on the cross-sections for the production of the isotope in the telescope material, in particular, the D1 detector and has to be determined for each individual isotope from a normalization of the model to measured activities.

---

[39] The natural radioactivity of ^{40}K and ^{208}Tl does not noticeably change with time over the duration of the CGRO mission of several years. The activity of short-lived isotopes such as ^{2}H and ^{28}Al is also fairly constant in time as there is no build-up.

[40] The plastic scintillators of the CAL-units are sensitive to the protons, but hardly to secondary γ-ray photons (see Sec. 4.1.2).

[41] In addition, it is assumed that the spectrum of the incident SAA protons is independent of their intensity, which changes with altitude and time (see Fig. 4.1). If the SAA-proton spectrum does vary

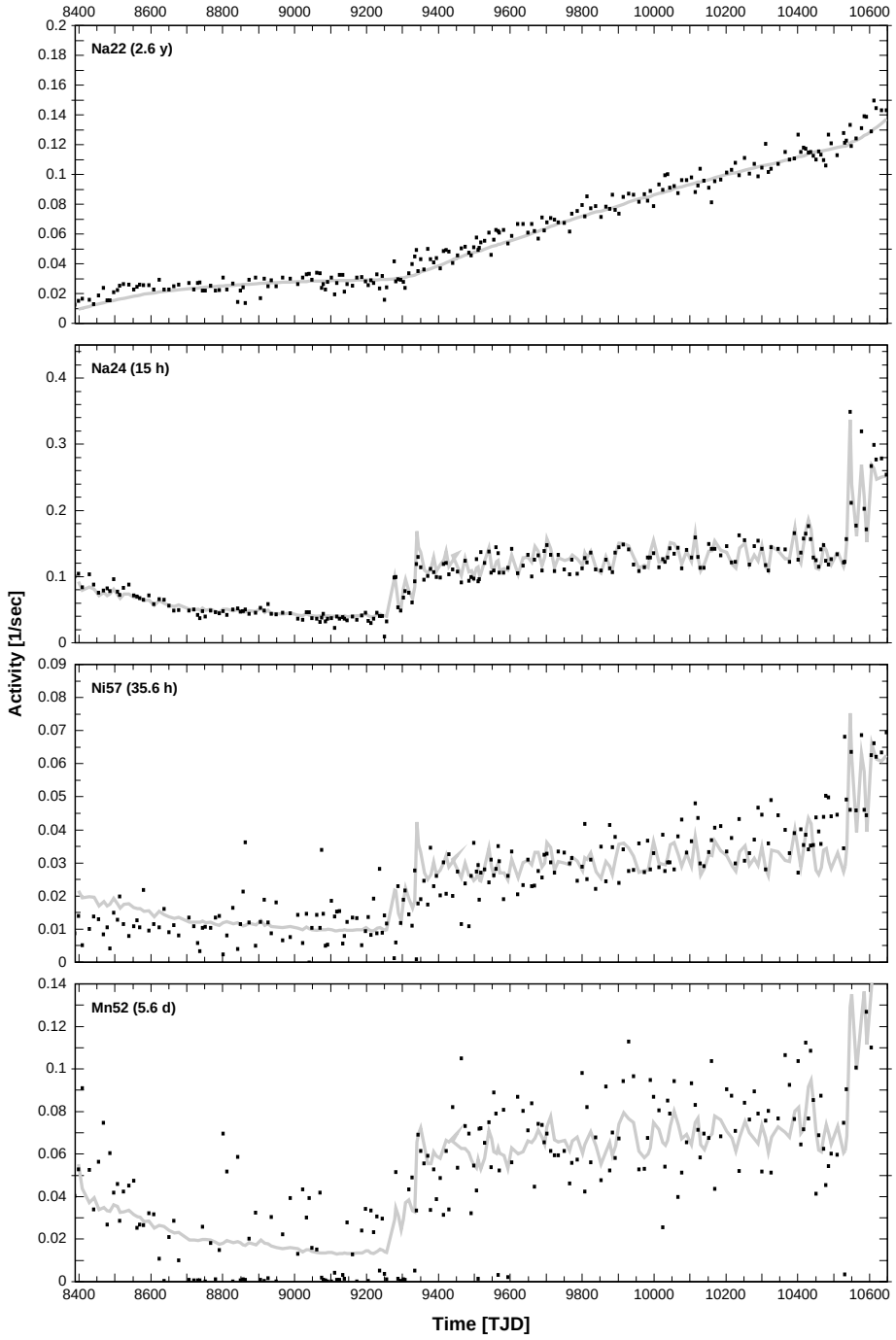

Figure 4.47: *Comparison of the measured activities of the long-lived isotopes ^{22}Na, ^{24}Na, ^{52}Mn, and ^{57}Ni produced in the D1 detector and the predictions of the activation model (solid grey lines). The activities were determined as a function of time by applying the CDG instrumental line-fitting procedure described in Sec. 5.3 to the analysis of the galactic ^{26}Al 1.8 MeV line emission (Plüschke 1998, private communication).*

with intensity, then the activation model is still valid provided that spectral changes have the same effect on both the activation of radioactive isotopes and on the trigger rate of the CAL-units.

A comparison of the measured activities[42] of the long-lived isotopes ^{22}Na, ^{24}Na, ^{52}Mn, and ^{57}Ni with the predictions of the normalized activation model is depicted in Fig. 4.47. In general, the activation model can reproduce the time variation of the isotopes' activities very well. This not only confirms the correctness of the basic model assumptions, but also serves as a valuable double-check on the isotope identifications, as the activity of an isotope depends, among other parameters, on its half-life (see Eqs. 4.10 and 4.11). The increases in activation and hence in activity following the two reboosts can clearly be seen for each isotope (compare Fig. 4.4 depicting the orbit altitude as a function of time). The scatter in the measured activities results from statistical and systematic uncertainties in the fits to the data. Since the instrumental lines due to ^{24}Na and ^{22}Na are more pronounced than those due to ^{52}Mn and ^{57}Ni, the activities of the two former isotopes can be determined more reliably and therefore exhibit less scatter than the activities of the latter two. Also, the production of an isotope varies due to the variation of the orientation of the satellite relative to the anisotropic incident SAA proton flux (see e.g. Watts *et al.* 1989), resulting in an intrinsic scatter of the isotope activity which is increasingly blurred with increasing half-life.

Additional confirmation of the activation model comes from a first-order estimate of the average incident proton flux derived from the modelled ^{22}Na actitvity[43]. The average number of ^{22}Na nuclei produced over one day, ΔN_{22}, can be derived from the modelled average increase in the isotope activity, ΔA_{22}:

$$\Delta N_{22} = \frac{\Delta A_{22}}{\varepsilon_{22} \cdot \lambda_{22}} \tag{4.12}$$

with ε_{22} being the detection efficiency for ^{22}Na decays as determined in Monte Carlo simulations (see Sec. 4.4.2.4) and λ_{22} being the ^{22}Na decay constant. The bulk of the ^{22}Na activity in the ToF forward-peak is due to SAA proton intercations with the aluminium in and around the D1 detector, with a total mass of $m_{Al} \approx 125$ kg. Neglecting for simplicity proton absorption, ΔN_{22} can be determined from the average daily incident SAA proton flux Φ_p:

$$\Delta N_{22} = N_A \frac{m_{Al}}{\mu_{Al}} \cdot \int \Phi_p(E) \sigma_{22}(E)\, dE \tag{4.13}$$

with N_A being Avogadro's number, μ_{Al} being the atomic weight of aluminium, $\sigma_{22}(E)$ being the ^{22}Na production cross-section for aluminium (see Fig. 4.31) and $\Phi_p(E)$ being the SAA proton flux (see Fig. 4.1). At the beginning of the mission, close to solar

[42]The activities were determined as a function of time for event selections used in standard COMPTEL analysis as part of the background modelling for the study of the galactic ^{26}Al 1.8 MeV line emission. This model, described in Oberlack (1997), was improved by Plüschke (1998) based on the CDG instrumental line-fitting procedure explained in Sec. 5.3.

[43]From the four identified long-lived isotopes ^{22}Na is best suited for this purpose for two reasons. First, it is exclusively produced by protons (in contrast to ^{24}Na), and second, the ^{22}Na can be determined with relatively little statistical and systematic uncertainty.

maximum and for an orbit altitude of $\sim$ 440 km (see Fig. 4.4), the average daily production of ^{22}Na according to the activation model was $\Delta N_{22} = 1.7 \times 10^7$, from which a daily incident fluence of SAA protons with energies above 100 MeV of

$$F_p(E_p > 100 \text{ MeV}) = \int_{100 \text{ MeV}} \Phi_p(E)\, dE = 2.3 \times 10^5 \text{ cm}^{-2} \qquad (4.14)$$

can be inferred (Varendorff *et al.* 1997). This first-order estimate is reasonably close to a much more detailed prediction of $F_p(E_p > 100 \text{ MeV}) = 5 \times 10^5$ cm^{-2} for an altitude of 462 km at solar maximum by Dyer *et al.* (1994).

4.6 Variation of Long-Lived Activity with Veto Rate — the Veto-Rate Bump

Similar to the time-variation, the veto-rate variation of the activity from long-lived isotopes is much more complex than that due to natural radioactivity, which is constant (see e.g. Fig. 4.35), or that from prompt and short-lived isotopes, which varies linearly with veto rate (see e.g. Fig. 4.18). The complexity of the variation of long-lived activity with veto rate was first realized by Weidenspointner and Varendorff (1997), who demonstrated that it is due to a number of reasons, depending on the isotope half-life and on the encountered geophysical environment and its time-variation (a summary of these results can also be found in Kappadath 1998). In the following discussion, the various effects are exemplified with the variations of the activity from the isotopes ^{22}Na ($T_{1/2} = 2.6$ y) and ^{24}Na ($T_{1/2} = 15$ h) only, as the variation of the activity from the other two long-lived isotopes, ^{52}Mn ($T_{1/2} = 2.6$ d) and ^{57}Ni ($T_{1/2} = 35.6$ h), are very similar to that of ^{24}Na.

The veto-rate variation of the activity from ^{22}Na and ^{24}Na over relatively short periods of time, during which the geophysical environment did not change significantly, is exemplified in Fig. 4.48 for data from Phase I–II and from Cycle 4. To a good approximation, the ^{22}Na activity is independent of veto rate, which is expected as its half-life is much longer than the orbital period of about 90 min. The average ^{22}Na activity, however, increased with time due to build-up during SAA passages, which is also true for the average ^{24}Na activity (see Fig. 4.47). Other than the ^{22}Na activity, however, the activity of the isotope ^{24}Na in general decreases with increasing veto rate when studied over periods of time with little variation of the geophysical environment, despite the fact that its half-life is considerably longer than the orbital period. This correlation of ^{24}Na activity and veto rate can be explained by a correlation between the veto rate and the time after the last SAA transit. The orbit of CGRO is such that, on average, the satellite passes through the SAA for about 7 consecutive orbits, and then avoids the SAA for the next 7 consecutive orbits, with an orbit lasting about 90 min. During those orbits that pass through the SAA the net ^{24}Na activity is building up, during those orbits avoiding the SAA the isotope activity is decaying. On average, the

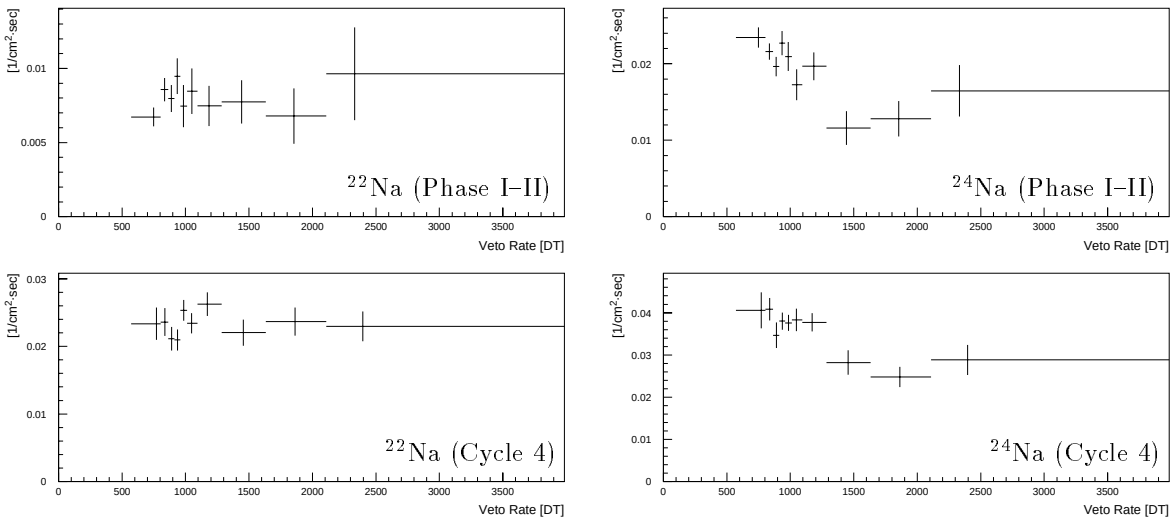

Figure 4.48: *The average variation of the ^{22}Na and ^{24}Na activity with veto rate for Phase I–II (1991–1993) and Cycle 4 (1994–1995), during of which there was little change in the geophysical environment.*

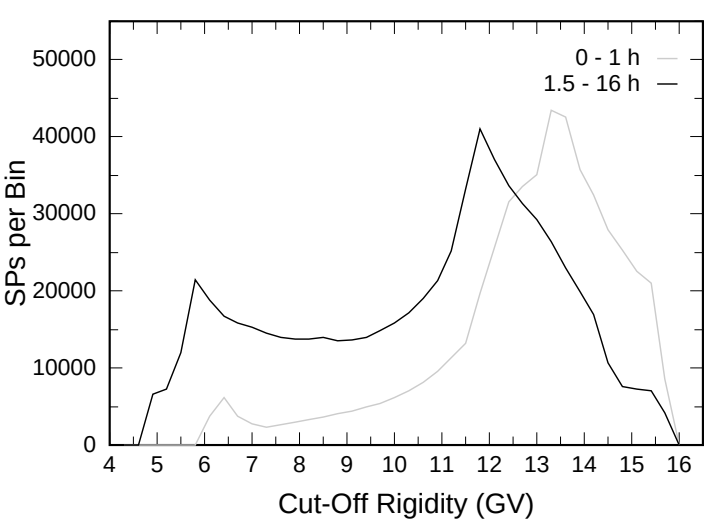

Figure 4.49: *Comparison of encountered cut-off rigidities for SAA-orbits ($t_{\mathrm{SAA}} < 1$ h) and non-SAA-orbits ($t_{\mathrm{SAA}} > 1.5$ h) for Cycle 4, with t_{SAA} denoting the time since the last exit out of an SAA. Clearly, the two distributions are not the same. In particular, the highest rigidities, corresponding to the lowest veto rates (see Fig. 4.2), occur more frequently shortly after an SAA exit, when the ^{24}Na is highest, as can be seen in the bottom left panel of Fig. 4.48.*

distribution of vertical cut-off rigidities (and hence of veto-rate values, see Fig. 4.3) encountered by the satellite for the two sets of orbits is different, as illustrated in Fig. 4.49. It follows that the ^{24}Na activity is not a constant when determined as a function of veto rate, the observed decrease being an artifact of the correlation of encountered rigidity or veto rate and ^{24}Na activation.

The average variation of the activity from ^{22}Na and ^{24}Na over the extended time period from Phase I through Cycle 5, during which the geophysical environment changed significantly due to the first reboost and the solar cycle, is depicted in Fig. 4.50. Typically, a bump-like feature, the so-called veto-rate bump, appears at low veto-rate

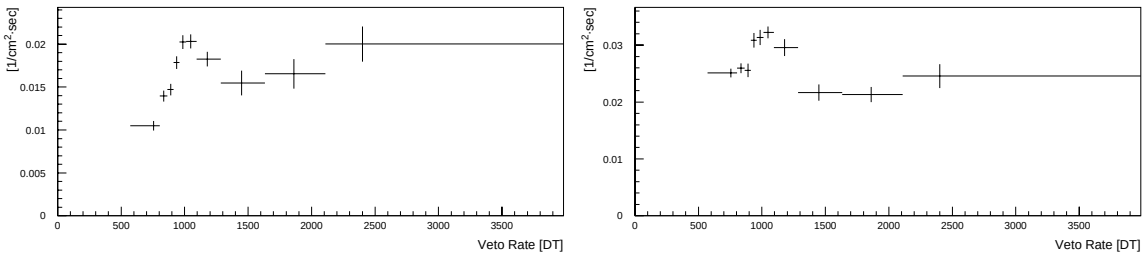

Figure 4.50: *The average variation of the ^{22}Na (left) and ^{24}Na (right) activity with veto rate for Phase I – Cycle 5 (1991–1996), during which the geophysical environment changed significantly due to the first reboost and due to the solar cycle.*

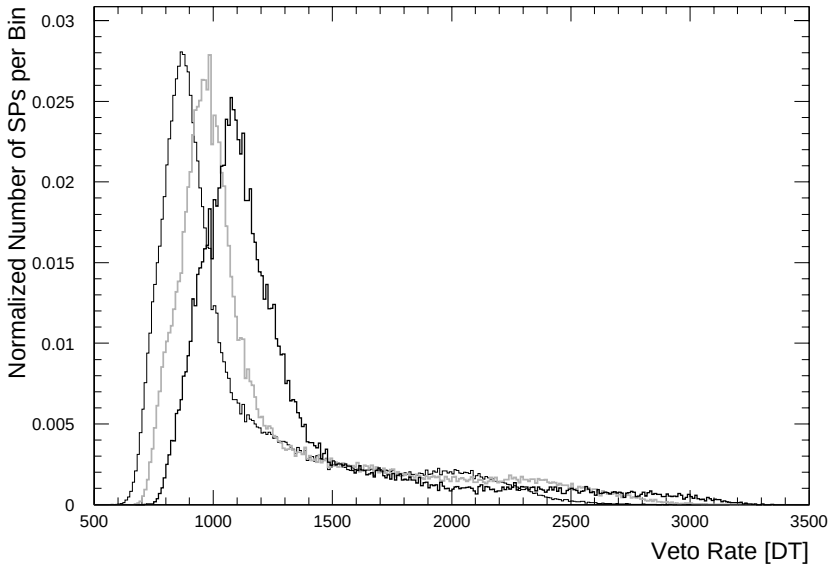

Figure 4.51: *The variation of the veto-rate frequency distribution with time, exemplified for* `SCV2M`*. Depicted are the normalized veto-rate frequency distributions, in units of superpackets per veto-rate bin, for Phase I (thin black line), Cycle 4 (grey line), and Cycle 7 (thick black line).*

values when studying the variation of the activity of long-lived isotopes with veto rate over extended periods of time — even for an isotope such as ^{22}Na, whose activity is independent of veto rate over short periods of time.

To understand the origin of the veto-rate bump it is necessary to realize that the changing geophysical environment not only affects the activity of long-lived isotopes (see Fig. 4.47), but also the veto-rate frequency distribution[44]. This is illustrated in Fig. 4.51, depicting the normalized veto-rate frequency distributions for Phase I, Cycle 4, and Cycle 7 (for clarity, the distributions for the other Phases/Cycles, which

[44]In general, any geomagnetic cut-off rigidity decreases with increasing altitude, resulting in an increasing flux of incident cosmic-ray particles. In addition, the solar modulation of the incident cosmic-ray intensity becomes more pronounced with increasing altitude.

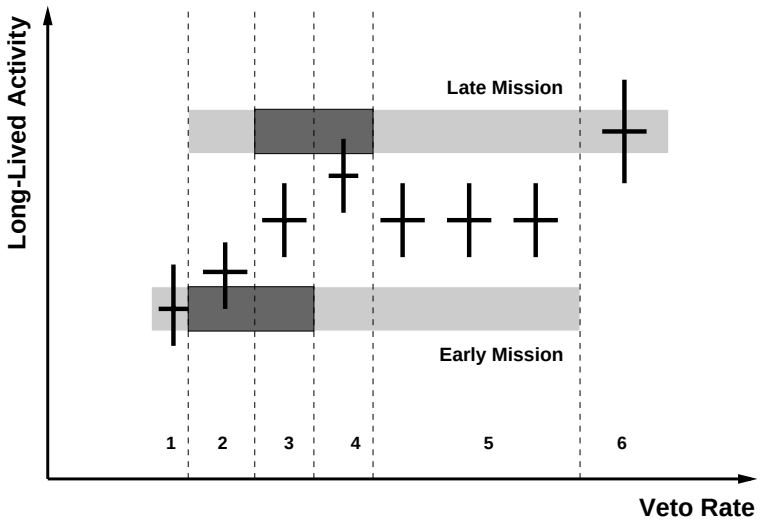

Figure 4.52: *Illustration of the origin of the veto-rate bump. Features such as the veto-rate bump result from the combined effects of the time-variation of the isotope activity (see Fig. 4.47) and of the veto-rate frequency distribution (see Fig. 4.51), as explained in detail in the text.*

interpolate the plotted distributions, were omitted). The generic veto-rate distribution is characterized by a pronounced peak centered at low veto-rates ($\sim$ 1000 DT for SCV2M), with a flat tail extending to higher veto-rate values. To a good approximation, the time variation of this generic veto-rate distribution can be described by a slow shift to higher veto-rates, with some slight changes of the shape of the distribution such as an increasing extension of the tail.

The veto-rate bump therefore is nothing but an artifact of the combined effects of the long-term variation in the activity of long-lived isotopes (see Fig. 4.47) and of the long-term shift of the veto-rate frequency distribution (see Fig. 4.51). The origin of the veto-rate bump is illustrated in Fig. 4.52. For simplicity, let us consider a long-lived isotope whose activity is independent of veto rate over periods of time during which the geophysical conditions do not change, such as ^{22}Na. Let us further consider a combination of two such time intervals of equal duration from early and late in the mission. Late in the mission the isotope activity is higher than early in the mission, and the veto-rate distribution is shifted to higher veto rates. The two sets of data are represented by the two bars in Fig. 4.52, with the grey-shading indicating the veto-rate distribution in terms of the number of superpackets per veto-rate interval (compare Fig. 4.51). When determining the average isotope activity of the combined data as a function of veto rate, indicated by the data points, the average activity of all superpackets in a given veto-rate interval is calculated (see Appendix B). The veto-rate interval 1 only contains superpackets from the early mission, hence the average activity is equal to the early-mission activity. Veto-rate bin 2 is dominated by early-mission data, but superpackets from the late mission contribute. Thus the average activity is somewhat higher than the early-mission level. Both data sets contribute

equally in interval 3, the resulting actvitity is thus the mean of the individual activities. Contrary to interval 2, superpackets from the late mission dominate in bin 4, the average activity being slightly below the level of the late mission. As in bin 3, both sets of data contribute equally in interval 5, the average activity again being the mean of the individual activities. Finally, only data from the late mission contribute to veto-rate interval 6. The net result for the average activity exhibits a general tendency to increase with increasing veto rate with a pronounced veto-rate bump on top — similar to what has been measured for ^{22}Na (compare to the left panel of Fig. 4.50).

As can easily be demonstrated following the above example, the veto-rate bump is an almost universal indicator for the presence of activation with half-lifes ranging from several minutes to several years when combining data covering extended periods of time, as exploited in the identification of the isotopes ^{52}Mn and ^{57}Ni (see Sec. 4.4.2.7). It has to be emphasized, however, that the veto-rate bump cannot be used to estimate the half-life of an isotope, as can be done with the activation model (see previous section).

To conclude, the generally complex variation of the activity of long-lived isotopes with veto rate can be explained by an interplay of the time-variation of the isotope activity, the distributions of cut-off rigidities or veto rates for different sets of orbits, and the time-variation of these distributions. As far as the CDG analysis is concerned, it is important to note that the activity of long-lived isotopes does *not* vary linearly with veto rate. Long-lived background components therefore have to be subtracted from the total event rate differently than prompt and short-lived background components, as described in detail in the following chapter.

Chapter 5

The CDG Analysis Method

5.1 Overview

The essence of the COMPTEL CDG analysis is to make use of the variable nature of the instrumental background for its separation from the CDG signal, which is constant in time. In this analysis COMPTEL is used as a pointed collimator. The CDG is determined by subtracting all identifiable instrumental as well as atmospheric background from the total event rate. The residual event rate then is attributed to the CDG intensity. The CDG spectrum is obtained by determining the CDG intensity independently for each of a set of energy intervals.

Atmospheric γ-rays can readily be removed from the data by using only data gathered at times during which the Earth was sufficiently far outside the instrument field-of-view (see Sec. 4.2).

The major challenge of the CDG analysis is the subtraction of the instrumental background. In the previous chapter, an overview of the instrumental-background signatures relevant to the CDG analysis was given. Specifically, in the CDG analysis full advantage is taken of the characteristic instrumental-background distributions in ToF and energy, as well as the characteristic instrumental-background variations with veto rate and time. Because of their fundamental importance for the following discussions of the CDG analysis method, the most important instrumental-background signatures are briefly summarized below.

The instrumental background by far dominates the sought-after celestial signal at all energies. A considerable fraction of the instrumental background, namely the ToF continuum-background, can be eliminated based on its distribution in ToF (see Sec. 4.3). The variation of the ToF continuum-background with veto rate and time, together with its smooth distribution in energy, strongly suggests that it is due to prompt processes such as bremsstrahlung emission or electromagnetic cascades.

The ToF forward-peak consists of the celestial signal and instrumental background,

with the latter being the dominant component. In marked contrast to the ToF continuum-background, the instrumental background in the ToF forward-peak is very complex. The forward-peak instrumental-background characteristics vary significantly with energy. At the highest energies, $\sim$ 9–30 MeV, the instrumental background is prompt, and mostly due to single photons, presumably of electromagnetic origin (see Sec. 4.3.3). At lower energies, below about 9 MeV, the forward-peak instrumental-background mostly arises from nuclear processes. In the $\sim$ 4.3–9 MeV range, these nuclear processes are prompt and predominantly give rise to multiple-photon events, whose ToF distribution is different from that of the celestial signal. At the lowest energies, below $\sim$ 4.3 MeV, the instrumental background in the ToF forward-peak is most complex. It is dominated by nuclear processes on time scales ranging from shorter than nanoseconds to longer than years. Some of these processes, in particular radioactive decays and de-excitations of long-lived isotopes, reveal themselves through the presence of lines and other features in the forward-peak energy spectrum. The identification of individual isotopes contributing to the instrumental-line background rests equally on the isotope's characteristic spectral distribution and on its half-life (see Secs. 4.4 and 4.5). Of particular importance for the CDG analysis are long-lived isotopes, which are mostly produced during SAA passages. These background components do not decay completely between successive transits through the radiation belts and hence may build up with time. In addition, unlike prompt and short-lived background components, long-lived background components do not vary linearly with veto rate, but in general exhibit a complex correlation with veto rate (see Sec. 4.6).

The COMPTEL CDG analysis — following the instructive examples of earlier investigations of the CDG (see Sec. 2.3) — is based on making use of the variable nature of the instrumental background for its separation from the CDG signal, which is constant in time. In particular, the instrumental background is exclusively, or to a large fraction, due to prompt processes above and below 4.3 MeV, respectively. The prompt instrumental background closely follows the local, instantaneous cosmic-ray intensity, which can, e.g., be parameterized by a cut-off rigidity or the trigger rate of the veto domes (see Sec. 4.1). Since all parts of the CGRO orbit are accessible to cosmic-ray particles, the prompt background cannot be eliminated by selecting observation times during which there is no incident cosmic-ray flux and hence no prompt background. The CDG analysis therefore relies on an extrapolation technique to eliminate the prompt background, similar to the extrapolation in rigidity utilized by satellite-borne experiments such as that of Mazets *et al.* (1975) and analogous to the extrapolation in atmospheric depth utilized by balloon experiments such as that of Schönfelder *et al.* (1980) (see Sec. 2.3.2). The event rate is described as a function of a parameter that quantifies the local cosmic-ray intensity. Extrapolation of this function to the parameter value representing a geophysical environment free of cosmic rays yields the event rate due to the CDG — provided no long-lived instrumental background is present (see below).

If the local cosmic-ray intensity is quantified by the vertical cut-off rigidity, the

prompt background to a good approximation varies exponentially with rigidity (see bottom panel of Fig. 4.3), with infinite rigidity corresponding to geophysical conditions free of cosmic rays. In addition to other drawbacks[1], however, such an exponential extrapolation is numerically unstable. This problem is less severe if the local cosmic-ray intensity is quantified by the trigger rate in the veto domes monitored in the veto rates (Kappadath *et al.* 1996), because the prompt background to a good approximation varies linearly with veto rate (see, e.g., top panel of Fig. 4.3 or Fig. 4.18), with a veto-rate value of zero, or close to zero, corresponding to a geophysical environment free of cosmic rays (see Sec. 5.5.2). A disadvantge of parameterizing the local cosmic-ray intensity with veto rate instead of rigidity is, however, that the veto rate only reflects the net rate of incident cosmic-ray particles, but not their composition or spectral distribution or directions of incidence. The CDG analysis presented in this thesis is based on linear extrapolation in veto rate to remove prompt instrumental-background components.

In the presence of long-lived background components, however, the situation is more difficult, because the veto-rate variation of these components in general is complex and very different from that of the prompt background. In particular, the activity of long-lived isotopes does not vary linearly with veto rate (see e.g. Figs. 4.48 and 4.50). Therefore the contributions of long-lived isotopes have to be subtracted as a function of veto rate *before* the extrapolation (Weidenspointner and Varendorff 1997). The validity of the veto-rate extrapolation for removing prompt instrumental backgrounds thus crucially depends on the absence of any long-lived background components, since only then can the event rate be assumed to vary linearly with veto rate[2]. Subtraction of long-lived background after the extrapolation is only justified for constant background components, such as natural radioactivity[3].

---

[1] A principal drawback of any cut-off rigidity is that a simple scalar value cannot properly take into account the complex variation of allowed directions of incidence at a given particle rigidity or the variation of allowed particle rigidities for a given incident direction. The calculation of the distribution of allowed particle rigidities as a function of direction of incidence and location (geographic longitude and latitude, together with altitude) is possible, based on a model of the (time-variable) geomagnetic field (see e.g. Smart and Shea 1994, and references therein). Such calculations are, however, extremely CPU intensive and not available for the CGRO orbit as a function of time. The principle advantage of such a detailed rigidity is that it not only describes the number of incident cosmic-ray particles, but also their composition and spectral distribution as a function of incident direction — invaluable input if the physics of the instrumental background were to be studied in detailed Monte Carlo simulations of cosmic-ray interactions in the satellite material (see e.g. Weidenspointner 1996b).

[2] For example, extrapolation of the 1.2–1.8 MeV ToF forward-peak event rate depicted in Fig. 4.18 without prior subtraction of the long-lived background indicated by the pronounced veto-rate bump, results in a systematic overestimate of the CDG event rate, which is the extrapolated event rate around veto rate zero.

[3] Depending on their lifetime, the activity of some long-lived isotopes such as ^{22}Na may be independent of veto rate over short periods of time, as exemplified in the left panels of Fig. 4.48. In general, however, the contributions from isotopes produced during SAA passages have to be subtracted *before* the extrapolation.

To conclude this overview of the CDG analysis method, the major steps of the analysis procedure are listed below. The CDG spectrum is derived by determining the CDG intensity in individual energy intervals. To extract the CDG signal from the total event rate, for each energy interval ToF spectra are summed as a function of veto rate. In some energy intervals it is possible to suppress instrumental background, and hence to increase the signal-to-background ratio, in the ToF spectra by tailored event selections (see Sec. 5.3). To determine and subtract the activity of long-lived isotopes, a set of $E_{\rm tot}$ and E_2 spectra is summed as a function of veto rate (see Sec. 5.3). Contrary with the ToF spectra, the signal from the background lines in the $E_{\rm tot}$ and E_2 spectra is maximized through application of optimized event selections, thereby facilitating the measurement of the isotopes' activities. The calculation of the ToF, $E_{\rm tot}$, and E_2 spectra is described in Appendix B. The veto-rate intervals were chosen such that each bin contains about the same number of superpackets.

1. *Fitting the ToF Spectrum*: The first step of the CDG analysis procedure to extract the CDG signal from the total event rate is to determine the ToF forward-peak flux[4] as a function of veto rate in each energy interval. For each energy interval and veto-rate bin, the ToF forward-peak flux is derived from a fit of the respective ToF spectrum. The ToF fit allows us to eliminate a considerable fraction of the instrumental background, namely the ToF continuum-background. The ToF forward-peak flux consists of the CDG signal and various background components, which, depending on energy, are exclusively prompt (above about 4.3 MeV), or both prompt and long-lived (below about 4.3 MeV).

2. *Subtraction of Long-Lived Instrumental Background*: Application of the veto-rate extrapolation requires prior subtraction of long-lived background components as a function of veto rate. The activities of the eight isotopes identified thus far (see Table 4.1) are self-consistently determined as functions of veto rate in an iterative line-fitting procedure using a set of $E_{\rm tot}$ and E_2 spectra. The contributions of each of these isotopes, including the prompt and short-lived isotopes, are subsequently subtracted, as a function of veto rate, from the ToF forward-peak flux in each of the individual CDG energy intervals that cover the energies below about 4.3 MeV. Ideally, at all energies the remaining ToF forward-peak flux now consists of the constant CDG signal and prompt background components only.

3. *Veto-Rate Extrapolation*: Finally, the remaining ToF forward-peak flux is linearly extrapolated to geophysical conditions free of incident cosmic radiation, which occur at or close to veto rate zero (see Sec. 5.5), to remove prompt background components. The residual flux after this extrapolation is then attributed to the CDG, and converted to intensity in units of $[1/(\mathrm{cm}^2 \cdot \mathrm{sec} \cdot \mathrm{ster} \cdot \mathrm{MeV})]$ through division by 2π ster (see Eqs. 3.18 and 3.19).

[4]As explained in Sec. 5.2, the ToF spectra are corrected for the instrument livetime and the instrument effective area, both of which vary in time. Hence the event rate in the ToF forward-peak is formally obtained in units of $[1/(\mathrm{cm}^2 \cdot \mathrm{sec} \cdot \mathrm{MeV})]$.

In the CDG analysis, two sets of $E_{\rm tot}$ binnings are utilized. The finer $E_{\rm tot}$ binning consists of nine energy intervals with boundaries at 0.8, 1.2, 1.8, 2.7, 4.3, 6.0, 9.0, 12.0, 17.0, and 30.0 MeV, the cruder binning consists of 6 intervals, with boundaries at 0.8, 1.2, 1.8, 2.7, 4.3, 9.0, and 30.0 MeV. The boundaries of the four lowest $E_{\rm tot}$ intervals reflect the structure of the instrumental-line background: the 1.2–1.8 MeV interval is dominated by the activity from ^{22}Na, ^{40}K, ^{52}Mn, and ^{57}Ni, the 1.8–2.7 MeV contains most of the ^{2}D activity, and the 2.7–4.3 MeV range is dominated by the activity from ^{24}Na. At higher energies, the 4.3–9 MeV and the 9–30 MeV ranges represent the regimes of dominating prompt multiple-photon and dominating prompt single-photon forward-peak backgrounds, respectively. The sub-divisions of these two high-energy intervals into 2 and 3 sub-ranges in the finer $E_{\rm tot}$ binning were chosen such that each of the two regimes is sub-divided into intervals containing about the same number of events. The finer $E_{\rm tot}$ binning is mostly used for determining the spectrum of the CDG, while the cruder binning is usually used for studying the CDG isotropy.

In the following sections, first each of the steps of the CDG analysis method is discussed in more detail, followed by a description of the final analysis method, and an assessment of the systematic uncertainties. Finally, a concise description of an alternative approach for determining the CDG with COMPTEL is given.

5.2 Fitting the ToF Spectrum

The first step of the CDG analysis procedure is to determine the ToF forward-peak flux[5] as a function of veto rate. In general, in each of the three models (see Eqs. 4.6, 4.7, and 4.8) described in Sec. 4.3, the ToF forward-peak is represented by a single Gaussian (see Fig. 4.11) in the ToF fits.

At energies between 4.3 MeV and 9 MeV, however, the ToF forward-peak is, in principle, better modelled by two Gaussians than by a single Gaussian (see Fig. C.6), as explained in detail in Appendix C[6]. The two forward-peak components are centered at $\sim$ 117.5 ch and $\sim$ 120.0 ch (see Table C.3)[7]. The lower Gaussian represents the

[5] As described in Appendix B, the ToF spectra have units of $[1/(\mathrm{cm}^2 \cdot \mathrm{sec} \cdot \mathrm{ch})]$ in each energy interval. The ToF forward-peak flux is determined by first integrating the fit result for the forward-peak Gaussian, followed by a division by the width of the energy interal ΔE. Hence the ToF forward-peak flux is obtained in units of $[1/(\mathrm{cm}^2 \cdot \mathrm{sec} \cdot \mathrm{MeV})]$.

[6] In fact, the ToF forward-peak was found to be better represented by two Gaussians than by a single Gaussian also at energies above 9 MeV(see Fig. C.7). At these high energies, however, both forward-peak components have very similar positions (see Table C.3). Within the statistics usually available in the CDG analysis, a reliable separation of the two components is not possible above 9 MeV, and therefore the ToF forward-peak is modelled by a single Gaussian.

[7] Based on the assumption that the forward-peak background and forward-peak signal components have the same widths when modelled with Gaussians, Kappadath (1998) obtained similar results.

prompt multiple-photon forward-peak instrumental background (see Sec. 4.3.2)[8]. The upper Gaussian consists of the celestial signal, in particular the signal from the CDG, and prompt instrumental background and will be referred to as "signal component" in the following.

Analogous to the single-Gaussian ToF models defined in Eqs. 4.6, 4.7, and 4.8, three two-Gaussian ToF models, each having nine parameters, were defined. With $\mathtt{t}$ denoting the ToF value in [channels]:

• *Parabolic Two-Gaussian Model*:

$$\begin{aligned} f_{\mathrm{p2}}(\mathtt{t}) &= p_1 \cdot \exp\left[-\frac{1}{2}\left(\frac{\mathtt{t}-p_2}{p_3}\right)^2\right] + p_4 \cdot (\mathtt{t}-p_5)^2 + p_6 + \\ & \quad p_7 \cdot \exp\left[-\frac{1}{2}\left(\frac{\mathtt{t}-p_8}{p_9}\right)^2\right] \end{aligned} \tag{5.1}$$

• *Exponential Two-Gaussian Model*:

$$\begin{aligned} f_{\mathrm{e2}}(\mathtt{t}) &= p_1 \cdot \exp\left[-\frac{1}{2}\left(\frac{\mathtt{t}-p_2}{p_3}\right)^2\right] + p_4 \cdot \exp\left(\frac{97.5-\mathtt{t}}{p_5}\right) + p_6 + \\ & \quad p_7 \cdot \exp\left[-\frac{1}{2}\left(\frac{\mathtt{t}-p_8}{p_9}\right)^2\right] \end{aligned} \tag{5.2}$$

• *Gaussian Two-Gaussian Model*:

$$\begin{aligned} f_{\mathrm{g2}}(\mathtt{t}) &= p_1 \cdot \exp\left[-\frac{1}{2}\left(\frac{\mathtt{t}-p_2}{p_3}\right)^2\right] + p_4 \cdot \exp\left[-\frac{1}{2}\left(\frac{\mathtt{t}-80}{p_5}\right)^2\right] + p_6 + \\ & \quad p_7 \cdot \exp\left[-\frac{1}{2}\left(\frac{\mathtt{t}-p_8}{p_9}\right)^2\right] \end{aligned} \tag{5.3}$$

Compared to a single-Gaussian ToF fit at energies in 4.3–9 MeV, a two-Gaussian fit explicitely accounts for a considerable fraction of the prompt forward-peak background present in the ToF forward-peak, and therefore increases the signal-to-background ratio in the forward-peak signal component. In principle, long-lived cascade events such as those from ^{24}Na or ^{22}Na could also be eliminated in the ToF fit, since their ToF signature is different from that of the CDG signal (see Secs. 4.4.2.2 and 4.4.2.4). This approach is not feasible, however, for two reasons. First, the ToF signature of an individual isotope thus far cannot be determined with sufficient accuracy in Monte Carlo simulations, because the various effects of the detector electronics on ToF have

[8]Note the expected similarity of the ToF signature of the prompt multiple-photon forward-peak instrumental background in 4.3–9 MeV with the ToF signatures of the ^{24}Na and ^{22}Na cascade events (see Secs. 4.4.2.2 and 4.4.2.4, respectively).

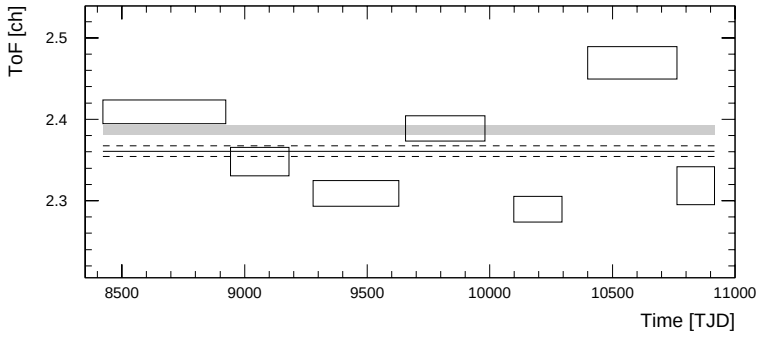

Figure 5.1: *The time-variation of the 17–30 MeV ToF forward-peak width (compare Fig. 3.15). The solid and dashed lines indicate the weighted mean of the inidividual values and its error, the thick grey line indicates the width and its error obtained for the combined data.*

not yet been included in sufficient detail. Second, the statistics of the ToF spectra in the CDG analysis is not sufficient to disentangle the individual contributions of a few components with rather similar ToF distributions.

In general, the statistics of the ToF spectra for a given energy interval ΔE and a given veto-rate interval Δv are insufficient for a robust and reliable determination of the six/nine model parameters in the ToF fits, in particular when analyzing subsets of the data to study the isotropy of the CDG. The robustness of the ToF-fitting procedure can be improved, however, by utilizing the results on the veto-rate variation of the individual model parameters as described in Sec. 4.3.5.

• *Single-Gaussian Fits (all $E_{\rm tot}$ intervals)*: The single-Gaussian models (Eqs. 4.6, 4.7, and 4.8) have six parameters, two of which exhibit very little variation with veto rate as depicted in Fig. 4.17: p_3, the width of the ToF forward-peak, and p_5, which describes the "shape" of the ToF continuum-background. These two parameters can therefore be fixed in the ToF fits as a function of veto rate. Their values are determined in a fit to the combined data in each energy interval ΔE, with all veto-rate intervals Δv summed. Fixing the parameters p_3 and p_5 in the fits of the ToF spectra for given energy and veto-rate intervals ΔE and Δv reduces the number of free parameters to four. When integrating the result for the forward-peak to determine the forward-peak flux, its statistical error is derived by propagation of the errors of the individual fit parameters, with the error of p_3 being the error from the combined fit.

• *Two-Gaussian Fits (4.3 MeV $< E_{\rm tot} <$ 9 MeV)*: The two-Gaussian models (Eqs. 5.1, 5.2 and 5.3) have nine parameters. The variation of the ToF continuum-background is unaffected by the modelling of the forward-peak, hence p_5 is again fixed at the result from the combined fit. The positions of the two Gaussians modelling the background and the signal component, p_8 and p_2, respectively, are fixed at the results obtained in the detailed ToF investigation as summarized in Table C.3. The widths of the two forward-peak components, p_3 and p_9, are not fixed at the results given in Table C.3, because the ToF investigation that revealed the drift of the forward-peak position in time (see Sec. 3.7) also revealed a small, erratic variation of the ToF resolution, illustrated in Fig. 5.1. Since this variation is expected to affect both forward-peak components in the same way, the *ratio* of the two widths is fixed in the fit of the combined data for energy interval ΔE to determine the values of the two parameters p_3

and p_9, which were then used in the fits as a function of veto rate. Hence the values of five parameters, p_2, p_3, p_5, p_8, and p_9, are fixed in the fits of the ToF spectra for given energy and veto-rate intervals ΔE and Δv, reducing the number of free parameters to four, as above for the single-Gaussian fits.

Which of the two models is to be preferred for analyzing the 4.3–9 MeV region? Both models have their advantages and disadvantages. The single-Gaussian fit is numerically robust and flexible with respect to systematic trends in the shape of the ToF forward-peak at the same time, thus providing a conservative approach. The two-Gaussian fit better represents the physical properties of the ToF forward-peak, and yields a significantly lower χ^2_ν when fitting the combined data for an energy interval. In the fits of the ToF spectra as a function of veto rate, which contain less events, both ToF models statistically describe the data equally well. A potential disadvantage of the two-Gaussian fit results from the restrictions that have to be imposed on it by fixing some parameter values. Although these restrictions are physically well founded, they may nevertheless, in general, introduce unwanted biases or systematic trends which could have significant influence on the final result after the veto-rate extrapolation.

Above 4.3 MeV the instrumental background is prompt. Hence both ToF models should yield the same result on the CDG intensity within statistical uncertainties. Comparing the results on the CDG intensity obtained with the two models in 4.3–6 MeV and 6–9 MeV indicates, however, that there is a significant discrepancy between both models in the 4.3–6 MeV range, while both results in general are consistent in the 6–9 MeV interval (examples are given in Chapter 6). The reason for the discrepancy in 4.3–6 MeV is not yet thoroughly understood, and since there is no *a priori* reason to favour either of the two results, both models have been considered in the analysis. It was not until the investigation of the isotropy of the CDG that independent evidence was obtained that the two-Gaussian model has to be considered inferior for the time being (see Sec. 6.2). The isotropy is not only studied by comparing CDG intensities, but also by direct comparison of ToF spectra — allowing us to estimate differences in intensity independent of any modelling of the ToF distribution. The results obtained from the subtraction of ToF spectra agree well with those obtained from the single-Gaussian model, but in general disagree with results from the two-Gaussian model. The final results therefore are derived with the single-Gaussian model. The behaviour of the two-Gaussian model for low-statistics ToF spectra will be further studied, however, since it is expected to be the superior model when implemented in a more refined way.

5.3 Subtraction of Long-Lived Instrumental Background

5.3.1 Overview

The variation of long-lived activity from nuclear decays and de-excitations with veto rate in general is complex, and in particular does not vary linearly with veto rate. Therefore, long-lived activity has to be subtracted from the ToF forward-peak flux as a function of veto rate *before* prompt and short-lived backgrounds can be eliminated by veto-rate extrapolation (Weidenspointner and Varendorff 1997).

In each veto-rate interval, the activity of the eight identified isotopes is self-consistently determined in an iterative procedure by fitting a set of three E_2 spectra and one $E_{\rm tot}$ spectrum[9]. The rationale of the iterative fitting procedure is illustrated in Fig. 5.2. In the top panel, the simulated E_1-E_2 distributions of the eight isotopes are schematically depicted for standard CDG selections (compare the detailed diagrams of the response to individual isotopes in Sec. 4.4.2). In general, there is considerable overlap in the E_1-E_2 distributions of individual isotopes (in particular around 1.3 MeV in E_2), which precludes separating each isotope from all other isotopes by suitable selections to independently determine each isotope activity. Therefore, an iterative procedure was introduced, which starts at the highest energies in E_1 and E_2, where the number of isotopes is smallest, and then proceeds down to the increasingly complex structures at lower E_1 and E_2 energies. The E_1-E_2 ranges of the four E_2 and $E_{\rm tot}$ spectra, chosen such as to enhance or suppress individual lines or spectral features, are indicated in the bottom panel of Fig. 5.2. As can be seen, the E_1-E_2 ranges covered by the second and third E_2 fit and by the $E_{\rm tot}$ fit overlap, hence the results of these fits are not statistically independent. The overlap is caused by the $E_{\rm tot}$ fit, which is necessary to properly separate the activites from ^{2}D and ^{28}Al. Hence inclusion or omission of the $E_{\rm tot}$ fit is a trade-off between systematic and statistical uncertainty. By iteratively fitting the second and third E_2 spectrum and the $E_{\rm tot}$ spectrum, both the systematic and the statistical uncertainty in the ^{2}D and ^{28}Al activities are minimized (all other isotopes are hardly affected by the overlap, see below). In additon, the iterative approach ensures the self-consistency of the determined isotope activities.

Also included in the lower panel of Fig. 5.2 are lines of constant $\bar{\varphi}$ and $E_{\rm tot}$. Comparison of the two panels of Fig. 5.2 provides a first indication of the many options for fitting individual lines, which can be enhanced or suppressed through the choice of the fit regions, and in addition through selections on $E_{\rm tot}$ and/or $\bar{\varphi}$. In particular, as ex-

[9]Ideally, the activity of the isotopes would be determined by fitting the two-dimensional event distribution in E_1 and E_2. At present, such two-dimensional fits are not feasible, however, for two reasons. First, in general the statistics is not sufficient in the CDG analysis, and second, we do not yet have a reliable model of the E_1-E_2 distribution of the continuum background, which is a blend of various components.

plained in Sec. 5.3.6.2, event selections may be used to suppress unidentified, long-lived spectral features, which cannot be eliminated by veto-rate extrapolation.

The purpose of the first E_2 spectrum, covering the E_1-E_2 region of 950–1250 keV in E_1 and 2000–3500 keV in E_2 (see Fig. 5.2), is to determine the activity from ^{24}Na. The signal from this isotope is optimized by selecting the E_1 range of the Compton edge of the 1.37 MeV photon interacting in D1 (see Fig. 4.22). The other three spectra are used to disentangle the activities from ^{2}D, ^{22}Na, ^{28}Al, ^{52}Mn, and ^{57}Ni. In these three spectra, the contributions from the natural radioactivity of ^{40}K and ^{208}Tl, as well as from the decay of ^{24}Na as determined from the first E_2 spectrum, can be calculated based on Monte Carlo simulations. The ^{2}D activity is assessed from fitting the $E_{\rm tot}$ spectrum ($E_{\rm tot}$ 1810–2800 keV, E_1 70–950 keV, and E_2 730–2800 keV, see Fig. 5.2). The second E_2 spectrum (E_1 500–950 keV, E_2 1500–3500 keV, see Fig. 5.2) is used to determine the activity from ^{28}Al, making use of the previous results on ^{24}Na and ^{2}D. Finally, the third E_2 spectrum is intended for determining the activities from the β^+-decays of ^{22}Na, ^{52}Mn, and ^{57}Ni, with the 270–350 keV range in E_1 being optimized for the Compton edge of 511 keV photons, and the E_2 range covering the energies 1100–3500 keV (see Fig. 5.2). Each of the four spectra is calculated as described in Appendix B. To optimize the ToF forward-peak instrumental-line signal in the spectra, the ToF range 110–130 channels is selected. All other selections, except the energy selections specified above, follow the CDG analysis standard (see Sec. 4.2.3).

In the fits the contributions from identified isotopes are modelled with templates obtained from Monte Carlo simulations. In deriving these templates, the same event selections have to be applied to the simulated events as to the data when calculating the respective spectra. In addition, the templates have to be corrected for the CDG effective area, just as the spectra. Because the changes of the shape of the templates for all isotopes and each spectrum due to the variation in the telescope configuration (see Table D.9) are negligible, all templates can be determined for a single, representative telescope configuration, which was chosen to be equal to that given in the last entry in Table D.9: all D1 modules on, D2 modules 01 and 02 off, and parts of D2 modules 11, 13, and 14 excluded due to PMT failure.

Finally, different CDG $E_{\rm tot}$ intervals contribute to the E_1-E_2 ranges covered by the three E_2 spectra. For standard CDG selections the CDG effective area varies with energy (see Fig. 3.12). This variation can be taken into account in the calculation of the E_2 and $E_{\rm tot}$ spectra and the respective templates. The resulting distortion of the shape of the continuum distribution in the E_2 spectra, however, cannot be modelled by a simple analytical function[10]. For this reason, and for the purpose of suppressing unidentified spectral features in the ToF spectra, optimized CDG event selections were used in the final CDG analysis, as described in Sec. 5.4.2, which were designed such that the CDG effective area is independent of $E_{\rm tot}$ in 1.2–4.3 MeV. Using these optimized

[10] An energy-dependence of $A_{\rm eff}$ does not degrade the $E_{\rm tot}$ fit, since the continuum function can be scaled with the respective effective area as a function of energy.

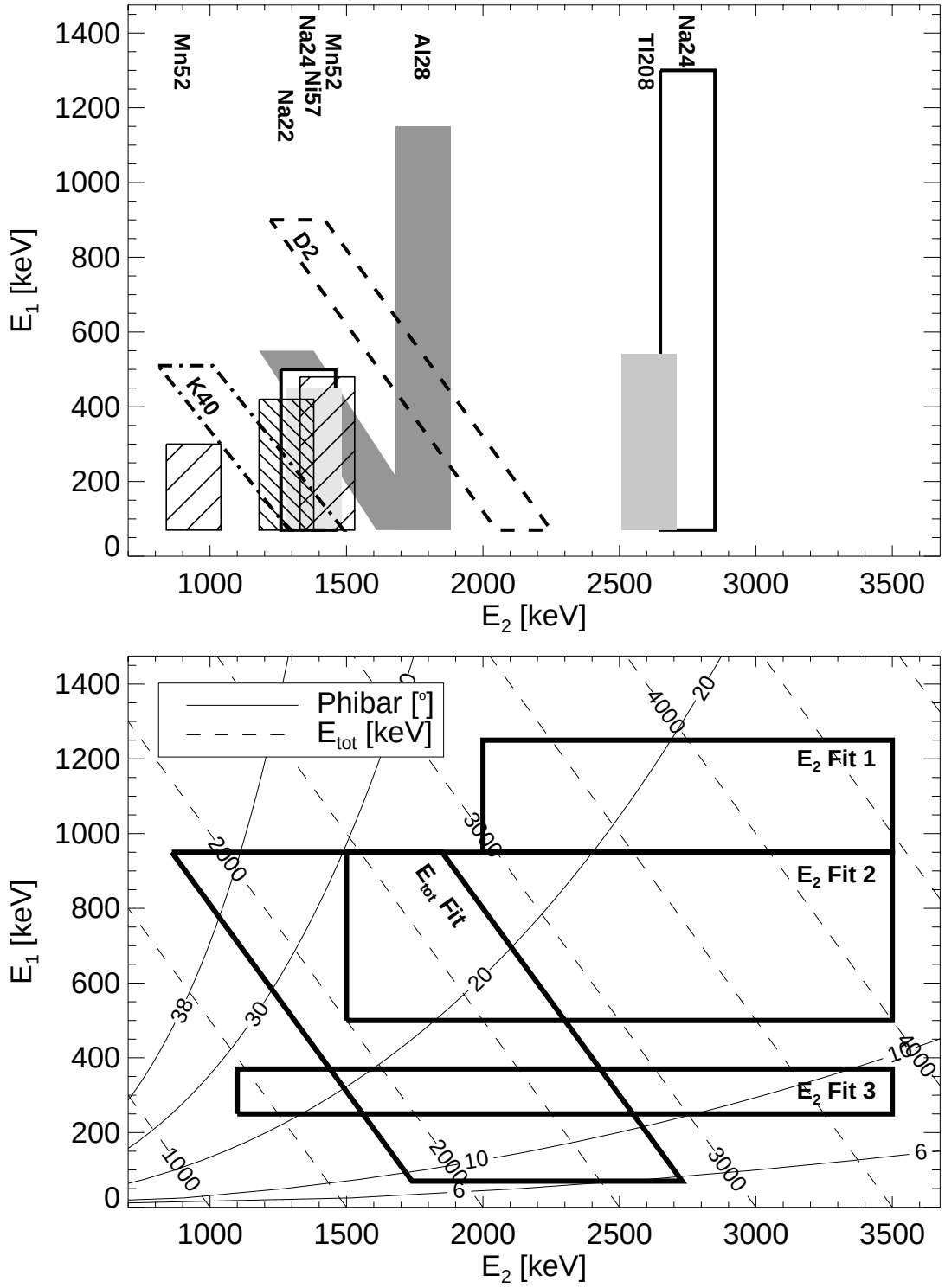

***Figure 5.2: Top Panel**: A schematic representation of the simulated E_1-E_2 distributions of the eight isotopes identified in the instrumental-line background. The "vertical" and "diagonal" bands represent multiple-photon and single-photon events, repectively (compare to the detailed individual diagrams in Sec. 4.4.2). **Bottom Panel**: An illustration of the E_1-E_2 ranges of the four E_2 and $E_{\rm tot}$ spectra used to determine the actvities from the background isotopes. Also plotted are lines of constant $\bar{\varphi}$ and $E_{\rm tot}$.*

CDG selections allows us to model the continua in the E_2 and $E_{\rm tot}$ spectra with an exponential in energy.

In the following, the eight individual fits of the iterative, self-consistent fitting procedure are briefly described[11]. The contributions from the naturally radioactive istopes ^{40}K and ^{208}Tl are not determined in these fits, but calculated from their known (^{40}K, see Sec. 4.4.2.3) or estimated (^{208}Tl, see Sec. 4.4.2.6) activities based on Monte Carlo simulations. Similarly, once the activity of an isotope has been determined from any spectrum, the isotope contribution to any other spectrum can be predicted using Monte Carlo simulation.

1. E_2 *Fit 1*: The activity due to the isotope ^{24}Na is determined.

2. $E_{\rm tot}$ *Fit*: The ^{2}D activity is estimated, with the contributions from ^{24}Na and ^{208}Tl being fixed. All other isotopes are neglected.

3. E_2 *Fit 2*: The ^{2}D and ^{28}Al activities are estimated, with the contributions from ^{24}Na and ^{208}Tl being fixed.

4. E_2 *Fit 3*: The activities due to the β^+-decays of ^{22}Na, ^{52}Mn, and ^{57}Ni are estimated, with the contributions from ^{2}D, ^{24}Na, ^{28}Al, ^{40}K, and ^{208}Tl being fixed.

5. $E_{\rm tot}$ *Fit*: The ^{2}D activity is determined, with the contributions from all other isotopes (^{22}Na, ^{24}Na, ^{28}Al, ^{40}K, ^{52}Mn, ^{57}Ni, and ^{208}Tl) being fixed.

6. E_2 *Fit 2*: The activity due to the isotope ^{28}Al is determined, with the contributions from ^{2}D, ^{24}Na, and ^{208}Tl being fixed.

7. E_2 *Fit 3*: The activities due to the β^+-decays of ^{22}Na, ^{52}Mn, and ^{57}Ni are determined. All other isotopes are fixed.

8. $E_{\rm tot}$ *Fit*: The ^{2}D activity is re-determined as in fit 5. Both results are compared to ensure the convergence of the procedure[12].

In the following sections, first each of the four different fits is discussed in detail, including the treatment of still unidentified spectral features, before the final subtraction of the isotope activities from the ToF forward-peak flux is explained. The spectra used to illustrate the line fitting procedure are in general based on the full CDG database (see Appendix D), which comprises observations from Phase I through Cycle 7. This

[11] A similar, albeit less involved, procedure consisting of four different fits was utilized by Kappadath (1998) to determine the activities of the five isotopes (^{2}D, ^{22}Na, ^{24}Na, ^{28}Al, and ^{40}K (fixed)) identified at that time.

[12] If the result for ^{2}D in fit 8 is the same as in fit 5, it follows that the next fit of the second E_2 spectrum would yield the same result as fit 6, and the next fit of the third E_2 spectrum would be the same as fit 7, implying that the result for ^{2}D from the next $E_{\rm tot}$ fit is identical to that of fit 8 ...

long-term database not only provides the best statistics available, but in additon allows us to distinguish crudely prompt and short-lived components from long-lived by virtue of their dependence on veto-rate. In particular, long-lived components reveal themselves through the presence of a veto-rate bump (see Sec. 4.6). Special attention is payed to unidentified long-lived components, since these can only be suppressed by tailored event selections (see Sec. 5.3.6).

5.3.2 E_2 Fit 1: Determining the ^{24}Na Activity

The fit of the first E_2 spectrum, which is used to determine the activity from ^{24}Na, is exemplified in Fig. 5.3. The veto-rate variation of the ^{24}Na activity has already been discussed in Sec. 4.6. The ^{24}Na template (and all other templates used in the line-fitting procedure) has not been smoothed in an attempt to reduce the statistical uncertainty, which is due to the limited number of available ^{24}Na simulations, because smoothing inevitably increases the systematic uncertainty due to distortions of the template shape. The "spikes" on the wings of the photopeak of the ^{24}Na template are an artifact of the fitting software.

Close inspection of the 2.75 MeV line in E_2 revealed that it cannot be fully accounted for by the decay of ^{24}Na. There is strong evidence for the presence of two additional, weak lines at $\sim$ 2.61 MeV and $\sim$ 2.93 MeV. In principle, these two additional lines could be artifacts of an incorrect modelling of the ^{24}Na response[13]. This hypothesis is unlikely, however, since the two lines differ in some important aspects from the ^{24}Na characteristics: their variation with veto rate and/or their dependence on E_1 and $\bar{\varphi}$. Both aspects will be exploited for the suppression of these unidentified lines, as explained in Sec. 5.3.6. In the fits, the two unidentified lines are each modelled by a Gaussian, with their positions and widths fixed[14].

5.3.3 E_{tot} Fit: Determining the ^{2}D Activity

The fit of the E_{tot} spectrum over the energy range 1810–2800 keV, which is used to determine the activity from ^{2}D, is exemplified in the top left panel of Fig. 5.4. Unexpectedly, detailed studies of the 2.2 MeV line lead to the conclusion that this line most likely is not exclusively due to thermal-neutron capture on hydrogen, but

[13]For example, if the energy resolution of the D2 detector is worse for in-flight conditions than during calibration on ground, the simulated template, which is based on the D2 resolution as determined in the instrument calibration (see Sec. 3.5), would be too narrow.

[14]In general, unidentified lines or spectral features are modelled by Gaussians in the line-fitting procedure. The position of such a Gaussian is fixed at the average of positions obtained in a series of test fits, in which all three parameters of the Gaussian (position, width and normalization) were allowed to vary freely. In addition, in the line fitting procedure the width of such a Gaussian is fixed at the nominal resolution at the line energy as determined in the instrument calibration (see Eqs. 3.6 and 3.7).

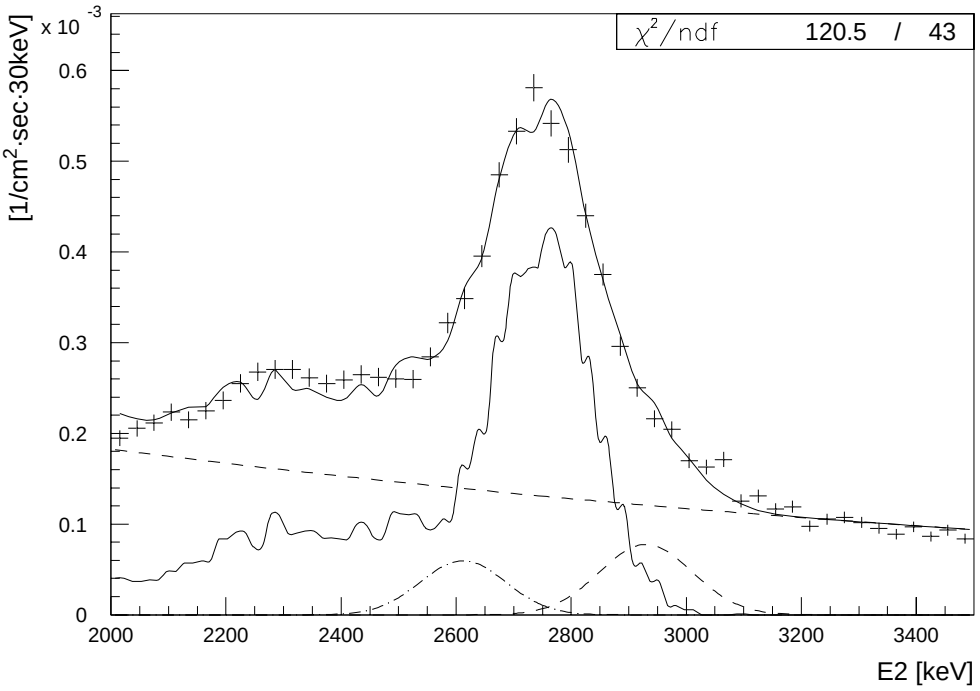

Figure 5.3: *An example of a fit of the first E_2 spectrum, which is used to determine the activity of ^{24}Na. In addition to the total fit, the ^{24}Na template, the two unidentified lines, and the exponential continuum are indicated.*

rather is a blend of at least two components. For the time being, the 2.2 MeV line is modelled as a blend of the internal 2.224 MeV photons from thermal-neutron capture on hydrogen, and an additional line at $\sim$ 2.29 MeV. Because of the importance of the veto-rate variation of the 2.2 MeV line as a probe of the systematics of the vero-rate extrapolation discussed in Sec. 5.5.2, the rationale for the existence of at least one additional component in the 2.2 MeV line is briefly summarized in the following.

In earlier studies the 2.2 MeV line was modelled by a single Gaussian (Weidenspointner 1994, Weidenspointner *et al.* 1996a)[15]. This simplistic approach was also pursued during the study of the 2.2 MeV line (see bottom right panel of Fig. 5.4) after the initial approach of modelling the 2.2 MeV line with the simulated ^{2}D template yielded unsatisfactory results (see bottom left panel of Fig. 5.4). The residual of the latter fit already provides strong evidence for the presence of additonal components in

[15]In these studies, the signal of the 2.224 MeV photons was optimized by accepting all $\bar{\varphi}$ values (the ^{2}D signal is strongest at high $\bar{\varphi}$ values, see Fig. 4.20), in contrast to the CDG selections. The position and the width of this Gaussian were found to be about 2228 keV and 82.2 keV, respectively, compared to the line energy of 2224 keV and the nominal width at this energy of 67 keV. Because the internal 2.224 MeV photons deposit relatively more energy in the D1 detector, which has a poorer energy resolution, than external photons at the same energy, some additional broadening of the instrumental 2.2 MeV line was expected. In addition, it was suspected at that time that statistical and systematic errors in the in-flight energy calibration may be responsible for additional line broadening and the line shift, respectively (Weidenspointner 1994).

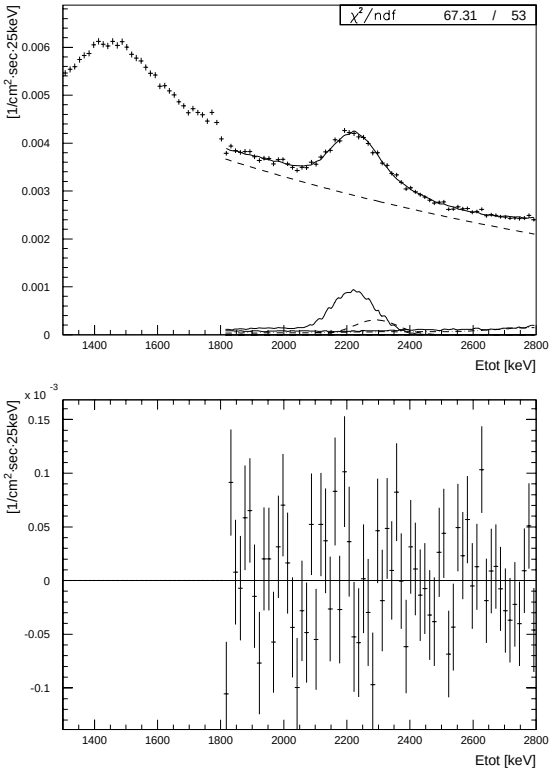

Figure 5.4: *Comparison of three different fit models for the 2.2 MeV line in E_{tot}. In addition to the fit, the fit components and the fit residuals are shown. The continuum is described by an exponential, with (fixed) contributions from ^{24}Na (solid line) and ^{208}Tl (dash dotted line).* ***Top left:*** *The 2.2 MeV line is modelled with two components: the ^{2}D template and a Gaussian at $\sim$ 2.29 MeV (dashed line) representing an unidentified line or spectral feature.* ***Bottom left:*** *The 2.2 MeV line is described with the ^{2}D template only. A significant residual indicates the presence of an additional component.* ***Bottom right:*** *A free Gaussian represents the 2.2 MeV line. The fit residual provides no clear evidence for an additonal component, however, the Gaussian parameters are inconsistent with what is expected for the ^{2}D line (see Fig. 5.5).*

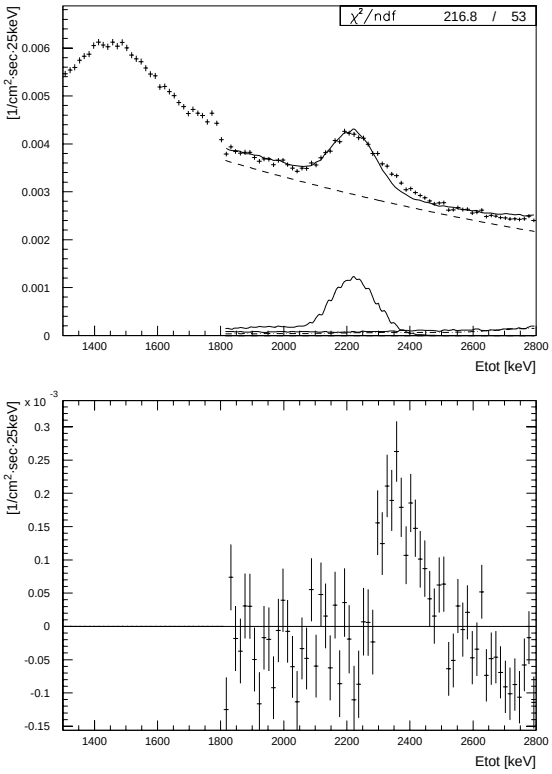

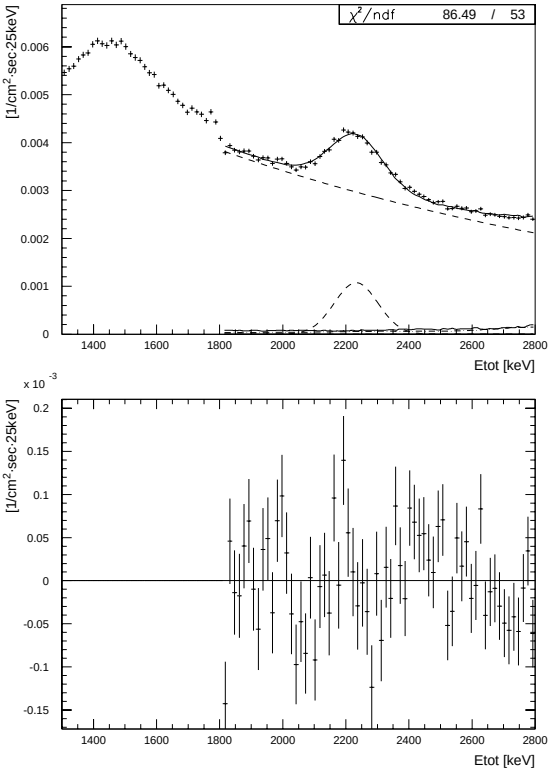

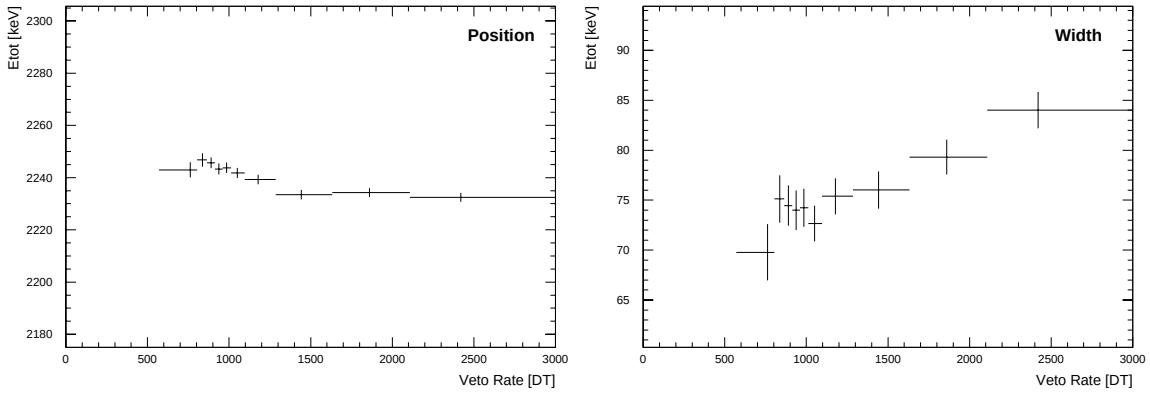

Figure 5.5: *The veto-rate variation of position (left panel) and width (right panel) of a Gaussian modelling the 2.2 MeV line in $E_{\rm tot}$ (see bottom right panel of Fig. 5.4). If the 2.2 MeV line were exclusively due to ^{2}D, both parameters should be indepenent of veto rate with values of 2224 keV and $\gtrsim$ 67 keV.*

the 2.2 MeV line, since the simulated template correctly accounts for the additional broadening of a line due to internal photons as compared to the width of line due to external photons. Further evidence for the presence of at least one additional component comes from the original modelling of the 2.2 MeV line as a function of veto rate with a single Gaussian. As depicted in Fig. 5.5, there is a trend for the position of the Gaussian to move to lower energies with increasing veto rate, and a pronounced increase of the width of the Gaussian with increasing veto rate. In addition, the position is persistently at energies above the nominal position, and similarly the width is significantly above the nominal width. Finally, if the 2.2 MeV line were due to a single component, this component so far would be the only one for which such shifts and additional, varying broadenings have been observed. Alternatively, the results on the 2.2 MeV line can be explained by assuming that at least one additional line or spectral feature is present. Introducing an additional Gaussian in the fit of the 2.2 MeV line suggested a line position of about 2.29 MeV, however, the residuals hint to either the presence of yet another, weaker line at slightly higher energy, or to the existence of a more extended feature that may include the suspecteded, unidentified 2.29 MeV line. The presence of an additional 2.2 MeV line component is supported by the fact that its veto-rate variation (see Sec. 5.3.6.1) is different from that of the ^{2}D activity (see Sec. 5.3.6.1).

5.3.4 E_2 Fit 2: Determining the ^{28}Al Activity

The ^{28}Al activity is determined from the fit to the second E_2 spectrum, exemplified in Fig. 5.6. The E_2 spectrum abruptly breaks down below about 1.4 MeV due to the E_1 selection of 500–950 keV. To minimize the effect of this break-down on the result, the fit range starts at 1500 keV. Also, the fit is stabilized at the lower end due to the fact that the ^{2}D contribution is fixed. Furthermore, by extending the fit range to the

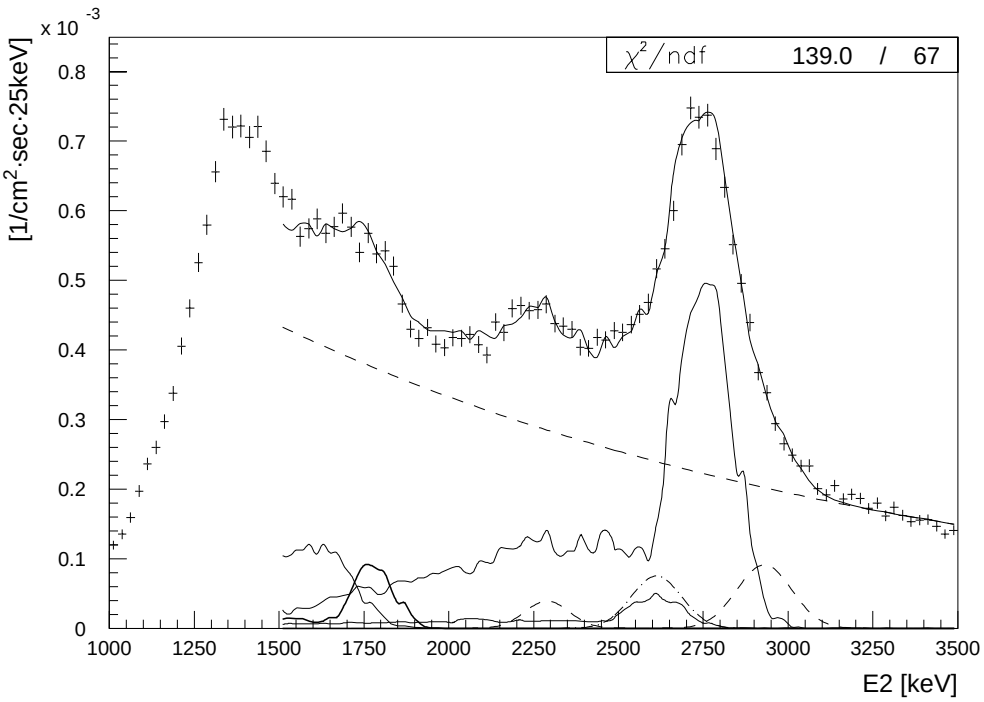

Figure 5.6: *An example for a fit of the second E_2 spectrum, which is used to determine the activity from ^{28}Al. In addition to the total fit, the templates for ^{2}D (the line-feature at $\sim$ 1.6 MeV, fixed), ^{28}Al (the 1.78 MeV line), ^{24}Na (the strong line at 2.75 MeV, fixed) and ^{208}Tl (the weaker line at 2.61 MeV, fixed), the three unidentified lines (dashed, dashed-dotted, and dashed lines), and the exponential continuum are indicated.*

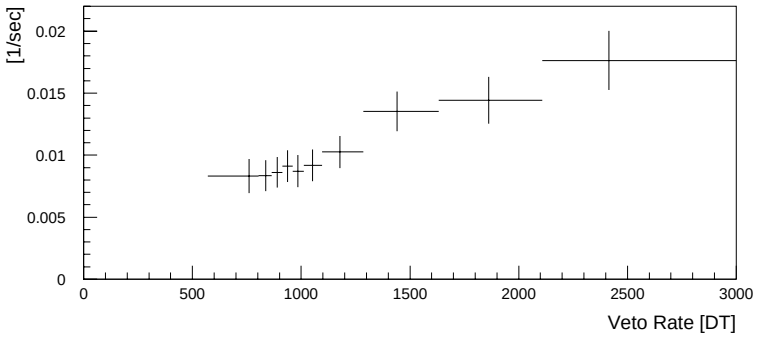

Figure 5.7: *The veto-rate variation of the ^{28}Al activity as determined from the fits of the second E_2 spectrum. As expected, the short-lived ^{28}Al activity varies linearly with veto rate (see Sec. 4.4.2.5).*

region of the (fixed) ^{24}Na line allows us to model the continuum background reliably .

In addition to the isotopes ^{2}D, ^{28}Al, ^{24}Na, and ^{208}Tl, and the unidentified E_2 lines at $\sim$ 2.61 MeV and $\sim$ 2.93 MeV (see Sec. 5.3.2), there is evidence for a weak, unidentified line, or rather extended feature or blend of lines, in 2.0–2.4 MeV (see also Kappadath 1998). In the fits, this feature is crudely modelled by a Gaussian at $\sim$ 2.29 MeV to minimize its effect on the exponential continuum background.

The observed variation of the ^{28}Al activity is shown in Fig. 5.7. As expected for a short-lived isotope, its activity varies linearly with veto rate, confirming its identifica-

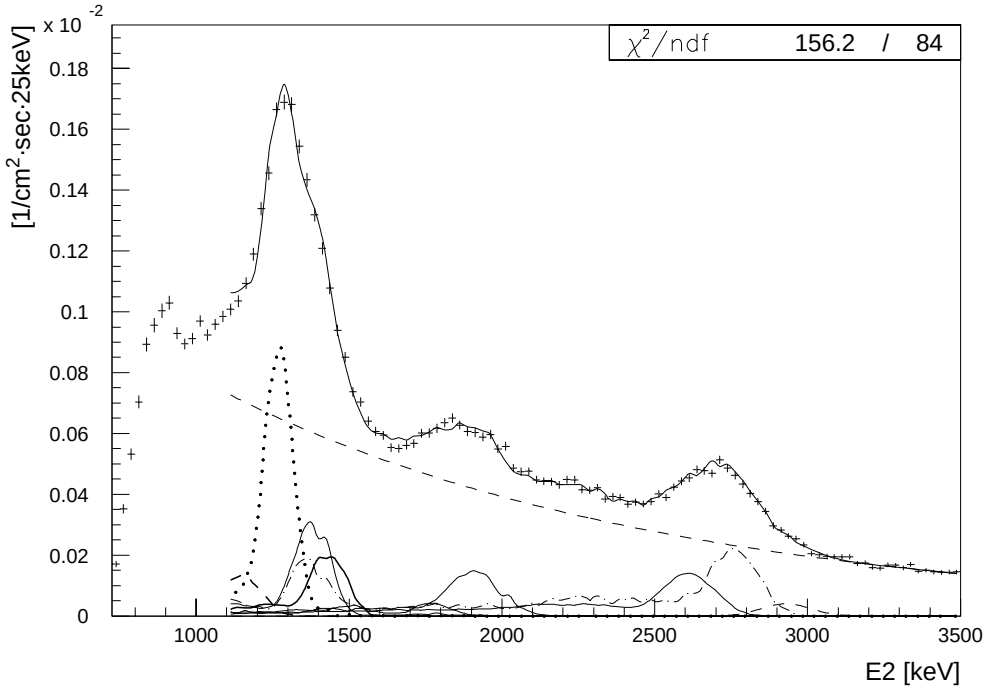

Figure 5.8: *An example for a fit of the second E_2 spectrum, which is used to determine the activities from ^{22}Na (dotted line), ^{52}Mn (thick solid line), and ^{57}Ni (thin solid line). Also depicted are the fixed components (^{2}D: solid line at 1.9 MeV, ^{24}Na: dash-dotted line, ^{28}Al: weak solid component below 1.9 MeV, ^{40}K: dashed line, ^{208}Tl: solid line at 2.6 MeV), as well as the total fit, the energy continuum, and the unidentified 2.93 MeV line.*

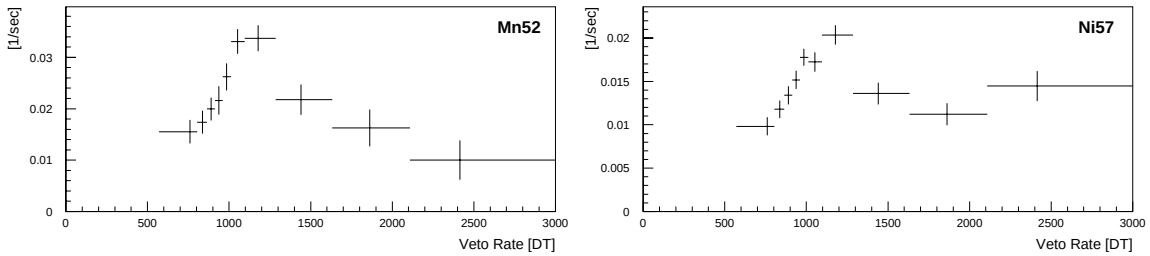

Figure 5.9: *The variation of the activity from ^{52}Mn (left) and ^{57}Ni (right) with veto rate. As expected, both isotope activities exhibit a pronounced veto-rate bump (see Secs. 4.4.2.7 and 4.4.2.8).*

tion (see Sec. 4.4.2.5).

5.3.5 E_2 Fit 3: Determining the Activities from ^{22}Na, ^{52}Mn, and ^{57}Ni

The activities due to the β^+-decays of ^{22}Na, ^{52}Mn, and ^{57}Ni are obtained from a fit of the third E_2 spectrum, exemplified in Fig. 5.8. Similar to the previous spectrum,

the third E_2 spectrum breaks down below about 1000 keV. The effect of this breakdown[16] is minimized by fitting only above 1100 keV. Except for the unidentified line at ~ 2.93 MeV, which as usual is modelled by a Gaussian, all other major spectral features can be accounted for by the eight identified isotopes. In particular, the fact that the spectral structures above 1.6 MeV are well reproduced by components (^{2}D, ^{24}Na, ^{28}Al, and ^{208}Tl)[17] which have been determined in the previous fits, supports the validity of the eight step fitting procedure. As can be seen in Fig. 5.8, the 1.3 MeV structure is accounted for by a blend of five isotopes: ^{22}Na, ^{24}Na (fixed), ^{40}K (fixed), ^{52}Mn, and ^{57}Ni. Disentagling this blend without prior knowledge of ^{24}Na and ^{40}K would hardly be possible.

The separation of ^{52}Mn and ^{57}Ni requires sufficient statistics, but in general is possible, as demonstrated in Figs. 4.47 and 5.9. As expected, both isotope activities exhibit a pronounced veto-rate bump. The veto-rate variation of the ^{22}Na has already been discussed in Sec. 4.6.

5.3.6 Unidentified Lines and Spectral Features

In the iterative line-fitting procedure described above four still unidentified lines or spectral features had to be modelled with Gaussians. The ~ 2.61 MeV and ~ 2.93 MeV lines in E_2 are present over a wide range of E_1 energies, suggesting that they are probably due to multiple-photon events. This may also be true for the 2.0–2.4 MeV feature in E_2 and the ~ 2.29 MeV line in $E_{\rm tot}$, but, at present a single-photon origin is also possible, especially for the latter line.

The activity due to unidentified background components cannot be explicitely subtracted from the ToF forward-peak flux, because their dataspace distribution is not known[18]. Two strategies can be pursued to eliminate or at least minimize the effect of unidentified background components on the result for the CDG spectrum. First, if the unidentified background can be shown to be prompt or short-lived, it will be eliminated or greatly reduced in the veto-rate extrapolation. Second, long-lived components, which cannot be eliminated by veto-rate extrapolation, may be suppressed in the ToF spectra by tailored selections on $\bar{\varphi}$ (or E_1).

---

[16] If the low-energy threshold is included in the fit, the results on the line activities hardly change. The "line" at about 950 keV is an artifact of the energy-dependence of the effective area at the lowest energies.

[17] As shown in Fig. 4.35, a small veto-rate dependence is observed for the ^{208}Tl activity when included as a free parameter in the third E_2 fit. This variation may be due to a contribution from the unidentified ~ 2.61 MeV line, which, however, in general is negligible.

[18] At best, the activity modelled by the Gaussian describing an unidentified line accounts for the photopeak. The full dataspace distribution, however, can be quite complex and extend over a wide energy range (see the dataspace distributions of identified isotopes in Sec. 4.4.2).

5.3.6.1 Veto-Rate Variation

The veto-rate variation of the four unidentified lines and spectral features is shown in Fig. 5.10[19]. The strong increase of the event rate in the $\sim$ 2.61 MeV line as well as in the $\sim$ 2.0–2.4 MeV excess exhibits a strong increase with increasing veto rate, suggesting that both components are prompt or at least sufficiently short-lived to be eliminated by the veto-rate extrapolation.

Similarly, the event rate in the $\sim$ 2.29 MeV line in $E_{\rm tot}$ increases with increasing veto rate, however, there is an indication of a weak veto-rate bump. The $\sim$ 2.29 MeV line may therefore be on the verge of being long-lived with a half-life of several minutes (compare the veto-rate variation of ^{28}Al in Fig. 5.7, which has a half-life of 2.2 min), but is still sufficiently short-lived to be severely reduced by the veto-rate extrapolation. The situation is different for the $\sim$ 2.93 MeV line in E_2, whose event rate exhibits a pronounced veto-rate bump, indicating that this line is due to a long-lived process.

Considering these veto-rate dependences it follows that the $\sim$ 2.93 MeV line is critical for the CDG analysis, since it can only be suppressed by applying tailored event selections when summing the ToF spectra, as discussed in the next section.

5.3.6.2 Dependence on $\bar{\varphi}$

To assess the potential of tailored $\bar{\varphi}$ selections for suppressing lines or spectral features, in particular those not identified, in the ToF spectra, the $\bar{\varphi}$ distribution of the ToF forward-peak was determined for standard CDG selections and compared to the simulated $\bar{\varphi}$ distribution of an $E^{-2.5}$ power-law CDG.

• *2.7–4.3 MeV*: The bulk of the events in the unidentified, long-lived E_2 line at $\sim$ 2.93 MeV are contained in the 2.7–4.3 MeV interval in $E_{\rm tot}$[20]. The 2.7–4.3 MeV ToF forward-peak $\bar{\varphi}$-distribution, obtained from ToF fits a function of $\bar{\varphi}$ for standard CDG selections, and the corresponding CDG $\bar{\varphi}$-distribution obtained from simulation are compared in Fig. 5.11. In the left panel, the absolute spectra are compared, with the CDG simulation being scaled based on the final result for the 2.7–4.3 MeV CDG intensity (see Sec. 6.3.3). It is interesting to note the $\sim 19^\circ$ peak in the forward-peak distribution due to ^{24}Na (compare Fig. 4.22). In the right panel, the ratio of the CDG and ToF forward-peak distribution is given, which serves as a measure of the signal-to-background ratio. This comparison suggests that rejecting all events with $\bar{\varphi} < 21^\circ$ severly reduces contributions from instrumental lines, both identified and

[19]The event rate in the 2.0–2.4 MeV feature was determined by summing the fit residuals in this energy range, including the event rate in the $\sim$ 2.29 MeV Gaussian in E_2. Similar results were obtained by Kappadath (1998), except for the $\sim$ 2.29 MeV Gaussian in $E_{\rm tot}$, which was not included in the his analysis.

[20]The event selections require than $E_1 \geq 70$ keV, and generally $E_1 \lesssim 1.2$ MeV (see the E_1 spectrum in Fig. 4.19)

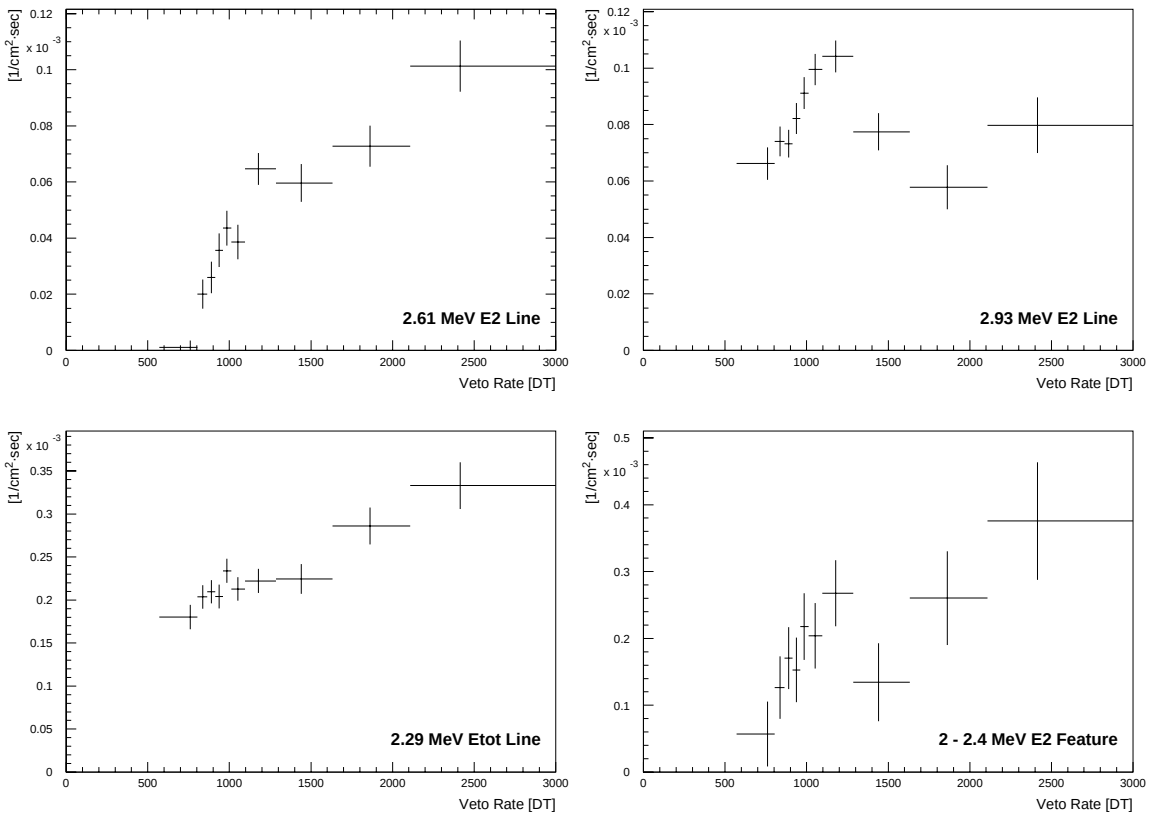

Figure 5.10: *The veto-rate variation of the most significant unidentified lines and spectral features: the E_2 lines at ∼2.93 MeV and ∼2.61 MeV, the $E_{\rm tot}$ line at ∼2.29 MeV, and the ∼ 2.0–2.4 MeV feature in E_2. The ∼2.61 MeV line and the ∼ 2.0–2.4 MeV feature both seem to be prompt or short-lived. The ∼ 2.29 MeV line appears to be on the verge of being long-lived (a weak veto-rate bump is indicated), but is still dominantly short-lived, while the ∼ 2.93 MeV line definitely is long-lived as can be seen from the pronounced veto-rate bump.*

unidentified. E_2 spectra for the standard CDG $6° - 38°$ $\bar{\varphi}$ selection, and for the $\bar{\varphi}$ ranges $6° - 21°$ and $21° - 38°$ are compared in Fig. 5.12. As expected, the $21° - 38°$ cut on $\bar{\varphi}$ practically removes the ^{24}Na photopeak as well as the unidentified lines at ∼ 2.61 MeV and ∼ 2.91 MeV, which is therefore applied in the final analysis of the CDG (see Sec. 5.6.1.1).

• *0.8–1.2 MeV, 1.2–1.8 MeV, and 1.8–2.7 MeV*: The unidentified spectral features in the $E_{\rm tot}$ 0.8–2.7 MeV range are either prompt or sufficiently short-lived for the veto-rate extrapolation to remove or severly reduce their contributions to the CDG result. The ToF forward-peak and CDG $\bar{\varphi}$ distributions in the three lowest energy intervals used in the CDG analysis (0.8–1.2 MeV, 1.2–1.8 MeV, and 1.8–2.7 MeV) for standard CDG selections are compared in Fig. 5.13. Other than in the 2.7–4.3 MeV $E_{\rm tot}$ interval, no significant suppression of indentified or unidentified lines and spectral features is possible below 4.3 MeV. An attempt to optimize the 1.2–1.8 MeV analysis by applying a $25° - 38°$ $\bar{\varphi}$ selection failed, since it enhanced the veto-rate bump relative

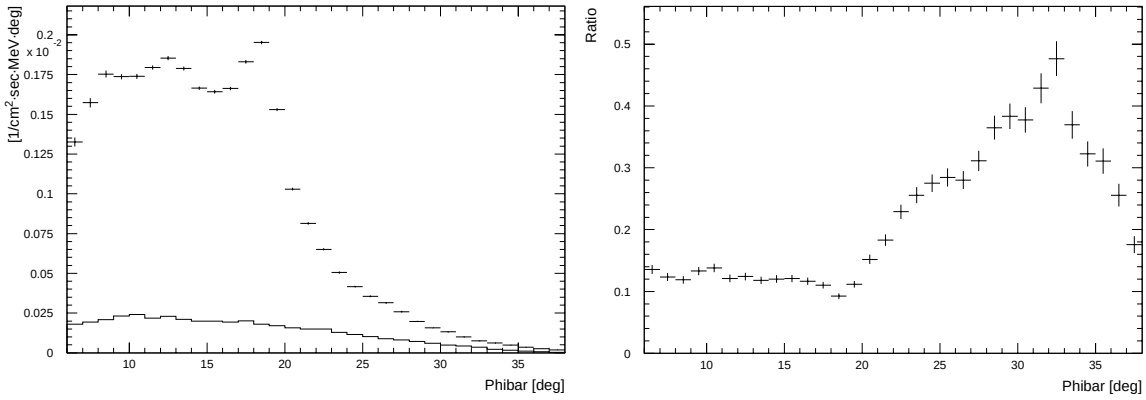

Figure 5.11: *A comparison of the ToF forward-peak and the CDG $\bar{\varphi}$-distributions for standard CDD selections in E_{tot} 2.7–4.3 MeV. The absolute spectra are shown in the left panel, with the data points and the histogram representing the forward-peak and the CDG, respectively. The right panel gives the ratio of CDG and forward-peak distribution.*

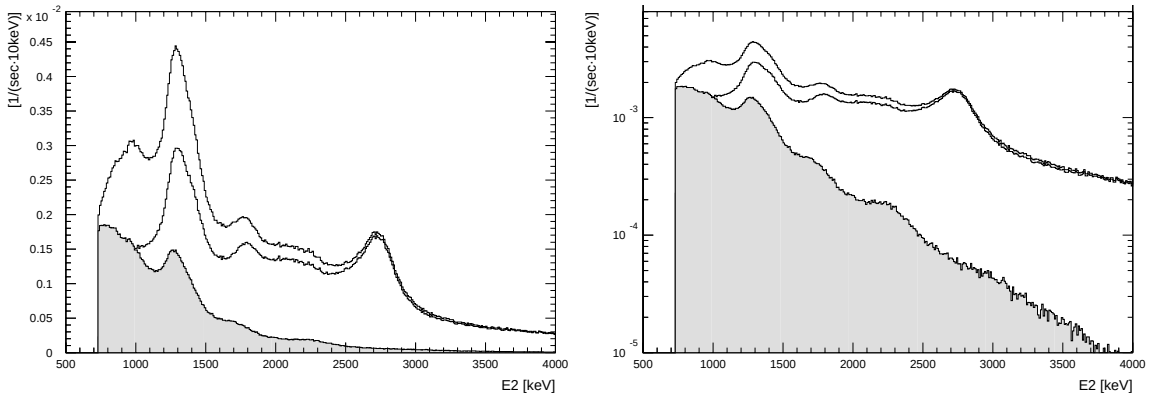

Figure 5.12: *A comparison of E_2 spectra for the standard CDG $6° - 38°$ $\bar{\varphi}$ selection (thick histogram), and for the $\bar{\varphi}$ ranges $6° - 21°$ (thin histogram) and $21° - 38°$ (filled histogram). The spectra are given in linear and logarithmic scaling in the left and right panel, respectively. The $21° - 38°$ cut on $\bar{\varphi}$ practically removes the ^{24}Na photopeak as well as the unidentified lines at $\sim$ 2.61 MeV and $\sim$ 2.91 MeV.*

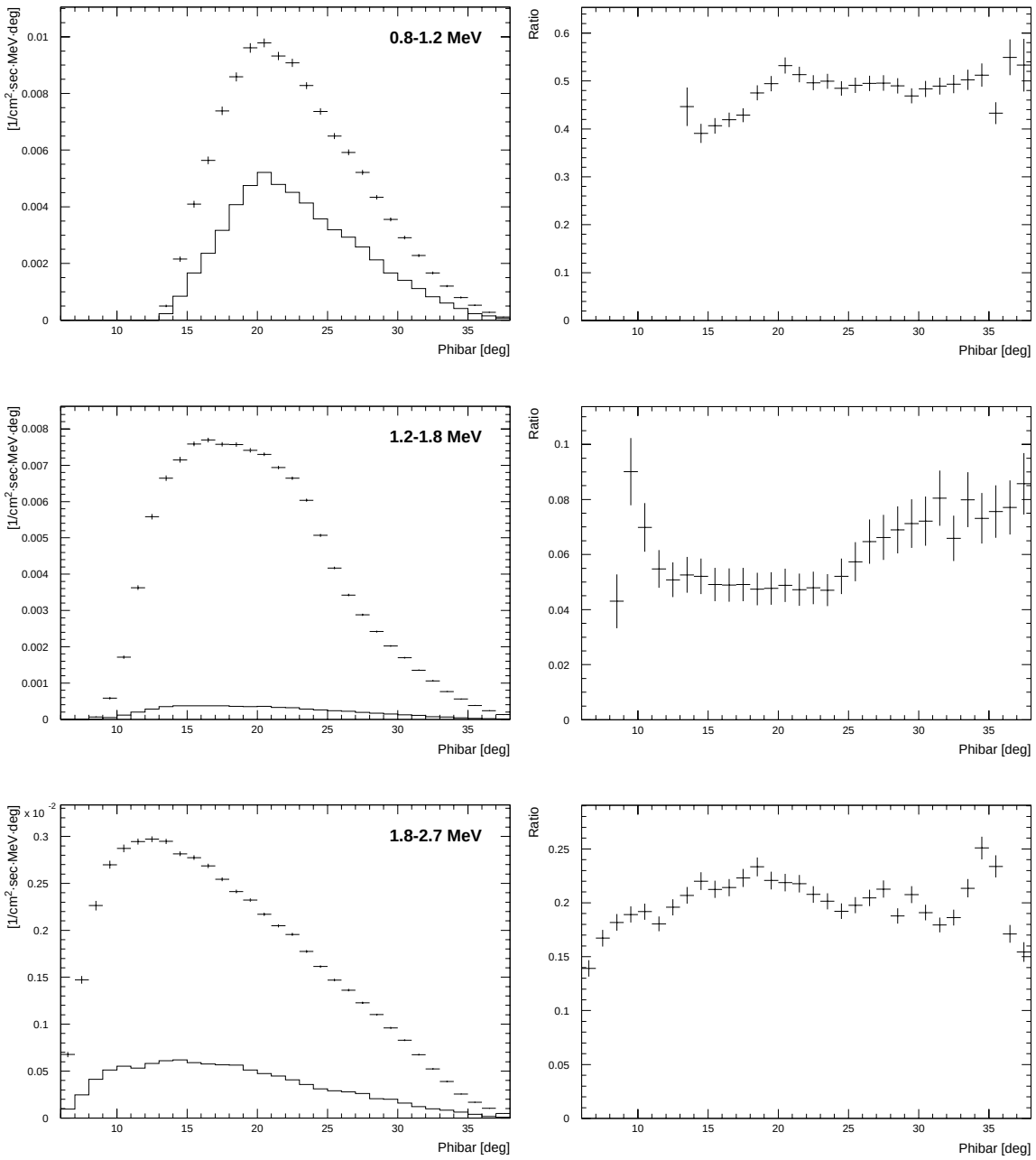

Figure 5.13: *A comparison of the ToF forward-peak and CDG $\bar{\varphi}$-distributions in the E_{tot} intervals 0.8–1.2 MeV (top), 1.2–1.8 MeV (middle), and 1.8–2.7 MeV (bottom) for standard CDG selections. The absolute spectra are shown in the left panels, with the data points and the histogram representing the forward-peak and the CDG, respectively. The right panels give the ratio of CDG and forward-peak distribution.*

to the general, prompt background. The veto-rate bump is due to remaining, still unidentified long-lived background components, as discussed in the following section.

5.3.7 Subtraction of Isotope Activities

As described above, the self-consistent determination of the activities due to the decay of long-lived isotopes inevitably requires the determination of all isotope activities, whether long-lived, short-lived or prompt. It is therefore possible to subtract not only the contributions from long-lived isotopes to the ToF forward-peak flux, but also those from short-lived and prompt components before the linear veto-rate extrapolation is performed. As discussed in detail below, subtraction of long-lived components removes, or at least significantly reduces, the veto-rate bump, while subtraction of prompt and short-lived components decreases the slope of the forward-peak flux variation, thereby reducing the systematic and the statistical uncertainty in the derived CDG intensity, respectively.

The activities of ^{2}D, ^{24}Na, and ^{28}Al subtracted from the respective ToF forward-peak fluxes are those obtained in fits 8, 1, and 6 (see Sec. 5.3.1), respectively. The subtraction of the activities due to the β^{+}-decays of ^{22}Na, ^{52}Mn, and ^{57}Ni is based on the results from fit 7. The simulated responses to each of these isotopes allows us to calculate their contributions to the ToF forward-peak flux in each of the CDG energy intervals based on the activity determined from a particular E_2 or $E_{\rm tot}$ spectrum, and taking into account the CDG selections. The contributions from the naturally radioactive isotopes ^{40}K and ^{208}Tl need not be determined from the line fits, but can be computed based on the known activities and Monte Carlo simulations.

A final point in the subtraction of isotope activities is that the ToF forward-peak flux is obtained from an integration of the full forward-peak, while the $E_{\rm tot}$ and E_2 spectra used in the line-fitting procedure were summed for a ToF selection of 110–130 channels, and therefore contain only a fraction of the total isotope ToF forward-peak contribution. This effect is accounted for in the subtraction by applying so-called flux-correction factors to the isotope activities. These factors, defined as the ratios of the total ToF forward-peak flux and the forward-peak flux in ToF channels 110–130, were derived assuming that the ToF distribution of the instrumental-line background is equal to that of the total ToF forward-peak. This is true to a good approximation, since the instrumental-line background is the dominant forward-peak component. The flux-correction factors, for each of the three ToF models (see Eqs. 4.6, 4.7, and 4.8) and each of the four lowest CDG energy intervals[21], are summarized in Table 5.1.

After these general considerations, the subtraction of isotope activities is discussed separately for each of the four CDG intervals below 4.3 MeV[22]. In addition, different $\bar{\varphi}$-

[21]The correction factors for the 4.3–6 MeV and 4.3–9 MeV intervals are not listed, since these energy bins are practically free of instrumental-line background.

[22]A few isotopes, such as ^{24}Na and ^{28}Al, make minor contributions to the ToF forward-peak flux

	0.8–1.2 MeV	1.2–1.8 MeV	1.8–2.7 MeV	2.7–4.3 MeV
Parabolic	1.108	1.075	1.031	1.020
Exponential	1.172	1.107	1.052	1.035
Gaussian	1.122	1.085	1.038	1.027

Table 5.1: *The flux-correction factors applied to the isotope activities upon their subtraction from the ToF forward-peak flux below 4.3 MeV for each of the three ToF models.*

selections are compared in the 1.2–1.8 MeV and 2.7–4.3 MeV energy intervals[23] based on the results on the $\bar{\varphi}$-variation of the signal-to-background ratio obtained in the previous section. The discussion commences with the highest of the four energy intervals, where the least number of instrumental components is present, and progresses down to lower energies with more complex line structures. For clarity, only results obtained with the Gaussian ToF model (see Eq. 4.8) are considered here. The systematic differences between the three ToF models will be discussed in Secs. 5.6.1.2 and 6.3.2.

5.3.7.1 Isotope Subtraction in 2.7–4.3 MeV

The 2.7–4.3 MeV ToF forward-peak flux before and after the subtraction of the instrumental-line background contributions for $\bar{\varphi}$ in $8.3° - 38°$ and $21° - 38°$ is depicted in the left and right panel of Fig. 5.14, respectively. In addition, the linear veto-rate extrapolations and the residuals of these fits are shown. The data used in this comparison consist of the full CDG database (see Appendix D), which not only minimizes statistical uncertainties, but also provides the best sensitivity for yet unidentified long-lived background components.

A pronounced veto-rate bump is present in the ToF forward-peak flux for both selections on $\bar{\varphi}$. As expected from the investigation of the 2.7–4.3 MeV ToF forward-peak $\bar{\varphi}$-spectrum (see Sec. 5.3.6.2), the amplitude of the veto-rate bump is less for the $21° - 38°$ $\bar{\varphi}$-cut, which suppresses the E_2 lines around 2.75 MeV than for the wider $8.3° - 38°$ selection. After subtracting the isotope activities as a function of veto rate, the bump is severely reduced in both cases, indicating that the isotope ^{24}Na produces the bulk of the veto-rate bump in the 2.7–4.3 MeV interval. The bump-like structure of both fit residuals strongly suggests, however, that not all long-lived

in the 4.3–6 MeV or 4.3–9 MeV energy intervals. These contributions are subtracted in the CDG analysis, but their subtraction is not explicitely discussed in the following.

[23] As will be summarized in Sec. 5.4.2, the two sets of $\bar{\varphi}$-selections are the so-called "adjusted-standard selections" and the so-called "optimized selections". The former are almost identical to the standard selections defined in Sec. 4.2.3, except for minor changes of the $\bar{\varphi}$ ranges in 1.2–4.3 MeV to achieve an effective area independent of energy. The latter result from the attempt to maximize the CDG signal in each $E_{\rm tot}$ interval (see Secs. 5.3.6.2 and 5.4.1).

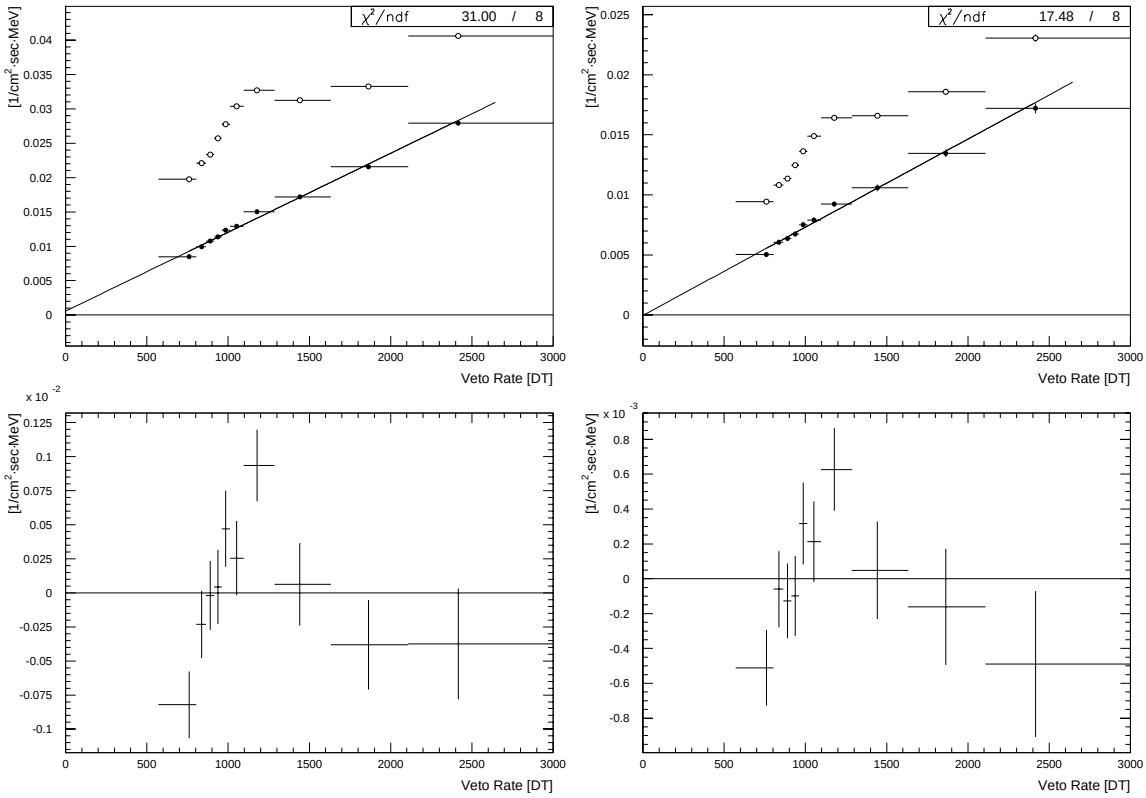

Figure 5.14: *A comparison of the 2.7–4.3 MeV ToF forward-peak flux before and after the subtraction of the instrumental-line background contributions for $\bar{\varphi}$ in $8.3° - 38°$ (left panels) and $21° - 38°$ (right panels) as obtained for the full CDG database (see Appendix D). In addition, the linear veto-rate extrapolations and the residuals of these fits are shown.*

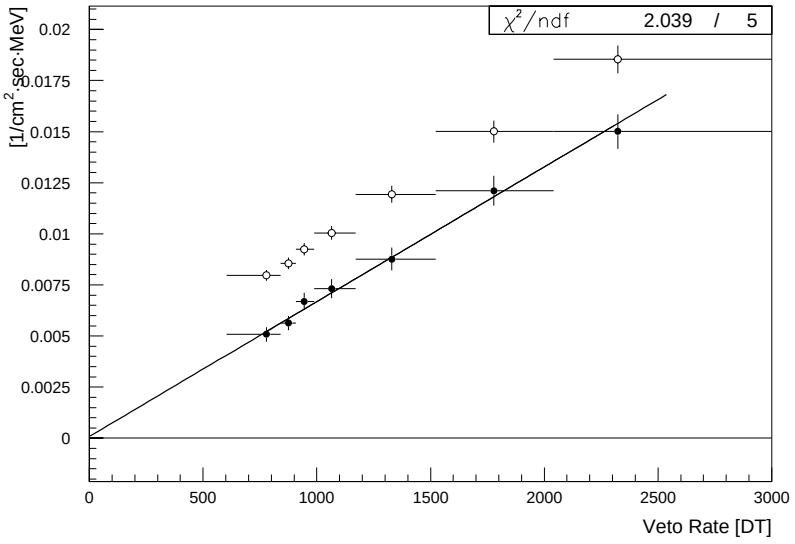

Figure 5.15: *The 2.7–4.3 MeV ToF forward-peak flux before and after the subtraction of the instrumental-line background contributions, together with the veto-rate extrapolation. The data are those used to derive the final result on the 2.7–4.3 MeV CDG intensity (see Sec. 6.2).*

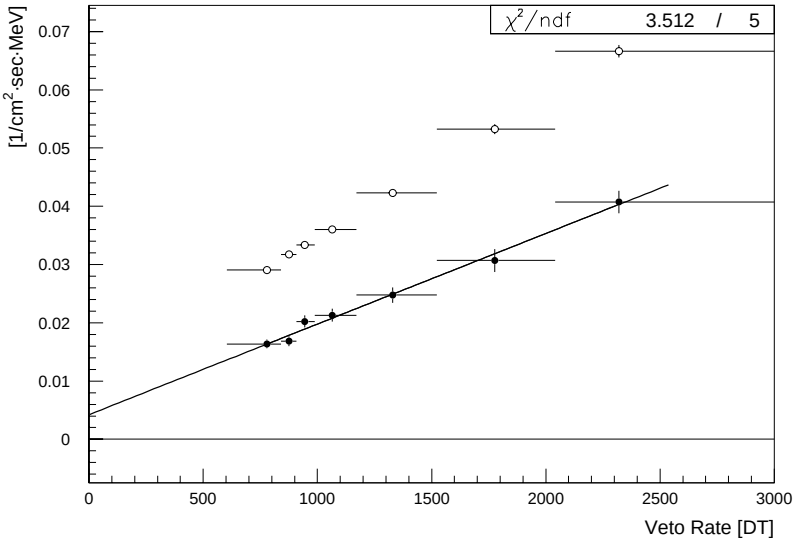

Figure 5.16: *The 1.8–2.7 MeV ToF forward-peak flux before and after the subtraction of the instrumental-line background contributions, together with the veto-rate extrapolation. The data are those used to derive the final result on the 1.8–2.7 MeV CDG intensity (see Sec. 6.2).*

instrumental background is yet identified or accounted for[24]. Close examination of the residuals shows that the optimized $\bar{\varphi}$-selection is slightly more effective in excluding yet unidentified long-lived background, and therefore a $21° - 38°$ $\bar{\varphi}$-selection is applied in the final CDG analysis (see Sec. 5.6).

The final result for the CDG intensities below 4.3 MeV is determined from a subset of the full CDG database, which comprises those OPs during which the general level of long-lived activity was at its absolute minimum, and which therefore is referred to as minimum-activity (MA) database (see Sec. 6.2). The 2.7–4.3 MeV ToF forward-peak flux before and after the subtraction of the instrumental-line background contributions, derived from this MA database for the optimized $21° - 38°$ selection on $\bar{\varphi}$, is depicted in Fig. 5.15, together with the veto-rate extrapolation. There is no indication of the presence of a veto-rate bump, and hence the systematic uncertainty of the extrapolation has been minimized.

5.3.7.2 Isotope Subtraction in 1.8–2.7 MeV

The comparison of the 1.8–2.7 MeV ToF forward-peak and CDG $\bar{\varphi}$-distributions in Sec. 5.3.6.2 suggested that no significant improvement of the signal-to-background ratio can be achieved by optimized $\bar{\varphi}$-selections in this energy range. This result was confirmed by deriving the 1.8–2.7 MeV CDG intensity for different ranges in $\bar{\varphi}$ — no significant differences could be found. Therefore the final result on the CDG intensity in this energy range was determined with the adjusted-standard CDG selection of $10.5° - 38°$ (see Sec. 5.4.2). The MA database 1.8–2.7 MeV ToF forward-peak flux before and after the subtraction of the instrumental-line background contributions and

[24]For example, the $21° - 38°$ selection may not completely eliminate the Compton tail of the unidentified ~ 2.93 MeV line.

the veto-rate extrapolation are shown in Fig. 5.16. Similar to the 2.7–4.3 MeV interval, no veto-rate bump impairs the reliability of the extrapolation. The slope of the increase of the forward-peak flux with veto rate is significantly reduced after the subtraction, mostly due to the removal of the strong, prompt ^{2}D activity. It has to be noted, however, that studies utilizing the full CDG database indicated the presence of yet unidentified long-lived background, similar to the 2.7–4.3 MeV interval.

5.3.7.3 Isotope Subtraction in 1.2–1.8 MeV

Based on the result of the $\bar{\varphi}$-dependence of the signal-to-background ratio in the 1.2–1.8 MeV energy range (see Sec. 5.3.6.2), the full CDG database 1.2–1.8 MeV ToF forward-peak fluxes, before and after the subtraction of the instrumental-line background contributions, are compared for $\bar{\varphi}$ in $6° - 38°$ and in $23.2° - 38°$ in Fig. 5.17. Also shown are the linear veto-rate extrapolations and the fit residuals.

For both selections the very pronounced veto-rate bump is strongly reduced after subtraction of contributions from identified isotopes, indicating that the bulk of the long-lived activitiy has been identified. The presence of a significant residual veto-rate bump, however, clearly indicates that some weak, long-lived background components still need to be accounted for. Contrary to expectations, the residual veto-rate bump is more significant for the "optimized" $23.2° - 38°$ selection than for the adjusted-standard selection of $6° - 38°$. In addition, the forward-peak flux obtained for optimized selections tends to be slightly larger than that obtained for adjusted-standard selections, and correspondingly the CDG intensity is lower for the adjusted-standard than for the optimized selections.

Given the fact that not all long-lived background has yet been identified, which of the two selections is more suited for deriving the final CDG intensity? In priniciple, the veto-rate extrapolation is only justified in absence of any long-lived background. In this case all $\bar{\varphi}$-selections should yield the same CDG intensity[25]. If unaccounted long-lived background is present, then it affects the residual ToF forward-peak flux in two ways: it increases the amplitude of the veto-rate bump, and it increases the general level of the residual flux[26]. Both indicators favour the adjusted-standard selection, which seems to be less succeptible for the yet unidentified long-lived background in 1.2–1.8 MeV and which is therefore applied in the final analysis.

The 1.2–1.8 MeV ToF forward-peak flux before and after the subtraction of the instrumental-line background contributions, derived from the MA database for the adjusted-standard $6° - 38°$ selection on $\bar{\varphi}$, is depicted in Fig. 5.18, together with the veto-rate extrapolation. The weak veto-rate bump present in the ToF forward-peak

[25] To a good approximation, this situation is realized above 4.3 MeV, as discussed in Sec. 5.4.1.

[26] The flux determination involves a correction for the CDG effective area, which takes into account all event selections. Therefore the flux due to the CDG is *independent* of the $\bar{\varphi}$-selection applied to the data, in contrast to the contribution from instrumental background.

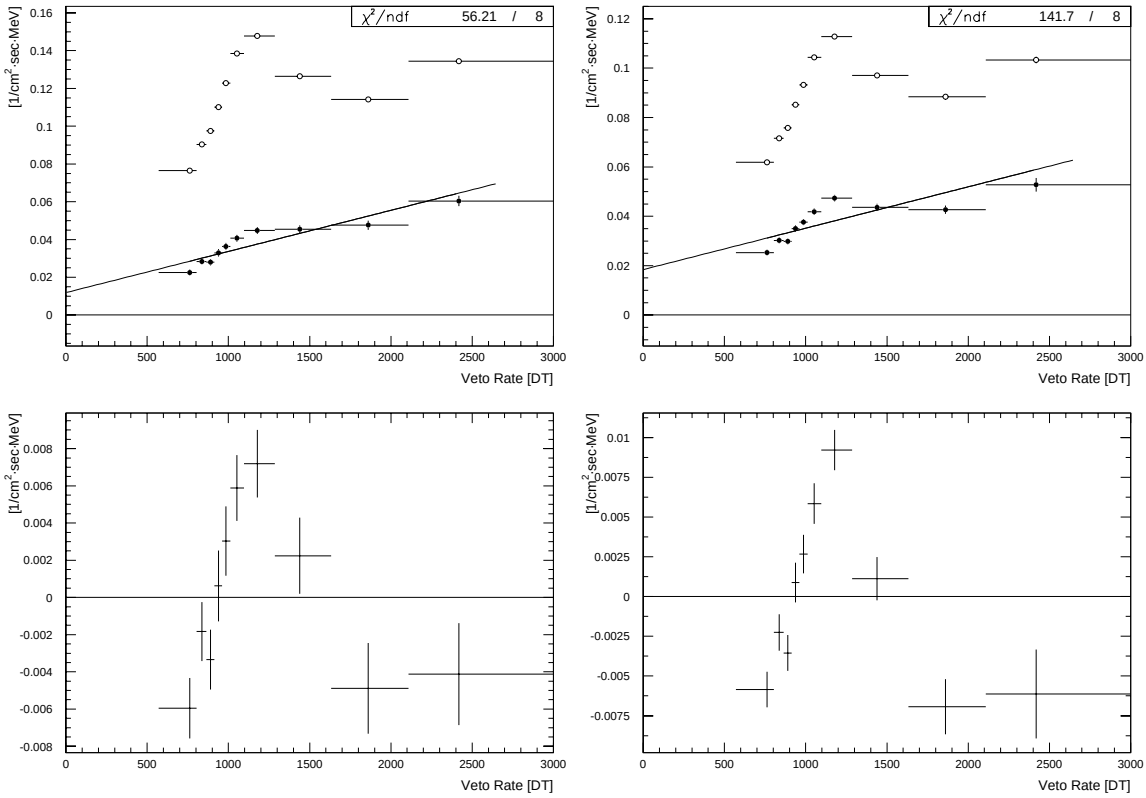

Figure 5.17: *A comparison of the 1.2–1.8 MeV ToF forward-peak flux before and after the subtraction of the instrumental-line background contributions for $\bar{\varphi}$ in $6° - 38°$ (left panels) and $23.2° - 38°$ (right panels) as obtained for the full CDG database (see Appendix D). In addition, the linear veto-rate extrapolations and the residuals of these fits are shown.*

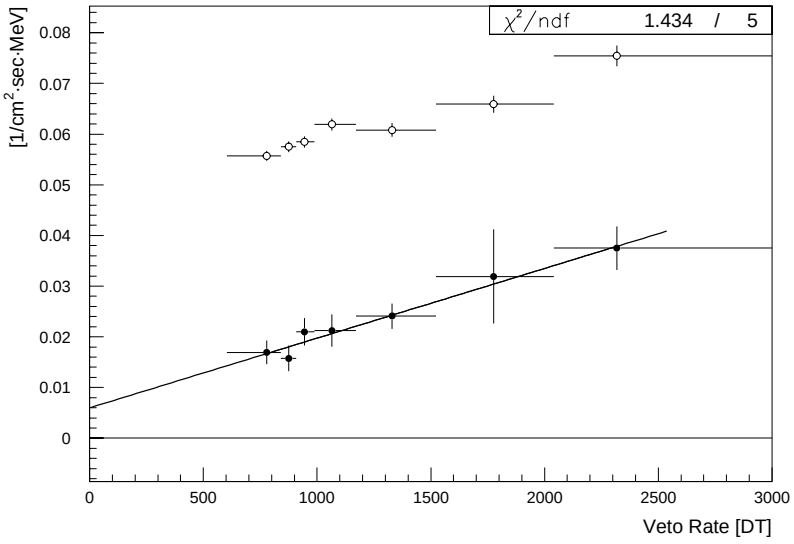

Figure 5.18: *The 1.2–1.8 MeV ToF forward-peak flux before and after the subtraction of the instrumental-line background contributions, together with the veto-rate extrapolation. The data are those used to derive the final result on the 1.2–1.8 MeV CDG intensity, which consist of those observations with the minimum isotope activity (see Sec. 6.2).*

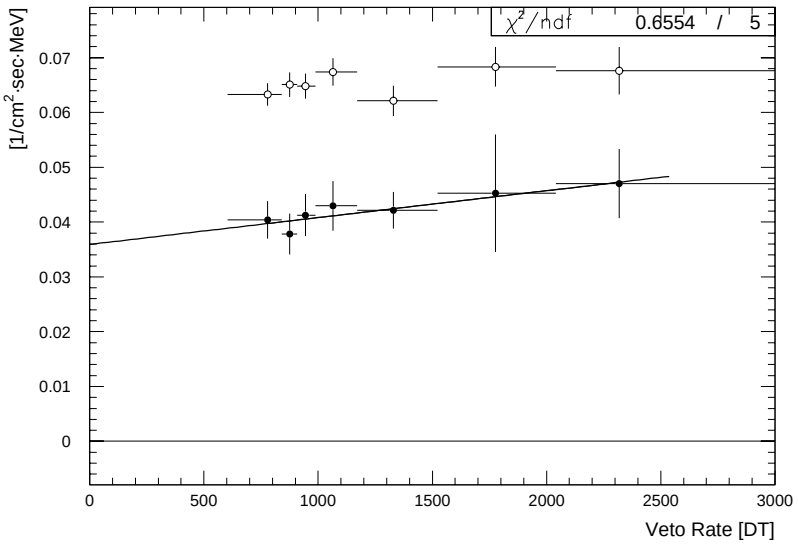

Figure 5.19: *The 0.8–1.2 MeV ToF forward-peak flux before and after the subtraction of the instrumental-line background contributions, together with the veto-rate extrapolation. The data are those used to derive the final result on the 0.8–1.2 MeV CDG intensity (see Sec. 6.2).*

flux is removed by the instrumental-line subtraction, but a weak contribution from yet unidentified long-lived background to the residual flux is expected.

5.3.7.4 Isotope Subtraction in 0.8–1.2 MeV

For the same reasons that apply to the 1.8–2.7 MeV range (see Sec. 5.3.7.2) the final result on the CDG intensity in the 0.8–1.2 MeV interval was determined with the adjusted-standard CDG selection of $6° - 38°$ (see Sec. 5.4.2). The corresponding MA database ToF forward-peak flux before and after the subtraction of the instrumental-line background contributions and the veto-rate extrapolation is shown in Fig. 5.19. Similar to the 1.8–2.7 MeV range, evidence exists for the presence of weak, yet unidentified long-lived background.

5.4 Final Data Selections

One of the objectives of the CDG analysis method was to improve the data selections, starting from the standard CDG selections summarized in Sec. 4.2.3. In the following, the possibilities for improving the signal-to-background ratio above 4.3 MeV through optimization of the selections on $\bar{\varphi}$ are investigated[27], and then the final data selections applied in the CDG analysis are summarized.

[27]Below 4.3 MeV the standard selections had to be changed for two reasons. First, introducing the weighting of the event rate with the effective area to account for the time variation of the telescope configuration entailed a refinement of the event selections such that the effective area is independent of energy in 1.2–4.3 MeV, as required by the line-fitting procedure (see Sec. 5.3.1). Second, in the 2.7–4.3 MeV interval the signal-to-background ratio can be improved by optimized $\bar{\varphi}$-selections (see Sec. 5.3.7.1).

5.4.1 Optimized Selections above 4.3 MeV

The potential of tailored $\bar{\varphi}$-selections for suppressing instrumental background above 4.3 MeV was assessed analogously to the investigations below 4.3 MeV (see Sec. 5.3.6.2) by comparing the ToF forward-peak and the simulated CDG ($E^{-2.5}$ power law) $\bar{\varphi}$-distributions.

For the 4.3–6 MeV, 6–9 MeV, and 4.3–9 MeV energy intervals this comparison is depicted in Fig. 5.20. In these energy ranges a small decrease in the signal-to-background ratio is found below about 14°, suggesting an optimized $\bar{\varphi}$-selection of $14° - 38°$.

A comparison of the ToF forward-peak and the simulated CDG $\bar{\varphi}$-distributions in the energy intervals 9–12 MeV, 12–17 MeV, 17–30 MeV, and 9–30 MeV is given in Fig. 5.21. In general, the variation of the ratio of forward-peak and CDG exhibits almost no trends in these energy ranges, at least partly due to the limited statistics in the simulations. In the 17–30 MeV range the CDG signal seems to decrease more strongly than the forward-peak flux above about 24°. Similarly, the CDG signal is very weak above 32° in the 12–17 MeV interval. In the 9–12 MeV and 9–30 MeV ranges there are no strong indications for a decrease of the ratio of forward-peak flux and CDG signal at the highest $\bar{\varphi}$-values. At the low end of the $\bar{\varphi}$-range covered by the standard CDG selections a decreasing trend for the ratio is indicated, which becomes very strong below 6°. As a precaution, a low-$\bar{\varphi}$ cut-off at 8° was introduced in the optimized selections above 4.3 MeV.

The instrumental background above 4.3 MeV is prompt, therefore an optimization of the event selections is not expected to yield different results for the CDG intensity, in contrast to energies below 4.3 MeV, where the effect of yet unidentified long-lived background components may be reduced through tailored $\bar{\varphi}$-selections. Suppression of prompt background results in a decrease of the slope of the veto-rate variation of the ToF forward-peak flux. A comparison of the slopes of foward-peak flux extrapolations in the five energy intervals above 4.3 MeV for adjusted-standard and optimized selections (summarized below), based on fits with the Gaussian models (see Eqs. 4.8 and 5.3) and for an effective area derived from $E^{-2.5}$ power-law simulations, is given in Table 5.2. As expected, the largest decrease in the slope occurs for the 4.3–6 MeV and 6–9 MeV bands, since there the differences between the two selections are greatest. In principle, decreasing the slope of the extrapolation decreases the statistical error of the derived CDG intensity, but the reduced number of events accepted for optimized selections increases the statistical error. A comparison of CDG intensities derived from the above-mentioned extrapolations, determined for the narrow ToF-range veto-rate offset (which is explained in detail in Sec. 5.5.2) for adjusted-standard selections and optimized selections is given in Table 5.3. In all energy intervals the two sets of CDG intensities are consistent within the statistical errors, whose magnitude is practically the same for both selections.

In the final analysis the optimized selections were used. The decrease in the slopes

	Adjusted-Standard Slope $[1/(\mathrm{cm}^2\,\mathrm{sec\,ster\,MeV\,DT})]$	Optimized Slope $[1/(\mathrm{cm}^2\,\mathrm{sec\,ster\,MeV\,DT})]$
4.3–6 MeV	$(0.196 \pm 0.007) \times 10^{-5}$	$(0.142 \pm 0.008) \times 10^{-5}$
6–9 MeV	$(0.530 \pm 0.037) \times 10^{-6}$	$(0.313 \pm 0.044) \times 10^{-6}$
9–12 MeV	$(0.257 \pm 0.013) \times 10^{-6}$	$(0.277 \pm 0.014) \times 10^{-6}$
12–17 MeV	$(0.145 \pm 0.006) \times 10^{-6}$	$(0.152 \pm 0.007) \times 10^{-6}$
17–30 MeV	$(1.038 \pm 0.028) \times 10^{-7}$	$(0.978 \pm 0.030) \times 10^{-7}$

Table 5.2: *A comparison of the slopes of veto-rate extrapolations above 4.3 MeV for adjusted-standard and optimized event selections. Further details on the comparison are given in the text.*

	Adjusted-Standard Intensity $[\mathrm{ph}/(\mathrm{cm}^2\,\mathrm{sec\,ster\,MeV})]$	Optimized Intensity $[\mathrm{ph}/(\mathrm{cm}^2\,\mathrm{sec\,ster\,MeV})]$
4.3–6 MeV	$(0.685 \pm 0.135) \times 10^{-4}$	$(0.698 \pm 0.137) \times 10^{-4}$
6–9 MeV	$(0.522 \pm 0.067) \times 10^{-4}$	$(0.479 \pm 0.080) \times 10^{-4}$
9–12 MeV	$(0.283 \pm 0.024) \times 10^{-4}$	$(0.300 \pm 0.026) \times 10^{-4}$
12–17 MeV	$(0.145 \pm 0.011) \times 10^{-5}$	$(0.155 \pm 0.012) \times 10^{-5}$
17–30 MeV	$(0.455 \pm 0.052) \times 10^{-6}$	$(0.452 \pm 0.057) \times 10^{-6}$

Table 5.3: *A comparison of CDG intensities above 4.3 MeV derived for adjusted-standard and optimized CDG data selections. Further details on the comparison are given in the text.*

of the extrapolations tends to yield more reliable results, and in addition the veto-rate offset tends to be slightly better behaved (see Sec. 5.5.2). The veto-rate extrapolations of the final CDG analysis above 4.3 MeV, for which the effective area was derived from simulations of an isotropic source with an $E^{-2.0}$ power-law spectrum, are given in Fig. 5.22.

5.4.2 Adjusted-Standard and Optimized CDG Selections

The various selections on $\bar{\varphi}$ discussed in the previous section for energies above 4.3 MeV, and in Sec. 5.3 for lower energies, can be combined to two different sets of CDG selections, the so-called adjusted-standard selections and the so-called optimized selections. Except for the energy-dependent selections on $\bar{\varphi}$, which are summarized in Table 5.4, these two sets of selections are identical to the standard CDG selections summarized in Sec. 4.2.3.

The adjusted-standard CDG selections are almost identical to the standard CDG selections, the only difference being a slight refinement of the $\bar{\varphi}$-selection in the 1.8–2.7 MeV and 2.7–4.3 MeV energy ranges. The only reason for this small difference is to

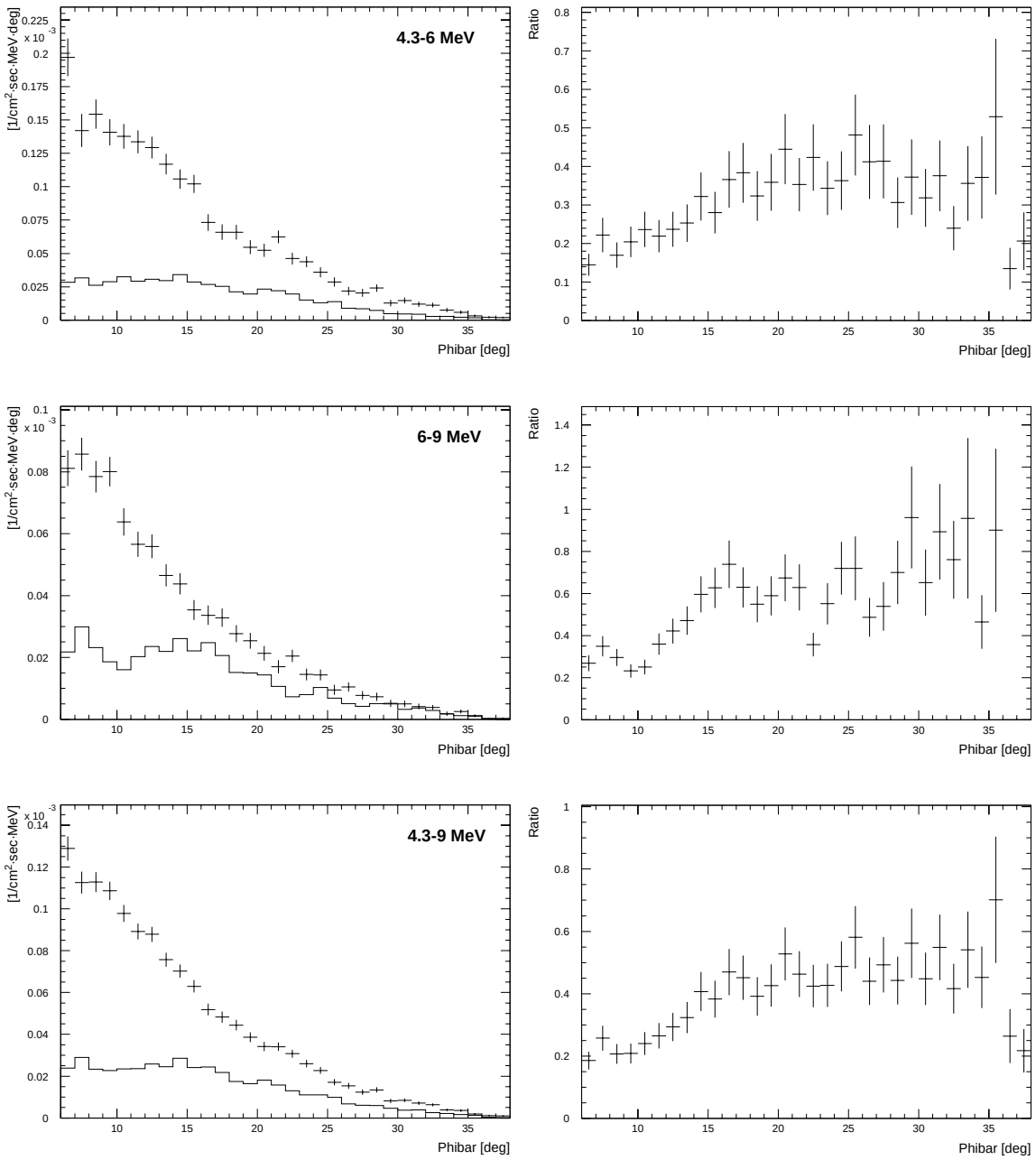

Figure 5.20: *A comparison of the ToF forward-peak and CDG $\bar{\varphi}$-distributions in the E_{tot} intervals 4.3–6 MeV, 6–9 MeV, and 4.3–9 MeV for standard CDG selections. The absolute spectra are shown in the left panels, with the data points and the histogram representing the forward-peak and the CDG, respectively. The right panels give the ratio of CDG and forward-peak distribution.*

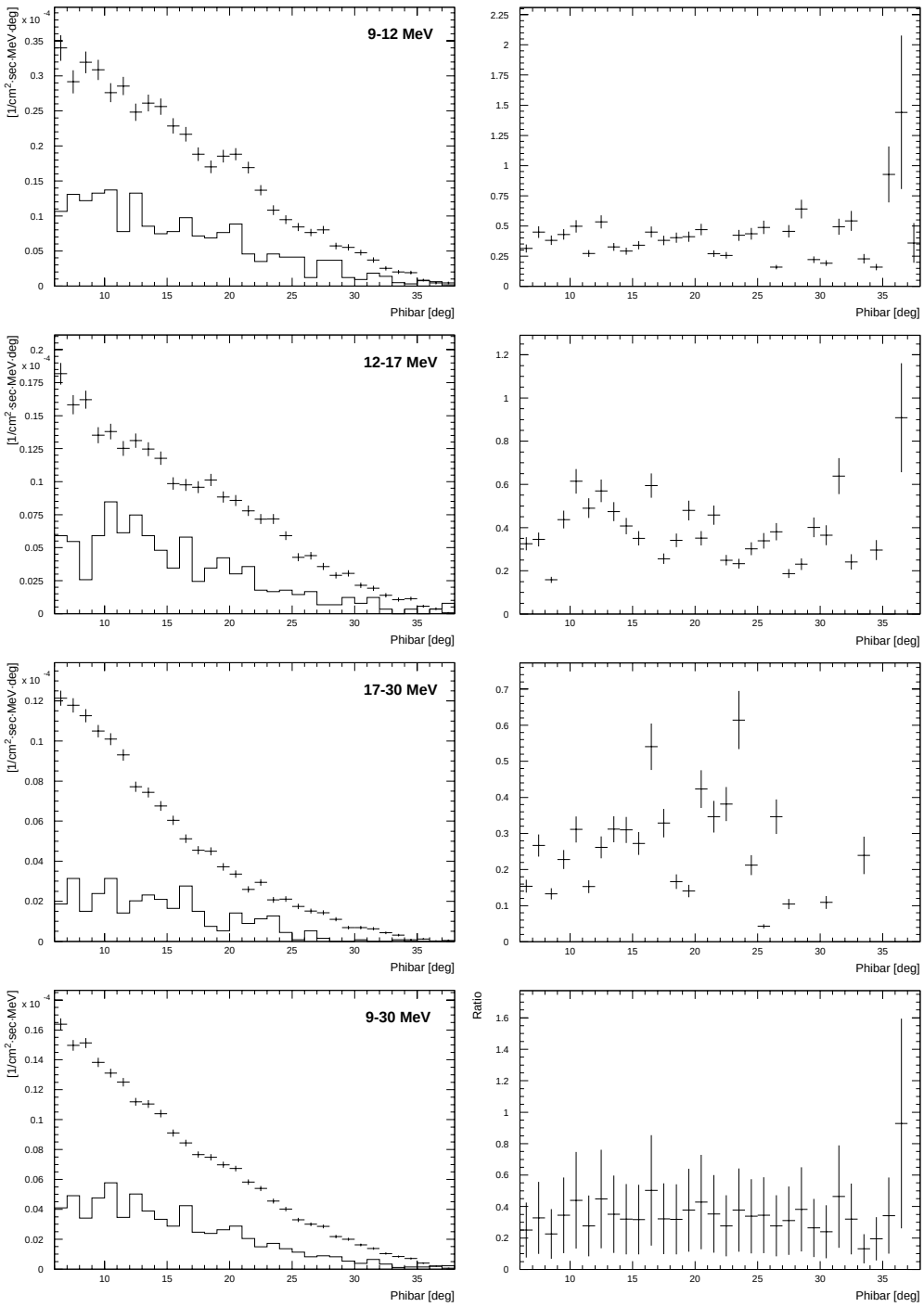

Figure 5.21: *A comparison of the ToF forward-peak and CDG $\bar{\varphi}$-distributions in the E_{tot} intervals 9–12 MeV, 12–17 MeV, 17–30 MeV, and 9–30 MeV for standard CDG selections. The absolute spectra are shown in the left panels, with the data points and the histogram representing the forward-peak and the CDG, respectively. The right panels give the ratio of CDG and forward-peak distribution.*

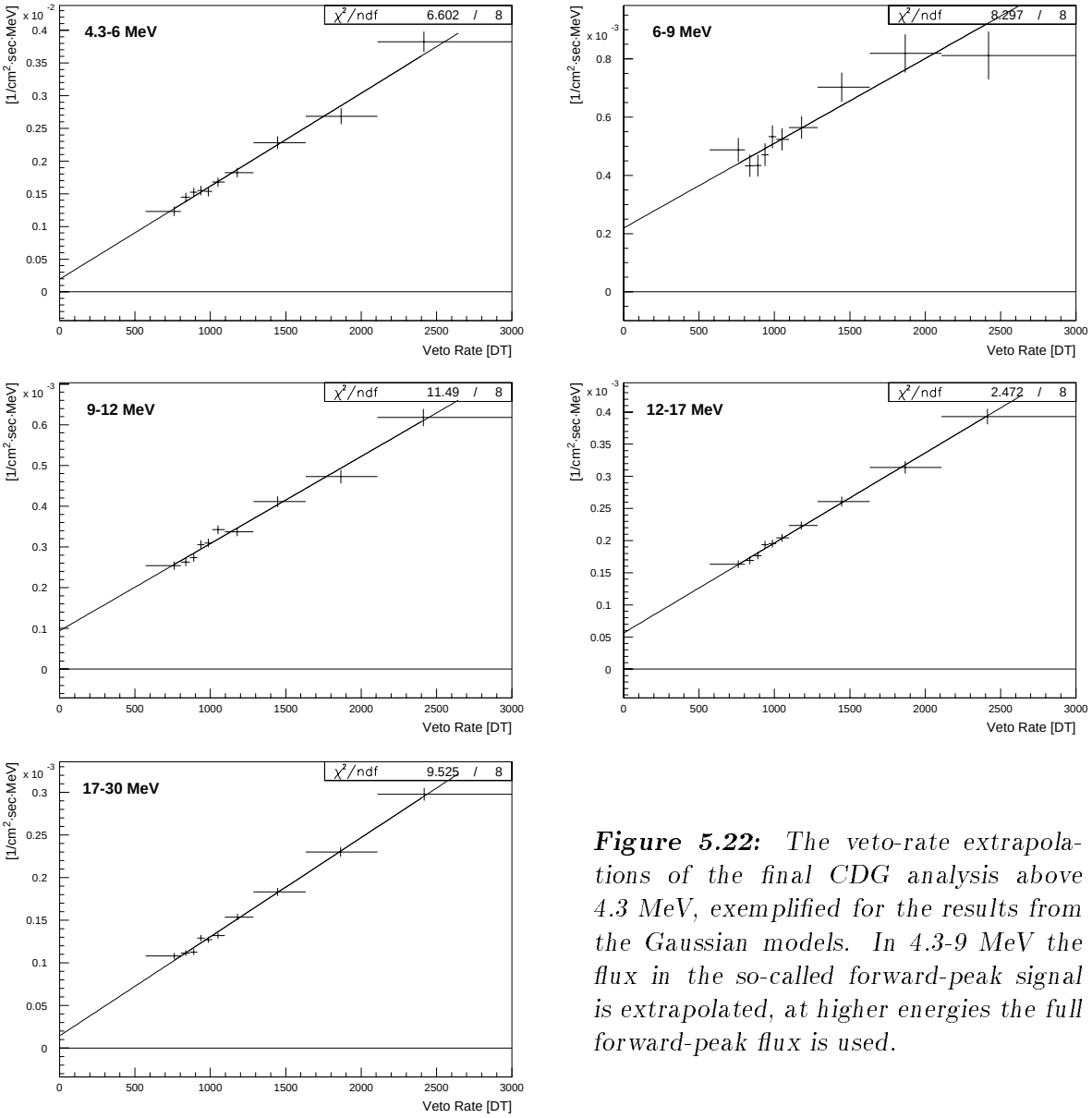

Figure 5.22: *The veto-rate extrapolations of the final CDG analysis above 4.3 MeV, exemplified for the results from the Gaussian models. In 4.3-9 MeV the flux in the so-called forward-peak signal is extrapolated, at higher energies the full forward-peak flux is used.*

render an effective area independent of energy in 1.2–4.3 MeV, as illustrated in Fig. 5.23 (compare the illustration of the effective area for standard selections in Fig. 3.12).

In contrast, the optimized and standard CDG selections differ in all energy ranges. The rationale for the optimized selections above 4.3 MeV has been described in the previous section. Below 4.3 MeV, the 2.7–4.3 MeV $\bar{\varphi}$-selection follows from an optimization of the signal-to-background ratio, as described in Sec. 5.3.7.1. The $\bar{\varphi}$-selections at lower energies merely serve to provide an effective area equal to that in the 2.7–4.3 MeV range.

	Adjusted-Standard Selections	Optimized Selections
0.8–1.2 MeV	$6° - 38°$	$20° - 38°$
1.2–1.8 MeV	$6° - 38°$	$23.2° - 38°$
1.8–2.7 MeV	$10.5° - 38°$	$22.25° - 38°$
2.7–4.3 MeV	$8.3° - 38°$	$21° - 38°$
4.3–6 MeV	$6° - 38°$	$14° - 38°$
6–9 MeV	$6° - 38°$	$14° - 38°$
4.3–9 MeV	$6° - 38°$	$14° - 38°$
9–12 MeV	$6° - 38°$	$8° - 38°$
12–17 MeV	$6° - 38°$	$8° - 32°$
17–30 MeV	$6° - 38°$	$8° - 24°$
9–30 MeV	$6° - 38°$	$8° - 38°$

Table 5.4: *The energy-dependent selections on $\bar{\varphi}$, for adjusted-standard selections and optimized selections, which are applied in the final CDG analysis.*

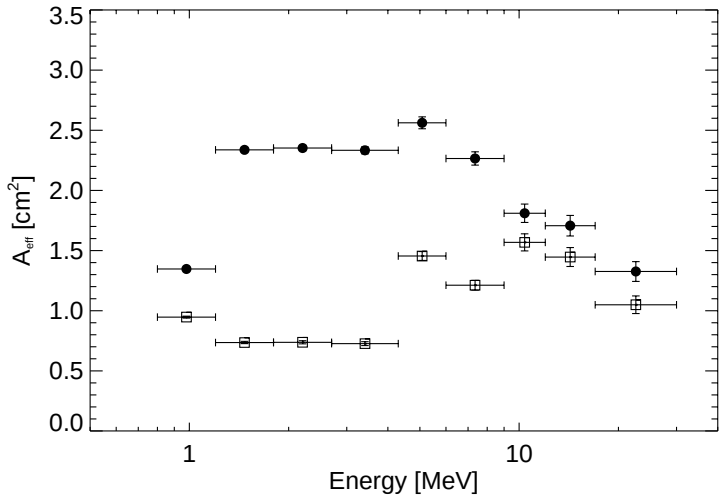

Figure 5.23: *The CDG effective area, calculated for an $E^{-2.5}$ power law and adjusted-standard (filled circles) and optimized (open squares) CDG selections (compare Fig. 3.12). All D1 and D2 detector modules were used in the simulations.*

5.5 Veto-Rate Extrapolation

The trigger rate in the COMPTEL veto domes is expected to monitor the local, instantaneous cosmic-ray intensity (see Secs.3.3 and 3.10), which also produces the prompt instrumental background. To a good approximation, both the veto rate and the prompt background should be proportional to the incident cosmic-ray intensity, and hence a linear correlation of prompt instrumental background and veto rate is expected (see Sec. 4.1.2). This linear correlation is the basis of the veto-rate extrapolation technique.

In this section the systematics of the veto-rate extrapolation are addressed. The

assumed linear correlation between prompt background and veto rate is examined, and the veto-rate level corresponding to conditions free of incident cosmic-ray particles is assessed. To begin with, however, first the individual veto domes are briefly compared.

5.5.1 Comparison of Individual Veto Domes

The variation of the veto rates, or more precisely the number of deadtime-clock counts per 2.048 sec (see Sec. 3.10), of each of the four veto domes during TJD 9725 is depicted in Fig. 5.24 (compare Fig. 4.2). Clearly, the variation of the four veto rates is very similar. Even more, the veto rates of the two larger (V1 and V3) and of the two smaller (V2 and V4) domes (see the COMPTEL scheme in Fig. 3.3), are almost identical. This is expected, since the frequency of triggers of a dome due to incident cosmic-ray particles should be proportional to the dome's geometrical area.

The correlation between the four different veto rates is exemplified in Fig. 5.25 for data from OP 204 with `GCEL` $> 45°$. The excellent linear correlation between the different veto rates is high-lighted by the fits with a linear function. To a good approximation, the magnitudes of the four veto rates are related through

$$\texttt{SCV1M} : \texttt{SCV2M} : \texttt{SCV3M} : \texttt{SCV4M} = 1 : 0.57 : 1.06 : 0.68 \tag{5.4}$$

The quality of these linear correlation implies that all four veto domes are equally suited to serve as a measure for the local, instantaneous cosmic-ray intensity. The results of the linear fits are very insensitive to the errors assigned to the individual veto rates. Assuming that the scatter of the data is purely statistical, the errors of individual veto-rate values are less than a factor of two above what is expected from Poisson statistics[28].

It is interesting to note that the linear fits to the veto-veto correlations in general do *not* intersect the origin, as would be expected if the individual veto rates and the incident cosmic-ray intensity were proportional. Possible origins of this small displacement are discussed in the following section.

5.5.2 Linearity and Veto-Rate Offset

The veto-rate extrapolation technique for removing prompt instrumental background rests on the assumption that the prompt-background event rate is proportional to the veto rate of each of the four veto domes. In the absence of long-lived background, the variation of the ToF forward-peak flux with veto rate should therefore be given by a linear function. Hence extrapolation of this linear relation to the veto-rate level corresponding to a geophysical environment free of cosmic rays, which is expected to be

[28]For example, the Poisson error of a veto-rate value of 1000 DT is $\sqrt{1000}$ DT ≈ 32 DT, while the scatter of the data suggests an error of ~ 50 DT at that veto rate.

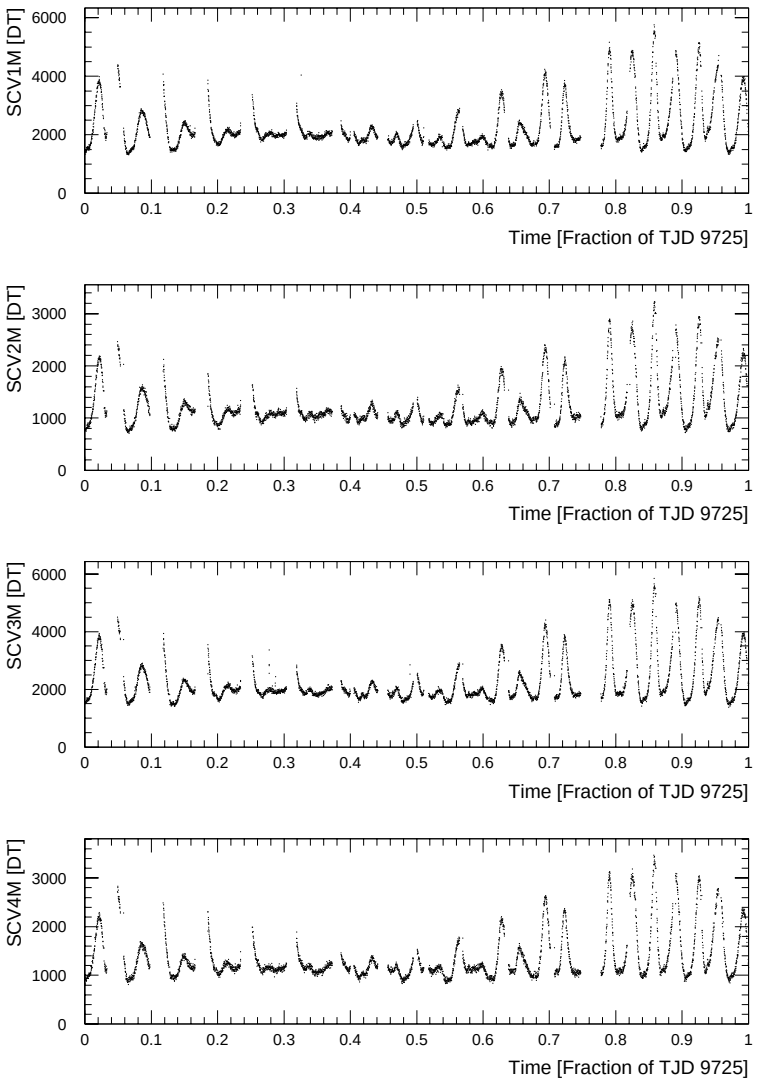

Figure 5.24: *The time-variation of the veto rates of the four veto domes on TJD 9725 (compare Fig. 4.2).*

at or close to veto rate zero, should yield the CDG intensity, as explained in Sec. 5.1. In the following, these assumptions are investigated by studying the veto-rate dependence of various prompt background components. In general, the results shown in the figures below were obtained using V2, hence the label "Veto Rate" stands for `SCV2M`, unless indicated otherwise[29].

[29]The reason for choosing V2 is mostly historic (see also Kappadath *et al.* 1996, Kappadath 1998). Originally, it was assumed that V2 is best suited of all four veto domes to monitor the incident cosmic-ray intensity. It was thought that the veto rate of V1 would be more noisy as it is exposed to time-variable X-ray emission, e.g. of solar origin. Also, it was feared that V3 and V4 would be shielded to some degree from the incident cosmic radiation by the mass of the spacecraft, which would make them imperfect monitors of incident cosmic-ray particles.

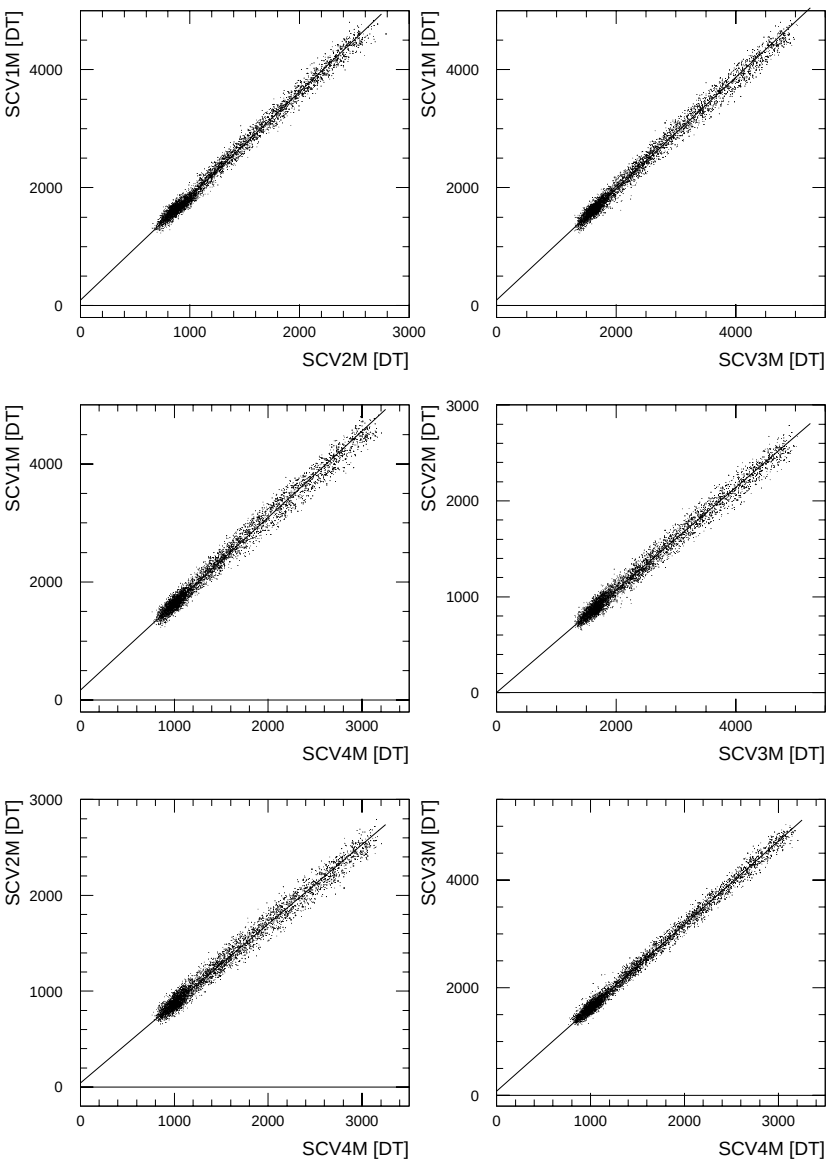

Figure 5.25: *The correlation between the four veto rates for* GCEL $\geq 45°$ *for OP 204. The correlations can be well described by linear functions which, however, in general do not intersect the origin. To a good approximation, the relative magnitudes of the four veto rates are described by Eq. 5.4.*

Above 4.3 MeV all instrumental-background components are expected to be prompt. Hence first insight into the veto-rate variation of prompt background components can be obtained from studying the veto-rate dependence of the event rate at high energies. To single out the CDG signal, which is independent of veto rate, this study was performed in different ToF-ranges, with the ToF interval 115–125 channels containing the bulk of the celestial event rate. The veto-rate variation of the 4.3–9 MeV and 9–30 MeV

event rate, as a function of ToF, is shown in Figs. 5.26 and 5.27, respectively[30]. In addition, linear fits of the event rates as a function of veto rate have been included for each ToF interval, together with the residuals of the fits.

To the first order, the veto-rate variation of the event rate in each ToF interval and energy band is indeed described by a linear function, with the data points agreeing to the fits, in general, within a few percent. At the highest veto rates, above about 3000 DT, the event rate tends to deviate further from the linear fit than at lower veto rates. Because such high veto rates do not occur very often, the Poisson error of the corresponding event rate is quite large, and hence the significance of this trend is limited. As a precaution, only veto rates up to 3000 DT are accepted in the CDG analysis for `SCV2M`.

In general, the scatter of the data points about the linear fit does not appear to be randomly distributed — rather, some systematic trends are indicated. Such trends are not unexpected, however, because there are some principal limitations to the application of the veto rate as a measure of the local, instantaneous cosmic-ray intensity. A fundamental drawback of the veto rate lies in the fact that it only represents a rate of veto-dome triggers[31], but does not provide any information on the composition, the spectral distribution or the distribution of the directions of incidence of the interacting particles[32]. Each of these characteristics of the incident cosmic radiation varies in time, hence a small variation in the proportionality between veto rate and event rate is expected due to changes in the proportionalities of the rate of incident cosmic-ray particles and event rate, as well as veto rate. In addition, these changes may be correlated with the orbit, which could give rise to systematic deviations from a linear correlation, analogously to the deviations due to the correlation between the activity of long-lived isotopes and the veto rate at energies below 4.3 MeV (see Sec. 4.6). Nevertheless, the assumption of a linear relation between the event rate due to prompt instrumental background and veto rate still appears to be warranted, as demonstrated below.

Ideally, the event rate due to prompt instrumental background should be proportional to the veto rate, implying that — in the absence of long-lived or constant components — the extrapolation of the linear fit intersects the origin of the veto-rate and event-rate axes. Therefore, if the event rate r is modelled as a function of veto rate `V`

[30] Analogous results have been obtained with the other three veto domes, V1, V3 , and V4.

[31] In addition, as described in Sec. 3.10, the rate of deadtime-clocks counts is not a physical trigger rate, but is to a good approximation proportional to the interaction rate in the veto domes (see Eq. 3.26).

[32] Another limitation of the veto system lies in the dependence of the veto signal on the interaction location in the domes. Interactions close to one of the PMTs lead to a stronger veto signal, and therefore are more likely to result in a deadtime-clock count, than interactions at the poles of the domes (Lichti 1987), which is another potential source of non-linearity. It has to be remembered that the veto system was built to reject charged-particle interactions in the D1 and D2 detectors, but not for any quantitative monitoring of the incident cosmic-ray intensity.

by

$$r(\mathtt{V}) = a + b \cdot \mathtt{V} \tag{5.5}$$

then it is expected that the value of a does not significantly deviate from zero. In other words, the veto-rate value at which the prompt background vanishes, $\mathtt{V}_0$, given by

$$\mathtt{V}_0 = -\frac{a}{b} \tag{5.6}$$

is expected to be consistent with zero. Geometrically, $\mathtt{V}_0$ is the intersect of the linear fit with the veto-rate axis, and any value of $\mathtt{V}_0$ unequal zero implies that the linear fit is off-set from the origin. Hence $\mathtt{V}_0$ will be referred to as veto-rate offset in the following. As can be seen in Figs. 5.26 and 5.27, in general the linear fit intersects the veto-rate axis at a positive veto-rate value ($\mathtt{V}_0 > 0$). Even more, there seems to be a trend for the veto-rate offset to increase with increasing ToF, as shown in Fig. 5.28. The ToF range 115–125 channels does not follow this trend, because it contains the bulk of the CDG signal. These celestial events, which give rise to a baseline event rate independent of veto rate, result in an increase of parameter a in Eq. 5.5, which geometrically amounts to a shift of the linear function to higher values on the ordinate, thus shifting the intercept with the abscissa to lower veto-rate values.

Physically, the existence of a positive veto-rate offset $\mathtt{V}_0$ in those ToF ranges that are dominated by prompt instrumental background could arise from various origins. For example, non-linearities in the correlation between event rate and veto rate, which are expected and indicated in the data, as discussed above, could result in such systematic deviations when modelled by a linear function. The presence of a positive veto-rate offset may also imply that the veto-domes are triggered even when the prompt-background event rate is zero, i.e. in the absence of incident cosmic-ray particles, which is also an expected effect. These possible origins of the veto-rate offset are further discussed in the following section.

For the CDG analysis the presence of a veto-rate offset implies that the ToF forward-peak flux due to the CDG signal, f_{CDG}, is not given by the flux at veto rate zero, but at veto rate $\mathtt{V}_0$. Analogous to Eq. 5.5, it follows that

$$f_{\mathrm{CDG}} = f(\mathtt{V}_0) = a + b \cdot \mathtt{V}_0 \tag{5.7}$$

The effect of the veto-rate offset on the CDG intensity obtained from the extrapolation depends on the slope a, but in general results is significant. Omission of the veto-rate offset results in an underestimate of the CDG intensity. Typically, the magnitude of the effect is comparable to the statistical error below 4.3 MeV, and comparable to the total error at higher energies (compare Sec. 6.3.2).

By interpolating the results on the veto-rate offset as a function of ToF depicted in Fig. 5.28, the value of the veto-rate offset in the ToF forward-peak region, which is the ToF range of the CDG signal, is expected to have a value of roughly 200 DT. A more accurate value of the veto-rate offset in the ToF forward-peak region can be

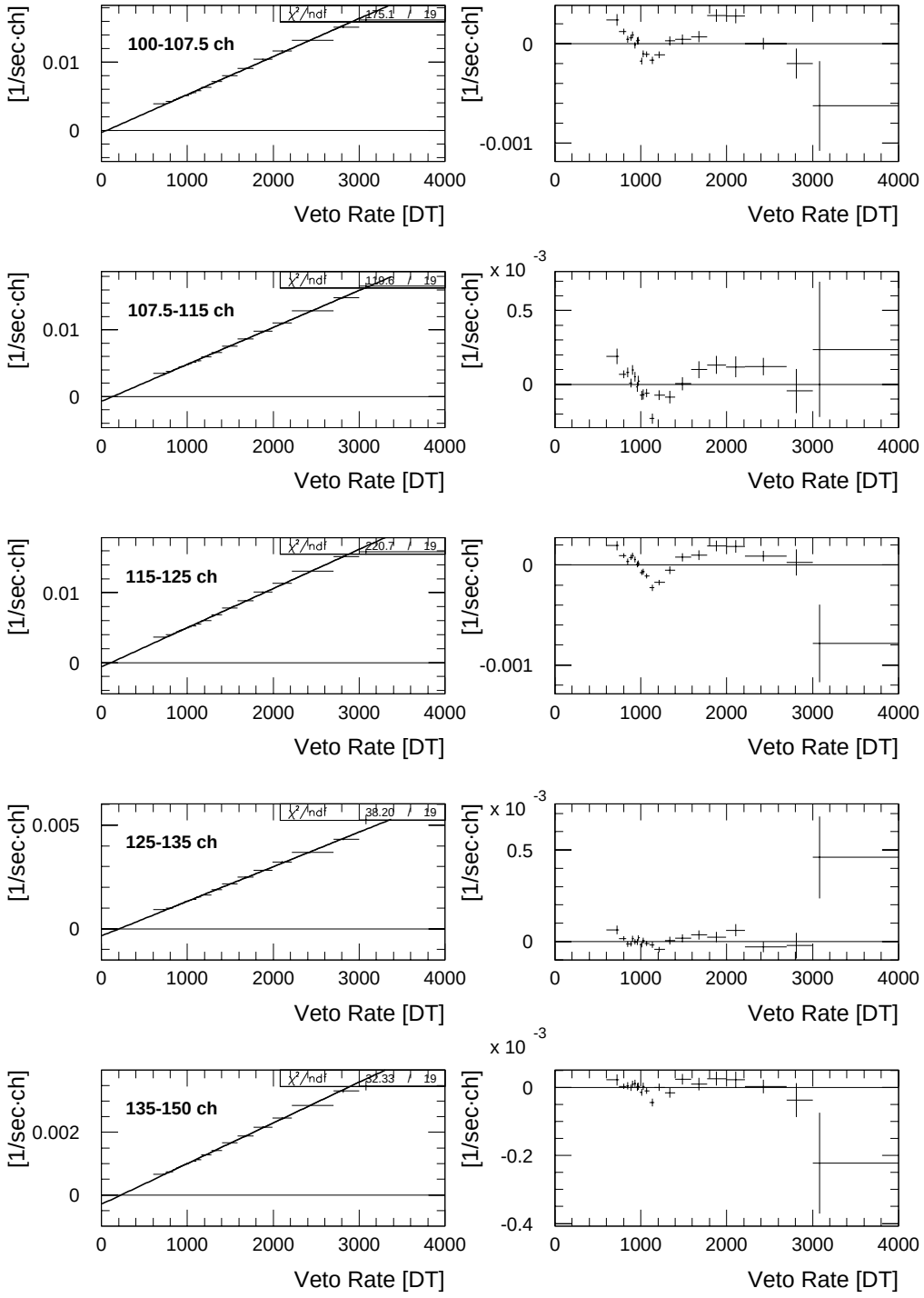

Figure 5.26: *An investigation of the veto-rate variation of the 4.3–9 MeV event rate as a function of ToF. The left panels depicted the linear veto-rate extrapolations in each ToF range, the right panels show the fit residuals.*

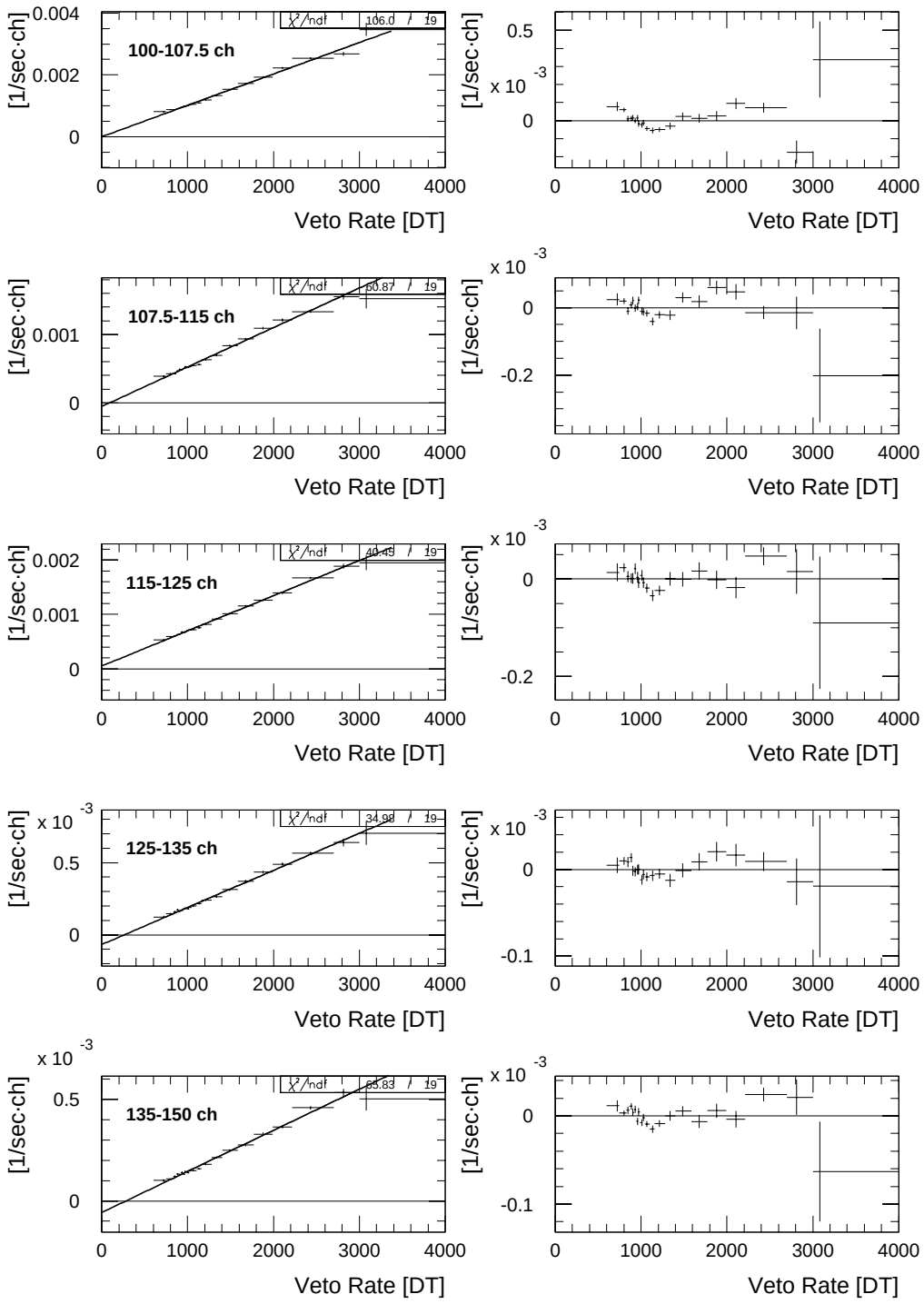

Figure 5.27: *An investigation of the veto-rate variation of the 9–30 MeV event rate as a function of ToF. The left panels depicted the linear veto-rate extrapolations in each ToF range, the right panels show the fit residuals.*

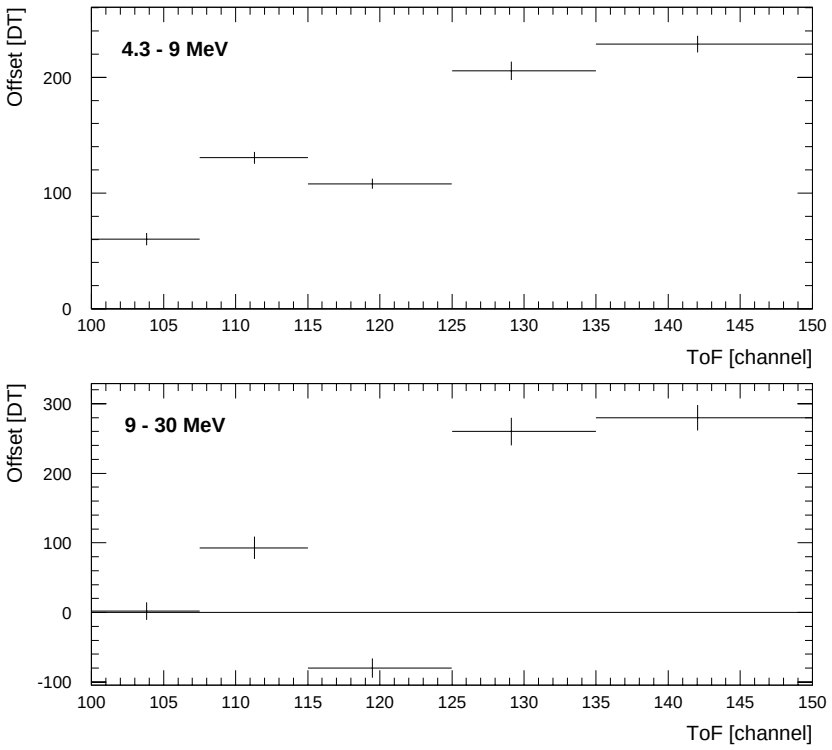

Figure 5.28: *The ToF-variation of the veto-rate offset in 4.3–9 MeV and 9–30 MeV, as obtained from the extrapolations shown in Figs. 5.26 and 5.27. As explained in the text, the presence of the CDG signal in the ToF interval 115–125 channels shifts the intercept of the extrapolation with the veto-rate axis to lower veto-rate values. The magnitude of the shift increases with the signal-to-background ratio.*

obtained from veto-rate extrapolations of prompt components of the ToF spectrum. As described in Secs. 4.3 and 5.2, the ToF-fitting procedure allows us to define seven different, prompt instrumental-background components in the nine energy intervals of the fine energy binning used in the CDG analysis, namely: ToF forward-peak background and ToF continuum-background in 4.3-6 MeV as well as in 6–9 MeV and ToF continuum-background in 9–12 MeV, 12–17 MeV and 17–30 MeV. To account for the ToF-dependence of the veto-rate offset, the flux in these seven, prompt background components, which is determined by integration of the ToF fit-function, is computed for two different sets of ToF ranges. The so-called narrow ToF-ranges, which are the ToF ranges of the maximum signal-to-noise ratio summarized in Table C.4, and the so-called wide ToF-ranges, which in all energy intervals are set to 110–130 channels. As an example, the veto-rate extrapolations of the seven prompt background components, determined with the Gaussian ToF models in the narrow ToF-ranges for the full CDG database under optimized CDG selections, are shown in Fig. 5.29. A linear function provides an acceptable description of the veto-rate variation of each of these prompt background-components. In additon, a fairly consistent, significant veto-rate offset is present for each of the seven components, as will be further discussed below.

In addition to these seven prompt components of the instrumental background above 4.3 MeV, a single, prompt background component exists below 4.3 MeV — the isotope ^{2}D produced in thermal-neutron capture on hydrogen (see Sec. 4.4.2.1). The ^{2}D activity, as a function of veto rate, is best obtained from the fits of the $E_{\rm tot}$-spectra used in the instrumental-line fitting procedure described in Sec. 5.3.3. Although this

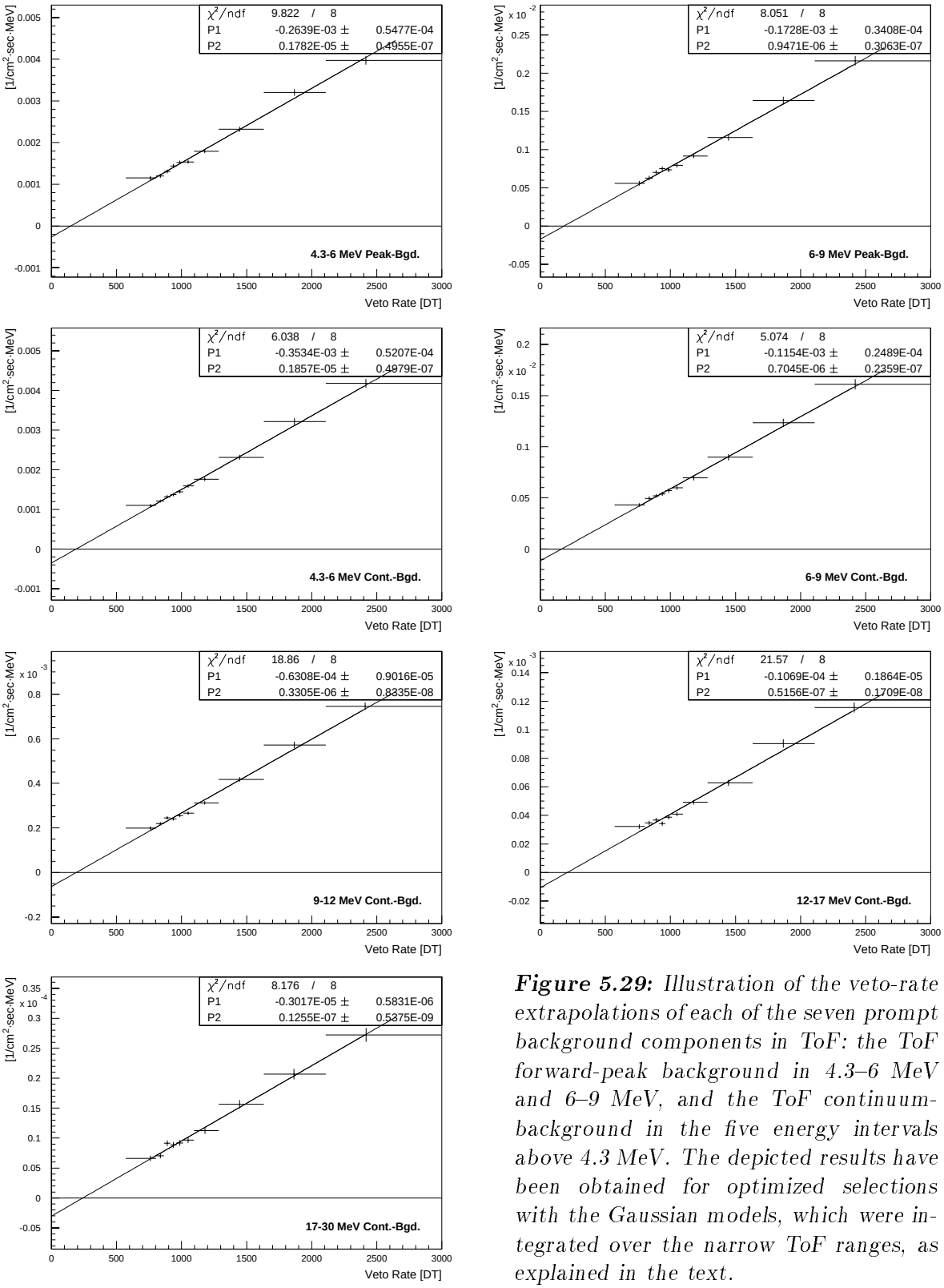

Figure 5.29: *Illustration of the veto-rate extrapolations of each of the seven prompt background components in ToF: the ToF forward-peak background in 4.3–6 MeV and 6–9 MeV, and the ToF continuum-background in the five energy intervals above 4.3 MeV. The depicted results have been obtained for optimized selections with the Gaussian models, which were integrated over the narrow ToF ranges, as explained in the text.*

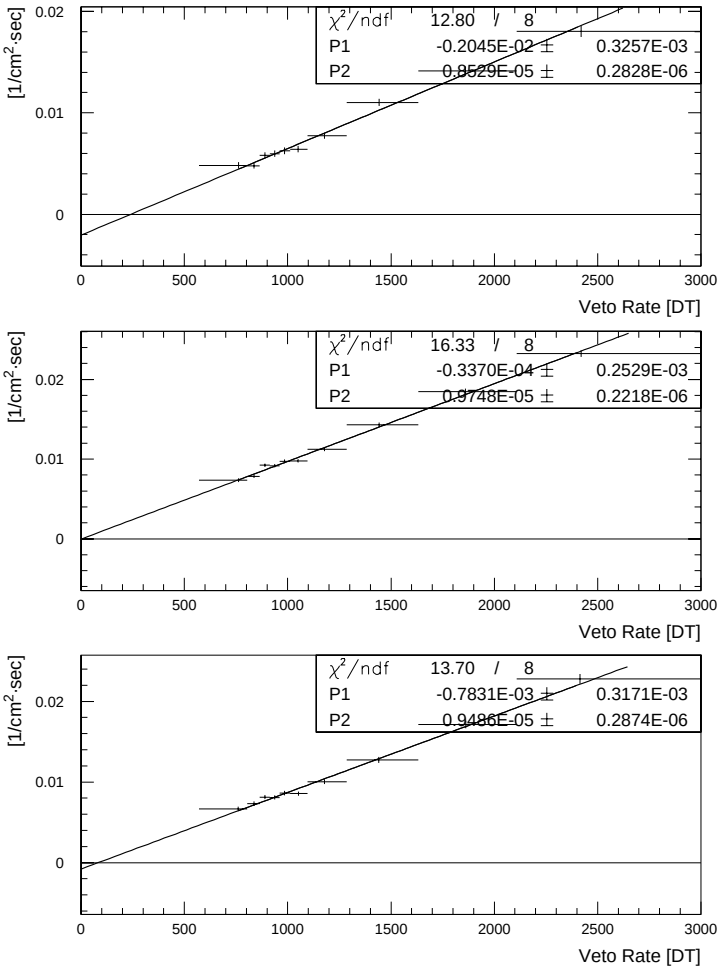

Figure 5.30: *Comparison of the veto-rate extrapolations of the ^{2}D activity as obtained with the three different fit models for the 2.2 MeV line in $E_{\rm tot}$ (see Fig. 5.4).* ***Top:*** *Extrapolation of the ^{2}D activity obtained from modelling the 2.2 MeV line with two components: the ^{2}D template and a Gaussian at $\sim$ 2.29 MeV, yielding a veto-rate offset of (239.8 $\pm$ 38.2) DT.* ***Middle:*** *The 2.2 MeV line was described with the ^{2}D template only, resulting in a veto-rate offset of (3.5 $\pm$ 25.9) DT.* ***Bottom:*** *Using a single Gaussian to fit the 2.2 MeV line results in an offset of (82.6 $\pm$ 33.5) DT.*

procedure yields a self-consistent result for the activities of the identified isotopes[33], the study of the ^{2}D veto-rate offset may be impaired by the remaing uncertainty in the 2.2 MeV fit due to the presence of additonal, yet unidentified instrumental background. The results on the ^{2}D veto-rate offset, obtained from the three different fits of the 2.2 MeV depicted in Fig. 5.4, are compared in Fig. 5.30. As expected, the ^{2}D activity obtained with the 2-component fit, which best represents the 2.2 MeV line, exhibits a significant veto-rate offset. The other two fit models, the ^{2}D template only, and a single Gaussian, yield no or a less significant veto-rate offset, which again is expected because in these models the result on the ^{2}D activity is contaminated by the yet unidentified, short-lived component. For the remainder of the discussion of the veto-rate offset, the ^{2}D offset refers to the result from the 2-component fit of the 2.2 MeV line in $E_{\rm tot}$.

The values of the veto-rate offsets from the eight prompt components of the instrumental background discussed above, obtained for the full CDG database with the

[33] In particular, the results on the veto-rate offset in the ^{2}D activity obtained from the 2-component fit of the 2.2 MeV line in $E_{\rm tot}$, discussed in the following, are consistent with results obtained from fits of the second and third E_2-spectrum with the ^{2}D activity being a free parameter.

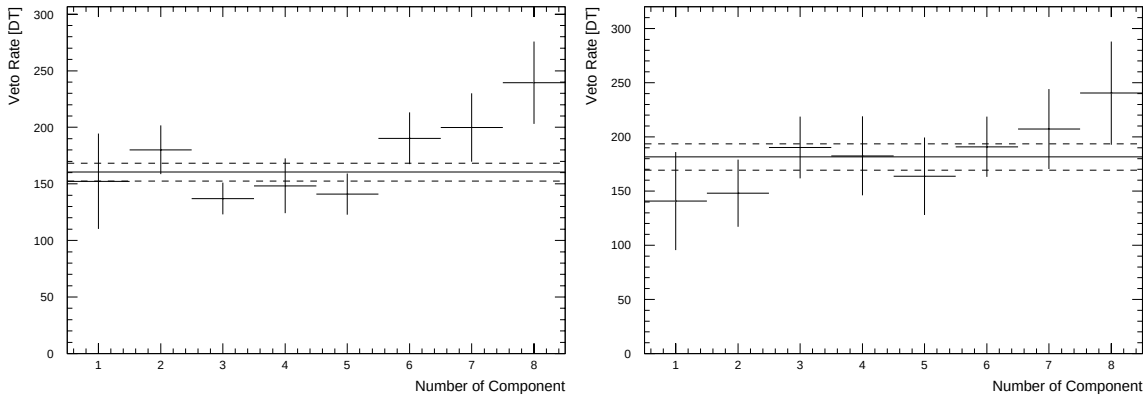

Figure 5.31: *A comparison of eight different estimates of the veto-rate offset obtained through extrapolation of the fluxes in of eight different, prompt components of the instrumental background for adjusted-standard selections (left) and optimized selections (right). The eight prompt components are: 1. isotope ^2D, 2.-3. and 4.-5. ToF forward-peak background and ToF continuum-background in 4.3–6 MeV and 6–9 MeV, respectively, 5.-8. ToF continuum-background in 9–12 MeV, 12–17 MeV, and 17–30 MeV. The ToF components have been evaluated in the narrow ToF-ranges. The solid and dashed lines indicate the weighted average of the eight veto-rate values, and its 1σ error.*

Gaussian ToF model, are shown for adjusted-standard and optimized event selections in the left and right panels of Fig. 5.31, respectively. Despite the fact that these components cover a wide range in energy and represent different types of background events (see Chapter 4), the different estimates of the veto-rate offset are quite consistent. In general, the scatter of the individual values about their weighted average tends to be smaller for optimized selections than for adjusted-standard selections, which also applies to the tendency of the veto-rate offset to increase with energy. This is one of the reasons why the optimized selections were favoured over the adjusted-standard selections in the final analysis of the CDG spectrum above 4.3 MeV.

A comparison of the veto-rate offsets determined for the narrow and wide ToF-ranges in individual phases/cycles of the mission (see Table D.1), as well as for the combined data is given in Fig. 5.32. In addition, the average veto-rate offset, defined as the average of the offsets for the narrow and wide ToF-ranges, is shown. It has to be noted that in this comparison, and in general for the remainder of this thesis, the veto-rate offset of a set of observations represents the weighted average of the respective eight individual offsets, as discussed above. In general, the narrow ToF-range offset exceeds the wide ToF-range offset by about 20 DT (for `SCV2M`). In the CDG analysis the full ToF forward-peak range is analyzed, not only the range of the maximum signal-to-noise ratio. Therefore, the average of the narrow and wide ToF-range offsets is used in the final extrapolations.

No significant variation of the veto-rate offset with time has been found so far. There may be a trend in the veto-rate offset to increase with time, or with the general level of long-lived isotope activities, however, no significant correlations could be identified to

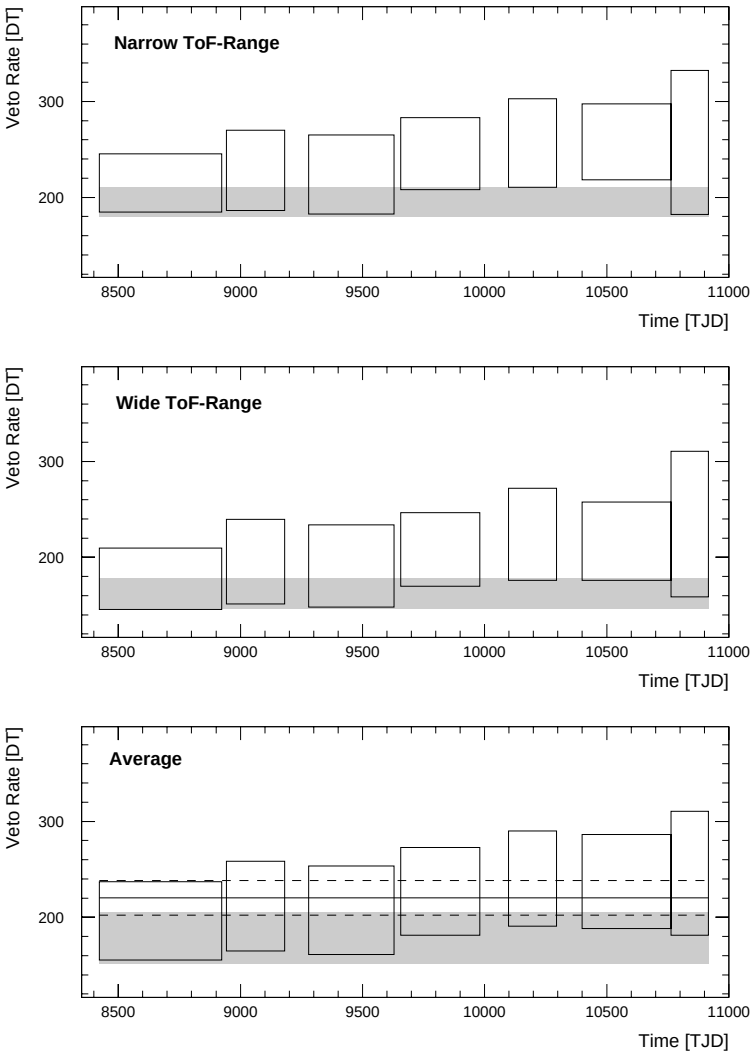

Figure 5.32: *The time-variation of the veto-rate offset derived for the narrow and wide ToF ranges, as well as for their average. The boxes give the results for individual phases or cylces (see Table D.1), the gray bars depict the results for the combined data. The solid and dashed lines in the bottom panel indicate the weighted average of the individual phases/cycles. All results are given as value $\pm 1\sigma$ error.*

date, suggesting that internal radioactivity from activation is not a significant source of the veto-rate offset (see Sec. 5.5.3.4). In general, the value of the veto-rate offset determined from a given set of observations tends to be smaller than the weighted average of the veto-rate offsets determined for disjunct subsets of the combined database, as can be seen in the bottom panel of Fig. 5.32. This behaviour may be an artifact of the non-linear CDG analysis procedure, in particular of a systematic trend in the results of the ToF fits depending on the available statistics. To account for the presence of this still unexplained behaviour a systematic uncertainty is assigned to each veto-rate offset (see below). In the final CDG analysis the veto-rate offset is determined from the analyzed set of observations, which appears to yield self-consistent results on the CDG intensity, as demonstrated in Sec. 6.1.

So far, the discussion of the veto-rate offset focused on veto dome V2. As already pointed out before, there is no qualitative difference between the four veto domes, hence the same characteristics of the veto-rate offset are obtained with either veto

	Veto Dome 1	Veto Dome 2	Veto Dome 3	Veto Dome 4
Offset [DT]	399.1 ± 12.1	181.5 ± 12.1	410.2 ± 22.0	229.5 ± 14.1

Table 5.5: *The value of the veto-rate offset in the four different veto domes, obtained from an analysis of the full CDG database with the Gaussian ToF model for optimized selections and the narrow ToF-ranges.*

dome. There is, however, a quantitative difference in the values of the veto-rate in the four veto domes, summarized in Table 5.5. It is interesting to compare the relative magnitudes of the veto-rate offsets,

$$\mathtt{V}_{0,1} : \mathtt{V}_{0,2} : \mathtt{V}_{0,3} : \mathtt{V}_{0,4} \approx 1 : 0.45 : 1.03 : 0.58 \tag{5.8}$$

with $\mathtt{V}_{0,i}, i = 1,4$ being the veto-rate offset in Vi, with the relative magnitudes of the veto rates given in Eq. 5.4. Within errors, the ratios between the two larger veto domes, V1 and V3, and between the two smaller veto domes, V2 and V4, are the same for both quantities. In addition, the magnitude of the veto-rate offsets in the two smaller veto domes relative to that in the two larger veto domes is only slightly less than the corresponding ratios for the veto rates themselfs. The consistency of these relations suggests that the size of the veto domes somehow affects the magnitude of the veto-rate offset, as would be the case if the offset is due to particles triggering the domes. The choice of the veto dome used in the final anlysis is irrelevant, as all four veto domes yield the same results, as demonstrated in Sec. 6.3.2.

To conclude, a brief description of the determination of the veto-rate offset used in the final analysis of the CDG spectrum is given[34]. As explained above, the different prompt background components utilized in estimating the magnitude of the veto-rate offset in general yield consistent results. The individual results exhibit, however, small systematic differences, depending on, e.g., the event selections applied to the data, the ToF range for which the ToF components are computed, or the energy of the component — thus precluding a unique determination of the veto-rate offset value. Considering the complexity of the COMPTEL instrumental background, however, a unique veto-rate offset may not even exist. A final answer to this question has to wait for the identification of the physical origin(s) of the veto-rate offset, which at present

[34]In contrast to the findings presented in this section, Kappadath (1998) did not find evidence supporting the existence of a significant veto-rate offset, and hence the CDG intensity is derived from a linear extrapolation of the ToF forward-peak flux to veto rate zero in his analysis. It has to be emphasized, however, that Kappadath (1998) did only study the veto-rate variation of a single prompt background component to investigate the existence of a veto-rate offset, namely the 2.2 MeV line in $E_{\rm tot}$, which he modelled with a single Gaussian. This study of the 2.2 MeV line yielded consistent results with those described here, in particular the unusual variation of the Gaussian parameters with veto rate (see Sec. 5.3.3). The values of the 2.2 MeV line veto-rate offset determined by Kappadath (1998) for different subsets of his database scattered about zero, and hence he arrived at the conclusion that a veto-rate offset, if present at all, is insignificant.

remains obscure (see next section). In the final analysis, the veto-rate offset therefore is determined self-consistently, i.e. the offset is derived from the data under study, using the same ToF model and the same event selections. No "prior knowledge" from studies of other datasets is used. The veto-rate offset for a given ToF model and given event selections is obtained by first determining the offsets in each of the eight prompt instrumental-background components for both the narrow and the wide ToF-ranges. Then for each of the ToF ranges the weighted averages and their statistical 1σ errors are computed, yielding the so-called narrow-ToF and wide-ToF veto-rate offsets. The final veto-rate offset then is the average of the narrow-ToF and wide-ToF offsets, and its statistical error is defined as the average of the statistical errors of these two offsets, which are very similar. In addition, to reflect the existing systematic uncertainties with respect to dependencies on time and energy (see Figs. 5.31 and 5.32), the final veto-rate offset is assigned a systematic error of 25 DT (for `SCV2M`).

5.5.3 Possible Origins of the Veto-Rate Offset

As already mentioned in the previous section, the positive veto-rate offset could arise from a number of origins, such as non-linearities in the correlation between event rate and veto rate, or the triggering of the veto domes even in the absence of cosmic radiation. Possible causes for non-cosmic-ray triggers of the veto system include electronic noise, such as dark counts of the PMTs watching the veto domes, or photon-interactions in the veto system. Candidate photon sources are the XRB (see Sec. 2.1.6), as well as the internal radioactivity of the spacecraft.

In the following, some of these potential origins are briefly discussed. Whenever possible, upper limits on the expected veto-dome trigger rates are derived. In general, these limits are quite generous, but sufficient for the purpose of this discussion. In the discussion, it is important to remember that the number of deadtime-clock counts in veto dome Vi per packet, `SCViM`, $i = 1, 4$, is related to the trigger rate $r_{\mathrm{V}i}$, through (compare Eq. 3.26)

$$r_{\mathrm{V}i} = 12.8 \times \frac{\texttt{SCViM}}{2.048 \text{ sec}}, \qquad i = 1, 4 \tag{5.9}$$

5.5.3.1 Non-Linearities in the Correlation between Event Rate and Veto Rate

As explained in the previous section, non-linearities in the correlation of event rate and veto rate are expected at some level due to orbital/temporal variations of composition, energy spectum and distribution of incidence directions of the interacting cosmic-ray particles. In addition, different ranges of the ToF spectrum are dominated by different types of background events (see Chapter 4), hence a ToF-dependence of the veto-rate offset is conceivable. As expected, weak non-linearities in the correlation of event rate and veto rate can be found (see Figs. 5.26 and 5.27), however, there is no significant

change in these small deviations with ToF which could account for the ToF-dependence of the veto-rate offset.

Assessing the extent to which the observed veto-rate offset arises from non-linearities requires an improved physical model for the correlation of event rate and veto rate — which is not available at present. For the time being, it cannot be ruled out that the veto-rate offset is an artifact of non-linearities in the framework of a linear model. Even if the veto-rate offset were known to arise from non-linearities, however, the extrapolation for removing prompt instrumental background should be performed self-consistently. Hence, if prompt background components in the ToF forward-peak region vanish at some offset value $\mathtt{V}_0$ due to the fact that an incorrect model is used in the extrapolation, then the same apparent behaviour is to be expected for the prompt ToF forward-peak background, and the CDG intensity should be determined at the offset level, and not at veto rate zero.

5.5.3.2 Dark Counts in the PMTs

Electronic noise, such as dark counts in the PMTs watching the veto domes, could possibly contribute to the veto-rate offset. The dark counts are the thermal noise in a PMT and arise from thermally emitted electrons from one of the dynodes. Typical dark-count rates measured for the PMTs used in the veto-system range from a few ten to a few hundred counts per second (Macri 1997c, private communication), with the average dark-count rates being less than 100 cts/sec.

Since the beginning of the mission, the veto domes were operated at threshold level 5 (Macri 1997b, private communication), corresponding to thresholds, in units of photoelectrons, of about 1.4, 6.4, 3.6, and 3.5 for veto domes V1–V4, respectively (Lichti 1988). Each veto dome is watched by 24 PMTs, hence we expect a total dark-count rate of less than 2400 cts/sec per veto dome. The V1 threshold is close to the noise level. Assuming that all dark counts lead to a veto trigger, an upper limit on the resulting veto rate `SCV1M` of about 384 DT is obtained from Eq. 5.9. The actual number of veto triggers is is expected to be lower by at least a factor of two, because only a fraction of the single-photoelectron dark counts do actually trigger the veto system (Lichti 1998, private communication). The triggering of the other veto domes, V2–V4, requires the coincidence of at least two dark counts because of the higher thresholds. The probabilty p for the coincidence of two dark counts is given by

$$p = 1 - \exp(\Delta t \cdot r) \approx \Delta t \cdot r \tag{5.10}$$

with r being the dark-count rate, and Δt being the length of the PMT signal, which is less than the duration of the veto signal of 200 nsec. It follows that $p < 2 \times 10^{-5}$, rendering veto triggers from coincidences of two or more dark counts negligible. It follows that PMT dark counts are only expected to contribute to the veto-rate offset in V1, but not in the other three veto domes. The measured veto-rate offsets in V1

and V3, however, are consistent within the statistical error of $\lesssim 20$ DT (see Table 5.5), and thus the contribution of the dark-count rate to the V1 offset should not exeed a few 10 DT, which corresponds to $\lesssim 10\%$ of the observed value.

5.5.3.3 XRB Photons

Photons from the XRB, and to a much lesser extent (because they are much less numerous, Table 2.1) from the EGB, can trigger the veto system[35] and thereby contribute to the veto-rate offset. To assess the rate of veto-dome triggers due to XRB and EGB photon-interactions, the spectra of these photon components were modelled using the final result of this thesis (see Sec 6.3.3), extrapolated to lower energies when necessary, and the result of Sreekumar *et al.* (1998) at higher energies.

The XRB photons were assumed to isotropically irradiate the spacecraft from a solid angle $\Omega_{\rm sky}$ of about 8.6 ster[36]. The thickness of the veto domes is 1.5 cm, the density of the plastic scintillator is 1.032 g/cm^3 (see Sec. 3.3). Most photons will enter the veto domes under an angle less than 90° and hence traverse a geometrical path in the domes exceeding their thickness. Therefore the veto domes are assumed to have an effective thickness of 2 g/cm^2 in the following. For each veto dome, the effective geometrical area exposed to the photons, $A_{\rm veto}$, was assumed to be equal to the average of the projected areas of the domes as seen from the top and from the side[37]. The energy-dependence of the linear attenuation coefficient τ of the plastic scintillator was approximated by $\tau(E) = 0.07 \cdot E^{-0.5058}$, with E in [MeV] (Lichti 1998, private communication). The in-flight threshold levels of the four veto domes V1–V4 correspond to energy thresholds of about 156 keV, 384 keV, 365 keV, and 265 keV, respectively (Lichti 1988).

An upper limit on the trigger rate $r_{{\rm V}i}$ of veto dome Vi due to XRB and EGB photons can be obtained from

$$r_{{\rm V}i} = A_{{\rm V}i} \cdot \Omega_{\rm sky} \cdot \int_{E_{\rm thr}} I(E) \cdot (1 - e^{-x\,\tau(E)})\, dE \qquad (5.11)$$

with $I(E)$ being the XRB/EGB intensity, assuming that each interacting photon with an incident energy above the energy threshold $E_{\rm thr}$ triggers the veto dome. The resulting upper limits for V1 through V4 are 2605 cts/sec, 248 cts/sec, 441 cts/sec, and

[35]The self-veto effect, i.e. the triggering of the veto system by a photon that simultaneously underwent a proper double-scattering process, is taken into account in the response simulations.

[36]As mentioned in Sec. 4.1.2, the angle between the direction to the geocenter and the Earth horizon is about 70° as seen from an altitude of about 450 km. Hence the Earth subtends a solid angle of about 4 ster, leaving $(4\pi - 4) \approx 8.6$ ster of unobscured sky.

[37]The diameter and the height of veto domes V1 and V3 were assumed to be about 154 cm and 85 cm, respectively (see Fig. 3.3). Approximating the side view of the domes by a square, the areas of the top and side views are about 18600 cm^2 and 13100 cm^2, respectively. The estimates of diameter and height of veto domes V2 and V4 are 140 cm and 44 cm, respectively, resulting in top and side view areas of 15400 cm^2 and 5600 cm^2.

553 cts/sec, respectively. These values are very sensitive to the energy threshold. For example, if each of the energy thresholds is increased by 255 keV to crudely include the effect of the Compton edge, then the estimates for the trigger rates in V1 through V4 reduce to about 323 cts/sec, 81 cts/sec, 136 cts/sec, and 147 cts/sec, respectively.

The relative ratios of these veto rates clearly are very different from those given in Eq. 5.8. In addition, the veto domes V2, and in particular V3 and V4, are to some degree shielded from external photons by the spacecraft material, hence the trigger rate in V1, compared to the other domes, will be even larger, making the discrepancy with the observation even more pronounced. Hence a significant contribution of XRB photons to the veto-rate offset appears unlikely.

5.5.3.4 Internal Radioactivity

There are various sources of internal radioactivity that potentially contribute to the veto-rate offset. In this context, natural radioactivity is of particular interest, since it is constant in time. The following discussion is focused on V1 and V2, since the radioactivity in the D1 detector has been studied in much more datail than that in the D2 detector.

• *EGRET spark-chamber frame*: A major source of natural radioactivity onboard CGRO is the frame of the EGRET spark-chamber, which is manufactured of MACOR glass ceramic[38] that is known to contain a considerable amount of potassium, and hence ^{40}K (see Sec. 4.4.2.3). Unfortunately, the manufacturer considered the potassium mass fraction in MACOR proprietory information. Hence the potassium content of a small piece of MACOR was estimated using γ-ray spectroscopy. From preliminary measurements with a Ge-spectrometer (Georgii and Wunderer 1998, private communication) a potassium mass fraction of about 33% was derived. Based on the approximate geometrical dimensions of the EGRET spark-chamber plates (Kanbach 1998a, private communication) and the density of the glass ceramic of 2.5 g/cm^3 a total potassium mass of about 13.7 kg was estimated, implying a ^{40}K activity $A \approx 4.5 \times 10^4$ sec^{-1}.

In assessing the veto-system trigger rate due to this activity, the EGRET spark chamber was modelled as a point source at a distance d of 2 m from the veto domes V1 and V2 (see Fig. 3.1). As above, the effective thickness of the veto domes was assumed to be 2 g/cm, the geometrical area exposed to the 1.4 MeV photons was approximated by the area $A_{\rm veto}$ of the side view of the domes. The solid angle $\Omega_{\rm veto}$ subtended by the domes was estimated by $\Omega_{\rm veto} = A_{\rm veto}/d^2$. Finally, each photon interaction was assumed to trigger the veto system. The trigger rate $r_{{\rm V}i}$ of veto dome Vi can be estimated by

$$r_{{\rm V}i} = \frac{\Omega_{\rm veto}}{4\pi} \cdot (1 - e^{-x\,\tau(E)}) \cdot A \qquad (5.12)$$

[38]MACOR is produced by Corning Inc., NY, USA.

For the ^{40}K radioactivity in the EGRET spark-chamber frame this yields upper limits for the trigger rate in V1 and V2 of about 118 cts/sec and 55 cts/sec, respectively.

• *Natural radioactivity in COMPTEL PMTs*: Similarly, the veto triggers due to the natural ^{40}K and ^{208}Tl radioactivity in the D1 PMTs was estimated, assuming that V1 and V2 subtend a solid angle of 2π as seen from the PMTs. The estimate for the trigger rate in V1 and V2 due to ^{40}K and ^{208}Tl is about 12 cts/sec and less than 1 cts/sec, respectively.

• *COMPTEL CAL-units*: At the time of launch the activity of the two CAL-units A and B was about 20.2 nCi and 16.8 nCi, respectively (Schönfelder *et al.* 1993). Upon each decay, the ^{60}Co calibration sources emit two photons at 1.17 MeV and 1.33 MeV, resulting in a total photon-emission rate of about 2700 sec^{-1}. The CAL-units are at a distance of about 1 m from the centers of the veto domes. Approximating the geometrical area subtended by the domes with their top-view areas, subtended solid angles of about 1.9 ster and 1.5 ster are obtained for V1 and V2, respectively. Assuming further that each photon-interaction results in a veto-dome trigger, Eq. 5.12 yields estimates for the V1 and V2 trigger rates of about 49 cts/sec and 39 cts/sec, respectively.

• *Long-lived activity in COMPTEL*: Finally, the summed long-lived activity from isotopes such as ^{24}Na or ^{22}Na is estimated to result in less than 100 cts/sec. From the line-fitting procedure and simulated efficiencies it follows that the activity of ^{24}Na and ^{22}Na in the upper aluminium structure on average is about 200 sec^{-1} and 120 sec^{-1}, respectively. Each decay of ^{24}Na and ^{22}Na gives rise to two and three photons, respectively. Assuming an average solid angle of 1π, 10 cts/sec and 14 cts/sec are expected in V1 and V2 from ^{24}Na and ^{22}Na, respectively. As demonstrated in Sec. 6.1, the activity of long-lived isotopes varied by at least a factor of $\gtrsim 5$ over the mission, hence, in principle, a corresponding variation in the contribution of the isotopes to the veto-rate offset is to be expected. The expected contribution from long-lived isotopes is too small, however, for its variation to be noticable.

To conclude, the summed upper limits on the veto-dome trigger rates due to internal radioactivity imply total rates of about 155 cts/sec and 92 cts/sec for V1 and V2, respectively. According to Eq. 5.9, this correponds to offset values of about 25 DT and 15 DT, for V1 and V2 — which is less than 10% of the observed value (see Table 5.5). Therefore a significant veto-rate offset due to identified internal radioactivity appears unlikely. In additon, no ToF-dependence is expected for the veto-rate offset contribution due to natural radioactivity. It is interesting to note, however, that the ratio of the expected contributions, which were derived taking into account the geometrical dimensions of the domes, agree quite closely to the observed ratios of the veto rates and the veto-rate offsets.

5.5.4 Summary

Despite the fact that clear and consistent evidence for the existence of a veto-rate offset has been obtained from a number of prompt instrumental-background components, its physical origin still remains obscure for the time being and requires further investigation. The fact that the relative magnitudes of the veto-rate offsets in the four veto domes (see Eq. 5.8) are very similar to the relative magnitudes of the veto rates (see Eq. 5.4) suggests that the size of the veto domes has an important effect on the veto-rate offset value. In contrast, the threshold level of individual domes seems to be unimportant. Finally, the veto-rate offset varies considerably with ToF, and may also exhibit a small variation with energy.

The upper limits on the contributions from dark counts in the veto PMTs and from the internal radioactivity identified to date indicate that these components together fall short of accounting for the observed veto-rate offset by at least a factor of 10. In addition, the rate of veto triggers due to these components should be independent of ToF, in contrast to the observations. Hence none of these components constiutes a viable origin of the veto-rate offset.

In general, if the veto-rate offset is due to particles triggering the domes, the size-dependence of the value of the offset follows naturally, and the independence from the threshold level implies that the energy deposited in each interaction is much larger than the threshold energy. The latter characteristic excludes a significant contribution from XRB photons. In principle, natural radioactivity could account for these characteristics of the veto-rate offset, however, natural radioactivity is not expected to give rise to a ToF-dependence of the offset level.

Non-linearities in the correlation of event rate and veto rate could account for all features of the veto-rate offset. In this picture cosmic-ray particles almost exclusively trigger the veto domes, and the dependence of the veto-rate offset level on the size of the domes, and its independence from the threshold levels, follow naturally. In addition, differences in the physics of the processes responsible for the background in different regions of the ToF spectrum could account for the ToF-dependence. To date, however, no significant changes in the small deviations of the event rate from a linear dependence on veto rate as a function of ToF have been found.

To conclude, the veto-rate extrapolation for removing prompt instrumental background in the CDG analysis should be performed self-consistently — irrespective of the origin of the veto-rate offset. Hence, if prompt background components are observed to vanish at some offset value $\mathtt{V}_0$ when linearly extrapolated, then the same behaviour is to be expected for the prompt ToF forward-peak background, and the CDG intensity should be determined at the offset level (see Eq. 5.7), and not at veto rate zero.

5.6 Final Analysis Methods

In this section the final methods employed to study the spectrum and the isotropy of the CDG are described. The results of these analyses are presented and discussed in the next chapter.

5.6.1 Analysis of CDG Spectrum

The procedures for determining, in each energy interval, the CDG intensity and its statistical, systematic and total error are involved as they reflect the complexity of the COMPTEL instrumental background. In deriving the final result a number of systematics and uncertainties have to be considered.

5.6.1.1 CDG Intensity and Statistical Error

The basic approach to determining, in each energy interval, the final results on both the CDG intensity as well as its statistical error is to first derive provisional results from each of the ToF models, which are then combined to give the final results. Depending on the energy range under study, different selections are applied to the data. As explained in Sec. 5.3.7, adjusted-standard selections are best suited to derive the CDG intensity in 0.8–2.7 MeV, while optimized selections are preferred for the 2.7–4.3 MeV range. Above 4.3 MeV, optimized selections are applied in the CDG analysis, as discussed in Sec. 5.4.1. Both selection sets are summarized in Sec. 5.4.2.

For each of the three ToF models (see Secs. 4.3.2 and 5.2) the intensity of the CDG is derived as follows:

- The veto-rate offset used in the final extrapolations is the average of the wide-ToF and narrow-ToF offset values. Similarly, the statistical error of this average veto-rate offset is approximated by the average of the statistical errors of the wide-ToF and narrow-ToF veto-rate offsets, which in general are very similar.
- The CDG intensity is obtained through linear extrapolation of the forward-peak flux as a function of veto rate, after subtraction of long-lived background if present, down to the average veto-rate offset (see Eq. 5.7). The statistical error is obtained through error propagation of the statistical errors from the ToF and instrumental-line fits, as well as from the veto-rate extrapolation, including the statistical error of the average veto-rate offset .

In each energy interval, the final CDG intensity, $I(E)$, and its statistical error, $\sigma_{\rm stat}$, result from averaging the results obtained with each valid ToF model. As explained in Sec. 5.2, below 9 MeV three ToF models are equally suited for modelling the ToF spectrum, hence the results from all three models are averaged at these energies. At

higher energies, however, the parabolic model can be discarded, and consquently the final results above 9 MeV represent the averages of the Gaussian and the exponential model.

5.6.1.2 Systematic and Total Error

In addition to the statistical error derived above, four sources of systematic uncertainty have been identified (see also Kappadath 1998): the ToF modelling, the veto-rate offset value, the telescope efficiency, and the choice of the veto dome used for the extrapolation. The procedures for assessing each of the these errors are briefly described below, before the calculation of the total error is given.

• *Systematic difference between ToF models*: The systematic uncertainty in the CDG intensity due to the different ToF models, $\sigma_{\mathrm{syst,ToF}}$, is estimated by first calculating the difference between the maximum and minimum intensity obtained from the valid ToF models. Subsequent division of this difference by two yields the final value of $\sigma_{\mathrm{syst,ToF}}$. Below 9 MeV all three ToF models are taken into account, while at higher energies only the Gaussian and the exponential model are considered.

• *Systematic uncertainty in veto-rate offset*: As discussed in the previous section, at present a systematic uncertainty of about 25 DT remains in the determination of the veto-rate offset in veto-dome V2, which is used in the final analysis. The resulting uncertainty in the CDG intensity is assessed by first determining, for each ToF model, the CDG intensity at a veto-rate value that is 25 DT above and below the respective average veto-rate offset, yielding an upper and a lower intensity, respectively. Then the upper and lower intensities from the valid ToF models are averaged, and the final systematic error due to the uncertainty in the veto-rate offset, $\sigma_{\mathrm{syst,offset}}$, is estimated to be half the difference between the average upper and lower intensities.

• *Systematic uncertainty in telescope efficiency*: The COMPTEL response has been calibrated for point sources at a number of different positions (see Sec. 3.5). A calibration of the instrument response to an isotropic γ-ray source, however, is not feasible. Hence the determination of the effective area used in the CDG analysis relies entirely on Monte Carlo simulation, as described in Sec. 3.6. The effective area obtained from these simulations can be assigned a statistical error based on the number of simulated events accepted under the appropriate CDG selections, which at present is on the order of a few percent (see Figs. 3.12 and 5.23). In principle, this Poisson error can be reduced below any level through simulation of a sufficient number of photons. A principle limitation of the accuracy of the simulations, however, arises from the uncertainty in the models of the instrument mass distribution used in the simulation, and from uncertainties in the empirically determined instrument characteristics, such as energy resolution (see Secs. 3.5.1 and 3.5.2), which by far dominate the total uncertainty. As a conservative estimate of the systematic uncertainty of the simulated effective area, a value of 15% has been adopted at all energies (Kappadath, 1998, and Kippen, 1998, private communication). Hence the systematic error of the CDG intensity due to the

uncertainty in the effective area, $\sigma_{\mathrm{syst,A_{eff}}}$, is approximated by 15% of the final CDG intensity value.

• *Systematic difference between individual veto domes*: Basically, all four veto domes are equally suited for the veto rate extrapolation, however, in the final analysis only V2 is used. To assess the uncertainty due to this choice of the veto dome, the CDG intensity was determined using each veto dome with the Gaussian model, as this model best represents the average of all models at all energies. It has to be noted that for each dome the respective veto-rate offset was used (see Table 5.5). As will be discussed in Sec. 6.3.2, there is no clear systematic trend in the CDG intensities obtained with different veto domes. Therefore, in each individual energy interval, the variance of the four CDG intensity values was determined, $\sigma_{\mathrm{syst,dome}}$, which is treated like a *statistical* error in the determination of the total error (see also Kappadath 1998).

Finally, in each energy interval the total error, σ_{tot}, of the CDG intensity can be computed. A conservative estimate of the total error is obtained from a summation of the total statistical error and the various systematic errors. The total statistical error, $\sigma_{\mathrm{stat,tot}}$, is obtained from adding the individual statistical errors, σ_{stat} and $\sigma_{\mathrm{syst,dome}}$, in quadrature:

$$\sigma_{\mathrm{stat,tot}} = \sqrt{\sigma^2_{\mathrm{stat}} + \sigma^2_{\mathrm{syst,dome}}} \tag{5.13}$$

The total systematic error, $\sigma_{\mathrm{syst,tot}}$, is conservatively defined as the linear sum of the individual systematic uncertainties:

$$\sigma_{\mathrm{syst,tot}} = \sigma_{\mathrm{syst,ToF}} + \sigma_{\mathrm{syst,offset}} + \sigma_{\mathrm{syst,A_{eff}}} \tag{5.14}$$

The total error of the CDG intensity is then given by

$$\sigma_{\mathrm{tot}} = \sigma_{\mathrm{stat,tot}} + \sigma_{\mathrm{syst,tot}} \tag{5.15}$$

5.6.2 Analysis of CDG Isotropy

The study of the CDG spectrum is aimed at determining the absolute intensity of the CDG in a number of energy bands. The analysis of the isotropy of the CDG, on the other hand, focuses on determining differences between the CDG intensity from different regions of the sky. In particular, it is the significance of the differences that is the primary interest in the investigation of the CDG isotropy. Two approaches have been pursued in the analysis of the CDG intensity, comparison of CDG intensities and comparison of ToF spectra, both of which are briefly described below.

5.6.2.1 Comparison of CDG Intensities

The isotropy of the CDG intensity can be studied by comparing the intensity values obtained for different regions of the sky. In these comparisons, only the statistical

error is taken into account. The systematic errors are expected to be independent of the sky region under study and reflect the absolute uncertainty in the CDG intensity. In studying the CDG isotropy, however, only those differences are relevant that arise from the fact that data from different parts of the sky are compared. The analysis of the CDG isotropy therefore is based on the intensities and statistical errors obtained with a single ToF model, chosen to be the Gaussian model, with the statistical error reflecting the statistical uncertainty in the ToF fits and the veto-rate extrapolation.

As discussed in the next chapter, the first step in the analysis of the CDG isotropy is a search for significant intensity differences. To quantify the significance of the differences in the CDG intensities the χ^2-statistic is employed[39]. A set of CDG spectra, consisting of n identical energy ranges, is analyzed by comparing each individual spectrum against all other spectra and against the weighted average of all other spectra. In comparing spectra i and j, the value of the reduced chi-squared, $\chi^2_{n,ij}$ is determing from

$$\chi^2_{n,ij} = \frac{1}{n} \sum_n \frac{(I_{n,i} - I_{n,j})^2}{(\sigma^2_{n,i} + \sigma^2_{n,j})} \tag{5.16}$$

with $I_{n,i/j}$ and $\sigma_{n,i/j}$ being the intensities and statistical errors for energy range n in spectrum i and j. As will be discussed in Sec. 6.4, no significant anisotropies could be detected.

Assuming that the CDG is, indeed, isotropic, the second step of the isotropy investigation is to derive a quantitative limit on the deviations from isotropy. For this purpose, each set of (statistically consistent) CDG spectra, consisting of n identical energy intervals, is modelled by the weighted average of all individual spectra. This average spectrum is now assumed to represent the true CDG spectrum, hence it has no error, and is referred to as best-model spectrum in the following. To obtain a limit on the deviations allowed by the data, the average of the spectra from the different sky regions, including its statistical errors, the so-called best-measured spectrum, is compared to the best-model spectrum, again employing the χ^2-statistic. The normalization of the best-measured spectrum is increased/decreased, until the value of χ^2_n obtained from a comparison to the best-model spectrum exceeds a defined χ^2_n limit, chosen to correspond to a 95% confidence level. For example, in a single energy interval the χ^2_1 difference between an individual measurement and the true value is expected to be less than 3.841 in 95% of all cases. In this example, the normalization of the best-measured spectrum corresponding to a χ^2_1 value of 3.841 is defined as a upper/lower limit on the deviations from isotropy at the 95% confidence level. Because the intensity errors are symmetric, so are the resulting limits.

[39] In principle, other statistical tests, such as the Kolmogorov-Smirnov test could also be used, but are not expected to yield additional insight due to the limited statistical significance of the data (see Sec. 6.4)

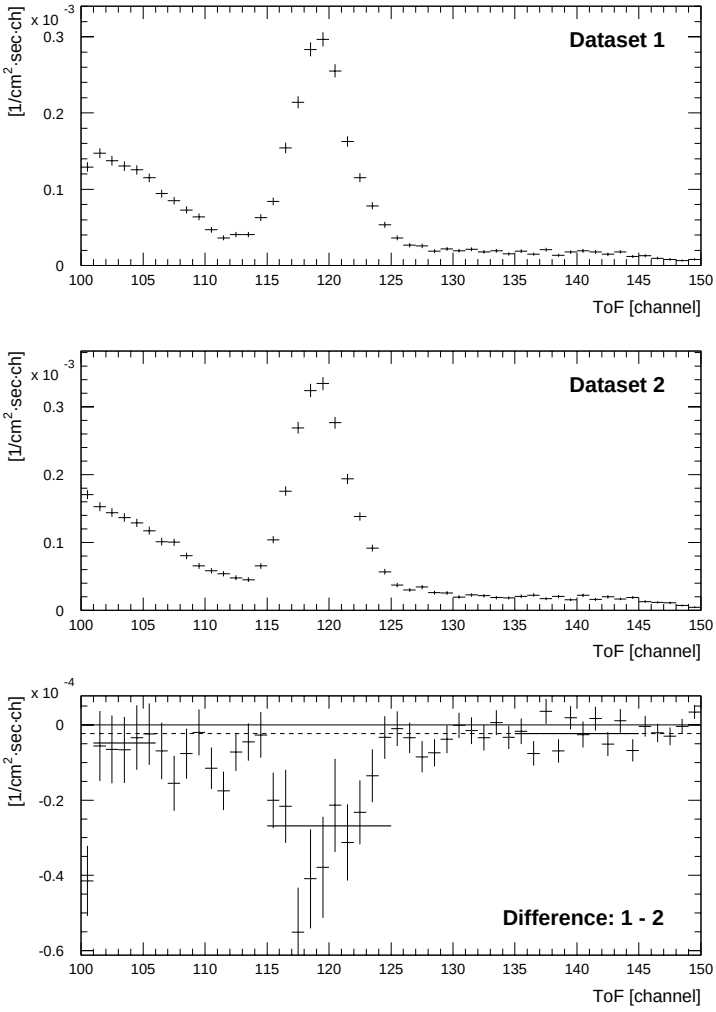

Figure 5.33: *An illustration of the subtraction of ToF spectra for studying the CDG isotropy. To assess the difference in intensity between two regions of the sky the corresponding ToF spectra (Dataset 1 and 2) are subtracted (Difference: 1 - 2). The general difference in the ToF continuum-backgrounds is determined by averaging the event rate in the difference ToF spectrum in the range 135–145 channels (see solid line at these ToF values). The difference event rate in the ToF forward-peak is derived from the ToF range 115–125 channels (see corresponding solid line), and corrected for the general difference in the ToF continuum-backgrounds (indicated by the dashed line). In general, the difference in the ToF continuum-backgrounds in ToF 101–106 channels (see corresponding solid line) is very close to that determined for 135–145 channels.*

5.6.2.2 Comparison of ToF Spectra

A principle drawback of studying the isotropy of the CDG by comparing the intensity measured from different regions of the sky, as described above, is that the intensities are obtained from an involved, non-linear fitting procedure. Therefore an alternative and much more straight-forward approach for determining intensity differences between different regions was investigated — the direct comparison of ToF spectra. At present, this approach is not sufficiently advanced to be utilized for deriving quantitative limits on the CDG isotropy, but it serves as an important cross-check for assessing the extent to which the CDG intensities from different sky regions deviate.

The basic idea of this approach is illustrated in Fig. 5.33. The intensity differences from different regions of the sky are assessed by subtracting corresponding ToF spectra in identical energy and veto-rate binnings. A possible difference in the general level of ToF continuum-background is determined by averaging the event rate in the difference ToF spectrum in 135–145 channels. The difference event rate in the ToF forward-

peak, which is assumed to be exclusively due to differences in the celestial signal, is derived from the ToF range 115–125 channels. The total ToF forward-peak difference is obtained by applying flux correction factors, based on position and width of the forward-peak as given in Table C.3. This correction is minor, on the order of a few percent, and applied to allow the differences to be compared to differences of CDG intensities. It is only in this small correction that results from ToF fits are applied in this approach.

In principle, the direct subtraction of ToF spectra circumvents practically all difficulties and uncertainties related to the complex ToF-fitting and veto-rate extrapolation, rendering the Poisson error in the data the dominant source of uncertainty. In practice, however, some additional sources of uncertainty are still present, which mainly arise from the veto-rate dependence of the prompt instrumental background. For example, in general the frequency distribution of different datasets is different. Because the prompt background increases with veto rate, different veto-rate distributions in the two datasets can result in systematic differences in the prompt ToF forward-peak background levels in each veto-rate bin, analogous to the veto-rate bump (see Sec. 4.6). In addition, the magnitude of this systematic effect may be different in different veto-rate intervals. As depicted in Fig. 4.51, the time-variation of the veto-rate frequency distribution is most pronounced at the lowest and highest veto rates, and in the vicinity of the peak in the distribution. These effects can be minimized by performing the comparison in a very fine veto-rate binning, and in addition by comparing only datasets with similar overall veto-rate frequency distribution, which will be done in future refinements of this approach.

5.7 An Alternative Approach

An alternative to the approach described in this thesis and in Kappadath (1998) for studying the CDG with COMPTEL is being developed by Bloemen *et al.* (1999). In the former approach, COMPTEL is used as a pointed collimator, instrumental-background components are explicitely identified and subtracted from the total event rate, the residual is attributed to the CDG. The latter, alternative approach fully exploits the imaging capability of the instrument and is based on all-sky model fitting through maximum-likelihood optimization in different energy bands, as briefly outlined below.

In each energy interval, the 3-dimensional dataspace-model in $(\chi, \psi, \bar{\varphi})$ utilized in the alternative approach consists of models for the diffuse emission of our galaxy (truncated at $|b| = 30°$), strong galactic sources, an isotropic component representing the CDG, and a model of the instrumental background (for details, refer to Bloemen *et al.* 1999, and references therein). In principle, the celestial components can be distinguished from the dominant instrumental-background component for two reasons. First, the instrumental and celestial components are expected to have different distributions in $\bar{\varphi}$ (the various celestial components should be distinguishable by their

(χ, ψ) distributions). Second, and very important, in contrast to the celestial components, the instrumental-background components vary in time, in particular in the energy range of the long-lived isotopes below about 4.3 MeV — hence the variability of the instrumental background is also at the core of this alternative approach. In the all-sky model-fitting analysis, all OPs are treated separately to account for changes in the instrumental background during the mission. For each individual OP, background models are determined in an iterative procedure, while the model distributions for the celestial components, which are independent of time, are simultaneously fitted to the combined set of observations. It has to be emphasized, however, that this iterative decomposition of the dataspace is not based on a physical model of the instrumental background in $(\chi, \psi, \bar{\varphi})$. In general, the dataspace distributions of isolated point sources and the instrumental background are sufficiently different to allow the point sources to be detected, but these differences decrease as the source distribution becomes more and more extended. In case that signal and background exhibit similar distributions over large regions of the dataspace their iterative separation becomes unreliable.

The alternative approach provides a cross-check for the studies presented in this thesis and in Kappadath (1998). The various results are compared and discussed in the following chapter.

Chapter 6

Results and Discussion

In the following, the results obtained on spectrum and isotropy of the CDG with the analysis methods described in the previous chapter, are presented and their astrophysical implications are discussed.

6.1 Long-Term Variation

The CDG is expected to be constant in time, in contrast to the instrumental background. In particular, there is a significant long-term variation in the instrumental background below 4.3 MeV due to the activity from long-lived radioactive isotopes (see e.g. Sec. 4.5), while at higher energies no such long-term variation is observed (see e.g. Sec. 4.3.4). Moreover, the eight isotopes identified thus far cannot account for all the long-lived instrumenal background (see Sec. 5.3). It is therefore expected that the residual forward-peak flux, which is attributed to the CDG intensity, to some extent varies with time below 4.3 MeV due to unaccounted long-lived instrumental background, but is consistent with a constant intensity at higher energies.

The result of this study is summarized in Fig. 6.1. Above 4.3 MeV the full CDG database was analyzed for each phase/cycle separately (see Tables D.2–D.8). At lower energies, Cycles 3 and 6 were subdivided into two time intervals, comprising those observations before and after the first and second reboost, to be more sensitive to their influence on the instrumental background. The Cycle 3 pre-reboost data consist of OPs 304 through 308, the post-reboost data of all other OPs in Table D.4. Similarly, the Cycle 6 pre-reboost data consist of all observations in Table D.7 up to OP 617.8, with the remaining OPs comprising the post-reboost data.

In each of the five energy intervals above 4.3 MeV the observed variation of the CDG intensity is consistent with a constant intensity in time. It follows that the CDG analysis at these high energies is unaffected by long-term systematics, or long-lived background. Hence data from all phases/cycles can be used for studying the CDG. A

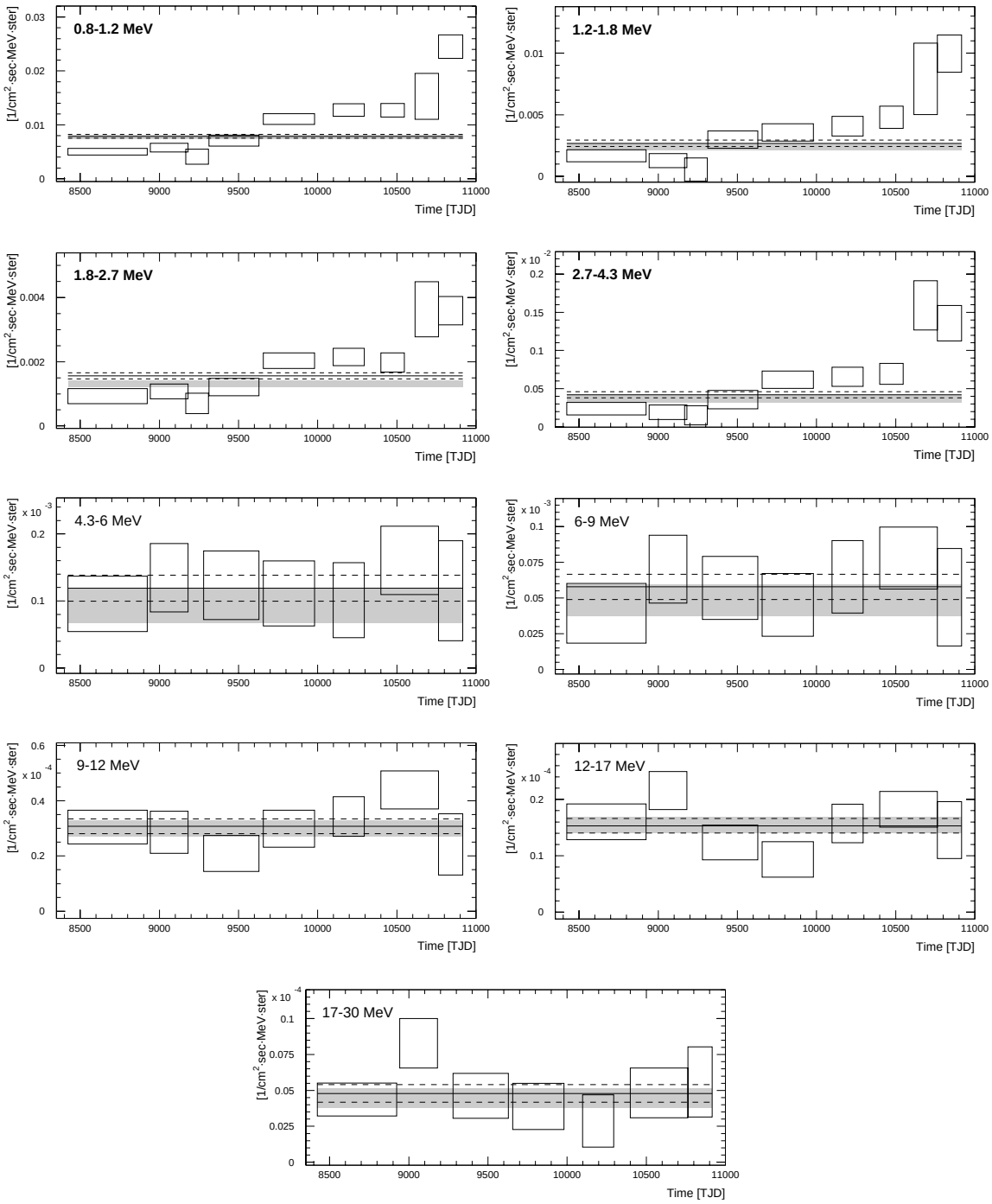

Figure 6.1: *The time-variation of the CDG intensity, as obtained with the Gaussian model at the average veto-rate offset, for adjusted-standard selections and an $E^{-2.5}$ power-law response at all energies. The open boxes represent the results, including the $\pm 1\sigma$ error, for individual time intervals. The grey-shaded band is the corresponding result obtained with the combined dataset. The solid and dashed lines give the weighted average of the results from the individual time intervals, including the 1σ error.*

comparison of the results obtained in the seven time intervals (open boxes) with the result obtained from the combined data (grey-shaded band) yields reduced-χ^2 values (assuming 6 degrees of freedom) of 0.42, 0.47, 0.97, 1.25, and 0.87 in these energy intervals, ordered according to increasing energy. In addition, the fact that in each energy interval the result derived from the combined data is very close to the corresponding weighted average of the results from individual phases/cycles, supports determining the veto-rate offset self-consistently from the data under study (see Sec. 5.5.2).

Below 4.3 MeV the residual forward-peak flux is clearly influenced by unidentified, long-lived instrumental background. The long-term variation of the residual forward-peak flux is very similar to the long-term variation of the activity of identified long-lived isotopes such as ^{22}Na and ^{24}Na (see Fig. 4.47). The rather low residual forward-peak flux obtained from the combined data is artificial, because an extrapolation has been performed for these data despite the presence of a very strong veto-rate bump. To mininize the influence of yet unidentified background components on the CDG intensity, the analysis below 4.3 MeV therefore is restricted to data with the lowest level of activity, which occurred during Phase 2 and early Phase 3 before the first reboost. These data, consisting of OPs 202 through 308 (see Tables D.3 and D.4) will hereafter be referred to as minimum-activity (MA) database. As demonstrated in Sec. 5.3.7, no significant veto-rate bump is present for these data, which further minimizes the influence of unidentified background on the final results.

6.2 Final Analysis Overview

Below, a concise overview of the final analysis of spectrum and isotropy of the CDG is given. Depending on energy, different selections, effective areas, and subsets of the full CDG database were used.

The full CDG database, summarized in Appendix D, comprises all observations pointed at $|b| > 30°$. Observations at lower galactic latitudes b were excluded to minimize the diffuse foreground emission from the galactic plane. The extent to which significant galactic emission and evidence for general anisotropies in the diffuse emission at these intermediate and high galactic latitudes could be detected is discussed in the following two sections.

At energies below 4.3 MeV the minimum-activity (MA) database is used for determining the CDG spectrum to minimize the effect of yet unidentified long-lived instrumental background, as described in the previous section. The MA database comprises all Phase 2 observations (see Table D.3) and the Phase 3 observations (see Table D.4) before the completion of the first reboost, i.e. OPs 202 through 308. The pointing direction of each of these observations, and their combined effective sky exposure[1] under

[1]The effective exposure takes into account the observation time of each individual observation period and its effective area relative to the ideal telescope configuration. Typically, the effective area

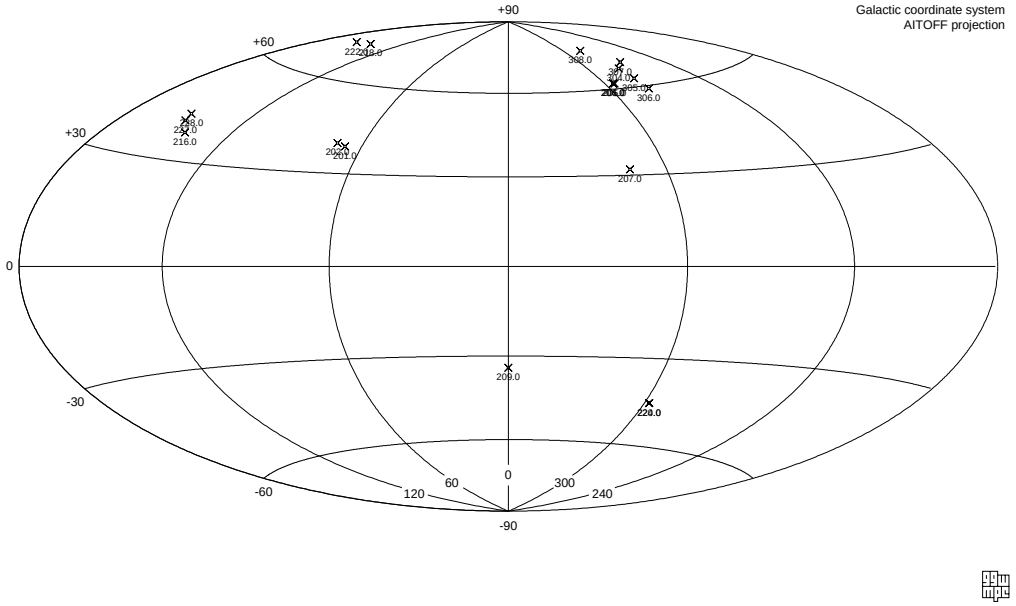

Figure 6.2: *The pointing directions of the observations included in the minimum-activity database in galactic coordinates.*

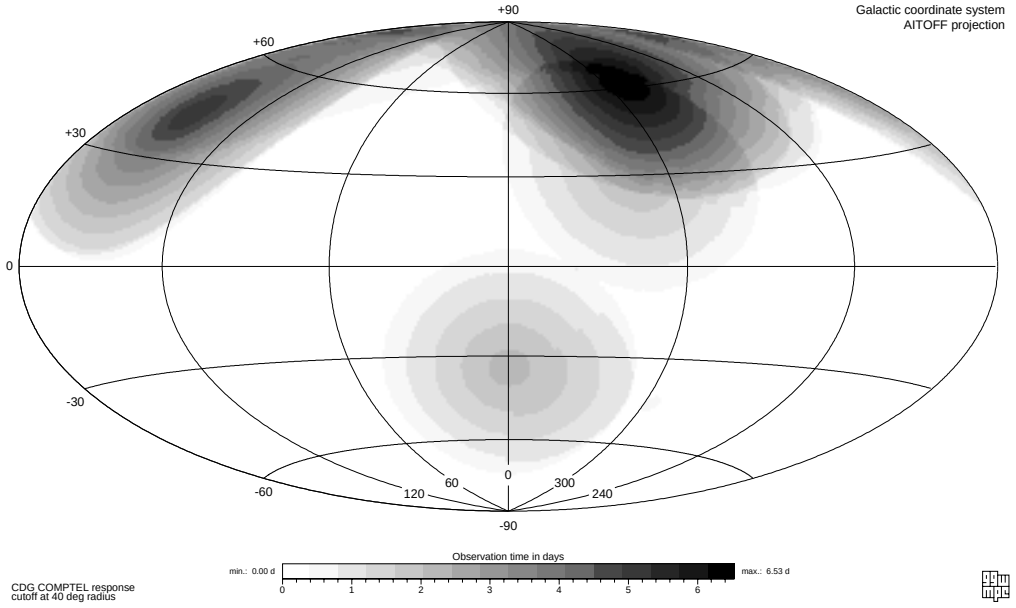

Figure 6.3: *The effective CDG exposure of the observations included in the minimum-activity database in galactic coordinates.*

---

is about 85% of its ideal value for all D1 and D2 modules working properly. The zenit-angle variation of the senisitivity within the field-of-view is approximated by a triangular shape.

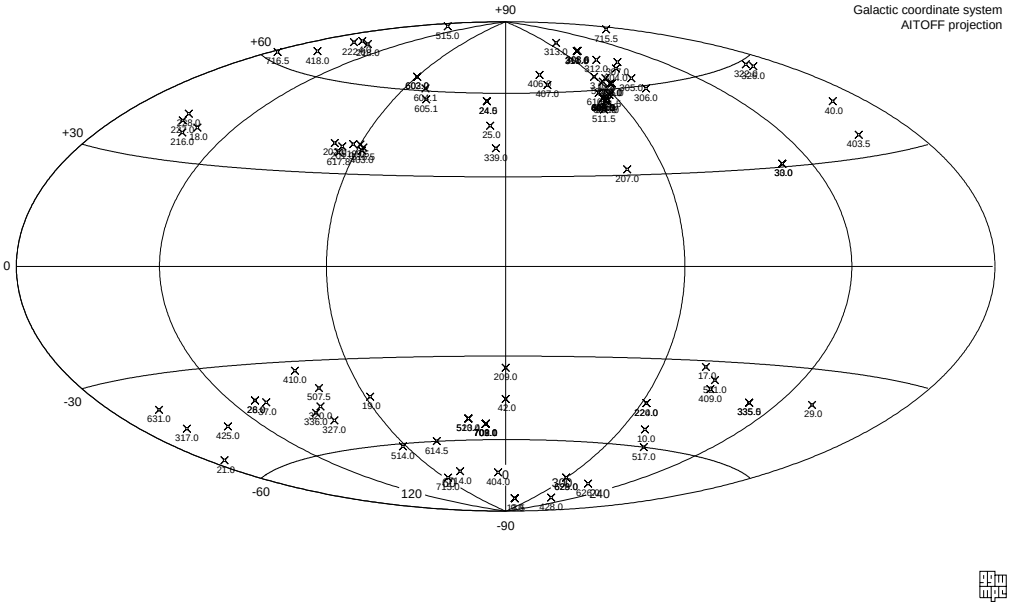

Figure 6.4: *The pointing directions of the observations included in the full CDG database in galactic coordinates.*

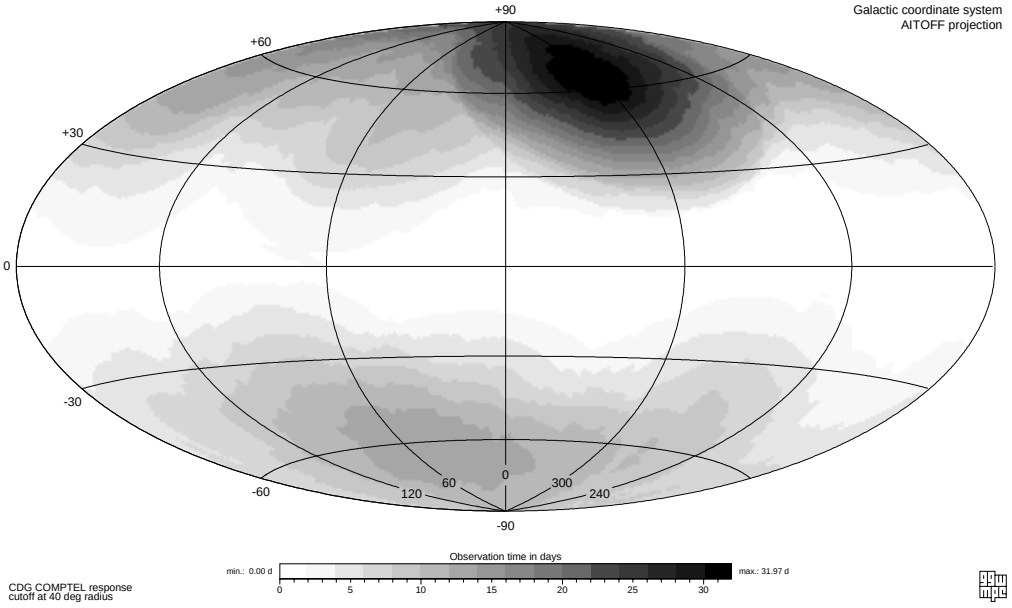

Figure 6.5: *The effective CDG exposure of the observations included in the full CDG database in galactic coordinates.*

CDG selections are depicted in galactic coordinates in Figs. 6.2 and 6.3, respectively. In the final analysis, adjusted-standard selections and optimized selections are applied in the 0.8–2.7 MeV and 2.7–4.3 MeV ranges, respectively (see Sec. 5.3.7). The effective area is determined for an isotropic source distribution with an $E^{-2.5}$ power-law spectrum.

At energies above 4.3 MeV the full CDG database is employed for studying spectrum and isotropy of the CDG. Optimized selections are applied in all energy intervals. The effective area is determined for an isotropic source distribution with an $E^{-2.0}$ power-law spectrum.

6.3 The Energy Spectrum of the CDG

In the following, the final results on the CDG spectrum, determined according to the analysis method described in Sec. 5.6.1, are summarized and discussed.

6.3.1 Intensity and Statistical Error

For each ToF model, the results on the CDG intensity $I(E)$ and its statistical error σ_{stat} are summarized in Table 6.1, together with the final result obtained by averaging the individual results (see Sec. 5.6.1.1). The statistical error reflects the combined statistical uncertainty in the ToF fits and the instrumental-line fits, as well as in the veto-rate extrapolations. In addition to the results obtained from the ToF fits with the single-Gaussian model, at the bottom of the table the results obtained from the two-Gaussian ToF fits in the 4.3–6 MeV and 6–9 MeV energy intervals are included, marked with an asterisk. In the 6–9 MeV range both ToF models yield very similar results, the difference in the 4.3–6 MeV range is not (yet) statistically significant.

6.3.2 Systematic Error and Total Error

The procedure for determining the systematic and total errors of the CDG intensity is decribed in Sec. 5.6.1.2.

The systematic uncertainty of the result on the CDG intensity due to the differences between the three ToF models can be inferred by comparing the results obtained with individual models as summarized in Table 6.1. These differences, depicted as relative deviations with respect to the Gaussian model, are illustrated in Fig. 6.6. It is interesting to compare the deviations in the CDG intensity to the deviations in the ToF forward-peak fluxes shown in Fig. 4.14. The general systematic difference between the three ToF models is preserved after the veto-rate extrapolation — which is the reason this difference is considered a systematic uncertainty. Moreover, in general the magnitude of the relative difference is little affected by the extrapolation, albeit the

Energy Range [MeV]	Intensity [ph/(cm^2 sec ster MeV)]			
	Parabolic	Exponential	Gaussian	Final
0.8–1.2	$(4.69 \pm 0.24) \times 10^{-3}$	$(8.04 \pm 0.09) \times 10^{-3}$	$(5.83 \pm 0.78) \times 10^{-3}$	$(6.18 \pm 0.64) \times 10^{-3}$
1.2–1.8	$(0.74 \pm 0.52) \times 10^{-3}$	$(2.14 \pm 0.56) \times 10^{-3}$	$(1.27 \pm 0.53) \times 10^{-3}$	$(1.38 \pm 0.54) \times 10^{-3}$
1.8–2.7	$(0.87 \pm 0.20) \times 10^{-3}$	$(1.14 \pm 0.21) \times 10^{-3}$	$(1.02 \pm 0.20) \times 10^{-3}$	$(1.01 \pm 0.21) \times 10^{-3}$
2.7–4.3	$(1.68 \pm 0.90) \times 10^{-4}$	$(2.03 \pm 0.94) \times 10^{-4}$	$(2.02 \pm 0.91) \times 10^{-4}$	$(1.91 \pm 0.92) \times 10^{-4}$
4.3–6	$(0.86 \pm 0.18) \times 10^{-4}$	$(1.01 \pm 0.18) \times 10^{-4}$	$(1.05 \pm 0.18) \times 10^{-4}$	$(0.97 \pm 0.18) \times 10^{-4}$
6–9	$(3.89 \pm 0.81) \times 10^{-5}$	$(4.30 \pm 0.77) \times 10^{-5}$	$(4.46 \pm 0.75) \times 10^{-5}$	$(4.21 \pm 0.78) \times 10^{-5}$
9–12	$(1.82 \pm 0.18) \times 10^{-5}$	$(2.01 \pm 0.19) \times 10^{-5}$	$(2.14 \pm 0.20) \times 10^{-5}$	$(2.08 \pm 0.19) \times 10^{-5}$
12–17	$(0.99 \pm 0.12) \times 10^{-5}$	$(1.26 \pm 0.11) \times 10^{-5}$	$(1.31 \pm 0.11) \times 10^{-5}$	$(1.29 \pm 0.11) \times 10^{-5}$
17–30	$(5.01 \pm 0.71) \times 10^{-6}$	$(5.53 \pm 0.70) \times 10^{-6}$	$(5.79 \pm 0.71) \times 10^{-6}$	$(5.66 \pm 0.71) \times 10^{-6}$
4.3–6 (*)	$(6.65 \pm 1.33) \times 10^{-5}$	$(7.01 \pm 1.42) \times 10^{-5}$	$(7.09 \pm 1.38) \times 10^{-5}$	$(6.92 \pm 1.38) \times 10^{-5}$
6–9 (*)	$(4.07 \pm 0.72) \times 10^{-5}$	$(4.34 \pm 0.74) \times 10^{-5}$	$(4.31 \pm 0.73) \times 10^{-5}$	$(4.24 \pm 0.73) \times 10^{-5}$

Table 6.1: *The results on the CDG intensity and its statistical error obtained with each of the three single-Gaussian ToF models. The final result $I(E)$ is the average of the three inidividual results, its statistical error σ_{stat} is the average of the individual statistical errors. The systematic differences between the ToF models are accounted for in the systematic error $\sigma_{\mathrm{syst,ToF}}$ (see Table 6.5). At the bottom of the table, marked with an asterisk, the results obtained with the two-Gaussian model in the 4.3–9 MeV range are included for comparison.*

significance of the difference is reduced. This is particularly true for the 1.2–1.8 MeV and to a lesser extent for the 2.7–4.3 MeV intervals, in which the relative background due to long-lived isotopes is largest. In the 1.2–1.8 MeV interval the magnitude of the relative difference even increases, which most likely arises from uncertainties in the substantial instrumental-line background that is subtracted before the extrapolation (see Fig. 4.14). In the 4.3–9 MeV range the exponential model yields a larger forward-peak flux before the extrapolation, and a lower residual forward-peak flux after the extrapolation. This behaviour is not yet fully understood, but occurs persistently. In the 9–12 MeV and 12–17 MeV intervals the relative deviation of the parabolic model slightly decreases and increases, respectively, but this model does not provide an adequate description of the ToF spectrum at these energies (see Sec. 4.3.2.2). The absolute values of the systematic uncertainty due to the differences between the ToF models, $\sigma_{\mathrm{syst,ToF}}$, can be found in Table 6.5.

For each ToF model, the systematic errors in the CDG intensity due to the systematic uncertainty in the veto-rate offset of 25 DT in `SCV2M` are given in Table 6.2. Also included is the average of these individual errors, denoted $\sigma_{\mathrm{syst,offset}}$, which is used as the final estimate of the uncertainty. In the 0.8–1.2 MeV range no error is quoted for the exponential model, because in this particular case the ToF forward-peak flux decreases with increasing veto-rate, which results from a systematic trend in the curvature of the exponential describing the ToF continuum. Since this variation of the forward-peak flux is unphysical, no extrapolation was performed, but an average value was computed unstead. This average value is independent of the uncertainty in the veto-rate offset.

In the final analysis the veto rate of veto dome V2 is used in the extrapolations. Any of the other three veto domes could be employed as well. To assess the uncertainty

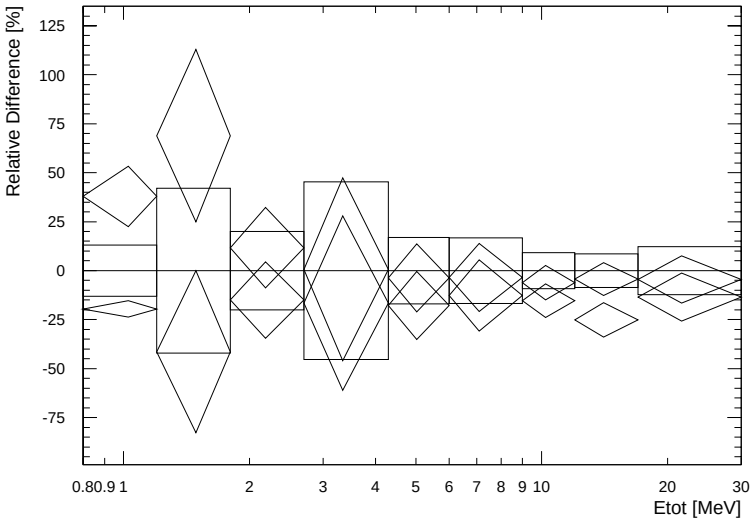

Figure 6.6: *The relative differences in the CDG intensity as obtained from the three ToF models. The differences are normalized to the Gaussian-model results (boxes). The results from the exponential and the parabolic model are depicted with thick and thin diamonds, respectively. (Compare to the relative differences in the forward-peak fluxes shown in Fig. 4.14.)*

Energy	Systematic Veto-Rate Uncertainty [ph/(cm^2 sec ster MeV)]			
Range [MeV]	Parabolic	Exponential	Gaussian	Average
0.8–1.2	8.74×10^{-5}	-	1.94×10^{-5}	3.56×10^{-5}
1.2–1.8	3.95×10^{-5}	8.65×10^{-5}	5.46×10^{-5}	6.02×10^{-5}
1.8–2.7	5.07×10^{-5}	7.44×10^{-5}	6.19×10^{-5}	6.23×10^{-5}
2.7–4.3	2.33×10^{-5}	2.93×10^{-5}	2.62×10^{-5}	2.63×10^{-5}
4.3–6	1.82×10^{-5}	2.12×10^{-5}	2.00×10^{-5}	1.98×10^{-5}
6–9	7.19×10^{-6}	8.02×10^{-6}	7.66×10^{-6}	7.62×10^{-6}
9–12	5.20×10^{-7}	7.57×10^{-7}	8.51×10^{-7}	8.04×10^{-7}
12–17	5.03×10^{-7}	5.27×10^{-7}	5.57×10^{-7}	5.42×10^{-7}
17–30	4.19×10^{-7}	4.55×10^{-7}	4.62×10^{-7}	4.59×10^{-7}

Table 6.2: *The systematic uncertainty in the CDG intensity due to the systematic uncertainty in the veto-rate offset. The final uncertainty, $\sigma_{\mathrm{syst,offset}}$, is estimated by averaging the uncertainties from the individual ToF models.*

due the choice of the veto dome, the CDG intensities were determined with all four veto domes for the Gaussian model at the respective veto-rate offset. As can be seen in Table 6.3, the differences between the individual results are well within the statistical uncertainty. In addition, there is no systematic trend in the differences between the individual results. Therefore the uncertainty due to the choice of the veto dome used in the final analysis, $\sigma_{\mathrm{syst,dome}}$, is considered being statistical in nature, and not systematic. The magnitude of this statistical uncertainty, which is the smallest of all individual errors, is estimated by calculating the variance of the four individual results[2] (see also Kappadath 1998).

[2]The values given in Table 6.3 were determined using an $E^{-2.5}$ power-law effective area at all energies. In addition, in 4.3–9 MeV the two-Gaussian ToF model was employed. Since the variance of the four values is expected to be insensitive to the absolute intensity value, these values were not redetermined for an $E^{-2.0}$ power-law effective area above 4.3 MeV.

	V1	V2	V3	V4	$\sigma_{\mathrm{syst,domes}}$
1	$(6.55 \pm 0.81) \times 10^{-3}$	$(5.84 \pm 0.77) \times 10^{-3}$	$(6.47 \pm 0.77) \times 10^{-3}$	$(6.18 \pm 0.86) \times 10^{-3}$	3.24×10^{-4}
2	$(1.63 \pm 0.58) \times 10^{-3}$	$(1.29 \pm 0.53) \times 10^{-3}$	$(1.48 \pm 0.53) \times 10^{-3}$	$(1.48 \pm 0.57) \times 10^{-3}$	1.40×10^{-4}
3	$(1.11 \pm 0.23) \times 10^{-3}$	$(1.05 \pm 0.20) \times 10^{-3}$	$(1.06 \pm 0.22) \times 10^{-3}$	$(1.12 \pm 0.24) \times 10^{-3}$	3.58×10^{-5}
4	$(2.33 \pm 0.91) \times 10^{-4}$	$(2.24 \pm 0.92) \times 10^{-4}$	$(2.10 \pm 0.92) \times 10^{-4}$	$(2.28 \pm 0.92) \times 10^{-4}$	1.09×10^{-5}
5	$(6.52 \pm 1.38) \times 10^{-5}$	$(6.29 \pm 1.32) \times 10^{-5}$	$(6.50 \pm 1.36) \times 10^{-5}$	$(6.91 \pm 1.33) \times 10^{-5}$	2.58×10^{-6}
6	$(3.58 \pm 0.33) \times 10^{-5}$	$(3.58 \pm 0.32) \times 10^{-5}$	$(3.68 \pm 0.33) \times 10^{-5}$	$(3.57 \pm 0.32) \times 10^{-5}$	5.24×10^{-7}
7	$(2.24 \pm 0.21) \times 10^{-5}$	$(2.24 \pm 0.20) \times 10^{-5}$	$(2.31 \pm 0.21) \times 10^{-5}$	$(2.24 \pm 0.20) \times 10^{-5}$	3.28×10^{-7}
8	$(1.39 \pm 0.12) \times 10^{-5}$	$(1.40 \pm 0.11) \times 10^{-5}$	$(1.39 \pm 0.12) \times 10^{-5}$	$(1.44 \pm 0.17) \times 10^{-5}$	2.50×10^{-7}
9	$(5.00 \pm 0.66) \times 10^{-6}$	$(4.73 \pm 0.64) \times 10^{-6}$	$(5.04 \pm 0.66) \times 10^{-6}$	$(5.01 \pm 0.65) \times 10^{-6}$	1.45×10^{-7}

Table 6.3: *The CDG intensities in the nine energy intervals as obtained from extrapolation with each of the four veto rates. The final uncertainty $\sigma_{\mathrm{syst,domes}}$, which is statistical in nature, is estimated by calculating the variance of the four individual results.*

The systematic error in the CDG intensity arising from the systematic uncertainty in the instrument effective area as determined from Monte Carlo simulation, $\sigma_{\mathrm{syst,A_{eff}}}$, is conservatively approximated as being 15% of the final intensity value. The absolute values of this uncertainty are given in Table 6.5.

To conclude, the various statistical and systematic errors are compiled in Tables 6.4 and 6.5, respectively, together with the total statistical error $\sigma_{\mathrm{stat,tot}}$ and the total systematic error $\sigma_{\mathrm{syst,tot}}$. These were calculated according to Eqs. 5.13 and 5.14, respectively. The magnitude of these uncertainties varies differently with energy, reflecting the charcteristics of the instrumental background. The total error therefore is dominated by different uncertainties in different energy intervals (see next section).

6.3.3 Final CDG Spectrum

The final result on the CDG intensity $I(E)$, as listed in Table 6.1, its total statistical error $\sigma_{\mathrm{stat,tot}}$, total systematic error $\sigma_{\mathrm{syst,tot}}$, and total error σ_{tot} are summarized in Table 6.6. The total error is conservatively estimated to be the linear sum of the total statistical and total systematic error (see Eq. 5.15). The systematic error is larger than the statistical error at all energies except for the 2.7–4.3 MeV interval. At the lowest energies, below 1.8 MeV, the total error is dominated by the systematic uncertainty in the ToF models. At higher energies, the uncertainites in the veto-rate extrapolation and in the effective area are dominant.

The CDG intensity is most significantly determined at the highest energies. In the 9–30 MeV band the combined intensity is $(9.54 \pm 1.88) \times 10^{-6}$ ph/(cm^2 sec ster MeV), corresponding to a significance of 5.1σ. In the 4.3–30 MeV band an intensity of $(1.91 \pm 0.52) \times 10^{-5}$ ph/(cm^2 sec ster MeV) is measured at the 3.7σ level. The intensity over the full 0.8–30 MeV range is obtained at $(1.71 \pm 0.59) \times 10^{-4}$ ph/(cm^2 sec ster MeV) with a significance of 2.9σ. The quoted numbers are based on the total uncertainty of the results and quantify the significance at which the absolute intensity of the CDG is determined, and which is relevant for comparisons with model predictions or results from other experiments. The significance at which the signal of the CDG is detected,

Energy Range [MeV]	Statistical Errors [ph/(cm^2 sec ster MeV)]		
	σ_{stat}	$\sigma_{\mathrm{syst,domes}}$	$\sigma_{\mathrm{stat,tot}}$
0.8–1.2	6.42×10^{-4}	3.27×10^{-4}	7.19×10^{-4}
1.2–1.8	5.39×10^{-4}	1.40×10^{-4}	5.57×10^{-4}
1.8–2.7	2.05×10^{-4}	3.58×10^{-5}	2.08×10^{-4}
2.7–4.3	9.18×10^{-5}	1.08×10^{-5}	9.25×10^{-5}
4.3–6	1.80×10^{-5}	2.58×10^{-6}	1.82×10^{-5}
6–9	7.76×10^{-6}	0.52×10^{-6}	7.78×10^{-6}
9–12	1.92×10^{-6}	0.33×10^{-6}	1.95×10^{-6}
12–17	1.12×10^{-6}	0.25×10^{-6}	1.15×10^{-6}
17–30	7.06×10^{-7}	1.45×10^{-7}	7.21×10^{-7}

Table 6.4: *A compilation of the individual and the total statistical errors of the CDG intensity.*

Energy Range [MeV]	Systematic Errors [ph/(cm^2 sec ster MeV)]			
	$\sigma_{\mathrm{syst,ToF}}$	$\sigma_{\mathrm{syst,offset}}$	$\sigma_{\mathrm{syst,A_{eff}}}$	$\sigma_{\mathrm{syst,tot}}$
0.8–1.2	1.67×10^{-3}	0.04×10^{-3}	0.93×10^{-3}	2.34×10^{-3}
1.2–1.8	6.99×10^{-4}	0.60×10^{-4}	0.21×10^{-4}	9.67×10^{-4}
1.8–2.7	1.37×10^{-4}	0.62×10^{-4}	1.52×10^{-4}	3.51×10^{-4}
2.7–4.3	1.74×10^{-5}	2.63×10^{-5}	2.86×10^{-5}	7.23×10^{-5}
4.3–6	0.93×10^{-5}	1.98×10^{-5}	1.46×10^{-5}	4.37×10^{-5}
6–9	2.83×10^{-6}	7.62×10^{-6}	6.32×10^{-6}	16.8×10^{-6}
9–12	0.66×10^{-7}	0.80×10^{-7}	3.11×10^{-6}	4.58×10^{-6}
12–17	0.28×10^{-6}	0.54×10^{-6}	1.93×10^{-6}	2.75×10^{-6}
17–30	1.30×10^{-7}	4.59×10^{-7}	8.49×10^{-7}	14.4×10^{-7}

Table 6.5: *A compilation of the individual and the total systematic errors of the CDG intensity.*

irrespective of its precise, absolute magnitude, is much higher, since in this case only the smaller statistical error is relevant. For example, based on the statistical uncertainty, the CDG signal over the full 0.8–30 MeV range is detected at the 10σ level.

The CDG spectrum as summarized in Table 6.6 can adequately be described by a power law. Fitting a power-law spectrum of the form

$$I(E) = A \cdot (E/E_0)^{\alpha} \tag{6.1}$$

to the final CDG spectrum, with the reference energy E_0 being fixed at 5 MeV, yields the following results for the normalization A and the power-law index α:

$$A = (1.12 \pm 0.22) \times 10^{-4} \quad \mathrm{ph/(cm^2\ sec\ ster\ MeV)}$$

and

$$\alpha = -2.20 \pm 0.24$$

Energy Range [MeV]	Final CDG Spectrum [ph/(cm^2 sec ster MeV)]			
	$I(E)$	$\sigma_{\mathrm{stat,tot}}$	$\sigma_{\mathrm{syst,tot}}$	σ_{tot}
0.8–1.2	6.183×10^{-3}	0.719×10^{-3}	2.639×10^{-3}	3.358×10^{-3}
1.2–1.8	1.384×10^{-3}	0.557×10^{-3}	0.966×10^{-3}	1.523×10^{-3}
1.8–2.7	1.014×10^{-3}	0.208×10^{-3}	0.351×10^{-4}	0.559×10^{-3}
2.7–4.3	1.909×10^{-4}	0.925×10^{-4}	0.723×10^{-4}	1.648×10^{-4}
4.3–6	9.710×10^{-5}	1.820×10^{-5}	4.372×10^{-5}	6.192×10^{-5}
6–9	4.217×10^{-5}	0.778×10^{-5}	1.678×10^{-5}	2.456×10^{-5}
9–12	2.076×10^{-5}	0.195×10^{-5}	0.458×10^{-5}	0.653×10^{-5}
12–17	1.288×10^{-5}	0.114×10^{-5}	0.275×10^{-5}	0.390×10^{-5}
17–30	5.662×10^{-6}	0.721×10^{-6}	1.437×10^{-6}	2.158×10^{-6}

Table 6.6: *The final result on the CDG intensity, its total statistical error, total systematic error, and total error.*

with the reduced chi-squared of the fit being $\chi^2_\nu = 0.27$ with 7 degrees of freedom.

The final CDG spectrum, together with the power-law fit and its extrapolation to lower and higher energies, is depicted in Fig. 6.7. The bowtie illustrates the 1σ uncertainty of the power-law fit. Although consistent with a power-law spectrum, the data points hint at a steepening of the spectrum with decreasing energy. Modelling the lower five and the upper five data points in energy separately with a power law, or modelling the data points with a broken power law, indicates power-law indices of about -2.6 and about -1.8 for lower and higher energies, respectively[3]. The latest results on the hard XRB in the 80–400 keV range (Kinzer *et al.* 1997) and on the EGB above 30 MeV (Sreekumar *et al.* 1998) suggest a change in the slope of the CDG spectrum which, however, cannot be inferred significantly from the measured CDG spectrum. The result of a broken power-law fit to the combined results, which is practically identical to extrapolations of separate power-law fits of each of the individual results, is included in Fig. 6.7. The individual power-law indices of the XRB and EGB are -2.75 ± 0.08 and -2.10 ± 0.03, respectively. The slope of the final CDG spectrum is slightly steeper than that of the EGB spectrum, but still consistent with an extrapolation of the EGB spectrum. The COMPTEL data are also consistent with the broken power-law fit to the XRB and EGB result. Hence the final CDG spectrum in itself cannot significantly constrain the general shape of the extragalactic background, but suggests that the XRB and the EGB merge smoothly.

Also included in Fig. 6.7 is an illustration of the MeV-bump, exemplified by the result of Trombka *et al.* (1977), which was consistently measured by different groups in the 1970's and early 1980's (see Sec. 2.3.2, in particular Fig. 2.9). The existence of such an MeV-bump is ruled out by the COMPTEL data, suggesting that the MeV-bump

[3]This trend prompted the application of different effective areas below and above 4.3 MeV. As mentioned in Sec. 6.2, at low and high energies the effective areas used are derived for an isotropic source with an $E^{-2.5}$ and an $E^{-2.0}$ power-law spectrum, respectively.

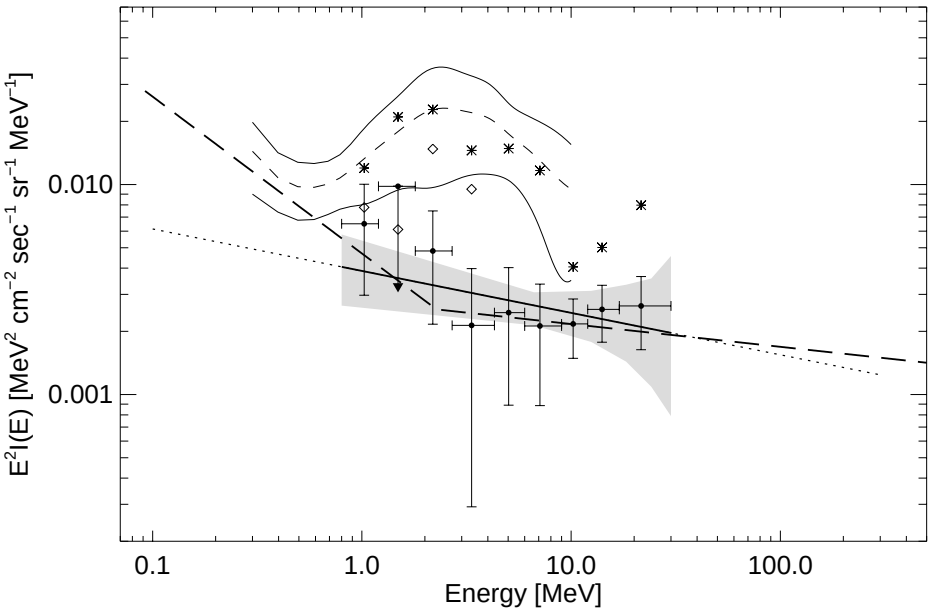

Figure 6.7: *The final result on the CDG spectrum (the arrow of the 2σ upper limit extends down to the measured intensity value). A power-law fit to the data and its extrapolation to lower and higher energies are represented by the solid and dotted lines, respectively. The bowtie illustrates the 1σ uncertainty of the power-law fit. A broken power-law fit to the hard XRB and EGB results by Kinzer* et al. *(1997) and Sreekumar* et al. *(1998) is shown as a thick dashed line. The thin dashed and solid lines indicate the result of Trombka* et al. *(1977), which exemplifies the MeV-bump measured consistently by different groups in the 1970's and early 1980's. The asterisks and open diamonds represent the lowest forward-peak flux measured in this COMPTEL analysis, converted to intensity, before and after the subtraction of the contributions from identified background isotopes (above 4.3 MeV no long-lived activity is present).*

measured in the past must have been due to unidentified instrumental background. As an illustration, the asterisks depict the lowest measured ToF forward-peak fluxes, i.e. the forward-peak flux in the lowest veto-rate bin, converted to intensity. The open diamonds represent the lowest measured forward-peak flux after subtraction of the contributions from identified background isotopes. The instrumental backgrounds of different experiments cannot be easily compared, hence the COMPTEL data cannot be used to explain the instrumental origin of the MeV-bump measured by other experimets. The asterisks and diamonds illustrate, however, the importance of both the veto-rate extrapolation and the subtraction of radioactivity from background isotopes in this analysis.

In this analysis of the CDG the emission from known point sources and, more importantly, the diffuse galactic emission, is not explicitely subtracted[4]. The potential

[4]In addition, it is conceivable that the γ-ray albedo of the Earth contributes to the final result,

contributions from these sources to the measured CDG intensity are discussed in the following.

Thus far the only point sources detected by COMPTEL at $|b| > 30°$ are AGN. Considering the time-averaged flux of these sources, i.e. the flux determined from the combined data available for each source, the two brightest AGN at high galactic latitudes are 3C 273 and 3C 279 (Collmar *et al.* 1996, 1999, Collmar 1999, private comunication), which can account for no more than a few percent of the CDG intensity. For example, the time-averaged flux of 3C 273 peaks in the 1–3 MeV band at $(14.5 \pm 2.2) \times 10^{-5}$ ph/cm^2 sec. This flux corresponds to an intensity of about 1.1×10^{-5}ph/(cm^2 sec ster MeV) when evenly spread over the sky at $|b| > 30°$, which is less than 1% of the CDG intensity at these energies (see Table 6.6). The contribution of AGN detected outside the COMPTEL energy band, in particular at higher energies, is difficult to estimate since the properties of these sources are not knownn well enough. It is therefore assumed that the contribution of known point sources to the measured CDG intensity is negligible.

Contributions from the diffuse galactic emission (see Sec. 2.2.2.3) are of much greater concern. Studies of the cosmic-ray composition and the diffuse galactic γ-ray continuum radiation suggest the presence of a large electron halo that gives rise to γ-radiation at high galactic latitudes via the inverse-Compton process (see e.g. Strong and Moskalenko 1998, Strong *et al.* 1999, and references therein). As an illustration, the CDG spectrum is compared to theoretical expectations on the diffuse galactic emission at $|b| > 30°$ for galactic halo sizes of 4 kpc and 10 kpc (Strong 1999, private communication), which span the currently favoured range according to Strong and Moskalenko (1998). Taking the model predictions at face value, the strongest contributions are to be expected at the highest energies, which in case of a 10 kpc halo could account for $\lesssim 40\%$ of the measured CDG intensity. To assess the possible contribution of the diffuse galactic emission, the CDG spectrum above 4.3 MeV, where the emission from the galaxy is most important, was also determined for a subset of the full CDG database, consisting of all observations pointed at $|b| > 50°$. The final CDG spectrum and the high-latitude spectrum are compared in Table 6.7. Both results agree well within the statistical uncertainty, suggesting that there is little variation in the total diffuse intensity above $|b| = 30°$. This is consistent with the theoretical models, which predict a difference of about 15% — less than the statistical uncertainty of the measurements — between the average intensity at $|b| > 30°$ and $|b| > 50°$.

In principle, the lack of latitude variation in the measured CDG intensities could

---

provided the `EHORA` selection applied in the CDG analysis is insufficient (see Sec. 4.2.2). To confirm that albedo γ-rays have, indeed, been excluded successfully, the analysis was repeated above 4.3 MeV for a `EHORA` $> 50°$ selection instead of the standard `EHORA` $> 45°$ cut. The spectrum of the γ-ray albedo is harder than that of the extragalactic radiation (see e.g. Ryan *et al.* 1979, Thompson and Simpson 1981), hence a comparison at high energies is most sensitiv. The resulting intensities agree within a few percent, with no systematic trend. Hence it is concluded that the standard `EHORA` selection successfully removed atmospheric γ-rays from the data.

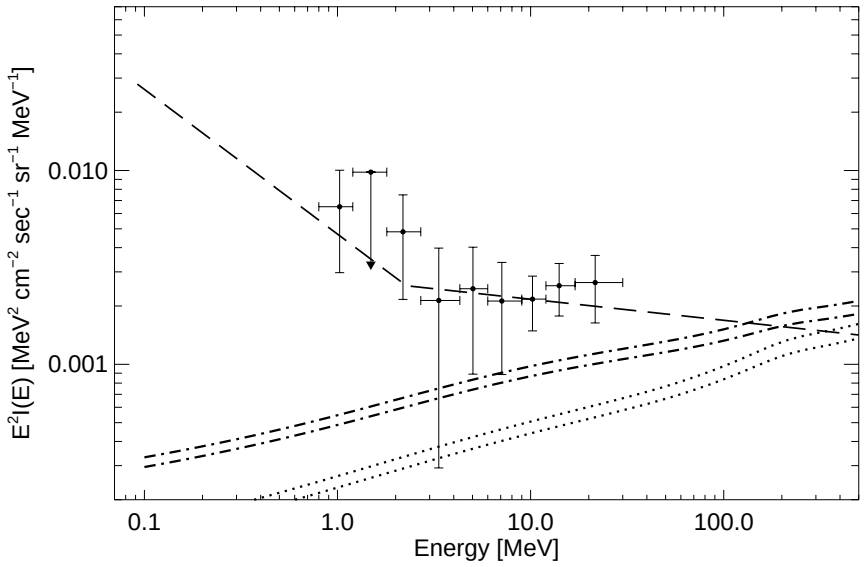

Figure 6.8: *A comparison of the CDG spectrum as determined from observations at* $|b| > 30°$ *with the predictions for the average intensity of the diffuse galactic emission according to the model of Strong* et al. *(1999). The two dash-dotted lines represent the predictions for the average intensity of the diffuse galactic emission at* $|b| > 30°$ *(upper line) and* $|b| > 30°$ *(lower line), assuming a 10 kpc halo. Analogously, the dotted lines illustrate the expected average emission in these two latitude ranges assuming a 4 kpc halo. The dashed line gives the broken power-law fit the latest results on the XRB (Kinzer* et al. *1997) and EBG (Sreekumar* et al. *1998). The contribution of the diffuse galactic emission to the XRB is negligible, and has been been modelled out in the analysis of the EGB.*

be due to a general deficiency of the analysis method. To verify that the CDG analysis method is sensitive to galactic emission, it was applied to 16 OPs[5] pointed within $\lesssim 10°$ of the galactic center. In each of the five energy intervals above 4.3 MeV the intensity inferred from these galactic-center observations is a factor of 3–4 higher than the CDG intensity, with a significance of 3–6σ, considering statistical errors only. The galactic plane, and in particular the galactic center, fill only a small fraction of the CDG field-of-view, which has a half-opening angle of 40°. In addition, the effective area used in the CDG analysis is only valid for isotropic emission. Therefore the derived ratio of the intensity from the galactic-center region to the CDG intensity is underestimated. Nevertheless, the emission from the galactic center is readily and significantly detected.

To further address the diffuse galactic emission, the ToF spectra from those observations in the CDG database with $30° < |b| < 50°$ were subtracted from the ToF spectra determined from the full CDG database. The differences are shown in Fig. 6.9. As expected, there are indications for possible systematic trends in the differences as a

[5]These observations are: 5, 210, 214, 223, 226, 229, 229.5, 232, 232.5, 302.5, 324, 334, 421, 422, 423, and 508.

Energy Range [MeV]	$\lvert b\rvert > 30°$			$\lvert b\rvert > 50°$		
	$I(E)$	$\sigma_{\rm stat}$	$\sigma_{\rm tot}$	$I(E)$	$\sigma_{\rm stat}$	$\sigma_{\rm tot}$
	[ph/(cm^2 sec ster MeV)]			[ph/(cm^2 sec ster MeV)]		
4.3–6	9.71×10^{-5}	1.80×10^{-5}	6.19×10^{-5}	9.03×10^{-5}	2.41×10^{-5}	6.75×10^{-5}
6–9	4.22×10^{-5}	0.78×10^{-5}	2.46×10^{-5}	4.84×10^{-5}	1.01×10^{-5}	2.81×10^{-5}
9–12	2.08×10^{-5}	0.19×10^{-5}	0.65×10^{-5}	2.25×10^{-5}	0.25×10^{-5}	0.74×10^{-5}
12–17	1.29×10^{-5}	0.11×10^{-5}	0.39×10^{-5}	1.23×10^{-5}	0.15×10^{-5}	0.41×10^{-5}
17–30	5.66×10^{-6}	0.71×10^{-6}	2.16×10^{-6}	5.68×10^{-6}	0.93×10^{-6}	2.37×10^{-6}

Table 6.7: *A comparison of the final CDG intensity, which is determined from the full CDG database ($|b| > 30°$), with the CDG intensity determined from those observations with $|b| > 50°$, in the five energy intervals above 4.3 MeV.*

function of veto rate (see Sec. 5.6.2.2). Nevertheless, the differences indicate that the ToF spectra from intermediate galactic latitudes ($30° < |b| < 50°$) contain more celestial signal than the ToF spectra from high galactic latitudes ($|b| > 50°$), as expected. The observed differences are, however, not significant. In addition, the differences and their errors are a few times larger than the predicted latitude variation according to the model of Strong *et al.* (1999).

It is therefore concluded that no significant differences in the CDG intensity between medium and high galactic latitudes can be found within the limits of the CDG analysis method, which therefore cannot yet be employed for investigating the diffuse galactic γ-ray emission at high latitudes, except for placing an upper limit on its intensity. Hence it cannot be ruled out at present that 20–40% of the measured CDG intensity is due to inverse-Compton emission from an extended galactic halo above 4.3 MeV as suggested by Strong *et al.* (1999), which is comparable to the total uncertainty of the determined CDG intensity. The predicted halo contribution decreases with energy to 10–20%. The issue of the latitude variation of the CDG intensity, and the CDG isotropy in general, is further addressed in the next section.

The final CDG spectrum derived in this analysis is compared to other current results on the CDG spectrum in Fig. 6.10. Other recent results on the CDG obtained with COMPTEL are those by Kappadath (1998), employing an analysis method similar to that in this thesis, and by Bloemen *et al.* (1999), using the alternative approach sketched in Sec. 5.7. A recent, preliminary result on the CDG spectrum in 0.3–7 MeV, obtained from an analysis of SMM/GRS data, has been reported by Watanabe *et al.* (1997). Also depicted are a recent measurement of the hard XRB in the 80–400 keV range obtained by Kinzer *et al.* (1997) with HEAO-1 and the lowest-energy data points in energy of the EGB as determined in the 30 MeV to 100 GeV range by Sreekumar *et al.* (1998) with EGRET (see Secs. 2.1.6 and 2.1.7). Finally, the MeV-bump found by earlier experiments is exemplified by the result of Trombka *et al.* (1977). In general, the different recent determinations of the CDG spectrum agree within their respective

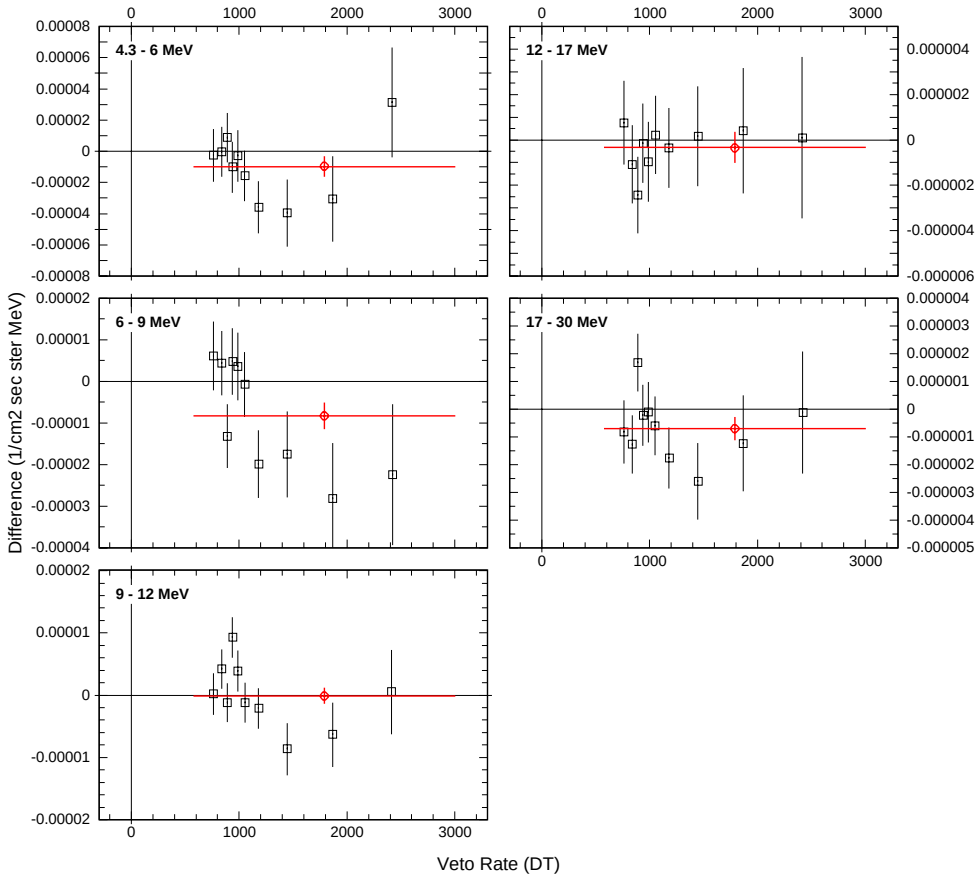

Figure 6.9: *The difference in the CDG intensity as determined from the subtraction of ToF spectra as a function of veto rate in the five energy intervals above 4.3 MeV. The ToF spectra of those observations in the full CDG database pointed at* $30° < |b| < 50°$ *have been subtracted from those observations pointed at* $|b| > 50°$.

uncertainties[6]. In addition, the various results are consistent with extrapolations of the hard XRB spectrum and the high-energy EGB spectrum to MeV energies. It is worth noting that contributions from the diffuse galactic emission to the XRB are negligible, while this foreground emission has been modelled out in the analysis of the EGB. As described in Sec. 2.3.3, the overall shape of the EGB spectrum above about 500 keV is now greatly simplified, compared to the historic spectrum depicted in Fig. 2.9. No evidence for the MeV-bump is found, instead the recent results indicate that there is a smooth transition from a softer, low-energy component to a harder, high-energy component in the extragalactic radiation, with the transition occuring at a few MeV. This transition may be due to the emission characteristics of different classes of point sources, as discussed in detail in the next section.

The result of Kappadath (1998) was derived in an analysis similar to that described

[6] This includes earlier COMPTEL results on the CDG presented by Kappadath *et al.* (1995, 1996, 1997) and Weidenspointner *et al.* (1999)

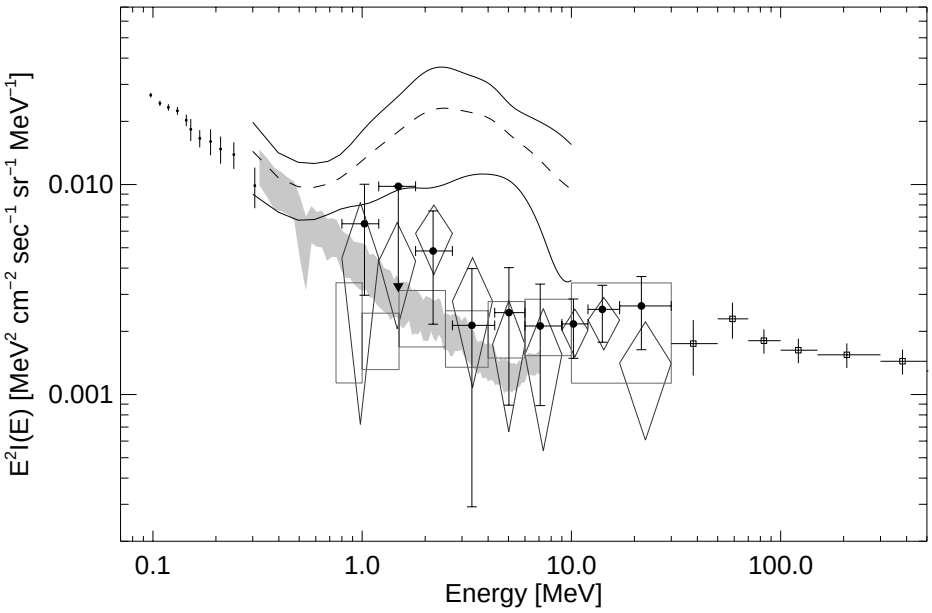

Figure 6.10: *A comparison of recent results on the CDG spectrum. The final CDG spectrum obtained in this thesis is depicted by the filled data points (the arrow of the 2σ upper limit extends down to the measured intensity value). Other current COMPTEL results on the CDG are those by Kappadath (1998) and Bloemen* et al. *(1999), represented by open diamonds and boxes, respectively. The grey-shaded band gives the preliminary result by Watanabe* et al. *(1997) derived from SMM data. The MeV-bump found by earlier experiments is exemplified by the result of Trombka* et al. *(1977). Also shown are the recent measurements of the hard XRB in 80–400 keV by Kinzer* et al. *(1997), and the recent determination of the EGB in the 30 MeV to 100 GeV range by Sreekumar* et al. *(1998).*

in this thesis. It is based on data from the Virgo region and from observations in the vicinity of south galactic pole from Phase I through Cycle 5, and hence represents the sky at high latitudes, similar to the result derived from observations at $|b| > 50°$ summarized in Table 6.7. In comparison, the result obtained in this thesis represents a much larger fraction of the sky (see Fig. 6.5). The results of both analyses agree well within uncertainites. For example, Kappadath (1998) derives a power-law index of -2.4 ± 0.2, compared to an index of -2.20 ± 0.24 as obtained in this work. There are, however, some small differences in the two analyses. In general, the total error quoted by Kappadath (1998) is smaller than the errors quoted in this work (see Table 6.6). The difference arises from the fact in this analysis statistical and systematic errors were combined linearly to obtain the total error (see Eq. 5.15), while all statistical and systematic errors were added in quadrature in the analysis of Kappadath (1998). Also, below 4.3 MeV the intensities obtained in this work are generally lower than those derived by Kappadath (1998), while above 4.3 MeV the opposite is the case. The difference at low energies is due to the fact that the isotopes ^{52}Mn, ^{57}Ni, and

^{208}Tl have not been explicitely subtracted in the analysis of Kappadath (1998). The 1.4 MeV line in E_2, which is due to the former two isotopes (see Secs. 4.4.2.7 and 4.4.2.8), was, however, tentatively modelled by a single Gaussian to account for this line to the first order. At higher energies the difference arises from the different veto-rate values assumed to correspond to geophysical conditions free of incident cosmic radiation. In this analysis the CDG intensity is determined by extrapolation to the veto-rate offset, while Kappadath (1998) determined the CDG intensity at veto rate zero (see Sec. 5.5.2).

The result of Bloemen *et al.* (1999) is derived from the alternative analysis method outlined in Sec. 5.7, which is still being developed. For example, the quoted errors of 30% (in the lowest and highest energy band 50%), although much larger than the formal statistical error of a few percent, have been assigned based on previous experience from studying point sources and also some extended sources. The magnitude of the errors suitable *in general* for the latter analyses is not necessarily applicable to the investigation of an isotropic source. The first result obtained with the alternative approach is in good agreement with the other two COMPTEL results, but does not exhibit any trend for the CDG intensity to increase with decreasing energy. Finally, the galactic high-latitude emission above $|b| = 30°$ has not been modelled or subtracted in the alternative approach, similar to the other two COMPTEL analyses.

The result of Watanabe *et al.* (1997) is still preliminary. In additon, the analysis has not yet been published in detail and is therefore not commented upon further.

6.4 The Isotropy of the CDG

In the CDG analysis method employed in this work COMPTEL is used as a pointed collimator with a circular field-of-view defined by a half-opening angle of 40° (see Sec. 4.2.1). It follows that the FoV covers a solid angle of about 1.5 ster, corresponding to about 12% of the celestial sphere, which implies that the isotropy of the CDG can only be probed on the largest angular scales. In addition, the long-term variation of the residual ToF forward-peak flux due to long-lived, unidentified background in general precludes an investigation of the CDG isotropy below 4.3 MeV, since it is not possible to combine data from different phases/cycles, which is necessary to obtain sufficient exposure of defined regions on the sky.

As described in Sec. 5.6.2.1, two approaches have been pursued to assess differences in the CDG intensity from different regions of the sky: comparison of absolute intensities and subtraction of ToF spectra. In the former approach the systematic errors are assumed to be independent of the sky region under study. Hence only the statistical error $\sigma_{\rm stat}$ is considered in the comparisons, based on ToF fits with the Gaussian model, which best represents the average of all three models. The final intensity value is determined at the average veto-rate offset.

In the following, the CDG intensity from the northern and southern hemispheres, defined to comprise all observations above $b = 30°$ and below $b = -30°$, respectively, is compared at energies above and below 4.3 MeV. Further investigations of the CDG isotropy above 4.3 MeV have been preformed for so-called sky quarters, defined as half-hemispheres, and as a function of latitude.

6.4.1 Isotropy in 0.8–4.3 MeV

As mentioned above, the isotropy of the CDG can only tentatively be addressed by comparing the intensities obtained from the northern and southern hemispheres. In principle, the minimum-actitvity database is best suited for this purpose. The effective exposure of the southern hemisphere is, however, very low for these observations because the `EHORA` selection rejects most of the minimum-activation observing time at southern latitudes (see Fig. 6.3). Therefore the CDG intensity from the two hemispheres was studied using all observations in Phases I through III until the first reboost, i.e. OPs 3–308 (see Tables D.2–D.4).

The CDG intensities obtained in the four energy intervals below 4.3 MeV for the individual hemispheres and the combined data are summarized in Table 6.8. The intensities are consistent within their statistical error, no significant anisotropy is found. Comparison of the hemispheres yields a reduced chi-squared of $\chi^2_\nu = 0.24$, assuming 4 degrees of freedom. Assuming that the CDG is isotropic, a formal upper limit of about 34% on the relative deviation of the CDG intensity from isotropy at the 95% confidence level is obtained based on the χ^2-statistic (see Sec. 5.6.2.1).

Energy Range [MeV]	CDG Intensity [ph/(cm^2 sec ster MeV)]		
	Total	North	South
0.8–1.2	$(5.28 \pm 0.44) \times 10^{-3}$	$(5.53 \pm 0.60) \times 10^{-3}$	$(5.26 \pm 0.94) \times 10^{-3}$
1.2–1.8	$(1.50 \pm 0.33) \times 10^{-3}$	$(1.57 \pm 0.46) \times 10^{-3}$	$(1.55 \pm 0.69) \times 10^{-3}$
1.8–2.7	$(9.86 \pm 1.41) \times 10^{-4}$	$(8.10 \pm 2.18) \times 10^{-4}$	$(10.9 \pm 2.37) \times 10^{-4}$
2.7–4.3	$(2.28 \pm 0.59) \times 10^{-4}$	$(2.35 \pm 0.81) \times 10^{-4}$	$(2.86 \pm 1.01) \times 10^{-4}$

Table 6.8: *A comparison of the CDG intensities and their statistical errors below 4.3 MeV obtained for the two hemispheres and the combined data. The intensities were derived with the Gaussian model for adjusted-standard selections.*

6.4.2 Isotropy in 4.3–30 MeV

6.4.2.1 Comparison of Hemispheres

In the comparison of the CDG intensity from the northern and southern hemispheres the full CDG analysis procedure is applied to obtain the statistical as well as the total error. The results for the two hemispheres, derived with the single-Gaussian models, are summarized in Table 6.9. In addition, the results in 4.3–6 MeV and 6–9 MeV derived with the two-Gaussian models are given in the last two lines, marked with an asterisk. While both approaches to model the ToF forward peak in the 4.3–9 MeV range yield consistent results in the northern hemisphere, there is a significant difference in the southern hemisphere. The intensities obtained for the two hemispheres with the single-Gaussian are consistent within their statistical error, while the two-Gaussian models suggest an anisotropy at 4.3–9 MeV.

Further insight into this problem was obtained from subtracting the southern-hemisphere ToF spectra from the northern-hemisphere ToF spectra (see Fig. 6.11). In each energy interval the difference is rather independent of veto rate, allowing us to reliability determine the average difference. The results are given in Table 6.10. The intensity from both hemispheres in general agrees within the statistical uncertainty, which is much smaller than that of the absolute CDG intensities of Table 6.9. Since no ToF fitting is involved in determining these differences, this approach can be employed to independently assess the reliabilty of the single-Gaussian and of the two-Gaussian ToF fits. Clearly, the results for $\Delta I(E)$ obtained from the subtraction of ToF spectra agree with the differences between the CDG intensities determined with the single-Gaussian model, while the two-Gaussian model — although superior in principle — is in conflict and therefore considered inferior in its present form.

Both the absolute CDG intensities and the subtraction of ToF spectra suggest that the emission from the northern hemisphere is slightly larger than from the southern hemisphere. Nevertheless, both sets of intensities agree within the statistic error limits and hence the assumption of isotropy cannot be rejected. Assuming isotropy, the results from a comparison of the intensities in three different energy ranges, and the

Energy Range [MeV]	$b > 30°$			$b < -30°$		
	$I(E)$	$\sigma_{\rm stat}$	$\sigma_{\rm tot}$	$I(E)$	$\sigma_{\rm stat}$	$\sigma_{\rm tot}$
	[ph/(cm^2 sec ster MeV)]			[ph/(cm^2 sec ster MeV)]		
4.3–6	9.33×10^{-5}	2.27×10^{-5}	6.70×10^{-5}	11.6×10^{-5}	2.82×10^{-5}	8.12×10^{-5}
6–9	4.34×10^{-5}	0.98×10^{-5}	2.72×10^{-5}	4.46×10^{-5}	1.25×10^{-5}	3.22×10^{-5}
9–12	2.17×10^{-5}	0.25×10^{-5}	0.73×10^{-5}	1.95×10^{-5}	0.31×10^{-5}	0.76×10^{-5}
12–17	1.32×10^{-5}	0.14×10^{-5}	0.43×10^{-5}	1.28×10^{-5}	0.18×10^{-5}	0.46×10^{-5}
17–30	6.13×10^{-6}	0.90×10^{-6}	2.44×10^{-6}	5.74×10^{-6}	1.11×10^{-6}	2.57×10^{-6}
4.3–6 (*)	9.13×10^{-5}	1.77×10^{-5}	3.86×10^{-5}	5.00×10^{-5}	2.22×10^{-5}	3.99×10^{-5}
6–9 (*)	5.21×10^{-5}	0.93×10^{-5}	1.89×10^{-5}	2.80×10^{-5}	1.20×10^{-5}	2.02×10^{-5}

Table 6.9: *A comparison of the CDG intensity and its statistical and total errors for the two hemispheres in the 4.3–30 MeV range. The intensities were derived with the single-Gaussian ToF models. In addition, the results in 4.3–6 MeV and 6–9 MeV derived with the two-Gaussian ToF models are given in last two lines, marked with an asterisk.*

Energy Range [MeV]	$\Delta I(E)$ from ToF Difference [ph/(cm^2 sec ster MeV)]
4.3–6	$(3.25 \pm 6.64) \times 10^{-6}$
6–9	$(6.01 \pm 3.21) \times 10^{-6}$
9–12	$(2.40 \pm 1.29) \times 10^{-6}$
12–17	$(3.58 \pm 6.88) \times 10^{-7}$
17–30	$(-1.86 \pm 4.27) \times 10^{-7}$

Table 6.10: *The average difference in the CDG intensity from the two hemispheres above 4.3 MeV as determined from the subtraction of ToF spectra (see Fig. 6.11).*

E. Band	E. Intervals	χ^2_ν	2σ U. L.
4.3–30	5	0.20	23.39%
4.3–9	2	0.30	39.44%
9–30	3	0.14	21.84%

Table 6.11: *. The results of a comparison of the CDG intensity above 4.3 MeV, determined for the two hemispheres in five energy intervals. In three energy bands 95% confidence limits on the deviations from isotropy allowed by the data are derived.*

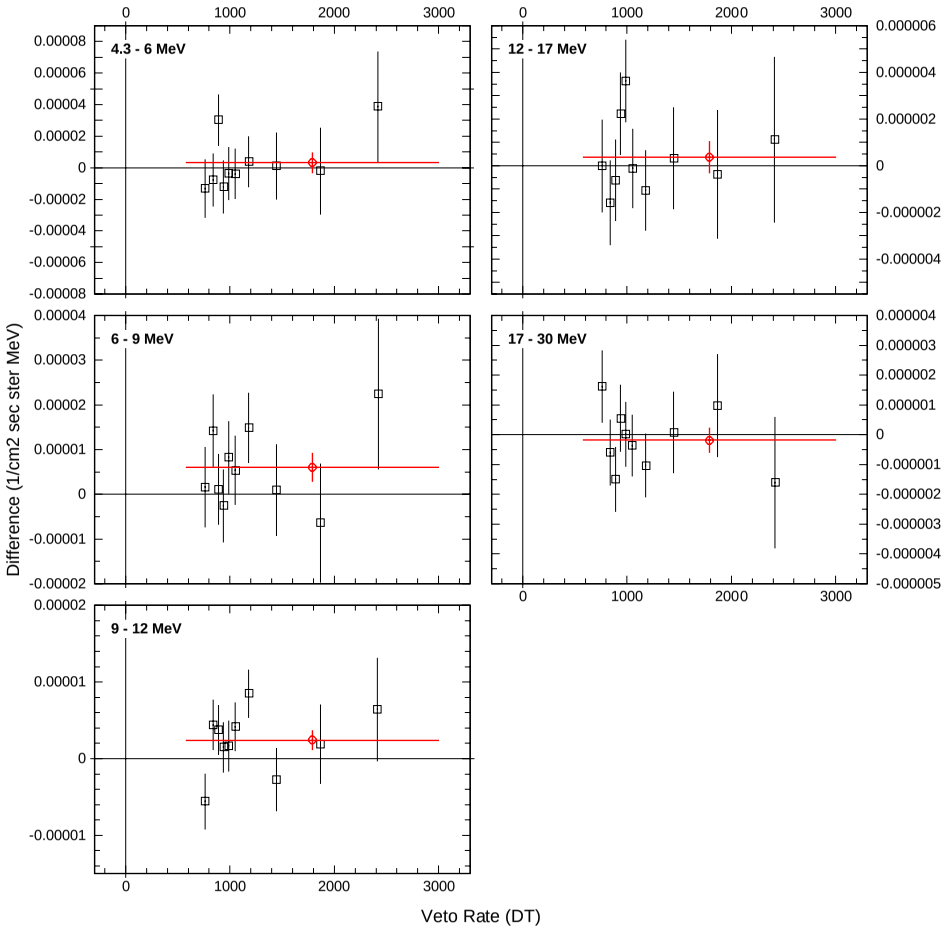

Figure 6.11: *The difference in the CDG intensity from the two hemispheres as determined from the subtraction of ToF spectra as a function of veto rate in the five energy intervals above 4.3 MeV. The ToF spectra of the observations in the southern hemisphere ($b < -30°$) have been subtracted from those of the observations in the northern hemisphere ($b > 30°$).*

inferred 95% confidence limits on the deviations from isotropy allowed by the data are summarized in Table 6.11.

6.4.2.2 Comparison of Sky Quarters

The next step in the isotropy study was to compare sky quarters, defined to be halved hemispheres as defined in Table 6.12. The χ^2_ν-values obtained from comparing the determined CDG intensities in the 4.3–30 MeV, 4.3–9 MeV, and 9–30 MeV bands are summarized in Tables 6.13–6.15. Each individual spectrum is compared with each of the other three spectra, and in addition the weighted average of the other three spectra. For each comparison the χ^2_ν-value is less than 1, hence again isotropy can be assumed. The inferred 95% confidence limits on the deviations from isotropy allowed by the data are summarized in Table 6.16.

Sky Quarter	Long. Range	Lat. Range
I	$0° \leq l < 180°$	$b > 30°$
II	$180° \leq l < 360°$	$b > 30°$
III	$0° \leq l < 180°$	$b < -30°$
IV	$180° \leq l < 360°$	$b < -30°$

Table 6.12: The definition of the sky regions corresponding to the sky quarters.

Sky Quarters in 4.3–30 MeV, 5 $E_{\rm tot}$ Intervals					
	I	II	III	IV	W. Avrg.
I	-	0.61	0.24	0.83	0.61
II		-	0.32	0.44	0.47
III			-	0.33	0.13
IV				-	0.54

Table 6.13: *The χ^2_ν-values obtained from the comparisons of the CDG intensities determined in the four sky quarters defined in Table 6.12 in 4.3–30 MeV.*

Sky Quarters in 4.3–9 MeV, 2 $E_{\rm tot}$ Intervals					
	I	II	III	IV	W. Avrg.
I	-	0.31	0.26	0.96	0.42
II		-	0.38	0.82	0.47
III			-	0.33	0.16
IV				-	0.81

Table 6.14: *The χ^2_ν-values obtained from the comparisons of the CDG intensities determined in the four sky quarters defined in Table 6.12 in 4.3–9 MeV.*

Sky Quarters in 9–30 MeV, 3 $E_{\rm tot}$ Intervals					
	I	II	III	IV	W. Avrg.
I	-	0.81	0.23	0.74	0.73
II		-	0.28	0.20	0.47
III			-	0.32	0.10
IV				-	0.37

Table 6.15: *The χ^2_ν-values obtained from the comparisons of the CDG intensities determined in the four sky quarters defined in Table 6.12 in 9–30 MeV.*

E. Band	E. Intervals	2σ U. L.
4.3–30	5	31.80%
4.3–9	2	49.10%
9–30	3	30.38%

Table 6.16: *. The results of a comparison of the CDG intensity above 4.3 MeV, determined for the four sky quarters in five energy intervals. In three energy bands 95% confidence limits on the deviations from isotropy allowed by the data are derived.*

Energy	CDG Intensity [ph/(cm^2 sec ster MeV)]		
Range [MeV]	$30° < \|b\| < 45°$	$45° < \|b\| < 60°$	$\|b\| > 60°$
4.3–9	$(6.83 \pm 1.47) \times 10^{-5}$	$(8.01 \pm 1.75) \times 10^{-5}$	$(5.82 \pm 1.70) \times 10^{-5}$
9–30	$(9.78 \pm 0.93) \times 10^{-6}$	$(10.7 \pm 1.06) \times 10^{-6}$	$(8.80 \pm 1.05) \times 10^{-6}$
4.3–9 (*)	$(3.32 \pm 1.07) \times 10^{-5}$	$(5.59 \pm 1.28) \times 10^{-5}$	$(7.75 \pm 1.21) \times 10^{-5}$

Table 6.17: *A comparison of the CDG intensity and its statistical error for three latitude ranges in the 4.3–30 MeV range. In addition, the result in 4.3–9 MeV derived with the two-Gaussian model is given in the last line, marked with an asterisk.*

6.4.2.3 Comparison of Latitude Regions

The lack of a significant deviation from isotropy in the comparisons of the hemispheres and the sky quarters was to be expected, since the diffuse galactic emission, which is the most likely source of anisotropy, is symmetric about $b = 0°$ and $l = 0°$. The most sensitive test for anisotropies due to the diffuse galactic emission is to study the latitude variation of the CDG intensity, which to some extent was already discussed in Sec. 6.3.3. For this purpose the observations were divided into three bands in latitude: $30° < |b| < 45°$, $45° < |b| < 60°$, and $60° < |b| < 90°$. The derived intensity values and their statistical errors are summarized in Table 6.17. Again, in the last line, marked with an asterisk, the intensities derived with the two-Gaussian model in 4.3–9 MeV are given. For comparison, the differences between the ToF spectra in $|b| > 60°$ and $30° < |b| < 45°$, as well as in $|b| > 60°$ and $45° < |b| < 60°$ are depicted in Figs. 6.12 and 6.13. As expected, the differences of the ToF spectra indicate that the celestial signal in the ToF forward-peak decreases with increasing latitude, with the difference between the two high-latitude bands being insignificant. The absolute magnitude of the difference of the CDG intensity from the lowest and highest latitude region as inferred from the ToF differences is consistent with that inferred from the ToF subtraction. In case of the difference between the medium and high latitude band there is, however, some inconistency. Similar to what has been observed in Sec. 6.3.3, the ToF differences indicate the expected latitude variation, whose magnitude, however, is smaller than the statistical error of the absolute intensity values. Hence again no significant deviation from anisotropy can be detected within the limits of the CDG analysis method. The

Latitude Regions in 4.3–30 MeV, 2 $E_{\rm tot}$ Intervals				
	$30° < \|b\| < 45°$	$45° < \|b\| < 60°$	$60° < \|b\| < 90°$	W. Avrg.
$30° < \|b\| < 45°$	-	0.40	0.35	0.00
$45° < \|b\| < 60°$		-	1.21	0.86
$60° < \|b\| < 90°$			-	0.87

Table 6.18: *The χ^2_ν-values obtained from the comparisons of the CDG intensities determined in three latitude ranges in 4.3–30 MeV.*

Latitude Regions in 4.3–9 MeV, 1 $E_{\rm tot}$ Interval				
	$30° < \|b\| < 45°$	$45° < \|b\| < 60°$	$60° < \|b\| < 90°$	W. Avrg.
$30° < \|b\| < 45°$	-	0.27	0.20	0.00
$45° < \|b\| < 60°$		-	0.81	0.61
$60° < \|b\| < 90°$			-	0.54

Table 6.19: *The χ^2_ν-values obtained from the comparisons of the CDG intensities determined in three latitude ranges in 4.3–9 MeV.*

Latitude Regions in 9–30 MeV, 1 $E_{\rm tot}$ Interval				
	$30° < \|b\| < 45°$	$45° < \|b\| < 60°$	$60° < \|b\| < 90°$	W. Avrg.
$30° < \|b\| < 45°$	-	0.41	0.48	0.00
$45° < \|b\| < 60°$		-	1.61	1.12
$60° < \|b\| < 90°$			-	1.20

Table 6.20: *The χ^2_ν-values obtained from the comparisons of the CDG intensities determined in three latitude ranges in 9–30 MeV.*

E. Band	E. Intervals	2σ U. L.
4.3–30	2	23.30%
4.3–9	1	46.72%
9–30	1	20.36%

Table 6.21: *. The results of a comparison of the CDG intensity above 4.3 MeV, determined for the three latitude ranges in two energy intervals. In three energy bands 95% confidence limits on the deviations from isotropy allowed by the data are derived.*

χ^2_ν-values obtained from comparing the determined CDG intensities in the 4.3–30 MeV, 4.3–9 MeV, and 9–30 MeV bands are summarized in Tables 6.17–6.20. The inferred 95% confidence limits on the deviations from isotropy allowed by the data are summarized in Table 6.21.

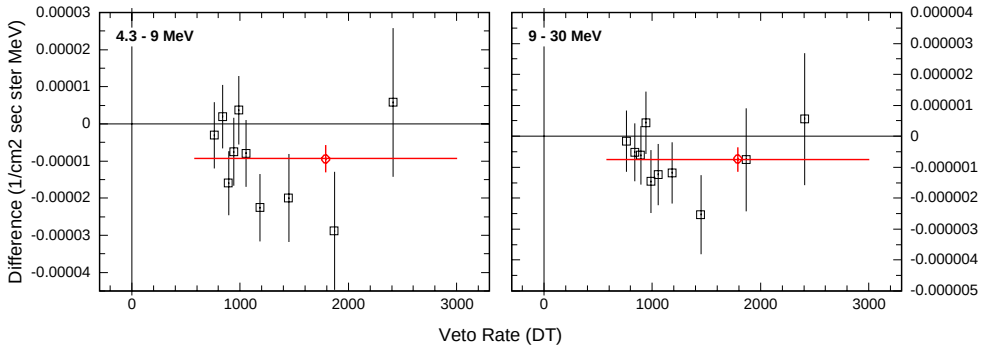

Figure 6.12: *The difference in the CDG intensity from two latitude ranges as determined from the subtraction of ToF spectra as a function of veto rate in two energy intervals above 4.3 MeV. The ToF spectra of the observations in* $30° < |b| < 45°$ *have been subtracted from those in* $|b| > 60°$.

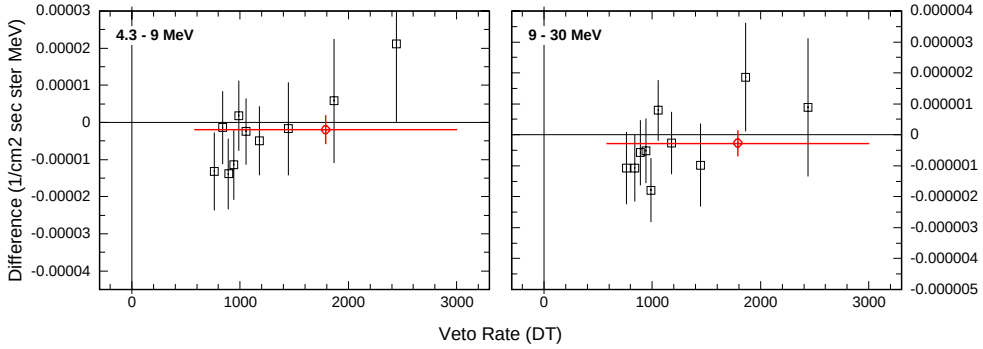

Figure 6.13: *Same as in Fig. 6.12. The ToF spectra of the observations in* $45° < |b| < 60°$ *have been subtracted from those in* $|b| > 60°$.

6.4.3 Summary

Within the limits of the CDG analysis method no significant anisotropies in the diffuse emission at $|b| > 30°$ could be found on large scales of a few steradian. This result is confirmed in other comparisons, not listed above. For example, in Phase I and Cycles 4 and 5 the effective sky exposures are sufficiently similar to allow us to determine the intensity in wide energy bands from both hemispheres for each of the three time periods. No significant anisotropy or time-variation was found. Futhermore, individual latitude regions on the southern and horthern hemisphere were compared. All intensities agree within statistical errors, but the magnitude of the statistcal error increases as the investigated sky regions are decreased and hence the comparisons become increasingly insensitive.

To conclude, a tentative upper limit on the relative deviations of the CDG from isotropy in the 0.8–4.3 MeV of about 34% has been obtained at the 95% confidence level from the comparison of both hemispheres, covering a solid angle of about π ster

each. At higher energies, the deviations could still be investigated with scales as small as about 1.5 ster. The upper limits on the deviations from isotropy in the 4.3–30 MeV, 4.3–9 MeV, and 9–30 MeV bands are about 26%, 45%, and 24%, respectively. These results are consistent with the assumption of an extragalactic origin of the CDG, which implies isotropy on large angular scales. The CDG analysis method is, however, not yet senitive enough to constrain predicted anisotropies in the CDG intensity at small angular scales. This topic is discussed in the next section.

6.5 Discussion

The origin of the extragalactic γ-ray background is still far from being understood. The measurement of spectrum and isotropy of the CDG/EGB is one of many small steps that need to be taken, together with studies of emission properties of γ-ray sources and their theoretical modelling, towards the goal of unravelling the origin of this background radiation. A general overview of the possible origins of the CDG/EGB is given in Sec. 2.2. A large variety of discrete sources and truly diffuse processes that could contribute to the CDG/EGB is described there. The following discussion will only address those models that can actually be constrained by currently available data.

In general, the current status of extragalactic γ-ray astronomy is reminiscent of the status of extragalactic X-ray astronomy about 20 years ago. On the one hand the initially diffuse extragalactic emission begins to resolve into discrete sources. On the other hand the properties of the extragalactic point sources observed thus far, all of which are AGN (see Sec. 2.2.1.2), are only poorly understood owing to their small observed number. To date about 60 blazars have been identified by EGRET above 100 MeV (Hartman *et al.* 1997), COMPTEL has detected ten AGN at MeV energies (Collmar *et al.* 1999), and OSSE has observed about 30 Seyfert galaxies in the 50–150 keV band (Johnson *et al.* 1997). These data firmly establish AGN as a viable source class contributing to the EGB, but considerable uncertainty remains concerning their "typical" emission characteristics. This uncertainty in the characteristics of individual source populations translates into a corresponding uncertainty in any model of the integrated emission of AGN. It is therefore not surprising that different investigators arrived at quite different conclusions concerning the EGB contribution from these sources.

Other populations of discrete sources that could contribute to the EGB, apart from AGN, include normal galaxies (see Sec. 2.2.1.1), infrared-luminous galaxies (see Sec. 2.2.1.3), and Type Ia SNe (see Sec. 2.2.1.4).

One of the models attributing the EGB to a truly diffuse origin is γ-radiation from the annihilation of matter and anti-matter in a baryon-symmetric universe (see Sec. 2.2.2.1). Among the truly diffuse models this annihilation model is distinguished by the fact that it predicts spectral features observable with current instruments, in particular an excess of emission at MeV-energies, the so-called MeV-bump.

The high-energy emission of these different source populations covers different energy ranges. To avoid unnecessary confusion, the models are compared in two groups to the current XRB and CDG/EGB data, depending on whether they describe emission that is predominatly present below a few MeV (see Fig. 6.14) or whether the emission extends to higher energies (see Fig. 6.15) The combined XRB and CDG/EGB data are those depicted in Figs. 2.3 and 2.4, with current COMPTEL results being only represented by the CDG spectrum derived in this thesis for clarity. As already mentioned in Sec. 6.3.3, the current results on the CDG/EGB suggest a much simplified shape of the extragalactic high-energy background as compared to the situation around 1982 (compare Fig. 2.9). In particular, the current COMPTEL and SMM results on the CDG at MeV energies provide no evidence for the existence of an MeV-bump. This excess emission above the extrapolations of the spectra at lower and higher energies was considered strong evidence for the cosmological annihilation radiation expected in a baryon-symmetric universe (see e.g. Stecker 1971, 1985). The disappearence of the MeV-bump is one of many pieces of evidence excluding a matter-antimatter symmetric universe (see Sec. 2.2.2.1). Instead, the overall spectrum appears to be much simplified, the XRB and EGB seem to merge smoothly without any additional spectral features being present.

It is instructive to start the discussion of the different models with the historical example of the so-called 30 keV-bump in the XRB, since it seems likely that γ-ray astronomy will evolve similarly as X-ray astronomy did over the last two decades. Originally, two different origins were proposed for this very pronounced spectral feature: a truly diffuse origin in a hot IGM and the superposition of unresolved, discrete soures (see Sec. 2.1.6). As X-ray astronomy evolved, an increasing fraction of the XRB was resolved into point sources, and finally the hot IGM hypothesis was convincingly eliminated by the FIRAS/COBE results on the spectrum of the CMB (Mather *et al.* 1994, see Sec. 2.1.2). Today, different models attributing the XRB to the superposed emission of radio-quiet AGN (Seyfert galaxies and QSOs) have been proposed (e.g. Madau *et al.* 1993, Zdziarski and Zycki 1993, Comastri *et al.* 1995, Zdziarski *et al.* 1995, Zdziarski 1996). As an illustration, the predicted emissions from Sy 1 (dotted line) and Sy 2 (dash triple-dotted line) galaxies in the model of Zdziarski (1996) are indicated in Fig. 6.14. All models can reproduce the overall XRB, despite the fact that the assumed source properties differ in detail. The bulk of the emission is attributed to heavily absorbed Sy 2 galaxies, in accordance with current AGN unification schemes (see e.g. Antonucci 1993, Urry and Padovani 1995). In these models the decrease of the XRB below about 30 keV results from intrinsic photoelectric absorption in the AGN, while the roll-over at higher energies arises from the red-shifted intrinsic exponential cut-offs at about 100 keV. As the data on source counts and redshift and absorption distributions improve, these models become more and more constrained. For example, the synthesis model of Comastri *et al.* (1995) (see Fig. 6.14) implies the existence of a large population of highly luminous, yet strongly obscured AGN. These objects should be observable with the next generation of X-ray telescopes.

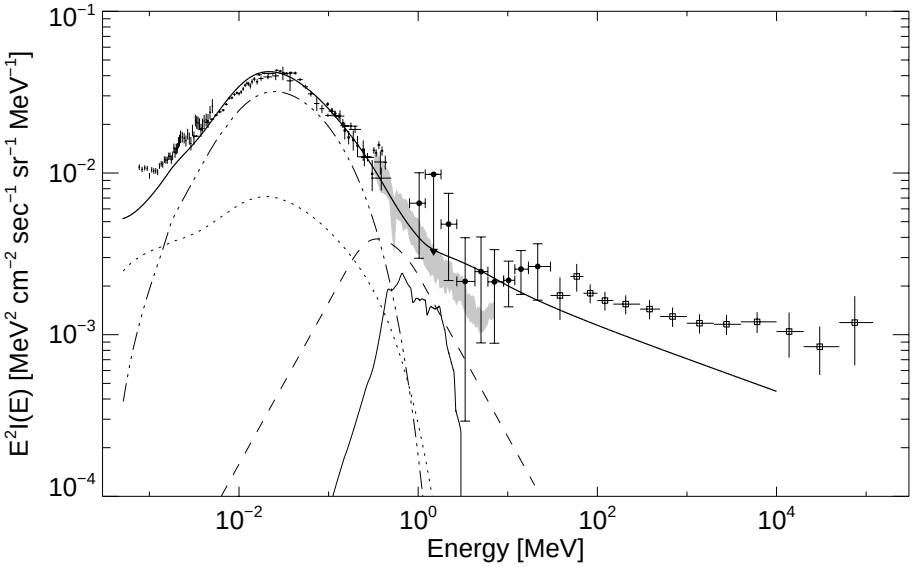

Figure 6.14: *A comparison of theoretical models to the current data on the XRB and CDG. The data are those depicted in Figs. 2.3 and 2.4. For simplicity, only the COMPTEL result obtained in this thesis is indicated. The thick solid line represents the XRB/EGB model of Comastri* et al. *(1996), which combines the XRB synthesis model of Comastri* et al. *(1995) with models for MeV-blazars (solid line) and FSRQ (see Fig. 6.15). The dotted and dash triple-dotted lines illustrate the XRB contributions of Sy 1 and Sy 2 galaxies, respectively, according to (Zdziarski 1996). A prediction of the integrated emission from SNe Tpye Ia (Watanabe* et al. *1999) is given as thin solid line.*

As illustrated in Fig. 6.14, the emission from Seyfert galaxies cuts off exponentially above about 100 keV (see e.g. Johnson *et al.* 1997), possibly implying that new source populations are needed to account for the hard XRB and CDG. Two candidates are indicated: MeV-blazars (see Sec. 2.2.1.2) and Type Ia SNe (see Sec. 2.2.1.4). Other possible sources of emission in the 100 keV to a few MeV region are so-called misaligned blazars or radio-loud Seyfert galaxies (see Sec. 2.2.1.2). Little data exists on these AGN types, hence their contribution to the CDG/EGB is hard to predict. In contrast, the γ-ray emission of Type Ia SNe is fairly well studied. The SN contribution to the XRB/CDG is of particular interest because it offers an independent tool for studies of the cosmic star-formation history (see e.g. Watanabe *et al.* 1999), which are difficult at UV and optical wavelengths due to the substantial extinction in the dense gas-clouds ambient in star-forming regions. The measured CDG intensity places an upper limit on the integrated emission from Type Ia SNe and hence constrains the cosmic star-formation history. The star-formation history is an important factor in the evolution of galaxies, hence the CDG and the EUB (see Sec. 2.1.5) and EBL (see Sec. 2.1.4) may be connected to some degree. A characteristic feature in the γ-ray emission of SNe is the sharp drop above about 3.5 MeV (see Sec. 2.2.1.4). In addition, steps are predicted in the CDG spectrum near the rest energies of the emitted γ-ray lines. No such edges

have yet been observed, nor any drop at about 3.5 MeV, which may imply that the SN contribution to the CDG is insignificant. A similar problem occurs at a few 100 keV. It is possible, however, that the emission of sources at higher and lower energy cuts off in such a way that their merged spectra do not exhibit any noticeable discontinuity. For the time being, SNe are promising contributors to the CDG at about 1 MeV, but a definite assessment of the intensity due to SNe may have to wait until the detection of the predicted steps and drops in the CDG spectrum. In addition to characteristic spectral features, a characteristic anisotropy is expected in the CDG intensity below the energies of the major lines emitted by SNe. This anisotropy arises because the line-photons close to the rest energy of the line are due to the nearest galaxies, which are non-uniformly distributed (Watanabe *et al.* 1999).

At higher energies the only extragalactic sources observed thus far are radio-loud blazars. As described in Sec. 2.2.1.2, the blazar class comprises two different AGN types, FSRQs and BL Lacs, whose γ-ray emission properties are similar but not necessarily identical. The close agreement of the average spectrum of radio-loud blazars above 100 MeV and the spectrum of the EGB immediately establishes γ-ray blazars as the prime candidate source population for the diffuse γ-ray background. Both spectra are described well by a power law, the spectral index of the EGB in the 30 MeV to 100 GeV range being 2.10 ± 0.03 (Sreekumar *et al.* 1998, see Fig. 6.15), the spectral index of the "average blazar" spectrum being 2.16 ± 0.31 (Hartman *et al.* 1997). In addition, a cosmological integration of a power law in energy yields the same functional form and slope (see Appendix A.3). There are, however, indications that blazars are observed only during flaring episodes, while being too faint to be detected when in the quiescent state, and that in addition the blazar spectra may become harder during a flaring episode (see e.g. Hartman *et al.* 1997, and references therein). Combination of these two effects results in a curvature in the EGB, as calculated by Stecker and Salamon (1996b) and Salamon and Stecker (1998) (see Fig. 6.15). The magnitude of the curvature depends on the duty-cycle, i.e. the ratio of the times spent in flaring and in quiescent state, as well as on the variation in luminosity. These blazar characteristics are very poorly constrained. Hence the fact that the predicted spectrum is not in agreement with the data does not necessarily imply that the blazar contribution to the EGB is small. It is possible that other sets of characteristic blazar parameters may provide an acceptable model. The model of Salamon and Stecker (1998) also exemplifies another potentially important feature of the blazar contribution to the EGB: a high-energy cutoff due to γ-γ pair-production of high-energy γ-ray photons with low-energy background photons. Observation of a high-energy cutoff in the EGB spectrum would provide constraints on the CIB (see Sec. 2.1.3), which is still quite uncertain. Moreover, observation of such a cutoff in the spectra of individual blazars as a function of z could provide an invaluable tool for understanding the diffuse photon background over cosmic time scales — once the intrinsic blazar properties over cosmic time scales are sufficiently well known.

Typically, a spectral break is observed for blazars at energies between about 1 MeV

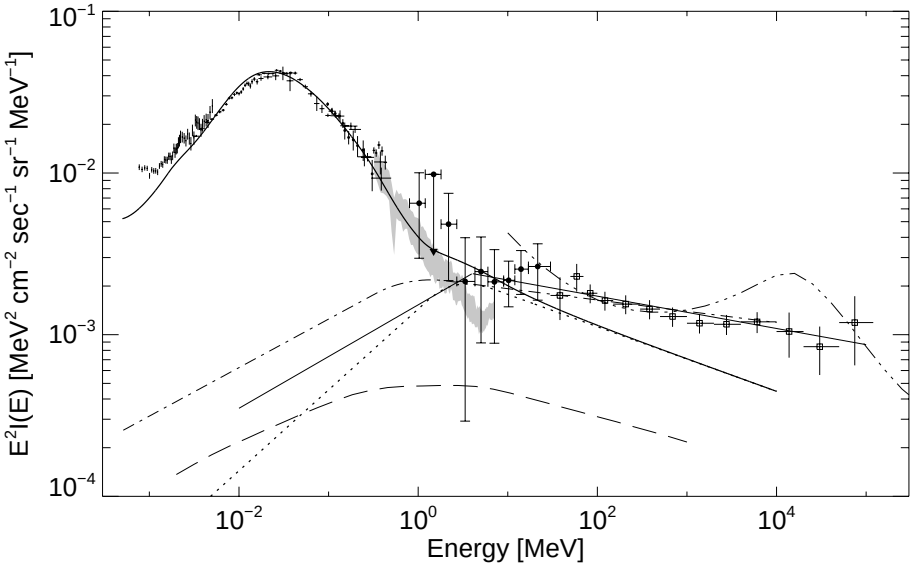

Figure 6.15: *A comparison of theoretical models to the current data on the CDG and EGB. The data are those depicted in Fig. 6.14. The thick solid line represents the XRB/EGB model of Comastri* et al. *(1996), which combines the XRB synthesis model of Comastri* et al. *(1995) with models for MeV-blazars (see Fig. 6.14) and FSRQ (dotted line). The dash-dotted line gives the FSRQ model of (Zdziarski 1996). The dash tripple-dotted line is the blazar model of Salamon and Stecker (1998). The straight, thin and solid lines represent a fit to the EGRET EGB data (Sreekumar* et al. *1998), which was extended to lower energies according to the "average" blazar spectrum derived by McNaron-Brown* et al. *(1995). The long-dashed line gives an estimate for the contribution of farinfrared-luminous galaxies (Soltan and Juchniewicz 1999).*

and 100 MeV (see e.g. McNaron-Brown *et al.* 1995, Collmar 1996). This is also indicated by the COMPTEL results on the CDG above a few MeV, which suggest a hardening of the spectrum around 30 MeV. The "average" blazar spectrum derived by McNaron-Brown *et al.* (1995), with a break energy of ~ 4 MeV and power-law indices of about -1.7 and -2.1 below and above the break is indicated in Fig. 6.15. Similarly, the two FSRQ models included in Fig. 6.15 are based on "typical" or "average" properties of these sources, again illustrating the lack of precise knowledge on the source properties. According to Fossati *et al.* (1999), the break energy is related to the luminosity of the blazar. Hence, a determination of the average break energy from the CDG/EGB could provide a valuable constraint on models for the blazar population.

As described in Sec. 2.2.1.2, most calculations of the blazar contribution to the EGB are based on the proposition that there is a correlation between the radio and the γ-ray emission of these objects. Albeit quite uncertain, most of the EGB is attributed to unresolved blazars in these integrations (e.g. Padovani *et al.* 1993, Comastri *et al.* 1996, Stecker and Salamon 1996b). The degree and nature of the correlation between the radio and the γ-ray emission is, however, still under debate (Padovani *et al.* 1993,

Mücke *et al.* 1996, Mattox *et al.* 1997). An alternative approach was pursued by Chiang *et al.* (1995) and Chiang and Mukherjee (1998), who deduced the γ-ray luminosity function from the γ-ray data itself. This analysis is complicated by the variable nature of the blazar emission. While the former analysis yielded a blazar emission at a level consistent with the observed EGB intensity, the latter analysis, based on a larger blazar sample, reduced the emission of unresolved blazars to $\sim 25\%$ of the observed EGB intensity. Clearly, a much improved evaluation of the γ-ray luminosity function is needed. Finally, Mücke and Pohl (1999) estimated the contribution of unresolved radio-loud AGN to the EGB assuming the blazar emission is mostly due to EIC process, with the SSC process being of minor importance (see Sec. 2.2.1.2), in the context of the AGN unification paradigm. The model was constrained, analogous to the synthesis models for the XRB, by observations of resolved BL Lacs and FSQRs: their $\log N - \log S$ distribution, their relative number, and their redshift. It was found that the model is consistent with the observed FSRQ number density, but underpredicts the number of BL Lacs, which might indicate that the SSC process is more important than the EIC process in these objects. This model can only account for 20–40% of the EGB. If the model is relaxed, however, so that it also reproduces the BL Lac number density, then unresolved BL Lacs and FSRQs can produce the observed EGB, with BL Lacs contributing 70–90% of the intensity.

The fact that no extragalactic sources except AGN have been detected thus far does not imply that other sources do not contribute to the EGB. For example, Soltan and Juchniewicz (1999) estimated that farinfrared-luminous galaxies may account for up to 20% of the EGB (see Fig. 6.15). Although too faint to be observed individually, the large number of these sources, compared to the much more luminous, but also much rarer AGN, can give rise to a considerable integrated intensity. This argument also applies to normal galaxies, which are usually thought to contribute about 10%, whose contribution, however, depends strongly on the assumed galaxy evolution (see Sec. 2.2.1.1).

Anisotropies in the CDG/EGB thus far have been mainly considered in the context of truly diffuse source models. For example, exotic, relic elementary particles from the early universe not yet discovered may reveal themselves in anisotropies due to the annihilation or decay in a galactic halo or enhanced emission above the general EGB intensity from other galaxies or clusters of galaxies (e.g. Kamionkowski 1995, and Sec. 2.2.2.2). A detection of the predicted characteristics is, however, beyond the capabilities of current instruments. This is also true for the large-scale fluctuation patterns or anisotropies resulting from annihilation in symmetric universes and from active galactic nuclei, which were investigated by Cline and Gao (1990) and Gao *et al.* (1990b,a). They found that the fluctuations produced by annihialtion on the boundaries of matter and antimatter domains, which resemble diffuse "ridges" in the 100 MeV range, are intrinsically different from EGB fluctuations produced by AGN, thus providing a probe for cosmological antimatter. Similarly, the possible anisotropies in the CDG at MeV energies arising from SNe, which have already been discussed above, will

remain unobservable in the near future.

To conclude, the recent results on the XRB, CDG, and EGB provide the overall picture of the high-energy extragalactic background radiation over more than six orders of magnitude in energy. In addition, there is a variety of viable source candidates that could give rise to the observed spectrum. The spectrum is, however, not determined with an accuracy sufficient to allow us to discern the contributions of the various source classes. In turn, the properties of individual source populations are not yet well enough constrained to allow us detailed predictions on shape and intensity of their integrated emission. Thus there is ample opportunity for future work.

Appendix A

Notes on Extragalactic Astronomy

In Sec. 2.1 of this thesis an overview of the extragalactic background radiation (EBR) across the electromagnetic spectrum was given. In doing so, miscellaneous issues in astronomy, and in particular extragalactic astronomy, came up which deserve closer attention than what can be given in a footnote. These issues are briefly addressed below.

A.1 Fluxes, Intensity, and Spectral Energy Distribution

Unfortunately, the nomenclature and notation customarily used in multiwavelength astronomy is somewhat sloppy. Often the term "flux" is used rather generously, even if "intensity" would be appropriate. To make matters worse, both quantities are denoted by the same symbols. These ambiguities can be alleviated by referring to the measured quantity in the case of observing a point source, which cannot be resolved any further, as flux, whereas the measured quantity in case of observing an extended source is referred to as intensity (Unsöld and Baschek 1988). Despite its ambiguity, the following notation customary in multiwavelength astronomy is adopted (Gehrels 1997). The (differential) photon number flux, which is the number of incident photons per unit area, unit time and unit energy interval, is denoted by I_E or, as is more common, $I(E)$:

$$I(E) = \frac{dN_\gamma}{dA\,dt\,dE} \tag{A.1}$$

The (differential) photon number intensity, which is the number of incident photons per unit area, unit time, unit energy interval and unit solid angle, is also denoted by $I(E)$, so that only the terminology and the quoted units allow to tell what is really referred to. The following considerations are given for fluxes only, since their application to intensities is straight forward.

Analogously to $I(E)$, the photon number fluxes per unit frequency and unit wavelength interval are denoted by I_ν and I_λ, respectively:

$$I_\nu = \frac{dN_\gamma}{dA\,dt\,d\nu} = h \cdot I(E) \tag{A.2}$$

$$I_\lambda = \frac{dN_\gamma}{dA\,dt\,d\lambda} = \frac{h\,c}{\lambda^2} \cdot I(E) \tag{A.3}$$

Usually, the photon number flux is the measured quantity for photon counting experiments, particularly in X-ray and γ-ray astronomy. At lower energies (longer wavelengths), however, the measured quantity normally is the energy flux F_E, the incident energy per unit time, unit area and unit energy interval:

$$F_E = E \cdot I(E) \tag{A.4}$$

and analogously

$$F_\nu = E \cdot I_\nu \tag{A.5}$$

$$F_\lambda = E \cdot I_\lambda \tag{A.6}$$

In particular in radio astronomy, the energy flux F_ν is customarily referred to as flux density (incident energy per unit time, unit area and unit bandwidth interval) and denoted by S_ν.

The quantity most appropriate for multiwavelength studies, however, is the spectral energy distribution (SED), defined as $E^2\,I(E)$, which best represents the amount of energy associated with different regions of the spectrum. The SED is also often denoted by $\nu\,F_\nu$ or $\lambda\,F_\lambda$. From Eqs. A.1 – A.3 the useful identity

$$E^2\,I(E) = \nu\,F_\nu = \lambda\,F_\lambda \tag{A.7}$$

can easily be obtained. Since

$$\nu\,F_\nu = \nu\,\frac{dF}{d\nu} = \frac{dF}{d(\ln\nu)} = F_{(\ln\nu)} \tag{A.8}$$

it follows that the SED is the energy flux per natural logarithmic frequency interval (as was pointed out by Gehrels (1997), the common statement that it is the energy flux per decade of photon frequency is incorrect). Similarly, $\lambda\,F_\lambda$ and $E^2\,I(E)$ describe the energy flux per natural logarithmic wavelength and energy interval, respectively.

A.2 Luminosity

The ultimate goal of astronomical observations is to study the intrinsic properties of the emitting objects. To that end the luminosity of the individual sources, quantifying their intrinsic radiative power, has to be determined from the observed quantities. This

is of particular importance in extragalactic astronomy, because cosmological effects can result in significant differences between the observed and the intrinsic properties of an object. Unfortunately, the terminology and nomenclature customarily used concerning "luminosity" are again ambiguous.

In the following, the bolometric (or total) luminosity and the integral luminosity of an emitting object, L, refer to the total emitted energy per unit time, and the emitted energy per unit time in a specified bandwidth or energy range of observation, respectively. The differential luminosity, L_E, denotes the emitted energy per unit time and unit energy interval[1]. The most appropriate quantity for comparing the intrinsic emission properties of different objects, however, is the luminosity per natural logarithmic frequency bandwidth, $\nu\, L_\nu$, the intrinsic analogon to the observed $\nu\, F_\nu$ (which equals $E^2\, I(E)$ and $\lambda\, F_\lambda$, see Eq. A.7).

Let us consider a point source at redshift z in a Friedmannian universe. Because $E = h\nu$, the observed photon energy E or frequency ν can easily be converted to the restframe energy E_0 or restframe frequency ν_0 of the source:

$$E_0 = (1+z)\, E \qquad \text{and} \qquad \nu_0 = (1+z)\, \nu \tag{A.9}$$

Since $d(\ln(\nu_0)) = d(\ln(\nu))$, there is no effect of the cosmological frequency shift on $\nu\, F_\nu$ (see Eq. A.8), and thus the SED in the object's restframe is given by the observed SED, $\nu\, F_\nu(\nu = \nu_0/(1+z))$, evaluated as a function of the intrinsic frequency ν_0 (Gehrels 1997).

Assuming isotropic emission, the bolometric flux observed from a nearby, stationary point source at distance d in euclidian space is related to its bolometric luminosity through $L = 4\pi d^2\, F$. For objects at cosmological redshift z, the luminosity calculation must include the frequency redshift, the time dilation and the change of the emission solid angle at the source for photons that cross a unit area at the observer by the curvature of space. These three cosmological effects can be combined to a distance variable, the so-called luminosity distance d_L, which is defined such that formally the euclidian relation between bolometric flux and luminosity holds true in curved space:

$$L = 4\pi d_L^2\, F \tag{A.10}$$

The so-defined luminosity distance is a function of the redshift z, Hubble's constant H_0 and the deceleration parameter q_0. For a Friedmannian universe (Weinberg 1972):

$$d_L = \frac{c}{H_0\, q_0^2}\, [z q_0 + (1-q_0)(1-\sqrt{2q_0 z + 1})] \quad \text{for} \quad q_0 > 0 \tag{A.11}$$

where c is the speed of light. Another distance measure in curved space is the so-called proper distance, which is defined as the light travel time along a null geodesic divided

[1] Analogously, L_ν and L_λ denote the emitted energy per unit time and unit frequency or wavelength interval, respectively.

by the speed of light. The proper distance d and the luminosity distance d_L are related through

$$d_L = d \cdot (1+z) \tag{A.12}$$

The flux per unit frequency interval and the differential luminosity are related by

$$L_{\nu_0}(\nu_0)\, d\nu_0 = 4\pi d_L^2\, F_\nu(\nu)\, d\nu \tag{A.13}$$

with $d\nu_0$ and $d\nu$ being the corresponding frequency bands in the rest frame of the source and the observer, respectively. Using Eq. A.9, it follows that

$$L_{\nu_0}(\nu_0) = 4\pi d^2\, (1+z)\, F_\nu(\nu) \tag{A.14}$$

If the source sprectrum has a power law form, $L_{\nu_0}(\nu_0) \propto \nu_0^{-\alpha}$, this relation becomes, using Eq. A.9

$$L_\nu(\nu) = 4\pi d^2\, (1+z)^{1+\alpha}\, F_\nu(\nu) \tag{A.15}$$

Finally, using Eqs. A.9 and A.14, the intrinsic source luminosity per natural frequency interval is given by (Gehrels 1997)

$$\nu_0\, L_{\nu_0} = L_{\ln \nu_0}(\nu_0) = 4\pi d_L^2 \cdot \nu\, F_\nu(\nu = \nu_0/(1+z)) \tag{A.16}$$

A.3 Luminosity Function

The intrinsic properties of a source class may change with cosmic epoch. The evolution of the space density and the luminosity of a source class are expressed in the luminosity function (see e.g. Weedman 1986), which again is a term that is often used ambiguously. In the following, let the differential luminosity function or space density function, $\rho(L,z)$, be defined as the number of sources with luminosity L per unit comoving volume at redshift z per unit luminosity. Very often, $\rho(L,z)$ is simply referred to as luminosity function. The integrated luminosity function, $\Psi(L_c,z)$, describes the number of sources with luminosity L greater than the cutoff luminosity L_c per unit comoving volume at redshift z:

$$\Psi(L_c,z) = \int_{L_c}^{\infty} \rho(L,z)\, dL \tag{A.17}$$

One way to derive the luminosity function $\rho(L,z)$ is by first determining $\rho(L)$ for different shells in z and by then finding a mathematical function capable of describing all these distributions (see e.g. Chapter 5 in Weedman 1986). All observations are inevitably flux limited, therefore there is always the possibility that objects exist which are fainter than what we are able to see. To allow us a consistent statistical treatment of the distribution of the source class of interest it is therefore necessary to base the derivation of a luminosity function on a so-called complete sample. Such a complete

sample is defined as a set of members of the source population of interest found to a precisely defined flux limit (or apparent magnitude limit) with a precisely defined search technique. For each member of the complete sample flux and redshift have to be determined, from which then the luminosity can be obtained (see Eqs. A.10, A.12 and A.14). It is important to note that the cutoff luminosity L_c in Eq. A.17 corresponding to the flux limit of the complete sample is a function of redshift z.

Allowing evolution of both the space density and the luminosity of a source class can result in very complicated luminosity functions, which can only be determined on the basis of a large database. Many studies therefore are restricted to the simpler cases of either pure density evolution (the number density of sources changes the same at all luminosities) or pure luminosity evolution (the source luminosities change the same at each density). It is important to note that the terms "density evolution" and "luminosity evolution" first of all refer to the type of mathematical function used to describe the variation of $\rho(L)$ as a function of z, and *not* to the actual physical evolution of the source population under study.

Commonly used parameterizations for pure density evolution are

$$\rho(L(z), z) = \rho(L(z=0), 0)\, \exp(\gamma \tau H_0) \quad \text{or} \quad \rho(L(z=0), 0)\, (1+z)^{\gamma} \tag{A.18}$$

Here τ is the so-called look-back time, the difference in the age of the universe between the the time of light emission and the time of light observation, which usually is a complicated function of z, H_0 and q_0 (see Weinberg 1972). The parameter γ determines the amount of evolution. Analogously, pure luminosity evolution is often parameterized by

$$L(z) = L(z=0)\, \exp(\beta \tau H_0) \quad \text{or} \quad L(z=0)\, (1+z)^{\beta} \tag{A.19}$$

at a given density with the evolution parameter β.

Another frequently used parameterization of the luminosity function is

$$\rho(L, z) = \Phi_0(L)\, f(z) \tag{A.20}$$

with $\Phi_0(L)$ being the local differential luminosity function and $f(z)$ being the so-called evolution function, here assumed to depend only on redshift, which takes the value 1 if the source distribution does not change with cosmic epoch. Depending on the forms of $\Phi_0(L)$ and $f(z)$ this parametrization can be used to describe evolution which can be considered density evolution as well as luminosity evolution.

A.4 Extragalactic Background Intensity

Below, the most common methods to determine the intensity of the extragalactic background radiation are summarized (a more comprehensive account of these issues can be found in, e.g., Chapter 4 of Longair 1994b).

A.4.1 Integration of Luminosity Function

Integration of the luminosity function is the most illuminating, yet most difficult way of determining the background intensity due to a source population. The difficulty lies in the determination of the luminosity function, as pointed out above. If the luminosity function is available, however, it is possible to follow the emission of this source population through cosmic history.

The volume of a spherical shell of thickness dr at proper distance d is

$$dV = 4\pi\, d^2 dr \tag{A.21}$$

with dr being a proper line element along the proper distance d. In Friedmannian world models, the relation between proper line element dr and redshift z is (see e.g. Weinberg 1972)

$$dr = \frac{c}{H_0}\,\frac{1}{1+z}\,\frac{1}{\sqrt{1+2q_0 z}}\,dz \tag{A.22}$$

It follows from Eq. A.21 that in the case of an isotropic distribution the number of sources per solid angle with luminosity L in an increment comoving coordinate distance dr centered on proper distance d and density $\rho(L, z(d))$ is

$$dN(L, z(d)) = \rho(L, z(d))\; dL\; d^2 dr \tag{A.23}$$

Each of these sources contributes a flux $F_\nu(\nu) = L_{\nu_0}(\nu_0)/(4\pi d^2(1+z))$ to the background intensity (see Eq. A.14), hence the total background intensity is given by

$$\begin{aligned} I_\nu(\nu) &= \int\int \frac{1}{4\pi d^2(1+z)}\, L_{\nu_0}(\nu_0)\, \rho(L,z)\; dL\; d^2 dr \\ &= \frac{c}{4\pi H_0}\int\int \frac{1}{(1+z)^2\sqrt{1+2q_0 z}}\, L_{\nu_0}(\nu_0)\, \rho(L,z)\; dL\, dz \end{aligned} \tag{A.24}$$

Assuming that the source spectrum has a power law form, $L_{\nu_0}(\nu_0) = L_0 \nu_0^{-\alpha}$, and using Eq. A.15 this relation becomes

$$I_\nu(\nu) = \frac{c}{4\pi H_0}\int\int \frac{1}{(1+z)^{2+\alpha}\sqrt{1+2q_0 z}}\, L_\nu(\nu)\, \rho(L,z)\; dL\, dz \tag{A.25}$$

It is important to note that for $L_\nu \propto \nu^{-\alpha}$ it follows that $I_\nu \propto \nu^{-\alpha}$, hence the spectral shape of the background intensity is identical to that of its sources if the sources have a power law spectrum.

Assuming further that the luminosity function can be parameterized as $\rho(L, z) = \Phi_0(L)\, f(z)$ (see Eq. A.20), the background intensity is given by

$$\begin{aligned} I_\nu(\nu) &= \frac{c}{4\pi H_0}\int L_\nu(\nu)\, \Phi_0(L)\, dL \int_0^{z_{max}} \frac{f(z)\, dz}{(1+z)^{2+\alpha}\sqrt{1+2q_0 z}} \\ &= \frac{c\,\rho_\nu(\nu)}{4\pi H_0}\int_0^{z_{max}} \frac{f(z)\, dz}{(1+z)^{2+\alpha}\sqrt{1+2q_0 z}} \end{aligned} \tag{A.26}$$

with z_{max} being the epoch of formation of the source population under study, and

$$\rho_\nu(\nu) = \int L_\nu(\nu)\,\Phi_0(L)\,dL \tag{A.27}$$

being the so-called local differential luminosity density.

A.4.2 Integration of log N – log S Distribution

The $\log N - \log S$ distribution of a source population is easier to obtain than the luminosity function, as the former requires only the measurement of the source fluxes in a given energy range. The lack of redshift information, however, allows us to draw only limited conclusions from studies of the $\log N - \log S$ distribution. The $\log N - \log S$ distribution is an integral distribution, namely the integral of the differential $N(S)$ function:

$$N(>S) = \int_S^\infty N(S')dS' \tag{A.28}$$

with $N(S)$ being the number of sources per steradian with flux in $[S, S+dS]$. The name $\log N - \log S$ distribution stems from the fact that $N(>S)$ is usually plotted in the form $\log N(>S)$ versus $\log S$.

The integration of the $\log N - \log S$ distribution is done by integration of the differential distribution $N(S)$. The intensity due to the source population under study is given by

$$I = \int N(S)\,dS \tag{A.29}$$

It is a well-known fact that in euclidian space and in absence of evolution the number of sources seen to limiting flux S is given by

$$\begin{aligned} N(>S) &= \int_L \int_0^{r_{max}(L)} \rho(L)\, r^2 dr\, dL \\ &= \frac{1}{3} S^{-\frac{3}{2}} \int_L \rho(L)\, (\frac{L}{4\pi})^{\frac{3}{2}}\, dL \\ &\propto S^{-\frac{3}{2}} \end{aligned} \tag{A.30}$$

with the euclidian distance $r_{max}(L)$ being defined through $S = L/(4\pi r_{max}^2)$ and $\rho(L)$ being the spatially homogeneous luminosity function. It has to be noted that this result is independent of $\rho(L)$.

A.4.3 Integration of Number-Magnitude Counts

The integration of number-magnitude counts is completely analogous to the integration of the $\log N - \log S$ distribution, the only difference being that in the former the brightness of the sources is expressed in magnitudes instead of fluxes. Similar to the

$\log N - \log S$ distribution, the number-magnitude relation is usually plotted as $\log N(m)$ versus m, with the relation between magnitude m and flux S being defined by

$$m = \text{const} - 2.5 \log S \tag{A.31}$$

The value of the constant in this relation is a complicated function of the passband of the observations and of the spectrum of the sources, e.g. the spectral type if stars are observed (see e.g. Lamla 1965, Allen 1973). It follows that

$$S \propto 10^{-\frac{2}{5}m} \tag{A.32}$$

Often the number-magnitude relation is approximated by a power law distribution:

$$\frac{d \log N(m)}{dm} \propto \alpha \tag{A.33}$$

Using Eq. A.30 it is straight-forward to show that for $\alpha = 0.4$ this corresponds to

$$dN(S) \propto S^{-2} dS \tag{A.34}$$

For multiwavelength comparisons it is more convenient to use fluxes instead of magnitudes. The background intensity then is, with $dN \propto S^{-\beta} dS$:

$$I = \int_{S_{\min}}^{S_{max}} S dN \propto \int_{S_{min}}^{S_{max}} S^{-(\beta-1)} dS \propto (S_{max}^{2-\beta} - S_{min}^{2-\beta}) \tag{A.35}$$

For $S_{min} \to 0$ this result diverges if $\beta \geq 2$, corresponding to $\alpha \geq 0.4$. Therefore $\alpha = 0.4$ is referred to as critical slope for number-magnitude relations.

A.4.4 Integration of Emissivity

The background intensity arising from a diffuse source of radiation can be calculated analogously to the integration of the emission of point sources as given by Eq. A.24. If the diffuse source is characterized by an isotropic emissivity $\Gamma(\nu, z)$, defined to be the emitted energy per unit time, unit frequency interval, and comoving volume at redshift z, the resulting background intensity is given by

$$I_\nu(\nu) = \frac{c}{4\pi H_0} \int \frac{\Gamma(\nu_0, z)}{(1+z)^2 \sqrt{(1+2q_0 z)}} dz \tag{A.36}$$

A.5 Photon Density and Energy Density

It is often useful to characterize the extragalactic background intensity in terms of a photon number density or an energy density. The extragalactic background radiation

can be assumed to be isotropic in all wavebands, hence it is straight forward to convert the differential photon number intensity $I(E)$, the number of inicident photons per unit area, unit time, unit energy interval and unit solid solid angle (see Eq. A.1) to a differential photon number density $n(E)$, the number of photons per unit volume and unit energy (see e.g. p. 322 in Longair 1994b)[2]:

$$n(E) = \frac{4\pi}{c}\, I(E) \tag{A.37}$$

with c denoting the speed of light. The energy density $\varepsilon(E)$ associated with the intensity $I(E)$ is then given by

$$\varepsilon(E) = \frac{4\pi}{c}\, E \cdot I(E) \tag{A.38}$$

Both the photon number density $n(E)$ and the energy density $\varepsilon(E)$ refer to the current cosmological epoch. The total photon density n or total energy density ε in an energy range of interest ΔE corresponding to the extragalactic intensity can be easily determined by integrating the differential quantities:

$$n = \int\limits_{\Delta E} n(E)dE \qquad \text{and} \qquad \varepsilon = \int\limits_{\Delta E} \varepsilon(E)dE \tag{A.39}$$

A.6 Conversions

Finally, a brief list of useful conversion factors for multiwavelength studies is given. The standard SI energy flux unit is 1 Jansky, which is defined as

$$1 \text{ Jansky} = 10^{-26} \frac{\mathrm{W}}{\mathrm{m^2\,Hz}} \tag{A.40}$$

It follows that in SI units intensities are usually quoted in [Jansky/steradian], and spectral energy distributions in [W/(m^2 ster)]. These SI flux and intensity units are customarily used in radio, microwave and infrared astronomy. The SI unit Jansky can easily be expressed in cgs units:

$$1 \text{ Jansky} = 10^{-26} \frac{\mathrm{W}}{\mathrm{m^2\,Hz}} = 10^{-23} \frac{\mathrm{erg}}{\mathrm{cm^2\,sec\,Hz}} \tag{A.41}$$

In optical astronomy, the differential photon intensity F_λ is often quoted in csg units, which can be converted to SI units through

$$1\ \frac{\mathrm{erg}}{\mathrm{cm^2\,sec\,ster\,\mathring{A}}} = 10^7\ \frac{\mathrm{W}}{\mathrm{m^2\,ster}}\ \frac{1}{\mathrm{m}} \tag{A.42}$$

[2]Following Eqs. A.2 and A.3 the differential photon densities n_ν and n_λ, the number of photons per unit volume and unit frequency or unit wavelength, respectively, can easily be obtained.

In ultraviolet astronomy, photon intensities are mostly quoted in so-called "units" or "photon units" (see Sec. 2.1.5), which are defined as the differential photon intensity per unit wavelength interval in cgs units:

$$1 \text{ unit} = 1 \ \frac{\text{photon}}{\text{cm}^2 \,\text{sec}\,\text{ster}\,\text{Å}} \tag{A.43}$$

For multiwavelength comparisons, these photon units for I_λ can be converted to SI units for the spectral energy distribution [$\text{W}\,\text{m}^{-2}\,\text{ster}^{-1}$] for $\lambda\, F_\lambda$ according to (see Eqs. A.3, A.6 and A.7):

$$h\,c \cdot \frac{1 \text{ photon}}{\text{cm}^2 \,\text{sec}\,\text{ster}\,\text{Å}} = 1.986 \times 10^{-11} \frac{\text{W}}{\text{m}^2\,\text{ster}} \tag{A.44}$$

At higher energies, in X-ray and γ-ray astromony, the preferred energy unit is [eV] instead of [erg]. A useful identity between the energy fluxes $E \cdot I_\nu$ and $E \cdot I(E)$ is

$$\frac{1}{\text{h}} \cdot \frac{\text{erg}}{\text{cm}^2 \,\text{sec}\,\text{Hz}} = 1.509 \times 10^{26} \frac{\text{eV}}{\text{cm}^2 \,\text{sec}\,\text{eV}} \tag{A.45}$$

To conclude, the following conversions for angels and solid angles are given:

$$1\,\text{rad} = \frac{180}{\pi}\,\text{deg} = \frac{180}{\pi} \cdot 3600\,\text{arcsec} \tag{A.46}$$

$$1\,\text{sr} = (1\,\text{rad})^2 = 3.283 \times 10^3\,\text{deg}^2 = 4.255 \times 10^{10}\,\text{arcsec}^2 \tag{A.47}$$

Appendix B

Flux and Intensity Calculation in the CDG Analysis

As outlined in Sec. 5.1, in this analysis the CDG is determined by subtracting all identifiable instrumental as well as atmospheric background from the total event rate. The residual event rate then is attributed to the CDG intensity. In step 1 and 2 of the analysis procedure (see Sec. 5.1), the calculation of ToF, $E_{\rm tot}$, and E_2 spectra as function of energy and/or veto rate is required. These spectra not only have to be corrected for the varying livetime of the telescope (see Sec. 3.9), but also for the changing effective area of the instrument (see Sec. 3.6). Due to failures of individual PMTs some D1 and D2 detector modules had to be switched off or cannot be used for scientific analysis for some periods of time, hence the effective area is not constant in time. The changing telescope configurations used in the CDG analysis are summarized in Table D.9. Because of the livetime and effective-area corrections applied to the event rate, the ToF, $E_{\rm tot}$, and E_2 spectra have units of $[1/(\mathrm{cm}^2 \cdot \mathrm{sec} \cdot \mathrm{bin})]$, with "bin" representing the width of the ToF or energy bins, which formally corresponds to a photon flux per "bin".

In the following, the algorithm to determine the livetime and effective-area corrected event rate in a given energy interval ΔE and a given veto-rate range Δv is derived. This algorithm can then be generalized easily to include additional selections on event parameters or orbit and house-keeping parameters.

Let the data consist of N superpackets with veto-rate values v_s, $s = 1, \ldots, N$. Let $N_{\Delta v}$ of these superpackets be such that v_s is in Δv and let $S_{\Delta v}$ be the set of indices s:

$$S_{\Delta v} = \{s \mid 1 \leq s \leq N \quad \text{and} \quad v_s \in \Delta v\}. \tag{B.1}$$

Let $n_s(\Delta E)$ be the number of events in superpacket s with energies in ΔE. Then the total number of counts detected in ΔE and Δv is:

$$c_{\Delta v}(\Delta E) = \sum_{s \in S_{\Delta v}} n_s(\Delta E) \tag{B.2}$$

On average the instrument livetime is about 97% (see Fig. 3.19), which means that during an observation the instrument cannot detect incident photons over the full length of a superpacket, $L_0 = 16.384$ sec, but only for about 15.9 sec. Therefore the number of events in ΔE that would have been detected in superpacket s with livetime L_s if the instrument had worked perfectly is:

$$\tilde{n}_s(\Delta E) = n_s(\Delta E) \cdot \frac{L_0}{L_s}. \tag{B.3}$$

Hence the number of counts in ΔE and Δv that would have been detected with an ideal instrument is:

$$\tilde{c}_{\Delta v}(\Delta E) = \sum_{s \in S_{\Delta v}} \tilde{n}_s(\Delta E) = L_0 \cdot \sum_{s \in S_{\Delta v}} \frac{n_s(\Delta E)}{L_s} \tag{B.4}$$

Since L_s varies in time and hence in general has a different value for each superpacket, this summation cannot be further simplified.

The average rate $r_{\Delta v}(\Delta E)$ of events in ΔE and Δv which we would have detected with an ideal instrument is the number of counts $\tilde{c}_{\Delta v}(\Delta E)$ divided by the total observation time:

$$r_{\Delta v}(\Delta E) = \frac{\tilde{c}_{\Delta v}(\Delta E)}{N_{\Delta v} \cdot L_0} = \frac{1}{N_{\Delta v}} \cdot \sum_{s \in S_{\Delta v}} \frac{n_s(\Delta E)}{L_s} \tag{B.5}$$

Now the average flux of photons in ΔE and Δv, $F_{\Delta v}(\Delta E)$, can be obtained by dividing the event rate $r_{\Delta v}(\Delta E)$ by the effective area for the energy interval ΔE, $A_{\rm eff}(\Delta E)$ — provided it is independent of time during the observations:

$$F_{\Delta v}(\Delta E) = \frac{r_{\Delta v}(\Delta E)}{A_{\rm eff}(\Delta E)} \tag{B.6}$$

In general, however, $A_{\rm eff}(\Delta E)$ varies in time because of the changing telescope configuration[1]. Let the number of different telescope configurations that occurred during the observations be denoted by $n_{\rm tc}$. Let Δt_j be the duration of the $j^{\rm th}$ telescope configuration ($j = 1, \ldots, n_{\rm tc}$). Let $A_{\rm eff,j}(\Delta E)$ be the effective area for the energy interval ΔE during Δt_j and let t_s be the start time of superpacket s. To derive the flux it is now necessary to correct $c_{\Delta v}(\Delta E)$ not only for the varying livetime, but also for the changing effective area of the telescope. If the instrument worked perfectly, the livetime of each superpacket would be equal to L_0, and the effective area of the telescope would always be equal to $A_{\rm eff,0}(\Delta E)$, the effective area for ΔE for the ideal telescope

[1]The telescope configuration describes the status of each detector module over time (see Table D.9). As described in Sec. 4.2, the selections on ξ and `GCEL` ensure that the field-of-view of COMPTEL is independent of time for the CDG analysis. Therefore the only time dependence of the effective area is introduced by the changing telescope configuration.

configuration with all modules performing perfectly. Then the total number of events in ΔE and Δv that would have been measured with an ideal instrument, $\tilde{\tilde{c}}_{\Delta v}(\Delta E)$, is:

$$\begin{aligned}\tilde{\tilde{c}}_{\Delta v}(\Delta E) &= \sum_{j=1}^{n_{\rm tc}} \sum_{s \in S_{\Delta v}} \left(n_s(\Delta E) \cdot \frac{L_0}{L_s} \cdot \frac{A_{\rm eff,0}(\Delta E)}{A_{\rm eff,j}(\Delta E)} \right) \\ &= L_0 \cdot A_{\rm eff,0}(\Delta E) \cdot \sum_{j=1}^{n_{\rm tc}} \sum_{s \in S_{\Delta v}} \frac{n_s(\Delta E)}{L_s \cdot A_{\rm eff,j}(\Delta E)} \end{aligned} \tag{B.7}$$

Now the actual average incident photon flux $F_{\Delta v}(\Delta E)$ in ΔE and Δv can again be obtained by dividing $\tilde{\tilde{c}}_{\Delta v}(\Delta E)$ by the total observation time and the ideal effective area:

$$\begin{aligned} F_{\Delta v}(\Delta E) &= \frac{1}{N_{\Delta v}\, L_0 \cdot A_{\rm eff,0}(\Delta E)} \cdot \tilde{\tilde{c}}_{\Delta v}(\Delta E) \\ &= \frac{1}{N_{\Delta v}} \cdot \sum_{j=1}^{n_{\rm tc}} \sum_{s \in S_{\Delta v}} \frac{n_s(\Delta E)}{L_s \cdot A_{\rm eff,j}(\Delta E)} \end{aligned} \tag{B.8}$$

The statistical error of the average flux is determined by the weighted Poisson errors of all counts from which it was derived (the statistical errors of the livetime and the effective area are negligible). As can be seen from Eq. B.8, the flux follows from a summation of $S_{\Delta v}$ terms, all of which are statistically independent since all individual detected events are statistically independent. Estimating the mean of the Poisson distribution for the number of events in ΔE in each superpacket with v_s in Δv by the number of actually detected counts, $n_s(\Delta E)$, the squared Poisson error of each of these terms is $n_s(\Delta E)/(N_{\Delta v} \cdot L_s \cdot A_{\rm eff,j}(\Delta E))^2$. Therefore the total statistical error of the flux is[2]:

$$\sigma^2_{F_{\Delta v}(\Delta E)} = \frac{1}{N^2_{\Delta v}} \cdot \sum_{j=1}^{n_{\rm tc}} \sum_{s \in S_{\Delta v}} \frac{n_s(\Delta E)}{(L_s \cdot A_{\rm eff,j}(\Delta E))^2} \tag{B.9}$$

As explained in Sec. 3.6, the flux F [photons/(cm^2 sec)] can be converted to intensity I [photons/(cm^2 sec ster)] by dividing the flux by 2π:

$$I = \frac{F}{2\pi} \tag{B.10}$$

[2]If there are no counts in ΔE and Δp the statistical flux error is approximated by

$$\sigma^2_{F_{\Delta v}(\Delta E)} = \frac{1}{(N_{\Delta v} \cdot L_s \cdot A_{\rm eff,j}(\Delta E))^2}$$

with the value of L_s set to 15.9 sec (the average livetime) and the value of $A_{\rm eff,j}(\Delta E)$ set to effective area for ΔE in the last occurring time interval Δt_j.

Appendix C

Perspectives for Improving COMPTEL Imaging Analysis

The background studies described in the main body of this thesis were intended to improve our physical understanding of the COMPTEL instrumental background, and to obtain qualitative, and possibly even quantitative, models for individual background components in order to account for the background in the CDG analysis. Some of these investigations have been extended to address background issues in (standard) imaging analysis as well. In the following, the results of one of these studies, which addressed the event selections in ToF and PSD, is summarized in fair detail, as it yielded important input for the CDG analysis: an improved fit of the ToF forward-peak in the 4.3–9 MeV range (see Sec. 5.2).

C.1 Improved Event Parameters and Optimized Event Selections

The latest corrections of event parameters, in particular ToF and PSD, have been described in Secs. 3.7 and 3.8. The basic motivation for these corrections is the attempt to improve the signal-to-noise ratio in the data used for CDG and imaging analyses by first improving the resolution in these parameters, and by subsequent optimization of data selections such that as much background as possible can be rejected.

A first step in this direction was to optimize the ToF and PSD selections for standard $\mathrm{ToF_{II}}$ and $\mathrm{PSD_{I}}$ data in the 10–30 MeV range (Collmar *et al.* 1997b). A more thorough study along these lines based on improved $\mathrm{ToF_{VI}}$ and $\mathrm{PSD_{II}}$ data, extending the energy range for which an optimization could be achieved to 4.3–30 MeV, was performed by Weidenspointner *et al.* (1997b). A comparison of the imaging results obtained with different data and different sets of event selections was given by Weidenspointner *et al.* (1997a).

The detailed investigations of the ToF spectrum as a function of energy and time described in Sec. 4.3 have returned a wealth of information. These studies were, however, limited by the fact that the ToF forward-peak was treated as a unit, despite the accumulating evidence that the ToF forward-peak is a combination of various components. In particular, these investigations did not allow us to extract the ToF signature of the celestial signal, because the ToF forward-peak is dominated by background events whose ToF distribution is insufficiently known.

Collmar *et al.* (1997b) advanced a potential solution to this problem, namely to utilize the signal of the Crab pulsar, the brightest point source in the COMPTEL energy range, as a calibration source. The basic idea is to reject as many background events as possible by making use of the ARM distribution (see Sec. 3.5.4), thereby achieving a significantly increased signal-to-noise ratio for investigating the ToF signature of a point source. The correlation of the ARM angle, calculated for the Crab position, and the ToF value is exemplified in Fig. C.1. The Crab signal can clearly be recognized around ARM = 0° in a ToF range of roughly 116–125 channels. The two-dimensional distribution in ARM and ToF was studied by fitting a simple analytical model to the one-dimensional ARM distribution in small ToF ranges, as depicted in Fig. C.2. The model consisted of a Gaussian and a constant describing the ARM continuum, and a second Gaussian modelling the ARM signature of the Crab[1]. Depending on the number of events in the ARM spectrum, the width of the ARM distribution of the Crab signal is more or less susceptible to statistical fluctuations in the data. Therefore the ARM distribution of the ToF range 119–121 channels, where the Crab signal is very pronounced, was used to obtain a best estimate for the width of the Crab ARM distribution (see Fig. C.2). Subsequently, the width of the Crab ARM signature was fixed at this best estimate in the fits of the ARM distribution as a function of ToF, the other six parameters were allowed to vary freely. Finally, the sought-after ToF signature of the Crab signal was determined from these fits, as depicted in Fig. C.3.

This procedure was first applied to comparing so-called on-axis Crab data of different ToF levels in the 10–30 MeV range. Let ζ_{Crab} be the zenith angle of the Crab, defined as the angle between the pointing direction of COMPTEL and the direction of the pulsar, then on-axis Crab data consist of observations for which $\zeta_{\mathrm{Crab}} < 7°$. The results for the position and width of the Crab signal in the Gaussian representation are summarized in Table C.1. It was to be expected from the results of the `IFCTCF` corrections (van Dijk 1996) and the additional `EVPTPC` selections (see Sec. 3.7.2) on the ToF forward-peak that the position of the Crab signal is lowest for standard $\mathrm{ToF_{II}}$ data, and that it is similar for the improved $\mathrm{ToF_{III}}$ and $\mathrm{ToF_{VI}}$ data. The results on the width of the Crab signal are somewhat inconclusive due the relatively large errors of the best fit values, not to mention the systematics involved. The results are, however, consistent with earlier findings. In particular, it seems that $\mathrm{ToF_{VI}}$ data do, indeed, yield the narrowest ToF distribution. Thus it was decided at this point to perform

[1]The true ARM distribution of a point source is not precisely Gaussian, as was explained in Sec. 3.5.4, but a Gaussian provides an acceptable analytical model for the purpose of this investigation.

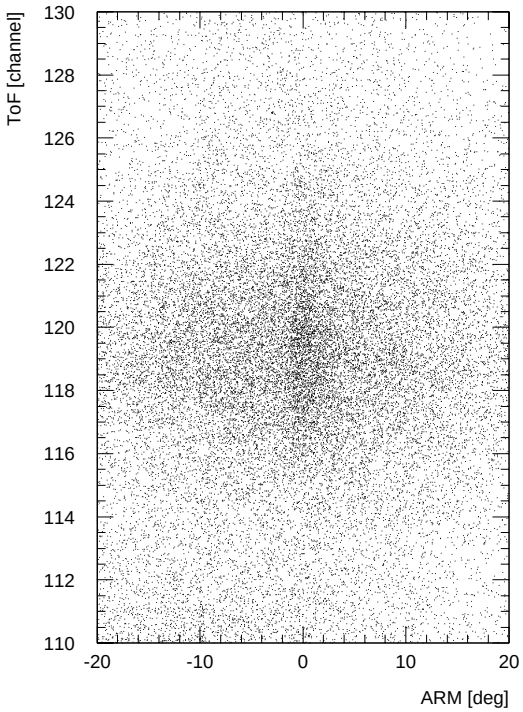

Figure C.1: *The ARM-ToF distribution of 10–30 MeV on-axis Crab data.*

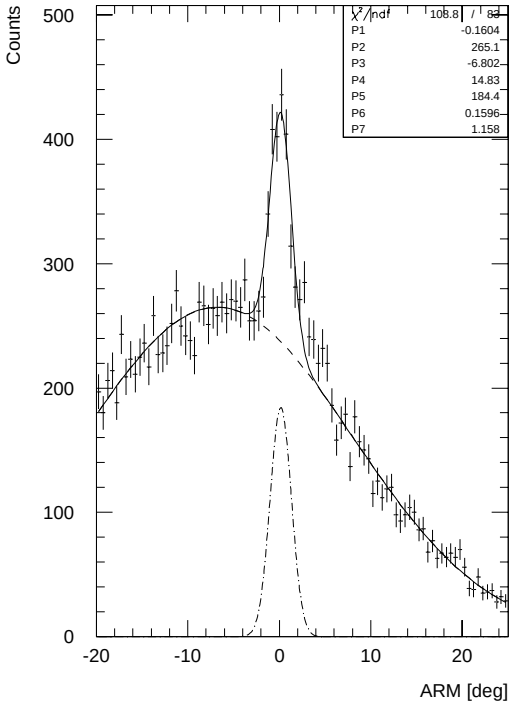

Figure C.2: *The fit of the ToF 119–121 ARM spectrum for 10–30 MeV on-axis Crab data (compare Fig. C.1).*

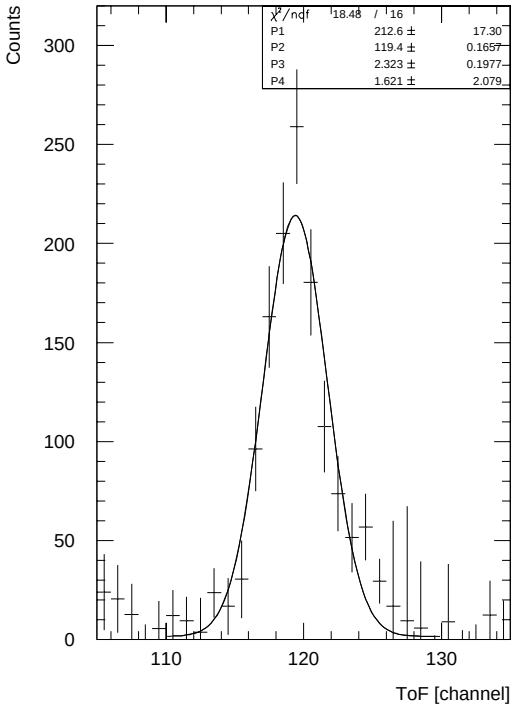

Figure C.3: *The Crab ToF spectrum from 10–30 MeV on-axis data (compare Figs. C.1 and C.2.*

	ToF_{II}	ToF_{III}	ToF_{VI}
Position	118.7 ± 0.3	119.6 ± 0.3	119.4 ± 0.2
Width	2.37 ± 0.40	2.57 ± 0.21	2.32 ± 0.20

Table C.1: *The position and width of the 10–30 MeV on-axis Crab signal in Gaussian representation for three different levels of ToF data.*

	Crab On-Axis		Crab Off-Axis		Crab On-Axis and Off-Axis	
	Position	Width	Position	Width	Position	Width
10-30 MeV	119.39 ± 0.17	2.32 ± 0.20	119.70 ± 0.14	2.29 ± 0.15	119.6 ± 0.10	2.25 ± 0.12
9-30 MeV	119.48 ± 0.15	2.14 ± 0.17	119.72 ± 0.13	2.33 ± 0.14	119.7 ± 0.10	2.38 ± 0.10
4.3-9 MeV	120.20 ± 0.15	2.78 ± 0.18	120.11 ± 0.12	2.88 ± 0.16	120.0 ± 0.10	2.97 ± 0.11

Table C.2: *The position and width of the on-axis, off-axis and combined on-axis and off-axis Crab signal in Gaussian representation for three different energy bands as obtained with* ToF_{VI} *data.*

the following, more detailed investigations, which required large amounts of additional off-axis Crab data (for which ζ_{Crab} ranges from 14° to 38°), with ToF_{VI} data *only*.

The next step was to compare the ToF spectrum for on-axis, off-axis and the combined on-axis and off-axis Crab data (on average, the off-axis Crab data contained about a factor of 1.5 more Crab events than the on-axis Crab data). The comparison was not only done for the standard 10–30 MeV range, but also for the 4.3–9 MeV and 9–30 MeV energy bands used in the CDG analysis. The results of this comparison are summarized in Table C.2 (the results obtained with the CDG selections are fully consistent). The ToF width of the Crab signal seems to be reasonably independent of the zenith angle of the Crab, ζ_{Crab}. This is also true for the position of the signal in the 4.3–9 MeV band. Above 9 MeV the position of the signal might increase with increasing ζ_{Crab}, however, considering the uncertainties involved, the evidence for such a trend is weak. In the following, it is therefore assumed that position and width of the Crab signal are independent of ζ_{Crab}. Consequently, all further investigations were performed exclusively with the combined on-axis and off-axis Crab data to minimize the statistical uncertainty.

If the position and the width of the ToF distribution of a point source are independent of its zenith angle, then the ToF distribution of a point source (such as the Crab), an extended source (such a supernova remnant or a gas or dust cloud) and a diffuse source (such as the galactic plane or the cosmic diffuse background) are identical. The results obtained above can therefore be applied to the analysis of the CDG, which is based on fits of ToF spectra to extract the signal. An analytical description of the ToF distribution of the signal is of fundamental importance for the CDG analysis, therefore

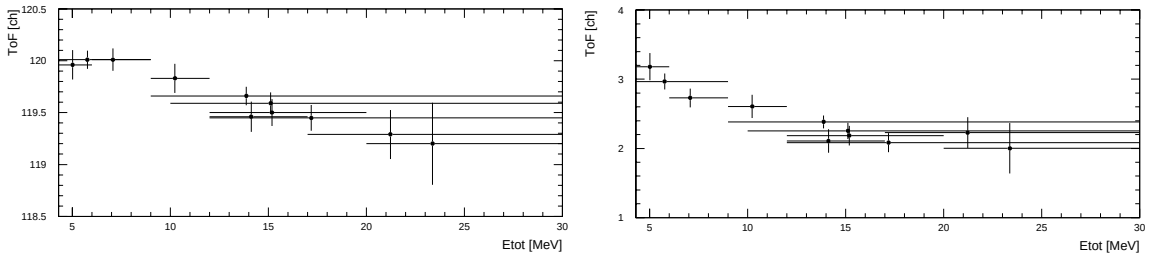

Figure C.4: *The position (left) and the width (right) of the Crab ToF spectrum in Gaussian representation as obtained for miscellaneous energy ranges with ToF_{VI} data. The data points are plotted at the average energy of each energy range, which is indicated by the horizontal lines.*

this analysis was also performed in the finer energy ranges used in the CDG analysis. The position and width of the Crab ToF signal for all energy intervals analyzed are depicted in the left and right panel of Fig. C.4, respectively. The numerical values will be given below in Table C.3. Below about 8 MeV the position of the signal is close to 120 channels. At higher energies the position seems to move to lower ToF values with increasing energy, but cannot be located very accurately above about 15 MeV. The width of the signal decreases with increasing energy.

Now the results on the ToF distribution of the Crab signal were applied to "traditional" ToF fits (as those in Sec. 4.3.2.2) in which the ToF forward-peak is modelled by a single Gaussian. ToF spectra were summed as a function of $|\mathrm{ARM}|_{\mathrm{max}}$, the maximal allowed absolute value of the ARM angle of an event (see Figs. C.1 and C.2). For example, the ToF spectrum for $|\mathrm{ARM}|_{\mathrm{max}} = 1°$ contains all events with an ARM angle between $-1°$ and $+1°$. If the ToF spectrum of these Crab selected data, which also contains instrumental background and events from other sources than the Crab (see Fig. C.3), is dominated by Crab events, then position and width of the ToF forward-peak should be consistent with the results shown in Fig. C.4. As the value of $|\mathrm{ARM}|_{\mathrm{max}}$ is increased, more and more events from other regions of the sky and more and more instrumental background events are included, allowing us to study the transition from a "signal dominated" ToF spectrum to a "background dominated" ToF spectrum.

In a first set of ToF fits all 7 fit parameters (3 parameters for the ToF forward-peak, 4 for the ToF continuum background) were allowed to vary freely. The results on the ToF spectrum of the Crab signal (as described above) were only used as start values. The fits revealed a dichotomy of the ToF spectrum as a function of energy: below 9 MeV the position of the ToF forward-peak increases with increasing $|\mathrm{ARM}|_{\mathrm{max}}$, above 9 MeV the position is independent of $|\mathrm{ARM}|_{\mathrm{max}}$, as shown in the left and right panel of Fig. C.5 for the 4.3–9 MeV and 9–30 MeV energy bands. At all energies (except the 9–12 MeV range, see below) the width of the ToF peak is significantly larger than the width of the Crab signal and varies little with $|\mathrm{ARM}|_{\mathrm{max}}$. The small values of the ToF width for the lowest $|\mathrm{ARM}|_{\mathrm{max}}$ values are artifacts of the fitting procedure (remember: all parameters of the ToF continuum are free). The dichotomy was to be expected from

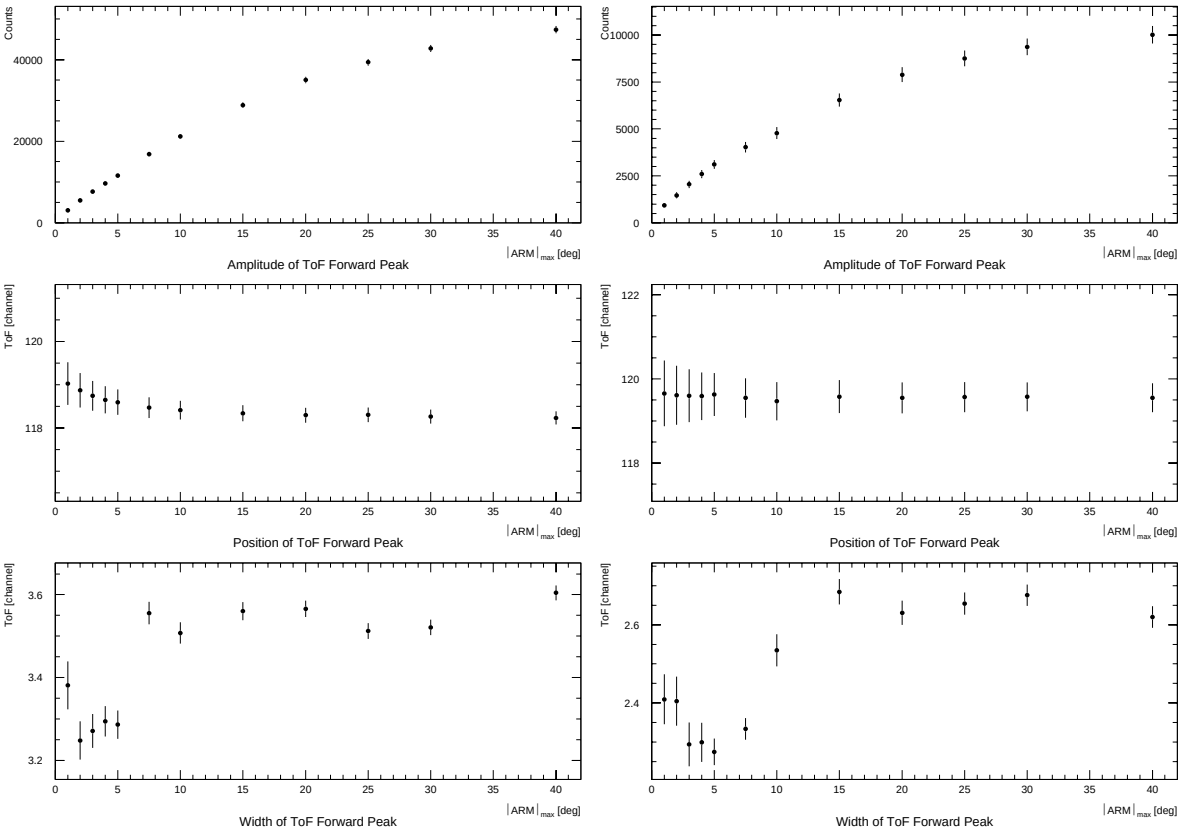

Figure C.5: *The amplitude (top), the position (middle) and the width (bottom) of the ToF forward-peak as a function of* $|\mathrm{ARM}|_{\max}$ *in the energy ranges 4.3–9 MeV (left) and 9–30 MeV (right).*

previous results on the ToF spectrum as a function of energy (see Sec. 4.3.3). Below 9 MeV the ToF forward-peak is dominated by prompt background produced in the material of the D1 detector and the Al-structure. As $|\mathrm{ARM}|_{\max}$ increases, the fraction of background events (centered around ToF 117–118 channels) increases relative to the fraction of source events (centered around ToF 120 channels), resulting in a decrease of the position of ToF forward-peak. Above 9 MeV the ToF forward-peak is also dominated by prompt background, but the processes responsible for and the locus of its production are different and, unfortunately, still poorly understood (see Sec. 4.3.3).

The obvious next step was to attempt a second set of fits in which the ToF forward-peak is described by two components: the signal as determined above and a second, Gaussian component describing some fraction of the background. At first, only the width and the position of the signal were fixed in the fits, leaving 5 parameters free. This was sufficient to clearly identify a second ToF forward-peak component below 9 MeV and, with less ease, also above 12 MeV. In the 9–12 MeV range the situation is not that clear, for reasons outlined below. The χ^2_ν values of these 2-component fits were a factor of 2–4 lower than the χ^2_ν values of the "traditional" 1-component fits, depending on the energy range. Below 9 MeV the results for position and width of

	Signal Component		Background Component	
	Position	Width	Position	Width
4.3-9 MeV	120.0	2.85	117.3	3.7
9-30 MeV	119.65	2.35	119.15	5.0
10-30 MeV	119.6	2.25	119.2	4.8
12-30 MeV	119.35	2.1	119.9	4.3
4.3-6 MeV	120.0	3.2	117.0	3.8
6-9 MeV	120.0	2.7	117.6	3.4
9-12 MeV	119.8	2.6	119.6	3.0
12-17 MeV	119.4	2.1	119.9	4.0
17-30 MeV	119.3	2.1	120.2	4.4

Table C.3: *The "average" results for position and width of the signal and the background component of the ToF forward-peak in miscellaneous ToF ranges as obtained with ToF$_{\rm VI}$ data.*

the ToF forward-peak background component were independent of $|\mathrm{ARM}|_{\max}$. Above 9 MeV some fits of the lowest $|\mathrm{ARM}|_{\max}$ values yielded inconsistent results for position and width of the second component, but even in these cases the values converged and remained stable for $|\mathrm{ARM}|_{\max}$ larger than about 10°. This problem of the fitting procedure could be solved by fixing the width of the background component in addition to position and width of the signal, leaving 4 parameters free. This had no effect on the fits of the energy bands below 9 MeV, but now the position of the background was independent of $|\mathrm{ARM}|_{\max}$ also for the higher energy ranges. The two-component fits with 4 free parameters in the 4.3–6 MeV and the 17–30 MeV energy ranges are depicted in Figs. C.6 and C.7, respectively. As expected, the ToF forward-peak fraction of the background component increases with increasing $|\mathrm{ARM}|_{\max}$. The ratio of the events in the ToF forward-peak background to the events in the signal is shown in the top and bottom panels of Fig. C.8 for the 4.3–6 MeV and the 17–30 MeV energy ranges, respectively. The increase of this ratio with increasing $|\mathrm{ARM}|_{\max}$ strongly supports the correctness of the identified ToF forward-peak signal and background components. These fits were also performed with CDG selections. The "average" results of these two sets of fits in miscellaneous energy ranges, which are used in the following, are summarized in Table C.3.

In the 4.3–9 MeV energy range, as expected from earlier investigations of the ToF spectrum, the ToF forward-peak background component is centered in the ToF range 117–118 channels. The uncertainties in the values for position and width of the background component are about 0.1 channels and 0.2 channels, respectively. As can be

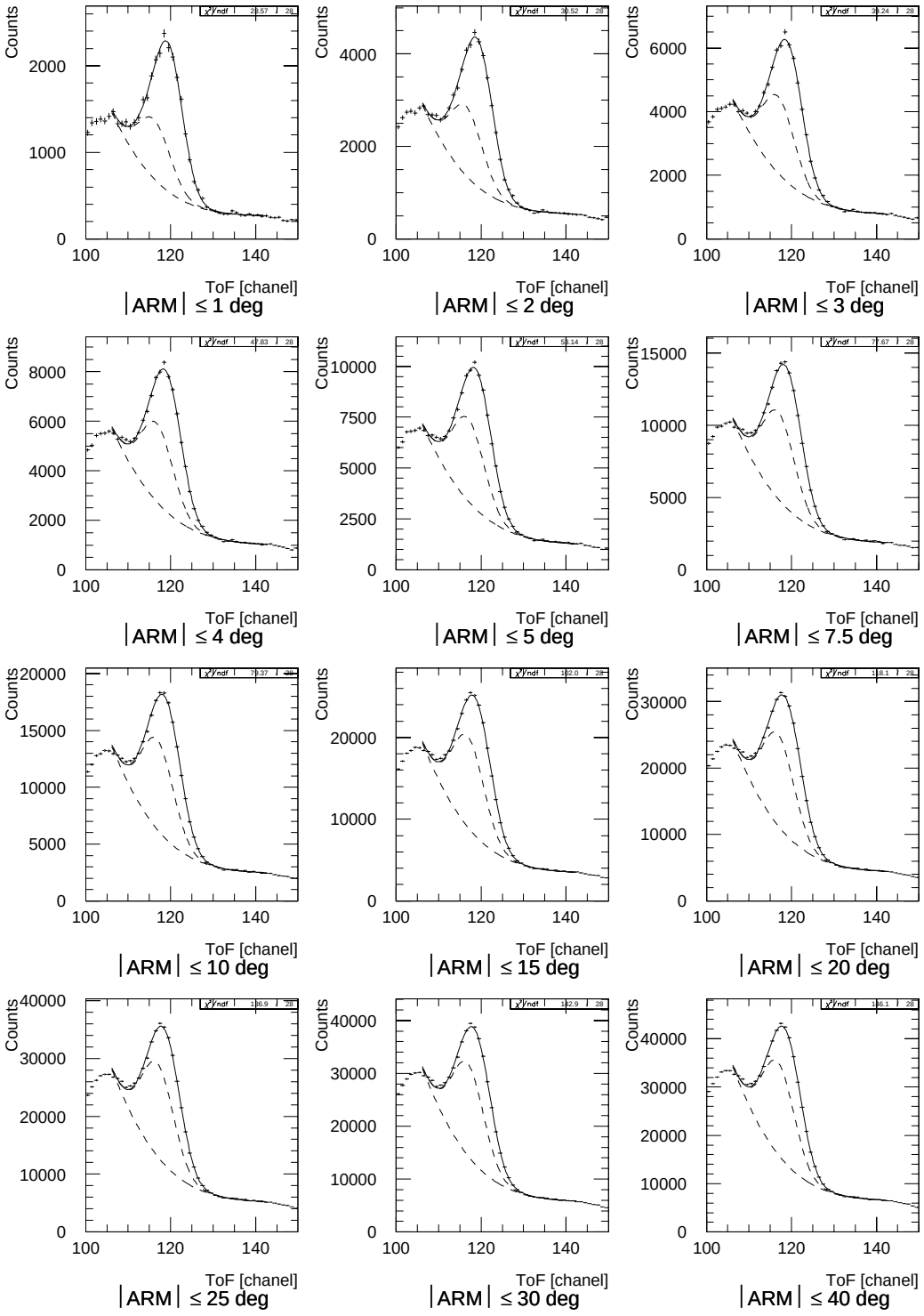

Figure C.6: *The two-component ToF fits with 4 free parameters for the 4.3–6 MeV energy range. The ToF continuum background and the ToF forward-peak background are indicated by dashed lines.*

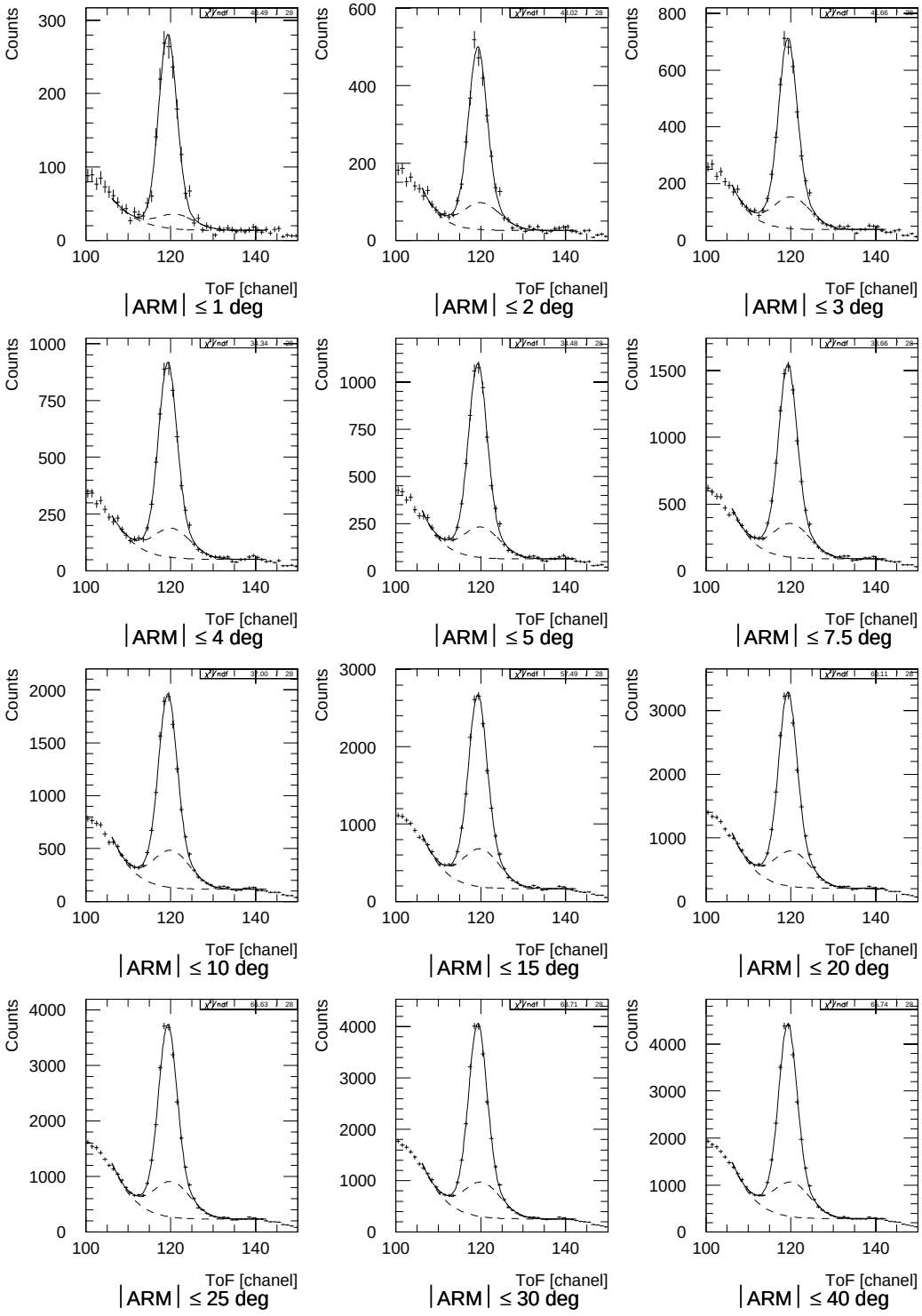

Figure C.7: *The two-component ToF fits with 4 free parameters for the 17–30 MeV energy range. The ToF continuum background and the ToF forward-peak background are indicated by dashed lines.*

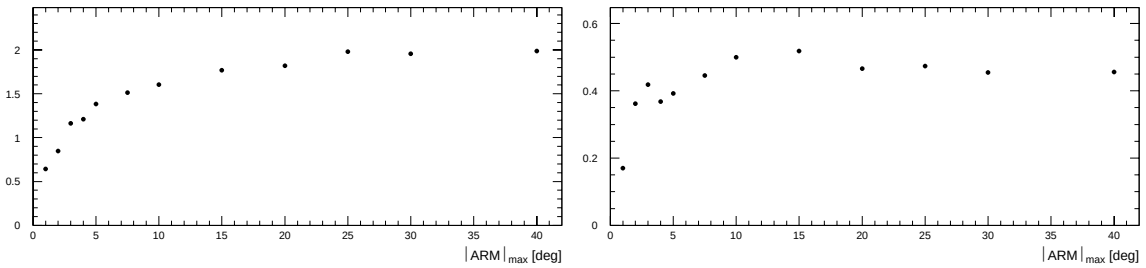

Figure C.8: *The ratio of the events in the ToF forward-peak background to the events in the signal for the 4.3–6 MeV (left) and the 17–30 MeV (right) energy intervals (compare Figs. C.6 and C.7).*

seen in Table C.3, the signal and the background component are separated by more than 2 channels in this energy range, in addition to having significantly different widths. Therefore both components could readily be identified and separated in the ToF fits. Application of these results on the ToF distribution to the spectral CDG analysis allowed us to improve the fit of the ToF forward-peak in the 4.3–9 MeV range (see Sec. 5.2).

In the 9–12 MeV range, the transition region between the low-energy prompt background dominated by nuclear cascades and the high-energy prompt background, the situation is much more difficult. Signal and background component are quite similar and therefore very hard to separate in the ToF fits, despite the excellent statistical quality of the ToF spectra. The uncertainty of position and width of the background component is about 0.2 channels and 0.3 channels, respectively.

Above 12 MeV the uncertainty in the ToF distribution of the ToF forward-peak background is about the same as in the 9–12 MeV range. Due to the siginificantly different widths of signal and background, however, these two components can be separated more easily than in the energy range below. It is interesting to note that the background component seems to be centered at higher ToF values than the signal.

In the "combined" energy ranges 12–30 MeV, 10–30 MeV, and in particular 9–30 MeV, the background component is rather poorly constrained. This is due to the energy dependence of the background component above 9 MeV, which reflects a transition in the physics of the prompt background. In general, the results above 12 MeV have to be used with care. At the current state of the investigation it is clear that the ToF forward-peak above 12 MeV has more than one component. It seems that a second, rather wide background component is supported by the data. The shape of this background component, however, which may not be Gaussian, is hard to determine because of the interplay of the shape of the ToF continuum background with the shape (width) of the ToF forward-peak background, even for excellent statistics.

With these results on the ToF spectrum the final step of this investigation could be taken, as summarized in Table C.4: the ToF windows of maximum signal-to-noise

Energy Range	ToF Range	Flux Correction
4.3-9 MeV	117.25 - 126.5	1.22
9-30 MeV	116.5 - 123.5	1.16
10-30 MeV	116.5 - 123.25	1.16
12-30 MeV	116.25 - 122.5	1.16
4.3-6 MeV	117.0 - 127.5	1.22
6-9 MeV	117.25 - 126.5	1.20
9-12 MeV	116.0 - 126.0	1.09
12-17 MeV	116.25 - 122.75	1.14
17-30 MeV	116.0 - 122.5	1.14

Table C.4: *The ToF window of maximum signal-to-noise ratio and the corresponding flux correction factors for miscellaneous energy ranges as obtained with ToF$_{\rm VI}$ data.*

ratio and the corresponding flux correction factors[2] for miscellaneous energy ranges were determined based on the ToF fits for the largest $|\mathrm{ARM}|_{\rm max}$ range. These are the ToF selections used in Weidenspointner *et al.* (1997a) for the preliminary ToF$_{\rm VI}$ analysis of 3C 273 and 3C 279. As already pointed out there, the application of ToF$_{\rm VI}$ data is currently under further investigation.

C.2 First Results

For a first, preliminary assessment of the potential improvements of COMPTEL imaging analyses due to the improved event parameter values and the optimized selections OPs 511 and 511.5 were analyzed for different types of `EVP` data and event selections. During these two OPs the blazar 3C 279 was observed in a flaring state by COMPTEL (Collmar *et al.* 1997a) and EGRET (Wehrle *et al.* 1997). The comparisons were performed in the two energy ranges 4.3–9 MeV and 10–30 MeV. The standard `EVP` data (containing ToF$_{\rm II}$ and PSD$_{\rm I}$) was processed with the standard `EVP` selection set `MPE006`[3] For the corrected `EVP` data (containig ToF$_{\rm VI}$ and PSD$_{\rm II}$) the E_1-dependent PSD selection of Sec. 3.8 and the energy-dependent ToF selection of Table C.4 (4.3–9 MeV: 117.25–126.5, 10–30 MeV: 116.5–123.25) was used; all other selections were

[2]The flux correction factors take into account that only a fraction of the celestial signal is contained in the selected ToF range. For example, if a fraction of 75% of the ToF distribution of the celestial signal falls into the selected ToF range, then the flux correction factor is $1/0.75 = 1.33$.

[3]The `MPE006` standard selections are independent of energy and defined as follows: E_1 70–20000 keV, E_2 650–30000 keV, ToF 115–130 ch, PSD 0–110 ch, $\bar{\varphi}$ 0°–50°, $\zeta > 0°$, with ζ being the angle between the Earth horizon and the event circle.

identical to `MPE006`. In addition, in the 10–30 MeV range the standard `EVP` data was processed with the PSD and ToF selections of Collmar *et al.* (1997b): PSD 65–85 ch, ToF 113–126 ch, all other selections as in `MPE006`. All maximum-likelihood maps[4] (`MLM`) compared in the following were generated with the COMPASS task `SRCLIX`, using the standard point-spread functions[5] (PSFs) for 3–10 MeV and 10–30 MeV.

The 10–30 MeV `MLM` maps obtained for the standard `EVP` data with the standard `MPE006` selection set, the standard `EVP` data with the selections of Collmar *et al.* (1997b) and the corrected `EVP` data with the optimized PSD and ToF selections given above are depicted in Figs. C.9, C.10, and C.11. In all maps identical grey scales and contour levels (6 step 3) were used for the maximum-likelihood ratios[6] (`MLR`) values. The triangle indicates the position of the blazar 3C 279, the circle marks the location of the quasar 3C 273. The standard map does not show any significant source-like feature and appears to be more dominated by "artifacts" than the other two maps — despite the fact that it was derived from the largest number of events. In marked contrast, the other two maps clearly show a source feature at the position of 3C 279. In addition, these two maps seem to be "cleaner" than the standard map. The highest significance for the blazar is obtained with the corrected `EVP` data. A more quantitative comparison of the three maps is given in Table C.5, which summarizes the number of events contained in each map, the MLR values and the significance at the positions of the two AGN (assuming one degree of freedom), and their fluxes (including ToF correction factors) as derived from a combined fit.

The 4.3–9 MeV `MLM` maps obtained for the standard `EVP` data with the standard `MPE006` selection set and the corrected `EVP` data with the PSD and ToF selections given above are shown in Figs. C.12 and C.13[7]. Again, the standard map and the map obtained with the corrected `EVP` data are markedly different. The standard map is dominated by a significant, somewhat extended feature centered about 3° off the position of 3C 273. This feature extends down to 3C 279, which is not really detected. Two other features, supposedly artifacts, are more significant than the latter blazar. Using the corrected `EVP` data and the optimized ToF and PSD selections described above, two source features of reduced significance close to the positions of the two AGN appear

[4]For a discussion of the maximum-likelihood approach and its application to COMPTEL analysis, refer to, e.g. de Boer *et al.* (1992) and references therein.

[5]The point-spread function describes the telescope response for a point source in terms of the probability distribution of the events in $(\chi, \psi, \bar{\varphi})$ in a given energy range. Detailed accounts of the COMPTEL PSF can be found, e.g., in van Dijk (1996) and Oberlack (1997).

[6]For a definition of the maximum-likelihood ratio λ_q, with q being the number of free model parameters, refer to , e.g. de Boer *et al.* (1992) or Blom (1997). At present, it is sufficient to realize that $-2\ln\lambda_q$ is distributed like a χ^2_q probability distribution. For example, a $> 3\sigma$ detection of a known source can be claimed when $-2\ln\lambda_1 > 9$ at the source position (χ_0, ψ_0), the free parameter being the source flux. The detection of an unknown source is a problem with three degrees of freedom (source flux and position), hence a $> 3\sigma$ detection requires that $-2\ln\lambda_3 > 14.2$. The `MLR` values depicted in the `MLM` maps are the values of $-2\ln\lambda_q$.

[7]Collmar *et al.* (1997b) could not derive improved selections below 10 MeV.

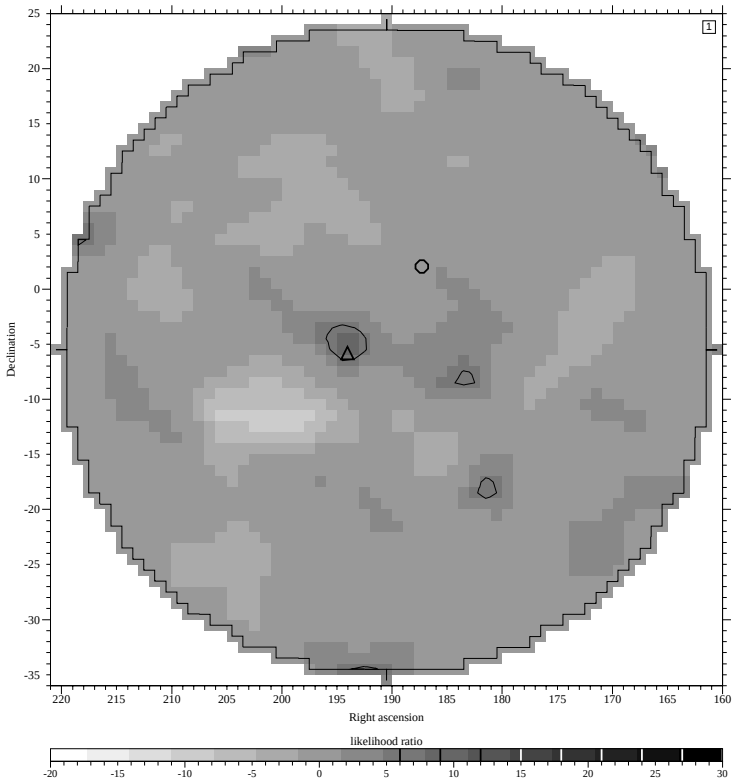

Figure C.9: *10–30 MeV standard* `MLM map` *derived with the standard* `EVP` *data, the standard selection set* `MPE006` *and the standard 10–30 MeV PSF. The circle and the triangle indicate the positions of the quasars 3C 273 and 3C 279, respectively.*

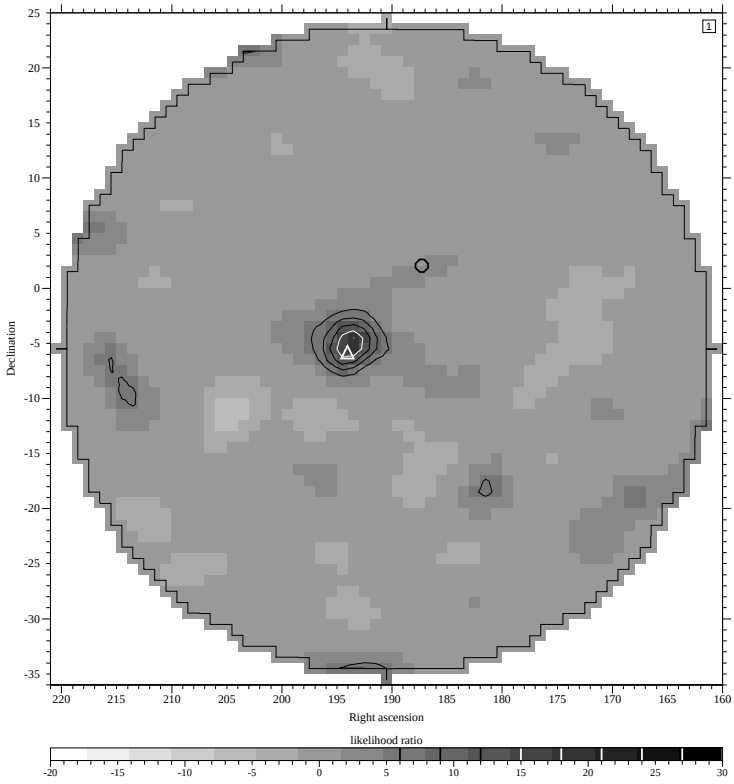

Figure C.10: *10–30 MeV* `MLM` *map derived with the standard* `EVP` *data, the selections of Collmar* et al. *(1997b) and the standard 10–30 MeV PSF. The circle and the triangle indicate the positions of the quasars 3C 273 and 3C 279, respectively.*

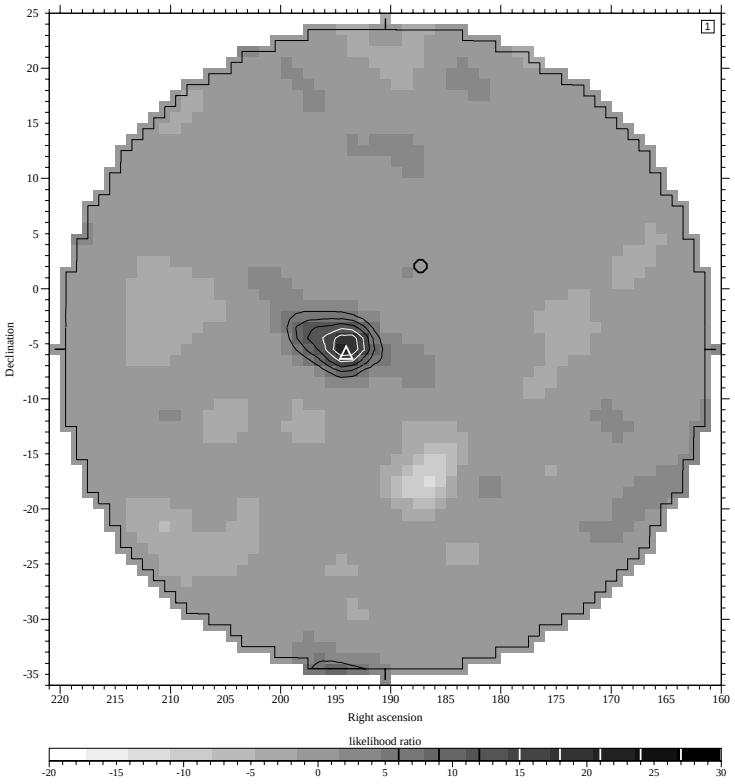

Figure C.11: *10–30 MeV* `MLM` *map derived with the corrected* `EVP` *data, the optimized ToF and PSD selections described above and the standard 10–30 MeV PSF. The circle and the triangle indicate the positions of the quasars 3C 273 and 3C 279, respectively.*

`EVP` data	standard `EVP`	standard `EVP`	corrected `EVP`
`EVP` selection	`MPE006`	Collmar *et al.* (1997b)	optimized (this thesis)
events in map	13377	9829	7618
3C 273 `MLR` value	0.2	1.6	1.0
3C 279 `MLR` value	8.5	17.3	20.8
3C 273 significance (1 dof)	0.4 σ	1.3 σ	1.0 σ
3C 279 significance (1 dof)	2.9 σ	4.2 σ	4.6 σ
3C 273 flux [10^{-4}/cm^{2}sec]	0.052 ± 0.066	0.087 ± 0.096	0.060 ± 0.057
3C 279 flux [10^{-4}/cm^{2}sec]	0.185 ± 0.066	0.256 ± 0.063	0.254 ± 0.059

Table C.5: Comparison of the three 10–30 MeV `MLM` maps of Figs. C.9, C.10, and C.11.

instead of the more significant, but extended source feature off 3C 273. Moreover, this map seems to be cleaner than the standard map. A quantitative comparison of the two maps is summarized in Table C.6.

Finally, the energy spectra of the two AGN 3C 273 and 3C 279 were derived for the corrected `EVP` data with optimized event selections by repeating the above analysis in a finer energy binning. The results are indicated by the circles in Fig. C.14 (see

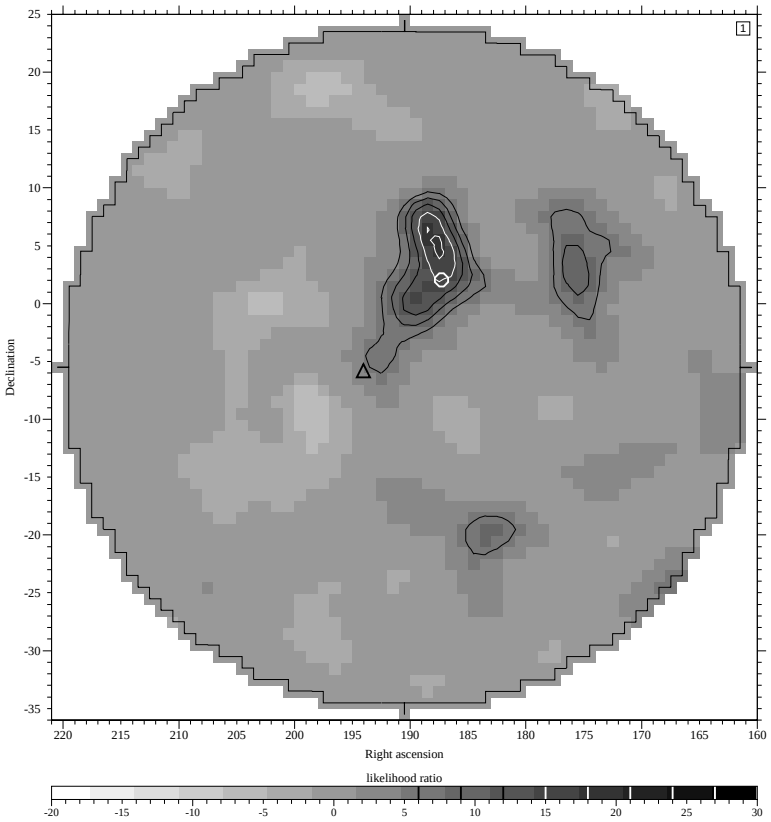

Figure C.12: *4.3–9 MeV standard* `MLM` *map derived with the standard* `EVP` *data, the standard selection* `MPE006` *and the standard 3–10 MeV PSF. The circle and the triangle indicate the positions of the quasars 3C 273 and 3C 279, respectively.*

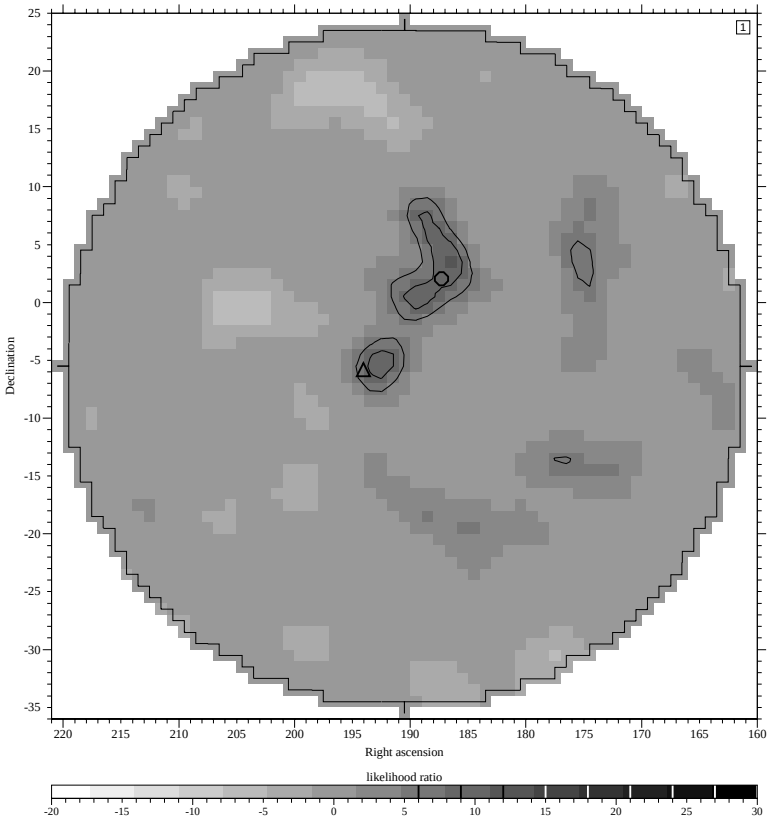

Figure C.13: *4.3–9 MeV* `MLM` *map derived with the corrected* `EVP` *data, the ToF and PSD selections described above and the standard 3–10 MeV PSF. The circle and the triangle indicate the positions of the quasars 3C 273 and 3C 279, respectively.*

EVP data	standard EVP	corrected EVP
EVP selection	MPE006	this report
events in map	83496	56274
3C 273 MLR value	15.9	10.0
3C 279 MLR value	3.8	6.6
3C 273 significance (1 dof)	4.0 σ	3.2 σ
3C 279 significance (1 dof)	2.0 σ	2.6 σ
3C 273 flux [10^{-4}/cm^{2}sec]	0.491 ± 0.124	0.347 ± 0.108
3C 279 flux [10^{-4}/cm^{2}sec]	0.262 ± 0.121	0.305 ± 0.106

Table C.6: Comparison of the two 4.3–9 MeV MLM maps of Figs. C.12 and C.13.

Weidenspointner *et al.* 1997a, for details). The squares are the result of the standard analysis according to Collmar *et al.* (1997b): below 10 MeV they were derived using standard EVP data and standard selections, in the 10–30 MeV band the selections of Collmar *et al.* (1997b) were used (a standard analysis returns at best fluxes of marginal significance above 10 MeV). It seems that the fluxes derived in these analyses are consistent with each other. In addition, the corrected EVP data seem to allow us to work with finer energy bins. In the case of 3C 279 there is no qualitative change of the overall spectrum. In the case of 3C 273, however, the spectrum now exhibits some resemblance to an MeV-blazar spectrum that was not present before.

These preliminary results obtained with different sets of EVP data and different selection sets are not sufficient to decide on the "quality" of different kinds of EVP data or selection sets. The selections of Collmar *et al.* (1997b) and the selections derived for the corrected EVP data are both intended to maximize the number of "source events" relative to the number of "background events", based on the assumption that this will facilitate the detection of any kind of source-like (cone-like) structure in the data space. All that can be said at the moment is that it seems easier for SRCLIX to find point sources when the signal to noise ratio is increased, even though this implies a reduction of the total number of events in the data. In addition, the 10–30 MeV maps indicate that SRCLIX might "prefer" the corrected EVP data over the standard EVP data. Work is in progress to address these questions by attempting to disentangle the effects of different kinds of EVP data and different selection sets.

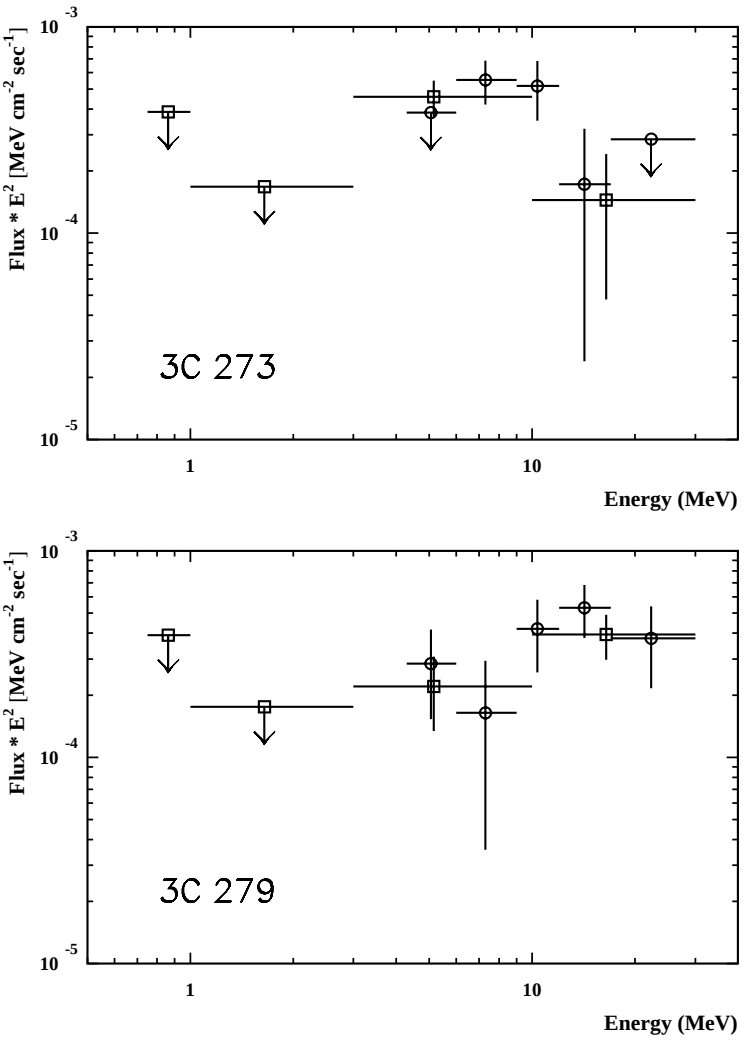

Figure C.14: *The energy spectra of 3C 273 (top) and 3C 279 (bottom) as derived with the corrected* `EVP` *data, represented by the circles. The squares were obtained from a standard analysis: standard below 10 MeV and according to Collmar* et al. *(1997b) above 10 MeV. 2σ upper limits are plotted if the flux is less than the 1σ error.*

Appendix D

Log of Observations used in the CDG Analysis

The CGRO observing program[1] is organized in four so-called Phases, which are further subdivided in Cycles of approximately one year in duration. During Phase I (Cycle 1), dedicated to the first all-sky survey at γ-ray energies, all observing time was reserved for the CGRO instrument teams. The fraction of reserved time decreased over the next two Phases, until all observing time was available to the general astronomical community starting with Phase IV. The start times (given in units of [TJD][2] and as ordinary date) of the individual Phases/Cycles are summarized in Table D.1.

Each Phase/Cycle consists of a sequence of so-called observation or viewing periods (OP/VP), which correspond to a period of time, typically 1 – 2 weeks, during which the pointings of the telescope axes remain unchanged. Individual OPs are identified by a unique number. Below all observations used in the CDG analyses presented in this thesis are summarized in Tables D.2 through D.8. The columns denote the identification number of the observation, the start and end time of the observation in [TJD] and [ticks][3], the start date of the observation, and the pointing direction of the telescope z-axis in galactic longitude l_z and latitude b_z. With a few exceptions, mostly due to unfavourable pointing directions relative to the orbital plane causing the CDG

[1]Detailed information on the CGRO observing program is e.g. available under `http://www.gamma.mpe-garching.mpg.de/~hcs/PLANS/plans.html` maintained by H. Steinle, MPE.

[2]In astronomy times are often quoted by the interval of time in days and fraction of a day since January 1, 4713 B.C., Greenwich noon (12:00), the so-called Julian Date (JD). Since JDs involve unwieldy large numbers, a more convenient numbering of days was introduced by defining Truncated Julian Days (TJDs):

$$\mathrm{TJD} = \mathrm{JD} - 2440000.5$$

whereby TJD zero corresponds to 24:00 on the night of May 23, 1968, i.e. 0:0 on May 24, 1968.

[3]Ticks count the time since the start of the day in units of 1/8 msec. It follows that a whole day corresponds to $(24 \cdot 3600 \cdot 8000 = 691,200,000)$ ticks.

	Start [TJD]	Start [Date]
Phase I, Cycle 1	8392	May 16, 1991
Phase II, Cycle 2	8943	Nov. 17, 1992
Phase III, Cycle 3	9216	Aug. 17, 1993
Phase IV, Cycle 4	9629	Oct. 4, 1994
Phase IV, Cycle 5	9993	Oct. 3, 1995
Phase IV, Cycle 6	10371	Oct. 15, 1996
Phase IV, Cycle 7	10763	Nov. 11, 1997
Phase IV, Cycle 8	11148	Dec. 1, 1998

Table D.1: The start dates of the CGRO observing Phases/Cycles.

`EHORA` cut (see Eq. 4.5) to reject the whole observation, these pointings comprise all viewing periods in Phase I through Cycle 7 with $|b_z| > 30°$.

Due to failures of individual PMTs some D1 and D2 detector modules had to be switched off or cannot be used for scientific analysis for some periods of time. These changes in the so-called telescope configuration, i.e. the set of D1 and D2 detector modules used in an analysis, strongly influence the effective area of the telescope and therefore had to be taken into account in the CDG analysis, as described in Appendix B. The changing telescope configurations used in the CDG analysis are summarized in Table D.9.

OP	Start [TJD:Ticks]	End [TJD:Ticks]	Start [Date]	l_z [°]	b_z [°]
3.0	8422 : 565440000	8435 : 562080000	Jun. 15, 1991	300.0	65.4
4.0	8435 : 581760000	8449 : 516608000	Jun. 28, 1991	156.1	72.2
9.0	8504 : 433440000	8511 : 386000000	Sep. 5, 1991	338.6	-83.6
9.5	8511 : 414720000	8518 : 388320000	Sep. 12, 1991	59.7	40.2
10.0	8518 : 420480000	8532 : 379680000	Sep. 19, 1991	287.8	-54.3
11.0	8532 : 408000000	8546 : 401760000	Oct. 3, 1991	294.5	63.6
13.5	8567 : 441600000	8574 : 453600000	Nov. 7, 1991	338.8	-83.6
17.0	8617 : 491040000	8631 : 468440000	Dec. 27, 1991	283.2	-31.2
18.0	8631 : 502624000	8644 : 394560000	Jan. 10, 1992	137.5	40.5
19.0	8644 : 423364000	8658 : 439200000	Jan. 23, 1992	58.1	-43.0
21.0	8672 : 462720000	8686 : 455520000	Feb. 20, 1992	171.5	-53.9
24.0	8714 : 388800000	8721 : 373920000	Apr. 2, 1992	9.5	57.2
24.5	8721 : 386880000	8728 : 359520000	Apr. 9, 1992	9.5	57.2
25.0	8728 : 372960000	8735 : 358560000	Apr. 16, 1992	6.8	48.1
26.0	8735 : 385440000	8740 : 366720000	Apr. 23, 1992	108.8	-41.4
28.0	8749 : 435840000	8756 : 405320000	May 7, 1992	108.8	-41.4
29.0	8756 : 436160000	8777 : 395744000	May 14, 1992	224.0	-40.0
30.0	8777 : 418560000	8784 : 439944000	Jun. 4, 1992	252.4	30.6
33.0	8805 : 418320000	8819 : 448776000	Jul. 2, 1992	252.4	30.6
37.0	8854 : 465360000	8861 : 485560000	Aug. 20, 1992	104.8	-42.1
40.0	8882 : 459840000	8903 : 397440000	Sep. 17, 1992	195.9	44.7
42.0	8910 : 498240000	8924 : 378840000	Oct. 15, 1992	0.0	-44.6

Table D.2: The Phase I (Cycle 1) OPs used in the CDG analysis in chronological order.

OP	Start [TJD:Ticks]	End [TJD:Ticks]	Start [Date]	l_z [°]	b_z [°]
201.0	8943 : 461760000	8950 : 471840000	Nov. 17, 1992	66.8	39.3
202.0	8950 : 485280000	8957 : 445920000	Nov. 24, 1992	70.9	40.5
204.0	8978 : 419440000	8985 : 447808000	Dec. 22, 1992	294.6	61.9
205.0	8985 : 461408000	8992 : 414120000	Dec. 29, 1992	294.5	61.6
206.0	8992 : 427888000	8999 : 429360000	Jan. 5, 1993	294.6	61.9
207.0	8999 : 447040000	9020 : 419328000	Jan. 12, 1993	314.1	31.5
209.0	9027 : 488560000	9040 : 464080000	Feb. 9, 1993	0.2	-34.0
216.0	9083 : 596592000	9089 : 366456000	Apr. 6, 1993	140.8	38.1
218.0	9097 : 443048000	9110 : 653360000	Apr. 20, 1993	151.4	71.3
220.0	9115 : 415072000	9120 : 445248000	May 8, 1993	298.1	-44.6
222.0	9131 : 465600000	9138 : 390504000	May 24, 1993	157.8	70.6
224.0	9141 : 452328000	9152 : 683992000	Jun. 3, 1993	298.1	-44.6
227.0	9167 : 432000000	9181 : 387760000	Jun. 28, 1993	148.1	41.2
228.0	9181 : 401688000	9195 : 366352000	Jul. 13, 1993	149.9	42.7

Table D.3: The Phase II (Cycle 2) OPs used in the CDG analysis in chronological order.

OP	Start [TJD:Ticks]	End [TJD:Ticks]	Start [Date]	l_z [°]	b_z [°]
304.0	9279 : 465352000	9285 : 418080000	Oct. 19, 1993	278.2	66.7
305.0	9285 : 431272000	9293 : 430280000	Oct. 25, 1993	277.7	62.7
306.0	9293 : 442896000	9300 : 378656000	Nov. 2, 1993	277.6	58.7
307.0	9300 : 392080000	9307 : 415272000	Nov. 11, 1993	268.6	69.3
308.0	9307 : 431360000	9310 : 288656000	Nov. 16, 1993	283.3	74.7
308.6	9314 : 633600000	9322 : 423536000	Nov. 23, 1993	283.2	74.6
311.0	9334 : 460416000	9336 : 318912000	Dec. 13, 1993	283.7	74.5
311.6	9339 : 000000000	9341 : 390184000	Dec. 17, 1993	283.7	74.5
312.0	9341 : 405720000	9348 : 444496000	Dec. 20, 1993	280.7	70.7
313.0	9348 : 458920000	9355 : 448488000	Dec. 27, 1993	289.2	78.7
317.0	9400 : 459360000	9412 : 390152000	Feb. 17, 1994	158.5	-45.4
320.0	9419 : 474512000	9426 : 404352000	Mar. 8, 1994	83.1	-45.5
322.0	9447 : 448224000	9461 : 426920000	Apr. 5, 1994	197.0	58.6
326.0	9482 : 454872000	9489 : 393200000	May 10, 1994	195.9	58.3
327.0	9489 : 424880000	9496 : 395832000	May 17, 1994	82.8	-49.6
329.0	9503 : 429600000	9510 : 404080000	May 31, 1994	253.4	-42.0
335.0	9545 : 444480000	9551 : 395272000	Jul. 12, 1994	253.4	-42.0
335.5	9558 : 432000000	9565 : 381608000	Jul. 25, 1994	253.4	-42.0
336.0	9565 : 426240000	9568 : 385120000	Aug. 1, 1994	88.4	-46.8
339.0	9615 : 426720000	9629 : 356296000	Sep. 20, 1994	4.1	40.4

Table D.4: The Phase III (Cycle 3) OPs used in the CDG analysis in chronological order.

OP	Start [TJD:Ticks]	End [TJD:Ticks]	Start [Date]	l_z [°]	b_z [°]
403.0	9657 : 436800000	9665 : 392928000	Nov. 1, 1994	58.2	37.5
403.5	9665 : 420104000	9671 : 410232000	Nov. 9, 1994	206.8	35.9
404.0	9671 : 439200000	9685 : 408896000	Nov. 15, 1994	7.15	-73.5
405.0	9685 : 440080000	9693 : 393552000	Nov. 29, 1994	306.7	56.6
405.5	9693 : 400552000	9699 : 413584000	Dec. 7, 1994	306.7	56.6
406.0	9699 : 428280000	9706 : 456088000	Dec. 13, 1994	336.4	67.2
407.0	9706 : 469296000	9720 : 413104000	Dec. 20, 1994	334.4	63.0
408.0	9720 : 427336000	9727 : 456576000	Jan. 3, 1995	305.17	57.1
409.0	9727 : 481080000	9741 : 464864000	Jan. 10, 1995	274.7	-39.2
410.0	9741 : 490200000	9762 : 457912000	Jan. 24, 1995	82.2	-32.6
418.0	9832 : 429600000	9846 : 370160000	Apr. 25, 1995	158.0	65.9
425.0	9923 : 440648000	9937 : 406680000	Jul. 25, 1995	137.4	-47.3
428.0	9967 : 425760000	9980 : 372960000	Sep. 7, 1995	270.5	-82.5

Table D.5: The Phase IV (Cycle 4) OPs used in the CDG analysis in chronological order.

OP	Start [TJD:Ticks]	End [TJD:Ticks]	Start [Date]	l_z [°]	b_z [°]
507.0	10049 : 452192000	10065 : 434400000	Nov. 28, 1995	77.5	-38.6
511.0	10098 : 469264000	10112 : 439200000	Jan. 16, 1996	298.4	62.9
511.5	10112 : 444960000	10119 : 432000000	Jan. 30, 1996	310.6	53.2
513.0	10119 : 461664000	10126 : 426720000	Feb. 6, 1996	17.6	-52.2
514.0	10126 : 442560000	10133 : 419368000	Feb. 13, 1996	62.3	-60.6
517.0	10147 : 493440000	10160 : 419760000	Mar. 5, 1996	276.8	-59.5
516.5	10163 : 460800000	10176 : 411360000	Mar. 21, 1996	61.0	41.2
519.0	10196 : 432000000	10210 : 441512000	Apr. 23, 1996	63.0	40.0
520.4	10224 : 412320000	10231 : 424320000	May 21, 1996	17.7	-52.3
521.0	10231 : 447360000	10245 : 366240000	May 28, 1996	275.6	-36.3
525.0	10287 : 433352000	10294 : 408080000	Jul. 23, 1996	338.8	-54.5

Table D.6: The Cycle 5 (Phase IV) OPs used in the CDG analysis in chronological order.

OP	Start [TJD:Ticks]	End [TJD:Ticks]	Start [Date]	l_z [°]	b_z [°]
602.0	10399 : 454560000	10406 : 423512000	Nov. 12, 1996	60.0	65.0
603.0	10406 : 435520000	10413 : 413760000	Nov. 19, 1996	55.7	64.2
605.1	10413 : 428160000	10420 : 457688000	Nov. 26, 1996	43.18	56.8
604.1	10420 : 470672000	10427 : 442640000	Dec. 3, 1996	48.4	60.7
606.0	10427 : 460040000	10434 : 433256000	Dec. 10, 1996	306.4	56.4
607.0	10434 : 446240000	10440 : 443520000	Dec. 17, 1996	306.5	56.4
608.0	10440 : 457440000	10447 : 436400000	Dec. 23, 1996	306.8	56.7
609.0	10447 : 448568000	10455 : 454560000	Dec. 30, 1996	306.9	56.8
610.0	10455 : 465472000	10462 : 444408000	Jan. 7, 1997	306.9	56.8
610.5	10462 : 457880000	10469 : 435360000	Jan. 14, 1997	306.7	58.9
611.1	10469 : 454080000	10476 : 425536000	Jan. 21, 1997	306.9	56.8
614.5	10490 : 436320000	10497 : 439400000	Feb. 11, 1997	39.8	-60.4
617.8	10547 : 422400000	10553 : 396312000	Apr. 9, 1997	66.8	37.2
621.5	10616 : 409488000	10623 : 405600000	Jun. 17, 1997	301.7	57.8
626.0	10686 : 400320000	10693 : 399272000	Aug. 26, 1997	270.0	-75.0
628.0	10700 : 400320000	10707 : 405296000	Sep. 9, 1997	300.1	-74.3
629.0	10707 : 418000000	10714 : 386936000	Sep. 16, 1997	300.1	-74.3
631.1	10755 : 448936000	10763 : 440560000	Nov. 3, 1997	156.8	-39.1

Table D.7: The Cycle 6 (Phase IV) OPs used in the CDG analysis in chronological order.

OP	Start [TJD:Ticks]	End [TJD:Ticks]	Start [Date]	l_z [°]	b_z [°]
701.0	10763 : 468464000	10770 : 424696000	Nov. 11, 1997	10.1	-54.1
702.0	10770 : 437312000	10777 : 446640000	Nov. 18, 1997	10.1	-54.1
708.0	10812 : 456800000	10819 : 416560000	Dec. 30, 1997	10.1	-54.1
709.1	10819 : 428520000	10826 : 438776000	Jan. 6, 1998	10.1	-54.1
714.0	10882 : 491360000	10889 : 489776000	Mar. 10, 1998	39.7	-72.3
715.0	10889 : 497040000	10892 : 466960000	Mar. 17, 1998	57.3	-73.7
715.5	10892 : 494160000	10899 : 441040000	Mar. 20, 1998	55.7	64.2
716.5	10899 : 458000000	10905 : 520560000	Mar. 27, 1998	176.6	61.9
716.7	10905 : 532720000	10917 : 406640000	Apr. 2, 1998	177.9	63.8

Table D.8: The Cycle 7 (Phase IV) OPs used in the CDG analysis in chronological order.

OP	D1 Off	D2 Off	D2 PMT-F.
3	—	2, 11, 13, 14	—
4 – 25	4	2, 11, 13, 14	—
26	4	2, 11, 14	13
28 – 37	—	2	11, 13, 14
40	—	2, 11, 13, 14	—
42 – 228	—	2	11, 13, 14
304 –	—	1, 2	11, 13, 14

Table D.9: *The telescope configurations used for individual OPs in the CDG analysis summarized in Tables D.2 – D.8. The table gives those D1 oand D2 detector modules that are not used in the analysis (D1/D2 Off). In addition, for some OPs failure of individual PMTs in the D2 detector modules 11, 13, and 14 (D2 PMT-F.) can be accounted for by excluding precisely defined sections of these modules from the analysis.*

Appendix E

Glossary of Acronyms

E.1 Astrophysical Acronyms

AGN *Active Galactic Nucleus* or *Active Galactic Nuclei* (see Sec. 2.2.1.2)

BH *Black Hole*

BL Lac *BL LACertae object*: a radio-loud AGN type (see Sec. 2.2.1.2)

BLRG *Broad-Line Radio-Galaxy*: a radio-loud AGN type (see Sec. 2.2.1.2)

CDG *Cosmic Diffuse Gamma-Ray Background*: often used as a synonym for EGB at low and medium γ-ray energies below about 30 MeV (see Sec. 2.1.7)

CIB *Cosmic Infrared Background*: the EBR in the infrared waveband (see Sec. 2.1.3)

CMB *Cosmic Microwave Background*: the EBR at microwave frquencies (see Sec. 2.1.2)

EBL *Extragalactic Background Light*: the EBR in the optical waveband (see Sec. 2.1.4)

EBR *Extragalactic Background Radiation*: all diffuse radiation across the electromagnetic spectrum arising external to our galaxy (see Sec. 2.1)

EGB *Extragalactic Gamma-ray Background*: often used for the EBR at γ-ray energies in general, and in particular above about 30 MeV (see Sec. 2.1.7)

ERB *Extragalactic Radio Background*: the EBR at radio wavelengths (see Sec. 2.1.1)

EUB *Extragalactic Ultraviolet Background* (see Sec. 2.1.5)

EIC *External Invers-Compton process*: leptonic model for the γ-ray emission of blazar jets (see Sec. 2.2.1.2)

FR *Faranoff-Riley radio-galaxy*: morphological classification of radio-galaxies (see Sec. 2.2.1.2)

FSRQ *Flat-Spectrum Radio-Quasar*: a radio-loud AGN type (see Sec. 2.2.1.2)

IGM *InterGalactic Medium*

IR *InfraRed*: the infrared waveband covers the wavelengths from about 1 μm up to about 400 μm (see Sec. 2.1.3)

$M_\odot$: The mass of our sun, often referred to as solar mass, is $M_\odot = 2 \times 10^{33}$ g

NLRG *Narrow-Line Radio-Galaxy*: a radio-loud AGN type (see Sec. 2.2.1.2)

QSO *Quasi-Stellar Object*: synonym for AGN (see Sec. 2.2.1.2)

SRF *Star-Formation Rate* (see Sec. 2.1.3)

SSC *Synchrotron Self-Compton process*: leptonic model for the γ-ray emission of blazar jets (see Sec. 2.2.1.2)

SSRQ *Steep-Spectrum Radio-Quasar*: a radio-loud AGN type (see Sec. 2.2.1.2)

Sy sl Seyfert galaxy: a radio-quiet AGN type (see Sec. 2.2.1.2)

UV *UltraViolet*: the ultraviolet waveband covers the wavelengths from about 3000 Å down to about 10 Å ($\sim$ 120 eV) (see Sec. 2.1.5)

XRB *Extragalactic X-Ray Background*: at X-ray energies (see Sec. 2.1.6)

E.2 Instrumental Acronyms

BATSE: *Burst And Transient Source Experiment*

CGRO: *Compton Gamma-Ray Observatory*

COMPASS: *COMptel Processing and Analysis Software System*

COMPTEL: *COMPton TELescope*

EGRET: *Energetic Gamma-Ray Experiment Telescope*

EHORA: *Earth-HORizon Angle* the angle between the pointing direction of the telescope and the Earth horizon (see e.g. Sec. 4.2.2)

FoV: *Field-of-View* (see Sec. 4.2.1)

GCEL: *GeoCenter ELevation* the angle between the pointing direction and the direction the center of the Earth (see e.g. Sec. 4.2.2)

OP: *Observation Period*

OSSE: *Oriented Scintillation Spectrometer Experiment*

PMT: *Photo-Multiplier Tube*

PSD: *Pulse-Shape Discriminator value* (see Sec. 3.8)

SCV2M: main deadtime-clock count rate of veto dome 2 (see Sec. 3.10)

TJD: *Truncated Julian Day* (see Appendix D)

ToF: *Time-of-Flight* (see Sec. 3.7)

List of Figures

List of Tables

Bibliography

Ait-Ouamer, F., A. Zych, R. S. White 1988, J. Geophys. Res. 93(A4), 2499

Alexander, J. K., *et al.* 1969, Astrophys. J. 157, L163

Allen, A. J. 1981, Mon. Not. R. Astron. Soc. 197, 679

Allen, C. W. 1973, *Astrophysical Quantities* (University of London, The Athlone Press)

Anderson, R. C., *et al.* 1979, Astrophys. J. 234, 415

Anger, H. O. 1958, Rev. Sci. Instrum. 29, 27

Antonucci, R. 1993, Annu. Rev. Astron. Astrophys. 31, 473

Armand, C., B. Milliard, J. M. Deharveng 1994, Astron. Astrophys. 284, 12

Armstrong, T. W., K. C. Chandler, J. Barish 1973, J. Geophys. Res. 78(16), 12

Arnold, J. R., *et al.* 1962, J. Geophys. Res. 67(12), 4878

Beckurts, K. H., K. Wirts 1964, *Neutron Physics* (Springer Verlag New York Inc.)

Bennett, A., C. L.and Kogut, *et al.* 1994, Astrophys. J. 436, 423

Bignami, G. F., *et al.* 1979, Astrophys. J. 232, 649

Blain, A. W., M. S. Longair 1993a, Mon. Not. R. Astron. Soc. 265, L21

Blain, A. W., M. S. Longair 1993b, Mon. Not. R. Astron. Soc. 264, 509

Bloemen, H. 1989, Annu. Rev. Astron. Astrophys. 27, 469

Bloemen, H., *et al.* 1995, Astron. Astrophys. 293, L1

Bloemen, H., *et al.* 1999, in 3^{rd} *INTEGRAL Workshop*, in press

Bloemen, H., A. M. Bykov 1997, in *Proceedings of the Fourth Compton Symposium*, eds. C. D. Dermer, M. S. Strickman, J. D. Kurfess, p. 249 (AIP Conference Proceedings 410)

Blom, J. J. 1997, *COMPTEL high-latitude gamma-ray sources*, Ph.D. thesis, Universiteit van Leiden, the Netherlands

Blom, J. J., *et al.* 1995a, Astron. Astrophys. 295, 330

Blom, J. J., *et al.* 1995b, Astron. Astrophys. 298, L33

Bodemann, E., *et al.* 1993, Nucl. Instrum. Methods Phys. Res., Sect. B 82, 9

Böhm, G. 1984, Master's thesis, Technische Universität München, Germany

Boldt, E. 1987, Phys. Rep. 146, 215

Bond, J. R., B. J. Carr, C. J. Hogan 1986, Astrophys. J. 306, 428

Bond, J. R., B. J. Carr, C. J. Hogan 1991, Astrophys. J. 367, 420

Bondi, H., T. Gold 1948, Mon. Not. R. Astron. Soc. 108, 252

Branch, D., K. Nomoto, A. V. Filippenko 1991, Comments Astrophys. 15(4), 221

Branduardi-Raymont, G., *et al.* 1994, Mon. Not. R. Astron. Soc. 270, 947

Bridle, A. H. 1967, Mon. Not. R. Astron. Soc. 136, 219

Cagnoni, I., R. Della Ceca, T. Maccacaro 1998, Astrophys. J. 493, 54

Chen, A., J. Dwyer, P. Kareet 1996, Astrophys. J. 463, 169

Chen, L.-W., A. C. Fabian, K. C. Gendreau 1997, Mon. Not. R. Astron. Soc. 285, 449

Chi, X., A. W. Wolfendale 1989, J. Phys. G 15, 1509

Chiang, J., *et al.* 1995, Astrophys. J. 452, 156

Chiang, J., R. Mukherjee 1998, Astrophys. J. 496, 752

Chupp, E. L. 1976, *Gamma-Ray Astronomy* (D. Reidel Publishing Company, Dordrecht)

Chupp, E. L., *et al.* 1973, Nature 241, 333

Clayton, D. D., S. A. Colgate, G. J. Fishman 1969, Astrophys. J. 155, 75

Clayton, D. D., J. Silk 1969, Astrophys. J. 158, L43

Clayton, D. D., R. A. Ward 1975, Astrophys. J. 198, 241

Cline, B. C., Y.-T. Gao 1990, Astrophys. J. 348, 33

Cline, D. B., W. Hong 1992, Astrophys. J. 401, L57

Cohen, A. G., A. De Rújula, S. L. Glashow 1998, Astrophys. J. 495, 539

Collmar, W. 1996, in *Proceedings of the Heidelberg Workshop on Gamma-Ray Emitting AGN*, eds. J. G. Kirk, M. Camenzind, C. von Montigny, S. Wagner, p. 9 (MPI H–V37–1996)

Collmar, W. 1999, *Intensities of COMPTEL AGN*, priv. comm.

Collmar, W., *et al.* 1996, Astron. Astrophys. Suppl. Ser. 120(4), C515

Collmar, W., *et al.* 1997a, in *Proceedings of the Fourth Compton Symposium*, eds. C. D. Dermer, M. S. Strickman, J. D. Kurfess, p. 1341 (AIP Conference Proceedings 410)

Collmar, W., *et al.* 1997b, in *Proceedings of the Fourth Compton Symposium*, eds. C. D. Dermer, M. S. Strickman, J. D. Kurfess, p. 1587 (AIP Conference Proceedings 410)

Collmar, W., *et al.* 1999, in *Proceedings of the* 3^{rd} *INTEGRAL workshop*, in press

Comastri, A., *et al.* 1995, Astron. Astrophys. 296, 1

Comastri, A., T. Di Girolamo, G. Setti 1996, Astron. Astrophys. Suppl. Ser. 120(4), C627

Connors, A., *et al.* 1992, in *Data Analysis in Astronomy IV*, eds. V. Di Gesù, L. Scarsi, R. Buccheri, P. Crane, M. C. Maccarone, H. U. Zimmermann, p. 271 (Plenum Press, New York)

Coppi, P. S., F. A. Aharonian 1997, Astrophys. J. 487, L9

Cowie, L. L., *et al.* 1994, Astrophys. J. 434, 114

Cummings, J. R., *et al.* 1993, in *Proc. of the* 23rd *Internat. Conf. on Cosmic Rays, Invited, Rapporteurs & Highlight Papers*, eds. D. A. Leary, R. B. Hicks, D. Venkatessan, p. 475

Daly, R. A. 1988, Astrophys. J. 324, L47

Daniel, R. R., G. Joseph, P. J. Lavakare 1972, Astrophys. Space. Sci. 18, 462

Daniel, R. R., P. J. Lavakare 1975, in *Proc. of the* 14th *Internat. Conf. on Cosmic Rays*, vol. 1, p. 23

Dar, A., N. J. Shaviv 1995, Phys. Rev. Lett. 75(17), 3052

de Boer, H., *et al.* 1992, in *Data Analysis in Astronomy IV*, eds. V. Di Gesù, L. Scarsi, R. Buccheri, P. Crane, M. C. Maccarone, H. U. Zimmermann, p. 241 (Plenum Press, New York)

De Jager, O. C., F. W. Stecker, M. H. Salamon 1994, Nature 369, 294

De Paolis, F., *et al.* 1995, Phys. Rev. Lett. 74(1), 14

De Rújula, A., S. L. Glashow 1980, Phys. Rev. Lett. 45, 942

de Vaucouleurs, G., *et al.* 1976a, *Third Reference Catalogue of Bright Galaxies, Vol. 1* (Springer Verlag)

de Vaucouleurs, G., A. de Vaucouleurs, H. G. Corwin Jr. 1976b, *Second Reference Catalogue of Bright Galaxies* (University of Texas Press)

de Vries, C. P. 1994, in *Astronomical Data Analysis Software and Systems III*, eds. D. R. Crabtree, R. J. Hanisch, J. Barnes, p. 399 (ASP Conference Series, Vol. 61)

de Vries, C. P. 1997, *Comments on the nature of the event parameter PSD*, priv. comm.

den Herder, J. M., *et al.* 1992, in *Data Analysis in Astronomy IV*, eds. V. Di Gesù, L. Scarsi, R. Buccheri, P. Crane, M. C. Maccarone, H. U. Zimmermann, p. 217 (Plenum Press, New York)

Dermer, C. D. 1996, in *Proceedings of the* 2^{nd} *INTEGRAL workshop, 'The transparent universe'*, eds. C. Winkler, T. J.-L. Courvoisier, P. Durouchoux, p. 405 (ESA SP-382)

Dermer, C. D. 1998, *Contribution of misaligned blazars to EGB*, priv. comm.

Dermer, C. D., N. Gehrels 1995, Astrophys. J. 447, 103

Dermer, C. D., S. J. Sturner, R. Schlickeiser 1997, Astrophys. J., Suppl. Ser. 109, 103

Di Cocco, G., *et al.* 1977, Nature 270, 319

Diehl, R., *et al.* 1992, in *Data Analysis in Astronomy IV*, eds. V. Di Gesù, L. Scarsi, R. Buccheri, P. Crane, M. C. Maccarone, H. U. Zimmermann, pp. 201–216 (Plenum Press, New York)

Diehl, R., U. Graser 1981, Nucl. Instrum. Methods Phys. Res. 186, 665

Dixon, D. D., *et al.* 1998, New Astron. 3(7), 539

Dolgov, A. D., J. Silk 1993, Phys. Rev. D 47, 4244

Done, C., A. C. Fabian 1989, Mon. Not. R. Astron. Soc. 240, 81

Dube, R. R., W. C. Wickes, D. T. Wilkinson 1979, Astrophys. J. 232, 333

Dudarewicz, A., A. W. Wolfendale 1990, Mon. Not. R. Astron. Soc. 268, 609

Dwek, E., *et al.* 1998, Astrophys. J. 508, 106

Dwek, E., J. Slavin 1994, Astrophys. J. 436, 696

Dyer, C. S., *et al.* 1994, IEEE Trans. Nucl. Sci. 41(3), 438

Ellis, J., *et al.* 1988, Phys. Lett. B 214(3), 403

Erlykin, A. D., *et al.* 1997a, in *25th Intern. Cosmic Ray Conf.*, eds. M. S. Potgieter, B. C. Raubenheimer, D. J. van der Walt, vol. 3, p. 125

Erlykin, A. D., A. Smialkowski, A. W. Wolfendale 1997b, in *25th Intern. Cosmic Ray Conf.*, eds. M. S. Potgieter, B. C. Raubenheimer, D. J. van der Walt, vol. 3, p. 113

Erlykin, A. D., A. W. Wolfendale 1995, J. Phys. G 21, 1149

Fichtel, C. E., *et al.* 1975, Astrophys. J. 198, 163

Fichtel, C. E., *et al.* 1992, Astrophys. J. 434, 557

Fichtel, C. E., G. A. Simpson, D. J. Thompson 1978, Astrophys. J. 222, 833

Fichtel, C. E., J. I. Trombka 1981, *Gamma Ray Astrophysics* (NASA Goddrad Space Flight Center, NASA SP-453)

Firestone, R. B., *et al.* 1996, *Table of Isotopes* (John Wiley & Sons, Inc.), 8th edn.

Fishman, G. J., *et al.* 1989, in *Proc. of the GRO Science Workshop (Greenbelt: NASA/GSFC*, ed. W. N. Johnson, pp. 2–39

Fixsen, D. J., *et al.* 1994, Astrophys. J. 420, 445

Fixsen, D. J., *et al.* 1996, Astrophys. J. 473, 576

Fixsen, D. J., *et al.* 1997, Astrophys. J. 486, 623

Fixsen, D. J., *et al.* 1998, Astrophys. J. 508, 123

Forrest, D. J. 1989, in *High-energy radiation background in space*, eds. A. Rester, Jr., J. I. Trombka, pp. 243–249 (AIP Conference Proceedings 186)

Fossati, G., *et al.* 1999, Mon. Not. R. Astron. Soc. in press

Fukada, Y., *et al.* 1975, Nature 254, 398

Gao, Y.-T., *et al.* 1990a, Astrophys. J. 361, L37

Gao, Y.-T., D. B. Cline, F. W. Stecker 1990b, Astrophys. J. 357, L1

Geandreau, K. C., *et al.* 1995, Publ. Astron. Soc. Jpn. 47, L5

Gehrels, N. 1997, Nuovo Cimento 112, 11

Gehrels, N., C. Cheung 1996, in Current Perspectives in High Energy Astrophysics", NASA Ref. Pub. 1391, 113

Gehrels, N., E. Chipman, D. Kniffen 1994, Astrophys. J., Suppl. Ser. 92, 351

Georgantopoulos, I., *et al.* 1996, Mon. Not. R. Astron. Soc. 280, 276

Georgii, R., W. Plass 1998, *Gamma-ray spectroscopy of a spare D1 PMT using a Ge-spectrometer*, priv. comm.

Georgii, R., T. Wunderer 1998, *Gamma-ray spectroscopy of a MACOR probe using a Ge-spectrometer*, priv. comm.

Giacconi, R., *et al.* 1962, Phys. Rev. Lett. 9(11), 439

Gnedin, N. Y., J. P. Ostriker 1992, Astrophys. J. 400, 1

Graser, U., V. Schönfelder 1977, J. Geophys. Res. 82(7), 1055

Gregorich, D. T., *et al.* 1995, Astron. Journal 110(1), 259

Griffiths, R. E., P. Padovani 1990, Astrophys. J. 360, 483

Gruber, D. E. 1992, in *The X-Ray Background*, eds. X. Barcons, A. C. Fabian, p. 44 (Cambridge University Press)

Gunn, J. E., B. A. Peterson 1965, Astrophys. J. 142, 1633

Gursky, A., *et al.* 1963, Phys. Rev. Lett. 11, 530

Hacking, P. B., B. T. Soifer 1991, Astrophys. J. 367, L49

Hagedorn, R. 1968, Nuovo Cimento A 56, 1027

Hall, R. D., *et al.* 1976, Astrophys. J. 210, 631

Halzen, F., *et al.* 1991, Nature 353, 807

Harrison, E. R. 1964, Nature 204, 271

Harrison, E. R. 1967, Phys. Rev. Lett. 18(23), 1011

Harrison, E. R. 1968, Phys. Rev. 167, 1170

Harrison, E. R. 1974, Phys. Today 27, 30

Harrison, E. R. 1987, *Darkness at Night: A Riddle of the Universe* (Harvard University Press)

Harrison, E. R. 1990, in *The Galactic and Extragalactic Background Radiation, Proc. of IAU Symp. No. 139*, eds. S. Bowyer, C. Leinert, p. 3 (Kluwer, Dordrecht)

Hartman, R. C., W. Collmar, C. D. von Montigny, C.and Dermer 1997, in *Proceedings of the Fourth Compton Symposium*, eds. C. D. Dermer, M. S. Strickman, J. D. Kurfess, p. 307 (AIP Conference Proceedings 410)

Hasinger, G. 1992, in *The X-Ray Background*, eds. X. Barcons, A. C. Fabian, p. 44 (Cambridge University Press)

Hasinger, G. 1996, Astron. Astrophys. Suppl. Ser. 120, C607

Hasinger, G. 1998, Astron. Nachr. 319, 37

Hasinger, G., *et al.* 1993, Astron. Astrophys. 275, 1

Hasinger, G., *et al.* 1998, Astron. Astrophys. 329, 482

Hauser, M. G. 1995, in *Extragalactic Background Radiation*, eds. D. Calzetti, M. Livio, P. Madau, p. 135 (Cambridge University Press)

Hauser, M. G. 1996, in *Unveiling the cosmic infrared background*, ed. E. Dwek, p. 11 (AIP Conference Proceedings 348)

Hauser, M. G., *et al.* 1998, Astrophys. J. 508, 25

Hawking, S. W. 1974, Nature 248, 30

Henry, R. C., J. Murthy 1995, in *Extragalactic Background Radiation*, eds. D. Calzetti, M. Livio, P. Madau, p. 51 (Cambridge University Press)

Herschel, J. F. W. 1848, Edinburgh Review 87, 170

Hogan, C. J., M. J. Rees 1979, Mon. Not. R. Astron. Soc. 188, 791

Holberg, J. B. 1986, Astrophys. J. 311, 969

Hoyle, F., A. Fowler 1973, Nature 241, 384

Hunter, S. D., *et al.* 1997a, Astrophys. J. 481, 205

Hunter, S. D., R. L. Kinzer, A. W. Strong 1997b, in *Proceedings of the Fourth Compton Symposium*, eds. C. D. Dermer, M. S. Strickman, J. D. Kurfess, p. 192 (AIP Conference Proceedings 410)

Jakobsen, P. 1995, in *Extragalactic Background Radiation*, eds. D. Calzetti, M. Livio, P. Madau, p. 75 (Cambridge University Press)

Jean, P. 1997, *Results of thin-target simulations of neutrons and protons incident on elements present in the D1 detector*, priv. comm.

Johnson, W. N., *et al.* 1993, Astrophys. J., Suppl. Ser. 86, 693

Johnson, W. N., *et al.* 1997, in *Proceedings of the Fourth Compton Symposium*, eds. C. D. Dermer, M. S. Strickman, J. D. Kurfess, p. 283 (AIP Conference Proceedings 410)

Kalberla, P. M. W., *et al.* 1998, Astron. Astrophys. 332, L61

Kamionkowski, M. 1995, in *The Gamma Ray Sky with CGRO and SIGMA*, eds. M. Signore, P. Salati, G. Vedrenne, p. 113 (Dordrecht, Kluwer Academic Publishers)

Kanbach, G. 1998a, *Geometrical dimensions of EGRET spark chamber*, priv. comm.

Kanbach, G. 1998b, *Instrumental Background of COS B*, priv. comm.

Kanbach, G., C. Reppin, V. Schönfelder 1974, J. Geophys. Res. 79(34), 5159

Kappadath, S. C. 1994, *An analysis of telescope event types and their contribution to the PSF*, Internal Report COM-RP-UNH-DRG-025, UNH, UNH, NH, USA

Kappadath, S. C. 1998, *Measurement of the Cosmic Diffuse Gamma-Ray Spectrum from 800 keV to 30 MeV*, Ph.D. thesis, University of New Hampshire, NH, USA

Kappadath, S. C., *et al.* 1995, in *Proc. of the* $24^{\rm rd}$ *Internat. Conf. on Cosmic Rays*, eds. N. Iucci, E. Lamanna, vol. 2, p. 230

Kappadath, S. C., *et al.* 1996, Astron. Astrophys. Suppl. Ser. 120(4), C619

Kappadath, S. C., *et al.* 1997, in *Proceedings of the Fourth Compton Symposium*, eds. C. D. Dermer, M. S. Strickman, J. D. Kurfess, p. 1218 (AIP Conference Proceedings 410)

Kashlinsky, A., J. C. Mather, S. Odenwald 1996, Astrophys. J. 473, L9

Kazanas, D., E. Pearlman 1997, Astrophys. J. 476, 7

Kazanas, D., R. J. Protheroe 1983, Nature 302, 228

Kellermann, K. I., *et al.* 1989, Astron. J. 98, 1195

Kimble, R., S. Bowyer, P. Jakobsen 1981, Phys. Rev. Lett. 46, 80

Kinzer, R. L., *et al.* 1997, Astrophys. J. 475, 361

Kippen, R. M. 1991, *Monte Carlo Simulation of the COMPTEL Gamma Ray Telescope*, Master's thesis, University of New Hampshire, NH, USA

Kippen, R. M. 1996, *Revised COMPTEL SIM Mass Model Description*, Internal Report COM-RP-UNH-SIM-047 Version 2, UNH, UNH, NH, USA

Klecker, B. 1996, Adv. Space Res. 17(2), 37

Kraushaar, W. L., *et al.* 1965, Astrophys. J. 141(3), 845

Kraushaar, W. L., *et al.* 1972, Astrophys. J. 177, 341

Kraushaar, W. L., G. W. Clark 1962, Phys. Rev. Lett. 8(3), 106

Krennrich, F., *et al.* 1997, Astrophys. J. 481, 758

Kurfess, J. D., *et al.* 1989, in *High-energy radiation background in space*, eds. A. Rester, Jr., J. I. Trombka, pp. 250–258 (AIP Conference Proceedings 186)

Lamla, E. 1965, in *Landolt-Börnstein Series*, ed. H. H. Voigt, vol. VI/1, p. p. 317 ff. (Springer Verlag, Berlin)

Leinert, C., *et al.* 1998, Astron. Astrophys. Suppl. Ser. 127, 1

Leising, M. D., G. H. Share 1990, Astrophys. J. 357, 638

Leventhal, M. D. 1973, Nature 246, 136

Lichti, G. 1987, *Veto-Dome Test Results*, Internal Report COM-RP-MPE-K38-29, MPE, MPE, Garching, Germany

Lichti, G. 1988, *Veto-Dome Test Results after Redesign*, Internal Report COM-RP-MPE-K38-46, MPE, MPE, Garching, Germany

Lichti, G. 1998, *Properties of COMPTEL veto domes and veto system*, priv. comm.

Lichti, G. G., G. F. Bignami, J. A. Paul 1978, Astrophys. Space. Sci. 56, 403

Lineweaver, C. H., *et al.* 1996, Astrophys. J. 470, 38

Lockman, F. J., K. Jahoda, D. McCammon 1986, Astrophys. J. 302, 432

Lockwood, J. A., *et al.* 1981, Astrophys. J. 248, 1194

Lockwood, J. A., S. O. Ifedili, R. W. Jenkins 1973, J. Geophys. Res. 78(34), 7978

Longair, M. S. 1992, *High Energy Astrophysics, Vol. 1* (Cambridge University Press), 2nd edn.

Longair, M. S. 1994a, *High Energy Astrophysics, Vol. 2* (Cambridge University Press), 2nd edn.

Longair, M. S. 1994b, in *The Deep Universe*, eds. B. Binggeli, R. Buser, p. 317 ff. (Saas Fee Advanced Course 23, Lecture Notes 1993, Swiss Society for Astrophysics and Astronomy, Springer)

Longair, M. S. 1995, in *Extragalactic Background Radiation*, eds. D. Calzetti, M. Livio, P. Madau, p. 223 (Cambridge University Press)

Lonsdale, C. J. 1995, in *Extragalactic Background Radiation*, eds. D. Calzetti, M. Livio, P. Madau, p. 145 (Cambridge University Press)

Loys de Chéseaux, J.-P. 1744, *Traité de Comète* (Lausanne, M. M. Bousequet)

Lubin, P. M. 1995, in *Extragalactic Background Radiation*, eds. D. Calzetti, M. Livio, P. Madau, p. 191 (Cambridge University Press)

MacGibbon, J. H., B. J. Carr 1991, Astrophys. J. 371, 447

Macri, J. 1996, *Comments on the veto deadtime meter*, priv. comm.

Macri, J. 1997a, *Electronic characteristic of PSD value*, priv. comm.

Macri, J. 1997b, *In-flight sensitivity level of veto system*, priv. comm.

Macri, J. 1997c, *Observed laboratory dark-count rate of veto-dome PMTs*, priv. comm.

Madau, P., G. Ghisellini, A. C. Fabian 1993, Astrophys. J. 410, L7

Marshall, F. E., *et al.* 1980, Astrophys. J. 235, 4

Martin, C., S. Bowyer 1989, Astrophys. J. 338, 677

Mather, J. C. 1995, in *Extragalactic Background Radiation*, eds. D. Calzetti, M. Livio, P. Madau, p. 169 (Cambridge University Press)

Mather, J. C., *et al.* 1994, Astrophys. J. 420, 439

Matsumoto, T. 1990, in *The Galactic and Extragalactic Background Radiation, Proc. of IAU Symp. No. 139*, eds. S. Bowyer, C. Leinert, p. 317 (Kluwer, Dordrecht)

Mattila, K. 1990, in *The Galactic and Extragalactic Background Radiation, Proc. of IAU Symp. No. 139*, eds. S. Bowyer, C. Leinert, p. 257 (Kluwer, Dordrecht)

Mattox, J. R., *et al.* 1997, Astrophys. J. 481, 95

Matz, S. M., *et al.* 1988, Nature 331, 416

Mazets, E. P., *et al.* 1975, apss 33, 347

McConnell, M., *et al.* 1997, in *Proceedings of the Fourth Compton Symposium*, eds. C. D. Dermer, M. S. Strickman, J. D. Kurfess, p. 1099 (AIP Conference Proceedings 410)

McNaron-Brown, K., *et al.* 1995, Astrophys. J. 451, 575

McVittie, G. L., S. P. Wyatt 1959, Astrophys. J. 130, 1

Metzger, A. E., *et al.* 1964, nat 204, 766

Michel, R., *et al.* 1995, Nucl. Instrum. Methods Phys. Res., Sect. B 103, 183

Mihalas, D., J. Binney 1981, *Galactic Astronomy* (W. H. Freeman and Company), 2nd edn.

Minkowski, R. 1941, Publ. Astron. Soc. Pac. 53, 224

Miyaji, T., *et al.* 1998, Astron. Astrophys. 334, L13

Morgan, I., S. P. Driver 1995, in *Extragalactic Background Radiation*, eds. D. Calzetti, M. Livio, P. Madau, p. 285 (Cambridge University Press)

Morris, D. J. 1996a, *Neutron singles measurements: solar modulation and neutron-induced background*, Internal Report COM-RP-UNH-F70-056, UNH, Durham, NH, USA

Morris, D. J. 1996b, *Parametrization of COMPTEL background energy spectra at 720–2600 keV by spectral fitting*, Internal Report COM-RP-UNH-DRG-046, UNH, Durham, NH, USA

Morris, D. J., *et al.* 1995, J. Geophys. Res. 100(A7), 12243

Morris, D. J., *et al.* 1997, in *1997 Conference on the High Energy Background in Space*, eds. J. I. Trombka, J. S. Schweitzer, G. P. Lasche, vol. IEEE catalog 97TH8346, p. 26, Institute of Electrical and Electronic Engineers

Morrison, P. 1958, Nuovo Cimento 7, 858

Much, R. P. 1994, *Analyse der COMPTEL Eichdaten und Anwendung der Ergebnisse auf die Messdaten vom Krebsnebel*, Ph.D. thesis, Technische Universität München, Germany

Mücke, A., *et al.* 1996, Astron. Astrophys. Suppl. Ser. 120(4), C541

Mücke, A., M. Pohl 1999, Mon. Not. R. Astron. Soc. submitted

Murdoch, H. S., *et al.* 1986, Astrophys. J. 309, 19

Mushotzky, R. F. 1984, Adv. Space Res. 3(10-12), 157

Newkirk, L. L. 1963, J. Geophys. Res. 68(7), 1825

Niemeyer, J. C., W. Hillebrandt, S. E. Woosley 1996, Astrophys. J. 471, 903

Oberlack, U. 1997, *Über die Natur der galaktischen ^{26}Al-Quellen - Untersuchung des 1,8-MeV-Himmels mit COMPTEL*, Ph.D. thesis, Technische Universität München, Germany

Oberlack, U., M. Varendorff, G. Weidenspointner 1996, *A new strong component in the COMPTEL background: build-up of ^{22}Na*, Internal Report COM-RP-MPE-DRG-166, MPE, MPE, Garching, Germany

Olbers, H. W. M. 1823, in *Astronomisches Jahrbuch für das Jahr 1826*, ed. J. E. Bodr (Späten, Berlin)

Omnès, R. 1969, Phys. Rev. Lett. 23(1), 38

Omnès, R. 1970, Phys. Rep. C 3, 1

Padovani, P., *et al.* 1993, Mon. Not. R. Astron. Soc. 260, L21

Page, D. N., S. W. Hawking 1976, Astrophys. J. 206, 1

Paresce, F., P. Jakobsen 1980, Nature 288, 119

Paresce, F., C. F. McKee, S. Bowyer 1980, Astrophys. J. 240, 347

Patridge, R. B., P. J. E. Peebles 1967, Astrophys. J. 148, 377

Peacock, J. A. 1995, in *Extragalactic Background Radiation*, eds. D. Calzetti, M. Livio, P. Madau, p. 237 (Cambridge University Press)

Penzias, A. A., R. W. Wilson 1965, Astrophys. J. 142, 419

Perotti, F., *et al.* 1981, Nature 292, 133

Pietz, J., *et al.* 1998, Astron. Astrophys. 332, 55

Plüschke, S. 1998, *Results of instrumental line fits as a function of time*, priv. comm.

Poe, E. A. 1848, *Eureka: A Prose Poem* (Putnam, New York)

Pohl, M., *et al.* 1997, Astrophys. J. 491, 159

Porter, N. A., T. C. Weekes 1977, Astrophys. J. 212, 224

Pozzetti, L., *et al.* 1998, Mon. Not. R. Astron. Soc. 298(4), 1133

Prantzos, N., O. Aubert 1995, Astron. Astrophys. 302, 69

Press, W. H., P. Schechter 1974, Astrophys. J. 187, 425

Preszler, A. M., S. Moon, R. S. White 1976, J. Geophys. Res. 81(25), 4715

Puget, J.-L., *et al.* 1996, Astron. Astrophys. 308, L5

Purton, C. R. 1966, Mon. Not. R. Astron. Soc. 133, 463

Ramana Murthy, P. V., A. W. Wolfendale 1993, *Gamma Ray Astronomy* (Cambridge University Press)

Rank, G. 1996, *Gamma-Stralung und Neutronen der solaren Flares am 11. und 15. Juni 1991 gemessen mit COMPTEL*, Ph.D. thesis, Technische Universität München, Germany

Rees, M. 1966, Nature 211, 468

Robson, I. 1996, *Active Galactic Nuclei* (John Wiley & Sons)

Rudaz, S., F. W. Stecker 1988, Astrophys. J. 325, 16

Ryan, J. M., *et al.* 1979, J. Geophys. Res. 84(A8), 5279

Ryan, J. M., *et al.* 1997, in *1997 Conference on the High Energy Background in Space*, eds. J. I. Trombka, J. S. Schweitzer, G. P. Lasche, vol. IEEE catalog 97TH8346, p. 13, Institute of Electrical and Electronic Engineers

Salamon, M. H., F. W. Stecker 1994, Astrophys. J. 430, L21

Salamon, M. H., F. W. Stecker 1998, Astrophys. J. 493, 547

Schiekel, T., *et al.* 1996, Nucl. Instrum. Methods Phys. Res., Sect. B 114, 91

Schmidt, M., *et al.* 1998, Astron. Astrophys. 329, 495

Schönfelder, V., *et al.* 1993, Astrophys. J., Suppl. Ser. 86, 657

Schönfelder, V., F. Graml, F.-P. Penningsfeld 1980, Astrophys. J. 240, 350

Schönfelder, V., U. Graser, J. Daugherty 1977, Astrophys. J. 217, 306

Schönfelder, V., A. Hirner, K. Schneider 1973, Nucl. Instrum. Methods Phys. Res. 107, 385

Schönfelder, V., G. Lichti 1974, Astrophys. J. 191, L1

Selesnik, R. S., *et al.* 1995, J. Geophys. Res. 100(A6), 9503

Setti, G., L. Woltjer 1994, Astrophys. J., Suppl. Ser. 92, 629

Shafer, R. A. 1983, Ph.D. thesis, University of Maryland, MD, USA

Share, G. H., R. L. Kinzer, M. S. Strickman 1989, in *High-energy radiation background in space*, eds. A. Rester, Jr., J. I. Trombka, pp. 266–277 (AIP Conference Proceedings 186)

Shectman, S. A. 1974, Astrophys. J. 188, 233

Sherman, R. D., J. Silk 1979, Astrophys. J. 231, L61

Silk, J., M. Srednicki 1984, Phys. Rev. Lett. 3(6), 624

Simon, A. J. B. 1977, Mon. Not. R. Astron. Soc. 180, 429

Smart, D. F., M. A. Shea 1994, Adv. Space Res. 14(10), 787

Smoot, G. F., *et al.* 1992, Astrophys. J. 396, L1

Snelling, M., K. Bennett, J. Clear 1986, Nucl. Instrum. Methods Phys. Res., Sect. A 248, 545

Soltan, A. M., J. Juchniewicz 1999, in *Proceedings of the* 3^{rd} *INTEGRAL workshop*, in press

Srednicki, M., S. Theisen, J. Silk 1986, Phys. Rev. Lett. 56(3), 263

Sreekumar, P., *et al.* 1992, Astrophys. J. 400, L67

Sreekumar, P., *et al.* 1993, Phys. Rev. Lett. 70(2), 127

Sreekumar, P., *et al.* 1998, Astrophys. J. 494, 523

Sreekumar, P., F. W. Stecker, S. C. Kappadath 1997, in *Proceedings of the Fourth Compton Symposium*, eds. C. D. Dermer, M. S. Strickman, J. D. Kurfess, p. 344 (AIP Conference Proceedings 410)

Stacy, J. G. 1995, *An Introductory Guide to COMPASS*, Internal Report COM-RP-UNH-DRG-037, UNH, Durham, NH, USA

Stacy, J. G., *et al.* 1996, Astron. Astrophys. Suppl. Ser. 120(4), C691

Stassinopoulos, E. G. 1989, in *High-energy radiation background in space*, eds. A. Rester, Jr., J. I. Trombka, pp. 3–63 (AIP Conference Proceedings 186)

Stecker, F. W. 1971, in Cosmic Gamma Rays", NASA SP-249 (US Govt. Printing Office, Washington, DC)

Stecker, F. W. 1985, Nucl. Phys. B, Part. Phys. 252, 25

Stecker, F. W. 1989, in *Proceedings of Gamma Ray Observatory Science Workshop*, ed. W. N. Johnson, pp. 4–73

Stecker, F. W., O. C. De Jager, M. H. Salamon 1992, Astrophys. J. 390, L49

Stecker, F. W., D. L. J. Morgan, J. Bredekamp 1971, Phys. Rev. Lett. 27(21), 1469

Stecker, F. W., J. L. Puget 1972, Astrophys. J. 178, 57

Stecker, F. W., M. H. Salamon 1996a, Phys. Rev. Lett. 76(20), 3878

Stecker, F. W., M. H. Salamon 1996b, Astrophys. J. 464, 600

Stecker, F. W., M. H. Salamon, M. A. Malkan 1993, Astrophys. J. 410, L71

Steigman, G. 1976, Annu. Rev. Astron. Astrophys. 14, 339

Steinle, H., *et al.* 1998, Astron. Astrophys. 330, 97

Størmer, C. 1955, *The Polar Aurora* (Calendon Press)

Strong, A. W. 1983, in 18^{th} *Intern. Cosmic Ray Conf.*, vol. 9, p. 90

Strong, A. W. 1984, Adv. Space Res. 3, 87

Strong, A. W. 1996, Space Sci. Rev. 76, 205

Strong, A. W. 1999, *Estimates on the average intensity of the diffuse galactic emission beased on the GALPROP model*, priv. comm.

Strong, A. W., *et al.* 1996, Astrophys. J., Suppl. Ser. 76(4), 205

Strong, A. W., I. V. Moskalenko 1998, Astrophys. J. 509, 212

Strong, A. W., I. V. Moskalenko, O. Reimer 1999, Astrophys. J. submitted

Strong, A. W., A. W. Wolfendale, J. Wdowczyk 1973, Nature 241, 109

Strong, A. W., A. W. Wolfendale, D. M. Worrall 1976, Mon. Not. R. Astron. Soc. 175, 23P

Strong, A. W., G. Youssefi 1995, in *24th Intern. Cosmic Ray Conf.*, vol. 3, p. 48

Sunyaev, R. A., Y. B. Zel'dovich 1980, Annu. Rev. Astron. Astrophys. 18, 537

Swanenburg, B. N. 1997, *Comments on the veto deadtime meter*, priv. comm.

Swanenburg, B. N., *et al.* 1978, Nature 275, 298

Tammann, G. A., W. Löffler, A. Schröder 1994, Astrophys. J., Suppl. Ser. 92, 487

Tennyson, P. D., *et al.* 1988, Astrophys. J. 330, 435

The, L.-S., M. D. Leising, D. D. Clayton 1993, Astrophys. J. 403, 32

Thielemann, F.-K., K. Nomoto, M. Hashimoto 1996, Astrophys. J. 460, 408

Thompson, D. J., *et al.* 1993, Astrophys. J., Suppl. Ser. 86, 629

Thompson, D. J., C. E. Fichtel 1982, Astron. Astrophys. 109, 352

Thompson, D. J., G. A. Simpson 1981, J. Geophys. Res. 86(A3), 1265

Thomson, W. 1901, Phil. Mag. 6(2), 161

Timmes, F.-X., S. E. Woosley, T. A. Weaver 1995, Astrophys. J., Suppl. Ser. 98, 617

Toller, G. N. 1983, Astrophys. J. 266, L79

Toller, G. N. 1990, in *The Galactic and Extragalactic Background Radiation, Proc. of IAU Symp. No. 139*, eds. S. Bowyer, C. Leinert, p. 21 (Kluwer, Dordrecht)

Trombka, J. I., *et al.* 1977, Astrophys. J. 212, 925

Tyson, J. A. 1995, in *Extragalactic Background Radiation*, eds. D. Calzetti, M. Livio, P. Madau, p. 103 (Cambridge University Press)

Unsöld, A., B. Baschek 1988, *Der neue Kosmos* (Springer), 4th edn.

Urry, C. M., P. Padovani 1995, Publ. Astron. Soc. Pac. 107(715), 803

van den Berg, S., G. A. Tammann 1991, Annu. Rev. Astron. Astrophys. 29, 363

van Dijk, R. 1994, *Potassium's Myths and Truth: PMT?*, Internal Report COM-RP-ROL-DRG-60, ROL, MPE, Leiden, The Netherlands

van Dijk, R. 1996, *Gamma-ray observations of X-ray binaries with COMPTEL*, Ph.D. thesis, Universiteit van Amsterdam, the Netherlands

van Dijk, R. 1997, *Comment on possible D2-sub-minitelescope dependence of ToF*, priv. comm.

Varendorff, M., *et al.* 1996, Astron. Astrophys. Suppl. Ser. 120(4), C699

Varendorff, M., *et al.* 1997, in *Proceedings of the Fourth Compton Symposium*, eds. C. D. Dermer, M. S. Strickman, J. D. Kurfess, p. 1577 (AIP Conference Proceedings 410)

Varendorff, M., G. Weidenspointner 1995, *Study of the Na-24 cascade*, Internal Report COM-RP-MPE-DRG-156. Issue 1, MPE, MPE, Garching, Germany

Vedrenne, G., *et al.* 1971, Astron. Astrophys. 15, 50

Vette, J. I., *et al.* 1970, Astrophys. J. 160, L161

Wall, J. V. 1990, in *The Galactic and Extragalactic Background Radiation, Proc. of IAU Symp. No. 139*, eds. S. Bowyer, C. Leinert, p. 327 (Kluwer, Dordrecht)

Watanabe, K. 1996, *Measurement of the Diffuse Gamma-Ray Background with solar maximum mission*, Ph.D. thesis, Clemson University, USA

Watanabe, K., *et al.* 1996, Bull. Am. Astron. Soc. 28(4), 28.02

Watanabe, K., *et al.* 1997, in *Proceedings of the Fourth Compton Symposium*, eds. C. D. Dermer, M. S. Strickman, J. D. Kurfess, p. 1223 (AIP Conference Proceedings 410)

Watanabe, K., *et al.* 1999, Astrophys. J. in press

Watts, J. W., T. A. Parnell, H. H. Heckman 1989, in *High-energy radiation background in space*, eds. A. Rester, Jr., J. I. Trombka, pp. 75–85 (AIP Conference Proceedings 186)

Wdowczyk, J., A. W. Wolfendale 1990, Astrophys. J. 349, 35

Weedman, D. W. 1986, *Quasar astronomy* (Cambrigde Astrophysics Series)

Weekes, T. C., *et al.* 1997, in *Proceedings of the Fourth Compton Symposium*, eds. C. D. Dermer, M. S. Strickman, J. D. Kurfess, p. 361 (AIP Conference Proceedings 410)

Wehrle, E. A., *et al.* 1997, in *Proceedings of the Fourth Compton Symposium*, eds. C. D. Dermer, M. S. Strickman, J. D. Kurfess, p. 1417 (AIP Conference Proceedings 410)

Weidenspointner, G. 1994, *Die Natur der 2.2 MeV Linie des Compton-Telescops COMPTEL*, Master's thesis, Technische Universität München, Germany

Weidenspointner, G. 1995a, *The dependence of the background lines on geophysical parameters*, Internal Report COM-RP-MPE-DRG-154, MPE, MPE, Garching, Germany

Weidenspointner, G. 1995b, *Minitelescope Livetime versus Composite Livetime*, Internal Report COM-RP-MPE-DRG-151, MPE, MPE, Garching, Germany

Weidenspointner, G. 1996a, *D1 PMT ^{40}K Simulations: Algorithm and first Results*, Internal Report COM-RP-MPE-SIM-2, MPE, MPE, Garching, Germany

Weidenspointner, G. 1996b, *Options for Rigidity Extrapolation*, Internal Report COM-RP-MPE-DRG-167, MPE, MPE, Garching, Germany

Weidenspointner, G. 1997, *The simulattion of ^{55}Co and ^{56}Co produced in the D1 detector*, Internal Report COM-RP-MPE-SIM-5, MPE, MPE, Garching, Germany

Weidenspointner, G., *et al.* 1996a, Astron. Astrophys. Suppl. Ser. 120(4), C631

Weidenspointner, G., *et al.* 1996b, *M-IDT-10025 The "^{40}K Mass Model"*, Internal Report COM-RP-MPE-SIM-1, MPE, MPE, Garching, Germany

Weidenspointner, G., *et al.* 1999, in *3^{rd} INTEGRAL Workshop*, in press

Weidenspointner, G., M. Varendorff 1996a, *Studying the ToF Spectrum as a Function of Energy Part 1: the Forward Peak Region*, Internal Report COM-RP-MPE-DRG-165, MPE, MPE, Garching, Germany

Weidenspointner, G., M. Varendorff 1996b, *Studying the ToF Spectrum as a Function of Energy Part 2: the Forward Peak Region*, Internal Report COM-RP-MPE-DRG-171, MPE, MPE, Garching, Germany

Weidenspointner, G., M. Varendorff 1997, *Status of Spectral CDG Analysis: Algorithm and Results*, Internal Report COM-RP-MPE-DRG-172, MPE, MPE, Garching, Germany

Weidenspointner, G., M. Varendorff, W. Collmar 1997a, *Correcting the Correction of the Correction ... ToF & PSD*, Internal Report COM-RP-MPE-DRG-174, MPE, MPE, Garching, Germany

Weidenspointner, G., M. Varendorff, W. Collmar 1997b, *Studying the ToF Spectrum as a Function of Energy Part 2: the Forward Peak Region above 4.3 MeV*, Internal Report COM-RP-MPE-DRG-175, MPE, MPE, Garching, Germany

Weinberg, S. 1972, *Gravitation and Cosmology* (John Wiley & Sons)

Weinberg, S. 1977, *The first three minutes* (Basic Books)

Wesson, P. S. 1991, Astrophys. J. 367, 399

Wesson, P. S., K. Valle, R. Stabell 1987, Astrophys. J. 317, 601

Wheeler, J. C., D. A. Swartz 1994, Space Sci. Rev. 66, 425

White, R. S., *et al.* 1977, Astrophys. J. 218, 920

Williams, R. E., *et al.* 1996, Astron. Journal 112(4), 1335

Willis, T. D. 1996, Ph.D. thesis, Stanford University, CA, USA

Withrow, G. J., B. D. Yallop 1965, Mon. Not. R. Astron. Soc. 130, 31

Woosley, S. E. 1997, Astrophys. J. 476, 801

Wright, E. L., *et al.* 1994a, Astrophys. J. 420, 450

Wright, E. L., *et al.* 1994b, Astrophys. J. 396, L13

Zamorani, G. 1995, in *Extragalactic Background Radiation*, eds. D. Calzetti, M. Livio, P. Madau, p. 237 (Cambridge University Press)

Zdziarski, A. A. 1996, Mon. Not. R. Astron. Soc. 281, L9

Zdziarski, A. A., *et al.* 1993, Astrophys. J. 405, 125

Zdziarski, A. A., *et al.* 1995, Astrophys. J. 483, L63

Zdziarski, A. A., P. T. Zycki 1993, Astrophys. J. 414, L81

Zel'dovich, Y. B. 1984, Sov. Sci. Rev. E Astrophys. Space Phys. 3, 1

Acknowledgements/Danksagung

Zum Gelingen dieser Arbeit, die im Rahmen der internationalen COMPTEL-Kollaboration durchgeführt wurde, haben viele Personen, direkt oder indirekt, durch Diskussionen, Ratschläge und Anregungen beigetragen. Ihnen allen will ich an dieser Stelle ein herzliches „Dankeschön“ sagen.

Besonders bedanken möchte ich mich zunächst bei Herrn Prof. Volker Schönfelder. Er gab mir die Möglichkeit, in der Gamma-Astronomie-Gruppe am Max-Planck-Institut für extraterrestrische Physik zu promovieren. Seine kritischen und konstruktiven Kommentare haben den Verlauf meiner Arbeit wesentlich beeinflußt.

Den größten Anteil am Gelingen dieser Dissertation hat ohne Zweifel mein Betreuer Herr Dr. Martin Varendorff. Er war ein stets aufgeschlossener, freundlicher und auch konstruktiv-kritischer Ratgeber, der sich darüberhinaus nicht davor gescheut hat, meine/unsere Arbeit bei den teils kontroversen Team-Meetings nach bestem Wissen und Gewissen mit dem gebührenden Nachdruck zu verteidigen. Neben unserer wissenschaftlichen Zusammenarbeit verbinden mich auch viele private Erlebnisse mit ihm und seiner Frau Hedda — sowohl in unserem zweiten Zuhause Neu-England als auch in der bayrischen Heimat. Ein einfaches „Danke“ wäre zuwenig, und so danke ich beiden mit einem herzlichen „Vergelt's Gott“.

Von den Mitgliedern der COMPTEL-Gruppe am MPE dürfte der Abschluß dieser Arbeit vor allem für Herrn Dr. Giselher Lichti eine willkommene Zäsur sein. Sein Wissen um die instrumentellen Eigenschaften des Teleskops und den Verbleib längst vergilbter Dokumentation war von unschätzbarem Wert für mich. Nach eigenem Bekunden kann er COMPTEL nun getrost vergessen. Ebenso erleichtert dürfte die „Gummibärchen-Connection“ sein, bestehend aus Herrn Dr. Thomas van Sant und Frau Doina Rehm, die mir die Reprozessierung und Verteilung einiger Datensatz-Typen zu verdanken haben. Außerdem gebührt Herrn Dr. van Sant mein Dank für die geduldige Korrektur meiner sprachlichen Unzulänglichkeiten. Bei Herrn Dr. Roland Diehl möchte ich mich vor allem für seinen ausgleichenden Einfluß und Beistand während diverser „trans-atlantischer Spannungen“ bedanken.

Unter meinen ehemaligen Mit-Doktoranden in der COMPTEL-Kollaboration möchte ich mich vor allem bei Herrn Dr. Gerhard Rank für viele hilfreiche Diskussionen und Anregungen bedanken, wie auch, unter anderem, für einen „coolen“ Aufenthalt auf Mt. Desert Island. Herr Dr. Uwe Oberlack war nicht nur eine stets willkommene Anspielstation im offensiven Mittelfeld unserer MPE-Fußballmannschaft, sondern vor allem einer der wenigen wirklichen Mit-Streiter im Ringen um ein Verständnis des intrumentellen Hintergrunds. Letzteres gilt auch für Herrn Dr. Rob „ToF“ van Dijk, einer

anerkannten COMPTEL-Autorität, dem ich für viele Einsichten und Anregungen und eine wirkliche Zusammenarbeit danke.

Without the interaction with Prof. Jim Ryan and Dr. Cheenu Kappadath my COMPTEL-years would have been much less of an experience. I also thank Dr. Dan Morris for his background work and many stimulating discussions, as well as John Macri for his patience and willingness to share his instrumental insight.

Den Langzeit-Rekord von Herrn Dr. Jakob Englhauser, Fels in der MPE-Abwehr, habe ich ebensowenig erreicht wie seine unvergleichliche und unverzichtbare PostScript-Expertise. Ebenfalls ungefährdet blieb der Seiten-Rekord von Herrn Dr. Konrad Dennerl, der für mich ultimativen Instanz in Fragen graphischer Gestaltung und moderner Camping-Ausrüstung.

Eine Analyse von COMPTEL-Daten ist ohne erheblichen Einsatz des Computers undenkbar. Deshalb bin ich dem COMPASS-Magier „Sir“ Mike Johnson, der routinemäßig Unmögliches möglich gemacht hat, zu größtem Dank verpflichtet. Nach seinem Weggang vom MPE war es nicht nur für mich ein Glücksfall, daß in Frau Beatriz Sanchez eine würdige Nachfolgerin gefunden werden konnte.

I'm deeply indebted to Miles Davis, Jimi Hendrix, Townes van Zandt, and many others too numerous to mention, for unwavering support and consolation during times when I felt *Kind of Blue*, *Manic Depression* or simply *High, Low and in Between* ...

Danken möchte ich auch Wolfgang Schmid und Christoph Sperger für viele gemeinsame Unternehmungen in Fels, Schnee und Eis, die es mir immer wieder ermöglichten wenige bis einige tausend Meter über den Isar-Niederungen zu stehen.

Leider läßt es sich, vor allem gegen das Ende einer Dissertation, nicht vermeiden, daß gerade die Menschen, die einem besonders nahe stehen, am meisten in Mitleidenschaft gezogen werden. Dies gilt zum einen für meine Familie, in der jede der vier Generationen, vom Basteln glücksbringender Kleeblätter bis zur unbegrenzten Versorgung mit „Knedln“, ihr Möglichstes zu meiner Aufmunterung und nicht nur moralischen Unterstützung getan hat. Ihnen allen, und besonders meinen Eltern, ein herzliches „Vergelt's Gott“. Vor allem aber gilt dies für meine bessere Hälfte Tanja Freyberg. Ich danke ihr für ihre unerschütterliche Zuversicht und für das Licht, das sie immer wieder in meinen grauen Alltag bringen konnte.